

# Mucin layer behaviour and its role in dental tribology

Pravin Alexander Smart

SID: 200697976

Submitted in accordance with the requirements for the degree of

Doctor of Philosophy in Integrated Tribology

The University of Leeds

Centre for Doctoral Training in Integrated Tribology

Institute of Functional Surfaces

School of Mechanical Engineering

March 2022

The candidate confirms that the work submitted is his own, except where work which has formed part of jointly-authored publications has been included. The contribution of the candidate and the other authors to this work has been explicitly indicated below. The candidate confirms that appropriate credit has been given within the thesis where reference has been made to the work of others.

- The publication *“Tribocorrosion of dental tissues: The role of mucin. Tribology International, vol 148, pp. 1-8”* was jointly-authored by Pravin Smart, Anne Neville and Michael Bryant. Pravin smart contributed to the conceptualisation, methodology, investigation, formal analysis, visualisation and writing - original draft writing. Anne Neville contributed to the conceptualisation, methodology, supervision and writing – review & editing. Michael Bryant contributed to the conceptualisation, methodology, supervision and writing – review & editing.
- The publication *“Stable oral lubrication enhancer obtained from thiolated polyethylene glycol and mucin, Friction (pending review)”* was jointly-authored by Xiaoyan He, Pravin Smart, Mohamad Taufiqurrakhman, Chun Wang and Michael Bryant. Xiaoyan He contributed to the conceptualisation, methodology, investigation, formal analysis, investigation and writing – original draft. Pravin smart contributed to the conceptualisation, methodology, supervision and writing – reviewing & editing. Mohamad Taufiqurrakhman and Chun Wang contributed to the methodology and formal analysis. Michael Bryant contributed to the conceptualisation, methodology, supervision and writing – review & editing.
- The publication *“Protection of dental materials: mucin layer growth kinetics & properties and their influence on lubrication, Biotribology”* (Pending revisions) was jointly-authored by Pravin Smart, Anne Neville and Michael Bryant. Pravin smart contributed to the conceptualisation, methodology, investigation, formal analysis, visualisation and writing - original draft writing. Anne Neville contributed to the conceptualisation, methodology, supervision and writing – review & editing. Michael Bryant contributed to the conceptualisation, methodology, supervision and writing – review & editing.

This copy has been supplied on the understanding that it is copyright material and that no quotation from the thesis may be published without proper acknowledgement.

The right of Pravin Alexander Smart to be identified as Author of this work has been asserted by him in accordance with the Copyright, Designs and Patents Act 1988.

## Acknowledgements

First, I would like to thank my primary supervisors. Dr Michael Bryant for his unwavering support, direction, motivation and general enthusiasm throughout my studies, and Professor Anne Neville for her invaluable advice, support, enthusiasm and patience throughout her time on this project. I am deeply grateful to have worked with these immensely knowledgeable and experienced individuals and have learnt a considerable amount working with them.

I would also like to thank the iT-CDT programme, and EPSRC, for enabling me to enrol onto the CDT programme, providing support towards my studies and nurturing my personal development. I would also like to thank Mrs Kimberly Hyde for all her hard work in managing myself and the CDT, and organising training / development activities, travel to conferences and helping me with purchasing issues.

I would like to thank the iFS technicians, for all their advice and support with CAD drawings, bespoke component manufacture and their helpful attitude during day-to-day laboratory activities.

I would like to thank Dr David Keeling for his expertise, experience and interest in developing a bespoke tribometer for in-situ friction assessment, which was invaluable to the project.

I would like to thank the members of iFS and the iT-CDT for fostering an environment where I could widen my knowledge and understanding within the world of surface engineering and tribology.

Finally, I would like to thank my parents and grandparents for their continued support and encouragement over the years. I would also like to thank my wife Issy, who has endured countless tantrums and periods of unresponsiveness from myself, as well as many repetitive presentations. I am also thankful she agreed to marry me after all of that, and continues to provide support and encouragement.

## Abstract

Over the past few decades, the prevalence of tooth loss has gained more attention within the realm of oral and dental tribology. Corrosion and tribocorrosion are areas for concern, with the potential to cause increased tooth loss in vulnerable populations who cannot naturally produce saliva to protect their tooth enamel. Improvements to therapies are required to provide enhanced protection to tooth enamel. This thesis investigates the role of mucin from the perspective of tooth enamel protection, by uncovering mechanisms of dental lubrication with mucin, whilst understanding mucin's contribution to of tooth tribocorrosion and its overall viability for protection.

Mucin-environments and mucin-surface adsorption experimented were completed using DLS, AFM, QCM-D, and in-situ QCM-D tribometer techniques, which provided further insight into the mechanical and rheological properties of mucin layers. Static and dynamic tribocorrosion experiments investigated the individual components of overall tooth wear, and whether mucin provided protection under these conditions.

Experiments indicated that solution composition and surface chemistries were critical factors of mucin layer adsorption, surface coverage, mucin structures and subsequent lubrication. The load-bearing properties of mucin were quantified by using an AFM, which was influenced by PBS. PBS significantly improved enamel wear resistance, which was linked to load-bearing, with evidence of increased mucin within wear sites. In-situ investigations were developed that examined the role of mechanical interactions, which provided insight into the potential compaction of mucin layer within the tribological interface, and subsequent tribofilm. Tribocorrosion experiments uncovered the components to quantify the total tooth degradation, and mucin was observed to not provide any additional benefit to lubrication, or surface protection within an acidic environment.

From the findings presented in this thesis, mucin has been shown to provide enhanced protection and lubrication within a neutral pH PBS environment. However, for mucin to protect enamel in an acidic environment, a complementary component is required.

## Contents

Acknowledgements.....	iii
Abstract .....	iv
Table of Figures.....	x
Table of Tables.....	xxiv
Chapter 1. Introduction – Motivation of research, Aims and Objectives .....	2
1.1 Motivation .....	2
1.2 Aims and Objectives .....	5
1.2.1 Aims.....	5
1.2.2 Objectives .....	5
1.3 Thesis Outline.....	6
Chapter 2. Background information and literature review .....	7
2.1 Introduction .....	7
2.2 Background information.....	7
2.2.1 Tooth materials and surfaces .....	7
2.2.2 Lubrication and protection .....	11
2.2.3 Dental tribology and the operational environment.....	32
2.3 Literature review of in-vitro experimental methods to investigate tooth tribocorrosion and the effects of protein layers.....	41
2.3.1 Tribology and tribocorrosion studies on tooth wear .....	41
2.3.2 Protein films on corrosion .....	49
2.3.3 Protein film modification.....	51
2.4 Summary.....	54
2.4.1 Background summary .....	54
2.4.2 Literature summary.....	55
Chapter 3. Experimental methodologies and surface analysis techniques.....	57
3.1 Introduction .....	57
3.2 Materials and Methodology .....	57

3.2.1	Tribological substrates .....	57
3.2.2	Lubricants and additives.....	59
3.2.3	Sample prep.....	63
3.2.4	Solution characterisation .....	67
3.2.5	Surface interaction methodologies and analysis.....	71
3.2.6	Static and dynamic experimental methodologies .....	84
3.2.7	Surface and chemical analysis techniques .....	89
3.2.8	Statistical analysis .....	105
3.3	Summary.....	105
Chapter 4.	General characterisation of mucin solutions, surfaces and interactions .....	106
4.1	Introduction .....	106
4.2	Results .....	107
4.2.1	The influence of solution composition on mucin .....	107
4.2.2	Surface characterisation of bovine enamel and steatite .....	117
4.2.3	Mucin interactions with surfaces at the nanoscale .....	122
4.3	Discussion .....	140
4.3.1	Mucin interactions with the lubricant environment.....	140
4.3.2	Steatite vs bovine enamel – from surface to mucin-surface interactions ....	144
4.3.3	Role of hydration state and salt composition on mucin layers .....	146
4.3.4	Influence of citric acid and mucin on solutions-surface interactions with bovine enamel	149
4.4	Summary.....	149
Chapter 5.	Tribocorrosion of dental tissues and mucin’s role.....	151
5.1	Introduction .....	151
5.2	Results .....	152
5.2.1	Friction behaviour comparison of steatite and bovine enamel under different artificial saliva environments.....	152
5.2.2	Calcium release under different artificial saliva environments.....	155

5.2.3	Tribocorrosive wear behaviour under different artificial saliva environments	156
5.2.4	Optical microscopy of bovine enamel surfaces .....	161
5.2.5	Surface chemistry and structural analysis with ambient pressure XPS, Raman spectroscopy and XRD. ....	164
5.3	Discussion .....	180
5.3.1	Lubrication performance of steatite .....	180
5.3.2	Influence of static vs dynamic conditions on overall tooth degradation .....	181
5.3.3	Influence of mucins on overall tooth degradation .....	183
5.3.4	Influence of the sliding environment of bovine enamel .....	185
5.4	Summary .....	192
Chapter 6.	Factors influencing mucin layer growth on dental surfaces.....	193
6.1	Introduction .....	193
6.2	Results .....	194
6.2.1	Kinetic adsorption modelling on QCM-D sensors .....	194
6.2.2	Viscoelastic modelling of mucin layers on QCM-D sensors.....	200
6.2.3	Mucin layer lubrication on QCM-D sensors.....	213
6.3	Discussion .....	217
6.3.1	Adsorption of commercial porcine gastric mucin onto gold and hydroxyapatite surfaces, and the influence of perturbing molecules.....	217
6.3.2	Viscoelastic changes and rheological properties of protein layers in relation to lubrication.....	220
6.3.3	Linking tribology with protein layer structure .....	223
6.4	Summary.....	229
Chapter 7.	The development of an in-situ QCM-D Tribometer .....	230
7.1	Introduction .....	230
7.2	Triborig Instrumentation .....	231
7.2.1	Force sensor calibration check .....	233
7.2.2	Triborig validation .....	234

7.2.3	Triborig data processing .....	235
7.3	Results .....	237
7.3.1	Force sensor calibration check .....	237
7.3.2	Validation of the Triborig with the NTR <sup>3</sup> .....	239
7.4	Discussion .....	247
7.5	Conclusion.....	251
Chapter 8.	The application of an in-situ QCM-D Tribometer .....	253
8.1	Introduction .....	253
8.2	QCM-D arrangement with Triborig .....	254
8.2.1	Experimental protocol with QCM-D Triborig.....	254
8.2.2	QCM-D data processing.....	256
8.2.3	QCM-D module comparison .....	258
8.3	Results .....	258
8.3.1	QCM-D module comparison .....	258
8.3.2	Combined QCM-D properties and tangential force response trends .....	261
8.4	Discussion .....	275
8.4.1	Influence of flow on mucin deposition .....	275
8.4.2	Influence of mechanical interactions and solutions changes on the properties of established and unestablished layers .....	279
8.5	Conclusion.....	282
Chapter 9.	Overall discussion, conclusions and future work.....	283
9.1	Overall discussion.....	283
9.2	Conclusions .....	290
9.3	Limitations of study and future work .....	291
9.3.1	Use of physiologically relevant mucin type and purity .....	291
9.3.2	Use of XRD on bovine enamel samples .....	291
9.3.3	Use of a static or incremental load profile for all tribometer tests .....	292
9.3.4	Use of XPS and location targeting specific areas .....	292



9.3.5	Use of the Triborig system combined with the QCM-D .....	292
9.3.6	Use of linear sliding motion on QCM-D sensors with the QCM-D tribometer 293	
9.3.7	Use of high contact pressure during tribo-tests, generally, and with the QCM-D tribometer .....	294
9.3.8	Use of static flow conditions with the QCM-D tribometer and NTR <sup>3</sup> tribo-tests 294	
9.4	Closing statement.....	295
Chapter 10.	References.....	296

## Table of Figures

<b>Figure 1-1 Percentage change in types of dental wear between 1998 and 2009 Adult Dental Health Surveys [8].</b> .....	<b>2</b>
<b>Figure 1-2 Outline of thesis structure.</b> .....	<b>6</b>
<b>Figure 2-1 Diagram of molar tooth anatomy [35].</b> .....	<b>7</b>
<b>Figure 2-2 Bovine enamel a) and bovine dentine b) surfaces examined under an optical microscope.</b> .....	<b>9</b>
<b>Figure 2-3 Bovine enamel a) and bovine dentine b) surfaces examined by SEM PDBSE, and SEM images of c) human enamel surface, and d) human dentine surface [44].</b> .....	<b>10</b>
<b>Figure 2-4 The multifunctional roles of salivary proteins and electrolytes [33].</b> .....	<b>13</b>
<b>Figure 2-5 Salivary gland locations in the oral cavity [64].</b> .....	<b>14</b>
<b>Figure 2-6 Condensation reaction process between amino acids.</b> .....	<b>15</b>
<b>Figure 2-7 Illustration of the four levels of protein structure.</b> .....	<b>16</b>
<b>Figure 2-8 Diagram of pellicle film formation on oral tissues and enamel in saliva (redrawn from reference) [59]. A dense Inner layer of precursor proteins, usually proline rich proteins and statherins, covers the enamel surface, followed by a more dispersed outer layer of larger proteins, such as mucin.</b> .....	<b>18</b>
<b>Figure 2-9 TEM image of in situ formed pellicle on enamel surface, Asterisk indicates pellicle basal layer and arrows toward layer indicate enamel surface [71].</b> .....	<b>19</b>
<b>Figure 2-10 Structure of a generic mucin monomer (a) displaying bottle brush / dumbbell type configuration (glycosylated central region and globular non-glycosylated regions) [96]. Structure of porcine gastric mucin (PGM) monomer (b) also displaying the same configuration with non-glycosylated regions in between glycosylated regions, the sequence of this which varies depending on mucin type [91].</b> .....	<b>24</b>
<b>Figure 2-11 Structure of a generic mucin oligomer; a chain of monomers linked by disulphide bonds [96].</b> .....	<b>25</b>
<b>Figure 2-12 Tooth contact diagram. A) Open phase. B) Closed phase. C) Thegosis/Bruxism [158]. Arrows indicate motion of teeth</b> .....	<b>35</b>
<b>Figure 2-13 Diagram of contact and contact free areas of occlusion [170].</b> .....	<b>37</b>
<b>Figure 2-14 Demineralisation and remineralisation of hydroxyapatite in teeth.</b> .....	<b>38</b>
<b>Figure 2-15 Calcium citrate complex example where two citrate anions have complexed a calcium cation.</b> .....	<b>39</b>

Figure 2-16 Schematic of friction and wear test rig [184]. Normal load is applied using the weight and pulley system, holding the flat sample against the ball. The piston reciprocates up and down to permit small scale displacement of the ball against the flat sample. ....	42
Figure 2-17 Friction of pure titanium against tooth dentin under dry and wet conditions over 5000 cycles [184]. After 100 cycles both present an increase in particle build up in contact when coefficient of friction increases. ....	42
Figure 2-18 Schematic of 3rd body wear testing rig [186]. ....	44
Figure 2-19 Wear areas of enamel surfaces under optical microscope. Two body wear tests are displayed for normal loads of 10 N a), 20 N b) and 40 N c). Three body wear tests are displayed for normal loads of 10 N d), 20 N e) and 40 N f) [186]. ....	45
Figure 2-20 Wear test configuration with lubricant flow [27]. ....	47
Figure 2-21 Focused ion beam images of subsurface enamel cracks after exposure to a) citric acid, b) lactic acid and c) acetic acid [28]. ....	48
Figure 2-22 X-ray diffraction patterns for control (original enamel before corrosion), eroded and remineralised enamel [32]. ....	49
Figure 2-23 a) Surface area and profile for baseline and eroded surfaces under the three test solutions, and b) the average surface roughness of surfaces [191]. ....	51
Figure 2-24 Micro hardness loss after three erosion cycles [73]. ....	52
Figure 2-25 Mean Ca loss ( $\mu\text{g}/\text{mm}^2$ ) after exposure to hydrochloric acid on bovine and human enamel [194]. ....	53
Figure 3-1 Bovine tooth processing from tooth to sample a) Bovine tooth, b) sectioned slabs and c) embedded and polished samples, and d) surface area roughness of bovine enamel samples taken from vertical scanning interferometry. ....	64
Figure 3-2 Images of a) over-ground enamel surface exposing subsurface dentine and b) ground enamel surface. ....	65
Figure 3-3 Steatite sample processing from a) ball to b) polished sample, and c) Surface area roughness of steatite samples taken from vertical scanning interferometry. ....	66
Figure 3-4 Malvern Zetasizer nano a) system, b) DLS cuvette and c) zetapotential capillary cell ...	67
Figure 3-5 Schematic of DLS measurement and light scattering intensity over time .....	68
Figure 3-6 Schematic representation of the zeta potential and electrical double layer. ....	69
Figure 3-7 Zetasizer output data for a) DLS particle size distribution and b) zetapotential. ....	70

Figure 3-8 a) Q-sense Analyzer QCM-D set up with flow cell modules and a gold QCM sensor showing the functional growth surface, b), and the reverse side c). Black arrows on the sensor images show the electrode placement on the sensor. ....	71
Figure 3-9 Example of frequency and dissipation shift when a sensor is treated with a given growth solution.....	72
Figure 3-10 Viscoelastic model a) a simple schematic of spring and dashpot viscoelastic Voight model where for a given interaction there is both a shear elastic and shear viscous response, and b) the geometry of the quartz crystal with a viscoelastic double layer in a bulk liquid environment [204]. ....	73
Figure 3-11 Example of processed data for mucin adsorption onto gold QCM sensors. ....	75
Figure 3-12 Flow cell configuration with liquid handling kit connected to A) the flow cells and B) the peristaltic pump set at a flow rate 0.4 ml/min. ....	76
Figure 3-13 Single flow module a) sensor interface and flow inlet/outlet locations marked by arrows and b) the inside of the flow cell. Black arrows indicate the direction of flow starting from the inlet on the out of the flow cell, through the heating channel.....	77
Figure 3-14 QCM open cell configuration.....	77
Figure 3-15 Multimode 8 AFM (Bruker). ....	78
Figure 3-16 Schematic representation of an AFM. ....	79
Figure 3-17 Force separation curve and extracted properties of interest [208].....	80
Figure 3-18 Diagram of AFM experimental protocol for air and liquid imaging.....	81
Figure 3-19 ScanAsyst-Fluid AFM tip.....	82
Figure 3-20 AFM workflow and analyses. ....	83
Figure 3-21 Bearing analysis a) mucin covered enamel surface highlighting surface features of interest and b) bearing area vs bearing depth showing 3 nm depth threshold and direction of surface features. ....	83
Figure 3-22 Erode example showing a) image before and b) image after a single erode function. .	84
Figure 3-23 Static immersion experiment protocol.....	85
Figure 3-24 NTR <sup>3</sup> nanotribometer.....	86
Figure 3-25 Front and side schematic of tribometer experiments.....	86
Figure 3-26 Hysteresis loop example showing frictional force, $F_t$ , vs linear position. The blue and red arrows represent the forward and reverse trace respectively and the shaded region shows the area of steady state sliding used to determine a cycle's mean $F_t$ . ....	89

Figure 3-27 Example of bovine enamel scar taken with VSI, showing X and Y cross-section profiles. .....	90
Figure 3-28 Example of surface roughness parameters calculated from profile height for a) $R_a$ and $R_q$ , and b) $R_k$ . .....	91
Figure 3-29 Example of volume calculations showing a) masked scar area, b) scar area below $Z = 0$ $\mu\text{m}$ and c) the output negative volume result.....	92
Figure 3-30 SEM a) Hitachi SU8230 high resolution and b) schematic. ....	93
Figure 3-31 Schematic of how the focused electron beam interacts with an atom showing the emission of a secondary electron (left) and the reflection of a back scattered electron (right). .....	94
Figure 3-32 Diagram of electron excitation and X-ray emission .....	95
Figure 3-33 Example of data output from EDX for a bovine enamel sample. ....	95
Figure 3-34 Bruker D8 X-ray Diffraction. ....	96
Figure 3-35 Schematic of X-ray diffraction and associated parameters to Bragg's Law. ....	97
Figure 3-36 Example data of XRD analysis of bovine enamel after surface preparation. ....	97
Figure 3-37 Example of data output from Raman spectroscopy for a bovine enamel sample. ....	98
Figure 3-38 Schematic of Enviro XPS system. ....	100
Figure 3-39 Example of output XPS data on CasaXPS for a bovine enamel sample showing a) a full survey of the binding energies, and b) a narrow-band survey over the O1s peak with curve fittings.....	101
Figure 3-40 Flame AAS (Agilent 200 series AA).....	103
Figure 3-41 Schematic of Flame AAS. 1) The nebulizer, 2) HC lamp, 3) Flame burner, 4) Monochromator, 5) Detector, 6) Amplifier, 7) Signal processing and electronic readout. ....	104
Figure 4-1 Flow chart of experimental methods and analyses in Chapter 4. ....	106
Figure 4-2 Zeta potential vs pH of 0.2% mucin solution. ....	107
Figure 4-3 0.2% mucin peak size vs peak area intensity for over the zeta potential pH range. ....	108
Figure 4-4 Mucin concentration vs solution pH in different environments. pH was taken as 3 readings within 0.01 of one another for each solution. ....	109
Figure 4-5 Mucin concentration vs zeta potential of mucin particles in different environments..	109
Figure 4-6 Mucin concentration vs average hydrodynamic diameter of mucin particles in different environments.....	110
Figure 4-7 Mucin concentration vs polydispersity index of mucin in solutions.....	111

Figure 4-8 Salt concentration comparison of mucin peak size vs size intensity area for different salts: a) NaCl, b) KCl, c) CaCl <sub>2</sub> and d) NaH <sub>2</sub> PO <sub>4</sub> .....	112
Figure 4-9 Salt concentration vs average hydrodynamic diameter of mucin particles for different salts: a) NaCl, b) KCl, c) CaCl <sub>2</sub> and d) NaH <sub>2</sub> PO <sub>4</sub> . ....	113
Figure 4-10 Salt concentration vs polydispersity index of mucin particles in solution for different salts: a) NaCl, b) KCl, c) CaCl <sub>2</sub> and d) NaH <sub>2</sub> PO <sub>4</sub> . ....	114
Figure 4-11 Salt concentration vs zeta potential of mucin particles in solution for different salts: a) NaCl, b) KCl, c) CaCl <sub>2</sub> and d) NaH <sub>2</sub> PO <sub>4</sub> . ....	115
Figure 4-12 CaCl <sub>2</sub> concentration in PBS solution comparison of a) mucin peak size vs size intensity area, b) average hydrodynamic diameter of particles, c) polydispersity index of particles in solution and d) zeta potential. ....	116
Figure 4-13 Optical microscope images of a) steatite and b) bovine enamel surfaces after grinding and polishing.....	117
Figure 4-14 SEM characterisation of steatite showing a) SE and b) PDBSE images of steatite surface, and c) SE and d) PDBSE images of steatite crater. ....	118
Figure 4-15 SEM characterisation of bovine enamel showing a) SE and b) PDBSE images of enamel surface. ....	118
Figure 4-16 EDS maps of a) steatite and c) bovine enamel surfaces. Bar charts of element weight % of b) steatite and d) bovine enamel. Bar colours correspond to elemental colours on their respective EDS map.....	119
Figure 4-17 VSI characterisation of surface profile show surface images of a) steatite and c) bovine enamel with profile traces in x and y directions of b) steatite and d) bovine enamel. ....	120
Figure 4-18 VSI surface profile comparison showing a) average profile traces of steatite compared to bovine enamel and b) calculated nominal roughness parameters R <sub>a</sub> , R <sub>k</sub> and R <sub>q</sub> of steatite (St) and bovine enamel (SE) surfaces.....	121
Figure 4-19 5 x 5 μm AFM height images of a) steatite and b) enamel in air.....	121
Figure 4-20 5 x 5 μm AFM height images of steatite and bovine enamel surfaces treated with Muc + DiW solution under static immersion conditions. Images were taken in an air environment, therefore mucins on the surface are partially dehydrated. Surface roughness parameter, R <sub>a</sub> , is displayed for each image. Red shapes indicate features of interest. ....	122
Figure 4-21 Mucin % area coverage on steatite and bovine enamel surfaces over time. Area coverage was determined by performing a bearing analysis on flattened height images with the bearing depth set such that the uncovered surface was excluded, focusing on the mucin coverages above this reference plane. ....	124

- Figure 4-22** 5 x 5  $\mu\text{m}$  Quantitative nanomechanical property maps of partially hydrated mucin on steatite after 30 minutes static immersion in 0.2% mucin showing maps of a) height, b) PeakForce error, c) adhesion, d) deformation, e) dissipation and f) logDMT modulus. Absolute scale used in images a) to e), where the lowest value is considered 0. ....125
- Figure 4-23** 5 x 5  $\mu\text{m}$  Quantitative nanomechanical property maps of partially hydrated mucin on bovine enamel after 30 minutes static immersion in Muc + DiW showing maps of a) height, b) PeakForce error, c) adhesion, d) deformation, e) dissipation and f) logDMT modulus. Absolute scale used in images a) to e), where the lowest value is considered 0. ....126
- Figure 4-24** Magnified QNM map and section profile of partially hydrated mucin for a) and b) adhesion, and c) and d) dissipation on bovine enamel. Absolute scale used in images a) and c), where the lowest value is considered 0. ....128
- Figure 4-25** 1 x 1  $\mu\text{m}$  AFM height images of mucin on bovine enamel after static immersion in a) and b) Muc + DiW, and c) and d) Muc + PBS. Partially hydrated mucin features are displayed in a) and c), while fully hydrated mucin features are displayed in b) and d). Absolute scale used in images a) to d), where the lowest value is considered 0. ....129
- Figure 4-26** 1 x 1  $\mu\text{m}$  Quantitative nanomechanical property maps of partially hydrated mucin on bovine enamel after 30 minutes static immersion in Muc + DiW showing maps of a) height, b) PeakForce error, c) adhesion, d) deformation, e) dissipation and f) logDMT modulus. Absolute scale used in images a) to e), where the lowest value is considered 0. ....131
- Figure 4-27** 1 x 1  $\mu\text{m}$  Quantitative nanomechanical property maps of fully hydrated mucin on bovine enamel after 30 minutes static immersion in Muc + DiW showing maps of a) height, b) PeakForce error, c) adhesion, d) deformation, e) dissipation and f) logDMT modulus. Absolute scale used in images a) to e), where the lowest value is considered 0. ....132
- Figure 4-28** 1 x 1  $\mu\text{m}$  Quantitative nanomechanical property maps of partially hydrated mucin on bovine enamel after 30 minutes static immersion in Muc + PBS showing maps of a) height, b) PeakForce error, c) adhesion, d) deformation, e) dissipation and f) logDMT modulus. Absolute scale used in images a) to e), where the lowest value is considered 0. ....133
- Figure 4-29** 1 x 1  $\mu\text{m}$  Quantitative nanomechanical property maps of fully hydrated mucin on bovine enamel after 30 minutes static immersion in Muc + PBS showing maps of a) height, b) PeakForce error, c) adhesion, d) deformation, e) dissipation and f) logDMT modulus. Absolute scale used in images a) to e), where the lowest value is considered 0. ....134
- Figure 4-30** 5 x 5  $\mu\text{m}$  AFM height images of bovine enamel after static immersion in Muc + Acid. Red dashed line refers to the location of section profiles, displayed next to the AFM images. White dashed line outline enamel rods. Surface roughness parameter,  $R_a$ , is displayed for each image. Absolute scale used in AFM images where the lowest value is considered 0. ...137

<b>Figure 4-31 1 x 1 <math>\mu\text{m}</math> AFM height image of bovine enamel after 1 minute static immersion in Muc + Acid. Absolute scale used in image where the lowest value is considered 0.....</b>	<b>138</b>
<b>Figure 4-32 5 x 5 <math>\mu\text{m}</math> Quantitative nanomechanical property maps of bovine enamel after 5 minutes static immersion in Muc + Acid showing maps of a) height, b) PeakForce error, c) adhesion, d) deformation, e) dissipation and f) logDMT modulus. Red dashed boxes indicate locations of depth surveys. Absolute scale used in images a) to e), where the lowest value is considered 0.....</b>	<b>139</b>
<b>Figure 4-33 Schematic of charge induced folding of mucin monomer.....</b>	<b>141</b>
<b>Figure 4-34 Mucin interactions with <math>\text{Ca}^{2+}</math> ions within the bulk solution. ....</b>	<b>142</b>
<b>Figure 4-35 Illustration of remineralisation with free ions compared to hypothesised mucin assisted remineralisation. ....</b>	<b>144</b>
<b>Figure 4-36 Cantilever tip interactions with partially hydrated mucin and fully hydrated mucin, illustrating load bearing and adhesive behaviour of mucin. ....</b>	<b>147</b>
<b>Figure 4-37 Load bearing of mucin without salts in deionised water and with salts in PBS solution. ....</b>	<b>149</b>
<b>Figure 5-1 Flow chart of experimental methods and analyses Chapter 5. ....</b>	<b>151</b>
<b>Figure 5-2 Coefficient of friction of a) steatite and b) bovine enamel with standard deviation shadow in deionised water (DIW) and 0.2% mucin only (Muc + DiW) solutions. ....</b>	<b>152</b>
<b>Figure 5-3 Coefficient of friction of a) steatite and b) bovine enamel with standard deviation shadow in PBS and 0.2% mucin and PBS (Muc + PBS) solutions.....</b>	<b>153</b>
<b>Figure 5-4 Coefficient of friction of a) steatite and b) bovine enamel with standard deviation shadow under pH 3.1 citric acid (Acid) and 0.2% mucin and pH 3.1 citric acid (Muc + Acid) solutions. ....</b>	<b>154</b>
<b>Figure 5-5 Mean coefficient of friction of last 500 cycles with SD bars for a) steatite and b) bovine enamel in all test solutions. ....</b>	<b>154</b>
<b>Figure 5-6 Calcium release into post-test solution in pairs of static and dynamic tests. Static tests are displayed as paler, patterned column on the left of the pairing, dynamic tests are displayed in the darker, non-patterned column on the right of pair.....</b>	<b>156</b>
<b>Figure 5-7 VSI images of Y-TZP balls showing no surface differences between a) control ball, b) ball used in steatite-DiW test and c) ball used in enamel-DiW test. ....</b>	<b>157</b>
<b>Figure 5-8 VSI image and cross section profile of enamel wear scars after dynamic tests in a) DiW, b) Muc + DiW, c) PBS, d) Muc + PBS, e) Acid and f) Muc + Acid. Cross sections are displaced to the same scale. ....</b>	<b>158</b>
<b>Figure 5-9 Estimated wear volume of bovine enamel wear scars.....</b>	<b>159</b>



Figure 5-10 pH 3.1 citric acid wear scar and area displayed by a) VSI image with a white dashed line showing the location of the b) cross-section.....	160
Figure 5-11 pH 3.1 citric acid comparison of scar volume and total sample volume loss.....	161
Figure 5-12 Example XPS survey of baseline bovine enamel reference samples before tribo-tests. ....	164
Figure 5-13 Chemical composition of the reference bovine enamel samples before testing shown by atomic percentage %. Argon % was removed to focus only on the material's composition, ignoring the measurement environment.....	167
Figure 5-14 Ca/P ratios of enamel samples after tribo-tests, inside and outside the wear areas. Percentage labels relate to the % difference between the Ca/P ratio within the wear area compared to the Ca/P outside the wear area. ....	173
Figure 5-15 Chemical composition of post tribo-test bovine enamel samples shown by atomic percentage %, showing a) inside the wear area and b) the surrounding surface outside the wear area. Composition is shown for tests in DiW, Muc + DiW, PBS, Muc + PBS, Acid, and Muc + Acid solutions. ....	174
Figure 5-16 Raman spectra of post-test enamel samples inside and outside wear locations, with and without mucins. The full spectra are shown in a) while b) shows the $\nu_1$ phosphate peak scaled in. ....	175
Figure 5-17 XRD sweep of bovine enamel showing pre-test reference and post tribo-test sample spectra. ....	178
Figure 5-18 Schematic of hypothesised wear contributions of bovine enamel under corrosive and tribocorrosive conditions (below the critical pH 5.5). ....	183
Figure 6-1 Flow chart of experimental methods and analyses Chapter 6. ....	193
Figure 6-2 Layer mass growth over time onto gold and hydroxyapatite coated QCM-D sensors with fitted kinetic adsorption models and fitting error parameters. Growth solutions used include a) and b) Muc + DiW, c) and d) Muc + PBS, and e) and f) Muc + Acid. In a), c), and e), gold (Au) surfaces adsorption is presented, while b), d), and f) show hydroxyapatite (Hap) surface adsorption. The red circles in b) present areas of poor model fit which required additional splits for analysis.....	196
Figure 6-3 Best kinetic model splits for mucin layer growth in Muc + DiW on Hap surfaces with fitting error parameters. ....	197
Figure 6-4 Layer mass growth over time onto gold coated QCM-D sensors with best fitting kinetic adsorption models and fitting error parameters. Growth solutions used include a) NaCl b) KCl, c) $\text{CaCl}_2$ d) $\text{NaH}_2\text{PO}_4$ , and e) $\text{CaCl}_2$ + PBS. Salt concentrations of 1, 10 and 100 mmol are	

presented. Solid lines represent the PFO mode, dash-dot lines represent the PSO model and dotted lines represent the Elovich model.....	199
<b>Figure 6-5 Average layer properties calculated from ‘Broadfit’ model comparing gold and Hap sensors after Muc + DiW adsorption and rinsing in DiW; showing a) thickness, b) mass, c) shear modulus and d) viscosity. Error bars represent standard deviation between samples (n = 3). Asterisks refer to level of statistical significance where (* - p &lt; 0.05, ** - p &lt; 0.01 and *** - p &lt; 0.001).....</b>	<b>201</b>
<b>Figure 6-6 Average layer properties calculated from ‘Broadfit’ model comparing gold and Hap sensors after Muc + PBS adsorption and rinsing in PBS; showing a) thickness, b) mass, c) shear modulus and d) viscosity. Error bars represent standard deviation between samples (n = 3).....</b>	<b>202</b>
<b>Figure 6-7 Average layer properties calculated from ‘Broadfit’ model comparing Muc + DiW (blue), Muc + PBS (magenta), Muc + Acid (green) growth solutions on gold and Hap sensors during the growth stage; showing a) thickness, b) mass, c) shear elasticity modulus, and d) viscosity. Error bars represent standard deviation between samples (n = 3). Asterisks refer to level of statistical significance where (* - p &lt; 0.05, ** - p &lt; 0.01 and *** - p &lt; 0.001).....</b>	<b>203</b>
<b>Figure 6-8 Average layer properties calculated from ‘Broadfit’ model comparing Muc + DiW (blue), Muc + PBS (magenta), Muc + Acid (green) growth solutions on gold and Hap sensors during the rinse stage; showing a) thickness, b) mass, c) shear elasticity modulus, and d) viscosity. Error bars represent standard deviation between samples (n = 3). Asterisks refer to level of statistical significance where (* - p &lt; 0.05, ** - p &lt; 0.01 and *** - p &lt; 0.001).....</b>	<b>205</b>
<b>Figure 6-9 Qualitative assessment of mucin layer viscoelasticity by comparing <math>\Delta D</math> vs <math>\Delta f</math> during the growth phase (blue), the rinse phase (green). Muc + DiW, Muc + PBS and Muc + Acid solutions onto gold are presented in a), c), and e) respectively, while the respective solutions adsorption to hydroxyapatite are presented in b), d), and f).....</b>	<b>207</b>
<b>Figure 6-10 Average layer properties calculated from ‘Broadfit’ model against salt concentrations comparing NaCl (green), KCl (purple), CaCl<sub>2</sub> (blue), NaH<sub>2</sub>PO<sub>4</sub> (cyan), and CaCl<sub>2</sub> in PBS (black) salt/mucin solutions on gold sensors during the growth stage; showing a) thickness, b) mass, c) shear elasticity modulus, and d) viscosity.....</b>	<b>209</b>
<b>Figure 6-11 Average layer properties calculated from ‘Broadfit’ model against salt concentrations comparing NaCl (green), KCl (purple), CaCl<sub>2</sub> (blue), NaH<sub>2</sub>PO<sub>4</sub> (cyan), and CaCl<sub>2</sub> in PBS (black) salt/mucin solutions on gold sensors during the rinse stage; showing a) thickness, b) mass, c) shear elasticity modulus, and d) viscosity. ....</b>	<b>210</b>
<b>Figure 6-12 Qualitative assessment of mucin layer viscoelasticity by comparing <math>\Delta D</math> vs <math>\Delta f</math> during the growth phase for 1, 10 and 100 mmol salt concentrations on gold with a) NaCl, b) KCl, c)</b>	

CaCl <sub>2</sub> , d) NaH <sub>2</sub> PO <sub>4</sub> , and e) CaCl <sub>2</sub> + PBS. Arrows and roman numerals indicate different phases of change and the direction of change. ....	211
Figure 6-13 Qualitative assessment of mucin layer viscoelasticity by comparing $\Delta D$ vs $\Delta f$ during the rinse phase for 1, 10 and 100 mmol salt concentrations with a) NaCl, b) KCl, c) CaCl <sub>2</sub> , d) NaH <sub>2</sub> PO <sub>4</sub> , and e) CaCl <sub>2</sub> + PBS. Arrows and roman numerals indicate different phases of layer change continuing from Figure 6-12 and the direction of change. ....	212
Figure 6-14 Mean tangential force from tribo-tests on gold and hydroxyapatite QCM-D sensors over incremental normal load lubricated in a) DiW, b) Muc + DiW, c) PBS and d) Muc + PBS. Error bars represent variation between mean tangential force over the sensor material samples (n=3) for each load increment.....	214
Figure 6-15 Mean tangential force from tribo-tests on gold QCM-D sensors over incremental normal load lubricated in mucin + salt solutions with concentrations of 1, 10 and 100 mmol for a) NaCl, b) KCl, c) CaCl <sub>2</sub> , d) NaH <sub>2</sub> PO <sub>4</sub> , and e) CaCl <sub>2</sub> + PBS. Error bars represent variation between mean tangential force over the 3 samples for each load increment. ....	216
Figure 6-16 Hypothesised mucin layer structure on a) gold and b) hydroxyapatite surfaces prior to sliding.....	225
Figure 6-17 Regression analyses comparing the relationship between the coefficient of friction on gold and hydroxyapatite sensors under Muc + DiW and Muc + PBS conditions compared with a) structural softness, b) layer thickness, c) layer shear modulus, and d) layer viscosity. ....	227
Figure 6-18 Regression analyses comparing the relationship between the coefficient of friction on gold and hydroxyapatite sensors all solution conditions compared with a) structural softness, b) layer thickness, c) layer shear modulus, and d) layer viscosity. ....	228
Figure 7-1 Flow chart of experimental methods and analyses Chapter 7. ....	230
Figure 7-2 Schematic of the Triborig. ....	231
Figure 7-3 Triborig system. ....	232
Figure 7-4 Force sensor check with mass balance for a) normal force sensor loading and b) tangential force sensor loading with an L-shaped probe. ....	234
Figure 7-5 Workflow diagram of MatLab script for processing NTR <sup>3</sup> and Triborig raw data. ....	235
Figure 7-6 a) Raw F <sub>n</sub> data over time during the initial 30 seconds of Triborig testing, b) Raw F <sub>t</sub> data over time during the initial 30 seconds of Triborig testing, and c) Raw slider displacement and calculated slider velocity, controlled by SMAC actuator over a 1.00 mm amplitude over the initial 30 seconds of Triborig testing.....	236

- Figure 7-7 a) Filtered  $F_n$  data with static periods removed compared to smoothed  $F_n$  data and b) offset, absolute and filtered  $F_t$  data with static periods removed compared to smoothed  $F_t$  data.....237
- Figure 7-8 a) Theoretical and experimental output force vs displacement for the normal force sensor. The gradient relate relates to the cantilever stiffness in the normal direction. b) Theoretical and experimental observed mass vs normal loading. ....238
- Figure 7-9 a) Theoretical and experimental Output force vs displacement for the tangential force sensor. The gradient relate relates to the cantilever stiffness in the tangential direction. b) Theoretical and experimental observed mass vs tangential loading.....239
- Figure 7-10 Raw Triborig friction loops under 0.25 mN loading, showing force output over linear position for several cycles. Presenting raw a)  $F_n$  loop in DiW, b)  $F_t$  loop in DiW, c)  $F_n$  in Muc + DiW and d)  $F_t$  in Muc + DiW. The coloured lines differentiate each cycle. ....240
- Figure 7-11 Raw NTR<sup>3</sup> friction loops under 0.25 mN loading, showing force output over linear position for several cycles. Presenting raw a)  $F_n$  loop in DiW, b)  $F_t$  loop in DiW, c)  $F_n$  in Muc + DiW and d)  $F_t$  in Muc + DiW.....241
- Figure 7-12  $F_t$  loops under 0.25 mN loading, smoothed with a median filter using a window size of 50 to remove excess noise. Smoothed Triborig  $F_t$  loops are shown for conditions in a) DiW and b) Muc + DiW. Smoothed NTR<sup>3</sup>  $F_t$  loops are shown for conditions in c) DiW and d) Muc + DiW.....242
- Figure 7-13 Velocity loop under 0.25 mN loading for the NTR<sup>3</sup> under DiW conditions. The red circle indicates where the velocity profile fluctuated towards the end of the NTR<sup>3</sup>'s forward trace, corresponding to the  $F_t$  drop in Figure 7-10c) and d).....243
- Figure 7-14 Comparison of Anton Paar's built-in algorithm to calculate the mean  $F_t$  compared to the MatLab scripted algorithm which processed the NTR<sup>3</sup>'s raw data. Figure shows results for DiW and Muc + DiW over the 0.05-0.50 mN loading range.....243
- Figure 7-15 Regression analysis comparing a) output  $F_n$  for NTR<sup>3</sup> and Triborig with SD bars for both rigs and b) output  $F_t$  for NTR<sup>3</sup> and Triborig with SD bars for both rigs. Tests were performed with a Y-TZP ball against on a glass substrate in DiW and Muc + DiW solutions. Mean and SD were taken from the last 20 cycles of each loading increment. ....244
- Figure 7-16 Mean tangential force with SD bars over incremental load with a) the NTR<sup>3</sup> under DiW and Muc + DiW conditions on a glass substrate, and b) the Triborig under the same conditions. Mean and SD were taken from the last 20 cycles of each loading increment. ...245
- Figure 7-17 Mean tangential force with SD bars over incremental load (ignoring loads < 0.20 mN) with a) the NTR<sup>3</sup> under DiW and Muc + DiW conditions on a glass substrate, and b) the

Triborig under the same conditions. Mean and SD were taken from the last 20 cycles of each loading increment. ....	246
Figure 7-18 Regression analysis comparing output $F_t$ for NTR3 and Triborig with SD bars for both rigs, ignoring the output $F_t$ corresponding to the $F_n$ range 0.05 – 0.15 mN. Tests were performed with a Y-TZP ball against on a glass substrate in DiW and Muc + DiW solutions. Mean and SD were taken from the last 20 cycles of each loading increment. ....	246
Figure 7-19 Raw $F_t$ and $F_n$ output, a), from the Triborig during 0.25 mN tests on glass in Muc + DiW and b) slider displacement and slider velocity between 50 - 60 seconds of testing. Red circles indicate where spikes in the slider's velocity occurred and red dashed boxed indicate dead zones where the slider's velocity remained a 0 mm/s and the slider was static. ....	250
Figure 8-1 Flow chart of experimental methods and analyses Chapter 8. ....	253
Figure 8-2 Triborig interaction with QCM-D open module, a) schematic of interaction and b) image of interaction. ....	254
Figure 8-3 Experimental protocols and timeline for QCM-D tribo-tests on mucin layers.....	256
Figure 8-4 Example of raw QCM-D data on Dfind software showing frequency and dissipation sensitivity during tribo-tests. R numbers represent rest phases during throughout protocol 1).....	257
Figure 8-5 Raw QCM-D data from a) flow and b) open modules. Both show growth the growth phase in Muc + DiW solution.....	259
Figure 8-6 Mean Structural softness of growth phase calculated from the 3 <sup>rd</sup> overtone by $\Delta D/\Delta f$ . ....	259
Figure 8-7 Average layer properties calculated from 'Broadfit' model comparing flow and open modules under Muc + DiW conditions; a) thickness b) mass, c) shear modulus and d) viscosity. ....	260
Figure 8-8 Retest of tribo- tests from protocol 1 under Muc + DiW conditions compared to pre-update $F_t$ results. ....	261
Figure 8-9 Protocol 1 - frequency and dissipation response over time under Muc + DiW conditions. Starting initially with a growth phase (G), followed by consecutive tribo-tests (T) and rest phases (R).....	262
Figure 8-10 Protocol 1 - frequency and dissipation response over time under Muc + PBS conditions. Starting initially with a growth phase (G), followed by consecutive tribo-tests (T) and rest phases (R).....	263
Figure 8-11 Comparison of Muc + DiW and Muc + PBS layer properties for each phase of protocol 1 showing a) structural softness, b) thickness, c) shear modulus and d) viscosity. ....	264

<b>Figure 8-12 Mean Ft for each tribo-test stage during protocol 1. ....</b>	<b>265</b>
<b>Figure 8-13 Protocol 2 - frequency and dissipation response over time under Muc + DiW conditions. Starting initially with a growth phase (G), followed by consecutive tribo-tests (T), rest phases (R) and solution changes (C). ....</b>	<b>267</b>
<b>Figure 8-14 Protocol 2 - frequency and dissipation response over time under Muc + PBS conditions. Starting initially with a growth phase (G), followed by consecutive tribo-tests (T), rest phases (R) and solution changes (C). ....</b>	<b>267</b>
<b>Figure 8-15 Comparison of Muc + DiW and Muc + PBS layer properties for each phase of protocol 2 showing a) structural softness, b) thickness, c) shear modulus and d) viscosity. ....</b>	<b>268</b>
<b>Figure 8-16 Mean Ft for each tribo-test stage during protocol 2. ....</b>	<b>270</b>
<b>Figure 8-17 Protocol 3 - frequency and dissipation response over time under a) Muc + DiW and b) Muc + PBS conditions. Starting initially with a growth phase (G), followed by consecutive tribo-tests (T) and rest phases (R). ....</b>	<b>271</b>
<b>Figure 8-18 Comparison of Muc + DiW and Muc + PBS layer properties for each phase of protocol 3 showing a) structural softness, b) thickness, c) shear modulus and d) viscosity. ....</b>	<b>272</b>
<b>Figure 8-19 Comparison of Muc + DiW properties for each phase of protocol 3 compared with the growth phase of protocol 1 showing a) structural softness, b) thickness, c) shear modulus and d) viscosity. ....</b>	<b>274</b>
<b>Figure 8-20 Mean Ft for each tribo-test stage during protocol 3. ....</b>	<b>275</b>
<b>Figure 8-21 Hypothesised influence of flow on mucin monolayer layer structure and viscoelastic layer properties. Under 0.4 ml/min flow rate, adsorbed mucin tilt to shield additional mucin from adsorbing to the surface leaving vacant sites, reducing potential H bonding within the mucin layer. Without any flow, mucin adsorbs on all available contact sites. Due to increased layer density, more H bonding within layer can take place, stiffening the layer and promoting the entrapment of water. ....</b>	<b>276</b>
<b>Figure 9-1 Hypothesised influence of mucin coverage and hydration in a tribological interface. Entrapment of water molecules within mucin's structure permit load bearing, separating surface from direct boundary contact, aided by repulsion of hydration layers. When partially hydrated with limited coverage, surfaces are more likely to come into boundary contact requiring a greater force to break adhesion forces.....</b>	<b>285</b>
<b>Figure 9-2 Hypothesis load bearing of mucin structures in a) deionised water and b) PBS solution. ....</b>	<b>287</b>
<b>Figure 9-3 Hypothesised mucin tribofilm illustration showing a) proposed mechanism of water movement out of mucin layers on gold leading to more elastic layers by mucin-mucin interactions, b) propose difference in mucin structures on bovine enamel after mechanical</b>	

interactions leading to a more condense layer within the wear contact, and c) the effect of the condensed mucin layer on trapping calcium ions close to enamel's surface, with additional fortification provided by phosphate ions in PBS. ....	289
Figure 9-4 Example of targeting the wear scar location with XPS system. ....	292
Figure 9-5 Raw displacement loops for a) $F_n$ and b) the piezo (PZ) stage displacement. ....	293
Figure 9-6 Illustration of how the Triborig's probe configuration can increase the area of effect on the QCM-D sensor. ....	294
Figure 9-7 Proposed modification to Tribo-QCM-D for tribocorrosion measurements of hydroxyapatite coated sensors. ....	295

## Table of Tables

Table 2-1 Mechanical properties of dentine and enamel [37].	8
Table 2-2 % Composition of dentine and enamel [38, 39].	8
Table 2-3 Composition of electrolytes and substances in saliva [23, 33, 55, 56, 57, 58].	12
Table 2-4 The properties of proteins that affect protein-surface interactions [65].	17
Table 2-5 The properties of surfaces that influence protein-surface interactions [66].	17
Table 2-6 Composition of artificial saliva used in [184].	43
Table 3-1 Composition of steatite [198].	57
Table 3-2 Salt composition of PBS [201].	60
Table 3-3 Standard test solutions used in this study.	61
Table 3-4 Compositions of 100 mmol salt solutions.	62
Table 3-5 Formalin solution composition.	63
Table 3-6 Tribometer quad beam cantilevers.	87
Table 3-7 Tribocorrosion test parameters for NTR <sup>3</sup> .	87
Table 3-8 QCM-D sensor test parameters for NTR <sup>3</sup> .	88
Table 3-9 XPS peak components and binding energies from the literature and databases with references.	102
Table 4-1 Mean zeta potential, Z-av and polydispersity index at 0.2% mucin concentration for each solution environment. Superscript lower-case letters imply significance between compared environments.	111
Table 4-2 Particle analysis data of mucin structures on steatite and bovine enamel after 30 minutes static immersion in 0.2% mucin solution.	123
Table 4-3 Mean quantitative nanomechanical properties and standard deviations of surface features on steatite and bovine enamel surfaces after 30 minutes static immersion in 0.2% mucin solution. Features relate to areas of no mucin (Surface), areas of partially hydrated mucin (Mucin) and the mean properties of the whole scan area (All).	127
Table 4-4 Particle analysis from 1x1 $\mu\text{m}$ AFM scans for partially and fully hydrated mucin after 30 minutes static immersion in either Muc + DiW or Muc + PBS solutions.	130
Table 4-5 Mean quantitative nanomechanical properties and standard deviations of surface features on bovine enamel surfaces after 30 minutes static adsorption in Muc + DiW and Muc + PBS. Features relate to areas of no mucin (Surface), areas of mucin (Mucin) and the	



mean properties of the whole scan area (All) under partially and fully hydrated conditions. .....	135
<b>Table 4-6 Mean quantitative nanomechanical properties and standard deviations of enamel rods on bovine enamel surfaces after 5 minutes static adsorption in Muc + Acid. Features relate to areas in the centre of the enamel rods (Centre) and the edges of the enamel rods (Edge). .....</b>	<b>140</b>
<b>Table 5-1 Comparison table of p values from t tests for the coefficient of friction on steatite between solutions. Significant values are labelled by asterisks, with a significance threshold chosen as p = 0.05. ....</b>	<b>155</b>
<b>Table 5-2 Comparison table of p values from t tests coefficient of friction on bovine enamel between solutions. Significant values are labelled by asterisks with a significance threshold chosen as p = 0.05 .....</b>	<b>155</b>
<b>Table 5-3 Maximum width, length and depth of wear scars. ....</b>	<b>159</b>
<b>Table 5-4 Optical microscope images of bovine enamel wear locations, presenting 34 µm x 36 µm images of.....</b>	<b>162</b>
<b>Table 5-5 XPS reference surveys of O 1s, C 1s, N 1s, Ca 2p and P 2s for bovine enamel tribo-test samples (pre-test). ....</b>	<b>165</b>
<b>Table 5-6 Peak positions of species in reference samples. ....</b>	<b>166</b>
<b>Table 5-7 Descriptive statistics of the atomic composition, At%, of reference bovine enamel samples. ....</b>	<b>168</b>
<b>Table 5-8 XPS surveys of O 1s, C 1s, N 1s, Ca 2p and P 2s for bovine enamel samples post tribo-test focussing within the wear area (inside wear scar). ....</b>	<b>169</b>
<b>Table 5-9 Peak positions of bovine enamel samples after tribo-tests within the scar area (inside). .....</b>	<b>170</b>
<b>Table 5-10 XPS surveys of O 1s, C 1s, N 1s, Ca 2p and P 2s for bovine enamel samples post tribo-test focussing outside of the wear area (outside wear scar). ....</b>	<b>171</b>
<b>Table 5-11 Peak positions of bovine enamel samples after tribo-tests outside the scar area (outside).....</b>	<b>172</b>
<b>Table 5-12 Peak analysis of v1 PO<sub>4</sub><sup>3-</sup> peak comparing the full width half maxima (FWHM), band position and degree of demineralisation, DD, for all bovine enamel samples. ....</b>	<b>176</b>
<b>Table 5-13 Comparison of full width half maximum (FWHM) of reference and post tribo-test bovine enamel samples for indices (002), (211) and (230). ....</b>	<b>179</b>
<b>Table 5-14 Mean crystallite sizes for all reference samples and samples after tribo-tests with standard deviation between crystallite sizes of individual peaks. ....</b>	<b>180</b>

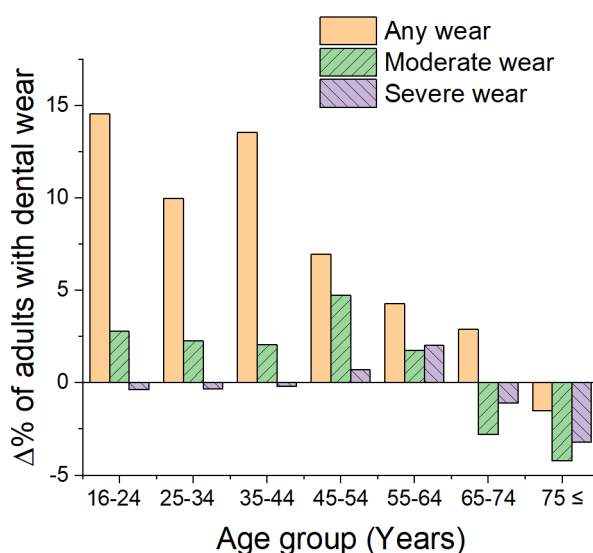
<b>Table 6-1 Kinetic adsorption model fitting parameters for mucin adsorption to gold and hydroxyapatite coated QCM-D sensors. Parameters in bold represent the best fitting model for each solution/material combination.....</b>	<b>197</b>
<b>Table 6-2 Kinetic adsorption model fitting parameters for salt influenced mucin adsorption to gold coated QCM-D sensors.....</b>	<b>200</b>
<b>Table 7-1 System components of the Triborig.....</b>	<b>233</b>
<b>Table 7-2 Summary of Triborig design issues, improvements and investigations.....</b>	<b>252</b>
<b>Table 8-1 Experimental protocols and rationale for QCM-D Triborig after baseline attained.....</b>	<b>255</b>
<b>Table 8-2 Model quality for all experimental protocols using default, moving average and flat FD fitting weights.....</b>	<b>258</b>
<b>Table 8-3 Mean QCM-D layer properties at the end of each phase of protocol 1 for Muc + DiW and Muc + PBS conditions.....</b>	<b>265</b>
<b>Table 8-4 Mean QCM-D properties at the end of each phase of protocol 2 for Muc + DiW and Muc + PBS conditions.....</b>	<b>269</b>
<b>Table 8-5 Mean QCM-D properties at the end of each phase of protocol 3 for Muc + DiW and Muc + PBS conditions.....</b>	<b>273</b>

# Mucin layer behaviour and its role on dental tribology

## Chapter 1. Introduction – Motivation of research, Aims and Objectives

### 1.1 Motivation

Dental erosion, a.k.a. corrosion, and tooth loss are areas of great concern in modern dentistry [1]. It is estimated that 3.5 billion people worldwide are affected by oral diseases, with 2 billion suffering from caries of permanent teeth [2]. Approximately 45% of the global cost of dental diseases (total cost = \$357 billion) related to dental caries, with direct treatment costs accounting for \$161 billion, and indirect costs from productivity losses accounting for \$84 billion [3]. Innovations in dental hygiene and tooth care products have ensured more durable teeth with improved aesthetic appearance over the long term [4]. However for low-income and developing populations, such treatments and interventions are out of reach leading to higher global populations with poorer oral and dental health [5, 2]. Increased consumption of acidic soft drinks and beverages or acidic foods can also lead to softening of tooth materials and eventually tooth material loss [6, 7]. It was revealed that people in the UK between the ages of 16-34 presented increased signs of moderate wear compared to the previous survey in 1998, demonstrated in Figure 1-1. Moderate wear is defined by the ADHS as combined tooth dissolution and abrasion from dietary/other acids and food particles/toothpaste or direct tooth grinding/sliding [8]. These combined interactions serve to have an impact on the long-term durability of younger teeth.



*Figure 1-1 Percentage change in types of dental wear between 1998 and 2009 Adult Dental Health Surveys [8].*

Private dental intervention is expensive, from £1905 for an artificial crown and implant, £2245 for a tooth extraction and up to £5100 for dental treatment under general anaesthetic [9, 10]. Treatments under general anaesthetic are usually reserved for tooth extractions in

the case of children, adults with learning disabilities and a last resort if multiple extractions are required. Comparatively extractions under the NHS comes under charge band 2, of £65.20 per treatment, increasing to £282.80 for restorative dental treatments [11]. Hospital extractions in 2019/2020 accounted for £54.6 million with the NHS, where £33 million was attributed to tooth decay for people under the age of 19, increasing financial pressures on the NHS [12, 13, 14]. This effectively accounts for 1% of the total annual spend of dental care by the NHS, approximately £3.5 billion [15]. Furthermore, these figures do not account for the additional costs of restorative dentistry required after extraction, nor the contribution of the adult population over an age of 19 years. As approximately 1.9 million tooth extractions and 627,000 crowns placement were recorded in the NHS dental statistics for adults in England 2019/2020, the overall cost of tooth decay to the NHS is likely to be greater [16].

Globally, it is estimated that 2.3 billion people suffer from tooth decay of permanent teeth [5]. Factors that can contribute to overall tooth decay and wear can be broken down into lifestyle, clinical and biological influences [6]. Gastro oesophageal reflux disease (GORD) is one condition where stomach acids (pH 1.5 – 3.5) enter the mouth to cause excessive tooth dissolution [17]. Another more prevalent condition is Xerostomia a.k.a dry mouth syndrome, which affects 22% of the overall population, increasing within elderly groups [18]. Xerostomia prevents adequate saliva production, reducing tooth protection and increasing the prevalence of tooth decay, and tooth loss in suffering patients [19, 20]. These conditions diminish the natural, biological mechanisms that would protect dental and oral tissues.

From a tribological perspective, saliva primarily acts a lubricant: ensuring transport of processed food to the back of the mouth for ingestion, reducing friction between food and dental/ oral surfaces. This function serves to protect both soft and hard tissues within the oral cavity. The various proteins and electrolytes of saliva also aid in acid neutralisation and permit tooth remineralisation [21]. This provides additional protection from a chemical interaction point of view. Proteins also adhere to the tooth surfaces to form a protective layer to underlying enamel [22, 23]. This layer serves as a barrier to protect against both mechanical and chemical interactions. Natural saliva is therefore a critical factor in permitting tooth longevity. Commercial artificial saliva aims to replicate the rheological properties and composition of natural saliva, primarily to relieve oral dryness. Some like AS Saliva Orthana contain a protein additive, Porcine Gastric Mucin, although this serves to enhance hydration of oral surfaces rather than protect of tooth enamel [24, 25].

One of the key interests is being able to preserve and protect tooth enamel under the acidic conditions of corrosion (dental erosion). Corrosion combined with the cyclic loading, impact and sliding of teeth during mastication is a potential mechanism for concern. For metals, mechanical exchanges within corrosive environments form a synergistic behaviour, further increasing surface wear, much more than each individual contribution [26]. This behaviour may translate over to the world of dental tribology considering the intermittency of eating and drinking within one sitting.

The conceptualisation of the research stemmed from the perspective of reducing the need for dental intervention by identifying methods of mitigating the loss of natural tooth enamel. To effectively develop dry mouth therapies that effectively protect tooth surfaces within the harsh environment that is the oral cavity, it is crucial to break down and understand the mechanisms of tooth tribocorrosion. Furthermore, it is important to understand how mucin, as an additive, influences tribocorrosion and lubrication of surfaces from the perspective of an adsorbed surface layer. Few studies have investigated this for mucin layers regarding dental tribology and enamel protection, and it is not clear how tribocorrosion and mucin layer formation contribute to overall tooth degradation. Conflicting theories exist to the contributions of tooth enamel loss when assessed in-vitro, especially within an acidic environment [27, 28, 29, 30]. At the time of conceptualisation of this thesis, purely mechanical indentation analysis of enamel surfaces after acidic interactions were used to assess the impact of an acid on enamel, ignoring the breakdown of calcium phosphate in the test solution itself [30, 31, 32, 27, 28]. Furthermore, this would provide a means to investigate the combined interactions of a mechanical and chemical nature, which was hypothesised to yield greater material loss overall compared to each individually.

No rehabilitative artificial saliva solution has effectively been observed to self-engineer a pellicle like layer on dental surfaces for the purposes of material protection. Therefore, artificial saliva solutions need to be assessed for adequate tooth and oral tissue protection in the absence of saliva. A mucin additive should be considered to effectively form a protective layer on these surfaces that is comparable in terms of protection and durability to that of the naturally occurring pellicle. Mucin is associated with oral lubrication and has been documented to contribute to the protective salivary pellicle [33, 23, 34]. It is also commercially available and may have potential as an additive. However, limited work exists on the adsorption of mucin only layers for the lubrication and protection of dental materials. Understanding the mechanisms of mucin interactions, its influence on tribology, and

exploring novel methods of investigating mucin behaviour may open new research areas in the future to further develop protective layer mechanisms.

## 1.2 Aims and Objectives

### 1.2.1 Aims

The aim of this thesis was to better understand the role of mucin-based saliva simulants on surface-layer formation, and its implications on tribological and tribocorrosion mechanisms on dental materials. This included an in-depth investigation into 1) the role of the simulated environment regarding surface layer adsorption, 2) the link between adsorbed mucin layers' mechanical and rheological properties in relation to tribology, and 3) identifying the tribocorrosion mechanisms on tooth enamel and how mucin provides protection.

### 1.2.2 Objectives

To reach the aims of this thesis, the following objectives were completed:

- Investigate mucin size and electrophoretic mobility within solution within deionised water and physiological salts solutions, to provide an insight into the state of free mucin within solution prior to surface adsorption.
- Characterise the surface structures on enamel and an alternative enamel material (steatite), to identify key surface properties of mucin layer adsorption and distribution of mucin, to determine implications of hydration and physiological salt interactions on mucin layers nanomechanical properties, and provide insights into how boundary lubrication occurs. Assess feasibility steatite for mucin adsorption study.
- Determine overall contributions to tooth wear, from physical surface wear and chemical dissolution of a representative tooth enamel material (bovine enamel) under deionised water, physiological saline and acidic environments. Compare static and dynamic contributions to wear, to provide an insight into the hypothesised mechanism of tooth tribocorrosion, and whether mucin layer surface material protection, chemical dissolution and lubrication.
- Investigate the adsorption kinetics of mucin layers onto specific dental surfaces, to determine specific surface chemistry implication on layer growth rates, rheological properties and indirect lubrication performance, in aqueous ionic environments.
- Develop a tribometer system and methodology to perform in-situ friction measurements whilst simultaneously measuring the rheological properties of mucin layer, to provide further understanding of mucin layer lubrication and changes

associated to mechanical interactions. mechanical interaction of surface layer formation experimental.

### 1.3 Thesis Outline

**Chapter 2** reviews the background and literature, identifying gaps within the data on mucin adsorption, tooth tribocorrosion and investigation methodologies. **Chapter 3** presents the numerous materials and methodologies used throughout this thesis. A general characterisation of functional surfaces and solutions, in addition to preliminary investigations of mucin-surface interactions, are presented in **Chapter 4**. Static and dynamic tribological tests on dental surfaces and post-test investigations into surface structures and chemistries are presented in **Chapter 5**. An in-depth assessment of the adsorption kinetics and layer properties of mucin, along with tribological evaluations, are presented in **Chapter 6**. **Chapter 7** builds on the development of a prototype QCM-D tribometer for the purpose of assessing soft, thin protein layers, which was trialled in **Chapter 8**. **Chapter 8** follows on from **Chapter 6**, by directly investigation of mucin layer lubrication while simultaneously measuring the layer properties. Finally, overall discussions, future work and closing statements are presented in **Chapter 9**. Figure 1-2 presents the outline of this thesis.

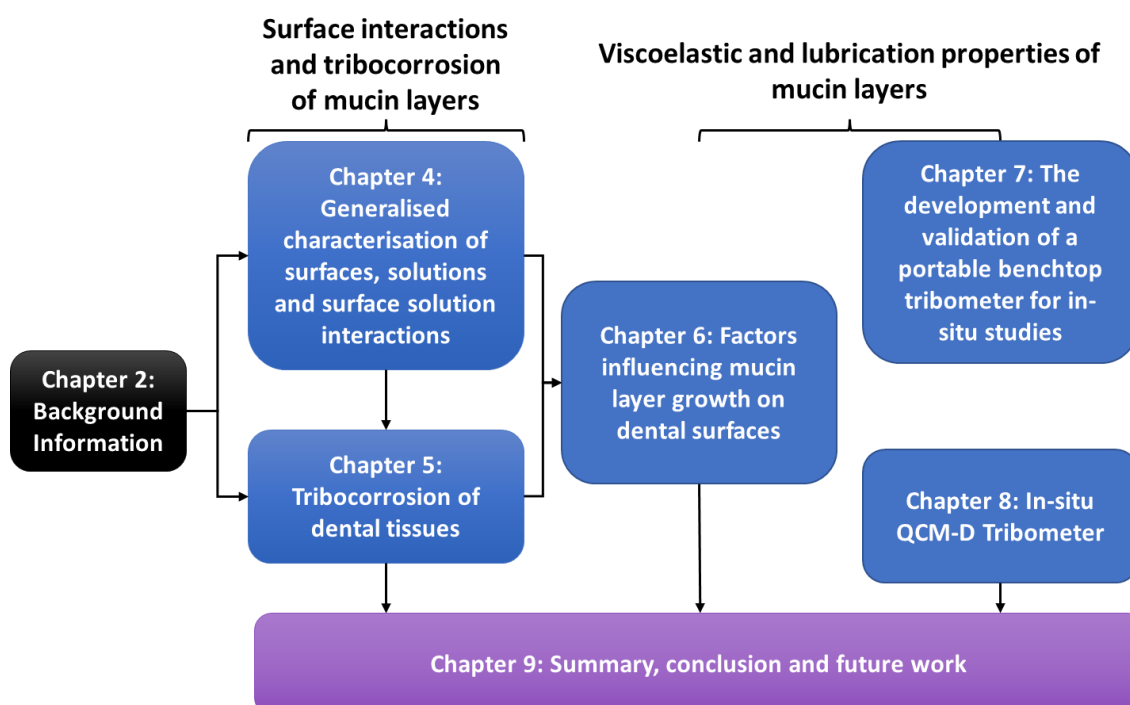


Figure 1-2 Outline of thesis structure.



## Chapter 2. Background information and literature review

### 2.1 Introduction

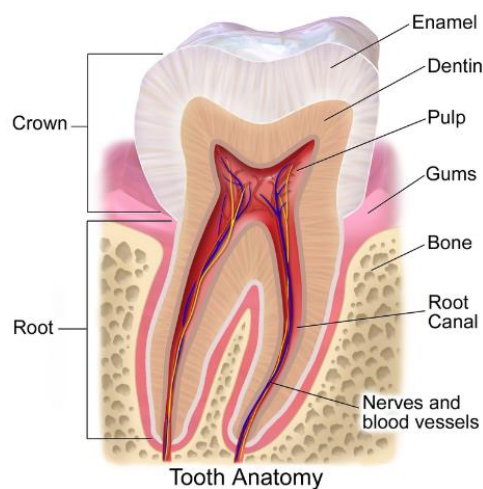
To understand how protein films form on and protect tooth materials, it is essential to understand all aspects of the project background. This section will initially cover the background of the anatomy, mechanical properties and chemical composition of teeth, materials used in dental wear testing, saliva, the pellicle, diseases which are linked to hyposalivation, the function of mucin, biomechanics of mastication and wear modes associated with teeth. Following this, a review of the literature will examine tooth tribology, tribocorrosion and the pellicle. This will cover studies on salivary film adsorption and protection from dental erosion, pellicle modification and impact of modification, and, tribological studies examining tribocorrosion test methods and theorised wear mechanisms.

### 2.2 Background information

#### 2.2.1 Tooth materials and surfaces

##### 2.2.1.1 Anatomy of a tooth and overall function

To start with, it is important to understand the composition and function of teeth. The tooth comprises of two different sections; the crown and the root. The crown serves as the functional surface aiding speech, mastication and tasting while the root anchors the tooth into the bone. The tooth is composed of enamel, dentine, and pulp which contains nerves and blood vessels. From a tribological perspective, the important sections of a tooth are the materials of the crown; dentine and enamel.



*Figure 2-1 Diagram of molar tooth anatomy [35].*

Enamel covers the exposed surfaces of healthy teeth and is the hardest tissue in the human body. It is mostly made from inorganic hydroxyapatite, which are crystalline calcium

phosphate prisms of 26 nm diameter forming keyhole shaped rods of approximately 5  $\mu\text{m}$  in diameter [36]. The enamel layer usually has a thickness of 2-3 mm before the enamel dentine junction, a transitional boundary between the enamel layer and underlying dentine.

### 2.2.1.2 Basic mechanical properties and chemical composition

Tooth enamel and dentine are composed of mineral, water, proteins and lipids. Table 2-1 provides data on the mechanical properties of dentine and enamel. The difference between the mechanical properties of enamel and dentine is related to its crystal structure and composition of the mineral and overall volume. The composition by percentage volume is displayed in Table 2-2.

*Table 2-1 Mechanical properties of dentine and enamel [37].*

Property	Dentine	Enamel
Young's modulus (GPa)	10.2-15.6	20.0-84.2
Shear modulus (GPa)	6.4-9.7	29
Bulk modulus (GPa)	3.11-4.38	45.65
Poisson's ratio	-0.11-0.07	0.23, 0.30
Compressive strength (GPa)	0.249-0.315	0.095-0.386
Tensile strength (GPa)	0.040-0.276	0.030-0.035
Shear strength (GPa)	0.012-0.138	0.06
Knoop hardness	57-71	250-500
Density ( $\text{kg}/\text{m}^3$ )	2900	2500

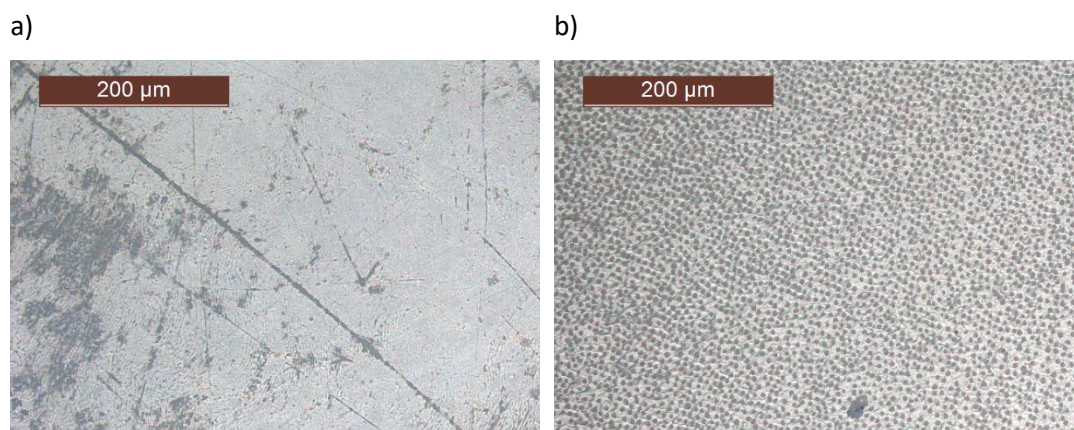
*Table 2-2 % Composition of dentine and enamel [38, 39].*

Composition	Dentine	Enamel
Inorganic minerals	47-65%	85-96%
Organic components and water	35-53%	4-15%

### Tooth material structure

Both enamel and dentine have quite different structures when prepared in a similar manner, shown in Figure 2-3. For example, microscope images of bovine teeth taken by the author demonstrate that bovine enamel presents a more compact structure, shown in Figure 2-3a) compared to bovine dentine's structure, shown in Figure 2-3b). Instead, dentine has a matrix of tubules which starts at the dentine enamel junction and end at the dental pulp. Tooth enamel protects the underlying dentine and comes in direct contact with the oral environment and foods which pass through the mouth. Once eroded or removed the enamel

cannot be regenerated. Dentine is harder than cortical bone but softer than enamel and supports the crown but also protects the underlying pulp.

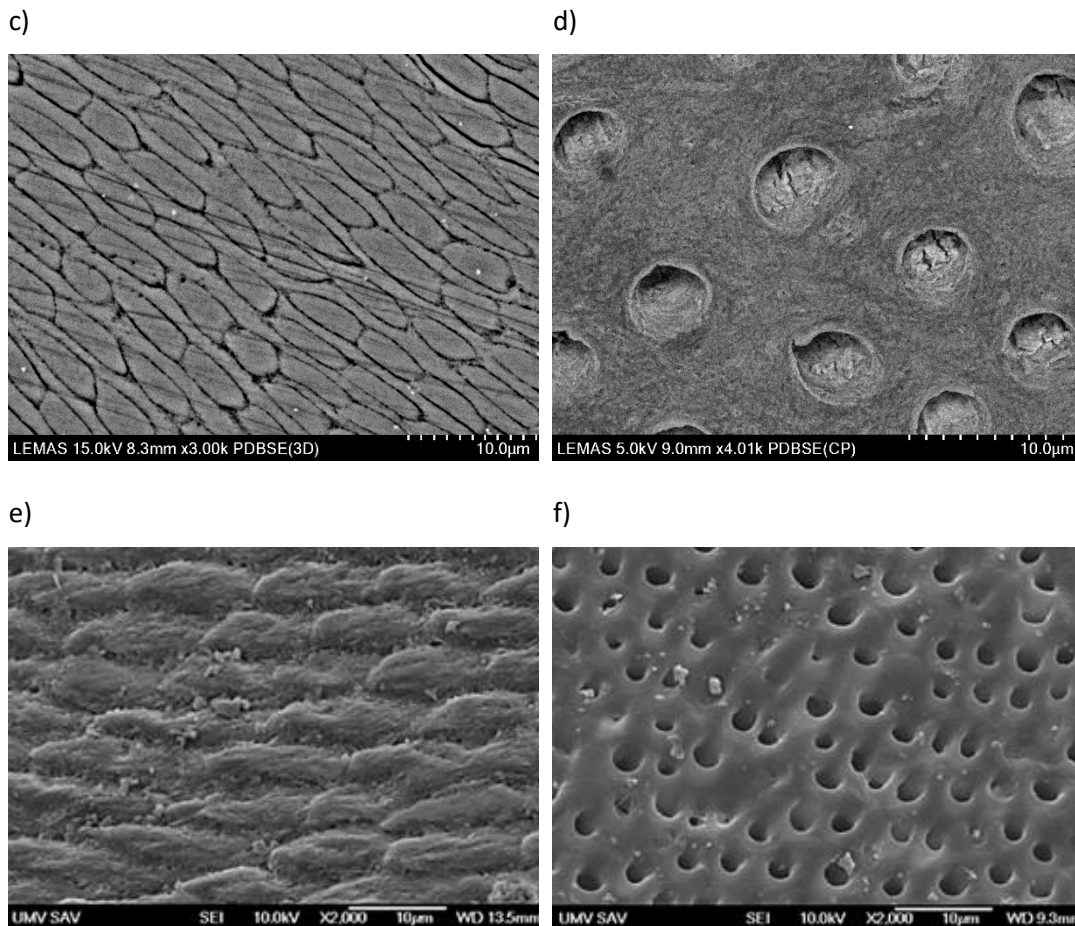


*Figure 2-2 Bovine enamel a) and bovine dentine b) surfaces examined under an optical microscope.*

Scanning electron microscopy (SEM) of these surfaces with a photo diode backscattered electron detector (PDBSE) exposes the presence of enamel rods on the surface, shown in Figure 2-3a). These rods are composed of smaller mineral crystals which give the enamel its overall strength. These hydroxyapatite prisms follow a hexagonal closed packed structure, are between 17-70 nm in width, and are orientated perpendicular to the occlusal surface [40, 41, 42, 43]. Figure 2-3c) shows the dentine tubules under the same technique. The differences in structure and composition inherently provide both enamel and dentine with unique mechanical properties.

### **Bovine tooth structures compared with human tooth**

Variation in both factors between types of teeth, individuals, and their dietary habits mean that there is a large amount of variation in their mechanical properties. It is therefore difficult to compare and determine tribological and erosive behaviour between samples from a range of backgrounds. To reduce this variability, different tooth models can be used given similarities in surface structure, bulk structure and chemical composition. For comparison with bovine enamel and dentine, Figure 2-3c) and d) shows SEM images of human enamel and dentine respectively. A similar key hole structures are shown in human enamel, with enamel rod widths of about 4  $\mu\text{m}$  which are slightly larger than those shown in Figure 2-3a) for bovine enamel. The size difference is attributed to a mature human tooth being compared to an adolescent bovine tooth. However, when comparing dentine, a similar diameter size is shown for both human and bovine sources, of approximately 3  $\mu\text{m}$  [44].



*Figure 2-3 Bovine enamel a) and bovine dentine b) surfaces examined by SEM PDBSE, and SEM images of c) human enamel surface, and d) human dentine surface [44].*

The chemical composition and nanostructure of human enamel have previously been compared to other tooth enamel models. Bovine enamel has previously demonstrated similarities to human enamel when compared to ovine and porcine models [41, 45]. Wavelength dispersive X-ray fluorescence spectrometry also demonstrated differences in chemical composition, with human enamel presenting a higher composition of calcium and phosphorus element, 34.91% and 16.8% respectively compared with 31.11% and 15.3% in bovine enamel [45]. Furthermore, hydroxyapatite crystals within human enamel are shown to be larger compared with those found in bovine enamel when examined by X-ray diffraction and Fourier Transform InfraRed (FTIR) spectroscopic methods [41]. Bovine enamel is generally accepted as an excellent tooth substitute from its similarities with human enamel compared with other available models in addition to bovine enamel's ease of availability and uniformity, however studies which do opt for bovine enamel need to consider its structural and compositional implications with when interpreting results [46, 47, 48].

### **Tooth enamel chemical structure, variations and impact on dissolution**

The minerals in dentine and enamel, and bone, are made up from a form of hydroxyapatite, a naturally occurring calcium phosphate mineral. Generally, the chemical formula for this is given as  $\text{Ca}_{10}(\text{PO}_4)_6(\text{OH})_2$ , however many substitutions can take place with other metals such as sodium, magnesium and potassium in place of calcium; with sodium being the most abundantly swapped. Furthermore, hydroxide ions can be substituted by fluoride ions and carbonate ( $\text{CO}_3$ ) groups can replace phosphate groups. Therefore, a more representative formula for this can be shown as  $\text{Ca}_{10-x}\text{Na}_x(\text{PO}_4)_6-y(\text{CO}_3)_z(\text{OH})_{2-u}\text{F}_u$  [38]. These substitutions can have an overall impact on the durability of tooth enamel, either to improve or reduce enamel's resilience.

Carbonate substitutions can have a considerable effect on the solubility of enamel and dentine. A study carried out by Featherstone et al [40] showed that carbonated apatites (CA) appear to show more reactivity to acids than non-carbonated apatites (NCA). The study examined the crystallinity and dissolution rates of NCA and CAs of 3% and 6.5% w/w  $\text{CO}_3$  with the addition of strontium and fluorides. It showed that the crystallinity of the CA, as measured by X-ray diffraction peak half widths, were comparatively different to NCA with decreased crystallinity on the (2 1 1) crystal plane [40]. Furthermore, the decreased half width value for (2 1 1) was linked to increased acid resistance with lower dissolution rates. As tooth enamel contains approximately 3% w/w  $\text{CO}_3$  and dentine contains 5-6% w/w  $\text{CO}_3$  this supports the increased dissolution rate associated with dentine compared to enamel [40]. This is not the sole factor that increases acid reactivity in teeth, as this study also indicated that strontium and fluoride substitution can decrease reactivity to acids.

It is important to note that the composition and chemical structure of teeth are heavily influenced by their surroundings, most importantly from saliva. The next section aims to expand on saliva's role for dental lubrication, fortification and protection of enamel.

#### 2.2.2 Lubrication and protection

##### 2.2.2.1 *Saliva, proteins and layer adsorption*

#### **The role of natural saliva**

Saliva possesses numerous qualities which are crucial for protection and upkeep of the oral environment and health. Regarding dental tissues, saliva's role can be subdivided into three main areas of protection: preventative defences, active defences and refortification. The preventative defences relate the film forming abilities of saliva, active defences relate to saliva's lubricating and natural buffering abilities, while refortification is related to the

remineralisation of dental tissues after mastication and acidic challenges [21, 22, 49, 23, 50, 51, 52, 53]. It has been documented that this layer forms via protein-surface electrostatic interactions, creating a layer which acts as a chemical diffusion layer and boundary lubricating film [21, 22, 49, 23, 50]. This layer effectively reduces friction between dental and oral surfaces while also controlling the movement of calcium and phosphate ions from the enamel surfaces [49, 53, 54]. Aside from the protection of dental tissues, its roles also range from digestion, taste and smell all the way to intraoral lubrication of hard and soft tissues, and aiding foodstuff transport/drug delivery.

### **Flow rate, composition and functionality**

On average between 600 – 1500 mL of saliva can be produced in a day, flowing into the mouth at 0.3-0.4 mL/min when unstimulated and up to 1.5 - 2.0 mL/min when stimulated [19, 23]. It is mostly composed of water, about 98%, with several enzymes, proteins, electrolytes, sugars and other organic substances. Some of these substances are listed in Table 2-3, where parts per million, ppm, is the measure of a chemical substance in each volume which is equal to mg/L.

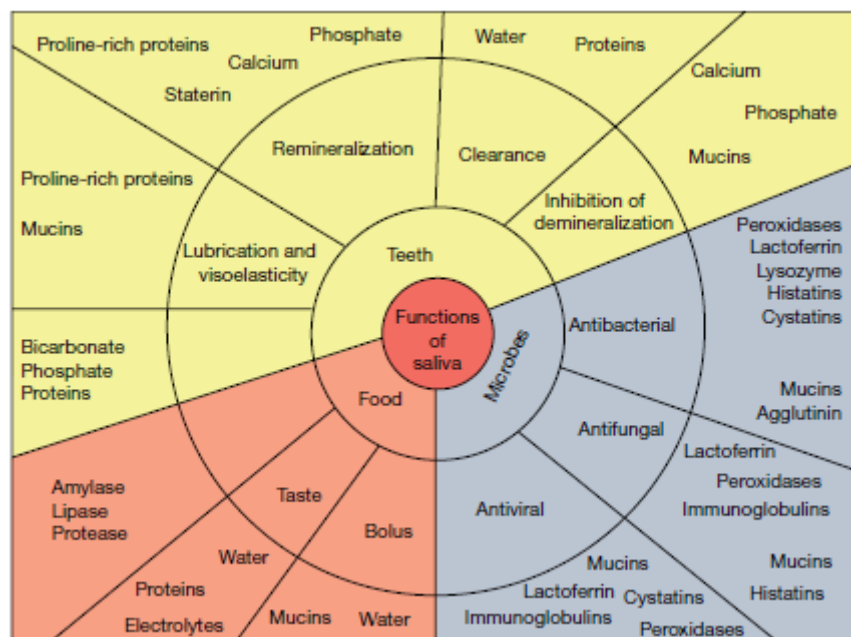
*Table 2-3 Composition of electrolytes and substances in saliva [23, 33, 55, 56, 57, 58].*

<b>Electrolytes</b>	<b>Approximate amount (ppm)</b>	<b>Organic substances</b>	<b>% Composition of total proteins in saliva</b>
<b>Sodium</b>	450-1150	<b>Glycoproteins</b>	20-30
<b>Potassium</b>	580-590	<b>Mucins</b>	20-30
<b>Calcium</b>	40-80	<b>Enzymes</b>	15-20
<b>Chlorides</b>	1060-1775	<b>Immune response proteins</b>	17-18
<b>Bicarbonates</b>	1220-1830		
<b>Phosphates</b>	190-380		
<b>Magnesium</b>	480-970		
<b>Urea</b>	130-270		
<b>Ammonia</b>	12-137		

Saliva has a neutral pH, about 6.8-7.0, and this is maintained with calcium, phosphate and bicarbonates which act as buffers against acids. The calcium and phosphate ions also aid in the remineralisation of tooth materials after acid attack [23, 33].

One function of saliva is to provide lubrication within the oral cavity. Proteins within saliva adhere to oral surfaces and form a thin film of proteins known as a pellicle. The pellicle can

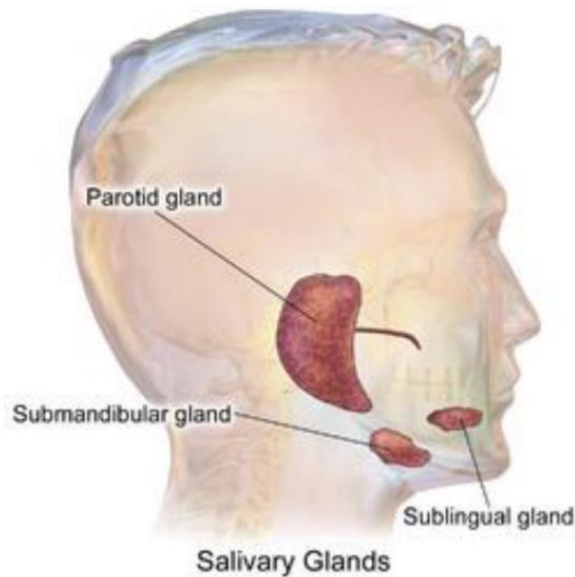
reduce the coefficient of friction of these surfaces and protect them during the initial stages of mastication and acidic attack [59]. There are many different types of protein in saliva, each with a specific function as shown in Figure 2-4. Mucins are one group of proteins which aid in intra oral lubrication and protection. Mucins are highly glycosylated glycoproteins, possessing several carbohydrates, which are secreted from submandibular and sublingual glands in the oral cavity. The presence of carbohydrate chains enables the entrapment of water molecules within mucin's structure, subsequently providing it with viscoelastic property when hydrated, which has been observed in QCM-D and viscometer studies [60, 61, 62]. This has implication of lubrication and protection of oral tissue in the transportation of food, in addition to lubrication and protection of teeth [33].



*Figure 2-4 The multifunctional roles of salivary proteins and electrolytes [33].*

Submandibular, sublingual and parotid glands can influence the lubricating properties of saliva. This is done by regulating the flow rate of saliva from these glands to alter the composition of saliva. When eating, a higher amount of friction is required to provide traction between food and oral surface to aid movement. When grip is not required, unstimulated mucin rich saliva is secreted [63]. Figure 2-5 shows where these glands are located. Prior to and during mastication, stimulated saliva is produced, with a larger proportion from the parotid gland. The parotid gland does not secrete mucins, which has demonstrated an overall higher coefficient of friction in comparison to the mucin-rich unstimulated saliva when tested within simulated oral surfaces (porcine tongue vs porcine oesophagus) [63]. For unstimulated saliva, a larger proportion is secreted from submandibular and sublingual glands. Unstimulated saliva has been seen to have a lower

coefficient of friction between soft oral surfaces compared to stimulated saliva, which may be down to with a larger mucin content [63]. This highlights the importance of proteins within saliva which control which properties are required for a given function. This can be attributed to the types and structures of proteins which will be looked at in the next section.



*Figure 2-5 Salivary gland locations in the oral cavity [64].*

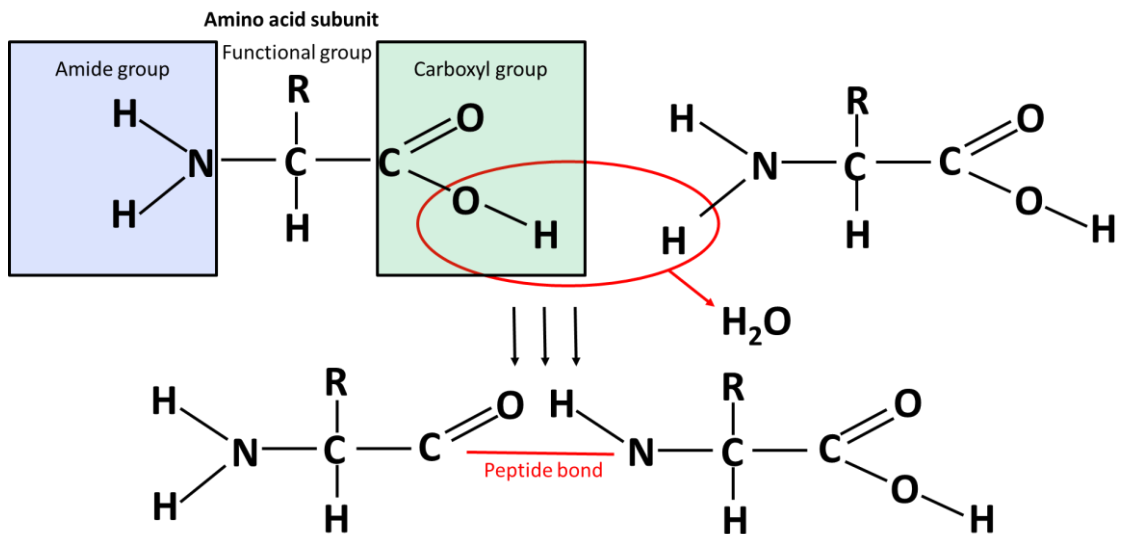
#### *2.2.2.2 Proteins and protein layer structures in the oral cavity*

##### **Protein build up and structure**

There are many different types of protein found in unstimulated and stimulated saliva. Each has a specific function in the oral cavity. These proteins are made up of individual amino acid sub units. There are 20 types of amino acid which can be split into 4 groups which are polar, non-polar, positively charged and negatively charged. The structure of an amino acid can be generalised to an amino group, a carboxyl group and a functional side chain which defines the type of amino acid, illustrated in Figure 2-6. Proteins are formed from chains of amino acids which bind to one another following a condensation reaction, also illustrated in Figure



2-6.



*Figure 2-6 Condensation reaction process between amino acids.*

In the condensation reaction, two amino acids bind together and release a water molecule. This water molecule comes from the oxygen – hydrogen (O-H) bond in the carboxyl group and a hydrogen (H) atom from the amide group. Once the water molecule (H<sub>2</sub>O) is removed, the carbon from one amino acid forms a bond with the nitrogen atom of the other amino acid, known as a peptide bond. This results in the formation of a dipeptide, made from two amino acids. If this process were to repeat itself, this would lead to a long chain of amino acids, known as a polypeptide. Protein synthesis is facilitated and controlled by enzymes which can influence the rate of reaction depending on concentration (amino acids and enzymes), pH, temperature and the presence of ions. These chains can pleat, coil and fold from primary structure proteins to tertiary structure proteins before binding to other proteins to form larger quaternary structured proteins. These structures are illustrated in Figure 2-7.

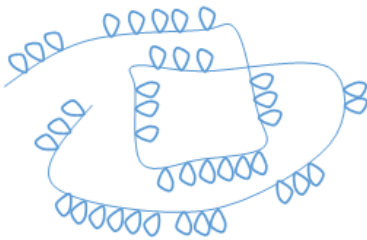
**Primary structure** – polypeptide chain



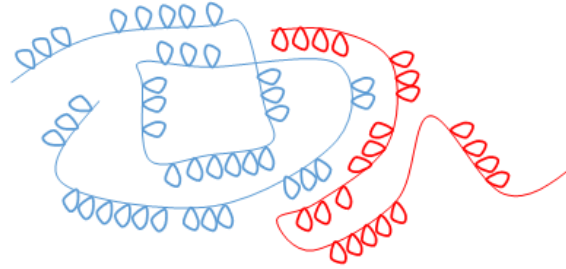
**Secondary structure** – coiled/helical chain



**Tertiary structure** – folded coiled chain



**Quaternary structure** – multiple peptide chain interactions



*Figure 2-7 Illustration of the four levels of protein structure.*

### Factors which drive protein interactions

The structure of a protein has a big influence on how it can adhere to other surfaces. This can be a result of the number of contact sites between a protein and surface which are dependent on the amino acid sequence in the primary structure. The number of contact sites can also vary on a protein depending on temperature, pH and ionic conditions which may reshape or denature a protein. Furthermore, protein-protein interactions can also alter the shape of a protein and increase surface adhesion by exposing more contact sites. When considering pH, the isoelectric point of a protein should be known along with the net charge of a protein when not at the isoelectric point pH [65]. When at the isoelectric point, the protein has no net charge which means the protein has a larger surface activity. This is a result of the protein exhibiting zero charge which reduces electrostatic repulsion between other proteins and the surface. This enables more proteins to bind to a given surface [65]. Structural changes of the protein film also occur as different amino acids contact the surface. Table 2-4 highlights the properties of proteins which influence surface interactions.

*Table 2-4 The properties of proteins that affect protein-surface interactions [65].*

<b>Property</b>	<b>Effect</b>
<b>Size</b>	Larger molecules have more contact sites with a surface compared to smaller molecules. E.g. Albumin weighs 67 kDa and has 77 contact sites on a silica surface while fibrinogen weighs 340 kDa and has 703 contact sites.
<b>Charge</b>	Protein surface charges can bind to corresponding area on a particular surface. Molecules near their isoelectric point can also adsorb more readily due to reduced protein – protein repulsion from no net charge. This can also change the shape of the protein to expose more amino acids and thus more contact sites.
<b>Structural stability</b>	Proteins with lower intermolecular bonding may unfold more readily and thus increase its number of contact sites with a surface.
<b>Unfolding rate</b>	Rapidly unfolding molecules can form more contact sites with a surface more quickly. When initially adsorbed, proteins may change conformation and increase its number of contact sites, promoting stronger adhesion.

The properties of the surface also influence protein surface interactions and adhesion. These are highlighted in Table 2-5. Topography, chemical composition, hydrophobicity, surface characteristics and potential all influence the way a protein can bind to a surface. It is therefore important to understand the materials and proteins in question when examining the formation and properties of protein films.

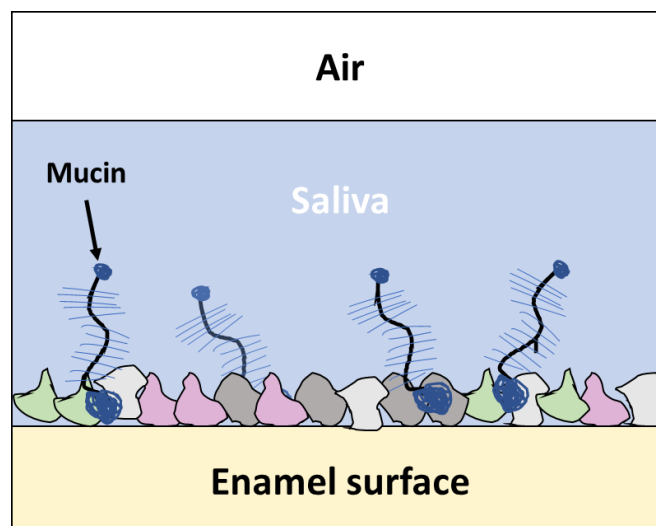
*Table 2-5 The properties of surfaces that influence protein-surface interactions [66].*

<b>Property</b>	<b>Effect</b>
<b>Topography</b>	Greater texture exposes more surface area and site-specific locations to enable protein interactions.
<b>Composition</b>	Chemical makeup of a surface determines the types of intermolecular forces governing protein interactions i.e. whether stronger covalent or ionic bonding occurs.
<b>Hydrophobicity</b>	Hydrophobic surfaces bind more proteins which possess hydrophobic non polar regions in aqueous environments.
<b>Heterogeneity</b>	Non-uniformity of the above surface characteristics result in areas that interact with proteins differently, forming connection points which promote protein networking through different combinations of exposed functional groups.
<b>Potential</b>	Surface potential will influence the distribution of ions in solution and interactions with proteins i.e., protein interactions to surface through surface ion intermediary.

### Formation and function of the pellicle

As mentioned previously, the pellicle is a proteinaceous structure that forms on the surfaces of teeth due to protein-surface electrostatic interactions which serves as a chemical diffusion barrier and a boundary-lubricating film [21, 22]. This layer effectively separates the surfaces of teeth from the surrounding environment, reducing the diffusion of calcium and phosphate ions into the surrounding environment as well as delaying the diffusion of an acid into the enamel [49]. This film initially forms when an oral or dental tissues encounter salivary proteins suspended in saliva (over a few minutes). Tooth enamel surfaces tend to be hydrophilic in nature and possess a net negative surface charge overall, although localised charge locations can exist on the surface depending on the crystal structure orientation [67, 68].

Figure 2-8 illustrates the pellicle layer which forms on tooth enamel, forming a 2-layer structure of condensed inner layer of low weight molecular weight proteins along with a dispersed outer structure of larger weight proteins such as mucin. Lower weight proteins, like statherins and histatins, have a high affinity to hydroxyapatite surfaces. These have been termed as precursor proteins that initiate the binding to the exposed tooth surface [69]. The secondary growth stage selectively adsorbs higher weight proteins. Mucins may interact with statherins and proline rich proteins, binding to them and the surface, changing its conformity in the process. The film's thickness grows until a plateau is reached after 2 hours of submersion [70].

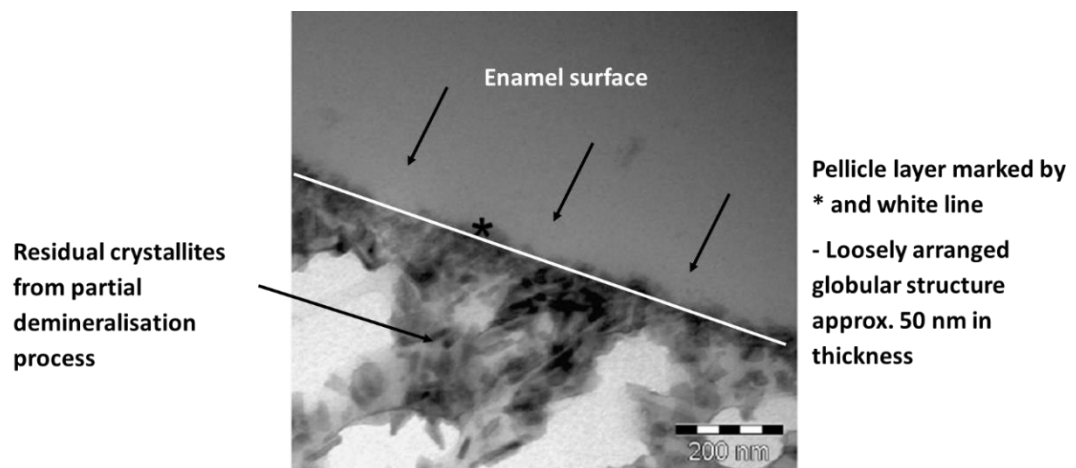


*Figure 2-8 Diagram of pellicle film formation on oral tissues and enamel in saliva (redrawn from reference) [59]. A dense inner layer of precursor proteins, usually proline rich proteins and statherins, covers the enamel surface, followed by a more dispersed outer layer of larger proteins, such as mucin.*

The pellicle's film formation is different to self-assembled layers observed in substitute saliva that only contain one type of protein or base material. Direct comparison of saliva to

substitutes, that contain either mucin, carbomethylcellulose or linseed extract, show saliva forms a layer with strong film retention properties on hydrophilic surfaces [24]. This is important to consider for the effectiveness of artificial and natural saliva on its overall protective capabilities.

While it is unclear how these films protect teeth from two body and three body abrasive wear in-vivo, in-vitro studies have shown that there is some sort of protection provided by the pellicle against toothbrush abrasion [71]. The study also used transmission electron microscopy (TEM) to determine the pellicle characteristics. Two regions were determined, a highly dense base layer around 10-40 nm thick and a more loosely arranged globular region between 50-500 nm [71]. An image of an enamel surface with an in-situ pellicle is presented in Figure 2-9.



*Figure 2-9 TEM image of in situ formed pellicle on enamel surface, Asterisk indicates pellicle basal layer and arrows toward layer indicate enamel surface [71].*

The variation of the pellicle's thickness was dependent on the location of film growth in-situ. This film was seen to be reduced to thickness 1-30 nm or was fully removed by brushing. However, after brushing it would be expected for a new pellicle to form quickly afterwards. An atomic force microscope study (AFM) also examined the pellicle formation on silica surfaces and showed there was a significant reduction in the lateral forces when comparing surfaces submerged in an electrolyte solution only and whole human saliva. This was from a coefficient of friction of 0.6 to 0.03 [22]. It was hypothesised that the pellicle film formed possesses load bearing properties that protect direct contact of asperities on interacting surfaces.

### **Pellicle composition**

Proteins in a pellicle have been examined by collecting natural pellicles from volunteers and conducting analysis on the ultra-structure. Siqueira et al [72] identified in vivo pellicle

proteins including amylase, MUC5B, carbonic anhydrase VI, proline rich proteins, albumins, statherins, histatin I, cystatins and lactoferrin to name a few. Some of these proteins, including histatins, statherins and other phosphoproteins, have been shown to reduce the effect of acid demineralisation with the hypothesis that these proteins adhere more strongly to tooth enamel, preventing acid attack of the surface in these areas [49]. Cysteine rich proteins like MUC5B have also been shown to reduce the effects of demineralisation of tooth enamel [73].

The formation, structure, composition, strength and protective properties are ultimately dependent on the ionic concentrations and components of the saliva. Without the saliva, there would be no transport of proteins and other substances around the oral cavity over the soft and hard tissues. Diseases and symptomatic conditions can influence saliva and consequently influence dental tissue protection and lubrication. The next sub section explores the impact of diseases and conditions on saliva and its implications.

#### *2.2.2.3 Diseases and conditions relevant to oral lubrication and protection*

One common condition to impact oral lubrication and protection is Xerostomia. Xerostomia, also known as dry mouth, is a chronic condition related to the hypofunction of salivary glands, reducing salivary flow and/or compromising salivary composition [74]. It has been estimated that the overall prevalence of dry mouth is 22% of the population, which increases in elderly groups [18]. It can be attributed to certain medications, irradiation of the head or neck from cancer therapies, diseases including Sicca Syndrome (Sjögren's syndrome) and Type 1 Diabetes, psychological conditions, age and gender [75, 76, 77, 20, 78, 79, 80]. This condition can be detrimental when it comes to dental hygiene, increasing the prevalence of tooth decay (dental caries) and demineralisation, and tooth enamel loss in patients presenting xerostomia symptoms [20]. This highlights the importance of saliva when it comes to the protection of dental tissues.

#### **Xerostomia and oral tribology**

Xerostomia is a condition commonly mentioned in the literature regarding dental and oral tribology. In most cases this subjective condition is usually diagnosed with questionnaires, evidence of dry lips, reduced salivation, buccal mucosa dryness and index score of decayed, missing or filled teeth [19, 23]. Hypofunction of the salivary glands can be measured by examining unstimulated and stimulated salivary flow using a technique known as sialometry [81]. Normally average stimulated and unstimulated flow rates have been observed as 1.5-2.0 ml/min and 0.3-0.4 ml/min respectively. Xerostomia/hyposalivation can reduce this to less than 0.5-0.7 ml/min for stimulated flow and less than 0.1 ml/min for unstimulated flow

[19, 78]. These conditions make it increasingly difficult to process food, swallow and even talk. They are also associated with forms of dental caries and erosion as the protective capabilities of saliva cannot fully prevent dental hard tissue loss in acidic conditions. This may also limit the formation of the dental pellicle, leading to an increased tooth material loss.

### **Underlying causes of Xerostomia**

The underlying cause of this dry mouth syndrome may be related to hypofunctional salivary glands in the oral cavity. Prescription medicines are the main cause of hyposalivation and have been suggested to be a potential factor in reduced salivary flow in older population. Villa et al [19] described the following medications as causes of this: anticoagulants, antidepressants, antihypertensives, antiretroviral, hypoglycaemics, multivitamins, supplements, anti-inflammatories and steroid inhalers. These tend to either repress saliva production in salivary glands or influence the way in which saliva flows and circulates within the oral cavity. This correlates with the general decrease in unstimulated salivary flow for increasing age groups of men and women [82]. Conditions like Sjögren's syndrome can impact the composition and quality of saliva, independent of salivary flow rate and quantity. It has been proposed that salivary mucins, which are linked to oral dryness symptoms, are impaired upon secretion from salivary glands [74]. The impairment relates to the structure of mucin and its ability to retain moisture for oral lubrication. This comes down to the negatively charged locations of mucin, the sialic acid and sulphate residues. It has been observed that Sjögren patients produced similar concentrations of mucin within their saliva compared to healthy individual, with reduced hydration and different rheological behaviour [74, 83]. Any treatments therefore need to consider how to improve the quality of saliva in addition to the quantity, which may differ from person to person.

#### *2.2.2.4 Symptom treatment and current artificial saliva substitutes*

### **Current types of treatments and therapies**

Given the high number of medications, diseases and therapies that induce dry mouth conditions, it would be complicated and costly to address each of them to prevent the effects of xerostomia. Considering this, there are several preventative treatments commercially available. Artificial saliva in the forms of gels, sprays and solutions are most prominent in the market, generally containing mineral salts, menthol oils and sugars like xylitol. These treatments aim to provide immediate relief, mimicking the viscosity of natural saliva while aiming to stimulate additional saliva production. Lozenges, gum, artificial saliva and other stimulates aim to relieve the symptoms of dry mouth, but all these treatments cannot provide proper relief compared to healthy saliva. Mucin based therapies also exist

with treatment from AS Pharma containing additional mucins to provide more effective protection as opposed to chemical only solutions. While providing short term relief, it is unclear if this provides protection to dental tissues within a tribological or tribocorrosive environment.

### **Commercial artificial saliva composition and influence on rheological properties**

Limited saliva substitutes exist for people who may suffer from dry mouth related conditions. As it would be expected, these cannot fully simulate the complex characteristics that natural saliva possesses. Within commercially available saliva substitutes there is a lot of variation on the type of saliva (what it's based on), the chemical compositions and its overall viscosity. Saliva bases include: mucins, carboxymethylcellulose (CMC), hydroxyethylcellulose, xanthan gum, linseed and polyethylene oxide [84]. Generally, it seems to be the case that mucin-based saliva substitutes are preferred to alternative commercially available substitutes under lab testing and clinically [84]. The aim of saliva substitute is to simulate aspects of natural saliva. Natural saliva is a non-Newtonian fluid, shown to possess a viscosity which is inversely proportional to the rate of shear [62]. Mucin containing solutions of porcine gastric mucin (PGM) and bovine submandibular mucin (BSM) dissolved in deionised water and an electrolyte solution, a.k.a simulating saliva solution (SSS), have also been assessed. These also exhibited non-Newtonian behaviour, with the PGM – SSS combinations showing similar viscosities to unstimulated human saliva [62]. Interestingly, the commercially available mucin-based saliva substitute Saliva Orthana did not show a dependency on the shear rate. In an earlier study of saliva substitutes and mucin containing solutions, commercial saliva substitutes containing either CMC, BSM or PGM showed no dependency with shear rate, and were generally more viscous [85]. This may be a result of sugar alcohols present in commercial saliva substitutes as opposed to the ionic concentrations as this was shown to not change the viscoelasticity of PGM [86]. Solutions containing PGM, BSM and a combination of the two with bovine serum albumin (BSA) were also examined [85]. While most of these protein solutions seemed to be independent on the shear rate, the combined BSM/BSA solution was shown to have a similar shear rate dependency to saliva.

### **Tribology of saliva substitutes**

While the rheology of the saliva substitute can differ to natural saliva, one study has shown that its viscosity may have little influence in terms of its lubricative ability [87]. A canine cusp was used on a rotating glass plate, using a pin on disc configuration, to measure the friction from different saliva solutions. A viscometer was also used to measure the solution's



viscosity. Mucin based, CMC based and whole human saliva all presented signs of boundary lubrication, with a decrease in friction observed with increasing speeds. The mucin based commercial saliva had a viscosity of 2.32 cP and coefficient of range of 0.04-0.15 compared to human saliva with a viscosity of 0.78-1.23 cP and a coefficient of friction range of 0.06-0.27 [87].

### **Polymers in saliva substitutes and influence on enamel protection**

PGM, CMC and other polymers were also looked at as thickening agents for artificial saliva solutions in terms of their protective capabilities under demineralisation and remineralisation processes. Most polymers tested were shown to reduce demineralisation due to their film forming abilities. It was also noted that some polymers, including PGM and CMC reduces that re-hardening potential of the solutions [88]. When comparing both PGM and CMC on their hardening ability, it was seen that there was no significant difference between the two [89]. Mucins contain numerous carbohydrate branches, which contain sialic acid groups that can form complexes with calcium ions, and thus reducing the passage of calcium ions from the liquid to the enamel surface [90]. One potential improvement to this may be to ensure the saliva substitute is supersaturated with calcium and phosphate ions which may also reduce demineralisation in the first place. An addition of 1 ppm fluoride as a control was also shown to increase the re-hardening potential of the solution, thus incorporation of this into an artificial saliva solution would be beneficial in erosion prevention and protection [88].

#### *2.2.2.5 Mucin as a potential additive for lubrication and protection*

To understand the role of mucin as a potential component of an artificial saliva, it is necessary to know about its structure and functionality. Mucins are glycoproteins consisting of a protein core/backbone decorated with numerous complex branches of “brush like” carbohydrate chains. These can be classified as either membrane-bound mucins or secreted mucins. These can vary considerably in size, structure, weight, viscoelastic and rheological properties. Typically, mucins can weigh in the range of 0.2 and 20 MDa depending on the length of the protein core, the level of glycosylation (carbohydrate chains) and the mucin type [91, 92]. With respect to saliva, mucins are secreted from sublingual and submandibular glands within the oral cavity and make up approximately 16% of the total protein present in whole human saliva [23, 93].

Early investigation into salivary mucins characterized two types of mucin glycoprotein; mucin glycoprotein 1 (MG1) and mucin glycoprotein 2 (MG2) [92, 94]. MG1 was characterized as a higher molecular weight glycoprotein (1 MDa) consisting of 15% protein,

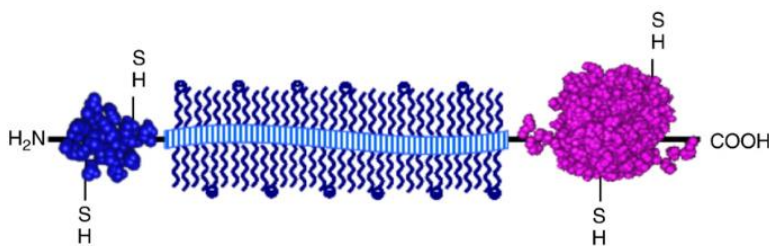
78% carbohydrate and 7% sulphate, suggesting that MG1 exhibited gel forming characteristics [94]. In contrast to this MG2 possessed a low molecular weight (200 KDa) and comprised of 30% protein, 68% carbohydrate and 1.6% sulphate [92, 94]. MG1 and MG2 are encoded by MUC5B and MUC7 genes respectively and are the main structural and functional mucins for hydration and lubrication in whole human saliva [93, 92, 94, 95, 96].

Porcine Gastric Mucin (PGM) type II (Sigma–Aldrich), a commercially available form of mucin, is derived from animal sources with similarities to MUC5B [97]. It is commonly used in academic research as an artificial saliva component for dental tribology, remineralization/demineralisation and other adsorption studies [97]. This sub section aims to cover the main characteristics and behaviours of mucin, touching on PGM as a specific mucin of interest.

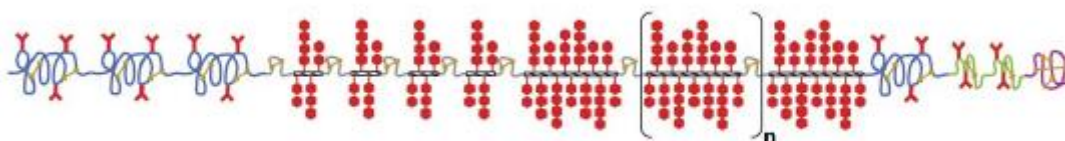
### Mucin Structure

The protein backbone of mucin is mostly composed of amino acids; serine, threonine, proline, alanine and glycine [95]. Hydroxyl groups found in serine and threonine form covalent bonds with the sialic acid subunits present in oligosaccharide chains (carbohydrates of  $\leq 20$  monosaccharide subunits), which are known as O-glycosidic bonds [98]. The level of glycosylation is determined by the regions which are rich in the amino acids proline, threonine and serine (PTS domains) which serve as attachment points for the glycans [99]. Examples of a generic mucin subunit and porcine gastric mucin (PGM) subunit are displayed in Figure 2-10 a) and b).

a)



b)

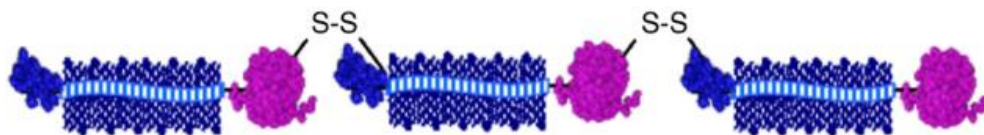


*Figure 2-10 Structure of a generic mucin monomer (a) displaying bottle brush / dumbbell type configuration (glycosylated central region and globular non-glycosylated regions) [96]. Structure of porcine gastric mucin (PGM) monomer (b) also displaying the same configuration with non-glycosylated regions in between glycosylated regions, the sequence of this which varies depending on mucin type [91].*

### Mucin functional groups and subsequent function

The glycan components of mucin make up at least 50-80% of its weight and links to the mucin's overall hydration [99, 100, 98]. This is due to monosaccharide subunits, such as sialic acid, fucose, N-acetyl glucosamine, N-acetyl galactosamine and galactose, which render mucin hydrophilic [100, 98]. Sialic acid and sulphate group residues are also negatively charged which gives mucin a net negative charge [95]. The glycan chains can associate with water molecules via hydrogen bonding which can trap large amounts of water [101, 102]. This is linked to mucin's lubrication properties as it can create a surface bound water layer under boundary lubrication conditions [100, 102]. The presence of these glycan chains within mucin has been shown to maintain a low coefficient of friction under boundary conditions compared to partially and fully de-glycosylated mucin by almost 2 orders of magnitude [102].

Non-glycosylated globular regions also exist within the structure of mucin. These exist as part of the amino (-NH<sub>2</sub>) or carboxyl (-COOH) terminals of the protein core and are also interspersed within the core [99, 96]. These regions tend to contain all the cysteine residues and are hydrophobic in nature [99]. Furthermore, the cysteine regions contain thiol (-SH) functional groups which facilitate the formation disulphide bonds between other mucin monomers and itself [91, 103]. Secreted mucins have been known to be arranged in a flexible chain of mucin subunits which may play a role in lubrication via disulphide bonding [103]. This is displayed for a generic mucin oligomer in Figure 2-11.



*Figure 2-11 Structure of a generic mucin oligomer; a chain of monomers linked by disulphide bonds [96].*

The overall structure of a mucin monomer is ultimately influenced by both hydrophobic and hydrophilic domains. Heavily glycosylated regions govern the chemical and physical properties of mucin with strong hydrophilic interactions. This subsequently prevents protein folding, as the hydrophobic non glycosylated regions are unable to overcome the superior hydrophilic nature of these carbohydrate chains [104]. Therefore, a combination of this phenomenon and the steric repulsion present between hydrated carbohydrate groups means a stiff linear structure is adopted [104].

### **Component functionality within an artificial saliva**

Mucin has been previously examined as a potential additive to artificial saliva substitutes [105, 106, 89]. It is a multifunctional component of saliva which possesses boundary lubricative, viscoelastic, anti-bacterial and digestive properties [107, 34, 23]. These characteristics make it a viable component for an artificial saliva substitute; however, it is important to assess how this component forms protective layer alone.

Studies have shown that mucin within an artificial lubricant adsorbs to surfaces, reducing surface wear by influencing the wear mechanisms [108, 105]. Reductions in abrasive wear and the prevention of adhesive wear mechanisms indicate the structural and lubrication properties of mucin-surface layers are important when it comes to surface protection [108]. It has been suggested that this relates to an aqueous boundary lubrication regime that depend on the adsorbed protein layer's "structural softness" (viscoelastic properties) and the layer's ability to retain water [109, 96]. These properties are essential for long term dry mouth relief and tooth enamel protection.

#### *2.2.2.6 Salivary protein and mucin adsorption pathways*

The properties of salivary proteins, the oral environment and the surfaces have an impact on the film formation process and subsequent viscoelastic behaviour of adsorbed protein layers. Saliva adsorption studies have previously examined the pathways to the formation of a pellicle on a range of surface materials. Most notably, quartz crystal microbalance with dissipation monitoring (QCM-D) studies have examined the growth of hydrated salivary films on gold, hydroxyapatite, zirconia, titania, silica and PDMS [110, 61, 111, 112, 113]. Differences in adsorption rate, adsorption behaviour (monophasic or multiphasic), layer thickness, layer viscoelasticity and the overall layer retention when subjected to different rinse solutions have been observed [110]. Furthermore, the surface's chemical composition, heterogeneity, potential, polarity and topography are factors which govern interactions with these proteins [111, 114, 70]. Therefore, protein and surface characteristics alike need to be scrutinised to engineer a particular protein layer within a given environment.

### **Mechanisms of salivary protein and mucin adsorption**

The mechanisms of protein adsorption come down to the inter- and intramolecular forces between a protein molecule and a particular surface. This can be broken down into two generalised types of adsorptions; chemisorption and physisorption. Chemisorption involves a chemical reaction between a given surface and an adsorbate which involves the sharing or transfer of an electron by either covalent or ionic bonding [115]. Physisorption on the other hand relates to weaker bonds that form on the surface from electrostatic interactions,

hydrophobic interactions, hydrogen bonding and London forces. The differences between the two modes of adsorption relate to the bond strength between the adsorbate (the salivary proteins) and the adsorbent surface (dental tissues/biomaterials).

Salivary proteins have been shown to adsorb via electrostatic and hydrophobic interactions [110, 61, 115, 116, 91]. Studies that have considered human saliva or isolated salivary protein alone (i.e., mucin, lysozyme, lactoferrin, statherin and other proline rich proteins) demonstrate progressive adsorption via these pathways on various surfaces as seen by QCM-D and ellipsometry [110, 61, 111, 112, 113, 117]. The next sub sections aim to break down the protein surface interactions dependant on the surface properties, starting with hydrophobic surfaces.

#### **Protein behaviour on hydrophobic surfaces**

Hydrophobic surfaces have been shown to adsorb larger amounts of salivary protein compared to hydrophilic surfaces [110, 117, 118, 112]. This has been observed when investigating bovine submaxillary mucin (BSM) and human MUC5B adsorption onto hydrophobic silica and hydrophilic silica surfaces [117, 61]. Mucin layers formed on hydrophobic silica showed a reduction in adsorbed mass with a more rigid layer while the opposite was seen for hydrophilic silica and gold surfaces [61]. However, when ellipsometry was performed on gold and hydrophobized silica surfaces the mass adsorbed was similar [119, 120]. This suggested that the mucin layer on the hydrophobic surface was less hydrated compared to layers formed on gold, and potentially a hydrophilic surface, indicating the layer structural conformation differs between surfaces. The hydrophobic interactions between the hydrophobic surfaces and the globular non-glycosylated regions of mucin facilitate initial adsorption, reducing the entropy of the system. In other words, the contact between both hydrophobic surfaces and non-polar regions of mucin with water are removed [121]. It appears to be the case that mucin forms a strongly adsorbed layer on hydrophobic surfaces which are more resistant to desorption [122]]. It may also be the case that for a hydrophobic surface, only hydrophobic interactions facilitate adsorption regarding whole human saliva, with little electrostatic interaction taking place [123]. PGM interactions with hydrophobic PDMS have also been shown to be driven by hydrophobic interactions, with glycosylated groups interacting with the bulk fluid [124].

#### **Protein behaviour on non-hydrophobic surfaces**

On hydrophilic and gold surfaces it seems to be the case that electrostatic interactions are more dominant for mucin adsorption compared to hydrophobic surfaces. The hydrophilic silica and mucin both possess a net negative charge, reducing mucin surface interactions due

to electrostatic of repulsion. This has been observed with atomic force microscopy of mucins on hydrophilic and hydrophobic silica. Larger mucin agglomerates were adsorbed onto the hydrophobic surfaces, while smaller globular structures were present on hydrophilic surfaces [122]. Structures adsorbed onto the hydrophilic surfaces via electrostatic interactions were limited in size due to electrostatic repulsion between other mucin structures. Electrostatic interaction between these surfaces is thought to be a result of the positively charged amino residues of mucin interacting with the negatively charged locations on the surface [121]. The degree of repulsion can also be reduced with the addition of salts within the system to reduce the overall net negative charge of mucin [121, 124]. Whole human saliva also imparts smaller protein agglomerates on hydrophilic surfaces; however, these were denser due to the additional cationic protein interactions with the mucin and the surface [122].

#### **Influence of surface material - gold surfaces**

Gold surfaces seem to adsorb considerably more protein in comparison to other surfaces [110, 61]. On gold surfaces, a combination of physisorption and chemisorption pathways are observed as studied by QCM-D and ellipsometry alike [110, 61, 111, 112, 113, 117]. Gold surfaces have the tendency to exhibit mirror charges, presenting active sites with an opposing charge to one presented by an adsorbing molecule, following the electrostatic model of image charges [110, 61]. As mentioned previously, cysteine is a functional amino acid within the structure of a mucin monomer due to its thiol group (S-H). Proteins with this thiol group can form strong covalent S-Au bonds which may promote a stronger layer adhesion [61, 125]. Mucins have been shown to adsorb to gold by this mechanism, rendering a stronger bound layer which was more resistant to elution compared to other non-thiolated proteins [126].

#### **Influence of surface material – hydroxyapatite surfaces**

Hydroxyapatite surfaces have been used to investigate salivary protein adsorption as these represent a similar surface chemistry and heterogeneity to tooth enamel. Hydroxyapatite surfaces are hydrophilic and possess a net negative charge [67]. Charges on the surface of hydroxyapatite are determined by the exposed crystal structure on the surface; positive charges from calcium ions on 'ac' and 'bc' faces, and negative charges from phosphate ions on the 'ab' face [68]. These have been referred to as C site and P sites [68]. These sites influence how proteins adsorb. Phosphate (P-OH) groups on the surface of hydroxyapatite serve as anionic binding sites which favour protein adsorption [127]. Naturally, precursor proteins like statherins and proline rich proteins (PRP1) form an initial layer; onto which

mucins can then interact and build up the pellicle in the early stages of formation [117]. In the absence of these proteins, mucin alone may adsorb by electrostatic interactions between their positively charged amino residues and the negatively charged P-OH regions on the surfaces of hydroxyapatite [127]. Furthermore, negatively charged regions of salivary proteins have been suggested to chelate surface calcium ions, which may further assist in additional localised protein-surface and protein-protein interactions [128]. In addition to the P-OH regions, hydroxyapatite has its own calcium sites on its surface onto which the negatively charged glycosylated regions (COOH groups) of mucin interact with [129]. It is also thought that the carboxyl groups of mucins bound via the calcium sites expose their amino group which promotes hydrogen bonding with nearby localised phosphate groups on hydroxyapatite [129]. The presence of additional negatively charged regions of a protein in proximity to a surface bound negative residue was also suggested to increase the possibility of adsorption to hydroxyapatite, potentially by cooperative binding [130].

#### **Influence of other surface characteristics**

Surface porosity and pore volume also impact the amount of protein which can adsorb onto hydroxyapatite, with bovine serum albumin showing a reduced surface adsorption with increasing pore volume [131]. This mostly effects larger globular proteins, as smaller proteins such as lysosome can adsorb inside pore [131]. Surface topography also can impact protein adsorption behaviour. A study investigating the effect of surface texturization on globular protein adsorption demonstrated significantly differences in layer thickness between flat and texturized surfaces of the same material [132]. Increasing surface root mean square roughness ( $R_q$ ) has been shown to increase fibrinogen adsorption on surface, which was attributed to the increase in surface area and conformational changes altering the orientation of the glycoprotein at the surface [133]. A subsequent effect of the conformational changes can influence the protein layer structure of surfaces of different surface morphologies. A study of bovine serum albumin adsorption demonstrated this behaviour with a QCM-D, showing different adsorption phases and layer structures on the roughness QCM-D sensor compared to untreated flat surface [134].

#### **Clarity with mechanism terminology – electrostatic interactions**

Ambiguity exists around the term 'electrostatic interactions' which has been used to describe the main driving force for salivary protein adsorption. 'Electrostatic interactions' is an umbrella term which relates to the interaction of charge molecules or entities within a molecule which covers ionic interactions, hydrogen bonding, dipole-dipole interactions and other Van der Waals forces. The issue is that the mechanism is not specified in the saliva

adsorption literature, to which no comment is made in relation to the binding energies involved in adsorption. It is therefore unclear whether the electrostatic interactions referred to in the literature relate to strong ionic bonding associated with chemisorption, or weak dipole-dipole/hydrogen bonding/London forces associated with physisorption [115]. This adds another layer of complexity to the exact mechanisms of salivary pellicle adsorption. To further understand the exact pathways of salivary proteins adsorption, additional techniques would need to be applied to further differentiate the mechanisms associated with electrostatic interactions.

### **Adsorption kinetics and modelling protein adsorption**

Adsorption kinetics describes the interactions between an adsorbate on an adsorbent surface with respect to time. This can provide an insight into the mechanisms of adsorption from a mass transfer point of view, with molecules in an aqueous solution forming an interface with a given surface which can be dependent on the solution's flow rate, pH and temperature [135]. Kinetic adsorption models are theoretical models which can be used to assess the efficiency of adsorbent systems, by describing/predicting the adsorption behaviour from a given model. These have been used previously to assess catalysis, the adsorption of heavy metals, dye adsorption and contaminant removal [135, 136, 137, 138, 139]. The most used empirical models are the Pseudo First Order, Pseudo Second Order and Elovich models. The next sections describe these in further detail.

#### **The PFO model**

The PFO model, aka Lagergren model [140], describes the adsorption capacity of adsorbate to adsorbent as described in Eq. 1.

$$\frac{dq_t}{dt} = k_1(q_e - q_t) \quad \text{Eq. 1}$$

Where  $q_t$  is the mass adsorbed onto the surface at time  $t$ ,  $q_e$  is the mass adsorbed at equilibrium and  $k_1$  is the rate constant. This was integrated using the boundary conditions  $q_t = 0$ ,  $q_t = q_t$ ,  $t = 0$  and  $t = t$  for Eq. 1 to be re-written as Eq. 2.

$$q_t = q_e(1 - e^{(-k_1 t)}) \quad \text{Eq. 2}$$

#### **The PSO model**

The PSO model describes the rate of adsorption as proportional available active sites on the surface. The amount of adsorbate adsorbed on the surface acts as the driving force for



adsorption as over time the number of active sites reduces, reducing the adsorption rate. This is described in Eq. 3.

$$\frac{dq_t}{dt} = k_2(q_e - q_t)^2 \quad \text{Eq. 3}$$

Using the same boundary conditions used for the PFO model, this was integrated and rearranged into Eq. 4.

$$q_t = \frac{k_2 q_e^2 t}{k_2 q_e t + 1} \quad \text{Eq. 4}$$

This model was used to describe valence forces through the sharing of electrons between adsorbent and adsorbate and ion exchange [140]. This model was hypothesised to represent adsorption of adsorbate to adsorbent surfaces with an abundance of active sites [136].

### The Elovich model

The Elovich model assumes the surface to be energetically heterogenous with no interactions between adsorbed species [138]. The model provides a good fit to heterogenous surfaces which favour chemisorption as the dominant mechanism of surface adsorption and is described in Eq. 5.

$$\frac{dq_t}{dt} = \alpha e^{-\beta q_t} \quad \text{Eq. 5}$$

Where  $\alpha$  is the initial adsorption rate and  $\beta$  is the desorption constant and is related to the extent of surface coverage and activation energy for chemisorption [141, 135]. Like before this equation is integrated with the same boundary conditions as for the PFO and PSO model and is re-written in Eq. 6.

$$q_t = \frac{1}{\beta} \ln(t) + \frac{1}{\beta} \ln(\alpha\beta) \quad \text{Eq. 6}$$

### Model application to mucin adsorption

The PFO and PSO model are commonly used in the literature for adsorption kinetics [142]. Multilayers are more associated with physisorption whereas monolayers are linked to chemisorption [115]. These PFO and PSO models indicate whether adsorption is more inclined towards physisorption and chemisorption respectively, while the Elovich model relates to chemisorption onto heterogenous surfaces in aqueous environments. These models do not appear to be widely used in the literature when it comes to protein or mucin adsorption onto surfaces. This seems odd considering a protein or mucin is essentially an

adsorbate within an aqueous solution which adsorbs onto an oral or dental adsorbent surface. Furthermore, mucin adsorption tends to be described qualitatively, as slow adsorption or quick adsorption, with no application of an adsorption model [143].

For general protein adsorption, alternative models like the Langmuir kinetic model have been used. This model is like PFO and PSO models, which examine the surface coverage with respect to time. The model assumes a fixed number of contact sites exist and the surface coverage relates to the proportion of free contact sites available during adsorption [144]. This is described by Eq. 7, where  $C$  is the protein concentration in solution,  $\theta$  is the area coverage,  $k_a$  &  $k_d$  are rate constants and  $B(\theta)$  is the blocking function. The blocking function relates to the of surface coverage as  $B(\theta) = \theta_\infty - \theta_t$  where  $\theta_\infty$  is the surface coverage at equilibrium and  $\theta_t$  is the surface coverage at time  $t$ .

$$\frac{d\theta}{dt} = k_a C B(\theta) - k_d \theta \quad \text{Eq. 7}$$

The Langmuir model is limited in terms of determining the adsorption pathways, providing a simplistic understanding of the adsorption rate onto a fixed number of sites. This universal model cannot therefore be used to determine the chemical/physical interaction during the adsorption process, especially when multilayers are concerned. Therefore, for the purposes of this work the PFO, PSO and Elovich models would be used to provide further insight into the mucin adsorption pathways onto dental surfaces.

### 2.2.3 Dental tribology and the operational environment

In order to investigate saliva substitutes in vitro, a suitable operational environment is required for testing. This sub section aims to address aspects suitable test materials, associated biomechanics for dental tissue/material testing, types of wear expected and the implications of a corrosive environment.

#### 2.2.3.1 Considerations for wear testing tooth enamel and dental biomaterials

In restorative dentistry, biomaterials are engineered and applied to restore functionality and enhance the quality of life of patients in need of therapeutic relief. The biomaterials used for artificial crowns aim to restore tooth functionality by emulating the mechanical durability of teeth within the oral environment. However, these materials need to be tested to understand how the material itself wears and how the material influences the wear of neighbouring or opposing teeth. The interface behaviour is important from a tribological point of view to prevent excessive wear of either the biomaterial or the opposing enamel surfaces, which may result in a further need for restorative dentistry [145]. Enamel and

biomaterial interactions must therefore be properly tested under relevant simulated conditions. ISO TS 14569 [146] provides guidance on several methods which can be used to conduct wear testing of dental restoration materials. Alumina, steatite and human tooth enamel are materials documented in the ISO as appropriate standard materials to new test materials against, to understand the effect of new materials interfaced against natural teeth. While this provides an indication of how to conduct standardised testing of materials, there are a few limitations to the methods presented relating to the test materials used.

Alumina is a ceramic which has been used as tooth crown material, however recent developments in the use of ceramics has seen a rise in the use of stabilised zirconia ceramics as a promising dental biomaterial [147, 148, 149]. Steatite is considered to be a suitable alternative to tooth enamel for wear testing purpose as it overcomes issue with shaping enamel counter surface. However, there is evidence steatite exaggerates wear rates on composite materials compared with enamel [150]. Whereas, human tooth enamel is an ideal material for wear testing, possessing the mechanical, chemical and structural properties expected for teeth in vivo. Once again there are drawbacks to this material for dental wear testing such as tooth variability of chemical composition and structure that manifest from varying lifestyles, age, gender and species. Furthermore, the complexity of manufacturing or preparing enamel test pieces can be particularly challenging if a hemispherical pin is required. The next subsections further expand on these materials.

#### **Yttria stabilised Zirconia Tetrahedral Polycrystalline (Y-TZP) ceramic**

Y-TZP ceramic is a yttria doped (3 mol %) zirconium dioxide ceramic material which is commonly used for the fabrication of artificial tooth crowns and fixed partial dentures. The addition of yttria permits structural stabilisation of the zirconia at room temperature in a tetragonal conformation. The use of Y-TZP became popular in 2008, due to the improved material properties from doping, which are important to prevent fractures that go on to cause excessive enamel wear [148]. It possesses a higher flexural strength and toughness, of 0.9-0.15 GPa and 2.2-4.5 MPa.m<sup>1/2</sup>, compared to glass ceramic and other metal-free alternatives used for tooth replacement purposes, and an elastic modulus between 200-210 GPa [148]. Monolithic Y-TZP crowns possess good long-term durability, biocompatibility, chemical inertness and aesthetics close to natural tooth enamel [148]. While alumina is suggested as a suitable test material, it is considerably more brittle in comparison to the toughened Y-TZP. As the use of Y-TZP is becoming more common, wear testing should adapt to mirror the material changes in current dental biomaterials. Y-TZP is therefore a suitable

standard material to perform tribological testing with, as it represents a modern cusp of an artificial crown.

Limitations do exist with Y-TZP ceramics for as it has the tendency for its crystal structure to change at relatively low temperatures and humid environments, a phenomenon known as low temperature degradation. A phase change occurs from a tetragonal crystal structure to one which is monoclinic, which has been associated with catastrophic failure of femoral heads in the field of orthopaedics [151]. On the other hand, assessment of this ageing behaviour for dental applications has concluded it is still clinically suitable [152].

### **Steatite**

Steatite is a magnesium silicate ceramic which classed as an antagonist wear material for the wear testing of dental materials [146]. It is a semi porous ceramic which has been observed to possess similar abrasive and friction characteristics to tooth enamel, and was suggested as a homogenous alternative to tooth enamel for frictional wear tests [150]. It has an elastic modulus of 100-103 GPa and flexural strength of 0.12-0.48 GPa, closer to the mechanical properties of tooth enamel [153, 154]. Contrary to this, another study concluded that steatite was not a suitable tooth enamel alternative as it was shown to be twice as hard as it's enamel counterpart and possessed a greater wear resistance [155]. Although it isn't an ideal alternative to tooth enamel, it is considered to a suitable antagonist material for in vitro material testing. It is not fully clear whether this material would be suitable in terms of wear testing in environments other than water, which would need to be investigated further to determine the feasibility of this material for artificial saliva testing.

### **Tooth enamel**

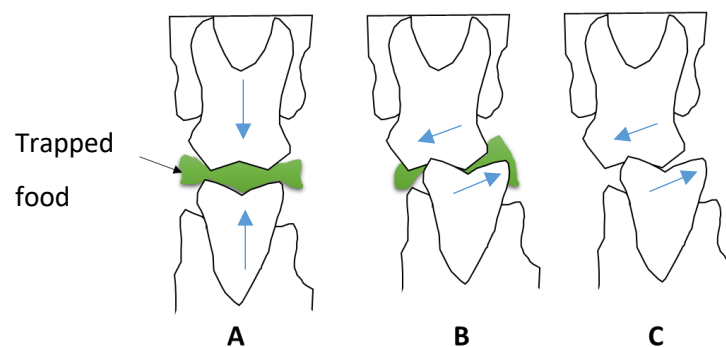
Tooth enamel has been commonly used in the literature in the area of dental tribology, oral tribology and dental erosion [156, 29, 31, 27] Bovine enamel has also been used in the literature for numerous wear and erosion studies due it's chemical composition and structure being the closest alternative to human tooth enamel [41, 48, 157]. The reason behind the use of alternative enamel models relates to the difficulties associated with the acquisition of sound human tooth enamel samples. Animal enamel models provide a more accessible alternative, with minimal variation to the raw samples compared to the age, diet and lifestyle factors that can influence the composition and structure of human enamel over time.

#### *2.2.3.2 Biomechanics of mastication*

Teeth are primarily used for the process of mastication, where food is sectioned, crushed and ground into smaller pieces before ingestion. Types of teeth include incisors, canines,

premolars and molars. Mastication occurs in two phases, open phase and closed phase as illustrated in Figure 2-12 [158]. Open phase begins the cycle where the jaws start in an open position and are brought together over the food bolus with no occlusal contact. The closed phase involves the continuation of jaw but with occlusal loading being applied throughout the food by opposing surfaces of the teeth. The food is dragged across the surfaces and crushed. A translational motion then occurs causing grinding of the food or teeth by indirect or direct loading.

Occlusion can occur outside masticatory conditions in the form of thegosis and bruxism, which are voluntary and pathological respectively. Both involve the direct contact and grinding of opposing teeth without food particles separating occlusal surfaces. Thegosis is the process of sharpening one's teeth by grinding, while bruxism is an involuntary clenching or grinding in stressful situations or during sleep [159]. Bruxism can cause significant wear and even damage, affecting approximately 8% of the adult population and being most common between the ages of 25-44 [160].



**Figure 2-12 Tooth contact diagram. A) Open phase. B) Closed phase. C) Thegosis/Bruxism [158]. Arrows indicate motion of teeth**

The mastication cycle lasts approximately 0.7 s with an occlusal time of 0.1 s [158]. When in contact, sliding distances between teeth range from 0.9-1.2 mm at speeds of 0.25-0.50 mm/s [161]. Loads during mastication vary throughout the cycle with initial contact loads of 10-20 N up to 50-150 N towards to the end of the chewing cycle [162]. The required load for mastication is ultimately dependent on the physical properties of the food with harder food requiring more force and softer food requiring less. Furthermore, this only amounts to a fraction of the total bite force produced by an individual which can vary depending on age, sex and muscle build. The maximum bite force can range from 600-1200 N with 80% of this being distributed over posterior teeth and 20% over anterior [163].

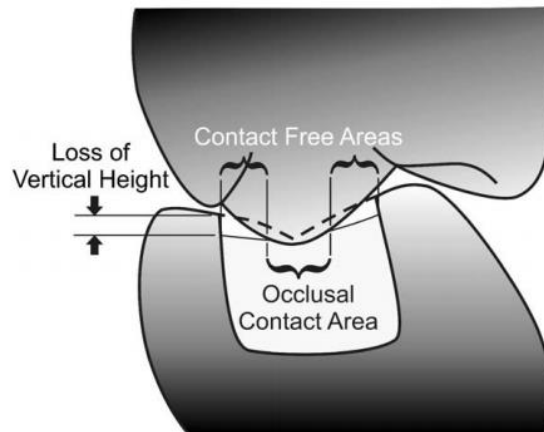
Finally, when considering the contact pressure observed during mastication there appears to be varying results observed. In the work of Anderson, maximum pressures of between 4-18 MPa were observed for processing biscuit, meat and carrot samples [164]. While on the

other hand a finite element model in another study predicted a maximum pressure for the mastication of a bone like substance to be 40 MPa [165]. This suggests that normal mastication pressures will change due to loading and the properties of the food being processed.

### *2.2.3.3 Mechanical wear types, contact mechanics and wear locations*

Wear of dental tissues and materials can be caused by four different factors; physiological, pathological, use of a toothbrush and dentifrice interaction [162]. The physiological processes of mastication result from 'attrition' and 'abrasion' (in dental terms). 'Attrition' is associated with tooth-on-tooth contact wear, during the impact and sliding of the closed phase of mastication. Thegosis and bruxism are also forms of attrition outside of mastication. 'Attrition' is more akin to two body abrasion in tribology, which relates to the mechanical loading of a body's surface asperities, cutting away the surface of a counter body when in relative motion [166]. 'Abrasion' relates to three body abrasion in tribology, where additional abrasive particles are present in the contact interface. These can include: abrasive particles from toothbrushing, or food particles during mastication.

Two body abrasion is the main cause of wear of the occlusal surface of human tooth enamel and leads to progressive material loss and flattening over the years [167, 166]. An in vivo study estimated steady state wear on occlusal contact areas ranged from 15 – 29  $\mu\text{m}$  per annum [168]. In addition to this, wear can occur on both the buccal surfaces (closest to lip) and lingual surfaces (closest to tongue) of teeth from abrasive food particles during mastication [167]. Normally during mastication, food can act as a lubricant over enamel – enamel contacts reducing the coefficient of friction and with a reduced pressure (as forces are distributed over a larger area) three body wear produces a smaller amount of wear compared to two body wear. However, in some studies on early composite functional surface materials it was noted that there was significant wear in locations where no occlusal contact occurred leading to the concept of the occlusal contact area and contact free occlusion area [169]. Figure 2-13 demonstrates the concept, where the cusps of the teeth come into direct occlusal contact with the opposing surface where two body wear is expected. Surrounding this area there is no direct contact between the teeth, however wear can still occur from entrained food particles, making up the rest of the wear in these locations [170]. Given the motion of teeth during mastication, it can be assumed that any wear track presents evidence of two-body wear in direct occlusion areas while evidence of 3 body wear directly outside of this in indirect occlusion areas.



*Figure 2-13 Diagram of contact and contact free areas of occlusion [170].*

The extent of wear from abrasion can depend on the hardness properties of the interacting bodies, the mechanical loading/ contact pressures and the amount of relative motion between bodies. These can contribute to different mechanisms of wear on the enamel surfaces. Ploughing, micro-cutting, chipping, polishing and micro-cracking are mechanisms associated with enamel abrasion which ultimately influence the material loss volume [171, 172]. The repetitive impact and sliding of mastication cycles also enhance the propagation of subsurface microcracks, referred to as fatigue wear [172]. When these cracks propagate to the surface, delamination can occur removing superficial fragments of tooth enamel.

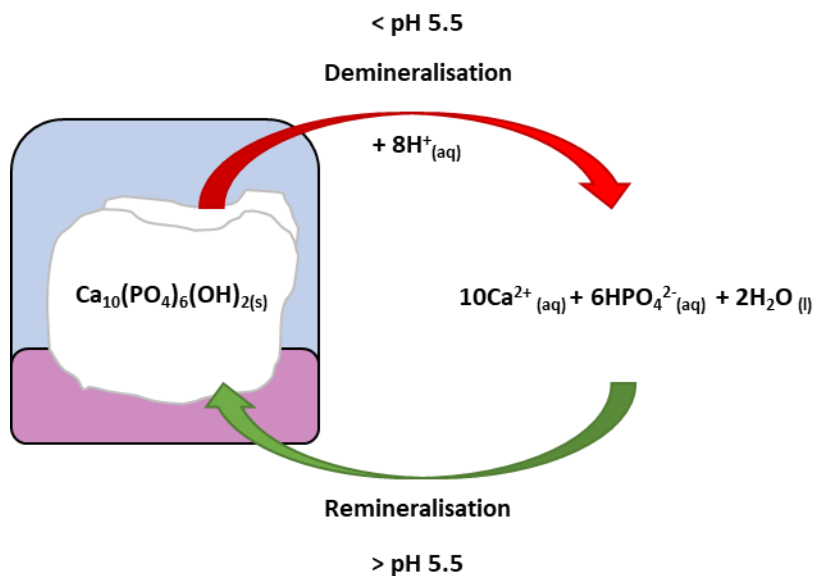
#### *2.2.3.4 Dental erosion (corrosion)*

##### **Defining corrosion in dentistry**

In tribology, “erosion” is the damage of a surface caused by the impact of solid or liquid particles. Consequently, the volume of erosive wear is dependent on the particle material, size, impact velocity and impingent angle [173]. This definition of wear is considerably different to what erosion refers to in dentistry. “Dental erosion” is a condition which is influenced by chemical, biological and behavioural factors. Cate and Infeld [174] define it as a pathological, chronic and localised loss of dental hard tissue resulting from chemical etching by acids or chelation, ignoring acidic products of bacteria. Rather than the impact of high velocity particles removing tooth material, extrinsic and intrinsic chemicals are associated with erosion in dentistry. This definition is closer to what engineers refer to as “corrosion”, where materials degrade due to chemical and/or electrochemical processes [26]. The common factor between corrosion and dental erosion is that fundamentally they are the result of a chemical reaction or influence leading to surface material degradation and loss. It could therefore be said that dissolution, demineralisation and dental erosion all come under the theme of corrosion.

## Teeth and corrosion

Corrosion of tooth enamel can occur in two stages. The initial stage of corrosion causes enamel softening by demineralisation, which can be reversed [175]. Demineralisation occurs under acidic conditions on the superficial surface of the tooth. This involves the removal of calcium mineral ions ( $\text{Ca}^{2+}$ ) from the hydroxyapatite crystals in the enamel, dentine or cementum which progressively lead to tooth degradation. This is usually caused by acidic attack from the diet, certain pathologies or acids produced by oral bacteria. Hydrogen ions within acidic solutions directly attack phosphate or carbonate groups of the hydroxyapatite prisms which make up the structure of tooth enamel, as shown in Figure 2-14 [38]. If acids that interact with teeth contain carboxylic acid groups, these can dissociate and become chelating agents. These go for the cations in teeth, the calcium, and can form strong complexes. Therefore, different types of acid lead to different rates of dissolution, independent of pH, releasing calcium and phosphate ions into the oral environment [176]. Figure 2-14 shows the chemical equations for the cycle of demineralisation and remineralisation.



*Figure 2-14 Demineralisation and remineralisation of hydroxyapatite in teeth.*

If acid is removed and the pH rebalanced by saliva, remineralisation can take place which is the reverse process of demineralisation. This occurs when conditions are no longer acidic, preferably above pH 5.5 or even slightly alkaline, and there is sufficient saliva saturated with calcium and phosphate ions to allow repair of partially demineralised hydroxyapatite crystals. Fluoride ions may also influence remineralisation, replacing the hydroxyl groups to form a fluorapatite crystal which is considerably less soluble than hydroxyapatite [177]. Statherins in saliva and the pellicle have also been seen to keep high concentrations of

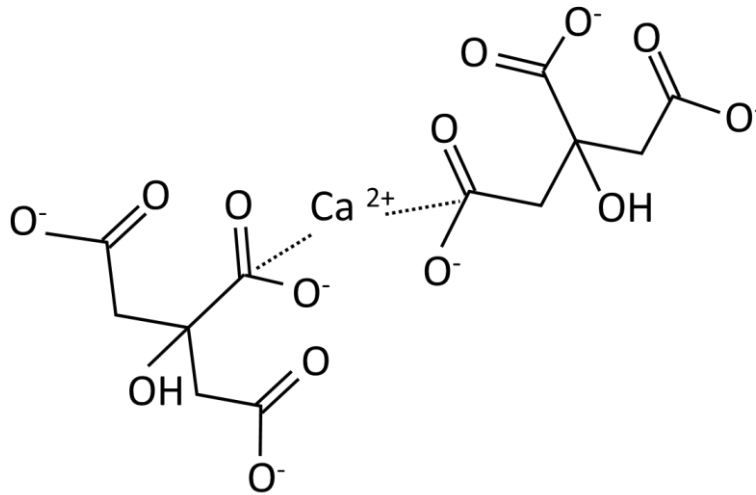


calcium and phosphate ions close to the tooth's surface, leading to slower dissolution rates in these regions [177].

### Causes/Factors influencing dissolution

As mentioned above, corrosion in dentistry can be influenced by 3 types of factors; chemical, biological and lifestyle factors. The saturation of calcium and phosphate in food stuff is of great importance regarding demineralisation. While an oversaturated solution has no effect on the dissolution of tooth enamel, under-saturated solutions can cause mineral ions to leave the enamel surface while also causing a local increase in pH. This occurs until the liquid layer surrounding the tooth enamel is saturated, softening the outer enamel.

Acids like citric acid can be quite problematic due to the way they attack teeth. When the acid dissociates in water, hydrogen ions and citrate anions are released. The hydrogen ions directly attack the crystal structure, usually going for carbonate or phosphate groups. The citrate anion on the other hand directs its attention to calcium, forming an anion calcium complex which can remove calcium ions from the crystal structure, an example of this is shown in Figure 2-15. The strength of these complexes can depend on the structure of the anion calcium complex and how easily it can attract calcium ions.



*Figure 2-15 Calcium citrate complex example where two citrate anions have complexed a calcium cation.*

In one study, 32% of calcium ions in saliva were observed to be complexed by the citric acid present in common fruit juice [178]. This reduced the supersaturation of the saliva with respect to the tooth enamel and resulted in the increase of demineralisation. While increasing the calcium and phosphate content of foodstuff and beverages does not completely stop corrosion in teeth, it can significantly reduce the amount of wear. This is shown in a study conducted by Hughes et al where calcium salts were added to blackcurrant

juice and compared to orange juice, reducing the erosive potential [178]. Fluorides may also provide additional protection, especially in terms of tribo-corrosion. Sodium fluoride solutions have shown a reduction in enamel corrosion and abrasion compared to non-fluoride solutions and dentine under the same treatment [179].

Exercise can also have an impact on tooth dissolution. Heavy exercise can lead to dehydration, resulting in reduced salivary flow, clearance and buffering capacity. Consuming sport drinks afterwards would also enhance demineralisation as there are less biological protective factors preventing this. Swimming also can influence this as, in some instances, the pH of a pool will be low due to the use of sodium hypochlorite for cleaning [6]. Again, drinking sports drinks straight after would enhance demineralisation. As well as the extrinsic acid interactions, there is also the risk of intrinsic factors. Vomiting, regurgitation, gastroesophageal reflux and rumination can introduce gastric acids to dental and oral tissues. These tend to have a pH between 1-1.5 which is considerably lower than that critical dissolution pH of enamel which is pH 5.5 [180]. Psychosomatic conditions like anorexia and bulimia, endocrine disorders, reflux and poor oral hygiene habits can also lead to increased tooth dissolution.

The erosive potential is a determining factor on the progression of tooth dissolution which is determined by 4 things; the type of acid interacting with dental hard tissues, the pH, the titratable acidity which is the total concentration of protons and undissociated acids in a solution that can be neutralised with a strong base, and the chelating properties. There are two ways of preventing erosion, either by decreasing the erosive potential or increasing tooth resistance and protection.

#### *2.2.3.5 Wear mechanism synergism - Tribocorrosion*

In the oral environment, a combination of corrosion and abrasion can occur simultaneously which can have a great effect on tooth material loss. Corrosion of enamel can result in a softened, degraded surface from demineralisation and dissolution. The enamel softening that occurs is dependent on the severity and frequency of acid exposure [181]. Should the enamel remain in contact with an acid, this can lead to a layer-by-layer loss of surface enamel, which cannot be reversed [175]. When combined with the mechanical sliding of an opposing body, approximately 200% more wear can be observed compared to alternative cycling of corrosion and abrasion [182]. This presents a potential area to further investigate the role of tribocorrosion.

## 2.3 Literature review of in-vitro experimental methods to investigate tooth tribocorrosion and the effects of protein layers

It is unclear what components of artificial saliva's are necessary for the protection of enamel against tribocorrosion. Most studies in the area utilise static corrosion models, where enamel samples are immersed in either an acid or artificial saliva, followed by subsequent surface hardness measurements and/or calcium ion release into solution [106, 183, 30]. While this does provide information on the effects of remineralisation and demineralisation of artificial saliva and acid solutions respectively, it focuses on the *corrosion* aspect of overall tooth material loss. However, a combination of mastication in a corrosive environment may enhance tooth material loss from these interactions and potentially their synergetic effects between mechanical and chemical wear.

### 2.3.1 Tribology and tribocorrosion studies on tooth wear

The tribology of teeth is an area which has gained interest in recent years. Due to the complexity of teeth in the oral cavity many of these studies were in vitro lab simulations. This allows more control to determine individual influences on friction and wear behaviour. Zhou et al [162] are one group which have looked at the microstructure and mechanical properties of teeth, the age of teeth and the predominant wear mechanisms of teeth under reciprocating sliding conditions. The sliding phase of mastication is an important area of study considering that peak loading occurs during this phase, in addition to the more severe sliding conditions associated bruxism. As well as the mechanical side of things, they have also integrated aspects of the oral environment in their testing to determine influential factors from both biological and chemical origins on the friction and wear behaviour of teeth.

#### 2.3.1.1 *Friction and two-body abrasive wear under wet and dry conditions*

Li et Zhou [184] examined the dry and lubricated sliding conditions on tooth wear. The artificial saliva used acted as a coolant and lubricant in the wear process compared to an unlubricated, dry condition; much like the hypo-salivary like conditions of xerostomia. The wear scar depth under lubrication was approx. 10  $\mu\text{m}$  compared to a depth of 21  $\mu\text{m}$  under no lubrication. While this was an in vitro preliminary study, it does provide an insight into how saliva might influence tooth wear in vivo. Reciprocating tests were conducted under a ball on flat configuration, using a pure titanium and a 52100-grade steel ball, as presented in Figure 2-16 [184]. Test conditions were conducted at 20 N, which would provide max contact pressures ( $P_{\text{max}}$ ) between 100 – 130 MPa as calculated by Hertzian contact

mechanics, assuming the elastic moduli of the dentin used was between 10 – 15 GPa as shown in Table 2-1.

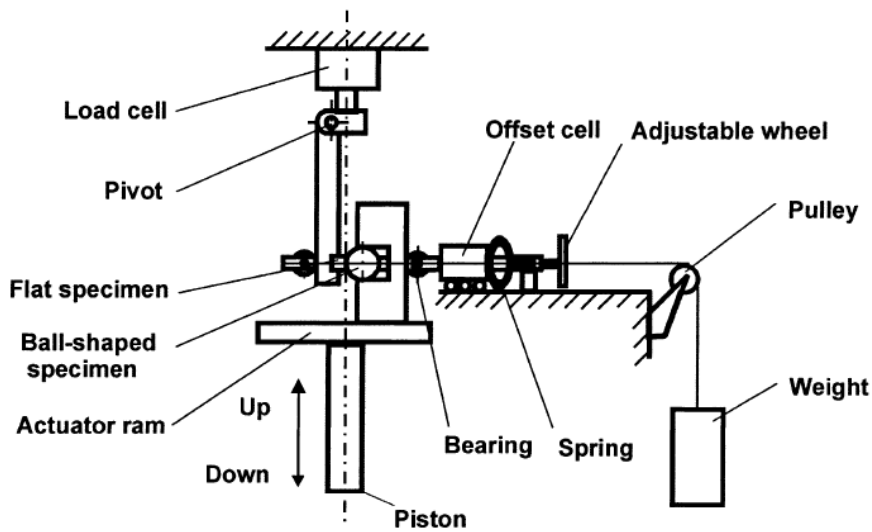


Figure 2-16 Schematic of friction and wear test rig [184]. Normal load is applied using the weight and pulley system, holding the flat sample against the ball. The piston reciprocates up and down to permit small scale displacement of the ball against the flat sample.

Pure titanium provided a more realistic contact pressure compared to steel, in addition to the oxidation of the steel surface and surface heating. While these results did not compare the impact of an artificial saliva on the friction and wear behaviour of a tooth enamel surface, they did indicate the role saliva has on reducing friction and wear. The coefficient of friction results are outlined in Figure 2-17.

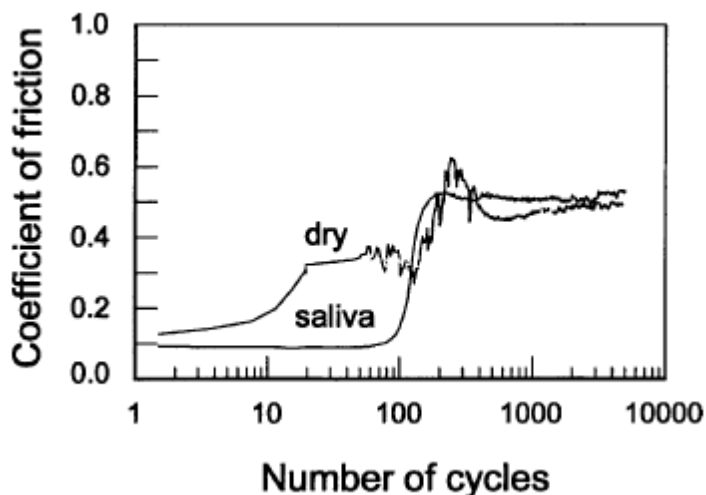


Figure 2-17 Friction of pure titanium against tooth dentin under dry and wet conditions over 5000 cycles [184]. After 100 cycles both present an increase in particle build up in contact when coefficient of friction increases.

Under dry conditions, the coefficient of friction (COF) increases to about 0.3, which become more unstable leading to a further increase up to over 0.6 before settling to 0.5. Conversely,

the friction remains low for the first 100 cycles before increasing and settling at 0.52 in artificial saliva [184]. Particle detachment and delamination could be one explanation to the destabilisation of the coefficient of friction under dry conditions. Interestingly the artificial saliva solution used contained 1 g of Urea, which changed to 2.2 g of porcine gastric mucin in later studies by the same authors. The composition of the artificial saliva use in the first study is displayed in Table 2-6. What is interesting is that the mass of urea is lower than the protein composition found within saliva.

*Table 2-6 Composition of artificial saliva used in [184].*

<b>Substance</b>	<b>Amount</b>
<b>NaCl</b>	0.4 g
<b>KCl</b>	0.4 g
<b>CaCl<sub>2</sub>.2H<sub>2</sub>O</b>	0.795 g
<b>NaH<sub>2</sub>PO<sub>4</sub>.2H<sub>2</sub>O</b>	0.78 g
<b>Na<sub>2</sub>S.9H<sub>2</sub>O</b>	0.005 g
<b>Urea</b>	1 g
<b>Distilled water</b>	1000 ml

Another study examined wet and dry sliding conditions on bovine enamel at the nanoscale [185]. Sliding tests were performed under a conical diamond indenter tip (radius of 1200 nm) with normal loads of 400  $\mu$ N, yielding a  $P_{\max}$  between 4.641 - 11.624 GPa. These pressures are much larger than previously mentioned study, and their results should be considered accordingly. The area of abrasion, from two body wear, was larger in the dry condition compared to the wet hanks balanced salt solution (HBSS) condition. While it was suggested that these differences may have been due to the method of cleaning the samples, it does also indicate that there is a resistance to two body wear under the HBSS condition, which highlights the importance of salt interaction with enamel [185].

A brittle fracture mechanism may have been observed in the later stages of wear testing under dry conditions conducted by Li et Zhou [184]. However, it's hard to compare the wear mechanisms described in these studies due to limiting factor related to test methodologies. The higher contact pressures from the diamond nano-scratch tip are physiologically unrealistic, which is attributed to the normal loading, counter face material and counter face geometry used for testing. Under these more physiological conditions, a different mechanism might be observed. Scratch tests on bovine enamel suggested plastic asperity

deformation and sub surface fatigue mechanisms occurred in both wet and dry conditions. Enamel wear under high contact pressures may initially start by plastic deformation at the surface which is followed by sub surface crack formation after repetitive loading/sliding cycles. Propagation of these cracks may then lead to surface enamel removal by delamination, exposing softer subsurface enamel into the interface. Particle detachment also introduces potential a 3<sup>rd</sup> body element to tests.

### 2.3.1.2 Friction and three-body abrasive wear in lubricated conditions

The impact of 3<sup>rd</sup> body particles on tooth wear was examined, using a rig which incorporated a food slurry bath as shown in Figure 2-18. Ground mill seeds and rice were used to simulate food particles under masticatory loads of 10 N, 20 N and 40 N [186]. This related to  $P_{max}$  between 120 – 385 MPa of the two-body system (titanium ball on enamel), excluding the 3<sup>rd</sup> body particles, which is much larger than the 40 MPa contact pressures observed during mastication [165].

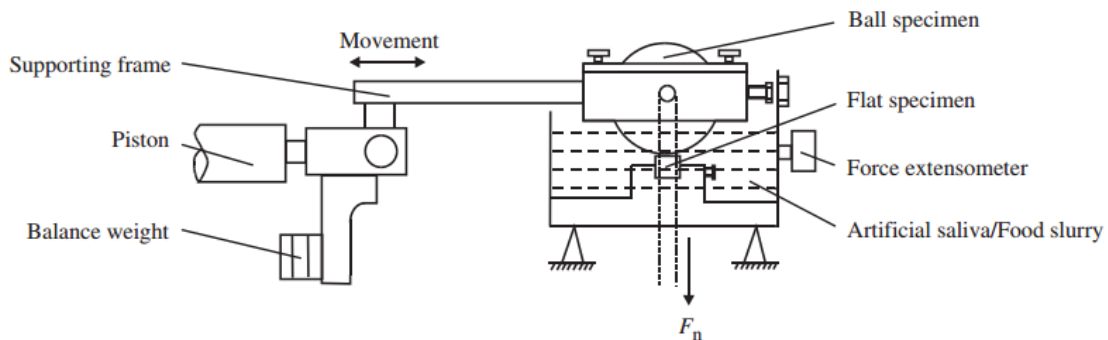
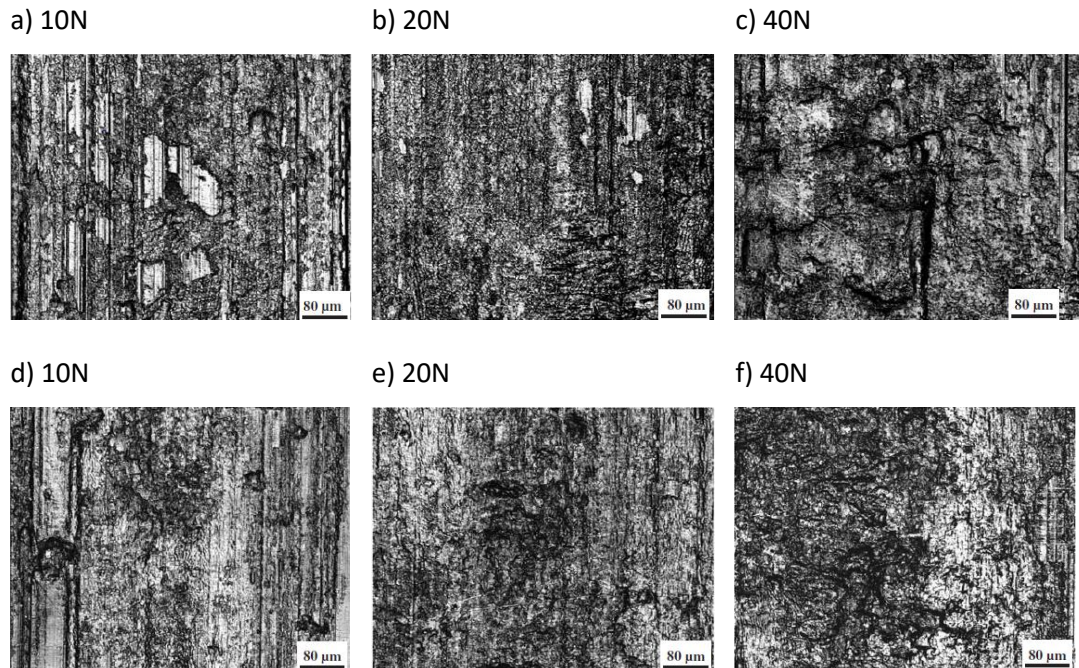


Figure 2-18 Schematic of 3<sup>rd</sup> body wear testing rig [186].

Test performed at 20 N under artificial saliva conditions presented a different friction behaviour to the previous study [184] as the coefficient of friction increased from 0.2 to 0.8 before reaching 100 cycles, which further increased to 1.0. Differences between the coefficients of friction, 0.52 when stabilised compared to > 1.00, might be attributed to the surface materials used, dentine in one study and enamel in the other. A similar friction behaviour was observed under 10 N. Under higher loads, 40 N, changes to the coefficient of friction occurred much earlier, however remained at 0.8 for the remainder of testing, lower than the lower loads [186]. The addition of a 3<sup>rd</sup> body element reduced the coefficient of friction towards the later stages of tests when compared to the two-body tests for all loads. Aside from the friction, the surfaces were also examined with an optical microscope to characterise the wear in terms of incremental loading and abrasion type, as shown in Figure 2-19. In both two and three body wear modes the wear volume was observed to increase

with normal load, which steadily increased under the three-body condition and considerably increased under the two-body condition [186]. Once again, evidence of ploughing leading to brittle surface delamination was observed for the two-body wear conditions, displayed in Figure 2-19a) b) and c).



**Figure 2-19** Wear areas of enamel surfaces under optical microscope. Two body wear tests are displayed for normal loads of 10 N a), 20 N b) and 40 N c). Three body wear tests are displayed for normal loads of 10 N d), 20 N e) and 40 N f) [186].

Under three-body conditions, evidence of ploughing was present along with pitting on the surface. No evidence of surface layer delamination was observed.

This study showed that that considerably more wear was attributed to two-body abrasion compared to three-body abrasion. These results also link to the habitual grinding of enamel by bruxism or thegosis. Ploughing and delamination wear mechanisms have also been observed in similar studies under more repetitive loading conditions [158]. When compared to the earlier two-body studies, the test conditions influenced the observed wear mechanisms, with surface ploughing appearing to be a more prominent factor leading to enamel wear.

### *2.3.1.3 Influence of an acidic environment on friction and wear behaviour*

Aside from two and three body contact under lubricated conditions, the role of acids within the operating environment have been investigated in vitro. This provided further insight into the chemical wear associated with tooth enamel.

Tribo-tests have been performed in solutions which may commonly enter the oral environment, including red wine and apple juice which contained tartaric acid and malic acid respectively [29]. An enamel cusp on enamel plane pin-on-disc configuration was used for tribometer set up. Loading was cyclical with a mean normal load of 35 N, relating to a calculated  $P_{\max}$  between 0.713-1.860 GPa, and the test solution's pH was varied [29]. Variation in the friction and wear were determined by splitting samples into two groups; high wear and low wear. The coefficient of friction of high wear sample increased over the test duration from 0.18-0.21 to 0.2-0.3 for pH 3.25 red wine and pH 3.46 apple juice respectively [29]. The low wear sample at the same pH displayed the opposite friction behaviour, with the coefficient of friction decreasing from 0.20-0.10 and 0.22-0.14 for red wine and apple juice respectively [29]. This behaviour indicated that the pH and acid type alone are not the only factors which influence the friction behaviour of the whole system.

Surface examination with scanning electron microscopy provided evidence of crater formation the removal of large fragments from the surfaces of high wear apple juice sample compared to smaller flake removal on low wear samples [29]. Red wine samples presented a smoother surface to the apple juice samples, and evidence of surface cracking on the high wear samples [29]. Differences to friction and wear behaviours were explained by the presence of a "dissipative structure" in these acidic environments, a term which isn't made particularly clear and was assumed to be related to the formation of a thin surface film/layer [29].

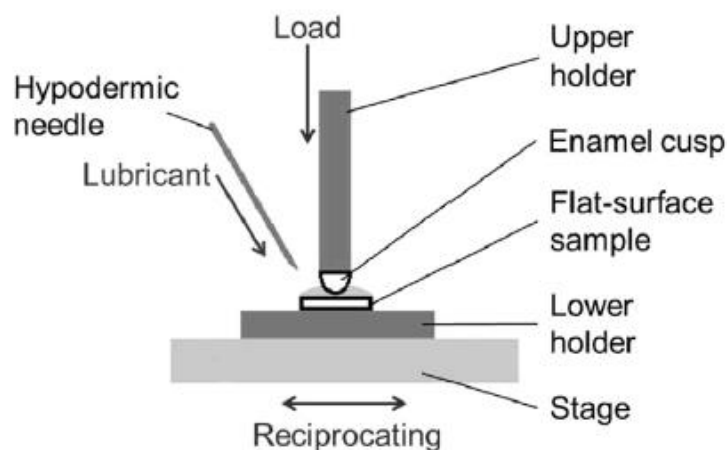
In other studies, isolated acids have been studied to mitigate the effects of additional components on the friction and wear behaviour. Acid reflux conditions were examined using hydrochloric acid for loads of 32 N, 36 N and 100 N ( $P_{\max}$  between 528 – 814 MPa) between enamel and dentine tribo-couples [187]. Below pH 2.2, enamel was observed to produce more wear than the dentine, an interesting behaviour considering the hardness of enamel compared to dentine. Above this pH, the reverse was observed. Furthermore, more surface wear was attributed to test performed in the control solution, deionised water, compare to pH 3 conditions [187]. This further illustrates the complexity of the role of acid on the friction and wear behaviour of tooth enamel. In this case, it was thought that the weaker acids interact with the enamel surfaces, leading to enamel softening and therefore reducing the contact pressure involved. This would change the wear mechanism from brittle fracture and surface delamination to a ploughing mechanism, attributed by a smoother wear scar [187]. Enamel softening (decreasing surface hardness), observed by nanoindentation methods, occurred rapidly within the first few minutes of exposure to citric acid, as the softening rate



decreased with exposure time [30]. Nanoscratch tests on the acid exposed enamel also increased the coefficient of friction with exposure time [30]. Despite different scales of testing, these results expand on the behaviour observed in the high wear samples discussed previously [29].

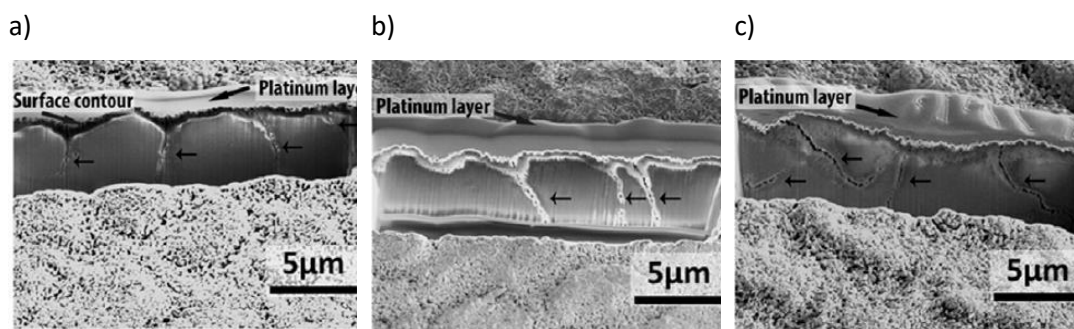
Further studies on the effect of erosion depth and its tribology after acid treatment showed changes to the enamel moving from the outside surface inwards. Hardness was shown to decrease from the outside of the tooth inwards while the substance loss and wear volume increased [31]. This suggests two things about the hardness of enamel, acid interactions reduced surface hardness and, hardness decreased with depth from the outer surface. Both aspects are important when it come to the preparation of samples for testing and subsequent test results. Furthermore, more dissolution occurred in the centre of the enamel rods compared which resulted in a rougher surface profile [31].

Further studies investigated the wear behaviour of enamel under low and high load sliding conditions in a citric acid environment to find corrosive wear to be more predominant under low loading conditions [188]. This is particularly the case for citric acid at lower pH values. Another study used a pin-on-disc tribometer with a hypodermic needle to simulate lubricant flow, as shown in Figure 2-20. The study compared the pH of acetic and citric acid on friction and wear behaviour [27]. Wear volumes were larger under low pH conditions compared to high pH conditions, presenting a reduced elastic modulus and surface hardness [27]. The coefficient of friction behaviour was similar to the low wear samples in the red wine and apple juice study [29] with a reduction in friction over the test duration. Brittle delamination was also observed, similar to [188], with visible surface flake removal from the surface. Removal of the outer enamel layer combined with acid softening also resulted in a smooth work area attributed to ploughing.



*Figure 2-20 Wear test configuration with lubricant flow [27].*

Interestingly, wear under acetic acid conditions was comparable to that of deionised water and less surface wear was observed under citric acid conditions. This may ultimately relate to how the solution interacts with surface which impact the wear mechanisms under these different environments. Furthermore, it was hypothesised that the penetration of the acid into the bulk material may also influence the surface and subsurface mechanical properties [27]. This was further investigated with a similar set up for lactic, acetic and citric acid between pH 3.2-3.5 [28]. Similar wear mechanisms were observed for deionised water and acidic conditions to the previously mentioned study [27], however focused ion beam examination provided a greater insight into the subsurface changes of enamel. Perpendicular subsurface cracking was observed for lactic and citric acid environments while U shaped cracks were observed for acetic acid, as shown in Figure 2-21.

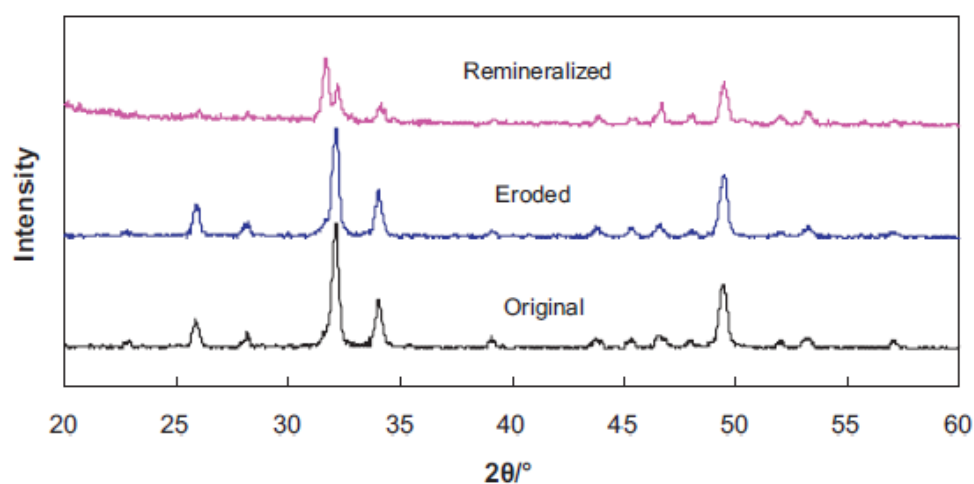


*Figure 2-21 Focused ion beam images of subsurface enamel cracks after exposure to a) citric acid, b) lactic acid and c) acetic acid [28].*

Both deionised water and acetic acid had a similar coefficient of friction, of 0.72 and 0.75 respectively, and produced rougher surfaces compared to the other acids [28]. Acetic acid was hypothesised to cause more dissolution due to its relatively smaller size in term of molar mass compared to lactic and citric acidic molecules. However, this fails to explain how citric acid possess a greater dissolution ability to lactic acid, as the molar mass of the former is greater. This is where the structure of citric acid may influence dissolution, as citrate anions possess a high affinity to calcium ions which may increase the rate of dissolution independent of size and surface penetration [28].

Aside from dissolution and corrosive wear, one study has studied the remineralisation effects of gallic acid on tooth enamel [189]. After acetic acid exposure gallic acid was used as a calcium ion carrier to remineralise the enamel, changing the wear behaviour from plastic deformation on untreated surfaces to brittle fracture on treated surfaces [189]. It was suggested a more brittle layer was formed in the absence of enamel matrix protein that would enable more energy dissipation. The same effects were observed for surfaces

exposed to acid and remineralised with an artificial saliva solution, where the hardness was partially restored [32]. X-ray crystallographic examination indicated that the peak intensities of the original and eroded samples were much higher compared to that of the remineralised samples [32], shown in Figure 2-22, indicating a reduction in enamel crystallinity. While teeth samples can be compared to some degree, these two studies indicated that remineralisation will not fully allow the enamel to regain its original properties after exposure to an acidic solution. Instead, a more amorphous hydroxyapatite structure is formed without organic components, creating a more brittle and rougher surface which may be easily removed later down the line.



*Figure 2-22 X-ray diffraction patterns for control (original enamel before corrosion), eroded and remineralised enamel [32].*

### 2.3.2 Protein films on corrosion

There are very few studies which examine both the tribology and protection of protein films that form on enamel surfaces. Studies have mainly focused on the influence of a protein or saliva film on enamel during corrosion alone. Pellicle formation studies which use whole human saliva can be complicated due to the time constraints of: gathering healthy volunteers, collecting saliva in a safe and responsible manner, pooling it together and storing it for a limited period. Once removed from the donor, it must be used as soon as possible before it begins to degrade and exhibit properties that are different to saliva in-vivo. A lot of work has used artificial saliva due to this issue as it is inexpensive and easier to get a hold of for in vitro testing for erosion studies. This provides an initial insight into the capabilities of artificial saliva substitutes.

The composition of an artificial saliva plays an essential role for the remineralisation of tooth enamel. A study conducted by Ionta et al [89] tested the influence of 5 different

artificial saliva compositions on the microhardness of enamel samples, before and after acid treatment and subsequent 2 hr immersion. Artificial saliva solutions which contained mucin did not present beneficial remineralisation compared to non mucin solutions, the later present a fractionally greater change to surface hardness [89]. It was suggested that the role of mucin may influence the mineral diffusion due to its viscosity. As mucin in whole human saliva has been observed to provide protection against citric acid [190], the inhibition of mineral diffusion is necessary for protection in an acidic environment.

An interesting follow up to this study [89] reversed the treatment process to examine the impact artificial saliva solutions on demineralisation [191]. Enamel surfaces were initially immersed in deionised water, a salt only artificial saliva and whole human saliva which represented a salt and protein solution. Surfaces were then subjected to repeated cycling of citric acid, followed by immersion in the test solution and surface height, roughness and hardness measurements taken after each cycle. Saliva provided the lowest step height for all solutions but did present the largest surface hardness change of 2.33 GPa and a rougher surface area [191], as shown in Figure 2-23. It was suggested that the proteins within natural saliva, which form a surface pellicle, also modify mineral diffusion on the enamel surface by retaining a high concentration of calcium and phosphorus ions close to the surface during demineralisation. After acidic attack, this concentration gradient ensures remineralisation to quickly occur and prevent further surface damage. Furthermore, artificial saliva solutions with mucin were observed to provide comparable enamel protection to whole human saliva in erosive conditions [106].

Acid treated enamel surfaces also influence the adsorption and protective capabilities of salivary proteins. Total protein content and the amount of statherins tended to be less on these surfaces compared to healthy surfaces in vivo [192]. The statherins are important to facilitate further adsorption of salivary proteins; a reduction in calcium and phosphate ions in localised regions may reduce this [192]. It is unclear how mucin may behave in the absence of similar pre-cursor proteins.

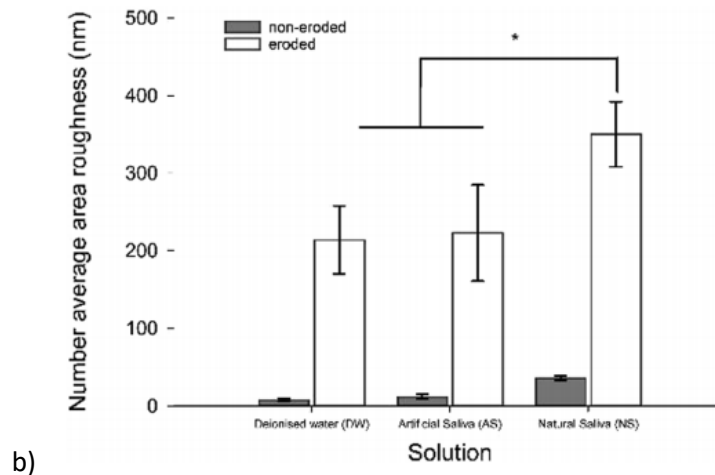
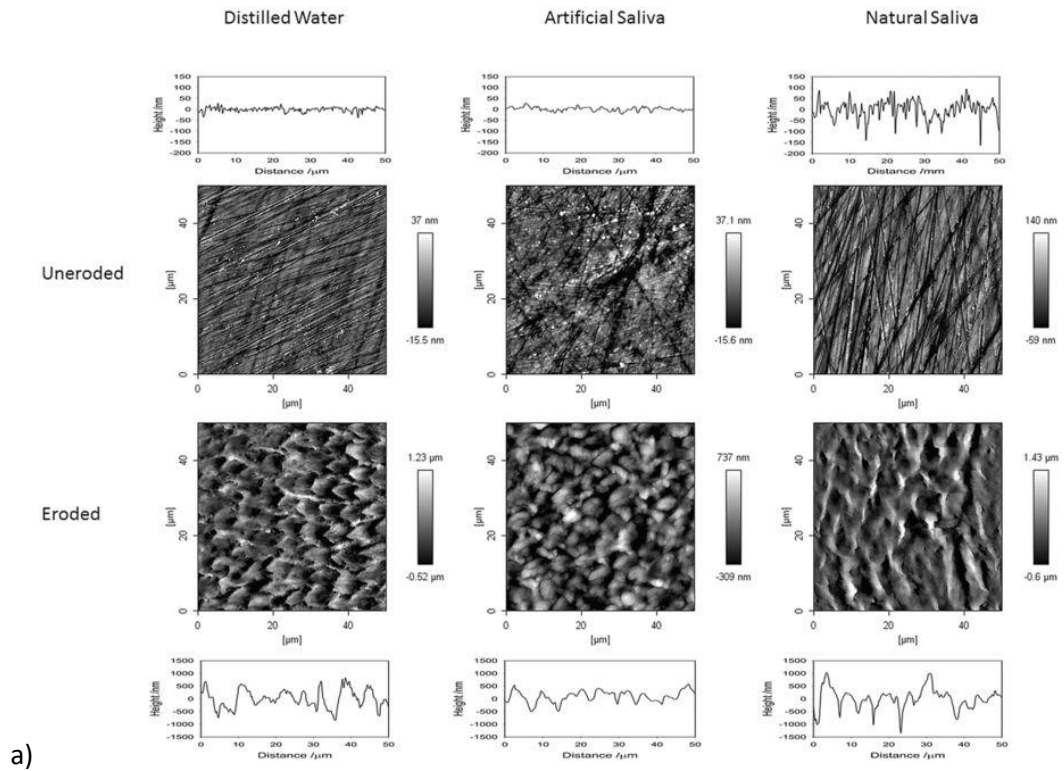


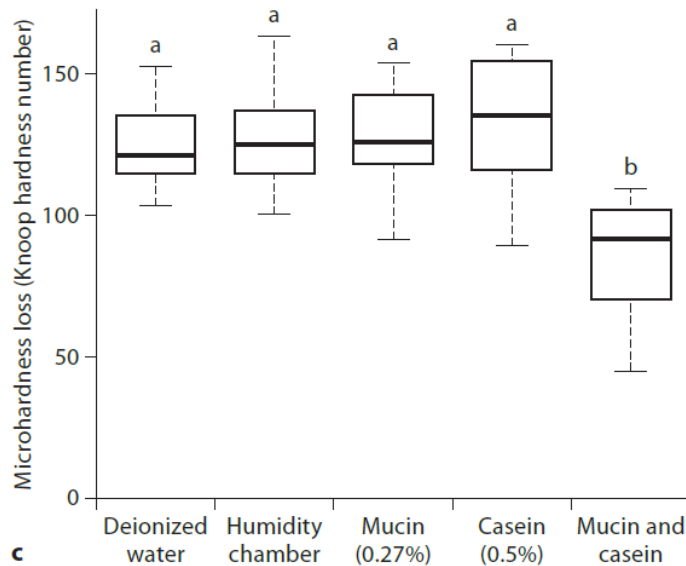
Figure 2-23 a) Surface are and profile for baseline and eroded surfaces under the three test solutions, and b) the average surface roughness of surfaces [191].

### 2.3.3 Protein film modification

To effectively reduce the effects of dental wear by corrosion, techniques have been applied to modify salivary films to enhance protection. This can either be done by treating a pre-formed layer or altering the saliva composition to self-assemble a layer with different structural properties that benefit tooth protection. The addition of specific salt ions and proteins have been previously investigated with salivary films.

Preformed salivary pellicles have been treated with combinations mucin and casein to assess the impact on demineralisation, measured by micro hardness [73]. Alone, both

proteins had little impact on the micro hardness change, but together a synergism was observed with less demineralisation overserved as shown in Figure 2-24. It was hypothesised that albumin was substituted with the casein on the enamel surface, enabling a strong protein-protein interactions with mucin to form a micellar surface structure that increases the layer's thickness and density [73].



**Figure 2-24** Micro hardness loss after three erosion cycles [73].

Increased calcium ion concentrations also improve the protective abilities of a salivary pellicle by promoting crosslinking of proteins within the layer, when adsorbed whole human and parotid saliva was examined with a quartz crystal microbalance with dissipation monitoring (QCM-D) [193]. Layers formed on gold sensors presented an increased layer thickness and mass, while the layer's dissipation decreased. This suggested that the increasing the calcium ion concentration altered the structural properties of the layer, and therefore the layer's viscosity and shear properties. It wasn't clear how this might have influence enamel protection under mechanical or chemical interrogation.

Future work by the same group further examined the impact of salt concentrations and alkaline pH solutions, with an additional focus on the layer's physical properties and lubrication [59]. Sodium bicarbonate treated saliva solutions demonstrated improved lubrication compared to the phosphate buffered control saliva, when assessed by a mini traction machine. However, when examined by QCM-D, repeated rinsing with sodium bicarbonate solution resulted in a reduction in adsorbed pellicle mass, while no significant changes were observed for sodium chloride, control and alkaline solutions [59]. It was thought that the ionic activity from the sodium bicarbonate may influence the protein structure by preventing protein crosslinking by effectively shielding the charges on the

pellicle proteins [59]. It was also thought that the alkaline phosphate buffer solution may have had an impact on the pellicle as a reduction in mass was observed. The structure may have been altered due to disruption of disulphide bridges in cysteine like proteins which contain thiol groups. This highlights the complexity of being able to modify the structure of the pellicle to improve its strength and functional performance. While the addition of one substance can improve a property, another may be altered as a result which may reduce its overall protective capacity.

The influence of fluoride ions on the pellicle has also been studied, as the addition of fluoride ions in various oral health related products have been shown to improve and reduce tooth loss. The fluorides can form fluorapatite crystals during remineralisation which are less soluble in acidic conditions. Hove et al [194] investigated titanium tetrafluoride treatment on both bovine and human enamel with an adsorbed pellicle under acidic conditions. A decrease in calcium ion loss from both bovine and human enamel was observed when pellicles were treated with titanium tetrafluoride compared to treatments without a pellicle or titanium tetrafluoride alone, as shown in Figure 2-25. Interestingly the presence of a pellicle had little impact on calcium loss compared to untreated enamel. Furthermore, total calcium loss after treatment with a pellicle and titanium tetrafluoride was significantly less in bovine enamel compared to human enamel. Aside from this, the combined treatment may exhibit a similar behaviour to calcium ion interactions with a pellicle; promoting protein crosslinking and strengthening the film's structure [193]. This improved protection has also been observed in other studies and linked to potential crosslinking [195, 196, 197].

Treatment	Mean Ca loss, $\mu\text{g}/\text{mm}^2$							
	bovine				human			
	1st acid exposure	2nd acid exposure	3rd acid exposure	total	1st acid exposure	2nd acid exposure	3rd acid exposure	total
No pretreatment	$13.4 \pm 1.4^a$	$12.2 \pm 1.3^a$	$13.3 \pm 1.6^a$	$38.9 \pm 2.7^a$	$12.0 \pm 3.1^a$	$12.5 \pm 3.1^a$	$15.3 \pm 4.2^a$	$39.8 \pm 9.1^a$
Pellicle	$12.2 \pm 2.8^a$	$12.0 \pm 1.2^a$	$12.6 \pm 1.4^a$	$38.7 \pm 4.3^a$	$13.2 \pm 2.7^b$	$13.0 \pm 2.6^a$	$13.7 \pm 2.3^a$	$39.8 \pm 5.8^a$
TiF <sub>4</sub>	$3.2 \pm 2.7^b$	$5.3 \pm 1.9^b$	$5.9 \pm 1.9^b$	$14.3 \pm 5.9^b$	$6.7 \pm 1.2^c$	$5.8 \pm 2.3^b$	$7.1 \pm 3.3^b$	$19.6 \pm 6.6^b$
TiF <sub>4</sub> + pellicle	$0.1 \pm 0.2^c$	$2.6 \pm 2.6^c$	$3.6 \pm 1.7^c$	$6.4 \pm 3.5^c$	$5.8 \pm 1.8^d$	$6.1 \pm 2.1^b$	$6.0 \pm 1.7^b$	$17.9 \pm 4.7^b$

Within columns (i.e. comparing the treatments), means sharing the same superscript letter are not significantly different ( $p > 0.05$ ).

**Figure 2-25 Mean Ca loss ( $\mu\text{g}/\text{mm}^2$ ) after exposure to hydrochloric acid on bovine and human enamel [194].**

An artificial saliva would need to be able to protect enamel much like a natural saliva does by creating a protein layer, the pellicle, on the surfaces of teeth. The pellicle serves to protect enamel from both mechanical and chemical forms of wear, so being able to artificially build a layer with similar properties would be a step forward to improving current therapies. It's therefore important to consider the biological implications of tooth loss by studying how it can reduce the impact of tribocorrosion.

Being able to maximize protection against tooth tribocorrosion is an area of growing interest for effective enamel protection [181]. Knowledge of this is essential for improved artificial saliva substitutes for the future of tribocorrosion testing and the development of enhanced commercial preventative therapies [6, 21, 181]. To engineer saliva substitutes, the underlying mechanisms of degradation need to be understood.

## 2.4 Summary

### 2.4.1 Background summary

This chapter covers the relevant background material of teeth within the harsh and ever-changing environment of the oral cavity. First, the composition, structure and properties of tooth enamel which is the functional surface of importance within this tribological environment with protection in mind. Alternative materials used in wear testing were also discussed for the purposes of wear testing and conducting research on in this project. Using Y-TZP as a standardised agonistic material for wear tests, steatite could be assessed against bovine enamel surfaces in terms of its feasibility as a representative tooth surface. Understanding the similarities and differences in surface characteristics, before and after wear testing, and lubrication behaviour in a mucin environment would provide a suitable assessment of steatite in future tooth tribology studies.

Secondly, the composition of electrolytes and proteins in natural saliva are important in terms of lubrication and tooth dissolution prevention. Salivary proteins have film forming abilities which adhere onto oral soft tissues and dental hard tissues. The adhesion of these proteins is influenced by other proteins and ionic components in natural saliva as well as the overall solution pH. In healthy individuals this can lead to the formation of a strong protein pellicle that can act as a boundary lubricant under sliding conditions and as a diffusion barrier to tooth dissolution. This can essentially reduce the overall tooth dissolution when introduced to acidic challenge from diet, lifestyle factors and health disorders which introduce intrinsic acids to the oral cavity.

Individuals who suffer from saliva inhibiting conditions like Xerostomia are more at risk of tooth dissolution from these acidic challenges due to a reduction in salivary flow, ensuring reduced protein film coverage and protection from the film and the neutralising ability of the saliva. There have been therapies aimed for these individuals in the form of artificial saliva. However, it seems to be the case that these commercially available substitutes fall short from natural occurring saliva. Being able to retain water on oral and dental surfaces being a key requirement for long term relief. Mucin-based saliva substitutes generally



perform better in terms of lubrication and tooth dissolution prevention, both in lab studies and clinically. To serve as an effective therapy for dry mouth relief, mucin substitutes would need to be further developed, with a supersaturation calcium and phosphate to further improve its protective ability against tooth dissolution. Furthermore, the addition other proteins or substances which can promote protein-surface adhesion and protein-protein bonding would be beneficial in encouraging a stronger protein film that is comparable to a natural dental pellicle.

Before this can occur, further information on mucin behaviour needs to be uncovered in terms of its adsorption mechanisms and kinetic pathways, rheological properties of surface layers and how these layers ultimately define its overarching lubrication behaviour. The composition of a mucin based artificial saliva needs to be broken down into a mucin only component without the complexity of addition electrolyte and synergistic proteins/polymers that may influence adsorption behaviour and layer properties. Assessment of these layers on uniform surfaces may uncover the underlying kinetics of adsorption in addition to the influence of surface composition on adsorption kinetics, layer strength and the subsequent layer's rheological properties.

#### 2.4.2 Literature summary

Most tribology studies incorporated the use of reciprocating sliding tests under a ball on flat configuration or conducted nano-scratch tests to understand tooth wear under specific conditions. Under dry conditions, wear seems to be dominated by the brittle fracture of asperities, exhibiting rougher worn areas compared lubricated conditions. This type of behaviour was hypothesised to be comparable to what might be expected for individuals with Xerostomia. Under lubrication with an electrolyte solution, plastic deformation and subsurface fatigue mechanisms seem to be more common. It would seem over longer testing conditions, both dry and lubricated tests would end up with three body debris generation with these mechanisms.

The addition of an acidic component to reciprocating tests allowed investigation into the mechanisms of enamel attrition-corrosion aka tribocorrosion. Instabilities in the friction and wear behaviour became more apparent under these conditions with some studies suggesting acidic environments reduce surface wear, while other studies increase this. Discrepancies like this may be attributed to what has been used to measure wear. Traditionally, comparing the material volume loss from a wear scar would serve as an indicator to the wear of the system. However, the penetration of acids into the subsurface of tooth enamel suggests corrosion may be occurring subsurface, softening the enamel.

Softening of the enamel changes the wear mechanism from brittle fracture and delamination to a ploughing mechanism which results in smooth worn surfaces.

When it comes assessing the demineralisation/remineralisation of enamel, the most common method of study relies on static dissolution cycling. This is done by alternating between acids or saliva type solutions and comparing the surface micro hardness after treatment to a benchmark. While micro hardness testing can provide an indirect measure to the level of demineralisation/remineralisation, this does not provide an answer to the level of overall tooth degradation or protection from the corrosive system. One method of interest compared the calcium loss after each dissolution cycle, providing a quantitative means which related to the overall tooth degradation. This method has not been used in tribology studies concerning tooth enamel and could serve to expand on what is known about the contributions to overall tooth degradation.

Natural saliva is best when it comes to the protection of teeth in acidic environments, however mucin containing artificial saliva solutions have been observed to provide comparable protection. Unfortunately, studies which examine mucin in terms of tooth protection under static and dynamic test conditions are lacking. Studies tend to focus on salivary protein layers and how additional components, be it ionic or proteinaceous in nature, can modify the layer for enhance enamel protection. Once again, it isn't clear how modification of a protein layer can influence the protection of teeth in a tribological environment. Salts and proteins have been shown to permit thicker and more elastic layer through protein crosslinking, but it is not clear how this might influence boundary lubrication or tooth enamel protection.

It is important to fully understand each the implications of each system component to make the necessary changes for improvement. For the tribocorrosion of tooth enamel, a suitable measure of wear needs to be established by determination of the individual wear contributions. Moreover, understanding the relevance of a protein layer's physiological properties and how it influences boundary lubrication would provide more meaningful insight into layer modification studies. These steps are important for the progression of artificial saliva substitute development in the future.

## Chapter 3. Experimental methodologies and surface analysis techniques

### 3.1 Introduction

The purpose of this chapter is to outline the various experimental procedures and analytical techniques used throughout this project. The information covered in this chapter include: the acquisition and preparation of bovine enamel and other dental material samples, protocols for formulating mucin based artificial saliva solutions, experimental equipment for solution characterisation, assessment of mucin - surface interactions, tribological measurements and surface analysis methods.

### 3.2 Materials and Methodology

#### 3.2.1 Tribological substrates

##### 3.2.1.1 Steatite

Steatite, a magnesium silicate ceramic, was used as an alternative material to human tooth enamel. This has been specifically used for the “Newcastle” test method in the ISO Standard ISO TS 14569 – 2:2001 [1]. It simulates the abrasive wear properties of human tooth enamel and is used as the antagonistic material during dental material testing. Steatite is composed of magnesia, silica, and alumina with trace amounts of iron (III) oxide and potassium oxide, the proportions are shown in Table 3-1 from a manufacturer’s notes [198]. These balls are manufactured through a hot isostatic pressing and sintering process. The rationale behind choosing this material for initial investigations was to assess whether steatite was a viable material for the study of oral tribology and lubrication. Outside of dental testing steatite is used as a grinding medium for size reduction purposes. Ø 6 mm steatite balls (Carl Stuart Ltd, UK) were used.

*Table 3-1 Composition of steatite [198].*

Component	Percentage
Magnesia (MgO)	31%
Silica (SiO <sub>2</sub> )	64%
Alumina (Al <sub>2</sub> O <sub>3</sub> )	4%
Iron (III) oxide (Fe <sub>2</sub> O <sub>3</sub> )	<1%
Potassium oxide (K <sub>2</sub> O)	<1%

### 3.2.1.2 *Bovine enamel*

To gain a proper understanding of the role mucins play in dental tribology and tribocorrosion, bovine enamel was used. This material has commonly been used in the literature for studying the effects of dental corrosion [199, 48, 90]. This has served as a suitable alternative to human enamel, possessing both similar structural and chemical compositions [48]. Bovine enamel was sourced from a local abattoir where cattle was slaughtered between the ages of 12 – 16 months, reducing any influences a wider age range might possess if collecting extracted teeth from a local dentist. Diet variation is also another factor which was reduced, as the diet of cattle is much more controlled compared to humans that have varied diets and eating habits. This ensured experiments were conducted on a more repeatable and consistent material of biological origin.

One of the drawbacks of bovine enamel is related to the use of deciduous teeth compared to fully mature permanent teeth. Deciduous teeth possess a thinner enamel layer, larger enamel pore structure and lower elastic modulus compared to permanent teeth, which makes deciduous teeth more susceptible to demineralisation [200]. Given this, deciduous bovine teeth were still chosen as they provided a representative chemistry similar to human tooth enamel, which was viable for the purposes of understanding protein layer adsorption, growth and lubrication. All enamel-focused studies were conducted on bovine enamel to concentrate on the differences from test solutions as opposed to changes from larger material variation due to different enamel sources.

### 3.2.1.3 *Y-TZP*

Y-TZP was used as a generic antagonist material for tribometer testing against steatite, bovine enamel and coated quartz crystal materials. Ø 3 mm Y-TZP balls (Goodfellow Cambridge Ltd, UK) effectively emulated the size and geometry of the cusp of a tooth. The use of Y-TZP was similar to the documented use of alumina for the purposes of wear testing dental materials [146]. Like steatite, Y-TZP ceramic balls were manufactured by a hot isostatic pressing method followed by high temperature sintering. Final grinding and cleaning ensure the spherical tolerance is  $\pm 5\%$  ball diameter, according to the manufacturer's notes.

#### 3.2.1.4 Quartz sensors - gold and hydroxyapatite

Gold quartz sensors (QuartzPro, Sweden) and hydroxyapatite sensors (Qsense, Biolin Scientific, Sweden) were used. These consisted of a thin layer of AT cut quartz sandwiched between two electrodes, with a material specific coating applied to the exposed surfaces. The purpose of the sensors was to assess how mucin layers formed over time on both surfaces. Most tests were performed on the gold sensors as these could be cleaned and re-used easily. Basic adsorption kinetics could be observed on gold and film properties could be compared using this universal surface. On the other hand, the hydroxyapatite coated sensors were single use only and were more expensive than the gold sensors. However, it was important to use hydroxyapatite sensors for growth tests as hydroxyapatite makes up a large proportion of tooth enamel. This allowed observation of mucin adsorption onto a more specific surface which could parallel adsorption behaviour on tooth enamel.

### 3.2.2 Lubricants and additives

#### 3.2.2.1 PGM type 2 – mucins

Commercially available porcine gastric mucin, PGM, (type II, Sigma Aldrich, USA) was acquired in powdered form. This was a crude form of mucin, as it possessed significantly less bound sialic acid functional groups, and contained a mixture of additional glycoproteins compared to mucin directly extracted from a pig's stomach [97]. PGM was chosen over the direction extraction method as a standardised additive to mitigate potential variations from stomach extraction and mucin purification methods. Variations within mucin solutions were assumed to have a negative influence on experiments that aimed to determine adsorption pathways, lubrication and protection mechanisms. Furthermore, if mucin was to be used in as an additive in an artificial saliva it would be important to be able to make large volumes of the solution with little expense. Ideally, bovine submaxillary mucin (BSM) would be the optimal mucin type due to a higher percentage of sialic acid groups and originating from salivary glands [97]. However, this type was only available in smaller quantities commercially with a larger material expense compared to the more cost effective porcine gastric mucin when considering the scale of testing. A crude and impurified form was therefore used as a benchmark additive.

### 3.2.2.2 Solution components: Salts

Other solution components were chosen to assess mucin interactions within a given environment. It was important to consider the components of natural saliva which included sodium, potassium, calcium, phosphate and chloride ions. A physiologically representative solution to this was a Phosphate Buffered Saline (PBS) solution which was used to emulate the neutral buffered saline properties of natural saliva. Table 3-2 shows the salt composition of a PBS solution. Other salts were considered individually to examine the impact of specific ions on aspects of mucin layer growth. These included sodium chloride (NaCl), potassium chloride (KCl), calcium chloride (CaCl<sub>2</sub>) and sodium dihydrogen phosphate (NaH<sub>2</sub>PO<sub>4</sub>).

*Table 3-2 Salt composition of PBS [201].*

Salt component	Concentration (mmol/L)
<b>Sodium Chloride (NaCl)</b>	137
<b>Potassium Chloride (KCl)</b>	2.7
<b>Sodium Phosphate (Na<sub>2</sub>HPO<sub>4</sub>)</b>	10
<b>Potassium Phosphate (KH<sub>2</sub>PO<sub>4</sub>)</b>	1.8

### 3.2.2.3 Solution components: pH modifiers

Citric acid (C<sub>6</sub>H<sub>8</sub>O<sub>7</sub>) was chosen to emulate an acidic environment throughout most tests. This aimed to simulate the acidity of several soft drinks and fruit juices which would commonly enter the oral cavity during oral processing. Tri-sodium citrate (Na<sub>3</sub>C<sub>6</sub>H<sub>5</sub>O<sub>7</sub>) was used alongside citric acid to ensure a buffered pH solution was attained. Sodium hydroxide (NaOH) was also used to examine changes to mucin's size and mobility characteristics in alkali environments.

### 3.2.2.4 All standard and salt solution compositions

Table 3-3 shows the standard test solutions used throughout this study and their composition per 100 ml of solution.

*Table 3-3 Standard test solutions used in this study.*

Solution	Composition per 100 mL	Rationale
<b>Deionised water (DiW) – pH 6.5</b>	<ul style="list-style-type: none"> <li>100 mL deionised water</li> </ul>	Control solution with no salts or mucin
<b>0.2% mucin (Muc + DiW) – pH 4.5-6.5</b>	<ul style="list-style-type: none"> <li>100 mL deionised water</li> <li>0.2 g PGM</li> </ul>	Mucin only solution based on mucin composition with whole human saliva to assess mucin behaviour without additional perturbation
<b>PBS – pH 7.4</b>	<ul style="list-style-type: none"> <li>100 mL deionised water</li> <li>0.98 g PBS salts</li> </ul>	Salt control solution with no mucin to assess salt implications on tribology
<b>0.2% mucin + PBS (Muc + PBS) – pH 7.4</b>	<ul style="list-style-type: none"> <li>100 mL deionised water</li> <li>0.98 g PBS salts</li> <li>0.2 g PGM</li> </ul>	Mucin and salt solution to assess interactions between the two components
<b>Citric acid (Acid) - pH 3.1</b>	<ul style="list-style-type: none"> <li>100 mL deionised water</li> <li>1.72 g 0.1 M citric acid monohydrate</li> <li>0.53 g 0.1 M trisodium citrate</li> </ul>	Control acid solution to assess corrosion without mucin. pH similar to soft drink acidity, with salts to maintain pH
<b>0.2% mucin + citric acid (Muc + Acid) - pH 3.1</b>	<ul style="list-style-type: none"> <li>100 ml deionised water</li> <li>1.72 g 0.1 M citric acid monohydrate</li> <li>0.53 g 0.1 M trisodium citrate</li> <li>0.2 g PGM</li> </ul>	Mucin and acid solution to assess mucin behaviour within an acid environment. pH similar to soft drink acidity, with salts to maintain pH

To examine the role of different salivary salts and salt concentrations on mucin size, mobility, layer growth kinetics, layer structural properties and lubrication, 100 mmol salt solutions were made up.

Table 3-4 shows the composition of the 100 mmol salt solutions examined in this study. 100 mmol was the maximum salt concentration used, and these solutions were further diluted with deionised water (excluding 100 mmol CaCl<sub>2</sub> + PBS) using a 1:9 ratio to make 10 mmol solutions, and once more for 1 mmol solutions. The same process was used for the 100 mmol CaCl<sub>2</sub> + PBS, using a PBS solution as the dilutant.

*Table 3-4 Compositions of 100 mmol salt solutions.*

Salt solutions	Composition per 100 mL	Rationale
<b>100 mmol NaCl</b>	<ul style="list-style-type: none"> <li>• 100 ml deionised water</li> <li>• 0.58 g sodium chloride</li> </ul>	Sodium and chloride ion interactions with mucin (single valency)
<b>100 mmol KCl</b>	<ul style="list-style-type: none"> <li>• 100 ml deionised water</li> <li>• 0.74 g potassium chloride</li> </ul>	Potassium and chloride ion interactions with mucin (single valency)
<b>100 mmol CaCl<sub>2</sub></b>	<ul style="list-style-type: none"> <li>• 100 ml deionised water</li> <li>• 1.47 g calcium chloride dihydrate</li> </ul>	Calcium and chloride ion interactions with mucin (double valency)
<b>100 mmol NaH<sub>2</sub>PO<sub>4</sub></b>	<ul style="list-style-type: none"> <li>• 100 ml deionised water</li> <li>• 1.19 g sodium dihydrogen phosphate</li> </ul>	Sodium and phosphate ion interactions with mucin (single valency)
<b>100 mmol CaCl<sub>2</sub> + PBS</b>	<ul style="list-style-type: none"> <li>• 100 ml deionised water</li> <li>• 0.98 g PBS</li> <li>• 1.47 g calcium chloride dihydrate</li> </ul>	Calcium, potassium, sodium, chloride and phosphate ion interactions with mucin (multiple valency)



### 3.2.3 Sample prep

#### 3.2.3.1 Bovine enamel samples

##### **Tooth extraction and sterilization**

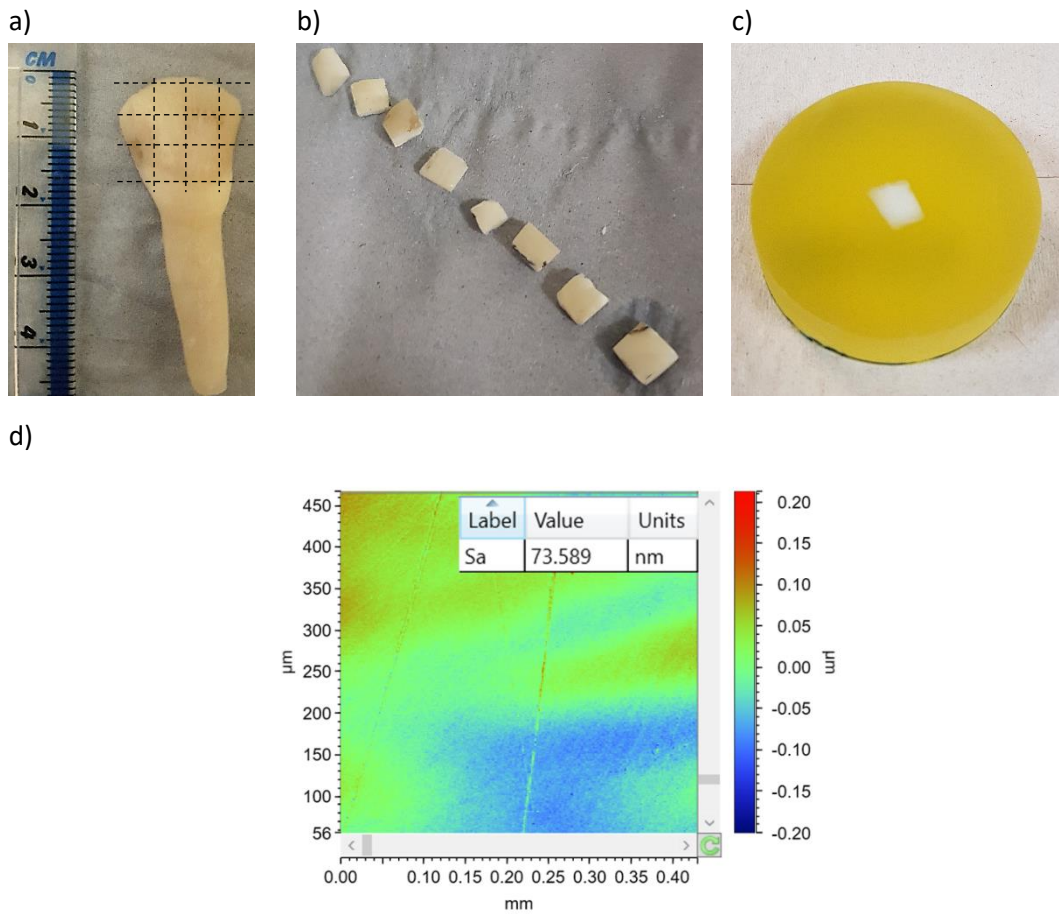
Enamel samples were acquired from a local abattoir in the form of a sectioned lower mandible. Dental excavators and pliers were used to separate whole incisors from the mandible without damaging the structure. Excess tissue was scraped off prior to sterilisation. Extracted teeth were treated in a 10 % formalin neutral buffer solution for a minimum of 7 days to disinfect and sterilise them [202]. The composition of this solution is shown in Table 3-5. After sterilisation the teeth were thoroughly rinsed and then refrigerated in deionised water until the next stage of processing.

*Table 3-5 Formalin solution composition.*

Solution	Composition per 100 mL	Rationale
<b>10 % neutral buffered formalin solution</b>	<ul style="list-style-type: none"> <li>• 10 ml 37% formaldehyde</li> <li>• 90 ml deionised water</li> <li>• 0.4 g sodium phosphate (monobasic)</li> <li>• 0.65 g sodium phosphate (dibasic/anhydrous)</li> </ul>	Sterilisation of bovine enamel

##### **Sectioning, embedding and grinding**

Teeth were processed by sectioning the surfaces into roughly 2 mm x 3 mm slabs for general testing, shown in Figure 3-1a). A root of an incisor was initially set in resin to aid in handling during the sectioning process. A rotary tool (Dremel 3000, USA) with a diamond cutting attachment was used for sectioning and deionised water was used as a coolant during cutting to prevent heat damage to the edges of the enamel. All sectioning was conducted in a fume cabinet to ensure debris was contained. The prepared slabs, shown in Figure 3-1b), were set in an acrylic resin (VariDur 200, Buehler, Germany) to form a Ø30 mm puck for further processing. Once set, samples were progressively and carefully ground with silicon carbide paper (Buehler, Germany) of grit sizes from 120 – 1200.

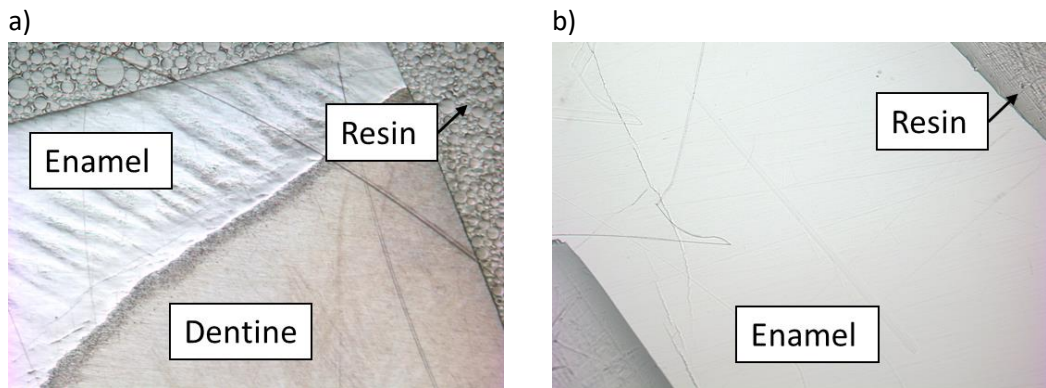


**Figure 3-1** Bovine tooth processing from tooth to sample a) Bovine tooth, b) sectioned slabs and c) embedded and polished samples, and d) surface area roughness of bovine enamel samples taken from vertical scanning interferometry.

For measurements which required a small sample size, the acrylic of the samples was further ground to ensure a fit within the equipment max sample dimensions. Finally, samples were polished with a polishing pad and diamond suspensions (Buehler, Germany) of 3  $\mu\text{m}$  and 1/2  $\mu\text{m}$  particle size, shown in Figure 3-1c). This would provide an approximate surface area roughness of < 0.1  $\mu\text{m}$ , as used in similar studies [31, 188], shown in Figure 3-1d).

### Quality assessment

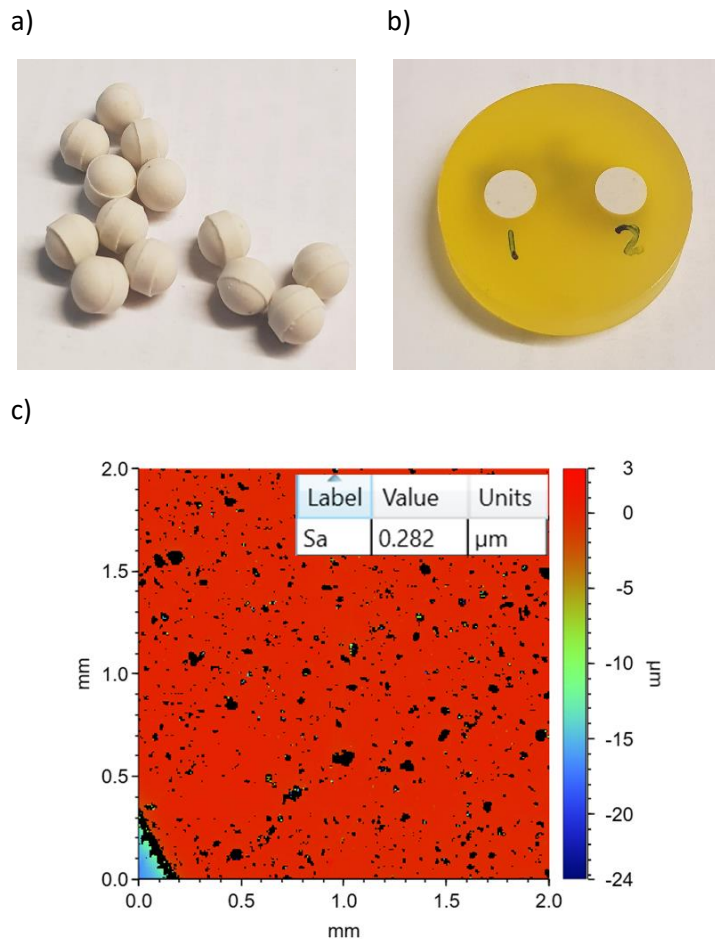
Checks were done throughout the grinding process using an optical light microscope. This ensured the most superficial enamel layer was removed, flattened and, not over ground, as shown in Figure 3-2a) and b). The thickness of the bovine enamel was between 1-3 mm and overgrinding could remove all the enamel, leaving the softer dentine surface exposed. Enamel and dentine were easily seen under an optical microscope.



*Figure 3-2 Images of a) over-ground enamel surface exposing subsurface dentine and b) ground enamel surface.*

#### 3.2.3.2 Steatite samples

Like the bovine enamel samples, steatite samples embedded in acrylic resin were progressively ground and polished in the same way as described in Section 3.2.1.2. The grinding process ensured an adequate area of steatite was exposed for all testing purposes. Figure 3-3 shows steatite before and after processing. It was intended that the surface area roughness value was  $< 0.1 \mu\text{m}$ , however determining this was difficult due to the nature of steatite's surface, shown in Figure 3-3c). The prepared steatite was covered in closed pores of varying size and geometry, which will be explained greater detail in Chapter 4.

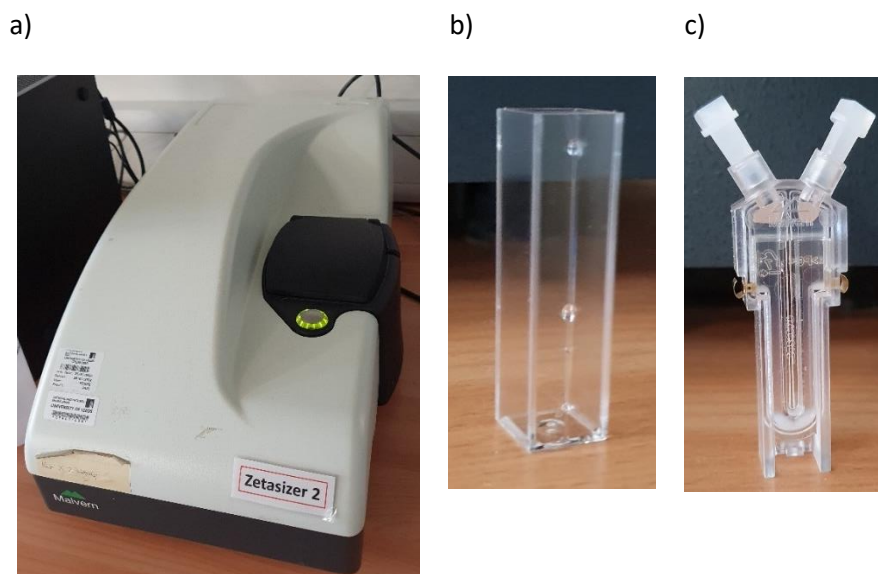


*Figure 3-3 Steatite sample processing from a) ball to b) polished sample, and c) Surface area roughness of steatite samples taken from vertical scanning interferometry.*

### 3.2.4 Solution characterisation

#### 3.2.4.1 Zetasizer

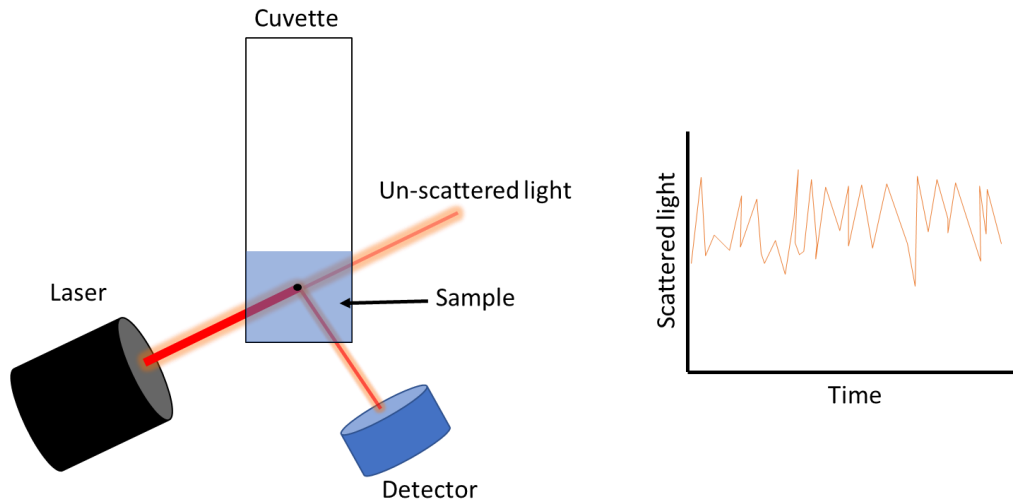
A Zetasizer nano (Malvern, UK) that combined dynamic light scattering (DLS) and laser doppler electrophoresis techniques was used to determine particle size and zeta potential of proteins (particles) within a solution, shown in Figure 3-4a). Particle size was measured in disposable polystyrene cuvettes, as shown Figure 3-4b), and the zeta potential measurements were performed in a capillary cell, as shown in Figure 3-4c). These differed from the cuvette in shape, with the addition of two electrodes which would apply a current to the solution.



*Figure 3-4 Malvern Zetasizer nano a) system, b) DLS cuvette and c) zetapotential capillary cell*

#### **Zetasizer theory**

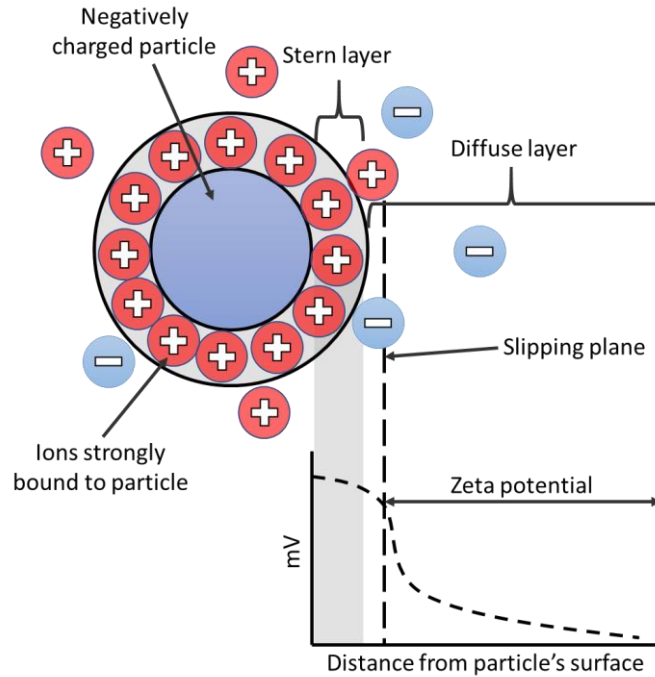
DLS investigated how mucin particle sizes varied in a particular solution environment which provided a further insight into film growth and tribological investigations. In a solution mucins or particles are in constant motion due to random collisions with surrounding molecules, a phenomenon known as Brownian motion. This is important to particle size measurements as smaller particles are more likely to move faster in a solution while larger ones move more slowly. A schematic of the measurement set up is shown in Figure 3-5.



*Figure 3-5 Schematic of DLS measurement and light scattering intensity over time*

The motion of the particles influences the fluctuations in light scattering intensity and this data is collected over time. A correlator is used to compare the similarity between scattering intensity signals at certain points in time and determine a correlation function which starts at one and decays to zero. The rate of decay is associated with the size of a particle, with larger particles exhibiting a large rate of decay and a slower fluctuation in scattering intensity. The reverse is observed for smaller particles. The Zetasizer software (Malvern, UK) calculated the size of particles in terms of a hypothetical hard sphere that diffuses at the same speed as the measured particles measured by the DLS methodology. A hydrodynamic diameter a.k.a Z-av in nm was estimated by the algorithm.

Zeta potential measurements provided an insight into the stability of the colloidal system of mucin dispersed in solution. This determined whether the mucins would repel, move apart from each other, or flocculate/aggregate, come together to form a larger structure with other mucins. This behaviour is dependent on the pH, composition and concentration of a solution. A zeta potential of 0 mV is known as the isoelectric point where a molecule in solution can exhibit a net zero charge as both positive and negatively charged functional groups exist on its structure. This can make a molecule less stable in solution, as the number of active sites is larger meaning high flocculation/aggregate may occur from molecule interactions. This point also indicates that there no net charge to the particle. Figure 3-6 presents a schematic of the zeta potential of a particle. The net charge of a particle's surface influences the distribution of counter ions, ions of an opposite charge, around that particle.



*Figure 3-6 Schematic representation of the zeta potential and electrical double layer.*

A larger concentration of counter ions may exist near the particle but as the distance from the particle's surface increases the counter ion concentration decreases. The area of high counter ion concentration, encompassing the particle's surface, is known as the stern layer, whereas the area of low ion concentration is referred to as the diffuse layer. This introduces an electrical double layer (EDL) around a particle which is the combination of the diffuse and stern layers. When the particle moves in a solution, ions within a boundary known as the slipping plane move with it, while ions outside the slipping plane remain static. The potential at this slipping plane is known as the zeta potential. The velocity of a particle, or electrophoretic mobility, is measured using laser doppler velocimetry and is converted into a zeta potential with the Henry equation in Eq. 8.

$$U_E = \frac{2\varepsilon\zeta f(\kappa\alpha)}{3\eta} \quad \text{Eq. 8}$$

Where  $\zeta$  is the zeta potential,  $\varepsilon$  is the dielectric constant,  $\eta$  is the viscosity,  $f(\kappa\alpha)$  is Henry's function a.k.a Smoluchowski approximation (1.5) and  $U_E$  is the electrophoretic mobility.

#### **Particle size measurement protocol**

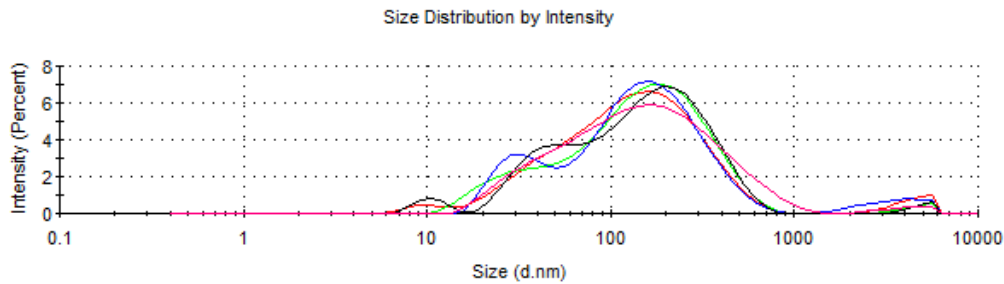
Prior to measurement cuvettes were rinsed with ultra-pure water (MilliQ, >18 M $\Omega$ ) to remove any small dust particles and other contaminants from the vessel. 1 mL of test solution was decanted into the rinsed cuvette and this was directly placed in the Zetasizer for testing. A standard protocol was set up for all experiments to run under. The protocol

took 5 measurements with 17 runs per measurement, an example is shown in Figure 3-7a). The mean peak size intensity was calculated for each measurement from the 17 runs, using a built-in peak fitting function. Peak sizes were exported to excel for distribution analysis.

### Zeta potential measurement protocol

Capillary cells were initially flushed with MilliQ water and then fill to the max level mark with the test solution. Approximately 1 mL test solution was required. Like the DLS measurements, a set protocol performed 5 measurements with 12 - 100 runs per measurement which depended on the data fit, an example is shown in Figure 3-7b). The software exemplified the peak fit of the data and determine whether more than 12 runs were needed for each experiment. Mean zeta potential determined from the central peak intensity and standard deviations were calculated from the full width at half maxima.

a)



b)

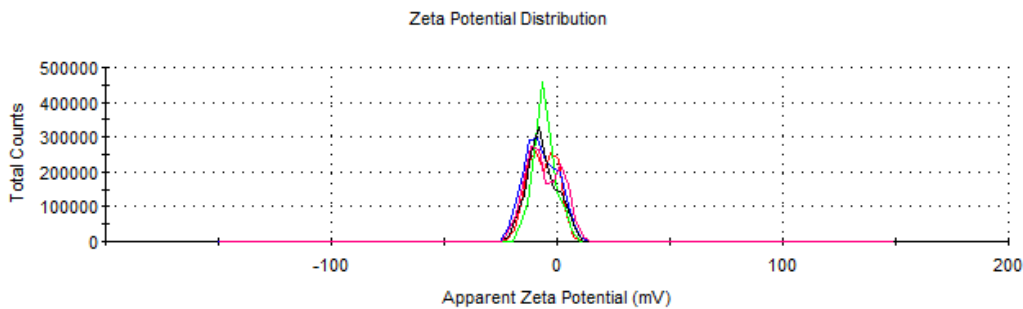


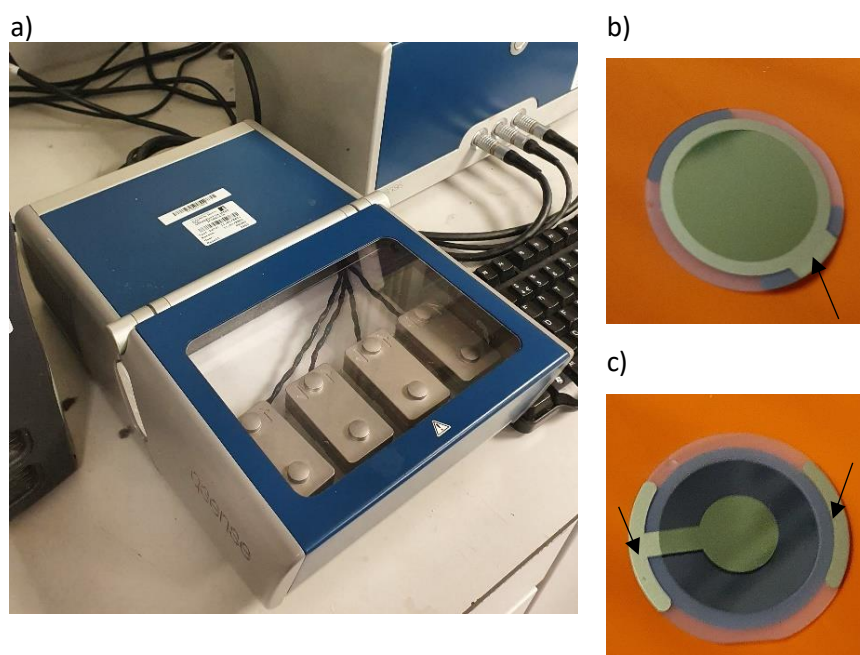
Figure 3-7 Zetasizer output data for a) DLS particle size distribution and b) zeta potential.



### 3.2.5 Surface interaction methodologies and analysis

#### 3.2.5.1 Quartz Crystal Microbalance with Dissipation monitoring (QCM-D)

To measure sensitive surface interactions on a particular surface material the quartz crystal microbalance (QCM) technique was utilised. Figure 3-8a) shows the QSense Analyzer instrument (Biolin Scientific, Sweden) used to perform these measurements. The instrument itself essentially tracked resonant frequency changes of an oscillating quartz crystal sensor and monitored the energy dissipation when solutions/molecules interacted with it. The sensors were made from thin AT-cut quartz in a disc shape with electrodes placed on either side of the sensor, as shown in Figure 3-8b) and c). Sensor materials from Qsense (Biolin Scientific) include, and are not limited to, gold, hydroxyapatite, stainless steel, titanium, polystyrene and zirconium oxide. For the purposes of this project, only gold and hydroxyapatite sensors were used.



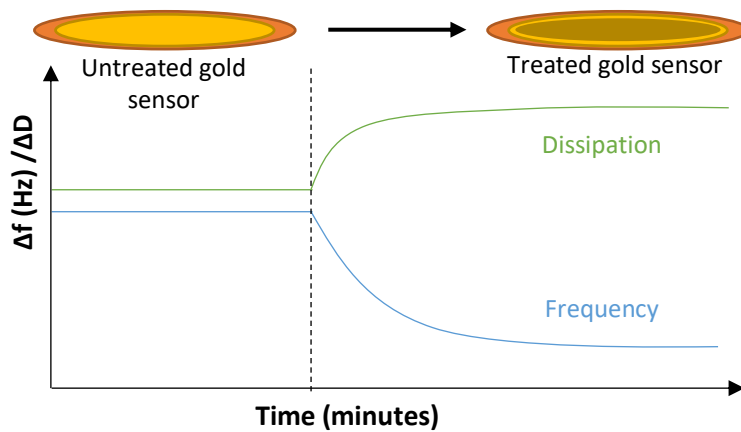
**Figure 3-8 a) Q-sense Analyzer QCM-D set up with flow cell modules and a gold QCM sensor showing the functional growth surface, b), and the reverse side c). Black arrows on the sensor images show the electrode placement on the sensor.**

The information provided by this technique allowed the properties of the adsorbed layer to be modelled and provided quantitative data for comparison. The modelled properties included the layer's mass, thickness, viscosity, shear modulus in addition to the rate of growth and probable adsorption kinetics in real time. These properties also served as an initial benchmark for comparing how the adsorbed layer reacted to environmental modifications, providing an insight into the behaviour of established layers. The next section

outlines the theory behind the QCM technique and the models associated with acquiring meaningful data.

### Theory

The theory of how a QCM works is relatively simple. A voltage is applied to a quartz crystal sensor which causes it to oscillate at a frequency specific to the sensor. In this case, 5 MHz sensors were used. The 5 MHz frequency relates to the relative resonant frequency of the sensor and first harmonic frequency a.k.a overtone. The QCM-D then directly measures two variables, the frequency response and the dissipation, a measure of the energy lost during one oscillation and the energy stored. Figure 3-9 highlights the changes in the raw data as a sensor is treated with a solution.



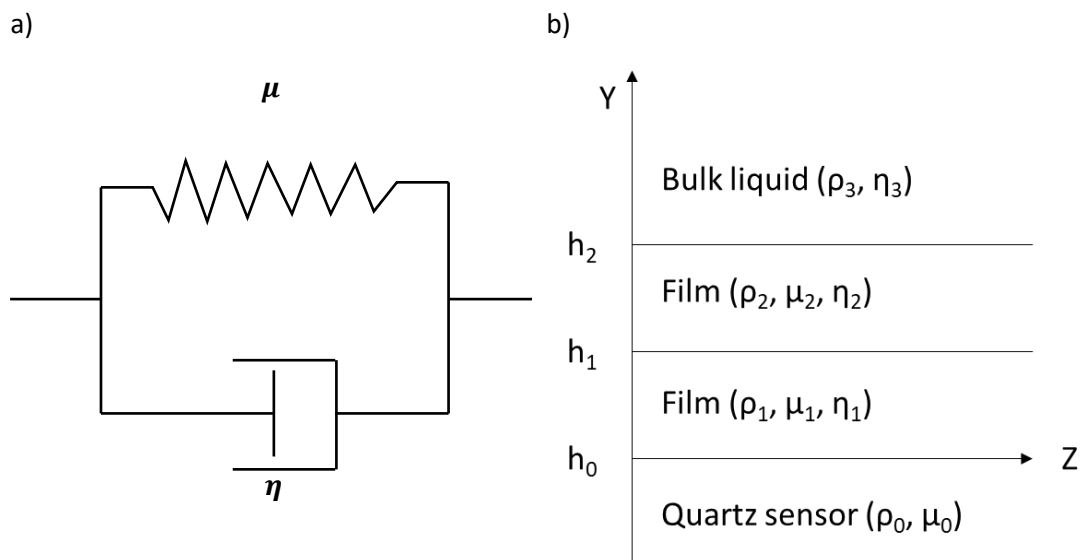
*Figure 3-9 Example of frequency and dissipation shift when a sensor is treated with a given growth solution.*

Frequency changes relate to nanogram scale changes in adsorbed mass on the sensor's surface over time i.e., an increased mass on the sensor reduces the resonant frequency over all measured harmonics. Simultaneously, the changes in dissipation are related to the rigidity of the formed surface layer over time. The Sauerbrey equation governs the relationship between the change in frequency and the change in mass as shown in Eq. 9.

$$\Delta m = -\frac{C}{n} \Delta f_n \quad \text{Eq. 9}$$

Where the mass adsorbed per unit area,  $\Delta m$ , is related to the change in frequency,  $\Delta f_n$ , for a given harmonic,  $n$ , and  $C$  is the mass sensitivity constant of the instrument [203]. This equation is only valid for thin and rigid layers, with negligible energy losses. If the change in dissipation ( $\Delta D$ ) was  $\approx 0$  for all resonant harmonic frequencies (a.k.a. overtones), then it could be assumed that the layer was thin and rigid, thus the Sauerbrey equation would adequately model the layer's mass and thickness properties.

However, if  $\Delta D > 0$  and the overtones were more spread out then the layer would indicate a thicker and softer layer with viscoelastic behaviour. In this case the viscoelastic model must be used to accurately predict thickness and viscoelastic properties of the layer following a Voight viscoelastic model as set out by Voinova et al [204]. The Voight model can be demonstrated as a spring and dashpot as shown by a simple schematic of a viscoelastic element in Figure 3-10a). The observed response from the sensor's oscillations presents both a shear elastic response,  $\mu$ , relating to the layer's shear modulus and a shear viscous response,  $\eta$ , which is related to the layer's viscosity. The geometric sandwich model used to model viscoelastic properties on the quartz slabs is displayed in Figure 3-10b), where  $\rho$  related to the density of a given layer,  $Y$  related to the height of layers, and  $Z$  related to the direction of shear.



*Figure 3-10 Viscoelastic model a) a simple schematic of spring and dashpot viscoelastic Voight model where for a given interaction there is both a shear elastic and shear viscous response, and b) the geometry of the quartz crystal with a viscoelastic double layer in a bulk liquid environment [204].*

The stress-strain relationship of the Voight model can be described by Eq. 10 where the shear stress,  $\sigma$ , is proportional to the elasticity,  $\mu$ , and the viscosity,  $\eta$ , of the overlayer.  $U_x$  related to the displacement in  $x$  and  $V_x$  related to its corresponding velocity.

$$\sigma_{xy} = \mu \frac{dU_x(y, t)}{dy} + \eta \frac{dV_x(y, t)}{dy} \quad \text{Eq. 10}$$

The Broadfit model (following the Voight viscoelastic model) in the Dfind software (Biolin Scientific, Sweden) was chosen to effectively model the layer's structural properties. This model assumed that the layer's formed on the surface were polymeric in nature, where layer structure was maintained with no observable flow, covering the entirety of the sensor's surface with a uniform density and thickness. The viscoelasticity in the Broadfit model was

described by a complex shear modulus where the real part is the energy storage modulus which is independent of frequency change, while the imaginary part relates to the loss modulus which linearly increases with the frequency [205]. The equation for bulk shear waves in a viscoelastic medium can be written as shown in Eq. 11. This includes  $\mu^*$  which is the complex shear modulus, made up of the real storage modulus and imaginary loss modulus.

$$\mu^* \frac{d^2 U_x(y, t)}{d^2 y} = \rho \omega^2 U_x(y, t) \quad \text{Eq. 11}$$

The model correlates density, elasticity, viscosity and thickness to the frequency and dissipation change according to the relationship between the shear wave response of the QCM-D and the layer's viscoelastic properties as researched by Voinova et al. [204]. In the context of a single viscoelastic layer, such as mucin on a sensor's surface, this can be described by Eq. 12 and Eq. 13. This is where  $\omega$  is the angular velocity of the shear wave,  $\delta$  is the viscous penetration depth of the shear wave into the bulk liquid and  $\eta_1$ ,  $\mu_1$ ,  $h_1$ , and  $\rho_1$  are the layer's viscosity, elasticity, thickness and density properties respectively.

$$\Delta f \approx -\frac{1}{2\pi\rho_0 h_0} \left\{ \frac{\eta_3}{\delta_3} + h_1 \rho_1 \omega - 2h_1 \left( \frac{\eta_3}{\delta_3} \right)^2 \frac{\eta_1 \omega^2}{\mu_1^2 + \omega^2 \eta_1^2} \right\} \quad \text{Eq. 12}$$

$$\Delta D \approx \frac{1}{\pi f \rho_0 h_0} \left\{ \frac{\eta_3}{\delta_3} + 2h_1 \left( \frac{\eta_3}{\delta_3} \right)^2 \frac{\eta_1 \omega}{\mu_1^2 + \omega^2 \eta_1^2} \right\} \quad \text{Eq. 13}$$

The model's algorithm initially determined a theoretical value for the frequency and dissipation response. This is based on the fixed parameters of the sensor's fundamental frequency and overtone number, and the fitting parameters which relate to the viscosity, shear modulus, density and thickness of the layer. The modelled frequency and dissipation output is compared to the measured response and the fit of the model is determined by a  $\chi^2$  value. The algorithm then adjusted the fitting parameters to improve the fit, following an iterative process. Once there was no significant change in the  $\chi^2$  value, its best fit was achieved. A representation of the output results with respect to time are displayed in Figure 3-11.

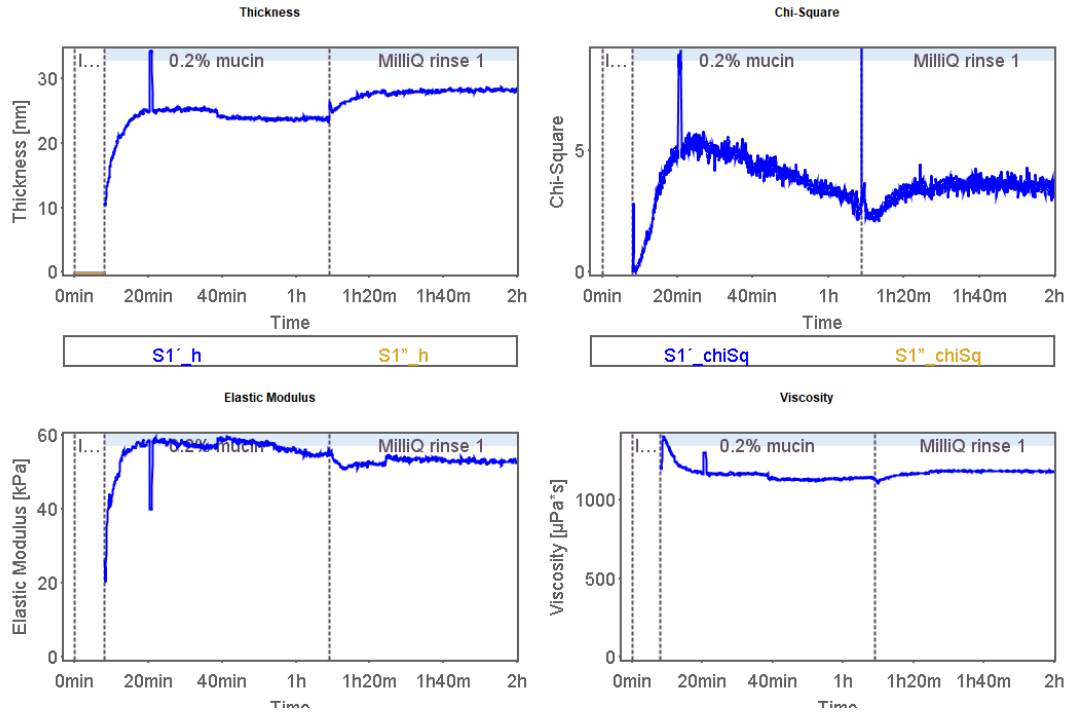


Figure 3-11 Example of processed data for mucin adsorption onto gold QCM sensors.

### Quartz sensor prep

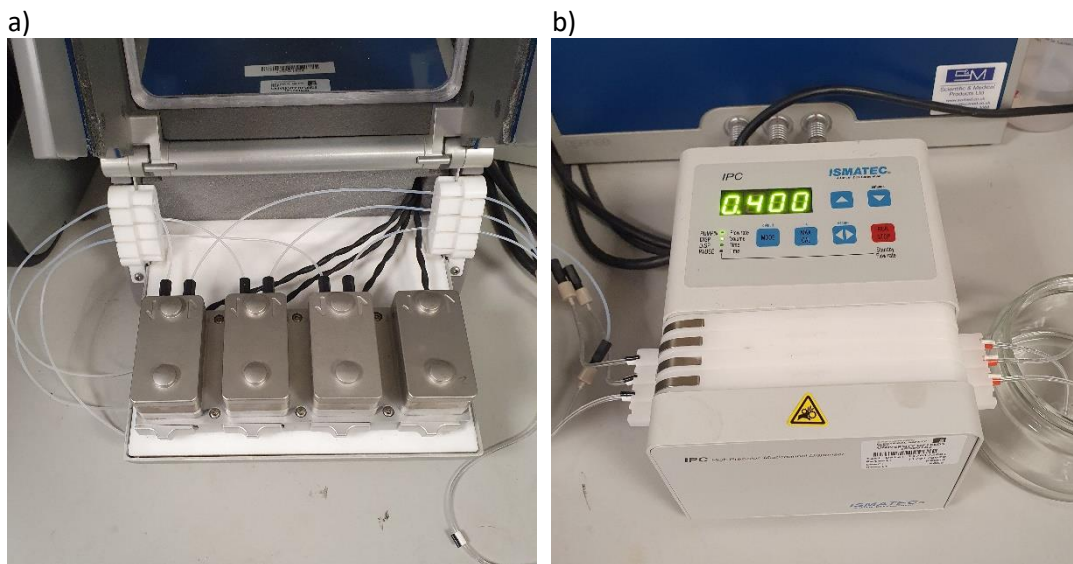
New sensors were used for all layer growth and tribological experiments with the NTR<sup>3</sup> tribometer. Sensors were prepared differently depending on their surface coating. Gold sensors were initially sonicated in 99% ethanol for 10 minutes at 30 °C. They were then rinsed with MilliQ water (>18 MΩ purity) followed by drying under a nitrogen gas flow. Hydroxyapatite sensors were submerged in 99% ethanol for 30 minutes, followed by thorough rinsing in MilliQ water and drying under a nitrogen gas flow.

Gold sensors which were previously used for layer growth experiments were also used for tribo-QCM-D tests. After initial growth testing these sensors were sonicated for 20 minutes in a Hellmanex III solution at 40 °C, followed by a thorough rinsing in MilliQ water. This solution would effectively remove anything which remained on the surface after layer growth experiments. Sensors were then prepared as previously mentioned prior to additional experiments.

### Cell configurations and protocol

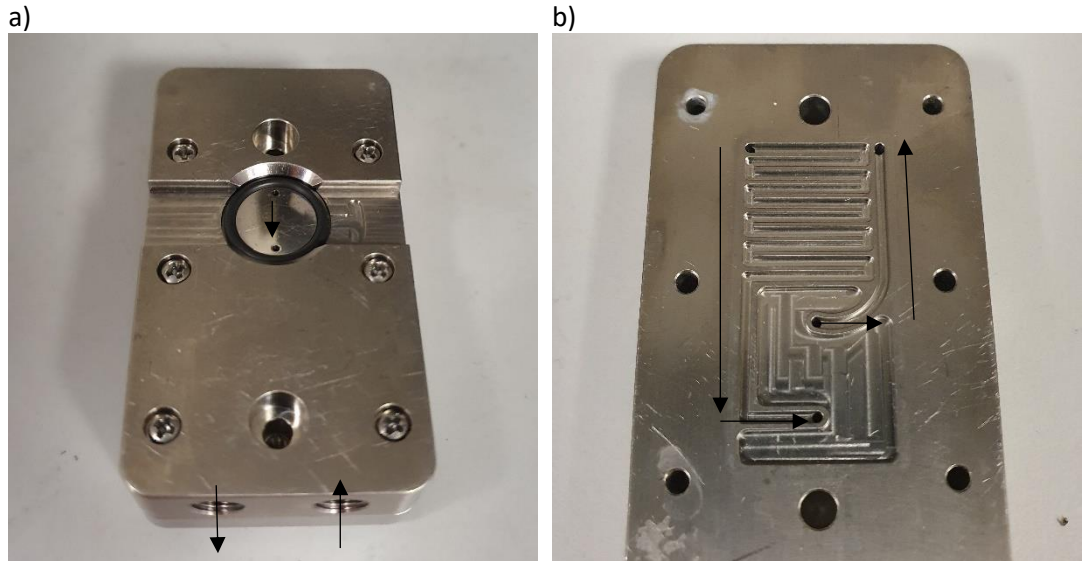
Two QCM-D configurations were used: a flow module and open module configuration. Flow experiments were performed with the flow module, shown in Figure 3-12a), which was connected to a peristaltic pump with the liquid handling kit (Qsense, Biolin Scientific, Sweden), shown in Figure 3-12b). The pump transferred solution from a reservoir into and out of the flow module at a constant flow rate of 0.4 ml/minute for all layer growth

experiments. Initially a baseline frequency and dissipation response were taken for no mucin solutions. This focused the study to assess mucin layer growth in each environment. Mucin solutions were introduced for 60 minutes after a stable baseline was established (less than 0.5 Hz drift per minute). After 60 minutes growth in mucin solutions, a rinse solution was reintroduced to determine if the layers were retained on the surface. The rinse solution was the same as the one used to take an initial baseline.



**Figure 3-12** Flow cell configuration with liquid handling kit connected to A) the flow cells and B) the peristaltic pump set at a flow rate 0.4 ml/min.

Figure 3-13a) and b) show the inside layout of the flow module. All liquids entered the module and passed through several channels prior to contact with the sensor's surfaces. The QCM instrument and the flow cell design allowed fluid within the cell and the sensor to remain at a constant temperature of 25 °C. After sensor contact, fluids passed through the flow cell's outlet. The flow cell was enclosed which meant no exterior contamination would influence the measurements. Fluid reservoirs were stored with a layer of parafilm on top to prevent contamination of the fluid during testing. Small holes were made in the film to permit entry of the tubing.



*Figure 3-13 Single flow module a) sensor interface and flow inlet/outlet locations marked by arrows and b) the inside of the flow cell. Black arrows indicate the direction of flow starting from the inlet on the out of the flow cell, through the heating channel.*

The open module, shown in Figure 3-14, enabled direct sensor interaction with the lab environment. This also allowed direct access to perform in-situ friction experiments as part of a bespoke rig combining the QCM with the Triborig. For all open cell experiments, 500  $\mu\text{L}$  of solution was maintained. Like flow cell experiments, a baseline was established prior to introducing mucin growth solutions. A micropipette was used to remove 250  $\mu\text{L}$  of the baseline solution and replace it with a 0.4% mucin solution. The rationale behind this was to ensure the resultant growth solution on the sensor equated to the standard 0.2% mucin solution used in other tests. Further alterations to the open module test protocol are described in 0



*Figure 3-14 QCM open cell configuration.*

### 3.2.5.2 Atomic Force Microscopy (AFM)

Atomic force microscopy was used to quantify the topography of steatite and enamel surfaces at the nanoscale. Furthermore, this provided a visual image along with quantitative data on distribution and size of mucin structures which adsorbed onto the enamel surfaces in greater detail. The results presented later in the thesis were collected with a Multimode 8 (Bruker, USA), shown in Figure 3-15. This had an X and Y resolution of approx. 5 nm, and a Z resolution of 100 pm. The multimode AFM system utilised a unique mounting configuration, using a bungee system to suspend the equipment during imaging. This minimised the impact from background noise.



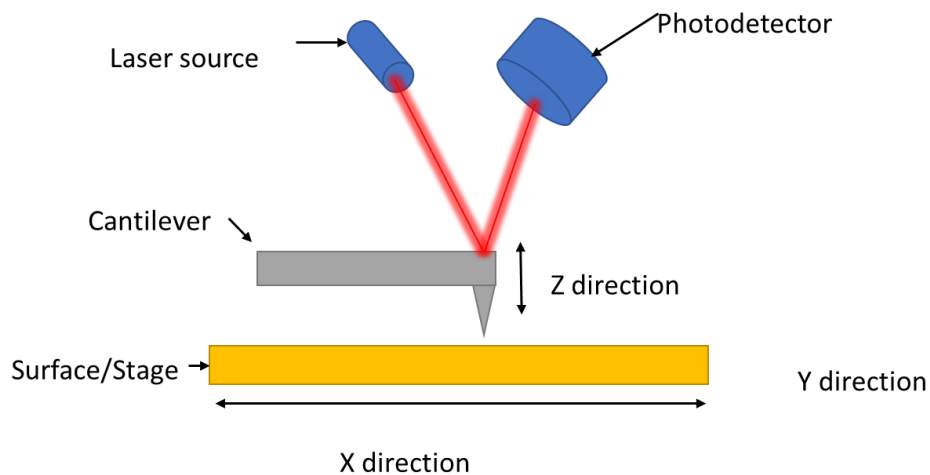
*Figure 3-15 Multimode 8 AFM (Bruker).*

Quantitative Nanomechanical property Mapping (QNM) imaging was utilised to gain additional insight into the properties of the mucin layers on bovine enamel and steatite surfaces. The technique was chosen to provide a more quantitative in-situ approach to examining the mucin layers in relation to an enamel surface and subsequent AFM probe interactions. Furthermore, other techniques like Scanning Electron Microscopy (SEM) or Cryo-SEM require a sample to be placed within a vacuum which would lead to dehydration of the enamel surface during testing. Data was exported from the NanoScope operating software (Bruker, USA) and imported into NanoScope Analysis (Bruker, USA) for post measurement processing.



### General imaging theory

The AFM is a scanning microscope with a very high resolution up to a fraction of a nanometre. It works by moving a sharp probe on the end of a cantilever over a desired surface to effectively “feel” the surface topography. This can be done by monitoring the deflections of the cantilever by directing a laser onto the cantilever, which reflects the light from the laser into a photodetector. The cantilever theoretically obeys Hooke’s law as the deflection is dependent on the force that influenced it. In this case the forces that dominate are van der Waals, electrostatic and capillary forces. The movement of the laser’s reflection on the photodetector relates to the vertical displacement of the tip relative to the surface. This can produce images of the surface’s topography. There are many types of imaging modes available but generally most AFMs follow this principle. Figure 3-16 gives a simple representation of this.



*Figure 3-16 Schematic representation of an AFM.*

The AFM can take measurements using several different imaging modes. Contact mode is the simplest mode whereby the probe is essentially dragged across the surface, taking topographical measurements of a surface. However, as probes are generally quite hard and sharp, this could lead to sample surface damage and a reduction to the lifespan of the probe. An alternative mode to contact is tapping. This mode makes the cantilever oscillate near to or at its resonant frequency relative to the surface. What this does is reduce to contact between sample and probe tip by systematically tapping across the samples’ surface, negating tip drag and lateral force influences that are seen in contact mode. An improved version of this mode is PeakForce tapping, which allow better force control of the probe on the surface such that more meaningful force data can be acquired [206].

### Quantitative nanomechanical property mapping (QNM) theory

PeakForce QNM uses the PeakForce tapping mode where the probe oscillates at  $\sim 2$  kHz and an amplitude of 150 nm, well below the cantilever's resonant frequency which can range between 22 – 525 kHz depending on the cantilever. The better force control allows higher quality images for softer samples, including biological ones. Each tap was an indentation on the surface which can be quantified from the acquired force curve of the surface tap. Force separation curves can be examined to extract properties of adhesion, dissipation, deformation and peak force of the tap. The DMT (Derjaguin, Muller, Toropov) model was used to estimate the reduced elastic modulus of the surface by rearranging Eq. 14 [207]. This model was relevant as it considered tip-surface adhesion, in addition to the contact forces during an indentation cycle, something which was useful for investigation of an elastic surface with a viscoelastic surface layer. The force on the AFM tip,  $F_{tip}$ , was proportional to the reduced DMT modulus,  $E^*$ , the root of the tip radius,  $R$ , and the cubed tip sample separation,  $d$ , plus the adhesion force,  $F_{adhesion}$ . Adhesion, the attraction between the tip and the surface, and the DMT and logDMT modulus were extracted from this equation. Figure 3-17 demonstrates how these values relate in terms of the force separation curve for a given indentation.

$$F_{tip} = \frac{4}{3}E^*\sqrt{Rd^3} + F_{adhesion} \quad \text{Eq. 14}$$

The deformation property related to the AFM tip's penetration into the sample's surface, which was directly quantified by the reflected laser onto the quad sectioned photodetector.

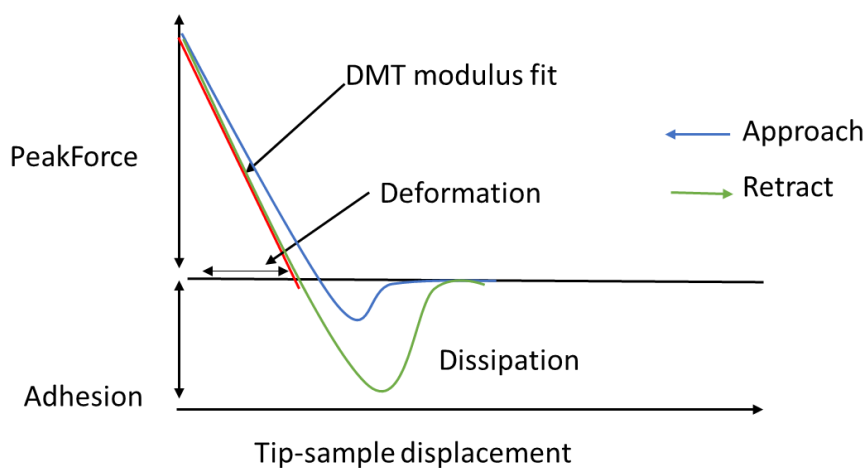


Figure 3-17 Force separation curve and extracted properties of interest [208].

Finally, the dissipation related to the hysteresis of the force displacement curve and thus related to the mechanical energy lost per indentation cycle in electron volts. For a purely

elastic indentation, this value was 0 and was calculated by integrating the area between the approach and retractions of a cycle. The dissipation,  $D$ , was extracted by Eq. 15, where  $F$  is the interaction force vector and  $Z$  is the displacement vector.

$$D = \int_0^T \overline{F} \cdot d\overline{Z} \quad \text{Eq. 15}$$

### AFM protocol and surface preparation

Growth experiments were performed by immersing the enamel surface in a mucin solution for up to 30 minutes, taking  $5 \mu\text{m}$  by  $5 \mu\text{m}$  images after 1, 5, 10 and 30 minutes. Quantitative nanomechanical property mapping mode (QNM) was enabled and used to provide a qualitative assessment of surface/tip interactions and what this meant in terms the surface properties. Figure 3-18 shows the experimental protocol in diagram form. A baseline image was taken to check the surface was clear of contaminants, which was followed by immersion in a mucin solution. After each immersion step, the mucin solution was removed and then pre-treated before imaging. Samples were dried under a nitrogen gas flow and then remounted for imaging in the air environment. In the liquid environment a non mucin solution replaced the mucin immersion solution, to permit further liquid imaging. This was done to ensure unbound mucin would not interfere with the AFM cantilever during scans.

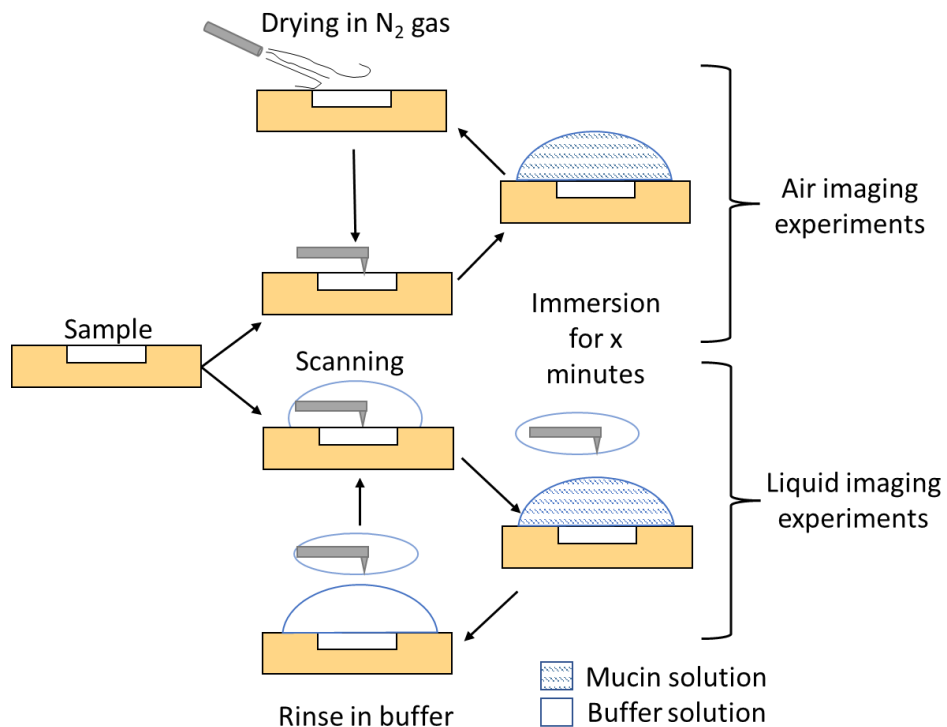
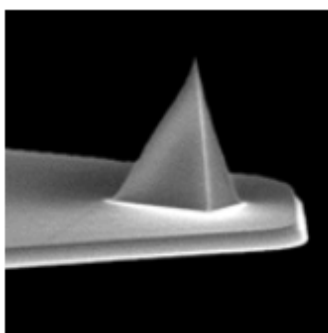


Figure 3-18 Diagram of AFM experimental protocol for air and liquid imaging.

ScanAsyst-FLUID AFM silicon nitride cantilevers (Bruker, USA) were used for all AFM experiments, shown in Figure 3-19, possessing a tip radius between 20 - 60 nm and a spring constant between 0.7 - 1.4 N/m. The cantilever's deflection sensitivity and spring constant was checked prior to any imaging. The deflection sensitivity was checked by performing 3 consecutive load ramps on a sapphire reference sample, enabling the AFM to convert the deflection from V to nm/V. The spring constant was calibrated by retracting the cantilever away from the reference sample and performing a harmonic thermal tune. Scans were performed on the sapphire reference sample to calibrate the sync distance and the Drive3 amplitude of the deflection separation curves.



*Figure 3-19 ScanAsyst-Fluid AFM tip.*

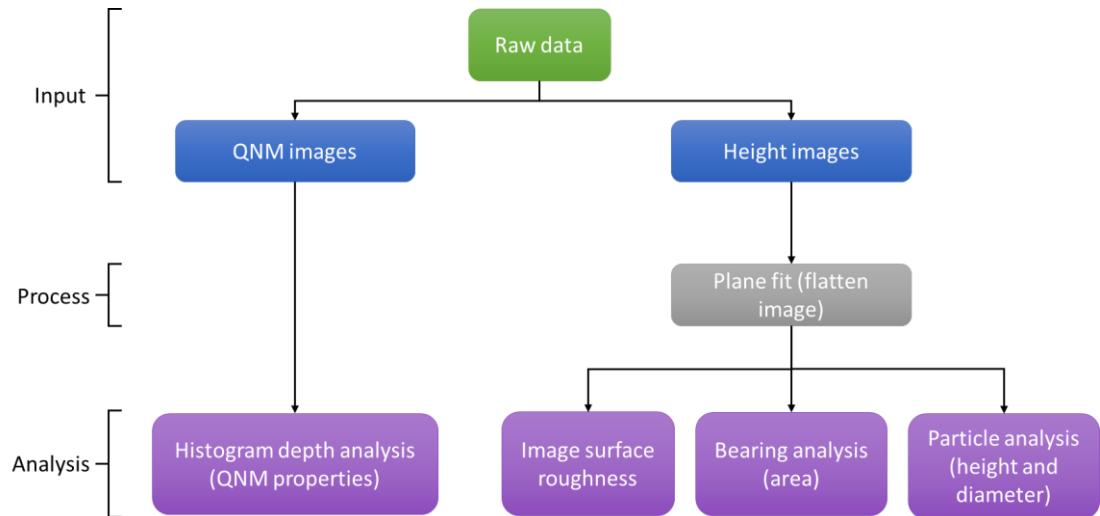
Experiments were performed on the standard mucin solutions, described in Table 3-3. Mucin surface interactions were initially examined in the absence of salts to characterise the size and spread of adsorbed mucin on the surface. This provided an idea to the level of surface coverage which was thought to provide surface protection. Experiments in PBS and citric acid aimed to assess mucin's interactions within these solutions and changes to size, spread and coverage within these different environments.

Due to the nature of testing a glycoprotein, mucin was susceptible to dehydration in the absence of a surrounding aqueous fluid. AFM scans performed in the air environment were therefore imaging a partially hydrated mucin layer compared to a fully hydrated mucin layer in the liquid environment. The two methods permitted a comparison between a simulated 'dry mouth' environment and a healthy hydrated environment. This aimed to examine possible mechanisms of dry mouth syndrome potentially further with a mucin layer.

### **AFM processing**

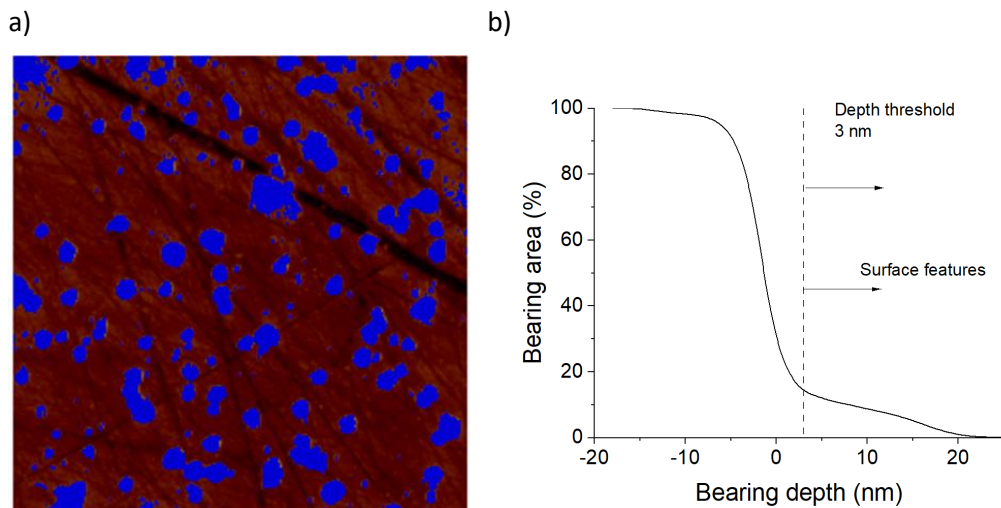
Aside from providing a visual assessment of mucin structures on surfaces, mucin size, area coverage, image roughness and properties were further analysed, shown by the workflow in Figure 3-20. Analysis was completed using NanoScope Analysis (Bruker, USA). Plane fit functions, a.k.a. image flattening functions, were applied to all height images to remove

image gradients before bearing, particle and image roughness analyses, while QNM images were directly assessed with an image depth analysis of regions of interest (ROI).



*Figure 3-20 AFM workflow and analyses.*

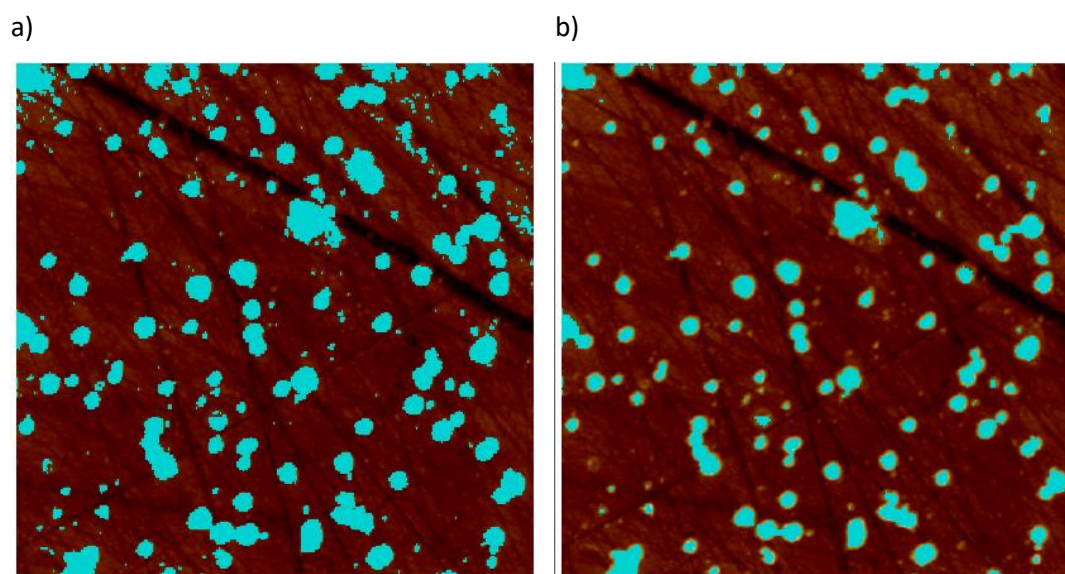
A depth threshold of 3 nm was applied for both particle and bearing analysis of mucin-surface structures, with the X-axis set to absolute. The meant all features above a reference plane 3 nm from the surface were assessed, demonstrated by Figure 3-21a) and b). Image surface roughness was determined using the roughness function in NanoScope Analysis.



*Figure 3-21 Bearing analysis a) mucin covered enamel surface highlighting surface features of interest and b) bearing area vs bearing depth showing 3 nm depth threshold and direction of surface features.*

The particle analysis function used the same depth threshold as the bearing analysis, and parameters were chosen to include boundary particles (incomplete particles on the edge of images). The function identified the features above the depth threshold for additional processing. The erode function was used to remove speckled datapoint. Erode is an image processing technique which removes pixels from the edges of identified particles, using a neighbourhood size of 3-pixel kernels. An example of an image before and after the erode

function is shown in Figure 3-22a) and b) respectively. The mean and standard deviation for particle heights and diameters of the remaining features were assessed by the algorithm afterwards.



*Figure 3-22 Erode example showing a) image before and b) image after a single erode function.*

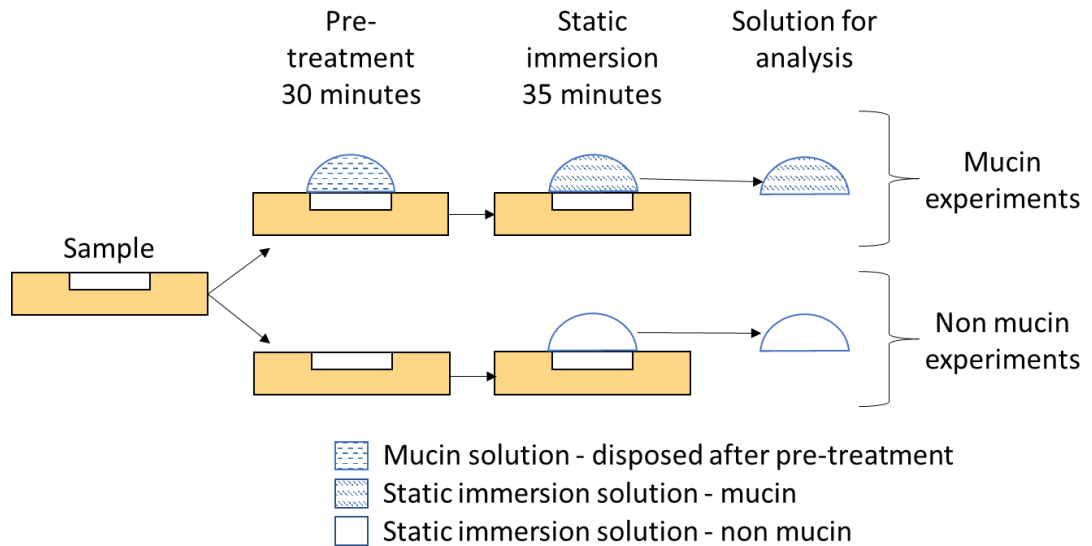
Finally, the image depth analysis function was used to assess the QNM properties of ROIs on the QNM images. Both mucin features and surface only features were assessed individually, and were compared to the composite properties of the whole image. Boxed areas were drawn around ROIs, producing a histogram of the image Z data, corresponding to adhesion, dissipation, logDMT modulus or deformation properties depending on the image channel. A mean and standard deviation from these histograms were taken from the ROIs for comparison.

### 3.2.6 Static and dynamic experimental methodologies

#### 3.2.6.1 Static immersion

Static immersion experiments assessed the pure corrosion properties of bovine enamel samples. Freshly prepared enamel samples were immersed in 300  $\mu\text{L}$  in an artificial saliva solution over a 35-minute period. The artificial saliva solutions are listed in Table 3-3. The time was chosen to equal the test duration of the dynamic tribocorrosion tests discussed later. Figure 3-23 shows the workflow of the static immersion protocol for mucin and non mucin pathways. For the former, samples were pre-treated in a neutral pH mucin solution i.e., Muc + DiW or Muc + PBS. This enabled mucin layer formation/adsorption before static tests. The pre-treatment solution was removed after 30 minutes and replaced with the corresponding static immersion solution to ensure all post-test analysis corresponded to the

same static immersion duration. Before experiments in Muc + acid, samples were treated with Muc + DiW to prevent excessive morphological changes in the pre-treatment phase. For non-mucin tests, samples were subjected to the static immersion solution as a corrosion control without mucin-surface interactions. All post-test solutions were refrigerated at 4 °C prior to chemical analysis.



**Figure 3-23 Static immersion experiment protocol.**

### 3.2.6.2 Dynamic tribological and tribocorrosion

A tribometer simulated the cyclical sliding conditions a tooth may experience in a controlled lab environment. The tribometer measured tangential and normal force data during simulation which was used to assess the friction and lubrication behaviour of a sample within a given environment. This was important to assess the protection mucin provided and how mucin layer viscoelastic properties linked to its dynamic friction in-situ. Experiments were performed on a NTR<sup>3</sup> nanotribometer (Anton Paar, Switzerland), shown in Figure 3-24, and another bespoke tribometer which will be discussed in greater detail in Chapter 7. Both tribometers investigated the sliding friction using a ball on flat configuration, i.e., a Y-TZP ball vs a flat/flattened sample.



Figure 3-24 NTR<sup>3</sup> nanotribo-meter.

### Tribometer theory

The system composed of a linear reciprocating stage which moved a mounted sample relative to a static probe within a range of  $5 \text{ mm} \pm 1.25 \text{ nm}$ , shown in Figure 3-25. The probe consisted of a pin with the  $\varnothing 3 \text{ mm}$  Y-TZP ball secured to the tip which served as the antagonist material for tribometer experiments. The probe was secured to pre-calibrated quad beam cantilever (Anton Paar, Switzerland) of a given stiffness in the normal force,  $F_n$ , and tangential force,  $F_t$ , directions which are quantified in Table 3-6.

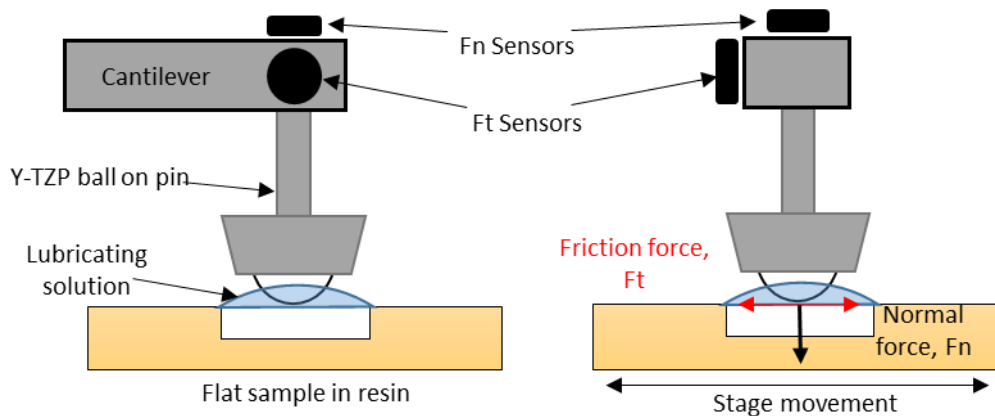


Figure 3-25 Front and side schematic of tribometer experiments.



The  $F_n$  applied to the sample was dependent on the cantilever stiffness and the displacement of a piezoelectric controlled stage, to a resolution of 0.05 - 0.1 nm. Capacitance displacement sensors measured the distance between the sensor and the cantilever, correlating to an output force measurement depending on the cantilever.

**Table 3-6 Tribometer quad beam cantilevers.**

Cantilever ID	$F_n$ stiffness (mN/ $\mu$ m)	$F_t$ stiffness (mN/ $\mu$ m)	Load range	Load resolution ( $\mu$ N)
ST-S 223	0.4704	1.1944	50 $\mu$ N – 100 mN	0.03-0.06
HR-S 220	0.0517	0.1712	5 $\mu$ N – 10 mN	0.003- 0.006

As the stage and sample moved relative to the loaded probe, a resistive force opposed the movement (friction). This manifested as a deflection of the cantilever beam in the  $F_t$  direction,  $x$ , measured by the capacitance displacement sensors. The output force,  $F$ , was then calculated following Hooke's law, where  $k$  was the cantilever's stiffness in the relevant direction.

### **NTR<sup>3</sup> Tribological protocol**

Two protocols were used to reflect different areas of study: to investigate the impact of tribocorrosive wear and to determine the friction and lubricating behaviour of mucin layers. As such different loading parameters were chosen. Tribocorrosion tests were performed on steatite and bovine enamel samples against Y-TZP balls. New balls were used for each dynamic test, which were cleaned in 70% ethanol and rinsed in deionised water prior to testing. Experimental conditions were chosen as a selection of the conditions used in *in-vitro* testing and in the ISO TS 14569-2:2001 for the wear testing of dental materials [146, 162, 161], which are displayed in Table 3-7. The experimental parameters were chosen to reflect the loading conditions and contact pressures associated with teeth mastication, < 140 MPa, compared to the contact pressures used by other researchers, > 200 MPa [164, 165, 187, 209, 184].

**Table 3-7 Tribocorrosion test parameters for NTR<sup>3</sup>.**

Parameter	Setting
Loading type	Constant
Load (mN)	10
Temperature ( $^{\circ}$ C)	20 - 25
Sliding amplitude ( $\mu$ m)	1000
Test duration	2000 cycles
Sliding frequency (Hz)	1

Friction and lubrication testing of mucin layers had different experimental parameters. Experiments were performed on QCM-D sensors after mucin layer deposition for 60 minutes. As the sensors and surface mucin layers were delicate, loading conditions were reduced. Incremental loads between 0.05 – 0.50 mN were used to assess the layer's load dependency behaviour on lubrication, which provided contact pressures between 15 – 60 MPa over the full test duration. Every 200 cycles, the load was increased by 0.05 mN. Table 3-8 shows the testing parameters used.

*Table 3-8 QCM-D sensor test parameters for NTR<sup>3</sup>.*

Parameter	Setting
Loading type	Incremental
Load increase (mN)	0.05
Load (mN)	0.05 – 0.50
Temperature (°C)	20 - 25
Sliding amplitude (µm)	1000
Test duration	200 cycles per load increment
Sliding frequency (Hz)	1

### **Triborig protocol**

The loading parameters of the Triborig were similar to the NTR<sup>3</sup> tests on the QCM-D sensors. These will be explained in further detail in Chapter 7.

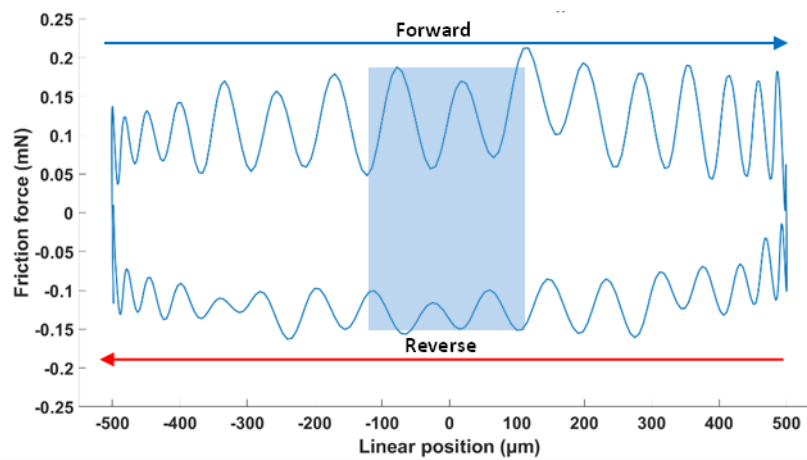
### **Output results and processing**

Amonton's law of friction describes the frictional force being proportional to the normal force applied to the system and the constant of proportionality is referred to as the coefficient of friction. Essentially, the magnitude of the frictional force,  $F_t$ , is the product of the applied normal force,  $F_n$ , and the coefficient of friction,  $\mu$ , plus an unknown interfacial adhesion force,  $C$ , as shown in Eq. 16. Its frictional force is assumed to be independent of surface contact area, sliding velocity and surface roughness.

$$F_t = \mu F_n + C \quad \text{Eq. 16}$$

In the context of tribology experiments, the mean  $F_n$  and  $F_t$  forces for steady state sliding were calculated by taking an average of the central 20% of the forward and reverse direction of a force displacement loop, over the last 25% of the total number of cycles. An example of

a  $F_t$  displacement loop and calculation region is shown in Figure 3-26. This was facilitated by the NTR<sup>3</sup> software (Tribometer, Anton Paar, Switzerland) which calculated the mean values for the coefficient of friction,  $F_n$  and  $F_t$  forces for each cycle. For incremental loading, the ‘system average’ was determined by the gradient of the average steady state  $F_t$  vs  $F_n$  curve according to Eq. 16. This provided an average coefficient of friction over a range of normal loading conditions. Testing under static loading conditions were calculated as an instantaneous coefficient of friction where  $\mu$  was calculated as  $F_t/F_n$  and averaged for the final 25% of the total number of cycles. One important point to note is the absence of the adhesion force,  $C$ , in this calculation. Given the scale of testing and the applied normal loading during tests, the adhesion force was considered negligible in this application.



*Figure 3-26 Hysteresis loop example showing frictional force,  $F_t$ , vs linear position. The blue and red arrows represent the forward and reverse trace respectively and the shaded region shows the area of steady state sliding used to determine a cycle's mean  $F_t$ .*

### 3.2.7 Surface and chemical analysis techniques

#### 3.2.7.1 White light interferometry

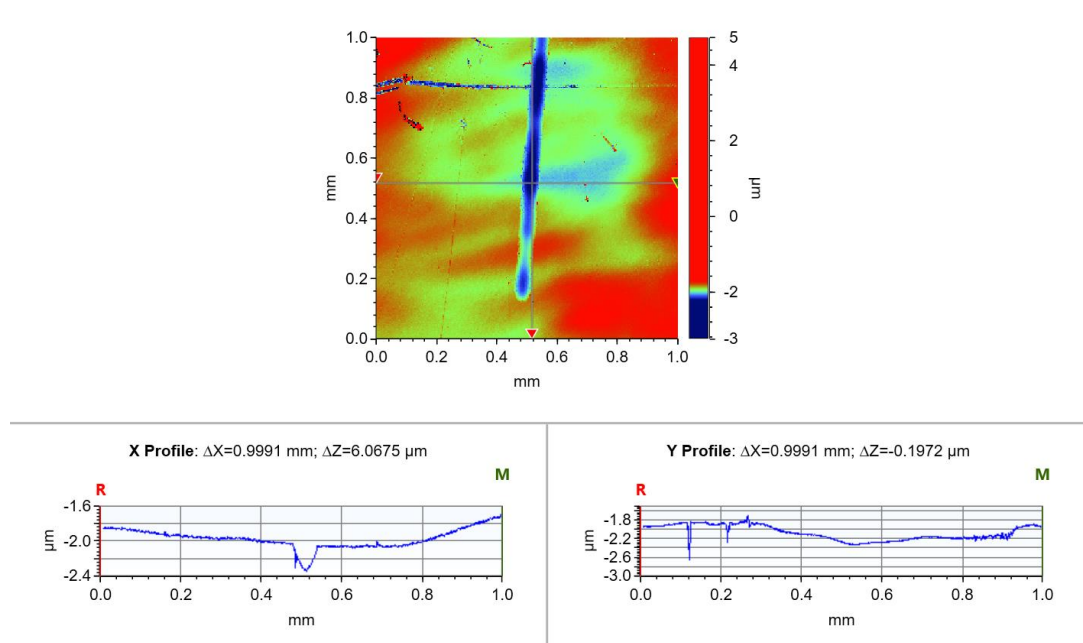
Surface profile measurements were performed using a NPFlex (Bruker, USA) white light vertical scanning interferometer (VSI). This profilometer enabled 3-D non-contact meteorological measurements to provide both quantitative and qualitative surface characterisation after tribological testing. Non-contact profilometry was preferred to prevent sample damage that might occur from conventional contact profilometry. Scar profiles were investigated to characterise the scar's depth and width. Volumetric analyses of tribo-contact areas were performed to determine surface material loss.

### Sample preparation before VSI

All samples were thoroughly rinsed in deionised water whilst being gently brushed with a nylon bristled toothbrush after testing. These were then dried under compressed air and wiped with a lint-free tissue prior to VIS surface examination. Y-TZP balls prepared in the same way to inspect their surfaces.

### Processing

Data was processed using Vision 64 (Bruker, USA). Raw data was processed by the 'Terms removal (F-operator)' function to remove sample curvature and tilt whilst a mask was applied on the wear location. Linear profiles of the scar were taken, measuring the width, length and depth from the X and Y trace data, shown in Figure 3-27. The scar depth was determined as the distance between the flattened surface and the lowest point of the wear scar at the central scar width cross section. Scar width was measured from this cross section too as the distance between the opposing scar edges at the flat reference surface. The length was also measured in a similar way, but from a scar length cross section.

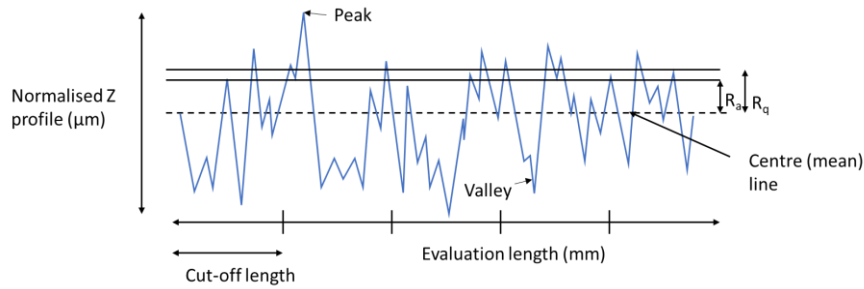


*Figure 3-27 Example of bovine enamel scar taken with VSI, showing X and Y cross-section profiles.*

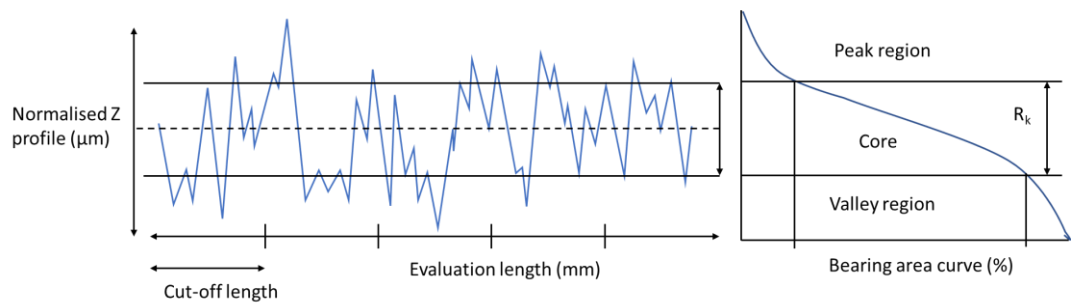
Surface roughness was calculated using the stylus analysis function in Vision64, where a sample evaluation length of 1.25 mm was used, with a 0.25 mm cut-off, performing 5 samples per length. Average asperity roughness,  $R_a$ , root mean square roughness,  $R_q$ , and core roughness,  $R_k$ , were assessed for steatite and bovine enamel surfaces.  $R_a$  is the arithmetic average of the absolute values of the profile height above the centre line for a given length, while  $R_q$  is the root mean square average profile height over the centre line, demonstrated by the profile in Figure 3-28a).  $R_k$  is calculated differently, applying a bearing

analysis curve on the normalised Z profile. Using the curve in bearing area plot, the Z profile values are taken from the minimum slope region to represent the core surface profile, shown in Figure 3-28b). The core roughness is an alternative roughness measure which ignore the impact of larger peaks and valleys within the profile.

a)

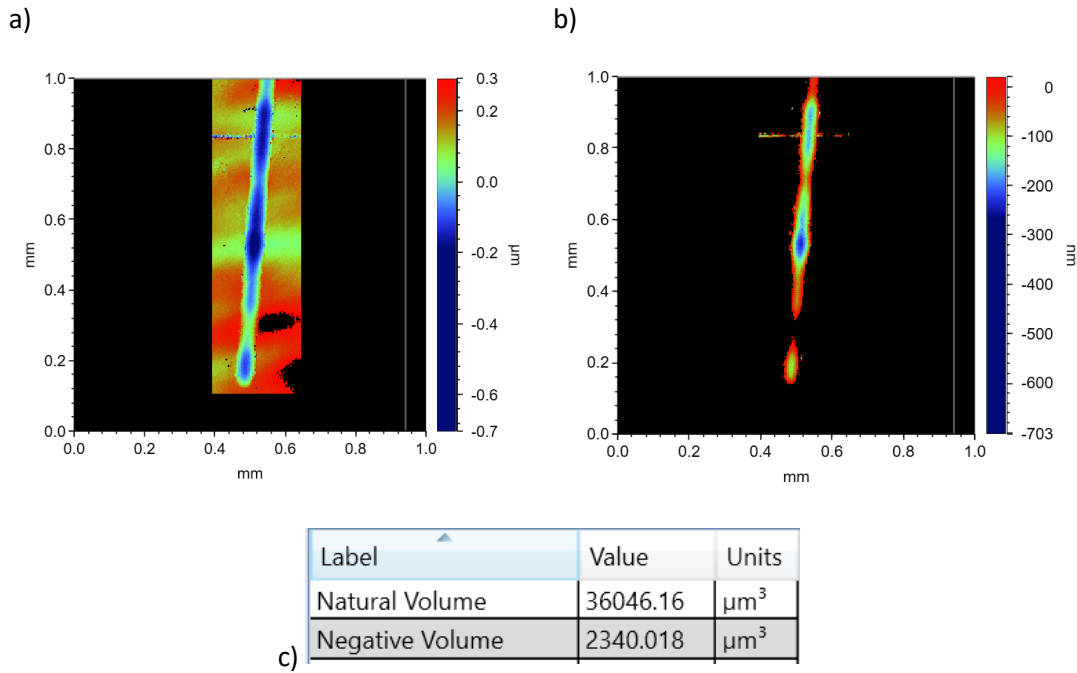


b)



**Figure 3-28** Example of surface roughness parameters calculated from profile height for a)  $R_a$  and  $R_q$  and b)  $R_k$ .

The wear scar volume was determined with further processing of the raw data. Images were adjusted such that the flattened reference surface possessed a depth value of  $Z = 0 \mu\text{m}$ . The depth value related to the surfaces at the edges of the wear scar, to enable the calculation of the volume below this depth. Sections were masked off to only focus on the scar area and the surrounding edges, shown in Figure 3-29a). The volume was then calculated as the negative volume from the reference plane as shown in Figure 3-29b), which determined the wear scar volume, shown in Figure 3-29c).



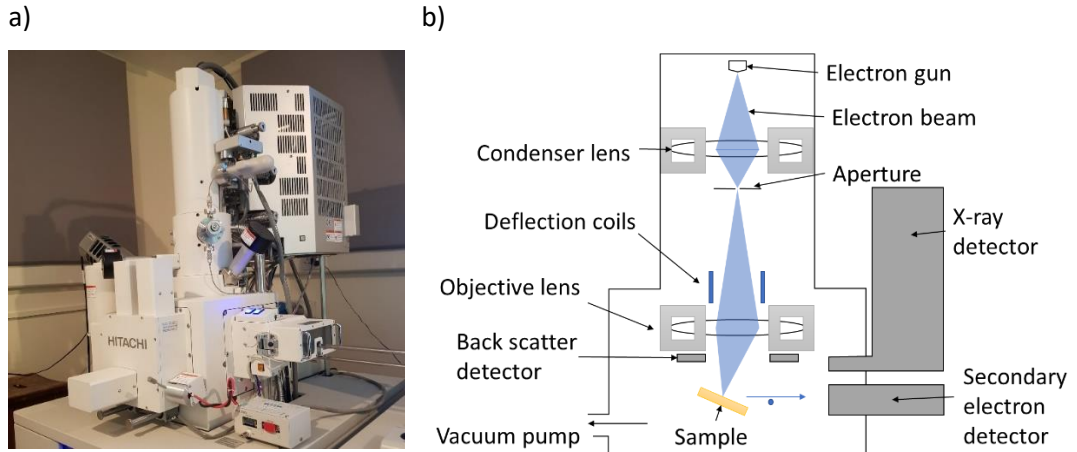
**Figure 3-29** Example of volume calculations showing a) masked scar area, b) scar area below  $Z = 0 \mu\text{m}$  and c) the output negative volume result.

### 3.2.7.2 Optical light microscope

Optical light microscopy (Leica, Germany) was used to perform quick examinations of bovine enamel and steatite samples throughout the grinding process, as part of managing the quality of samples as alluded to in Section 3.2.1.2. Bovine enamel surfaces were studied the surfaces of the two materials after tribological experiments to characterise the potential wear mechanisms. Examples of the output data can be found in Chapter 2 Section 2.2.1.2.

### 3.2.7.3 Scanning Electron Microscope (SEM)

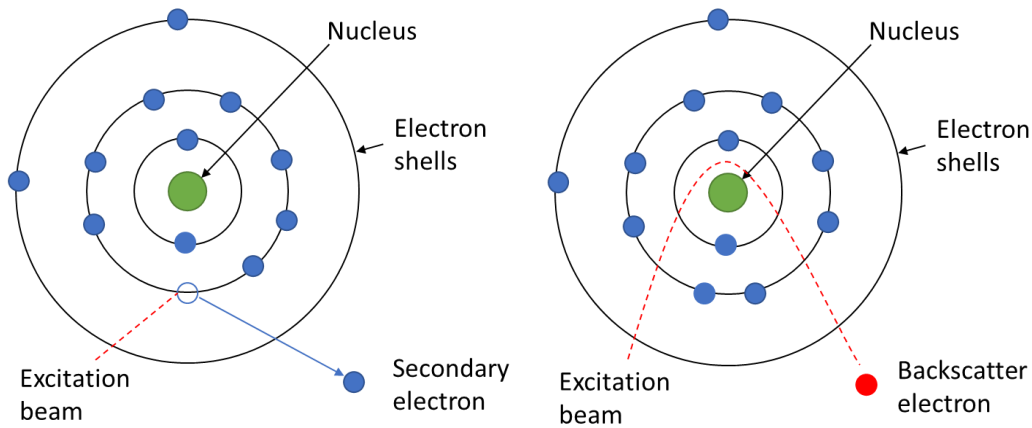
Scanning electron microscopy (SEM) was performed using a SU820 (Hitachi, Japan) high resolution SEM as shown in Figure 3-30. This enabled high resolution surface imaging in the scale of nanometres (nm) which permitted characterisation of surface features and wear areas. Compared to the wavelengths of visible light, an electron possesses a much shorter wavelength which permits higher resolution imaging of finer surface features compared to an optical light microscope. Images were captured using an accelerating voltage of 15 keV under vacuum conditions ( $<0.1 \text{ mPa}$ ) which also enabled EDX elemental characterisation, as described in section 3.2.7.4.



*Figure 3-30 SEM a) Hitachi SU8230 high resolution and b) schematic.*

### SEM theory

The image on the right of Figure 3-30 shows a schematic of how an SEM works. The SEM scans a surface with an electron beam which is focused on the surface with electromagnetic condenser and objective lenses. Depending on the penetration depth of the incident electron beam, signals are emitted from the surface in the form of secondary electrons, backscattered electrons and x-rays which are characteristic for a given element. Because secondary electrons possess a relatively low energy, they are more surface sensitive and are useful for examining the top few nanometres of a given surface. Backscatter electrons have a higher energy and are a result of the reflection of the incident electron beam from within the sample. An example of this is shown in Figure 3-31. The intensity of the background scatter changes when interacting with a surface with varying crystal orientation, which helps identify elemental regions when combined with the x-ray emission data. X-ray emissions can be used to identify the sample composition close to the surface, which is described in section 3.2.7.4. Each emission is detected by their respective detector and analysed on a computer. A representation of the data output has been presented previously in Chapter 2 Section 2.2.1.2.



*Figure 3-31 Schematic of how the focused electron beam interacts with an atom showing the emission of a secondary electron (left) and the reflection of a back scattered electron (right).*

### Sample preparation

As samples were non-metallic and did not possess any charge conducting properties, samples had to be pre-treated to prevent surface charges building up. Dry samples were mounted to metallic stubs with carbon double-sided adhesive discs. The resin sections of the sample were painted with a carbon paint, while the surface under examination was left exposed. Once dried, the exposed surface was sputter coated with a thin layer of graphite under vacuum conditions. These were then transported to a different room to perform SEM investigations.

#### 3.2.7.4 Energy Dispersive X-ray Spectroscopy (EDX or EDS)

Energy dispersive X-ray spectroscopy (EDX) is an analytical technique which allowed the identification of the elemental composition of a sample's surface and is integrated with the SEM. This was performed alongside SEM as vacuum conditions are required to perform this function. This enabled a semi-quantitative examination of the surface chemistry of steatite and bovine enamel.

### Theory

The SEM electron beam is fired at the surface, which excites electrons within an atom's inner shell. These electrons are ejected and electrons which inhabit the outer shells jump energy levels to replace the escaped electron. The movement from a higher energy shell to a lower energy shell releases the energy difference in the form of an X-ray which is detected by the SEM-EDX. A diagram of this is shown in Figure 3-32. The energy of the X-ray is characteristic of a given element and thus the elemental composition of a sample can be measured in counts per second per electron volt. An example of the data output is presented in Figure 3-33.



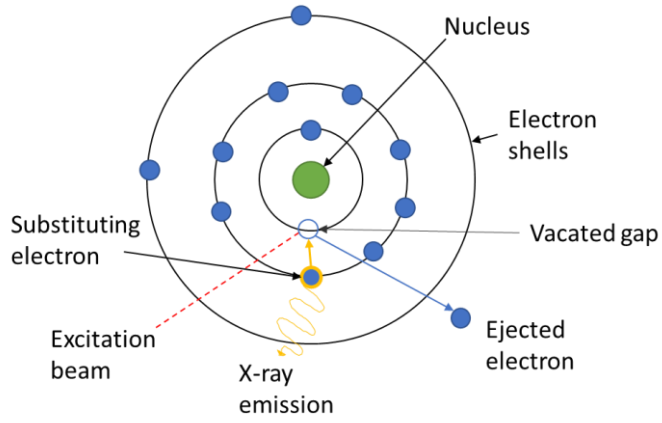


Figure 3-32 Diagram of electron excitation and X-ray emission

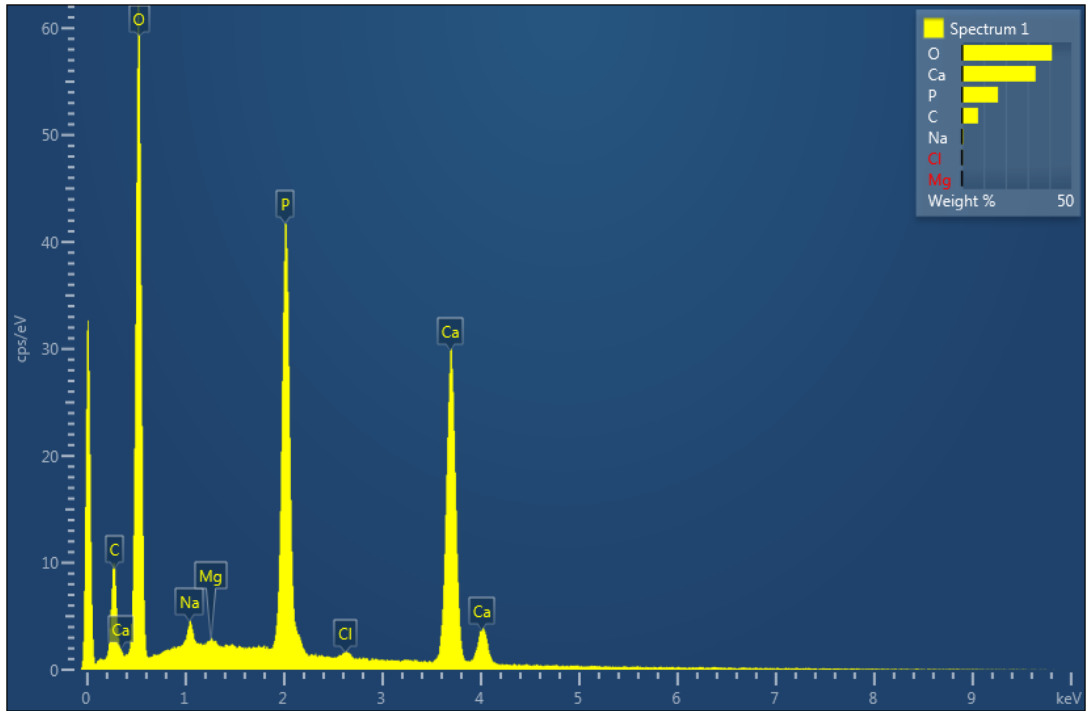


Figure 3-33 Example out data output from EDX for a bovine enamel sample.

### 3.2.7.5 X-ray Diffraction (XRD)

X-ray diffraction (XRD) was used to analyse the crystal arrangement of bovine enamel before and after tribological and tribocorrosion experiments. A D8 (Bruker, USA) X-ray diffractometer was used, as shown in Figure 3-34. Phase identification and structural deviations because of mechanical stress and corrosive environments were assessed.



*Figure 3-34 Bruker D8 X-ray Diffraction.*

#### **Theory**

The crystals within a substance are arranged in a regular array of atoms which are characteristically spaced in between planes. X-rays, with a wavelength in the same order of magnitude of the plane's spacing, can interact with the electrons of the atoms which scatter the X-rays. These scatterings interfere with each other, either destructively or constructively. For a specific angle of incidence, strong amplification can occur from constructive interferences which is referred to as diffraction and this interaction is defined by Bragg's diffraction law as shown in Eq. 17 and illustrated in Figure 3-35.

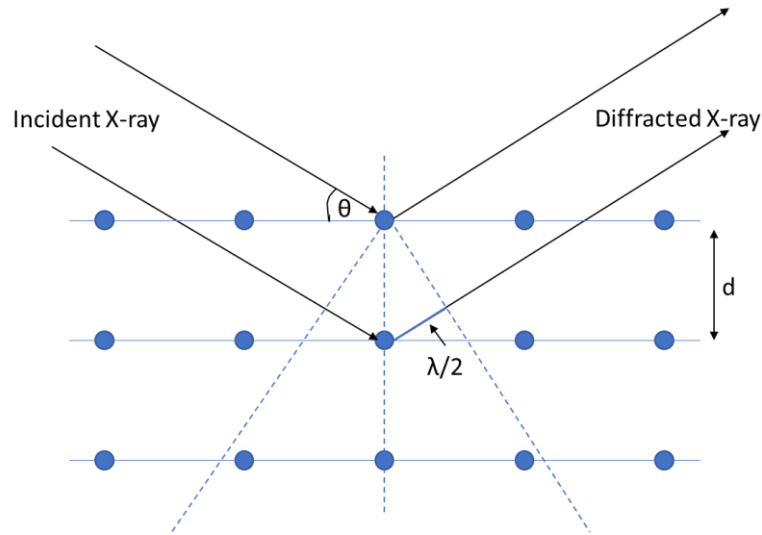


Figure 3-35 Schematic of X-ray diffraction and associated parameters to Bragg's Law.

$$2d\sin\theta = n\lambda$$

Eq. 17

### Sample preparation

All samples were thoroughly rinsed in deionised water whilst being gently brushed with a nylon bristled toothbrush after testing. These were then dried under compressed air and wiped with a lint-free tissue prior to XRD examination. Samples were placed in specialised mounts to ensure surfaces were aligned for analysis.

### XRD protocol and analysis

$2\theta$  scans between  $20-70^\circ$  with a step size of  $0.04^\circ$  and a scan time per step of 1.5 seconds were performed for all samples under a copper  $K\alpha$  x-ray source. An example of the output data is presented with the background subtracted in Figure 3-36.

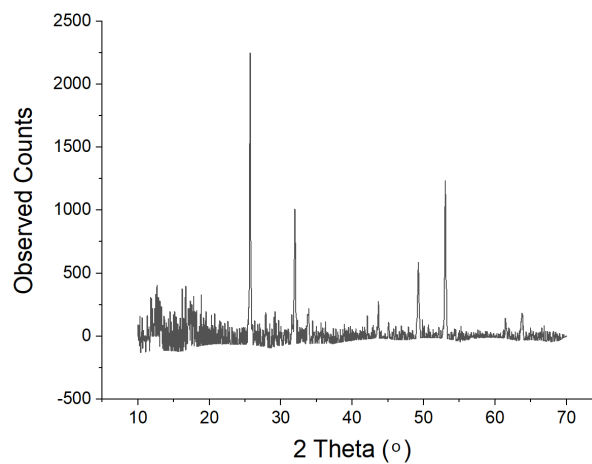


Figure 3-36 Example data of XRD analysis of bovine enamel after surface preparation.

Eq. 18 presents the Scherrer equation which was used to calculate the crystallite size,  $D$ , from the product of the incident emission wavelength,  $\lambda$ , and a Scherrer constant (0.9) over the product of the FWHM,  $\beta$ , and the cosine of the Bragg angle,  $\theta$  [41].

$$D = \frac{k\lambda}{\beta \cos\theta} \quad \text{Eq. 18}$$

Eq. 19 shows the Bragg equation which was rearranged to determine the d-spacing parameter,  $d$ , which also enabled the calculation of interplanar unit cell spacings  $a$  and  $c$ . Miller indices,  $h$ ,  $k$  and  $l$  were determined as (002) and (230) from the sodium carbonate hydroxyapatite reference [210] for the corresponding  $2\theta$  angles to calculate  $a$  and  $c$  [211].

$$d = \frac{n\lambda}{2\sin\theta} = \left[ \left( \frac{4}{3a^2} \right) (h^2 + k^2 + hk) + \left( \frac{l^2}{c^2} \right) \right]^{-\frac{1}{2}} \quad \text{Eq. 19}$$

### 3.2.7.6 Raman Spectroscopy

A Raman spectrometer (inVia, Renishaw plc, England) was used to determine whether any surfaces species existed within the wear tracks of enamel samples after tribological testing in different environments. This provided an assessment to the existence of a potential tribofilm (mechanically induced surface layer).

#### Sample preparation

Similar to before, all samples were thoroughly rinsed in deionised water whilst being gently brushed with a nylon bristled toothbrush after testing. These were then dried under compressed air and wiped with a lint-free tissue prior to Raman examination.

#### Raman protocol and analysis

The spectrometer used a near infrared laser with a wavelength of 785 nm and a 0.05% power filter. A spectral range from 400 – 1400  $\text{cm}^{-1}$  was investigated, as no peaks were observed outside of this range. Figure 3-37 presents an example of the data output.

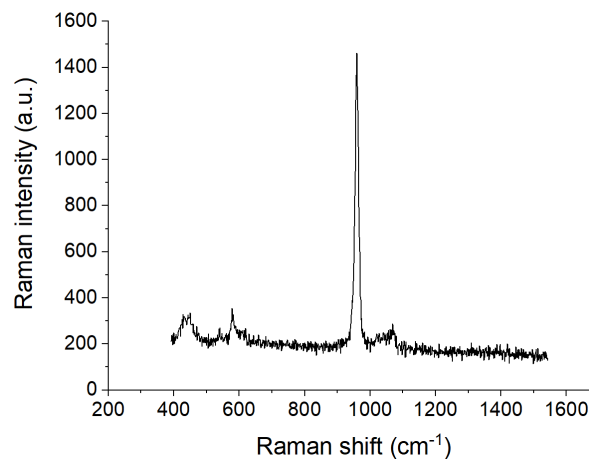


Figure 3-37 Example of data output from Raman spectroscopy for a bovine enamel sample.

The degree of demineralisation was calculated from the intensities of the v1 PO<sub>4</sub><sup>3-</sup> peak. Eq. 20 shows the formula for calculating the degree of demineralisation.  $I_{ref}$  was the v1 peak intensity for the deionised water samples outside of the wear location  $I_{demin}$  was the v1 peak intensity for other samples. The deionised water only spectra outside the wear location was chosen as a reference for this calculation in the absence of pre-test Raman spectra as it represented a baseline sample fresh from the storage. Intensities were taken from both raw and normalised spectra for analyses as it was not clear in previous studies whether this was taken from the former or the latter [212, 213].

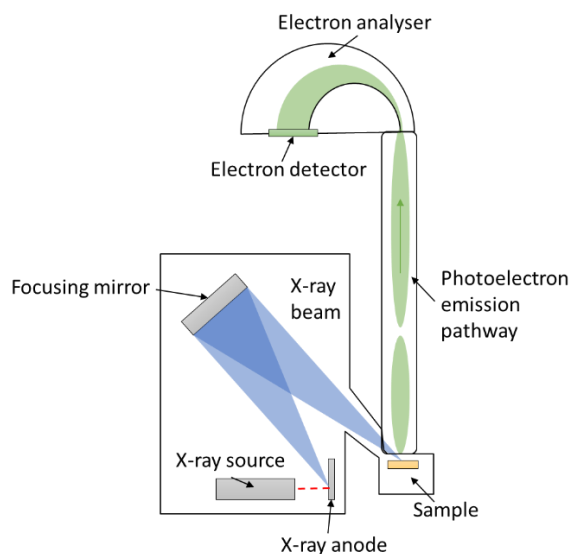
$$DD = 100 \times \left(1 - \frac{I_{demin}}{I_{ref}}\right) \quad \text{Eq. 20}$$

### 3.2.7.7 X-ray Photoelectron Spectroscopy - ENVIRO (XPS)

An Enviro ESCA (Electron Spectroscopy for Chemical Analysis) a.k.a X-ray Photoelectron Spectroscopy (XPS, Spec group, Germany) with an Al  $K_{\alpha}$  micro-focused monochromatic x-ray source (1486.7eV) was used to provide a quantitative evaluation of the chemical composition of bovine enamel surfaces before and after dynamic tribo-tests. Unlike a conventional XPS system which requires an ultra-high vacuum to operate, the EnviroESCA could work at near ambient conditions. This enabled the analysis of bovine enamel samples without fully dehydrating samples, which prevented the outgassing issues associated with ultra-high vacuum XPS. This investigated the surface chemistry of bovine enamel after testing in various artificial saliva solutions, to determine whether salts, acids or mucin had cause changes in the superficial enamel chemistry.

#### Theory

Figure 3-38 shows the XPS system used. Like the x-ray emissions explained in Section 3.2.7.4, the XPS generates an x-ray beam by firing an electron gun on an aluminium anode. Monochromatic x-rays are then focused onto the sample, which excite electrons within the top atomic layers of the sample, causing photoelectric emissions. The photoelectron emissions possess a specific kinetic energy which can be used to determine the electron's binding energy through knowledge of known incident x-ray photon energies. Photoelectrons move up towards an electron analyser, following a circular path with a radius dependent on its kinetic energy, before hitting the electron detector. The detector measures the intensity of electrons hitting it in counts per second. A photoelectric spectrum is produced by varying the voltage of the hemispherical capacitor to determine the sample's chemical composition.



*Figure 3-38 Schematic of Enviro XPS system.*

### Sample preparation

All samples were thoroughly rinsed in deionised water whilst being gently brushed with a nylon bristled toothbrush before XPS examination. These were then dried under compressed air and wiped with a lint-free tissue, before being carefully transported to a different lab for XPS analysis.

### XPS protocol

Analysis was performed before and after tribological tests to determine any changes to the chemical composition within areas of interest. Full surveys were taken to determine atomic composition at the specific sample locations and short scans were performed for specific binding energies related to the sample's composition. These included binding energies associated with calcium, phosphorus, carbon, nitrogen, and oxygen. To prevent sample charging, a problem alluded to in Section 3.2.7.3, a neutral argon gas was pumped into the 1 mBar atmosphere to deliver free charge to the surface. Each sample was scanned for approximately 45 minutes per location.

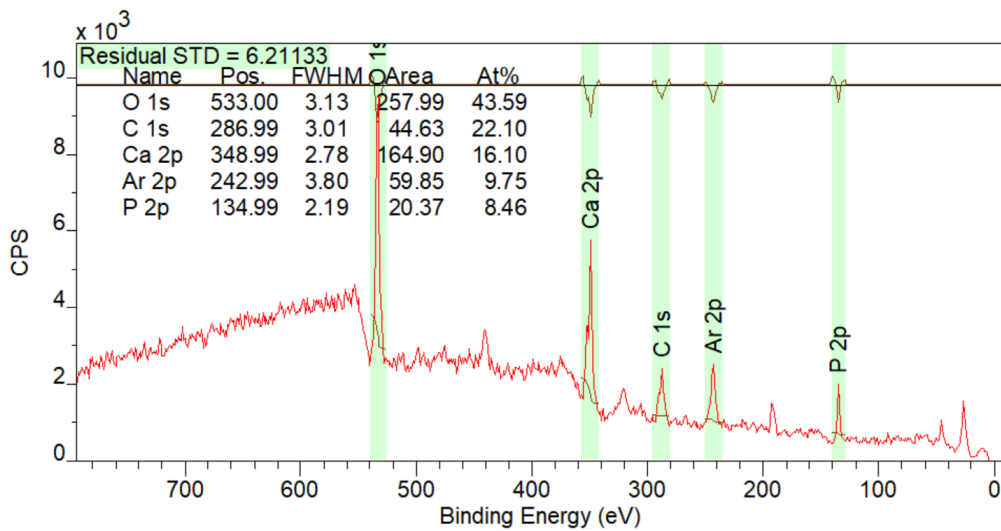
### Processing

The XPS curves were processed using the CasaXPS software to analyse survey data, including full sweep surveys and more specific elemental surveys. The binding energy scale was calibrated for the Ar-2p electrons at 243 eV, rather than the C-1s electrons at 284.5 eV. This decision was made due to the abundance of argon used to compensate the charge build up under ambient conditions. The Shirley background removal type was applied to all peaks to determine the atomic percentage of the full survey data, an example of which is shown in Figure 3-39a). This background type was also applied to individual elemental surveys to fit component peaks, an example of this is shown in Figure 3-39b). Fitting constraints were

applied to the full width half maxima (FWHM) of multiple peaks so that these were equal during the peak fitting process. Values for binding energies were taken from: the NIST XPS reference database, Thermo Scientific XPS data base, XPS reference handbook and the literature [214, 215, 216, 217].

Table 3-9 presents the XPS component data in relation to binding energies observed in the literature and XPS databases. This was used to identify components within deconvoluted peak data. For clarity in data analyses, components which presented more than one bond species for a single binding energy were used purely for providing a hypothesis of the surface features, rather than assigning both bond candidates to the observed binding energy.

a)



b)

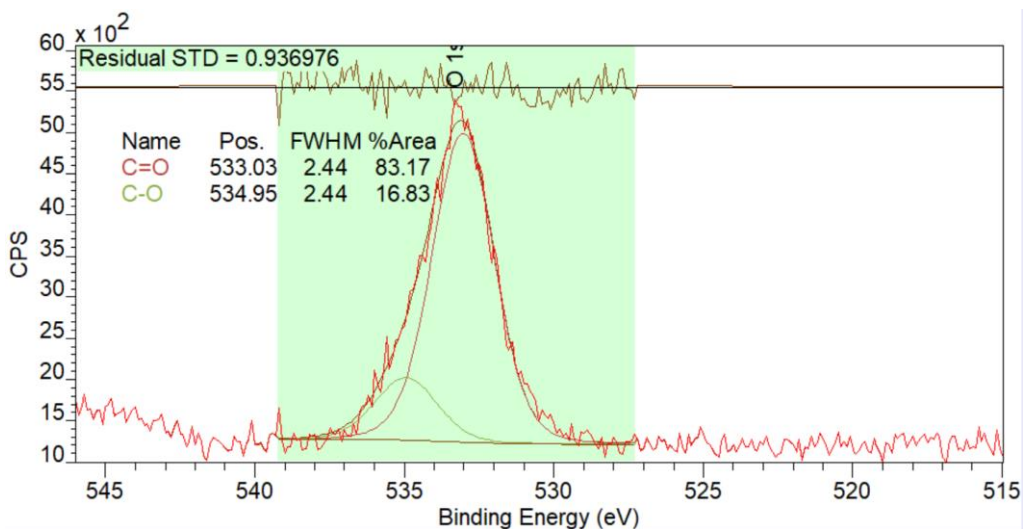


Figure 3-39 Example of output XPS data on CasaXPS for a bovine enamel sample showing a) a full survey of the binding energies, and b) a narrow-band survey over the O1s peak with curve fittings.

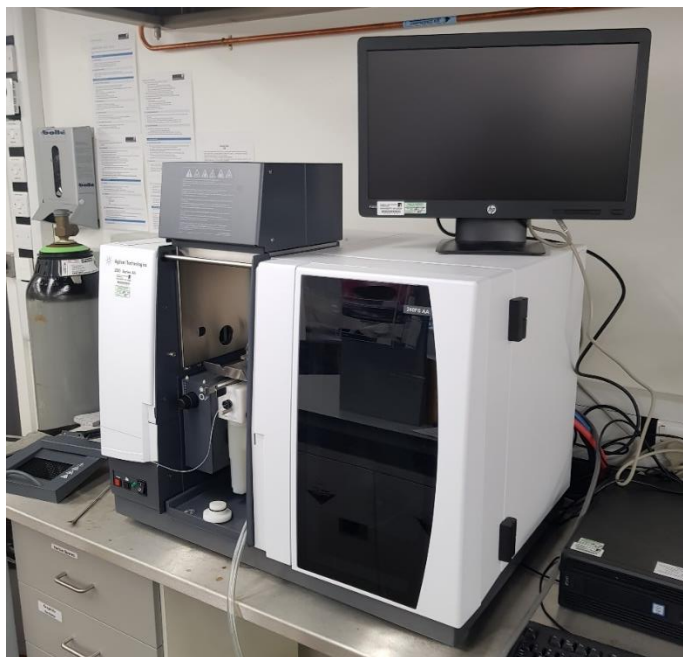
*Table 3-9 XPS peak components and binding energies from the literature and databases with references.*

XPS Peak	Component	Binding energy (eV)	Reference(s)
<b>O 1s</b>	O-H/O-C	533.1	[214, 109, 218, 219, 220, 221]
	O=C/O-P	531.5	[218, 215, 214, 109, 219, 221]
<b>C 1s</b>	C-C/C-H	285	[218, 222, 220, 216]
	C-O/C-N	286.5	[218, 222, 220, 216]
	C=O	288	[218, 222, 220, 216]
	CO <sub>3</sub>	289	[218, 222, 220, 216]
<b>N 1s</b>	N-H	400	[218, 215, 216]
	Satellite feature	401.8 - >405	[218, 215, 216]
<b>Ca 2p</b>	Ca 1/2p	351	[215]
	Ca 3/2p	347.3	[218, 215]
	Ca	344.9	[214]
<b>P 2s</b>	PO <sub>4</sub>	190.4	[223]
	P	188	[223]
<b>Cl 2p</b>	Cl 1/2p	198	[215]
	Cl/3/2p	200	[215]



### 3.2.7.8 Atomic Absorption Spectrophotometry (AAS)

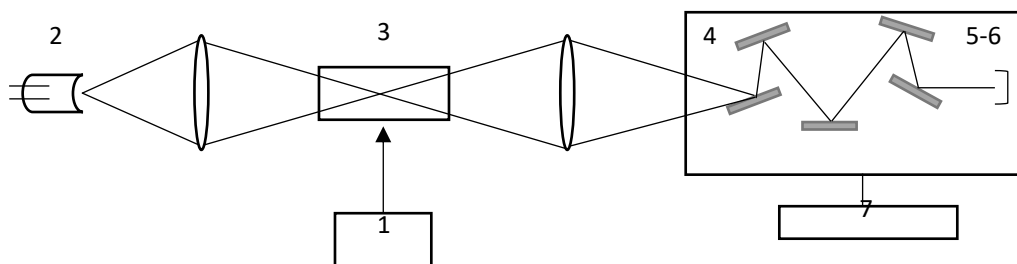
Atomic absorption spectrophotometry (AAS, Agilent 200 series AA, USA) was utilised for identifying and quantifying specific elements in each sample, shown in Figure 3-40. The technique measured and analysed the absorption of radiant energy of atomized elements, which quantified the concentration of calcium within static and dynamic post-test solutions.



*Figure 3-40 Flame AAS (Agilent 200 series AA)*

#### **Theory**

A sample solution was passed through a nebuliser which would disperse the solution into fine mist over a source of thermal energy. This dissociated compounds into a cloud of ground state atoms. In this case, an air-acetylene fuelled flame was used to achieve temperatures of around 2300 °C for dissociation. For examination of elements, such as calcium, higher temperatures were required for dissociation. An acetylene-nitrous oxide fuel was utilised to achieve flame temperatures of around 2700 °C. The atomised cloud was then irradiated by a chosen hollow cathode (HC) lamp which would excite electrons within a specific atom. This light was aligned to pass through the flame burner and atomized cloud towards a monochromator which isolated the light's wavelength. Light then passed to a detector/amplifier and absorption was measured on an electronic readout. A schematic of this is shown in Figure 3-41.



**Figure 3-41 Schematic of Flame AAS. 1) The nebulizer, 2) HC lamp, 3) Flame burner, 4) Monochromator, 5) Detector, 6) Amplifier, 7) Signal processing and electronic readout.**

The HC lamp emitted a characteristic wavelength of light which corresponded to a specific element. The atoms of this element would absorb the light energy causing electrons to move up an energy level. The more abundant an element was in a sample; the more energy was absorbed by the atoms. When the electrons relaxed, whereby electrons moved from the energy level above back to their original level, energy was released as photons. The intensity and wavelength of this emission was subsequently analysed to determine the presence of the element of interest and the concentration of it within a solution measured in ppm (parts per million) or mg/L.

#### 3.2.7.9 Solution preparation and protocol

Prior to any sample testing, a standard solution of a specific element was made up for the purposes of equipment calibration. Calcium standard solutions of 800 ppm and magnesium solution of 20 ppm were made up for this purpose. A SIPS, sample introduction pump system, was integrated into the AAS system to effectively dilute the standard solution prior the nebulizer. 7 calibration points were determined within the optimal working range for each element and the SIPS diluted the standard solution accordingly. A calibration curve was then established to analyse the test sample solutions.

A minimum volume of 1.5 ml was required for AAS analysis. Sample solutions were collected from tribometer tests and the initial volume was measured to the nearest 10  $\mu\text{l}$  by collection with a pipette. Samples were then diluted with 5 ml of MilliQ water (>18 M $\Omega$  purity) for AAS analysis. Once analysis was complete, the initial concentration ( $C_1$ ) of the solution was calculated from knowing the diluted concentration ( $C_2$ ), and the pre and post dilution volumes ( $V_1$ ,  $V_2$ ) as shown in Eq. 21.

$$\frac{V_2 C_2}{V_1} = C_1 \quad \text{Eq. 21}$$

### 3.2.8 Statistical analysis

A student's t-test was used to assess the significance of observed differences between samples for including friction, calcium release and scar volume results to name a few. Paired tests were performed on Microsoft Excel using a two-tail distribution and differences were statistically significant if  $p < 0.05$ .

## 3.3 Summary

The materials and methods presented in this chapter provide a means of analysing the role of a mucin additive as a component of an artificial saliva. This initially investigated the viability of using steatite as an alternative tooth material for tribological and adsorption-based studies with mucin, to which surface analysis methods were particularly helpful in characterising differences between materials. Growth experiments aimed to identify the mechanistic behaviour of mucin adsorption and its structural properties on dental materials, including tooth enamel. This provided insights into potential lubrication mechanisms under tribological contacts. Tribology and tribocorrosion based experiments examined the role of mucin for protection, measuring different aspects of surface and corrosive wear. Changes to surface chemistry and crystal phase were examined before and after tribological tests. Finally, a conceptual methodology to investigate the lubrication of mucin layers and their structural properties in-situ was trialled.

## Chapter 4. General characterisation of mucin solutions, surfaces and interactions

### 4.1 Introduction

This chapter aims to investigate the characteristics of mucin structures within different bulk lubricant environments, and understand how this influences the formation of mucin surface layers through the lubricant-surface interactions in the absence of tribology. Figure 4-1 shows a flow chart of the experimental methods and analyses used in this chapter. Mucin was characterised alone in different solution environments with DLS and zetapotential methods. Bovine enamel and steatite surfaces were characterised by optical microscopy, SEM, EDX and quasi-in situ AFM methods. Following the static immersion protocol with the AFM, mucin interactions with steatite and bovine enamel surfaces were investigated. This chapter also aimed to comment on the feasibility of steatite as an alternative test material to bovine enamel, investigate how solution composition influenced mucin and mucin layers, and, to further investigate the surface properties of partially hydrated and fully hydrated mucin layers.

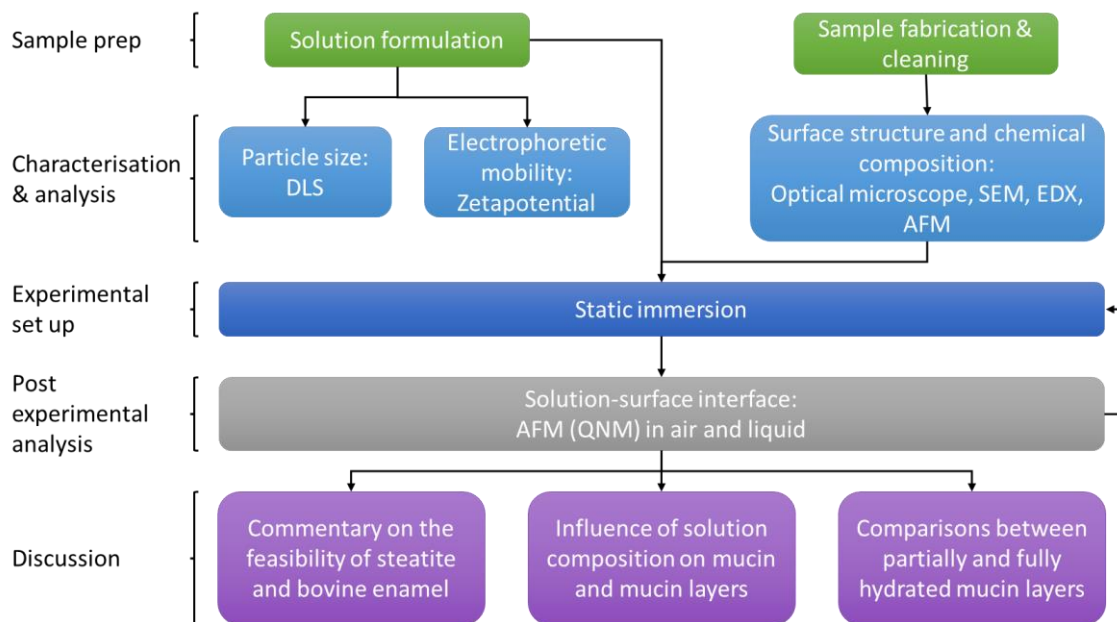


Figure 4-1 Flow chart of experimental methods and analyses in Chapter 4.

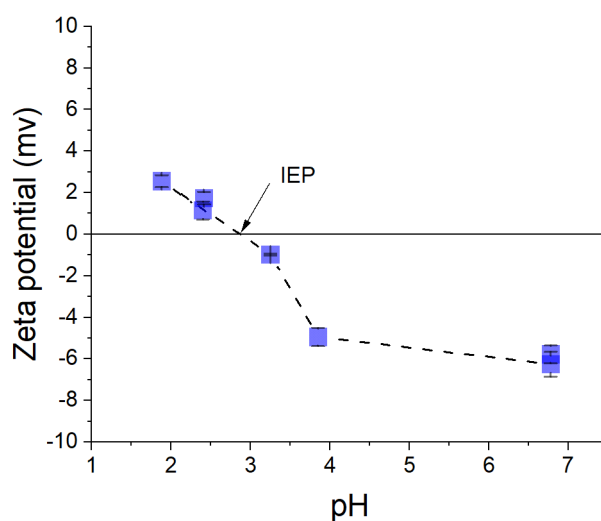
## 4.2 Results

### 4.2.1 The influence of solution composition on mucin

#### 4.2.1.1 Influence of pH on mucin isoelectric point and size variation

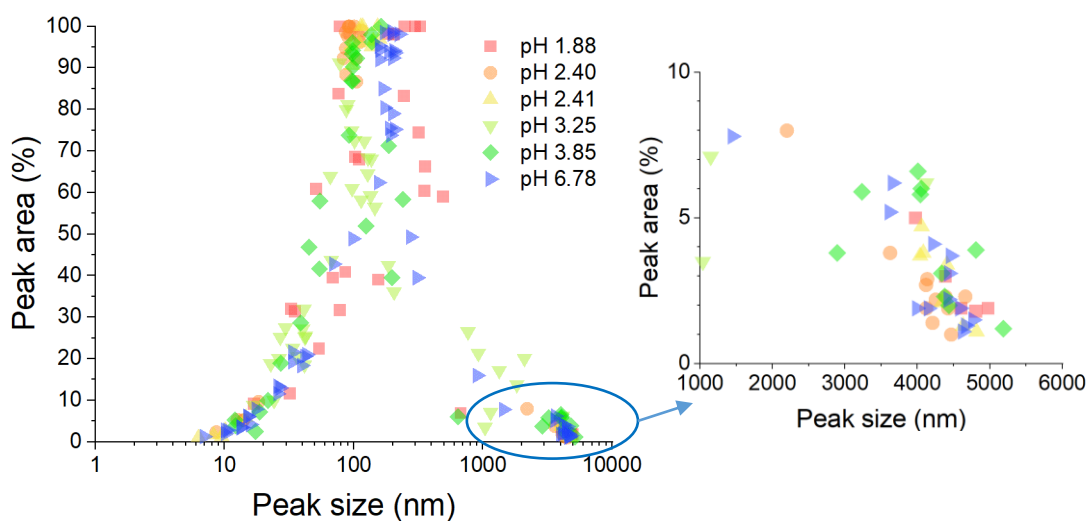
Solutions of different pH were made with citric acid to determine the isoelectric point of mucin. This provided an insight into the charge behaviour of mucin and how it might interact with solution components and surfaces. The pH was confirmed with 3 readings from a pH meter prior to experimental analysis to ensure all readings were within a pH of 0.01.

Figure 4-2 shows the zeta potential as a function of pH for a 0.2% mucin solution (Muc + DiW). The isoelectric point (IEP) was estimated to be between pH 2.4 – 3.25. Mucin was shown to have a negative zeta potential of  $-6.01 \pm 0.51$  mV in a neutral pH (6.78), suggesting mucin was negatively charged in this environment. The zeta potential was observed to increase as the pH decreased.



*Figure 4-2 Zeta potential vs pH of 0.2% mucin solution.*

Figure 4-3 shows the peak sizes distribution and area intensity of mucin. A range of mucin sized between 5 to 5000 nm was observed, presenting a large degree of size variation. The peak area intensity was the greatest between 100 – 300 nm, indicating this was the most common mucin size agglomeration. The pH variation did not appear to impact the size of mucin within the test solutions.

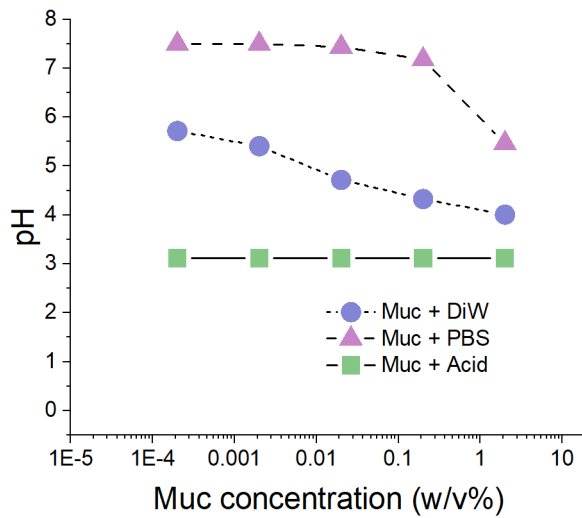


**Figure 4-3 0.2% mucin peak size vs peak area intensity for over the zeta potential pH range.**

#### 4.2.1.2 Influence of solution environment and mucin concentration on mucin size, zeta potential and polydispersity index

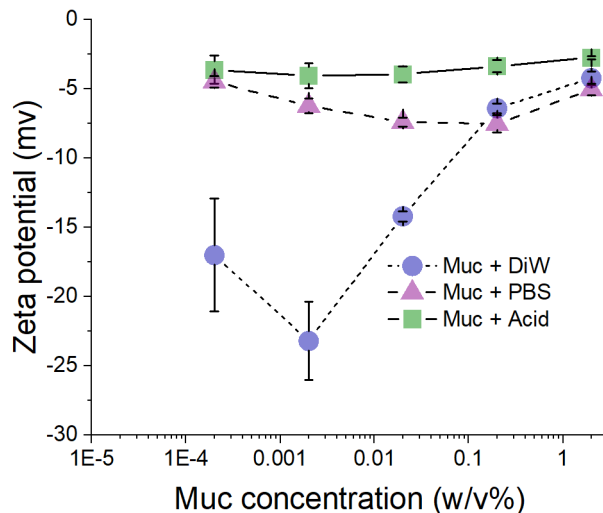
Mucin size, zeta potential and polydispersity index were investigated in three solution environments: deionised water (DiW), PBS solution (PBS) and citric acid (Acid). These solutions aimed to characterise mucins behaviour alone, interacting with salts and within an acidic environment over a range of mucin concentrations. A 2% mucin solution (20 g/L) was made up with the three base solutions and diluted such that 5 different concentrations could be investigated. The pH of each solution was confirmed in the same manner as before. Regression analyses were performed to determine relationships between dependent and independent measurements. Reported  $R^2$  values from this point onwards are considered significant, based on a 95% confidence interval ( $p < 0.05$ ) of the calculated regression coefficient.

Figure 4-4 shows how the concentration of mucin influenced the measured pH of each solution. The solution's pH decreased linearly ( $R^2 = 0.98$ ) in DiW from pH 6 – pH 4 with each logarithmic increment in mucin (Muc) concentration. The pH of PBS was consistent at pH 7.5 for Muc concentrations between 0.0002% - 0.02%. Muc concentrations after this see the pH drop to pH 7 in the 0.2% Muc concentration, followed by pH 5.4 for the 2% Muc solution. This indicated the buffer capacity of the PBS solution was exceeded by the pH change from an increased Muc concentration. No pH change was observed in the Acid solution, due to it being buffered to pH 3.1.



**Figure 4-4 Mucin concentration vs solution pH in different environments. pH was taken as 3 readings within 0.01 of one another for each solution.**

Figure 4-5 shows the corresponding zeta potentials for the three solution environments when examined over the Muc concentration range. Negative zeta potentials were observed in all solutions and the lowest zeta potential was observed in Muc + DiW,  $-23.2 \pm 2.8$  mV for the 0.002% Muc concentration, indicating a more stable mucin structure. A positive linear relationship was observed between the zeta potential and Log Muc concentration in Muc + DiW ( $R^2 = 0.89$ ), which brought the zeta potential closer to the IEP, reaching  $-4.24 \pm 0.49$  mV by the largest Muc concentration.

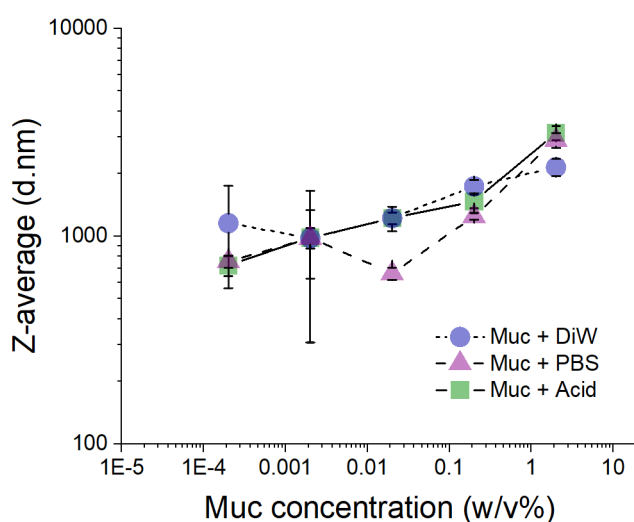


**Figure 4-5 Mucin concentration vs zeta potential of mucin particles in different environments.**

There were no large changes to zeta potential with increasing Muc concentration in the Muc + Acid solutions, with the zeta potential slightly increasing from  $-4.01 \pm 0.90$  mV to  $-2.76 \pm$

0.10 mV. A positive linear relationship was observed in the Muc + Acid solutions ( $R^2 = 0.85$ ). In PBS, the zeta potential was shown to decrease as the Muc concentration increased, from  $-4.50 \pm 0.42$  mV in 0.0002% Muc concentration to  $-7.53 \pm 0.61$  mV in 0.2% Muc concentration. At 2% Muc + PBS, the zeta potential increased to  $5.06 \pm 0.43$  mV. No relationship was determined for Muc + PBS.

Figure 4-6 shows the influence of Muc concentration on the mean hydrodynamic particle diameter (Z-av) of mucin within the solution environments. This was measured as d.nm which refers to the hydrodynamic diameter size in nm. Large variations in size existed at lower Muc concentrations, becoming less varied as the Muc concentration increased. A slight positive trend was observed between the Z-av and Muc concentration for both DiW and Acid environments ( $R^2 = 0.94$  and  $R^2 = 0.90$  respectively). This indicated that the Muc concentration within DiW and Acid environments had an impact on mucin's average size in solution. In the Salt environments, a slight positive relationship was observed between the Z-av and Muc concentration but not significantly ( $p > 0.05$ ).

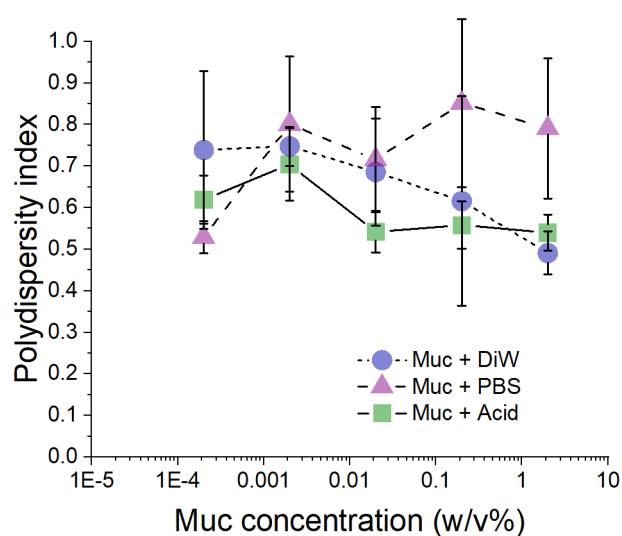


**Figure 4-6 Mucin concentration vs average hydrodynamic diameter of mucin particles in different environments.**

Figure 4-7 shows the polydispersity index (Pdl) changes over the Muc concentration, providing an insight into the size homogeneity of mucin with the solution environments. A Pdl of 0 indicated the dispersed particles were the same size (homogenous) whereas a Pdl of 1 indicated the opposite (heterogenous). Large variations in Pdl were observed for all environments, and mucin size was observed to be polydisperse in all cases. This was attributed to use of mucin in its crude form, without additional purification steps. DiW and PBS presented different relationships between the Pdl and Muc concentration. Increasing the Muc concentration decreased the Pdl in DiW significantly ( $R^2 = 0.98$ ) while the Pdl



increased in PBS ( $R^2 = 0.80$ ). No significant relationship was observed in the Acid environment.



*Figure 4-7 Mucin concentration vs polydispersity index of mucin in solutions.*

The 0.2% Muc concentration was chosen for future test solutions as this concentration reflected the quantity of mucin in whole human saliva [97]. Mean zeta potential, Z-av and Pdl were compared at this Muc concentration between each solution environment. The mean values are presented in Table 4-1. The zeta potentials for DiW ( $-6.41 \pm 0.36$  mV) and PBS of ( $-7.41 \pm 0.33$  mV) were significantly different to Acid environments ( $-3.37 \pm 0.45$  mV), where  $p < 0.005$  and  $p < 0.001$  respectively. No significant differences were observed between environments when comparing mucin size and poly dispersity.

*Table 4-1 Mean zeta potential, Z-av and polydispersity index at 0.2% mucin concentration for each solution environment. Superscript lower-case letters imply significance between compared environments.*

Environment	Zeta potential (mV)	Z-av (d.nm)	Pdl
<b>Muc + DiW</b>	$-6.41 \pm 0.36^a$	$1741 \pm 127$	$0.62 \pm 0.25$
<b>Muc + PBS</b>	$-7.41 \pm 0.33^b$	$1249 \pm 46.7$	$0.85 \pm 0.20$
<b>Muc + Acid</b>	$-3.37 \pm 0.45^{ab}$	$1475 \pm 112$	$0.56 \pm 0.06$

#### 4.2.1.3 Influence of salt type and concentrations on mucin size and zeta potential.

The influence of individual salt types and concentrations on mucin's solution characteristics were examined. Salt solutions were made up to 1, 10 and 100 mmol/L concentrations as described in Chapter 3. Section 3.2.2.2. The salt types were attributed to the salts found naturally in saliva and included  $\text{CaCl}_2$ , KCl, NaCl and  $\text{NaH}_2\text{PO}_4$ . Mucin was added to solutions to make up a concentration of 0.2% (w/v).

The peak size variation of mucin within these salt solutions is displayed in Figure 4-8. No trends between the salt concentration and peak size were observed, with the most intense peak sizes being between 900 – 3000 nm.

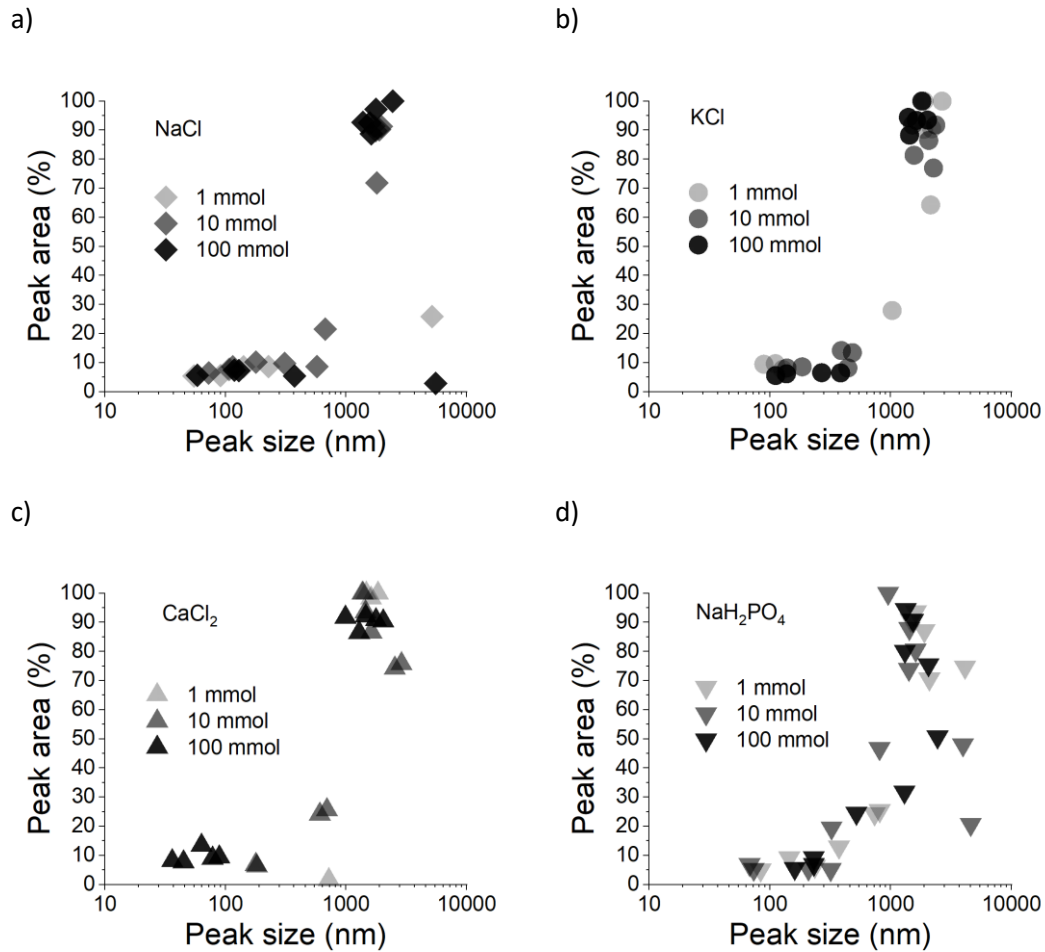
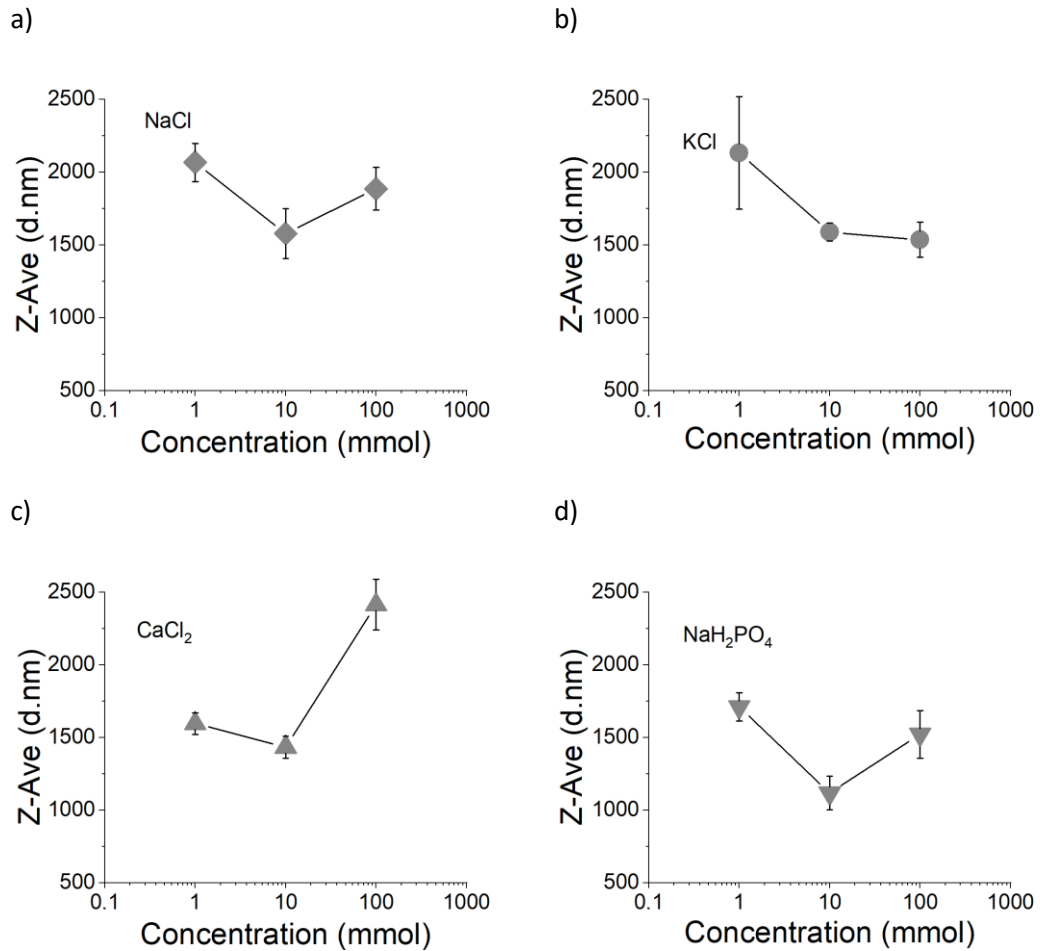


Figure 4-8 Salt concentration comparison of mucin peak size vs size intensity area for different salts: a) NaCl, b) KCl, c) CaCl<sub>2</sub> and d) NaH<sub>2</sub>PO<sub>4</sub>.

Figure 4-9 shows the Z-av compared to the salt concentration and salt type. Sodium containing salts, NaCl and NaH<sub>2</sub>PO<sub>4</sub>, presented a similar drop in the Z-av at 10 mmol salt concentrations. Further comparison of the salt types uncovered a mean Z-av difference between NaCl and NaH<sub>2</sub>PO<sub>4</sub> salts of  $393 \pm 128$  d.nm, which was statistically significant ( $p < 0.05$ ).

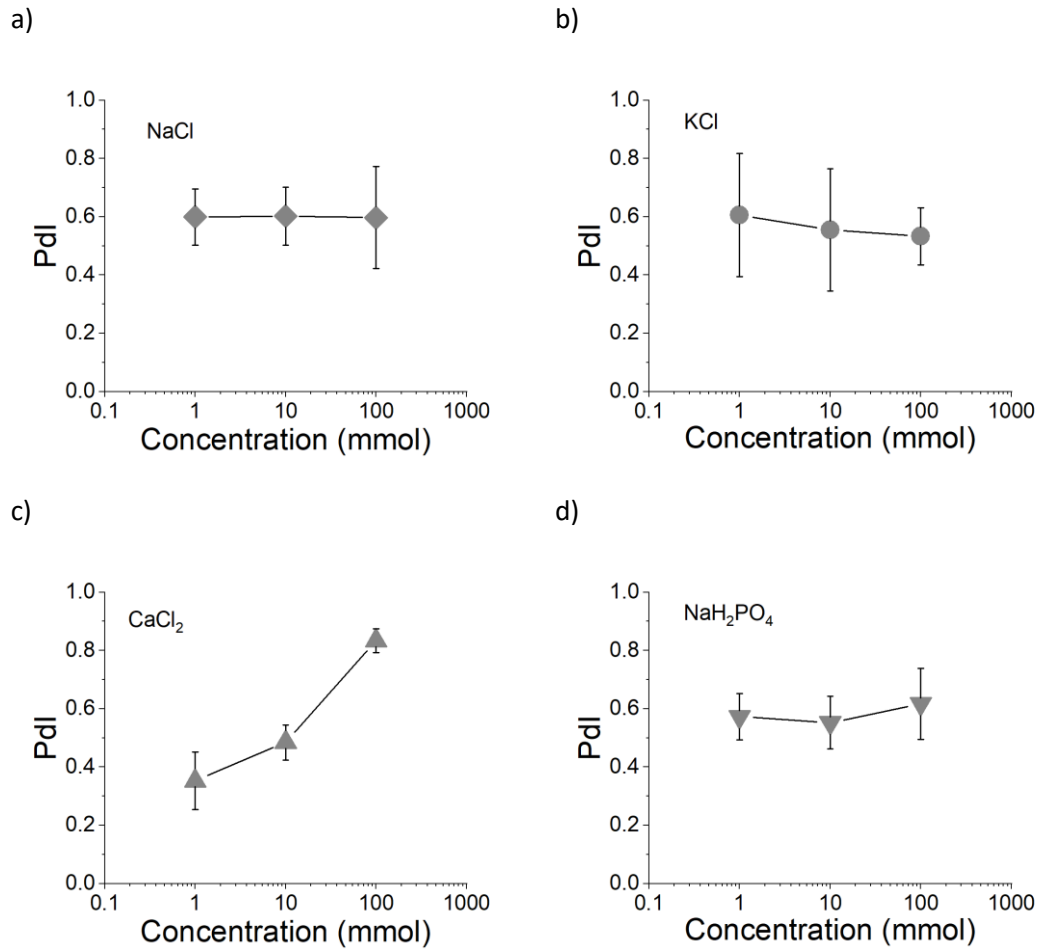


**Figure 4-9 Salt concentration vs average hydrodynamic diameter of mucin particles for different salts: a) NaCl, b) KCl, c) CaCl<sub>2</sub> and d) NaH<sub>2</sub>PO<sub>4</sub>.**

Although trends were observed for increasing CaCl<sub>2</sub> and KCl salt concentrations with the Z-av, no significant relationships were determined between the two variables. Further exploration of the results aimed to determine how the salt type influenced the Z-av at each salt concentration level. Significant differences ( $p < 0.05$ ) were observed for 100 mmol CaCl<sub>2</sub> ( $2412 \pm 195$  d.nm) compared to 100 mmol KCl ( $1534 \pm 119$  d.nm) and 100 mmol NaH<sub>2</sub>PO<sub>4</sub> ( $1520 \pm 183$  d.nm) only.

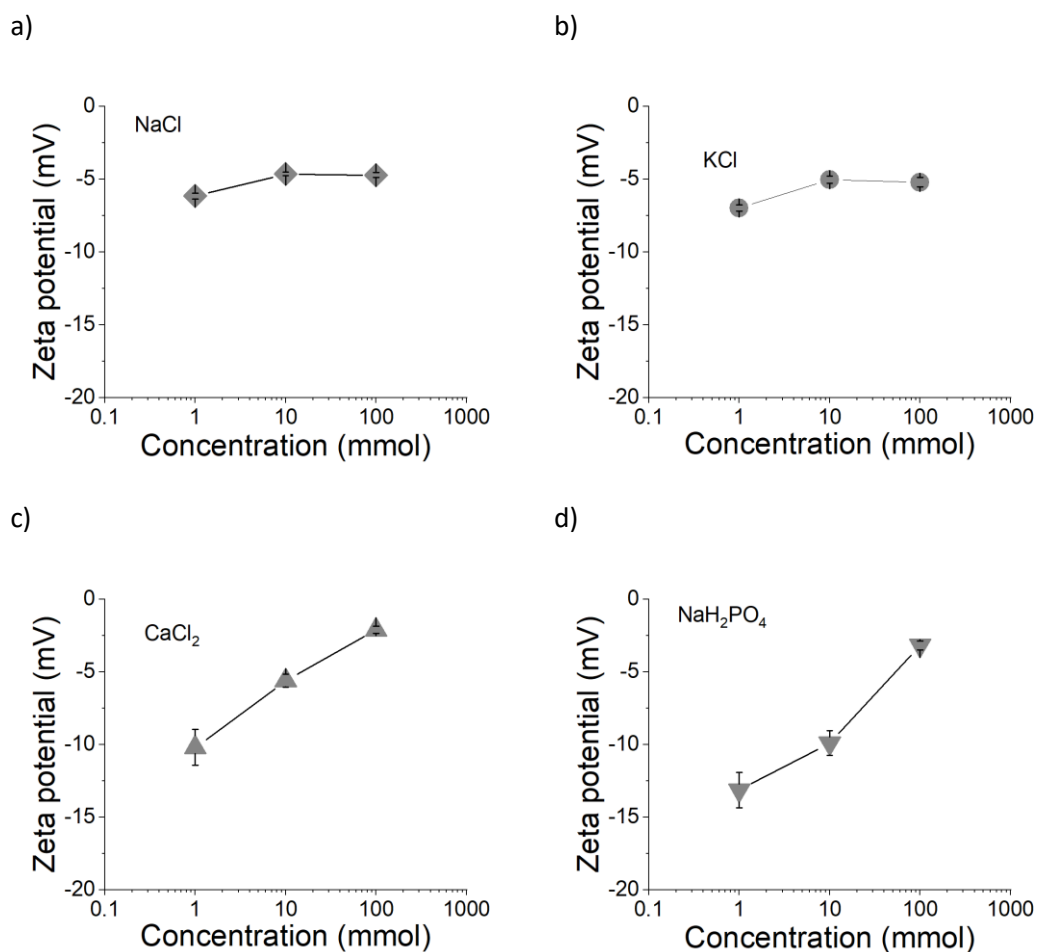
Figure 4-10 explored the polydispersity of mucin sizes compared to salt type and salt concentrations. No significant relationships between the salt concentration and PDI were observed. CaCl<sub>2</sub> presented a different trend to other the salts, where the size variation of mucin particles increased with salt concentration. Further investigation into each salt

concentration level showed that the Pdl of 100 mmol  $\text{CaCl}_2$  ( $0.83 \pm 0.05$ ) was significantly different to 100 mmol KCl ( $0.53 \pm 0.01$ ) ( $p < 0.05$ ).



**Figure 4-10 Salt concentration vs polydispersity index of mucin particles in solution for different salts: a) NaCl, b) KCl, c)  $\text{CaCl}_2$  and d)  $\text{NaH}_2\text{PO}_4$ .**

Figure 4-11 show the zeta potential of each of the salts compared to the salt concentration range. The zeta potential did not appear to change with increased NaCl and KCl salt concentrations, increasing slightly from  $6.27 \pm 0.24$  mV and  $6.99 \pm 0.30$  mV to  $4.65 \pm 0.22$  mV and  $5.22 \pm 0.36$  mV respectively. In  $\text{CaCl}_2$  and  $\text{NaH}_2\text{PO}_4$  salt solutions, the zeta potential did increase with salt concentration, from  $-10.21 \pm 1.37$  mV to  $-2.11 \pm 0.26$  mV for  $\text{CaCl}_2$  and  $-13.14 \pm 1.37$  mV to  $-3.19 \pm 0.36$  mV for  $\text{NaH}_2\text{PO}_4$ . This was significant for the  $\text{CaCl}_2$  solutions ( $R^2 = 0.99$ ). Despite the  $\text{NaH}_2\text{PO}_4$  salt solutions' zeta potential possessing a good fit with the salt concentration, this was not significant.



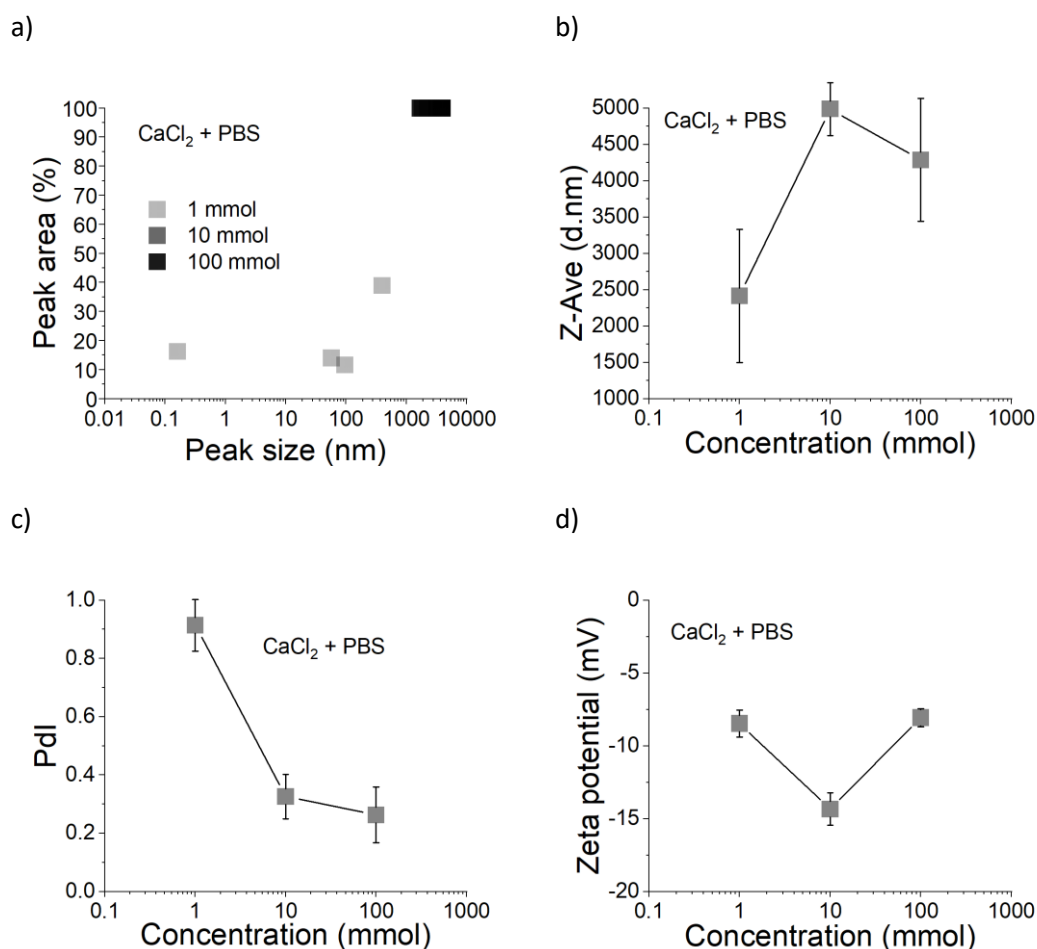
**Figure 4-11** Salt concentration vs zeta potential of mucin particles in solution for different salts: a) NaCl, b) KCl, c) CaCl<sub>2</sub> and d) NaH<sub>2</sub>PO<sub>4</sub>.

The zeta potential was further compared between salt types at each salt concentration. Significant differences were observed for a 1 mmol salt concentration ( $p < 0.05$ ), except for NaCl compared to KCl. At 10 mmol salt concentrations, KCl, CaCl<sub>2</sub> and NaCl zeta potentials were significantly different to NaH<sub>2</sub>PO<sub>4</sub> ( $p < 0.05$ ). At 100 mmol salt concentrations, the zeta potential of CaCl<sub>2</sub> was significantly different to NaCl and KCl zeta potentials ( $p < 0.05$ ). Furthermore, the zeta potential of KCl was significantly different to NaH<sub>2</sub>PO<sub>4</sub>.

Given that calcium and phosphate salts are essential components for tooth enamel remineralisation, it was important to consider how these components influenced mucin behaviour. As saliva contains a combination of salts, another solution composition was formulated to assess different concentrations of CaCl<sub>2</sub> in a PBS solution (CaCl<sub>2</sub> + PBS). This solution represented an artificial saliva in terms of its salt composition.

Upon formulation of the CaCl<sub>2</sub> + PBS solutions, it was observed that the solution's appearance became opaque with increasing CaCl<sub>2</sub> concentration, indicating precipitation. Figure 4-12 shows the summarised DLS and zeta results for CaCl<sub>2</sub> + PBS. Figure 4-12 a) and c) shows how the addition of calcium influenced the size variation of mucin in the solutions.

The Pdl decreased as the  $\text{CaCl}_2$  concentration increased, resulting in a single peak size cluster at 10 and 100 mmol concentrations. No significant trends in Pdl, average mucin size and zeta potential were observed with increasing  $\text{CaCl}_2$  concentration in PBS. Figure 4-12b) indicated that the Z-ave was much larger compared to observations in Figure 4-9, significantly for 10 and 100 mmol  $\text{CaCl}_2$  concentrations in PBS compared to all other salts at each respective concentration ( $p < 0.001$ ).



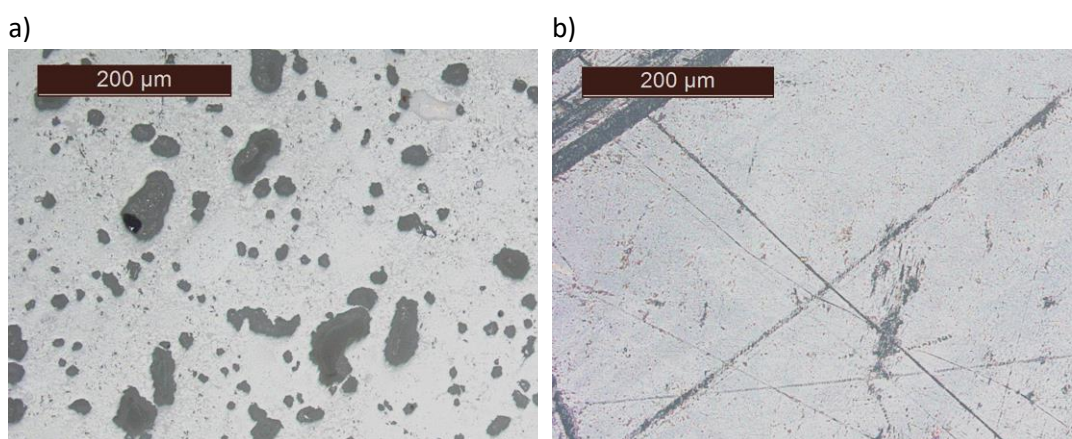
**Figure 4-12**  $\text{CaCl}_2$  concentration in PBS solution comparison of a) mucin peak size vs size intensity area, b) average hydrodynamic diameter of particles, c) polydispersity index of particles in solution and d) zeta potential.

The Pdl of 1 mmol  $\text{CaCl}_2$  + PBS was significantly different to other of salts of the same concentration ( $p < 0.05$ ). Pdl differences between 100 mmol  $\text{CaCl}_2$  + PBS and all other salts, excluding KCl, were significant ( $p < 0.05$ ). Finally, zeta potential differences between  $\text{CaCl}_2$  + PBS solutions at each concentration and all other salt types at corresponding concentrations were significant ( $p < 0.05$ ), excluding 1 mmol KCl.

## 4.2.2 Surface characterisation of bovine enamel and steatite

### 4.2.2.1 Initial observations with optical microscopy

Steatite and enamel samples were examined with optical microscopy after sample fabrication. Figure 4-13 shows the steatite and enamel surfaces to the same scale. Surface features were observed on the steatite, as illustrated in Figure 4-13a) by the irregular-shaped dark spots that were randomly distributed on the surface. Conversely, these features were not present on the bovine enamel surfaces as demonstrated in Figure 4-13b).

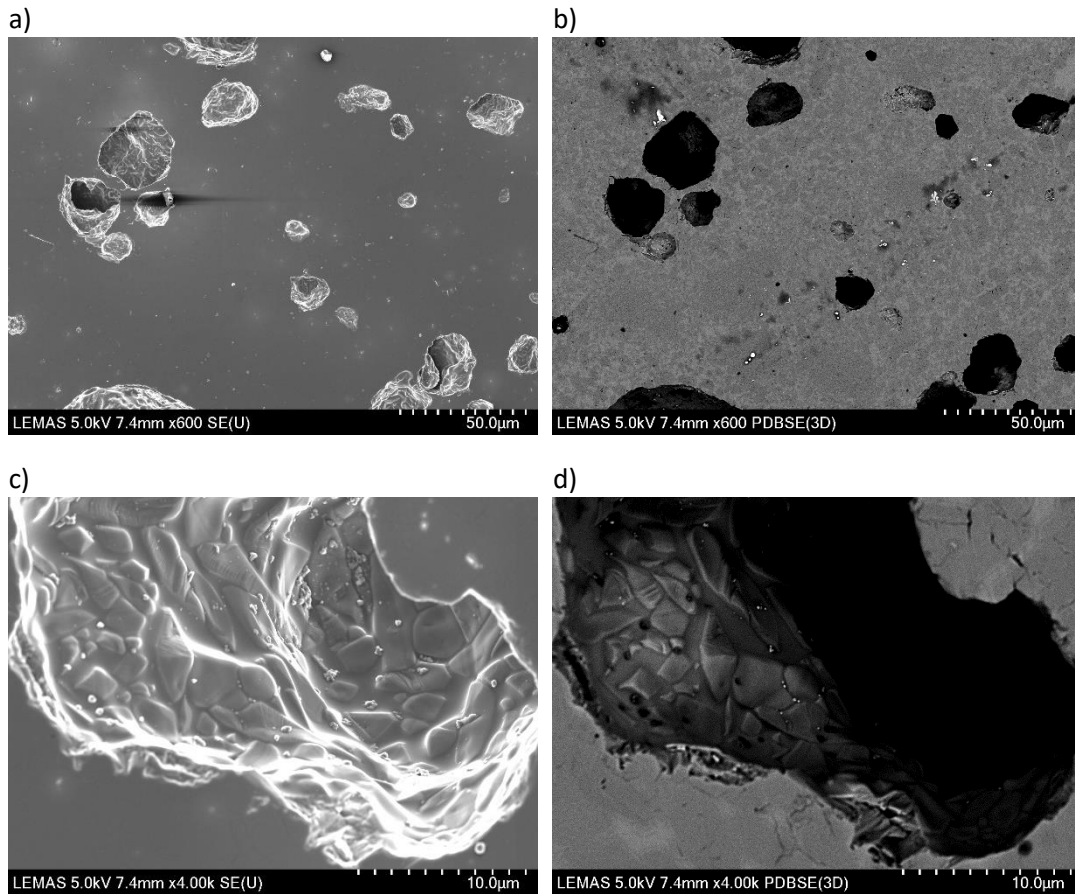


**Figure 4-13** Optical microscope images of a) steatite and b) bovine enamel surfaces after grinding and polishing.

### 4.2.2.2 Surface characterisation of steatite and bovine enamel with SEM/EDX

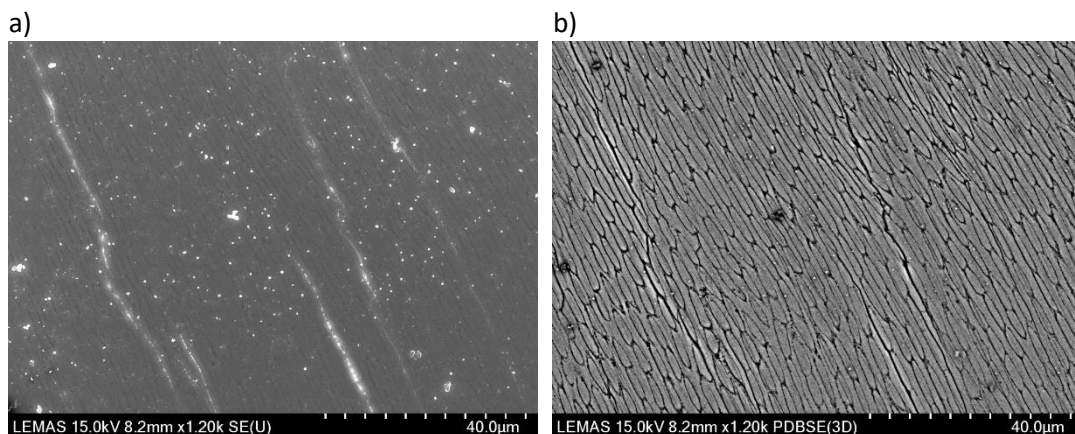
Further examination on steatite and bovine enamel surfaces was performed using SEM with EDX. This aimed to characterise the surface features and the chemical composition of each surface. Both secondary electron (SE) and backscatter electron (PDBSE) image modes were used to compare surface and subsurface features respectively. Figure 4-14 shows SEM image of steatite with corresponding SE and PDBSE images.

The features alluded to in Figure 4-13a) as dark spots were thought to be craters on the steatite surface when inspected with SEM, which is presented in Figure 4-14a). A faint grain structure was observed on the non-cratered surface regions, shown with the aid of PDBSE in Figure 4-14b). The grain structure was further defined within the crater, shown in Figure 4-14 c) and d), and faintly around the outside of the crater in Figure 4-14d). Grains within the crater were considered native compared to the grains on the exposed surface which were flattened by sample grinding. Grain size, geometry and distribution were not observed to be uniform.



**Figure 4-14 SEM characterisation of steatite showing a) SE and b) PDBSE images of steatite surface, and c) SE and d) PDBSE images of steatite crater.**

Figure 4-15 shows the bovine enamel surface imaged by SE and PDBSE imaging modes. In comparison to the steatite surface, the bovine enamel surface was considerably different. Figure 4-15a) presents a uniform flattened surface (ignoring the dust particles) with a few surface cracks. These cracks occurred on the edges of the observed enamel rods which are oriented in one direction, as shown in Figure 4-15b). The size, geometry and distribution of the enamel rods were uniform on the surface in contrast to steatite's grains, made up from approximately  $2 \times 7 \mu\text{m}$  rods.

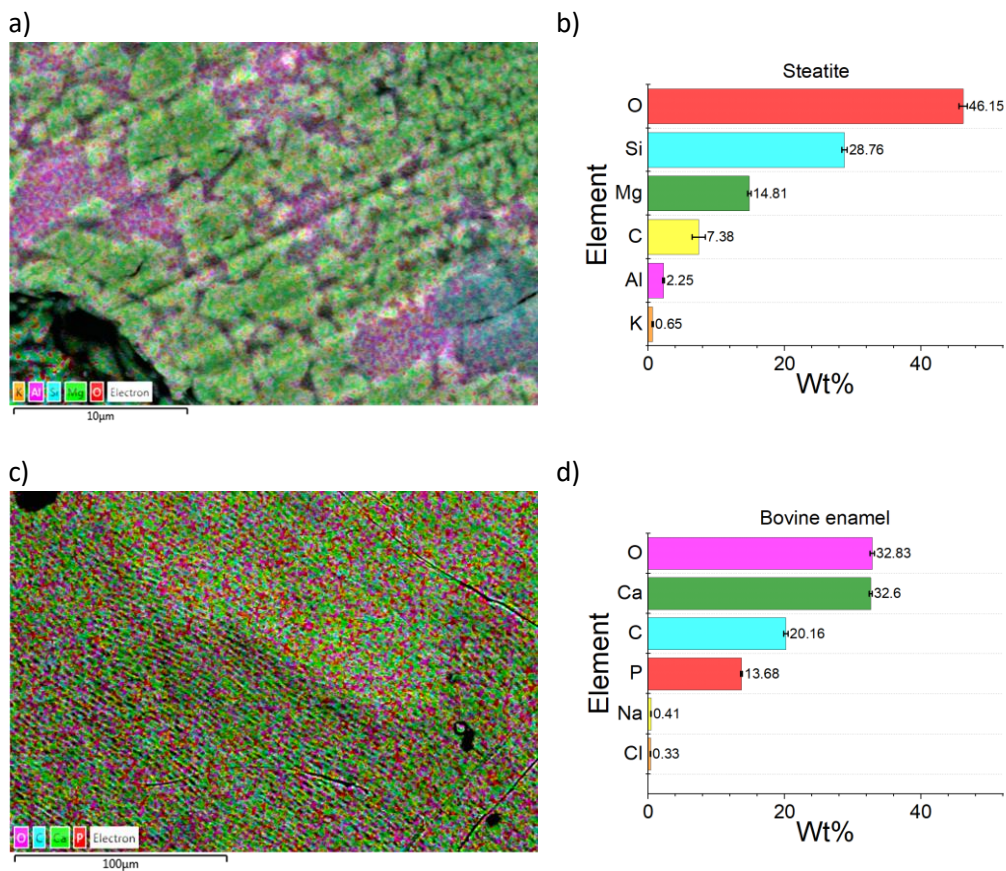


**Figure 4-15 SEM characterisation of bovine enamel showing a) SE and b) PDBSE images of enamel surface.**



Figure 4-16 compares the chemical composition of steatite and bovine enamel surfaces examined by EDX, showing EDX maps and their corresponding elemental composition by weight percentage up to 1  $\mu\text{m}$  in depth from the surface. The grain structure and grain composition of steatite was identified as Figure 4-16a) shows high density areas of magnesium rich granules that are both fine and coarse. In between the magnesium grains, there were localised areas with a higher percentage of aluminium, and one larger structure which was rich in silicon. The elemental composition of steatite was shown to be mostly made up of oxygen, silicon and magnesium, shown in Figure 4-16b). This was comparable to the expected composition of steatite. The carbon content was attributed to the carbon surface coating which was applied prior to SEM/EDX examination.

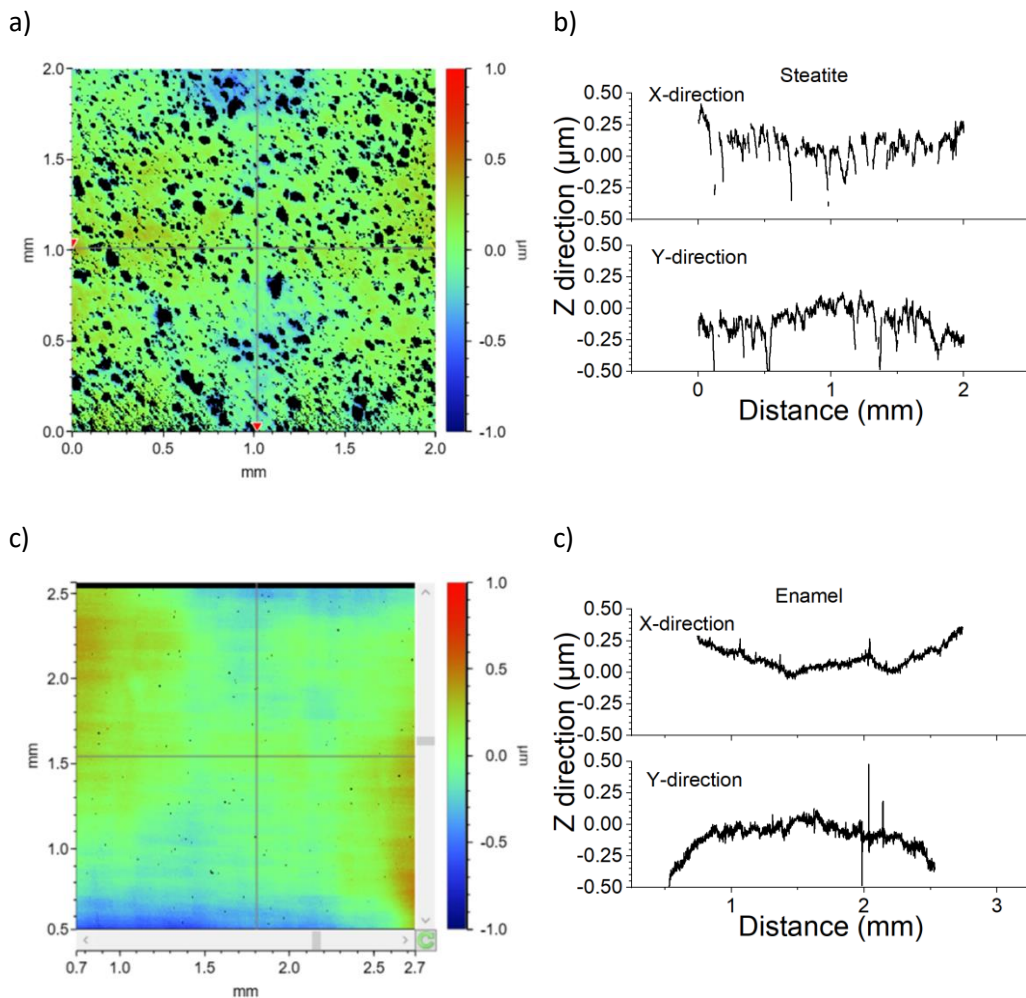
Compared to steatite, bovine enamel presented a uniform chemical composition across the entire surface with no localised element dense regions, as shown in Figure 4-16c). Bovine enamel was shown to be made primarily made up of oxygen, calcium, carbon and phosphorus, as shown in Figure 4-16d). The carbon weight percentage of bovine enamel was only part attributed to the pre-applied carbon coating, as tooth enamel has been described as a carbonated hydroxyapatite.



**Figure 4-16** EDS maps of a) steatite and c) bovine enamel surfaces. Bar charts of element weight % of b) steatite and d) bovine enamel. Bar colours correspond to elemental colours on their respective EDS map.

#### 4.2.2.3 Surface profile characterisation of steatite and bovine enamel with VSI prepared by the same methods

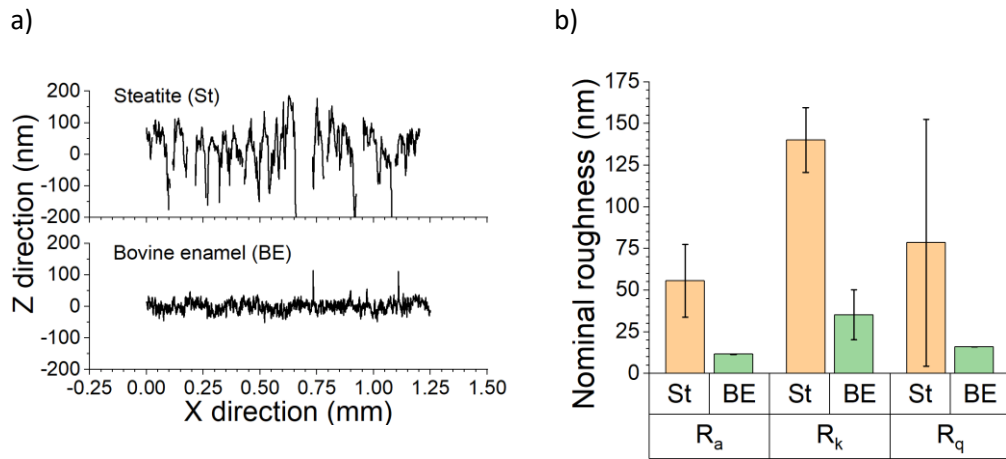
Steatite and bovine enamel surface areas and profiles were further characterised with VSI to compare surface profile differences after following the surface preparation methods in Chapter 3. Section 3.2.3. Figure 4-17 shows steatite and enamel surfaces their respective profile traces in the X and Y directions. Clear differences in the Z direction variation were observed between the two surfaces over the 2 mm profile trace, as shown in Figure 4-17b) and d). Variation in the Z direction was independent of the trace direction. The presence of craters on steatite were also confirmed by the valleys in X and Y steatite profiles, shown in Figure 4-17b).



**Figure 4-17** VSI characterisation of surface profile show surface images of a) steatite and c) bovine enamel with profile traces in x and y directions of b) steatite and d) bovine enamel.

Figure 4-18a) shows the profiles of each material corrected about a centre line, and the average roughness parameters  $R_a$ ,  $R_q$ , and  $R_k$  are displayed in Figure 4-18b). Variations in  $R_q$  were attributed to the mechanical interface of surface grinding and polishing with the variable chemical and structural composition on steatites surface. Differences were

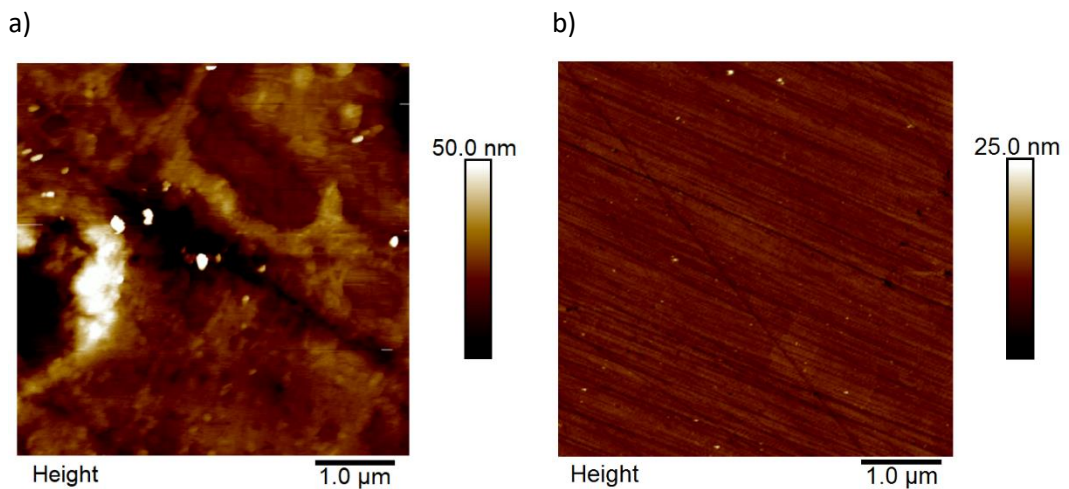
observed between the surface profiles and roughness parameters despite both surfaces being prepared with the same methodology. These were significant when comparing the average asperity roughness ( $R_a$ ) and the core roughness ( $R_k$ ) of the steatite compared to bovine enamel ( $p < 0.05$ ).



**Figure 4-18** VSI surface profile comparison showing a) average profile traces of steatite compared to bovine enamel and b) calculated nominal roughness parameters  $R_a$ ,  $R_k$  and  $R_q$  of steatite (St) and bovine enamel (SE) surfaces.

#### 4.2.2.4 Bare surface observations of steatite and bovine enamel with AFM (air)

Steatite and bovine enamel surfaces were examined at the nanoscale with an AFM in an air environment, illustrated in Figure 4-19. Prominent surface features were observed on the steatite surface while bovine enamel surfaces were uniform with no discernible features. Figure 4-19 serves as a baseline surface image to compare AFM images depicting mucin-surface interactions in the next section.

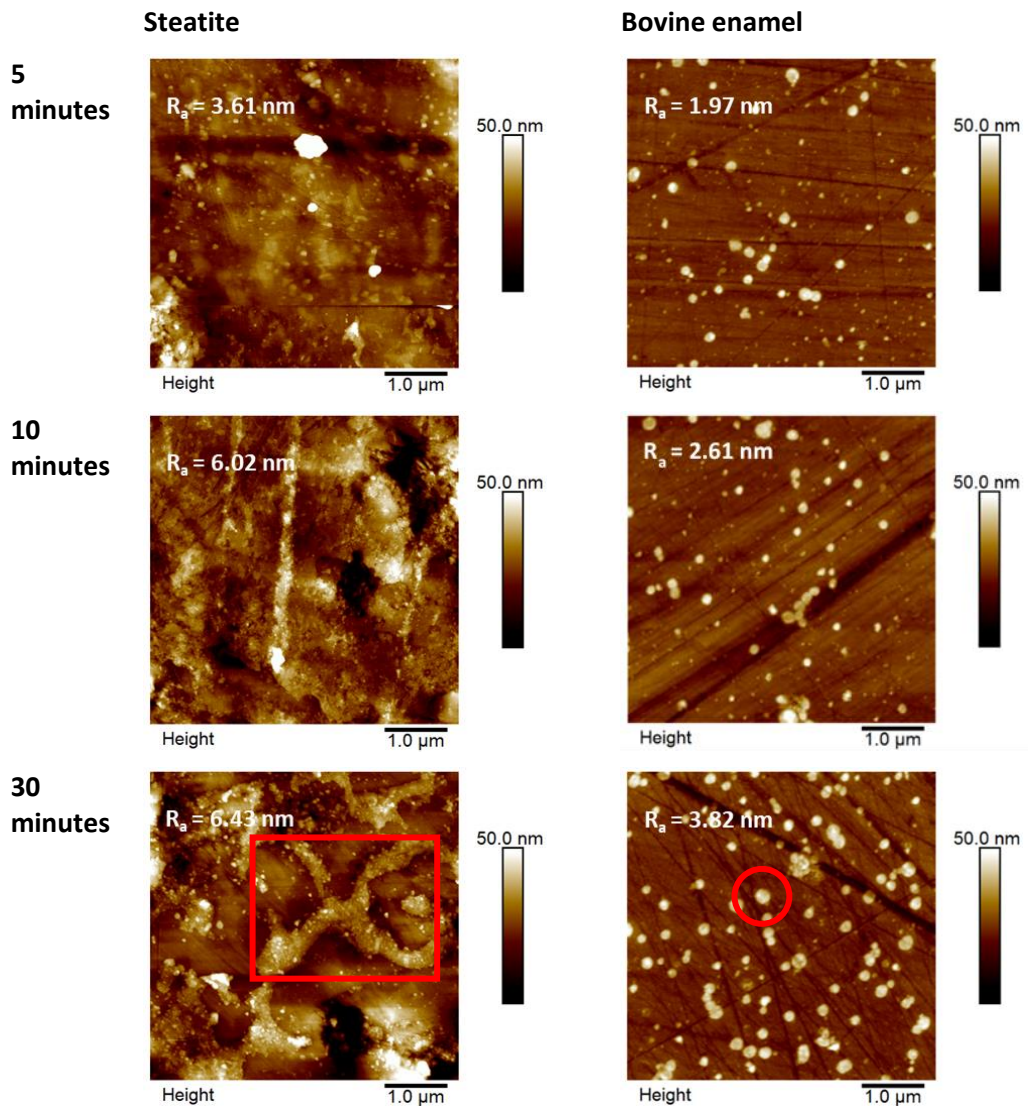


**Figure 4-19**  $5 \times 5 \mu\text{m}$  AFM height images of a) steatite and b) enamel in air.

### 4.2.3 Mucin interactions with surfaces at the nanoscale

#### 4.2.3.1 Influence of surface material on mucin surface interactions

AFM in an air environment after immersion in a Muc + DiW environment was employed to image mucin interactions with steatite and bovine enamel surfaces. Figure 4-20 shows mucin solution interactions with both surfaces after 5, 10 and 30 minutes of static immersion. The adsorbed mucins are partially hydrated given the air imaging environment, providing an experimental representation of what the oral state without continuous flow, simulating conditions akin to xerostomia.



**Figure 4-20** 5 x 5  $\mu\text{m}$  AFM height images of steatite and bovine enamel surfaces treated with Muc + DiW solution under static immersion conditions. Images were taken in an air environment, therefore mucins on the surface are partially dehydrated. Surface roughness parameter,  $R_a$ , is displayed for each image. Red shapes indicate features of interest.

Partially hydrated mucin structures on bovine enamel were different to structures formed on steatite. Dome like nodules appear to be distributed randomly on enamel, an example is annotated by the red circle in Figure 4-20, increasing in population density over time.

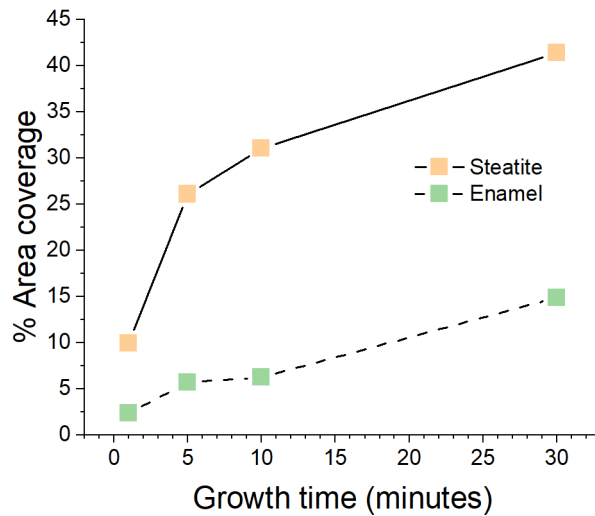
However, mucin structures on steatite formed larger clusters of smaller mucins above the surface with a surrounding film, annotated by the red square in Figure 4-20.

A particle analysis of the structures was performed on the NanoScope Analysis software (Bruker, USA), where particles above a given depth were isolated and assessed, using the surface depth as a reference plane. Height and diameter of structures were determined after 30 minutes static immersion, shown in Table 4-2. Mean heights and diameters of mucin structures on steatite were observed to be smaller than mucin structure on bovine enamel, however large variations existed with these which may have been an effect of the surface energy differences.

*Table 4-2 Particle analysis data of mucin structures on steatite and bovine enamel after 30 minutes static immersion in 0.2% mucin solution.*

	Surface	Mean	Minimum	Maximum	SD
<b>Height (nm)</b>	Steatite	4.77	0.01	48.32	6.50
	Bovine enamel	9.89	0.02	30.89	7.37
<b>Diameter (nm)</b>	Steatite	119.43	27.71	2033.27	231.43
	Bovine enamel	122.84	22.04	423.92	91.77

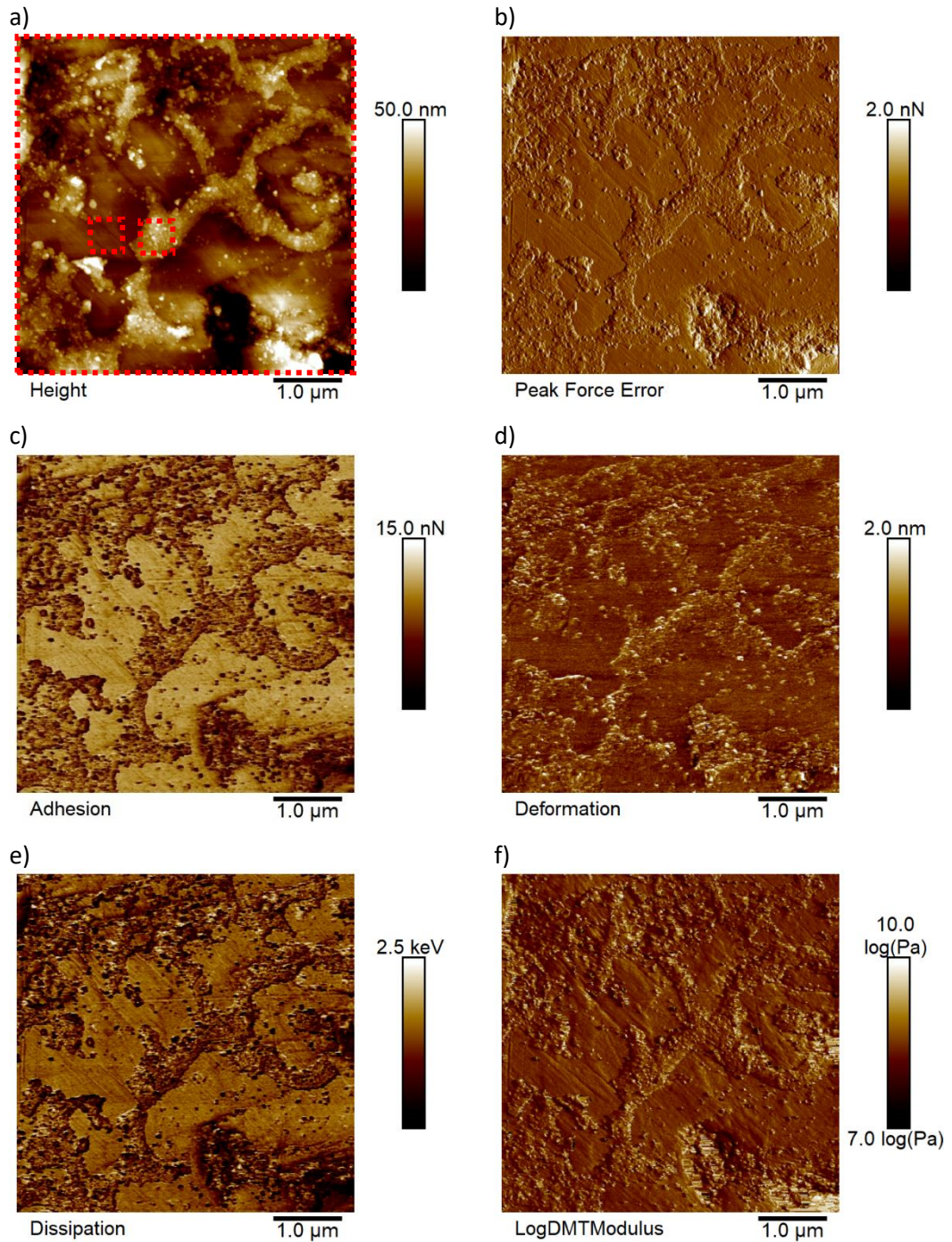
Figure 4-21 shows the estimated mucin area coverage on each surface over the growth period. Area coverage was determined using the bearing analysis tool on the NanoScope Analysis software (Bruker, USA). The bearing depth for the analysis was chosen to be above the material surface to estimate the area coverage of mucin above this reference plane. Steatite presented more surface coverage than bovine enamel for all adsorption periods, covering 41.34% of the 5 x 5  $\mu\text{m}$  scan area after 30 minutes static immersion. In contrast, only 14.87% of the surface was covered on bovine enamel after the same immersion time. These differences were attributed to larger structures formed on steatite that took up a larger portion of the surface area.



*Figure 4-21 Mucin % area coverage on steatite and bovine enamel surfaces over time. Area coverage was determined by performing a bearing analysis on flattened height images with the bearing depth set such that the uncovered surface was excluded, focusing on the mucin coverages above this reference plane.*

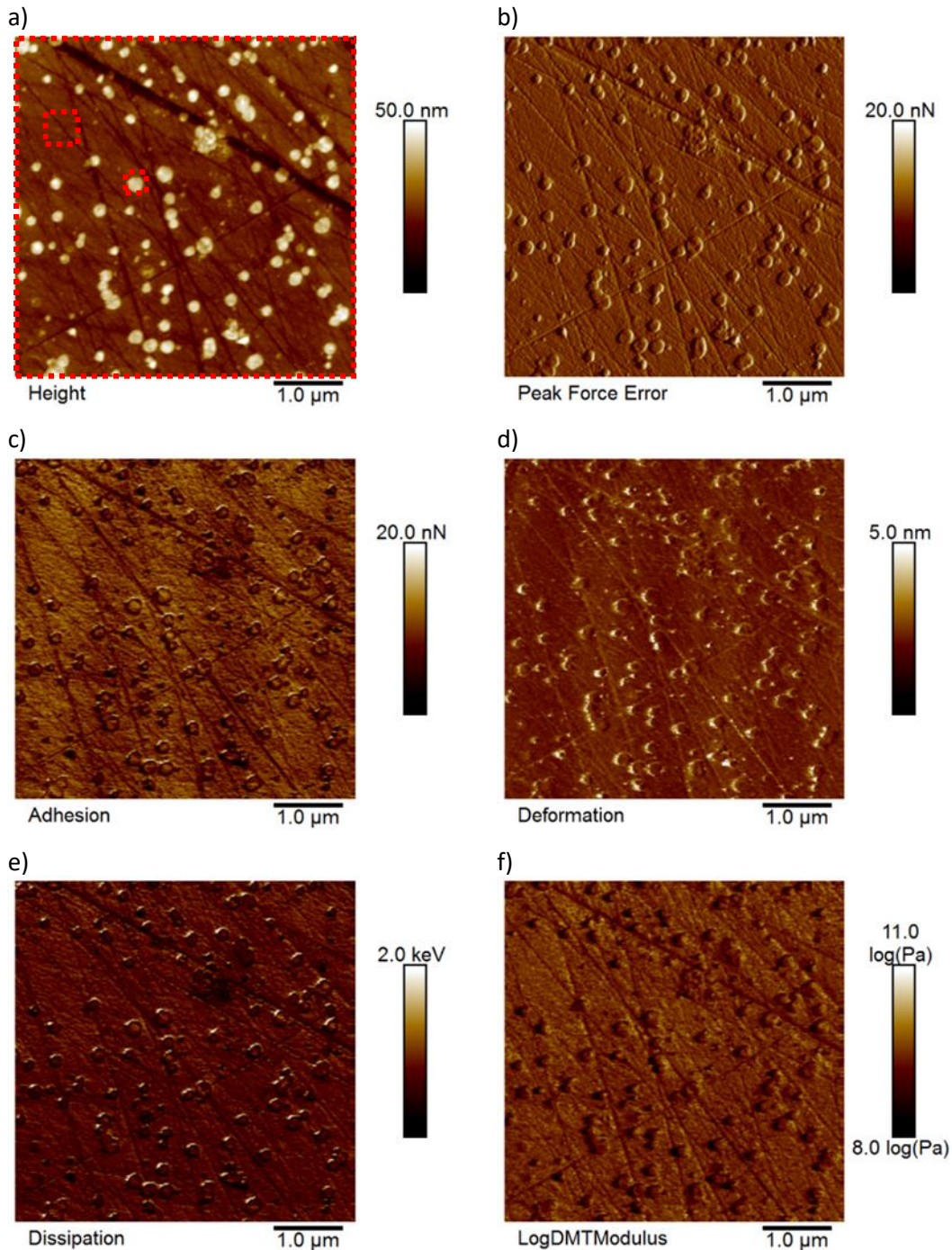
Quantitative nanomechanical property (QNM) maps of steatite and enamel were examined after 30 minutes static immersion to identify differences in the surface properties of partially hydrated mucin-surface structures. Figure 4-22 shows the QNM maps for steatite, displaying height, error, adhesion, deformation, dissipation and logDMT modulus. The maps highlight further differences in the surface properties where the mucin structures were located compared to the uncovered surface, as shown by image contrast differences throughout Figure 4-22. It should be noted that Peak Force error maps do not provide any quantitative assessment of the surfaces, merely providing more of a 3D visual representation to complement the rest of the acquired data.

For adhesion, deformation, dissipation and logDMT QNM maps of steatite, image depth surveys were taken for the whole scan, bare surface, and mucin-surface areas, shown by the red, dashed boxes in Figure 4-22a). Image depth was measured from an absolute X axis which plotted the real, measured quantities for each QNM property map. The mean calculated results of these image depth surveys on steatite are displayed in Table 4-3.



*Figure 4-22 5 x 5  $\mu\text{m}$  Quantitative nanomechanical property maps of partially hydrated mucin on steatite after 30 minutes static immersion in 0.2% mucin showing maps of a) height, b) PeakForce error, c) adhesion, d) deformation, e) dissipation and f) logDMT modulus. Absolute scale used in images a) to e), where the lowest value is considered 0.*

Figure 4-23 shows the QNM maps for mucin on bovine enamel surfaces. Clear differences in the surface properties were observed between the bare surface and mucin-surface locations. Depth surveys were performed on bovine enamel in the same way as on steatite, focussing on the red, dashed boxes shown in Figure 4-23a). The mean calculated results of these depth surveys on bovine enamel are displayed in Table 4-3.



*Figure 4-23 5 x 5  $\mu\text{m}$  Quantitative nanomechanical property maps of partially hydrated mucin on bovine enamel after 30 minutes static immersion in Muc + DiW showing maps of a) height, b) PeakForce error, c) adhesion, d) deformation, e) dissipation and f) logDMT modulus. Absolute scale used in images a) to e), where the lowest value is considered 0.*

Mucin structures in Figure 4-22 and Figure 4-23 both present a drop in dissipation, adhesion and logDMT modulus compared to the surrounding surface material, with an increase in deformation at the surface. This is quantified in Table 4-3, which presents the mean QNM properties of mucin-surface interactions on steatite and bovine enamel surfaces. Mucin structures on bovine enamel were observed to be softer relative to the bare bovine enamel surface compared to mucin structures on steatite compared to bare steatite. This was shown



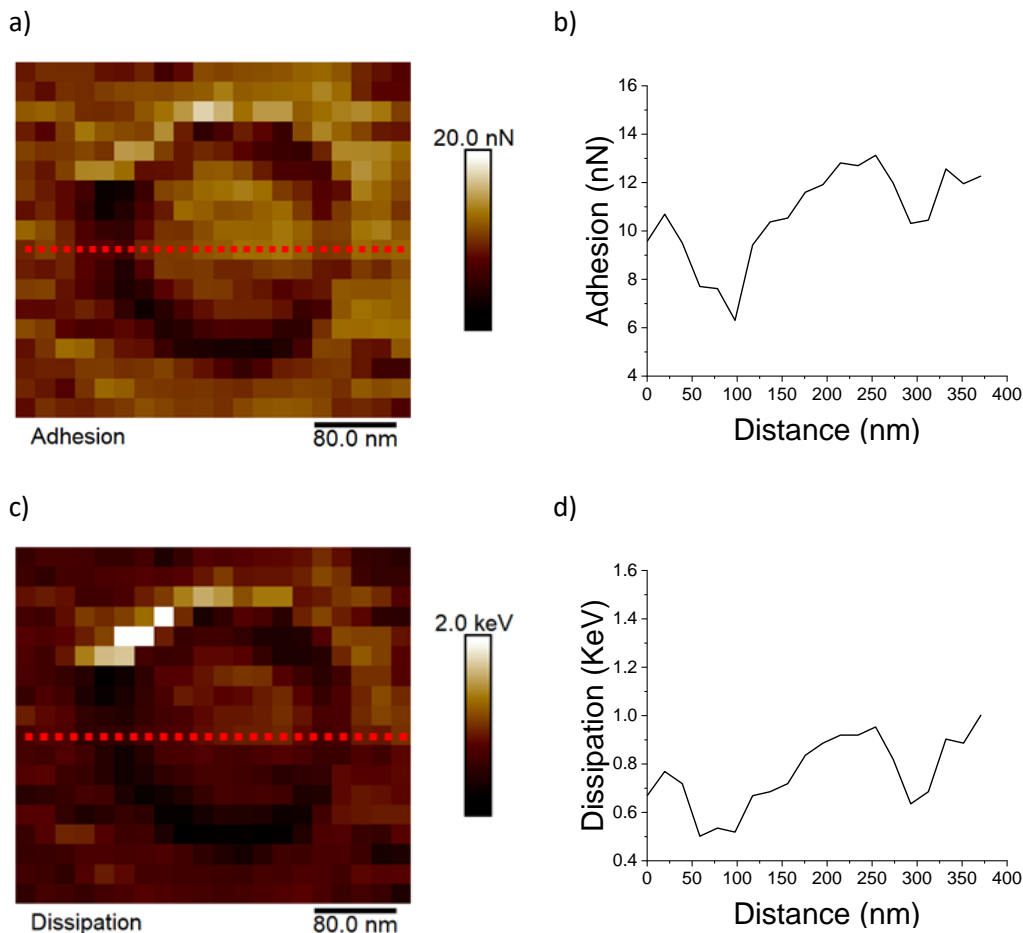
by differences in deformation and logDMT properties between the surface and mucin features. This was shown to have a minor effect on reducing the overall mean logDMT moduli on both surfaces. However, this has a greater effect on increasing the overall deformation. On the other hand, mucin structures on steatite appear to show less adhesion and dissipation properties relative to their base surface compared to mucin structures on bovine enamel. This effectively reduces the overall adhesion and dissipation properties on steatite, more than on bovine enamel.

*Table 4-3 Mean quantitative nanomechanical properties and standard deviations of surface features on steatite and bovine enamel surfaces after 30 minutes static immersion in 0.2% mucin solution. Features relate to areas of no mucin (Surface), areas of partially hydrated mucin (Mucin) and the mean properties of the whole scan area (All).*

	Feature	Steatite	Bovine enamel
<b>Adhesion (nN)</b>	Surface	10.67 ± 0.53	10.57 ± 1.38
	Mucin	7.60 ± 2.42	9.80 ± 2.66
	All	8.68 ± 2.40	9.24 ± 2.16
<b>Deformation (nm)</b>	Surface	0.27 ± 0.08	0.38 ± 0.11
	Mucin	0.53 ± 0.29	2.17 ± 2.72
	All	1.49 ± 0.26	3.58 ± 2.86
<b>Dissipation (keV)</b>	Surface	1.51 ± 0.11	0.74 ± 0.12
	Mucin	1.17 ± 0.43	0.63 ± 0.28
	All	1.33 ± 0.42	0.75 ± 0.20
<b>LogDMT (logPa)</b>	Surface	8.48 ± 0.14	9.50 ± 0.17
	Mucin	8.36 ± 0.41	8.88 ± 0.48
	All	8.44 ± 0.36	9.37 ± 0.30

#### 4.2.3.2 Differences between partially hydrated mucin and fully hydrated mucin interactions with bovine enamel and the influence of salts

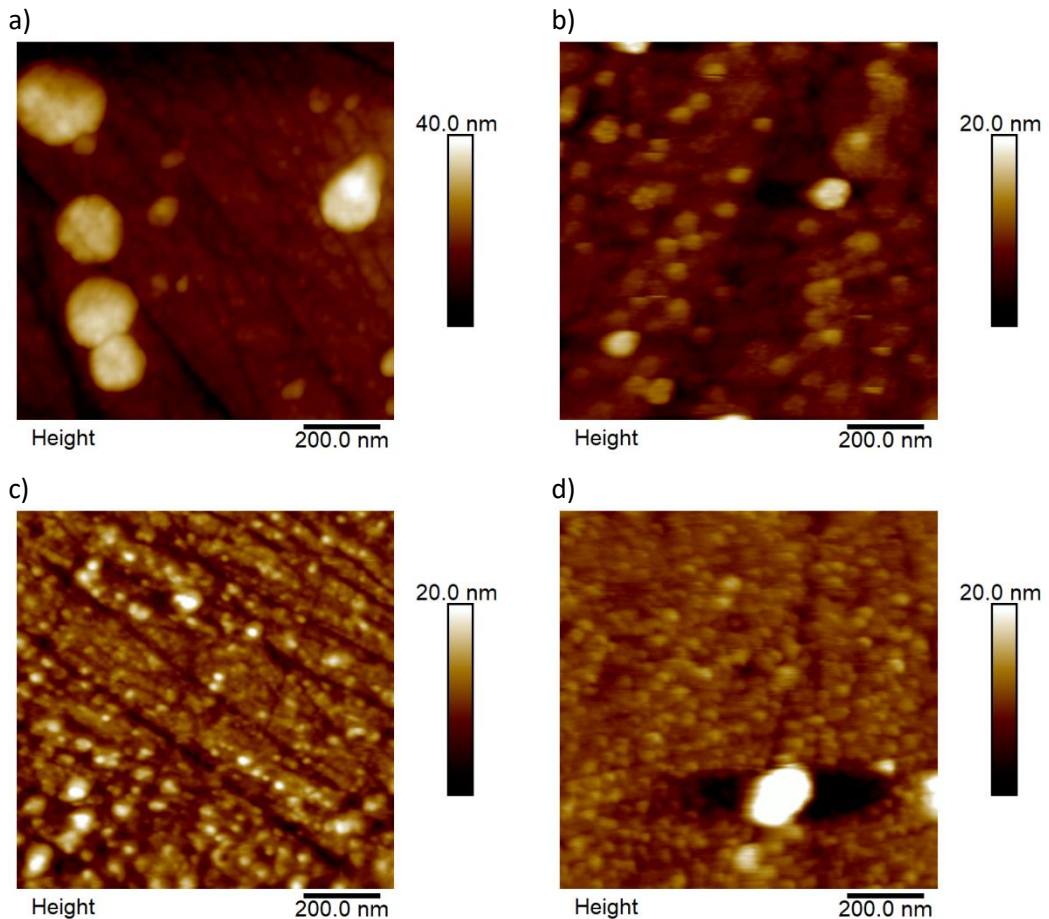
Partially hydrated mucin seen as the ROI in Figure 4-23c) and e) are shown in Figure 4-24 at an increased scale; contrast differences between the edge and centre of nodules are presented. The centre of these nodules shows QNM properties similar to surrounding bovine enamel, while the edges present a lower value. Adhesion and dissipation maps both show a drop at the nodule's edge, shown in Figure 4-24b) and d), which correspond to the dashed lines in Figure 4-24a) and c).



**Figure 4-24** Magnified QNM map and section profile of partially hydrated mucin for a) and b) adhesion, and c) and d) dissipation on bovine enamel. Absolute scale used in images a) and c), where the lowest value is considered 0.

Partially hydrated mucin structures on bovine enamel were further examined and compared with fully hydrated mucin structures at a greater magnification ( $1 \times 1 \mu\text{m}$  AFM scans). The term fully hydrated mucin structures refer the AFM method used to measure mucin structures in an aqueous environment, simulating a hydrated oral state. Furthermore, the influence of salts was assessed for both hydration states. Figure 4-25 show height images of mucin structure on bovine enamel after 30 minutes static immersion in 0.2% mucin and PBS

+0.2% mucin solutions, referred to as Muc + DiW and Muc + PBS from hereafter respectively. Smaller mucin nodules were observed on bovine enamel when fully hydrated, shown in Figure 4-25b) compared to partially hydrated mucin Figure 4-25a) after immersion in Muc + Muc. The nodule coverage also appeared to be greater under fully hydrated conditions. Immersion in Muc + PBS presented a greater coverage of finer nodules under both hydration conditions, shown in Figure 4-25c) and d).



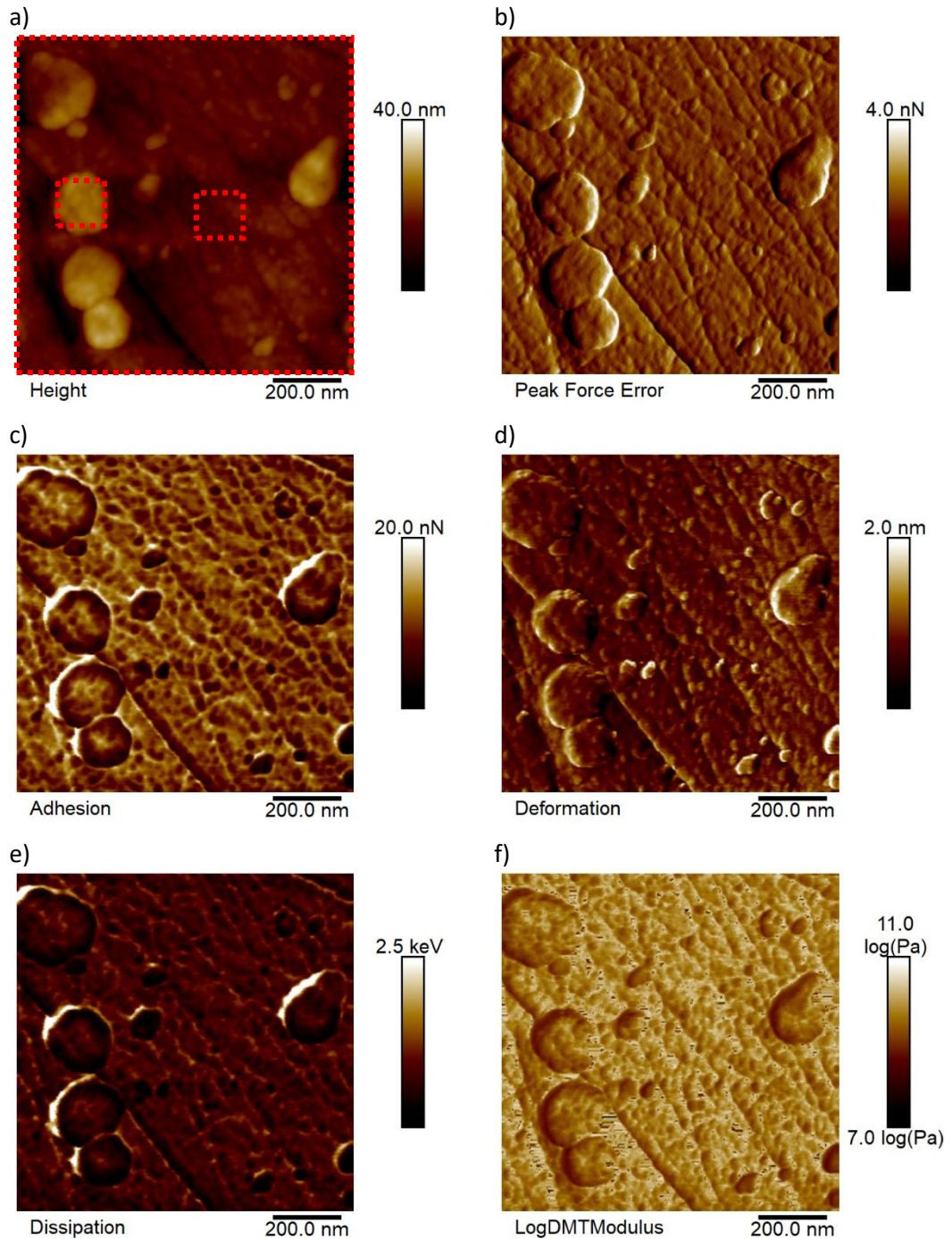
*Figure 4-25 1 x 1  $\mu\text{m}$  AFM height images of mucin on bovine enamel after static immersion in a) and b) Muc + DiW, and c) and d) Muc + PBS. Partially hydrated mucin features are displayed in a) and c), while fully hydrated mucin features are displayed in b) and d). Absolute scale used in images a) to d), where the lowest value is considered 0.*

Particle analyses of the height images in Figure 4-25 were performed and particle height and diameters were quantified, as shown in Table 4-4. After Muc + DiW immersion, the mean height and diameter of fully hydrated mucin structures were less than the partially hydrated structures, with a reduced particle range. Under partially hydrated and fully hydrated conditions, the presence of salts reduced the mean height and diameter of particles as well as the ranges of these properties. Large variations in height and diameter existed in all immersion and hydration conditions.

*Table 4-4 Particle analysis from 1x1  $\mu\text{m}$  AFM scans for partially and fully hydrated mucin after 30 minutes static immersion in either Muc + DiW or Muc + PBS solutions.*

	Hydration	Solution	Mean $\pm$ SD	Minimum	Maximum
<b>Height (nm)</b>	Partially	Muc + DiW	7.29 $\pm$ 6.6	0.49	23.23
		Muc + PBS	1.93 $\pm$ 1.94	0.06	8.89
	Fully	Muc + DiW	2.31 $\pm$ 2.41	0.01	10.34
		Muc + PBS	1.74 $\pm$ 1.01	0.54	3.90
<b>Diameter (nm)</b>	Partially	Muc + DiW	74.04 $\pm$ 77.67	13.94	241.78
		Muc + PBS	28.96 $\pm$ 14.13	4.41	77.86
	Fully	Muc + DiW	55.96 $\pm$ 35.86	13.22	186.95
		Muc + PBS	35.29 $\pm$ 18.50	18.7	66.56

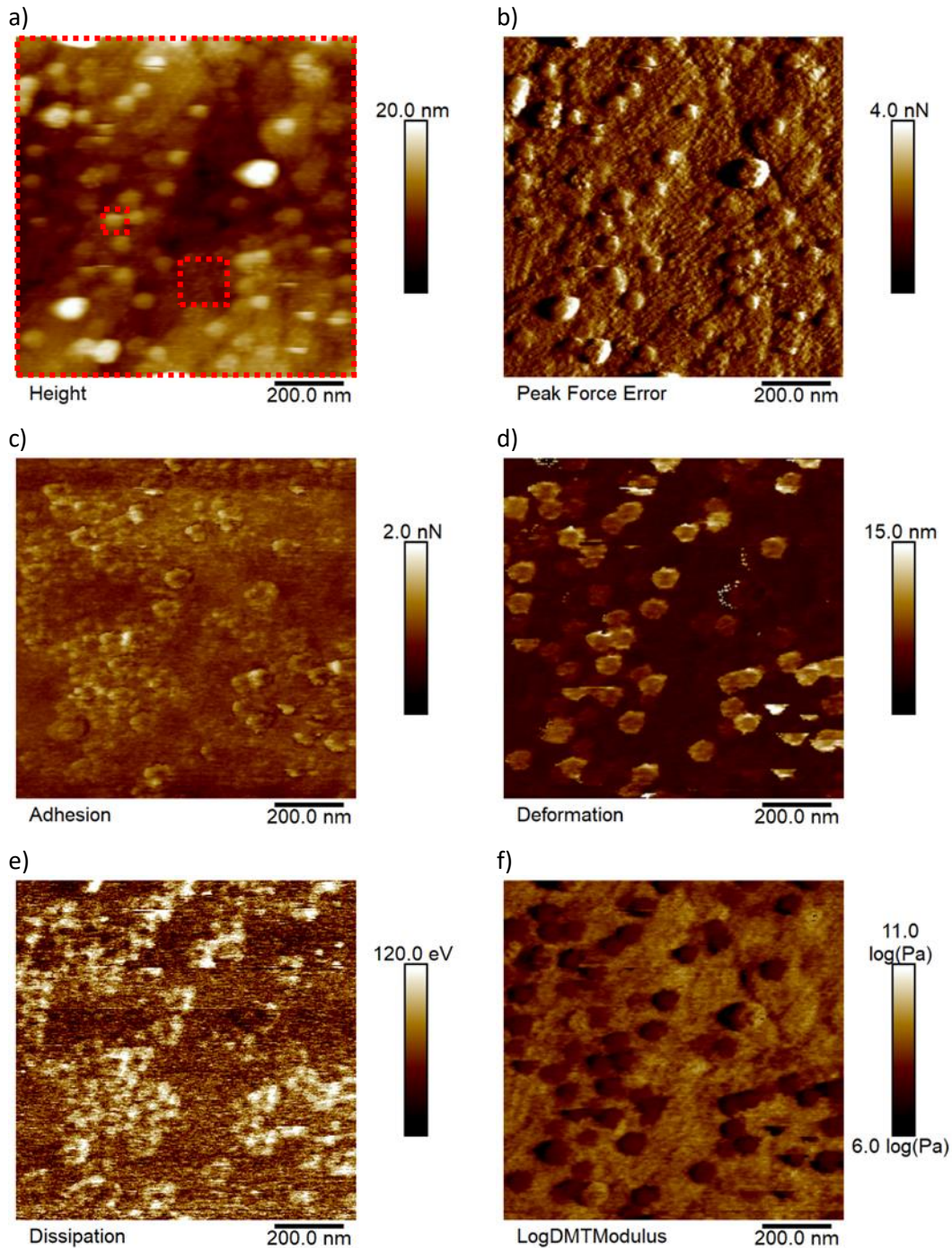
The surface properties of partially hydrated and fully hydrated mucin structures, after immersion in both Muc + DiW and Muc + PBS, were mapped out with QNM. Figure 4-26 shows 1 x 1  $\mu\text{m}$  QNM maps of partially hydrated mucin structure on bovine enamel after 30 minutes immersion in Muc + DiW. Figure 4-26 presents partially hydrated mucin structures and properties, similar to what was observed in Figure 4-23 but with increased scale. Surface abrasion marks were more clearly observed on bovine enamel from the surface preparation methods. In addition to the larger globular features observed on bovine enamel, smaller surface bound features were identified, from adhesion and deformation maps which was attributed size variation components within the Muc + DiW growth solution. It should be noted that the white lines associated with the edges of mucin features are a result of hysteresis of the piezo-controlled cantilever, caused by load control overshoots on the leading and trailing edge of features.



**Figure 4-26**  $1 \times 1 \mu\text{m}$  Quantitative nanomechanical property maps of partially hydrated mucin on bovine enamel after 30 minutes static immersion in Muc + DiW showing maps of a) height, b) PeakForce error, c) adhesion, d) deformation, e) dissipation and f) logDMT modulus. Absolute scale used in images a) to e), where the lowest value is considered 0.

Figure 4-27 shows  $1 \times 1 \mu\text{m}$  QNM maps of fully hydrated mucin on bovine enamel after 30 minutes static immersion in Muc + DiW. Unlike partially hydrated mucin, fully hydrated mucin presented more uniform properties throughout its whole structure, shown in Figure 4-27c), d), e) and f). Furthermore, the base surface is difficult to define in Figure 4-27b), as the ground enamel surface is not visible, indicating that a surface film might have formed.

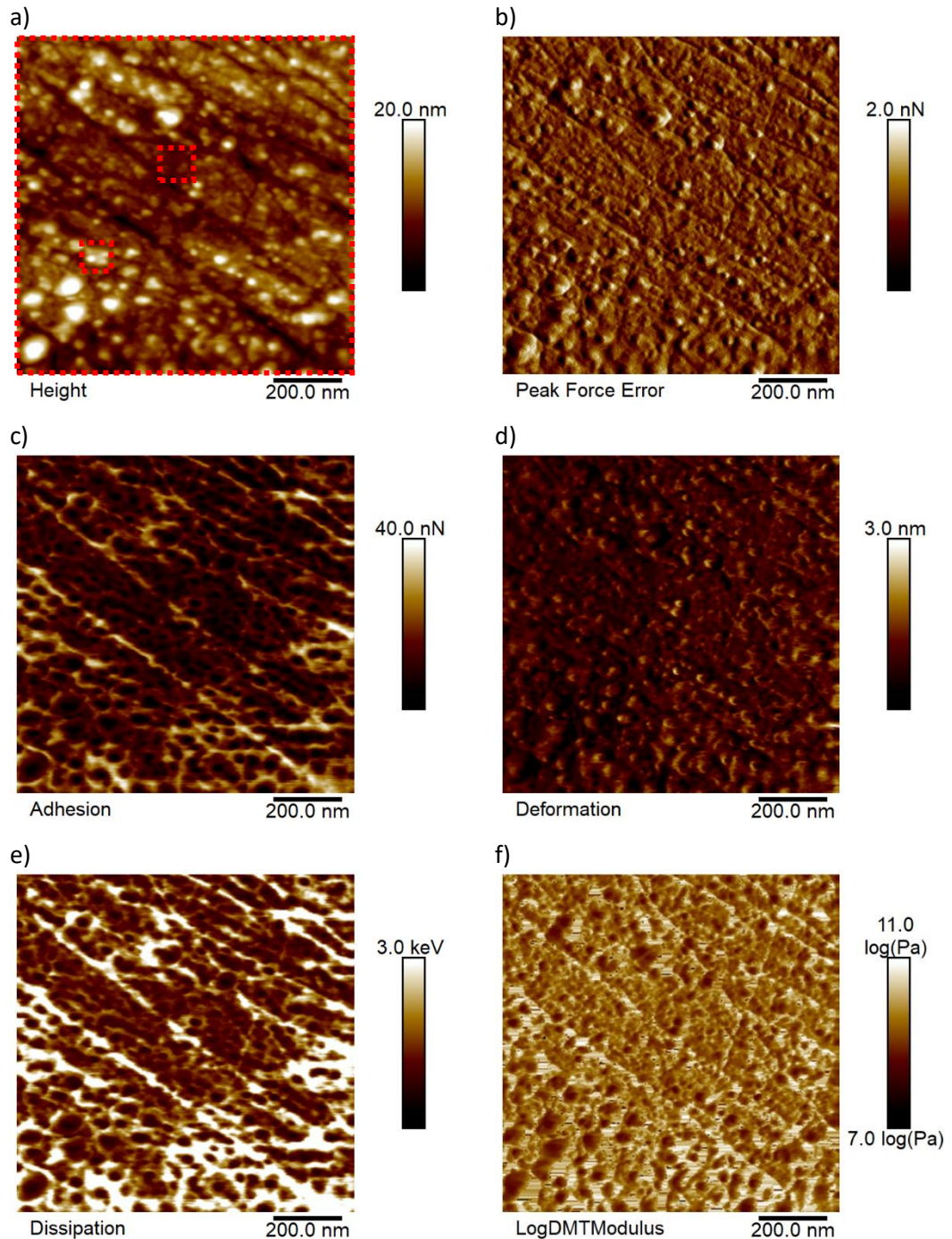
This was further evidenced by the maximum dissipation range of Figure 4-27e) of 120 eV (compared to 2.5 KeV in Figure 4-26e).



*Figure 4-27 1 x 1  $\mu\text{m}$  Quantitative nanomechanical property maps of fully hydrated mucin on bovine enamel after 30 minutes static immersion in Muc + DiW showing maps of a) height, b) PeakForce error, c) adhesion, d) deformation, e) dissipation and f) logDMT modulus. Absolute scale used in images a) to e), where the lowest value is considered 0.*

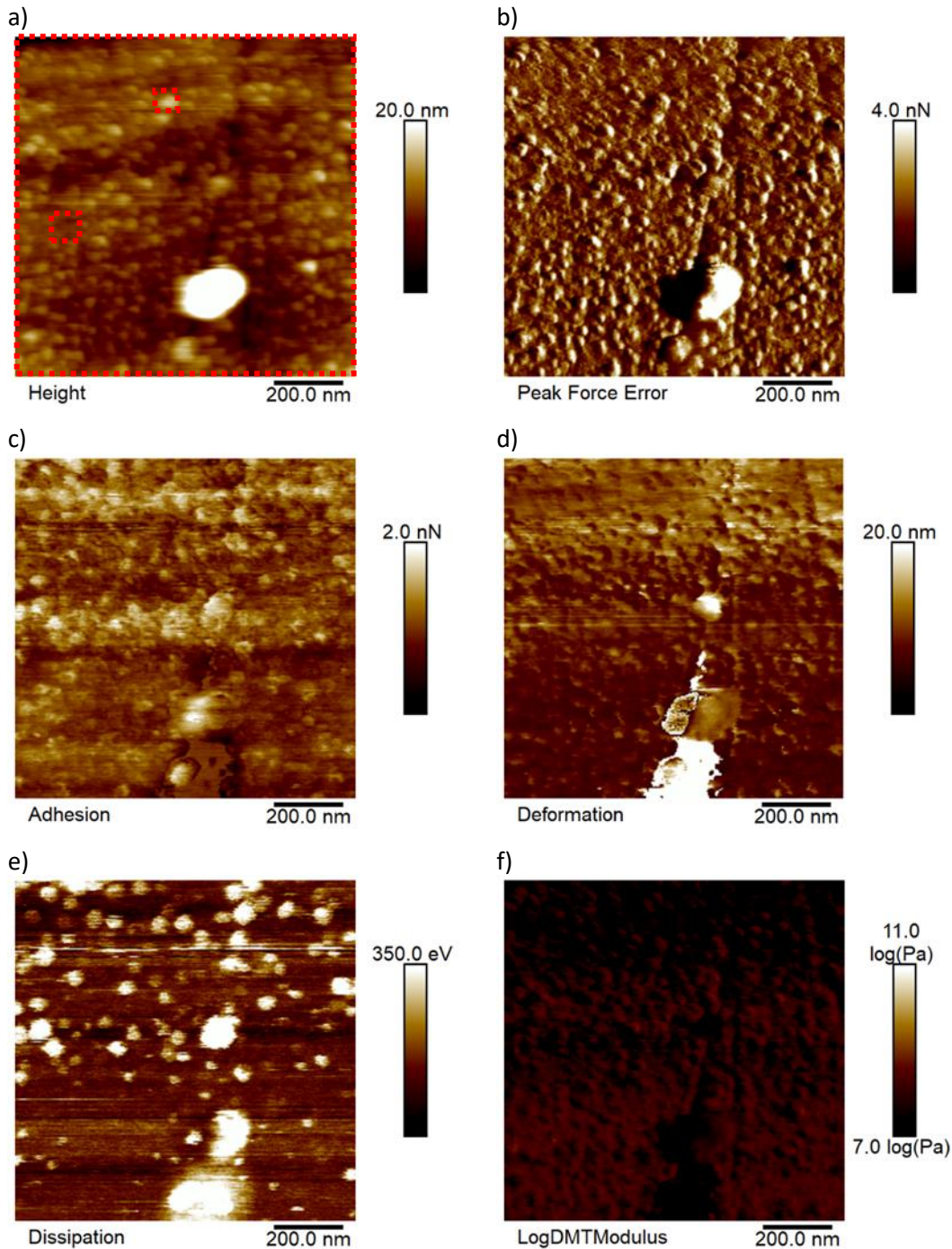
Figure 4-28 shows 1 x 1  $\mu\text{m}$  QNM maps of partially hydrated mucin on bovine enamel after 30 minutes static immersion in Muc + PBS. Uniform QNM properties were observed over these mucin structures, much like fully hydrated structures formed from Muc + DiW. Partially hydrated Muc + PBS structures were observed to be more evenly distributed over

the scan area compared to mucin structures without salt in Figure 4-26. The base surface was still defined, shown by the visible scratches from grinding in Figure 4-28b).



*Figure 4-28 1 x 1 μm Quantitative nanomechanical property maps of partially hydrated mucin on bovine enamel after 30 minutes static immersion in Muc + PBS showing maps of a) height, b) PeakForce error, c) adhesion, d) deformation, e) dissipation and f) logDMT modulus. Absolute scale used in images a) to e), where the lowest value is considered 0.*

Figure 4-29 shows 1 x 1 μm QNM maps of fully hydrated mucin on bovine enamel after 30 minutes static immersion in Muc + PBS. Fully hydrated Muc + PBS structures are evenly distributed over the enamel surface, similar to partially hydrated Muc + PBS structures.



*Figure 4-29 1 x 1  $\mu\text{m}$  Quantitative nanomechanical property maps of fully hydrated mucin on bovine enamel after 30 minutes static immersion in Muc + PBS showing maps of a) height, b) PeakForce error, c) adhesion, d) deformation, e) dissipation and f) logDMT modulus. Absolute scale used in images a) to e), where the lowest value is considered 0.*

Red dashed boxes in Figure 4-26a), Figure 4-27a), Figure 4-28a), Figure 4-29a) represent image depth survey locations for the adhesion, deformation, dissipation and log DMT modulus properties, displayed in Table 4-5. The boxed areas relate to mucin areas, potential surface areas with no mucin and the whole scanned area. Surface areas were estimated based on the PeakForce error maps for hydrated samples due to surface coverage.



*Table 4-5 Mean quantitative nanomechanical properties and standard deviations of surface features on bovine enamel surfaces after 30 minutes static adsorption in Muc + DiW and Muc + PBS. Features relate to areas of no mucin (Surface), areas of mucin (Mucin) and the mean properties of the whole scan area (All) under partially and fully hydrated conditions.*

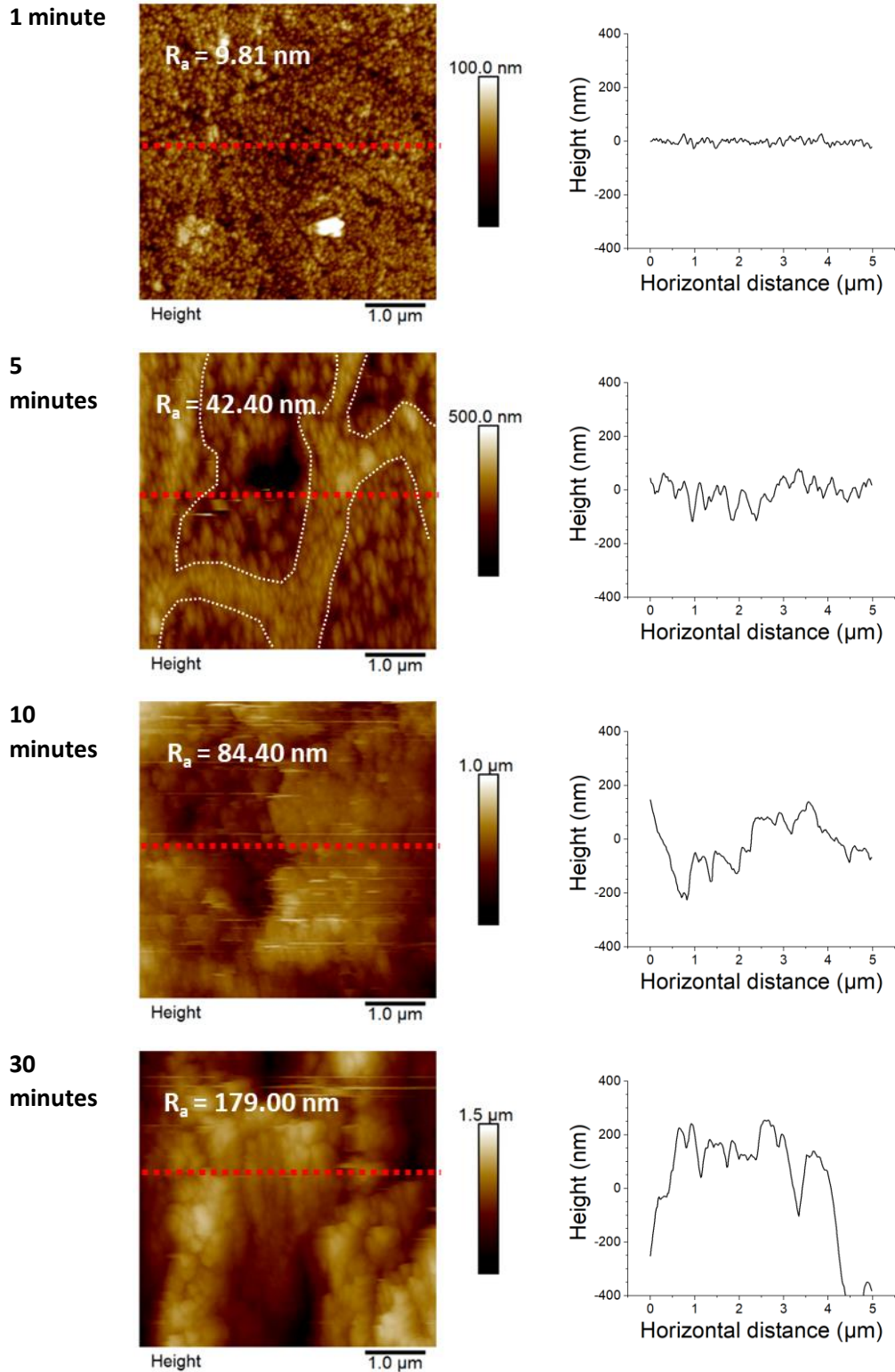
Feature		Partial hydration		Full hydration	
		Muc + DiW	Muc + PBS	Muc + DiW	Muc + PBS
<b>Mean ± SD</b>					
<b>Adhesion (nN)</b>	Surface	10.23 ± 1.76	9.49 ± 3.22	0.02 ± 0.04	0.06 ± 0.07
	Mucin	9.53 ± 2.83	6.57 ± 2.31	0.11 ± 0.11	0.71 ± 0.146
	All	10.05 ± 3.00	13.62 ± 6.66	0.04 ± 0.08	0.71 ± 0.146
<b>Deformation (nm)</b>	Surface	0.41 ± 0.14	0.34 ± 0.16	0.66 ± 0.19	1.84 ± 0.40
	Mucin	0.60 ± 0.19	0.92 ± 0.47	5.50 ± 1.18	9.27 ± 2.13
	All	1.28 ± 0.24	1.26 ± 0.33	1.88 ± 1.88	5.30 ± 7.70
<b>Dissipation (KeV)</b>	Surface	0.79 ± 0.17	1.25 ± 0.93	0.05 ± 0.01	0.04 ± 0.02
	Mucin	0.68 ± 0.22	0.39 ± 0.22	0.06 ± 0.02	0.15 ± 0.04
	All	0.76 ± 0.33	1.27 ± 0.89	1.25 ± 0.02	0.12 ± 0.08
<b>logDMT (logPa)</b>	Surface	9.79 ± 0.30	9.53 ± 0.39	8.82 ± 0.19	7.92 ± 0.32
	Mucin	9.94 ± 0.30	8.86 ± 0.29	7.38 ± 0.32	7.81 ± 0.21
	All	9.63 ± 0.36	9.53 ± 0.48	8.24 ± 0.62	7.68 ± 0.56

Adhesion and dissipation properties were reduced in a fully hydrated environment compared to the partially hydrated environment for both solutions. Salt interactions reduced mucin's adhesion and dissipation properties compared to the surface's when partially hydrated. However, the overall adhesion and dissipation of the whole area was shown to increase with the addition of PBS. The adhesion and dissipation properties of fully hydrated mucin were observed to increase with the addition salt. Differences between mucin and surface features were greater with the addition of salt in the partially hydrated environment. Furthermore, adhesion and dissipation properties of fully hydrated mucin with salt were similar to the whole area, suggesting the surface properties were dominated by mucin.

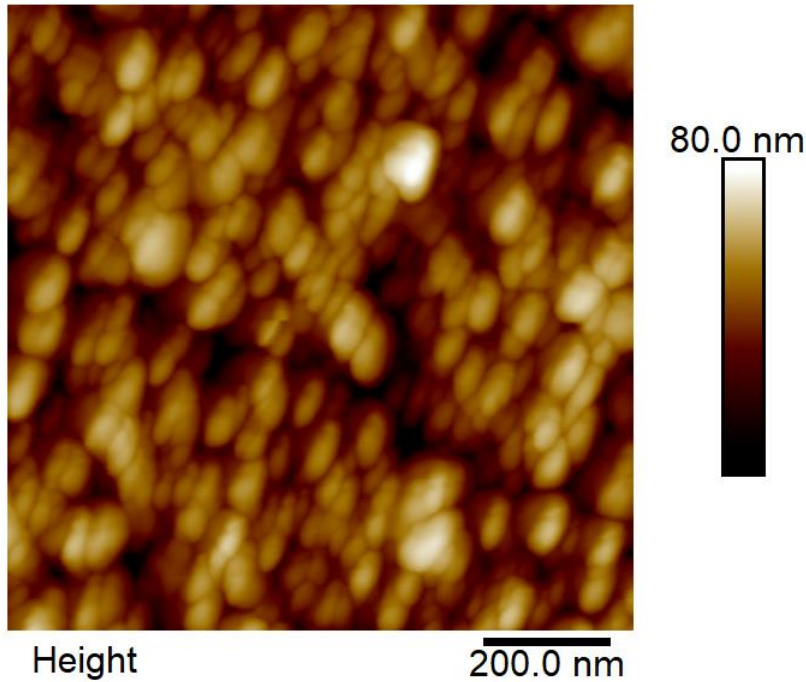
Comparison of deformation in partially hydrated and hydrated conditions indicated that area and mucin deformation were greater under hydrated conditions, while surfaces were similar. The addition of salts increased deformation of mucin in hydration conditions compared to the surface deformation. Both hydration and salts increased mucin deformation relative to the surface. Deformation links to the DMT modulus and there the logDMT modulus, which shows similar trends to deformation. This suggested mucin structures were softer with the addition of salt, within a hydrated environment and with the two combined.

#### *4.2.3.3 Influence of citric acid on mucin interaction with bovine enamel*

Static immersion tests in the pH 3.1 citric acid + 0.2% mucin solution (Muc + Acid) were performed on bovine enamel. Figure 4-30 shows the progressive degradation of bovine enamel with increase immersion time, evidenced by increasing surface roughness and changes to the surface profile at the red dashed section lines. No mucin was observed on these surfaces; no particle analysis was performed. Two surface features were noted: hydroxyapatite crystals and enamel rods. Hydroxyapatite crystals were characterised on bovine enamel surfaces after 1- and 5-minutes static immersion in the Muc + Acid by formation of fine sharp peaks over the surface. These peaks are magnified and displayed in Figure 4-31. Particle analyses were performed on 5 x 5  $\mu\text{m}$  and 1 x 1  $\mu\text{m}$  height images after 1 minute static immersion in Muc + Acid. The mean diameter of these peaks was estimated to be  $44.68 \pm 21.00$  nm and  $54.08 \pm 36.65$  nm for respectively. The peaks appeared to be homogenous and orientated along a particular direction.

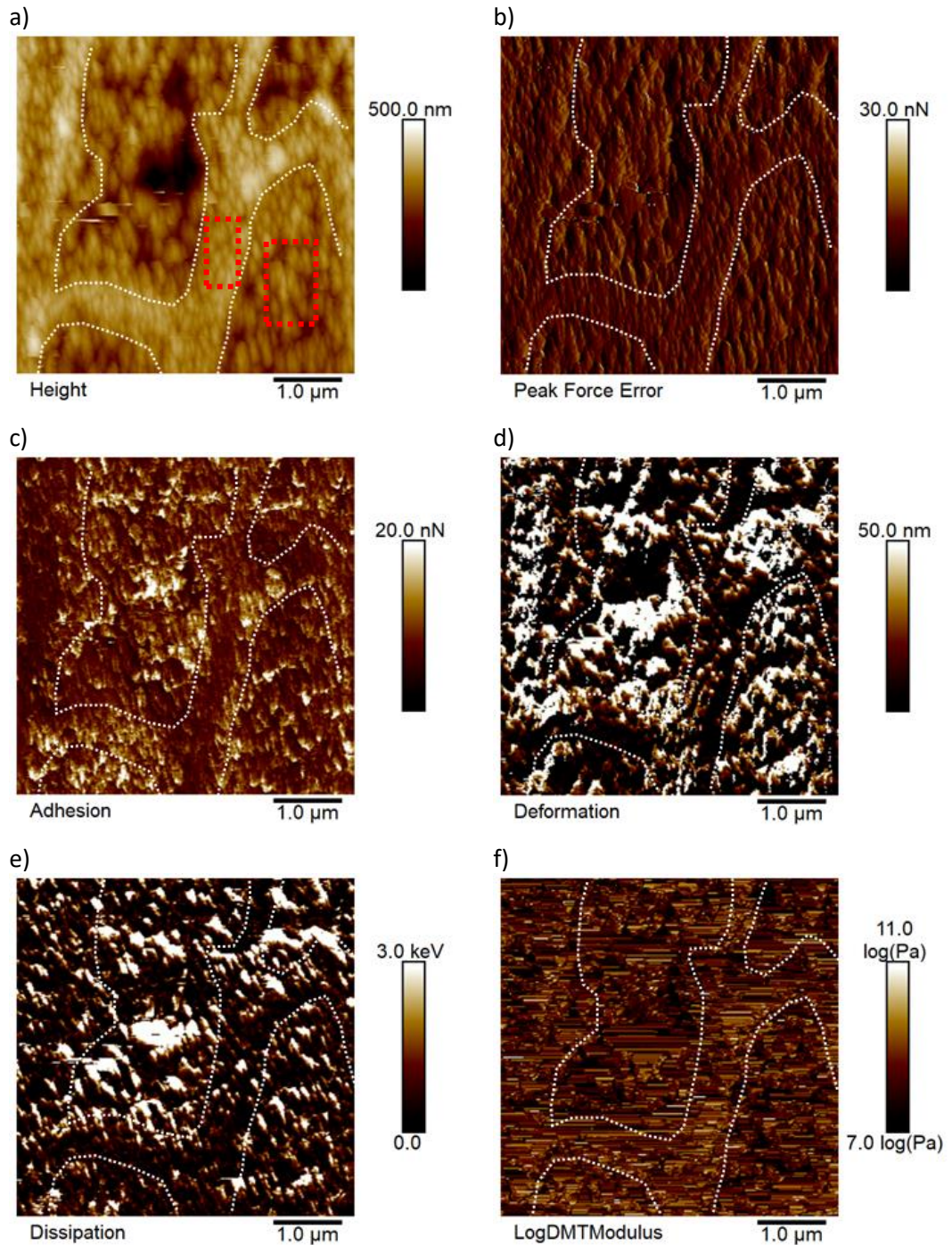


*Figure 4-30 5 x 5  $\mu\text{m}$  AFM height images of bovine enamel after static immersion in Muc + Acid. Red dashed line refers to the location of section profiles, displayed next to the AFM images. White dashed line outline enamel rods. Surface roughness parameter,  $R_a$ , is displayed for each image. Absolute scale used in AFM images where the lowest value is considered 0.*



*Figure 4-31 1 x 1  $\mu\text{m}$  AFM height image of bovine enamel after 1 minute static immersion in Muc + Acid. Absolute scale used in image where the lowest value is considered 0.*

Enamel rods became more visible with increased static immersion in Muc + Acid, as shown by the white outline in Figure 4-30. The central regions of the enamel rods appeared to degrade more than the enamel rod edges, which increased the step height between the two. The step height impacted addition investigations with QNM after more than 5 minutes static immersion in Muc + Acid. However, some QNM images were taken of the enamel rod location, displayed in Figure 4-32. Depth surveys were taken for adhesion, deformation and dissipation property maps at the centre and edges of enamel rod features. The mean and standard deviation of these properties are shown in Table 4-6.



**Figure 4-32**  $5 \times 5 \mu\text{m}$  Quantitative nanomechanical property maps of bovine enamel after 5 minutes static immersion in Muc + Acid showing maps of a) height, b) PeakForce error, c) adhesion, d) deformation, e) dissipation and f) logDMT modulus. Red dashed boxes indicate locations of depth surveys. Absolute scale used in images a) to e), where the lowest value is considered 0.

Depth surveys taken from the red boxed locations, shown in Figure 4-32a), suggested the edges of the enamel rods were softer compared to the rod's centre, shown by the difference in deformation properties in Table 4-6. This could not be determined with the logDMT map due to the image distortion from the variation in step height over the scan image. Adhesion and dissipation properties were observed to be lower towards the edge of enamel rods compared to the centre.

*Table 4-6 Mean quantitative nanomechanical properties and standard deviations of enamel rods on bovine enamel surfaces after 5 minutes static adsorption in Muc + Acid. Features relate to areas in the centre of the enamel rods (Centre) and the edges of the enamel rods (Edge).*

	Centre	Edge
<b>Adhesion (nN)</b>	6.81 ± 3.37	5.37 ± 2.35
<b>Deformation (nm)</b>	30.23 ± 28.70	17.30 ± 16.60
<b>Dissipation (keV)</b>	3.51 ± 2.22	2.94 ± 1.35

## 4.3 Discussion

### 4.3.1 Mucin interactions with the lubricant environment

The properties of a protein in solution are important to consider regarding protein adsorption and subsequent layers. Size, charge and structural stability may influence the number of contact sites a protein exhibits in solution prior to adsorption to a surface interface [66]. These were characterised with DLS and zeta potential experiments. The IEP of mucin in this work was close to the IEP of both bovine submaxillary mucin and porcine gastric mucin observed in the literature, between pH 2 - 3 [224, 91]. The measured zeta potential at a neutral pH in this work also supports observations from other studies on bovine submaxillary mucin and porcine gastric mucin, with zeta potentials between  $-5.99 \pm 0.46$  mV and  $-5.47 \pm 1.07$  mV respectively in a pH 7.4 solution [225]. Standard practice suggests a zeta potential greater than  $\pm 30$  mV is stable as the particle's electrostatic repulsion is strong enough to prevent aggregation [226]. Moving closer to the IEP, particles are unstable and more susceptible to aggregation due to the reduced net electrostatic repulsion [227]. This aggregation behaviour describes the larger mucin sizes observed over the tested pH range. Factors which decrease mucin's zeta potential are therefore important to promote initial adsorption on a given surface as larger proteins, unstable aggregating proteins and unfolding proteins all increase the number of potential contact sites [66].

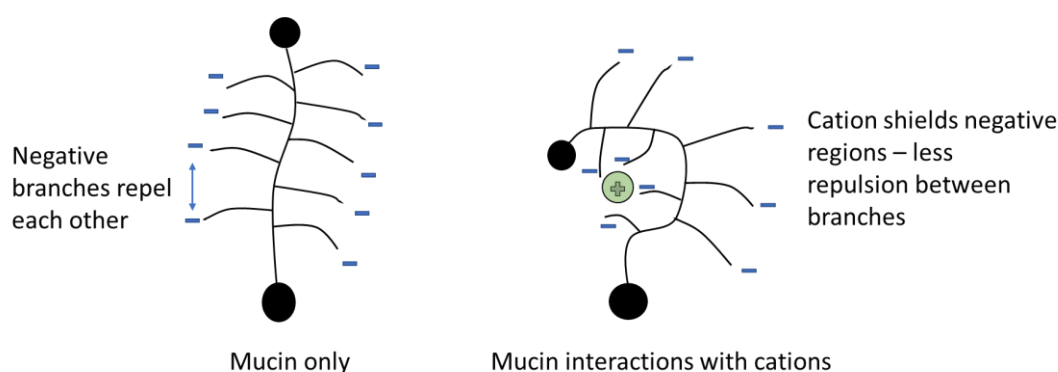
#### **Impact of mucin concentration**

Mucin concentration was shown to influence the zeta potential the most in deionised water compared to salt and acid solutions buffered pH 7.4 and pH 3.1 respectively. In the latter solutions, only slight changes in the zeta potential towards 0 mV were observed. However changes to the pH were observed with increasing mucin concentration, in both DiW and PBS buffered solution, which were attributed to the impurities from commercial porcine gastric

mucin [228]. This influenced the average hydrodynamic diameter of mucin, as increasing its concentration will increase the chances of interaction and agglomeration.

### Influence of salt type and salt concentrations

At the standard mucin concentration of 0.2% mucin, the addition of PBS reduced mucin's size and increased the zeta potential. This suggests that salts within PBS interact with the structure of mucin, potentially causing it to fold by shielding the negative regions of mucin [229]. Folding effects reduce mucin's size in solution, and the number contact sites for initial adsorption to a surface, shown by the schematic in Figure 4-33.

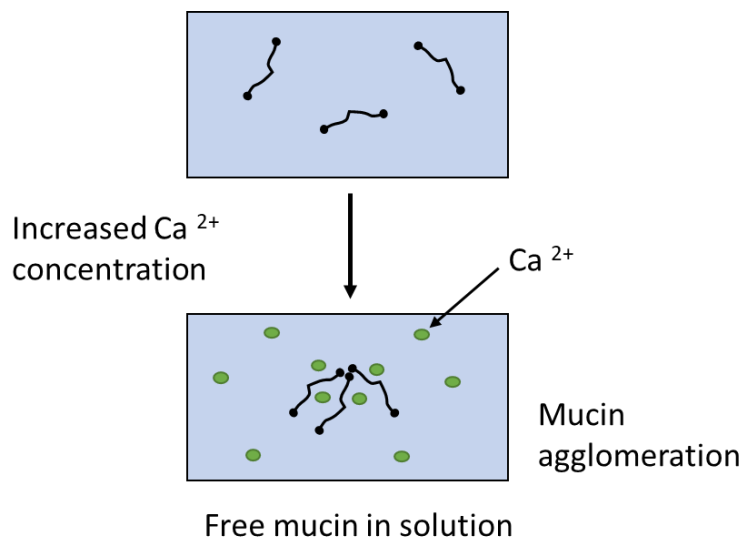


*Figure 4-33 Schematic of charge induced folding of mucin monomer.*

Ion strength and concentration were also investigated as factors which impact mucin's properties in solution. Salts containing calcium and phosphate groups presented a larger change in the zeta potential, with an overall increase. The movement closer to the isoelectric point of mucin supported the higher average hydrodynamic diameter size for mucin particle in the  $\text{CaCl}_2$  solutions, although this was not the case for the  $\text{NaH}_2\text{PO}_4$  solutions. Individually, it appeared that single valency salts paired with chloride ions had a minimal impact on altering particle charge and size dispersity over the concentration range. Large size variations in the mucin solutions meant that no meaningful size comparisons were made. However, the presence of either calcium or phosphate ions indicated more visible changes to particle charge over the concentration range.

The higher concentration of calcium ions presented an increase in the average mucin size compared to other salts at the same concentration. Usually, higher valency ions like calcium are thought to make a molecule more compact as the electric double layer is reduced [121, 229]. Previous work examined mucin interactions on a surface via QCM-D and AFM studies, observing mucin layer compaction with increased calcium concentration [121, 229]. However, this work solely relates to changes to surface-bound mucin layers, and cannot infer what mucin behaviour in the bulk fluid. In this work, calcium-mucin interactions at

similar calcium concentrations increased the aggregation of mucin within the bulk solutions, yielding a larger average particle size. This aggregation behaviour can be thought as salting-out, where higher salt concentrations drive proteins to form larger aggregates [230]; this is illustrated on the right-hand side of Figure 4-34. From an understanding of general protein adsorption and the Vroman effect, larger structures will adsorb more slowly to a given surface and form stronger bonds with the surface given due to the increase number of contact sites [231, 66]. Once adsorbed, further structural conformation changes may occur within the mucin structure, causing the adsorbed structure to spread over the surface [66]. This highlights key differences between the structures of free mucin and surface bound mucin regarding environmental composition, illustrated in Figure 4-34.



*Figure 4-34 Mucin interactions with Ca<sup>2+</sup> ions within the bulk solution.*

### **Precipitation formation in the bulk solution and implications**

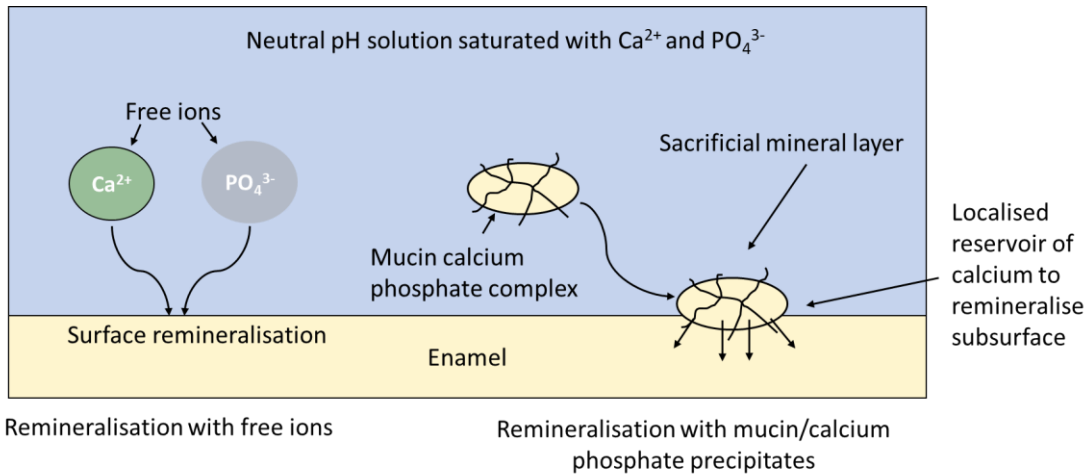
Finally, the cloudiness of CaCl<sub>2</sub> + PBS was attributed to the formation of calcium phosphate precipitates in the solution. The reduced Pdl and the more condensed peak size clusters for CaCl<sub>2</sub> concentrations over 10 mmol and the much larger mean hydrodynamic diameter could be explained a few possible reasons. Either the dominant molecule measured by DLS was from: the calcium phosphate precipitates, the mucins influenced by calcium and phosphate ions, or, the mucins influenced by both calcium phosphate precipitate and individual ions. It has been seen than human biliary mucin promotes the formation of amorphous magnesium-calcium phosphate particles and directly interacts with them [232]. The presence of calcium-binding regions of mucin, namely the sialic acid and sulphate groups, may provide crosslinking between molecules and cause larger structures/agglomerates to form [233,



234]. Furthermore, a relatively low concentration of sodium ions has previously been observed to enhance the binding of calcium ions to biliary mucin, which may in turn enhance the networking between mucins [234].

The calcification behaviour and the formation of calcium phosphate precipitates is what makes mucin an ideal component for an artificial saliva. In the absence of mucin, calcium and phosphate ions can facilitate remineralisation of tooth enamel at a neutral pH. One study which examined the use of a supersaturated calcium-phosphate rinse in patients with salivary hypofunction and observed an improvement in long term protection against dental caries [235]. It is unknown whether the addition of mucin to a supersaturated calcium phosphate solution Vroman would enhance tooth enamel remineralisation.

Salivary glycoproteins which complex calcium phosphate, termed as 'Salivary Precipitin', have been observed in the literature to become incorporated with dental plaque [236]. It is not clear which glycoprotein forms these complexes. However, it was shown to provide a reservoir of calcium and phosphate ions to promote remineralisation of decalcified tooth enamel and act as a sacrificial layer due to it being 8-10 times more soluble than tooth enamel [236]. Casein Phosphopeptide-Amorphous Calcium Phosphate (CPP-ACP), a remineralisation agent, behaves similarly. Casein proteins complex ACP, and bind well to plaque locations providing a calcium reservoir to reduce demineralisation and assist remineralisation in subsurface enamel [237, 238]. Similarly, mucin within an artificial saliva was seen to promote enamel remineralisation in vitro when combined with fluoridated toothpastes [239]. The literature suggests that a protein component which can promote localised calcium phosphate reservoirs is essential for demineralisation prevention and assisted remineralisation. Figure 4-35 illustrates remineralisation of enamel with free calcium and phosphate ions, compared to the potential adsorption of mucin-calcium phosphate complexes that initially bind to the surface and then facilitate enamel remineralisation acting as a localised reservoir for calcium and phosphate ions. Future work should aim to investigate the remineralisation effects of mucin + salt solutions by precipitate remineralisation of both the surface and subsurface enamel.



**Figure 4-35** Illustration of remineralisation with free ions compared to hypothesised mucin assisted remineralisation.

#### 4.3.2 Steatite vs bovine enamel – from surface to mucin-surface interactions

The use of steatite as an alternative tooth material is a controversial one. While recommended as a standard material for friction and wear testing [150, 146], it has also been deemed unsuitable due hardness and wear resistance properties [155]. The work in this chapter partially highlights the latter regarding sample surface preparation. Both steatite and bovine enamel were progressively ground and polished for the same duration, in the same media. Steatite was shown to possess a greater core roughness compared to bovine enamel, which inferred that steatite possessed greater wear resistant properties compared to bovine material during the grinding and polishing processes prior to analysis.

Qualitative surface characterisation of the two materials highlighted key differences in surface characteristics. Steatite was observed to be a granular ceramic with a randomly distributed closed pore structure, an artefact of the dry pressing and sintering temperatures of manufacture [240]. Subsequent grinding of steatite into a usable sample therefore produced surface pockets of various shapes and sizes, which has been previously seen in the literature [241]. Among these features, grains of different shape, size and arrangement were randomly distributed over the surface, yielding element dense locations. In contrast, bovine enamel is composed of a uniform organised structure of hydroxyapatite rods, with no element dense locations.

#### **Mucin adsorption to steatite and bovine enamel**

Topography, composition, heterogeneity, surface energy and potential are all surface characteristic which influence protein adsorption [66]. Rougher surfaces, porosity, pore size and pore distribution all have an impact on increasing the real surface area. While surface roughness has been observed to not influence protein adsorption at the nano scale, porosity

and pore sizes larger than the adsorbing protein have been shown to increase surface adsorption [242, 243]. Mucin interactions with both surfaces indicated a greater coverage on steatite compared to bovine enamel, producing different partially hydrated mucin structures overall. The greater coverage on steatite may be partly attributed to the greater real surface area attributed to its porosity. The chemical composition, surface potential of exposed grains and heterogeneity on steatites surface might also contribute to this. Protein adsorption onto magnesium silicates has not been documented in the literature while adsorption on its constituent ceramic components have. It has been documented that increasing silica content in yttria stabilised zirconia decreased the amount of adsorbed protein [244]. Furthermore, bovine serum albumin (a negatively charged protein) adsorbed onto silica and alumina surfaces showed stronger interaction and a faster rate of adsorption on the positively charged alumina, compared to the negatively charged silica at a neutral pH [245]. At a neutral pH, mucin is negatively charged and may therefore interact with alumina dense locations on steatite due to a stronger electrostatic attraction. It could be inferred that preferential adsorption of mucin occurred onto the exposed alumina grains on steatite.

#### **Mucin layer properties on steatite compared to bovine enamel**

Mucin location reduced adhesion and dissipation on both surfaces, with a greater difference observed on steatite. Adhesion means the tensile force required to separate the AFM cantilever from the surface, and the dissipation is the mechanical energy lost from this interaction. Furthermore, surface energies were also observed to be different with bare steatite surface expressing a higher dissipation property compared to bare bovine enamel. The average reduction in adhesion has been previously observed to relate a lower average frictional force under nanoscale loading [246]. It is unclear how these properties may influence friction at the microscale, however it is clear that surface substrate has an influence on adhesion, dissipation and deformation properties measure by AFM QNM. Assessment of the deformation properties indicated that mucin was stiffer on steatite compared to enamel. The deformation property, defined as the distance between the contact setpoint and the max peak force, is influenced by the localised stiffness and dissipation properties of the area. An increased deformation therefore indicates a combination a lower local stiffness and/or greater dissipation [246]. Indentations on mucin/steatite presented minimal deformation change compared to the bulk surface, suggesting mucin did not alter the previously mentioned surface properties. However, the opposite was observed on bovine enamel surfaces.

As a substitute tooth material for wear testing of dental materials, the similarities between steatite and an enamel material are limited. To effectively use steatite as a tooth material, it should behave similarly to enamel in terms of its surface properties and interactions with an artificial saliva solution. However, this was not the case. Study limitations existed with the imaging of mucin in air which rendered a partially hydrated mucin on the examined surfaces, where the relative hydration of mucin was not quantified, which should be considered in future investigations.

#### 4.3.3 Role of hydration state and salt composition on mucin layers

AFM imaging in MilliQ water uncovered key differences between partially hydrated and fully hydrated mucin structures on bovine enamel. AFM height images of partially hydrated mucin show dome like structures, however upon investigation of the adhesion and dissipation properties of these structures presented notable property differences. Partially hydrated structures had collapsed central regions, with adhesion and dissipation properties similar to neighbouring, uncovered bovine enamel, whereas hydrated mucin structures presented uniform adhesion and dissipation properties throughout. This suggested a potential link between mucin layer hydration with the layer's structure, and subsequent adhesion properties that may impact on their lubrication properties.

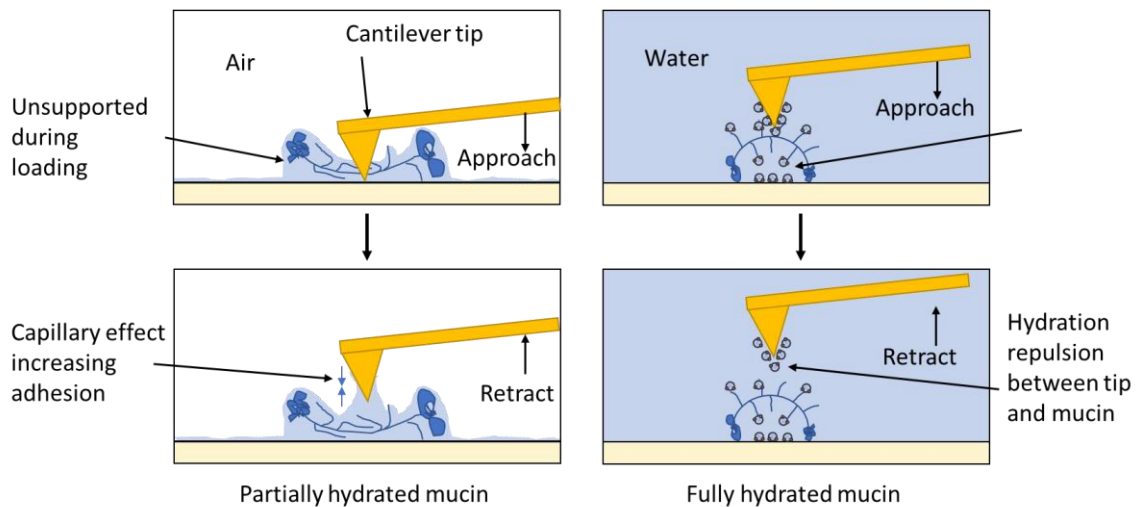
##### **Role of hydration on surface mucin size and distribution**

Size differences between partially hydrated and fully hydrated mucin were attributed to the drying method of samples before imaging. Larger partially hydrated mucin structures may have been retained on the surface compared to smaller structures because of the former possessing a greater number of contact sites for surface interactions [66]. No drying process was associated with fully hydrated mucin and thus mucin was not removed in this way. Fully hydrated mucin layers therefore formed with greater coverage, covering the bare enamel surface which made surface measurements difficult. For a better comparison of surface and mucin layer properties under these conditions, future work should have a clear separation between the two, either by scratching off mucin or taping of a control area.

##### **Role of hydration on mucin layer load bearing properties**

It has previously been observed that changing the hydration state of globular proteins has little impact changing aspects of secondary/tertiary structures, while for intrinsically disordered proteins this impacts unfolding/folding of the structure during film formation [247]. It was speculated that the intermolecular H-bonding between water molecules and the protein structure are removed in favour of intramolecular H bonding within the protein

when it's dehydrated [247]. Mucin contains between 20-40% (over 40% for some mucin types) intrinsically disordered regions which may therefore be influenced by changes to the hydration state [248]. Furthermore, from a liquid crystal perspective, decreasing hydration of porcine gastric mucin has been observed to decrease the structural order of the protein, examined by increasing the mucin concentration (well above what was used in the current work) [249]. Together, this suggests a potential mechanism for the structural changes that was observed in this work. Partially hydrated mucin is thought to be unsupported without sufficient water molecules, while fully hydrated mucin is supported, illustrated in Figure 4-36. This subsequently influences the adhesion and load bearing properties of mucin.



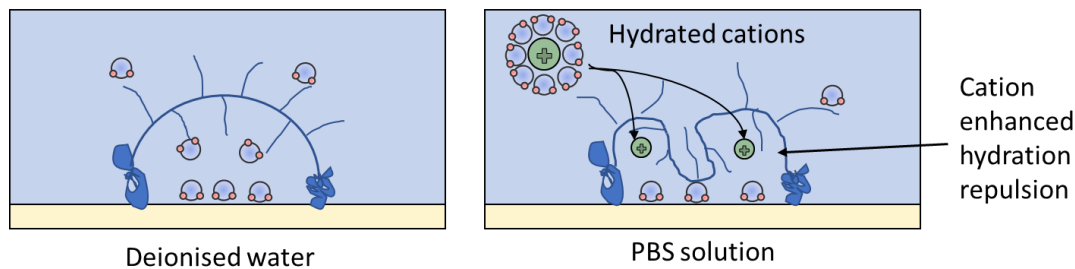
*Figure 4-36 Cantilever tip interactions with partially hydrated mucin and fully hydrated mucin, illustrating load bearing and adhesive behaviour of mucin.*

Fully hydrated mucins, supported by water molecules, are shown to reduce adhesion to the AFM cantilever compared to partially hydrated mucin and the bare enamel surface. Greater adhesion on the bare surfaces may be a result of the capillary effect, as the enamel is also partially hydrated from interactions with the growth solution. During indentation, the AFM cantilever experiences greater attraction to the surface and requires a larger tensile force to break free from the surface [250]. Partially hydrated mucin was shown to partly reduce this, but fully hydrated mucin reduced this considerably, reducing the overall surface area adhesion property. This may partly be due to the cantilever being fully immersed in the liquid and is permitted to approach and retract from the surface unencumbered. This is also illustrated in Figure 4-36. Future work should aim to include compliance testing on specific regions on partially hydrated and fully hydrated mucin layers to compare time dependent viscoelastic properties and how this relates to QNM properties [251].

QCM-D investigations of fully dehydrated porcine gastric mucin have previously shown that at 0% relative humidity the mucin layer behaves like a rigid solid layer, with no observable dissipation [252]. The measured dissipation property of the layer remained at 0, therefore rigid, until humidity reached 75% at which point the dissipation increased until a plateau was reached at 97% humidity [252]. This suggests that the rheological properties of mucin layers are dependent on their hydration level. It is important to note that dissipation in QCM-D studies relates to the energy lost from the shear wave during one oscillation. This infers the rheological properties of the layer without any physical interactions with a third body. This is different to dissipation properties of QNM, where dissipation is the mechanical energy lost during an indentation cycle and is linked to the adhesion property. The rigid layer behaviour may be partially observed when considering the deformation properties of partially hydrated mucin and fully hydrated mucin. The larger mean deformation of fully hydrated mucin indicated that it was a softer material relative to partially hydrated mucin and the bare enamel surface. Furthermore, the deformation of partially hydrated mucin was similar bovine enamel, which suggested either this layer exhibited rigid properties or its structure could not support the PeakForce loading, thus presenting the deformation property of the underlying bovine enamel. Considering that hydrated polymers at the nanoscale can bear load due to the trapping of water within its structure [253], fully hydrated mucin may also show this behaviour under indentation.

#### **Salt contribution to mucin surface layer structure and load bearing**

Salt contributions from the PBS solution present similarities to what was observed with DLS experiments; smaller mucin structures were shown on enamel under both hydration conditions due to structural folding. The load bearing capacity of polymers have been suggested to be augmented by trapped counterions with the polymer structure, which influences the osmotic pressure to support compressive loads [253]. In this case, sodium and potassium cations within PBS may promote additional load bearing support to mucin structures owing to protein folding around the hydrated cations, indicated by the increase in deformation in Table 4-5 and illustrated in Figure 4-37. The effect is greater under fully hydrated conditions.



*Figure 4-37 Load bearing of mucin without salts in deionised water and with salts in PBS solution.*

It was also stated that the counterion effects do not influence the lubrication under a hydration lubrication mechanism, contributing only to the load bearing behaviour for neutral polymer segments at the nanoscale [253]. The larger adhesion properties of fully hydrated mucin with PBS compared to fully hydrated mucin without PBS further suggests hydration lubrication is not salt dependent, however to confirm this further tribological work was required. the opposite is observed under partially hydrated conditions.

#### 4.3.4 Influence of citric acid and mucin on solutions-surface interactions with bovine enamel

The pH 3.1 citric acid + mucin solution was shown to influence the structure of bovine enamel at the nanoscale. No mucin adsorption was observed, mainly as the bulk acid solution dominated any surface interactions. As the solution was below the critical pH for enamel dissolution, this behaviour was expected. The lack of mucin suggests either the acid interaction with the surface prevents or removes any adsorbed mucin. As such, an acidic environment would not be suitable to grow a protective mucin layer.

The degradation behaviour observed followed what has been observed in the literature where the centre of the enamel rods degrades initially followed by the outer inter-rod locations, revealing a honeycomb like structure [30, 188, 31]. This in turn causes the surface roughness to increase, supporting similar work [254, 31, 255]. This behaviour is linked to the mineralisation of enamel rods and inter-rod locations, where rods tend to be highly mineralised, while inter-rod contain relatively more water and organic matrix protein [30]. Under acidic conditions, the rods are weakened considerably more than the inter-rod regions, something which is observed in the current work from the deformation property data in Table 4-6 [30]. Here the rod locations are softer compared to the inter-rod locations.

## 4.4 Summary

The work in this chapter aimed to characterise mucin solutions, surfaces and the interactions between the two at the nanoscale. DLS and zeta potential measurements have been used

to identify changes to the size and stability of mucin in various solution environments. Changes to mucin stability and size were observed which were used to predict how initial adsorption of mucin might be influenced. Atomic force microscopy with quantitative nanomechanical property mapping aimed to characterise interactions between a few of these mucin solutions and bovine enamel surfaces. It was seen that:

- Hydration influenced the measured adhesion properties of mucin layers on bovine enamel, and was also observed to enhance the layer's load bearing properties. Partially hydrated mucin layers were linked to increased surface adhesion, which was supported by similar behaviours observed with saliva in the literature.
- PBS salts reduced mucin's size in the bulk solution by structural folding caused by charge shielding, ultimately enabling enhanced surface coverage onto bovine enamel surfaces. Increased AFM tip deformation demonstrated enhanced load bearing capabilities under hydrated conditions compared to Muc only conditions.
- Muc + Acid presented no adsorption onto bovine enamel surfaces, with bulk lubricant interactions presenting clear demineralisation of the surface after 1 minute. It was inferred that mucin layers could not grow on bovine enamel within this environment which was a novel observation.
- Individual salt type and concentration were observed to have a various effect on mucin's size and stability within solution, however a greater influence on mucin size was observed with high  $\text{Ca}^{2+}$  concentrations because of mucin agglomeration. The addition of  $\text{CaCl}_2$  to PBS was observed to form even larger structures which were thought to be a combination of calcium phosphate precipitate and mucin.
- Finally, steatite and enamel surfaces were characterised by optical microscopy, SEM, VSI and atomic force microscopy. Both surfaces were shown to be different in terms core roughness after the same surface preparation procedures and were shown to present different interaction regarding mucin adsorption. This demonstrated that it was not feasible to use steatite as a tooth substitute material, however to confirm this additional tribology tests should be completed.



## Chapter 5. Tribocorrosion of dental tissues and mucin's role

### 5.1 Introduction

This chapter delves into the contributions of tooth material loss from wear and corrosion in different artificial saliva environments. First, the friction behaviour was assessed on steatite and bovine enamel surfaces, as a baseline feasibility study using steatite for tribological studies. The wear and corrosion behaviour of bovine enamel samples were evaluated, to provide a measure of surface dissolution in static corrosion and tribocorrosive (dynamic corrosion) settings. Alongside these experiments, mucin was evaluated for its protective capabilities regarding surface volume loss, total surface dissolution, surface crystallinity and surface interactions with bovine enamel. The outline of the work in this chapter is presented in Figure 5-1, following methods outlined in Chapter 3.

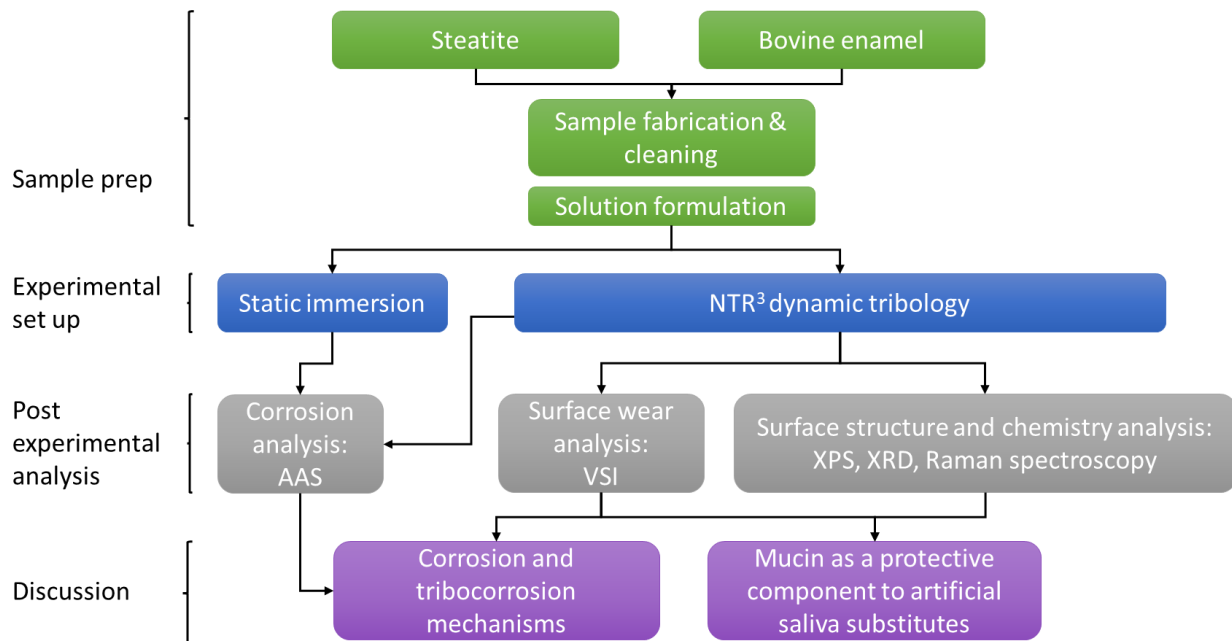
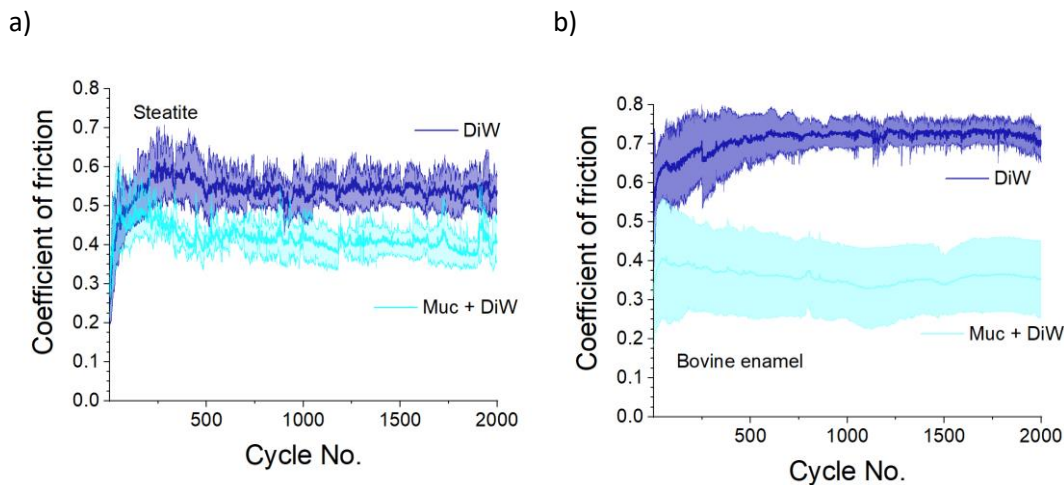


Figure 5-1 Flow chart of experimental methods and analyses Chapter 5.

## 5.2 Results

### 5.2.1 Friction behaviour comparison of steatite and bovine enamel under different artificial saliva environments

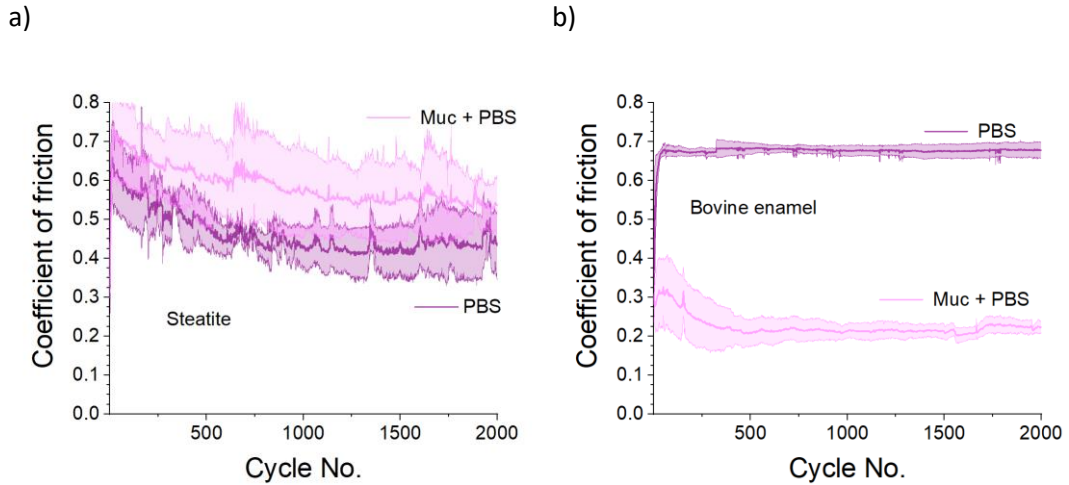
Figure 5-2, Figure 5-3 and Figure 5-4 show the effective coefficient of friction for each artificial saliva solution. Steatite and bovine enamel friction were compared, in mucin and non-mucin solutions. The coefficient of friction,  $\mu$ , is displayed as a line with an error shadow representing the standard deviation across samples. Figure 5-2a) shows reduction in the steatite's coefficient of friction, from  $0.54 \pm 0.08$  in DiW to  $0.39 \pm 0.03$  in Muc + DiW. Similarly bovine enamel's coefficient of friction, in Figure 5-2b), reduced from  $0.72 \pm 0.03$  in DiW to  $0.36 \pm 0.09$  in Muc + DiW. This indicated that mucin improved lubrication in DiW, under the chosen loading conditions for both steatite and bovine enamel samples. More variation was observed in bovine enamel samples with Muc + DiW compared to DiW, and steatite samples under both DiW and Muc + DiW conditions, suggesting instabilities with mucin lubrication on bovine enamel.



**Figure 5-2 Coefficient of friction of a) steatite and b) bovine enamel with standard deviation shadow in deionised water (DiW) and 0.2% mucin only (Muc + DiW) solutions.**

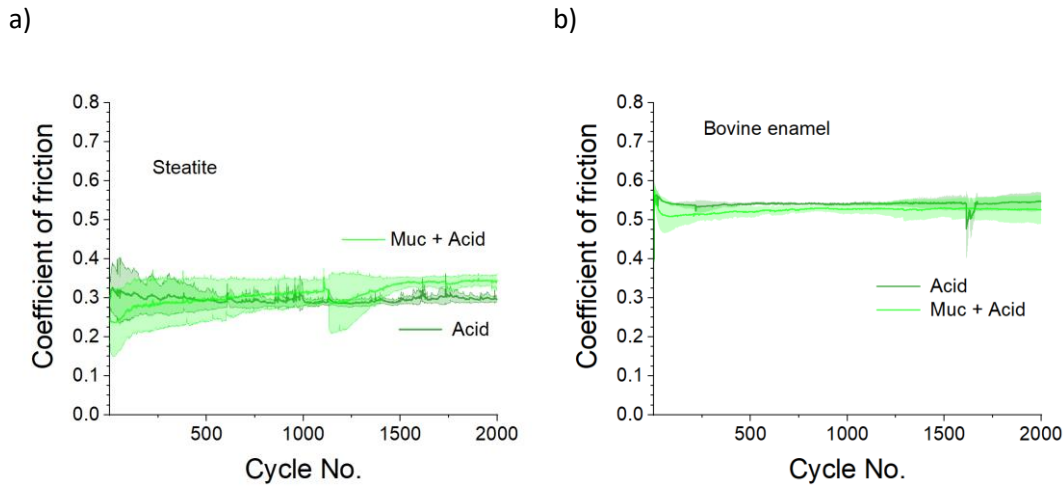
Steatite presented more varied friction behaviour in PBS and Muc + PBS solutions, shown in Figure 5-3a). Conversely, bovine enamel's friction behaviour in PBS and Muc + PBS appeared to be more stable, as shown in Figure 5-3b). Steatite's coefficient of friction increased from  $0.43 \pm 0.07$  in PBS to  $0.55 \pm 0.08$  in Muc + PBS. This differed to bovine enamel's coefficient of friction which decreased from  $0.68 \pm 0.02$  in PBS to  $0.22 \pm 0.02$  in Muc + PBS. The addition of PBS salts to the test environment did not influence the friction behaviour on bovine enamel in the absence of mucin when compared to DiW. On the other hand, steatite presented a lower coefficient of friction in PBS,  $0.43 \pm 0.07$ , compared to DiW conditions,  $0.54 \pm 0.08$ . Steatite's coefficient of friction in PBS was also closer to that of bovine enamel

in Muc + DiW,  $0.36 \pm 0.09$ . Muc + PBS appeared to enhance mucin's lubricating behaviour on bovine enamel, but not on steatite.



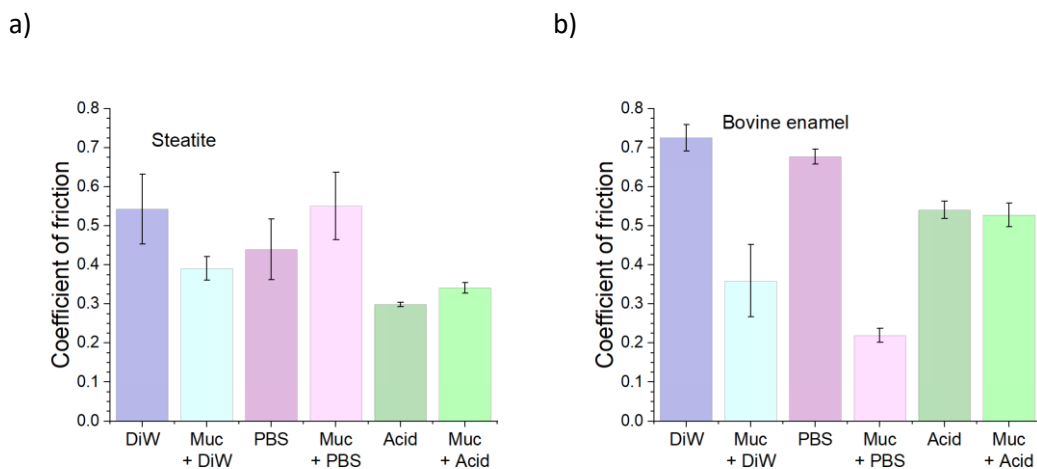
**Figure 5-3** Coefficient of friction of a) steatite and b) bovine enamel with standard deviation shadow in PBS and 0.2% mucin and PBS (Muc + PBS) solutions.

In the Acid and Muc + Acid environments on both steatite and bovine enamel, small differences in the friction behaviours were observed with the addition of mucin, as shown in Figure 5-4a) and b). This suggested that the acidic environment either inhibited the lubrication of mucin within the solution, or caused changes to these surfaces which dominated the friction behaviour. The possibility of the latter was suggested by the drop in the coefficient of friction in Acid compared to PBS and DiW tests for both steatite and bovine enamel samples. Furthermore, steatite's coefficient of friction under both Acid and Muc + Acid solutions was less than what was observed in bovine enamel, between  $0.29 \pm 0.01$  –  $0.34 \pm 0.01$  compared to  $0.54 \pm 0.02$  –  $0.52 \pm 0.03$  respectively. These differences were attributed to the way citric acid interacts with these surfaces, as a material dependent interaction.



**Figure 5-4** Coefficient of friction of a) steatite and b) bovine enamel with standard deviation shadow under pH 3.1 citric acid (Acid) and 0.2% mucin and pH 3.1 citric acid (Muc + Acid) solutions.

A comparison of the average effective coefficient of friction during the last 500 cycles is shown for steatite and bovine enamel in Figure 5-5a) and b) respectively. The comparison, in Figure 5-5a), indicated that mucin had little effect on reducing steatite's coefficient of friction in the neutral pH solutions ( $P > 0.05$ ), while a significant increase was observed with mucin in an acidic pH environment ( $P < 0.05$ ) when compared with DiW. The addition of salts did not have much of an impact on the friction behaviour of steatite compared to DiW ( $P > 0.05$ ). In Figure 5-5b), the comparison highlighted the effect of mucins reducing the coefficient of friction in the neutral pH solutions on the bovine enamel surfaces ( $P < 0.05$ ) compared to DiW. The addition of salts to the mucin solution reduced the coefficient of friction more than mucin alone, but above the chosen significance threshold when compared statistically ( $P = 0.053$ ).



**Figure 5-5** Mean coefficient of friction of last 500 cycles with SD bars for a) steatite and b) bovine enamel in all test solutions.

Table 5-1 and Table 5-2 present the P values for all tests on steatite and bovine enamel respectively.

*Table 5-1 Comparison table of p values from t tests for the coefficient of friction on steatite between solutions. Significant values are labelled by asterisks, with a significance threshold chosen as  $p = 0.05$ .*

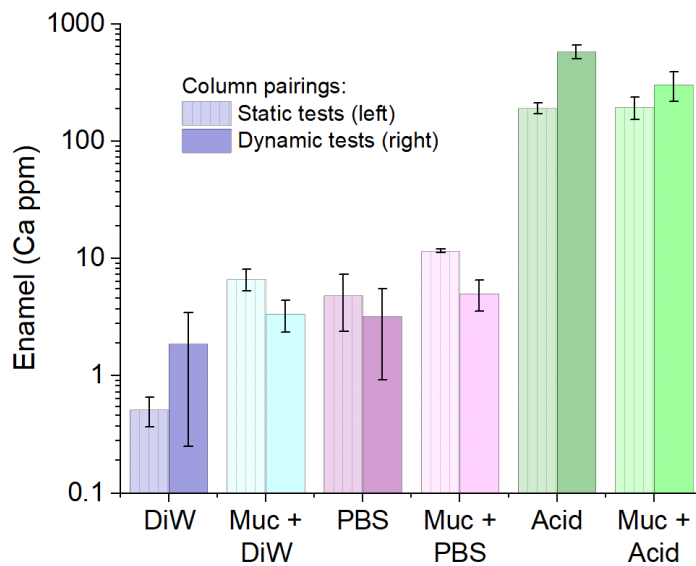
	DiW	Muc + DiW	PBS	Muc + PBS	Acid	Muc + Acid
DiW	-					
Muc + DiW	0.126	-				
PBS	0.284	0.476	-			
Muc + PBS	0.938	0.108	0.249	-		
Acid	0.060	0.043*	0.122	0.053	-	
Muc + Acid	0.082	0.131	0.211	0.072	0.036*	-

*Table 5-2 Comparison table of p values from t tests coefficient of friction on bovine enamel between solutions. Significant values are labelled by asterisks with a significance threshold chosen as  $p = 0.05$*

	DiW	Muc + DiW	PBS	Muc + PBS	Acid	Muc + Acid
DiW	-					
Muc + DiW	0.002**	-				
PBS	0.067	0.004**	-			
Muc + PBS	< 0.001***	0.053	< 0.001***	-		
Acid	< 0.001***	0.027*	0.002**	< 0.001***	-	
Muc + Acid	< 0.001***	0.029*	0.003**	0.003**	0.566	-

### 5.2.2 Calcium release under different artificial saliva environments

Figure 5-6 shows the Atomic Absorption Spectrophotometry (AAS) analysis of all solutions ( $n = 3$ ) for both static and dynamic tests. The highest concentration of calcium release was observed for citric acid in tribological conditions. The lowest calcium concentration was observed for deionised water in static conditions. Student t-tests were employed to compare static and tribocorrosion tests as well as the addition of mucins to solution. A significant increase in calcium release between static and dynamic tests was observed for the acid only ( $P < 0.02$ ) solutions and a significant decrease in calcium release was observed for salt and salt + mucin solutions ( $P < 0.01$ ).

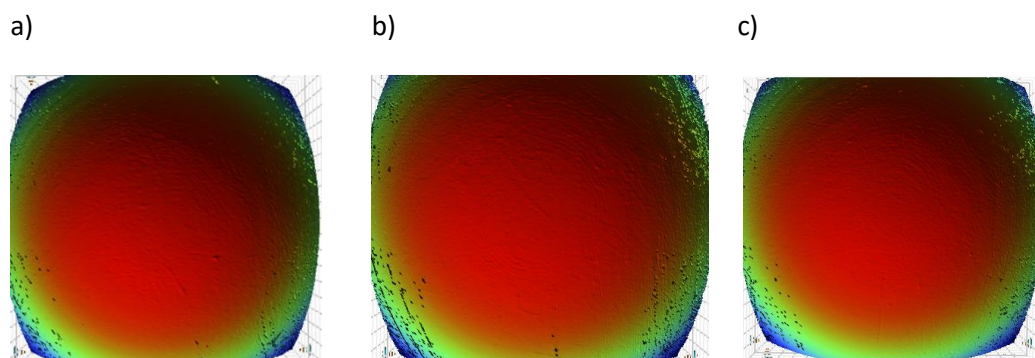


*Figure 5-6 Calcium release into post-test solution in pairs of static and dynamic tests. Static tests are displayed as paler, patterned column on the left of the pairing, dynamic tests are displayed in the darker, non-patterned column on the right of pair.*

Under dynamic test conditions, Muc + Acid significantly reduced the calcium release compared to Acid conditions ( $P < 0.05$ ). For all other solutions, Muc + DiW and Muc + PBS increased the calcium concentration compare to DiW and PBS post-test solutions respectively, under both static and dynamic conditions. It was acknowledged that these differences were a few magnitudes smaller than what was observed for citric acid solutions. Significant differences for static tests were observed between DIW and Muc + DIW solutions ( $p$  value  $< 0.03$ ) and PBS compared with Muc + PBS solutions ( $p$  value  $< 0.02$ ).

### 5.2.3 Tribocorrosive wear behaviour under different artificial saliva environments

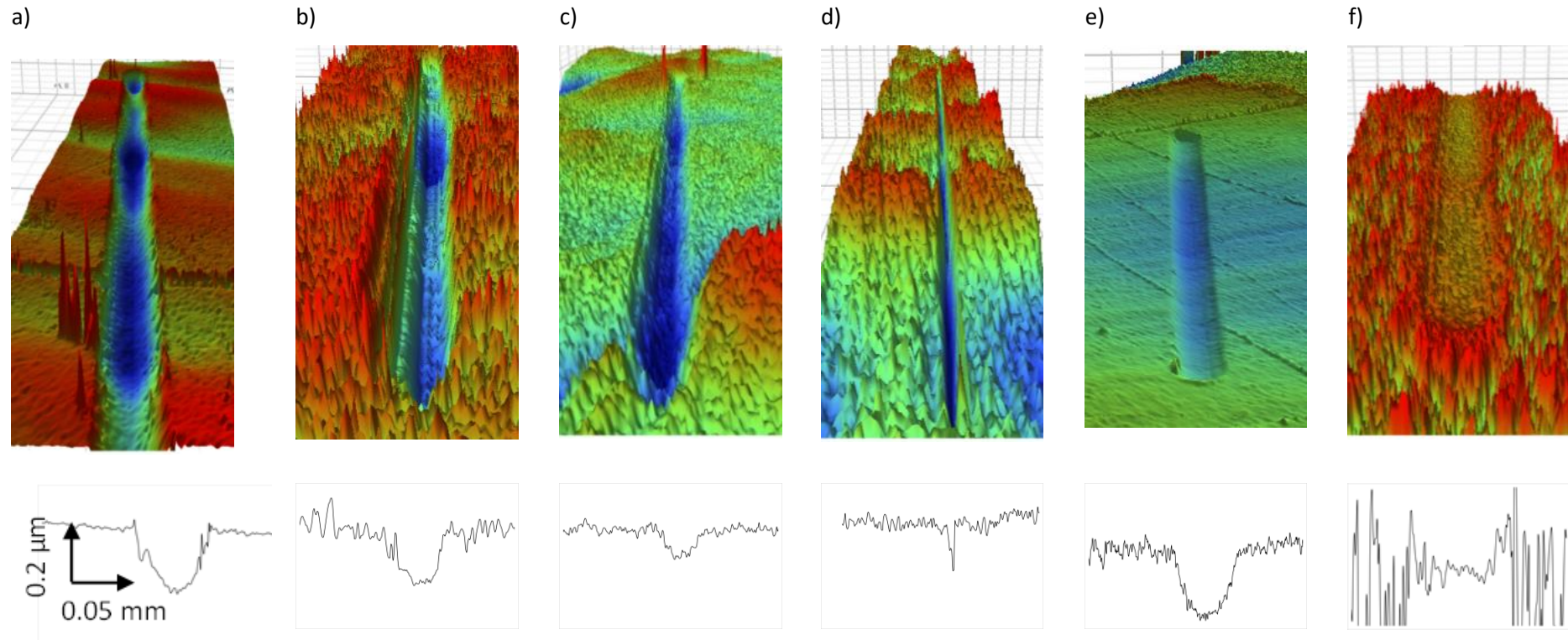
A Vertical Scanning Interferometry (VSI) investigation was performed on the Y-TZP balls after tribological testing to determine wear on the ball's surfaces. Figure 5-7 shows a visual comparison of a control Y-TZP ball compared to balls tested in DiW on steatite and enamel surfaces. No surface wear could be determined on these surfaces compared to the control sample. This indicated that the dynamic test conditions used for tribological testing did not impart a measurable amount of wear on the Y-TZP surfaces. This was attributed to the use of a new ball for each test along with a limited test duration to cause sufficient wear on the Y-TZP ball's surface. No further testing was performed on these surfaces hereafter.



*Figure 5-7 VSI images of Y-TZP balls showing no surface differences between a) control ball, b) ball used in steatite-DiW test and c) ball used in enamel-DiW test.*

The examination of the enamel surfaces with VSI highlighted variations of the wear scar characteristics as shown in Figure 5-8. The data on the wear scar characteristics in terms of maximum depth, length of scar and maximum width of scar taken at the centre of all samples is presented in Table 5-3. The scar profile width for DiW was larger than the Muc + DiW wear scar,  $0.059 \pm 0.007$  mm and  $0.027 \pm 0.010$  mm respectively, visualised in Figure 5-8a) and b). The scar profile depth followed a similar pattern. The depth of the DiW scar was slightly more than the Muc + DiW scar,  $0.232 \pm 0.068$   $\mu\text{m}$  and  $0.131 \pm 0.093$   $\mu\text{m}$  respectively. The area outside the wear scar was also interesting, with more micro scaled asperities presented on the Muc + DiW surface compared to DiW. It was noted that despite setting the stroke length to 1 mm, the resulting lengths of wear scars were less than this in most instances. This behaviour itself was attributed to systematic errors within the tribometer's reciprocating stage controller.

In PBS, the scar width was much smaller,  $0.038 \pm 0.001$  mm, and the Muc + PBS wear scar was much smaller,  $0.012 \pm 0.003$  mm, which is observed clearly in Figure 5-8c) and d) respectively. The Acid wear scar width,  $0.060 \pm 0.004$  mm was similar to the DiW wear scar. However, the Acid scar depth was much larger at a maximum depth of  $0.315 \pm 0.027$   $\mu\text{m}$ . Another feature of interest was the scar profile for the Muc + Acid scar, presented in Figure 5-8f). While other profiles exhibited a trough shaped scar, the surfaces either side of the Muc + Acid wear track were much more corroded and irregular. This was not the case for the Acid scar. These features prevented an accurate calculation of the scar volume as the reference plane could not be clearly determined.



**Figure 5-8** VSI image and cross section profile of enamel wear scars after dynamic tests in a) DiW, b) Muc + DiW, c) PBS, d) Muc + PBS, e) Acid and f) Muc + Acid. Cross sections are displaced to the same scale.



Table 5-3 Maximum width, length and depth of wear scars.

Solution	Length (mm)		Width (mm)		Depth ( $\mu\text{m}$ )	
	Average	SD	Average	SD	Average	SD
DiW (n=3)	0.800	0.046	0.059	0.007	0.232	0.068
Muc + DiW (n=3)	0.864	0.018	0.027	0.010	0.131	0.093
PBS (n=3)	0.854	0.007	0.038	0.001	0.116	0.002
Muc + PBS (n=3)	0.796	0.112	0.012	0.003	0.067	0.046
Acid (n=3)	0.935	0.001	0.060	0.004	0.315	0.027
Muc + Acid (n=3)	0.781	0.072	0.114	0.013	1.215	0.347

A wear volume analysis of the scars indicated that the Muc + DiW and Muc + PBS solutions influenced mechanical wear, shown in Figure 5-9. The largest wear volume was observed with the Acid solution, while the Muc + PBS solution showed the lowest scar volume. Student t-tests were performed and significant volume reductions were observed for the PBS solution compared with DiW ( $P < 0.02$ ) and for the Muc + PBS solution compared with DiW ( $P < 0.01$ ). Tests in the Muc + Acid solutions presented surfaces which made the current method for calculating volume loss challenging as there was no clear reference plane to take measurements from.

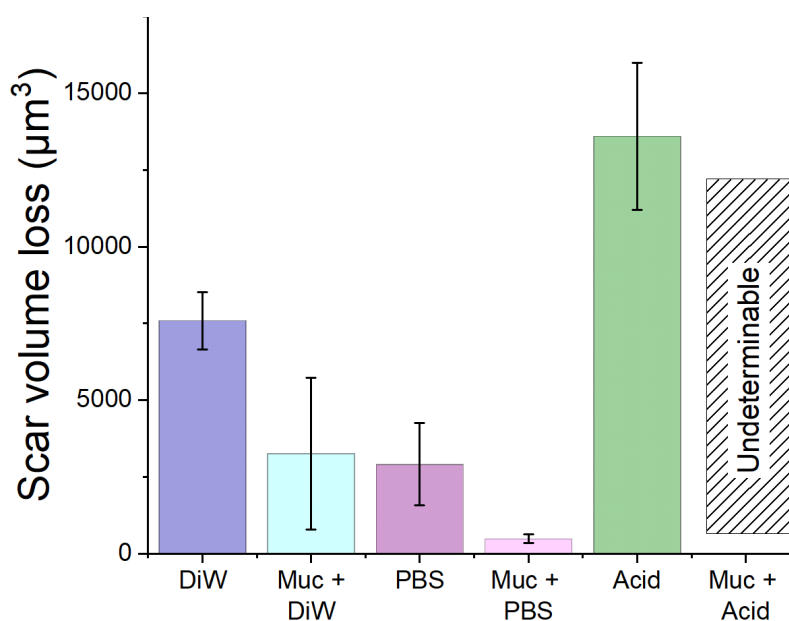
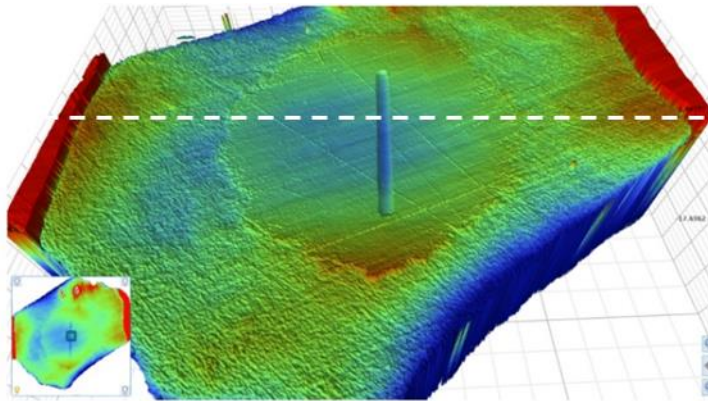


Figure 5-9 Estimated wear volume of bovine enamel wear scars.

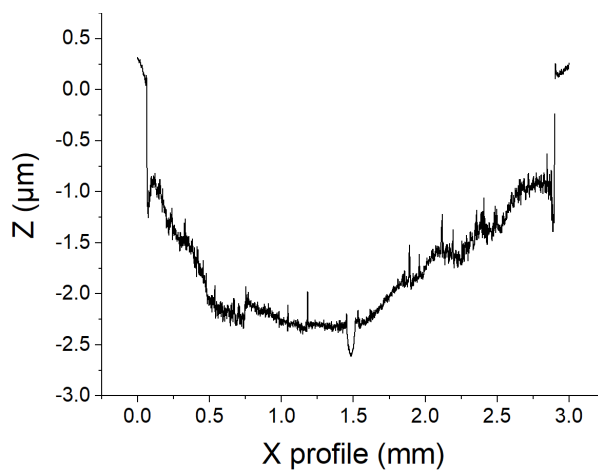
Upon examination of the whole sample, the citric acid wear scar was clearly defined in the centre, shown in Figure 5-10. There was a smooth surface area present around the wear

scar, while there was a rougher and more corroded enamel area outside of this before reaching the untouched enamel surfaces (in red). The overall volume lost appears to be dominated by corrosion from the citric acid, causing large-scale demineralization and dissolution over the test duration. This is highlighted in Figure 5-11 which compares the wear scar volume to the total visible volume lost from the enamel surface under acid only conditions.

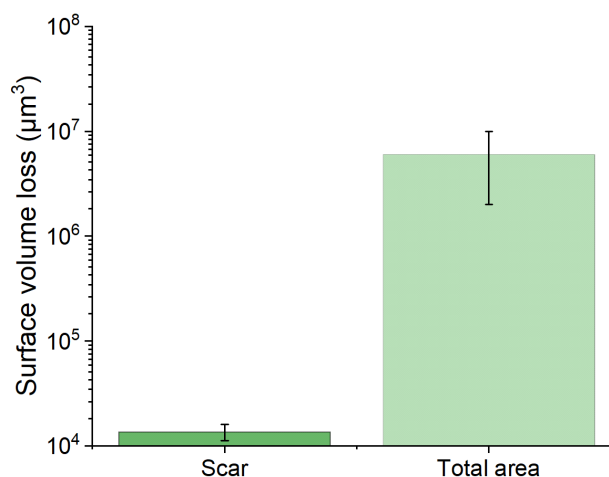
a)



b)



**Figure 5-10 pH 3.1 citric acid wear scar and area displayed by a) VSI image with a white dashed line showing the location of the b) cross-section.**

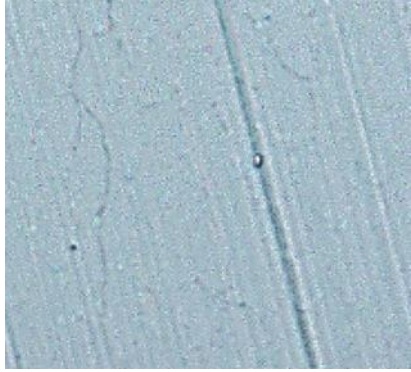
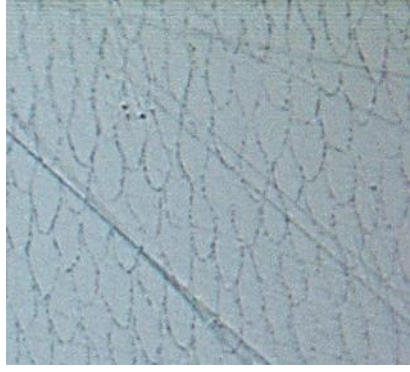


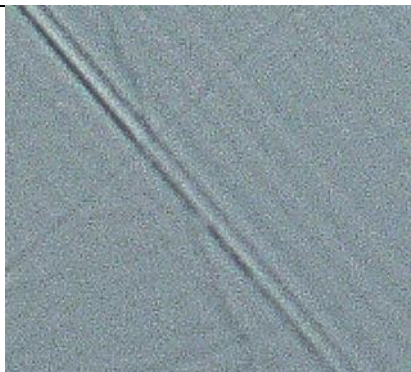

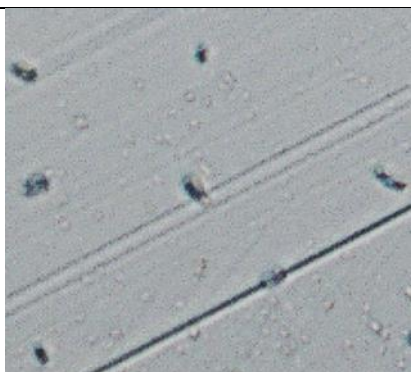
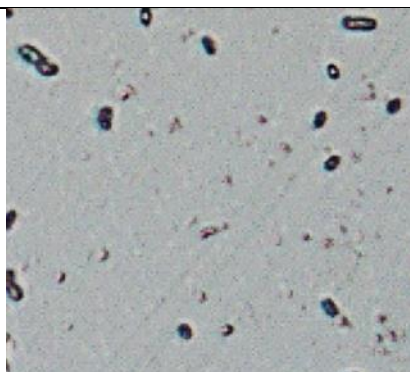


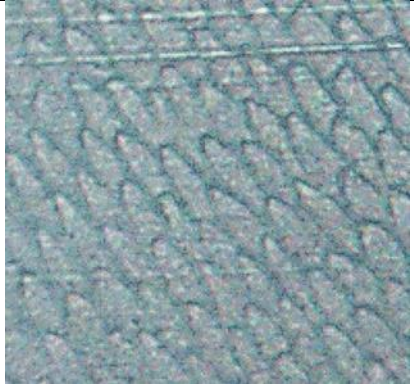

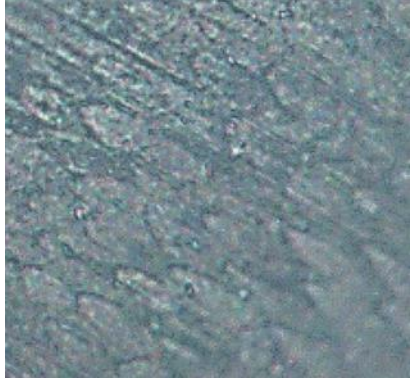
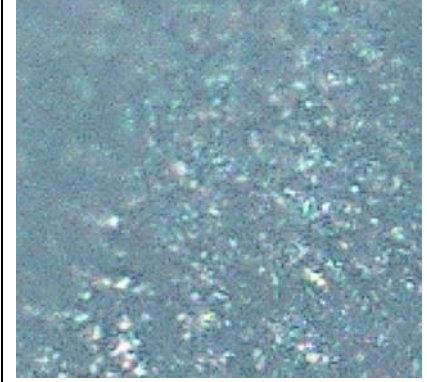
*Figure 5-11 pH 3.1 citric acid comparison of scar volume and total sample volume loss.*

#### 5.2.4 Optical microscopy of bovine enamel surfaces

Optical microscopy was used to further investigate surface texture within the wear scars and in the surrounding area outside of the wear scars after tribo-tests, shown in Table 5-4. This was to understand whether any preferential dissolution occurred on the surface. Evidence of dissolution was demonstrated outside of the wear scar in DiW by the outline of enamel rods. Rod outlines were observed within the DiW wear scar, but these were less prominent than outside due to mechanical smoothing by surface ploughing. Enamel rods were not visible within or outside the wear scars in Muc + DiW, PBS, and Muc + PBS samples. Acid and Muc + Acid sample presented dissolution both within and outside wear areas. Inside the wear areas, the enamel rods were clearly defined in the Acid sample, whereas the Muc + Acid sample presented a greater loss of texture from either dissolution between rods or delamination of weakened areas. It should be noted that the darker images of bovine enamel samples after citric acid tribo-tests were not a result of less illumination, but from changes to the surface texture. This is especially highlighted outside of the wear area of Acid and Muc + Acid samples. It was thought that these differences in surface texture outside of the wear scar were attributed to the continuous dissolution of surface enamel in the absence of the mechanical shearing of surface asperities.

*Table 5-4 Optical microscope images of bovine enamel wear locations, presenting 34  $\mu\text{m}$  x 36  $\mu\text{m}$  images of texture within the wear scar area and in the surrounding area outside of the wear scar, for all test solutions.*

Wear scar	Inside	Outside
DiW		
Muc + DiW		
PBS		
Muc + PBS		

Acid		
Muc + Acid		

## 5.2.5 Surface chemistry and structural analysis with ambient pressure XPS, Raman spectroscopy and XRD.

### 5.2.5.1 XPS examination of bovine enamel surfaces

Bovine enamel samples were investigated with XPS to determine and characterise any changes in enamel's surface chemistry, after tribocorrosion tests, up to a depth of 10 nm from the surface over a spot size of 200  $\mu\text{m}$ . Baseline data was collected on freshly prepared enamel samples before tribo-tests. Afterwards, both the wear scar area and the surrounding surface was assessed for direct changes from mechanical interactions compared to locations with zero contact. The next subsection covers the reference samples, which were freshly prepared bovine enamel samples that were precleaned with a toothbrush and deionised water before initial benchmarking with XPS.

#### Reference samples

Figure 5-12 shows the XPS sweep data for all baseline samples, a.k.a. reference samples. Six elements were identified by XPS sweeps, shown by clear peaks corresponding to oxygen (O1s), carbon (C1s), nitrogen (N1s), calcium (Ca2s and Ca2p), phosphorus (P2s and P2p), and finally argon (Ar2p). Table 5-5 and Table 5-6 present the deconvoluted XPS peak components and their measured binding energies respectively. Each sample was effectively a repeat to provide a means of traceability of sample composition changes due to tribocorrosion testing.

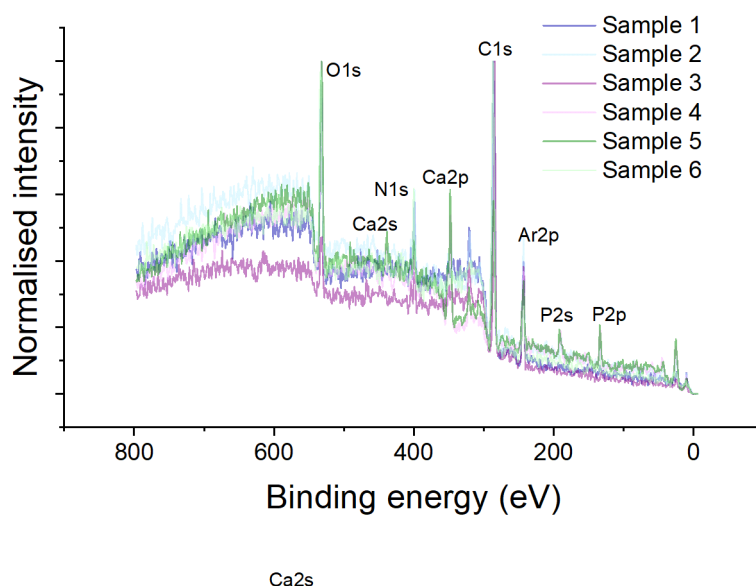
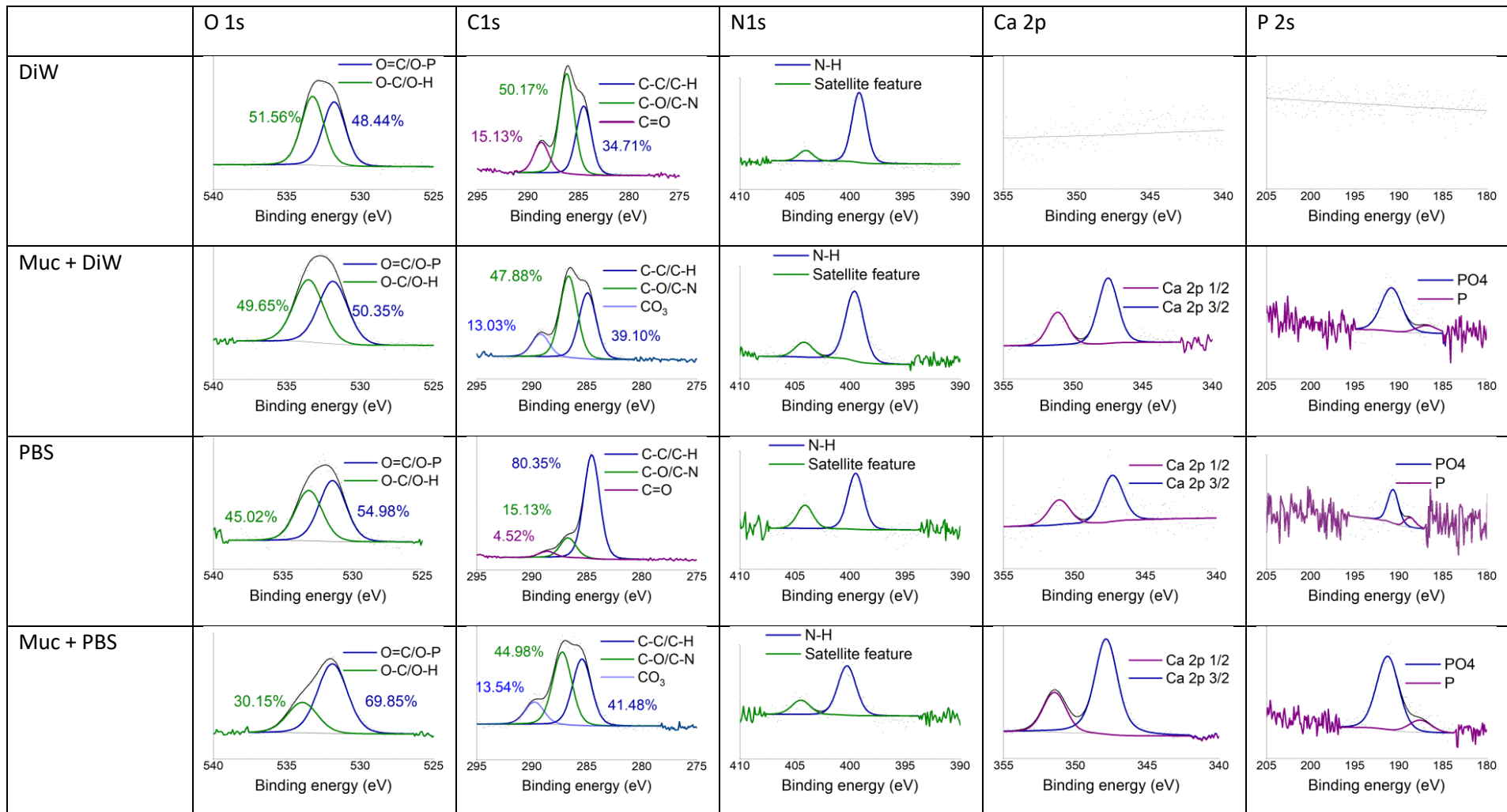


Figure 5-12 Example XPS survey of baseline bovine enamel reference samples before tribo-tests.

Table 5-5 XPS reference surveys of O 1s, C 1s, N 1s, Ca 2p and P 2s for bovine enamel tribo-test samples (pre-test).



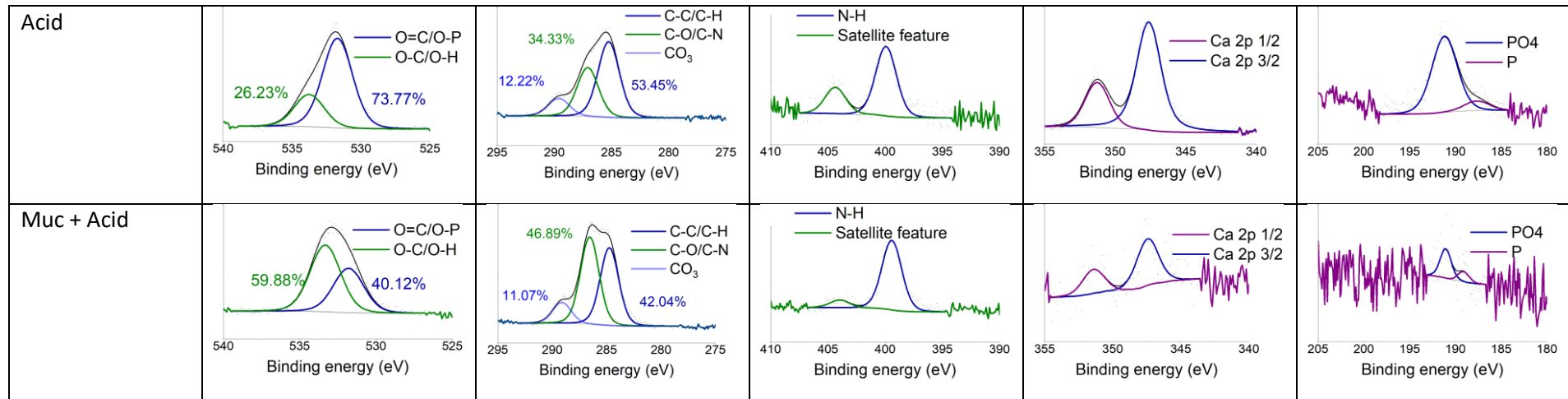
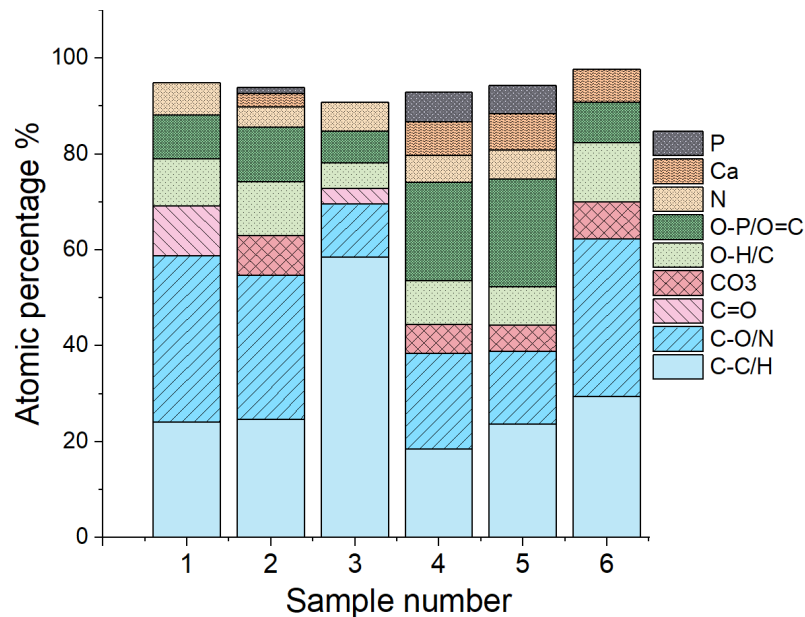


Table 5-6 Peak positions of species in reference samples.

Species	O 1s		C 1s				N 1s		Ca 2p		P 2s	
	O-C/H	O=C/O-P	C-C/H	C-O/N	C=O	CO <sub>3</sub>	N-H	Satellite	1/2p	3/2p	PO <sub>4</sub>	P
DiW	533.23	531.77	284.48	286.16	288.68	-	399.17	404.02	-	-	-	-
Muc + DiW	533.51	531.84	284.93	286.65	-	289.20	399.58	404.16	351.12	347.49	190.80	186.81
PBS	533.15	531.45	284.55	286.71	288.60	-	399.49	404.08	351.08	347.33	190.62	188.69
Muc + PBS	533.93	531.89	285.43	287.23	-	289.75	400.28	404.46	351.45	347.85	191.24	187.57
Acid	533.76	531.70	285.25	287.08	-	289.60	399.92	404.35	351.27	347.62	191.19	187.65
Acid + Muc	533.32	531.79	284.74	286.55	-	289.10	399.42	403.97	351.44	347.44	191.06	189.10



Figure 5-13 shows the deconvoluted % atomic composition for each sample. The presence of argon was removed from Figure 5-13 to focus on elements with the surface of bovine enamel. The atomic composition was deconvoluted by taking more specific XPS scans over the binding energies associated with O 1s, C 1s, N 1s, Ca 2p and P 2s. Reference samples presented an approximate 50:50 component split between the two O 1s components, O-H/O-C and O=C/O-P, relating to hydroxides/organic functional groups (carboxyl) and carbonates/phosphates respectively. C 1s components composed of C-C/C-H, C-O/C-N, C=O and carbonate bonds. The proportion of carbon species varied across reference samples, with larger peaks observed for C-C/C-H and C-O/C-N species compared to C=O species and carbonates which was attributed to a combination of adventitious surface carbon and sample variation. N 1s peaks mainly existed as an isolated peak, attributed to organic components (i.e., proteins) while additional unknown peaks were considered as satellite features. Ca 2p components existed as a split peak, corresponding to Ca 1/2p and Ca 3/2p with a 1:2 ratio respectively. Finally, peaks at P 2s components related to potential phosphate groups ( $\text{PO}_4$ ), while additional peak features were associated with phosphorus (P). No  $\text{PO}_4$ , P, or Ca 2p peaks were observed for the DiW reference sample.



*Figure 5-13 Chemical composition of the reference bovine enamel samples before testing shown by atomic percentage %. Argon % was removed to focus only on the material's composition, ignoring the measurement environment.*

Table 5-7 displays the descriptive statistics from the XPS surveys for the reference bovine enamel samples (n=6). Bovine enamel surfaces were shown to be mostly composed of carbon, ( $60.69 \pm 12.83$  %), followed by oxygen ( $22.44 \pm 7.03$  %) and then nitrogen ( $5.92 \pm 0.99$  %). These values and variations are consistent with what has been previously seen in the literature for XPS studies on human tooth enamel, despite these studies using ultra high

vacuum conditions for spectroscopy [218, 256, 220]. Calcium and phosphorus made up a mean composition of  $2.92 \pm 2.61$  % and  $1.99 \pm 2.71$  % respectively, lower than previous studies which presented  $4.33 \pm 1.13$  and  $5.58 \pm 2.27$  for calcium, and  $5.58 \pm 2.27$  and  $3.95 \pm 1.96$  for phosphorus [218, 256]. The coefficient of variance, calculated by the standard deviation of each element within the sample over the mean elemental composition, assessed the degree of variability for element between all samples. Calcium and phosphorus presented the largest coefficient of variance compared to all other elements, suggesting a varied mineral content between samples within a depth of 10 nm. Some samples did not show an abundance of either calcium or phosphorus. Half of the reference samples presented both Ca and P peaks, and these were used to determine the mean Ca/P ratio of  $1.59 \pm 0.54$ . The Ca/P ratio was somewhat different to the ratios of  $1.41 \pm 0.10$  and  $1.04 \pm 0.35$  observed in human tooth enamel studied by XPS [218, 256].

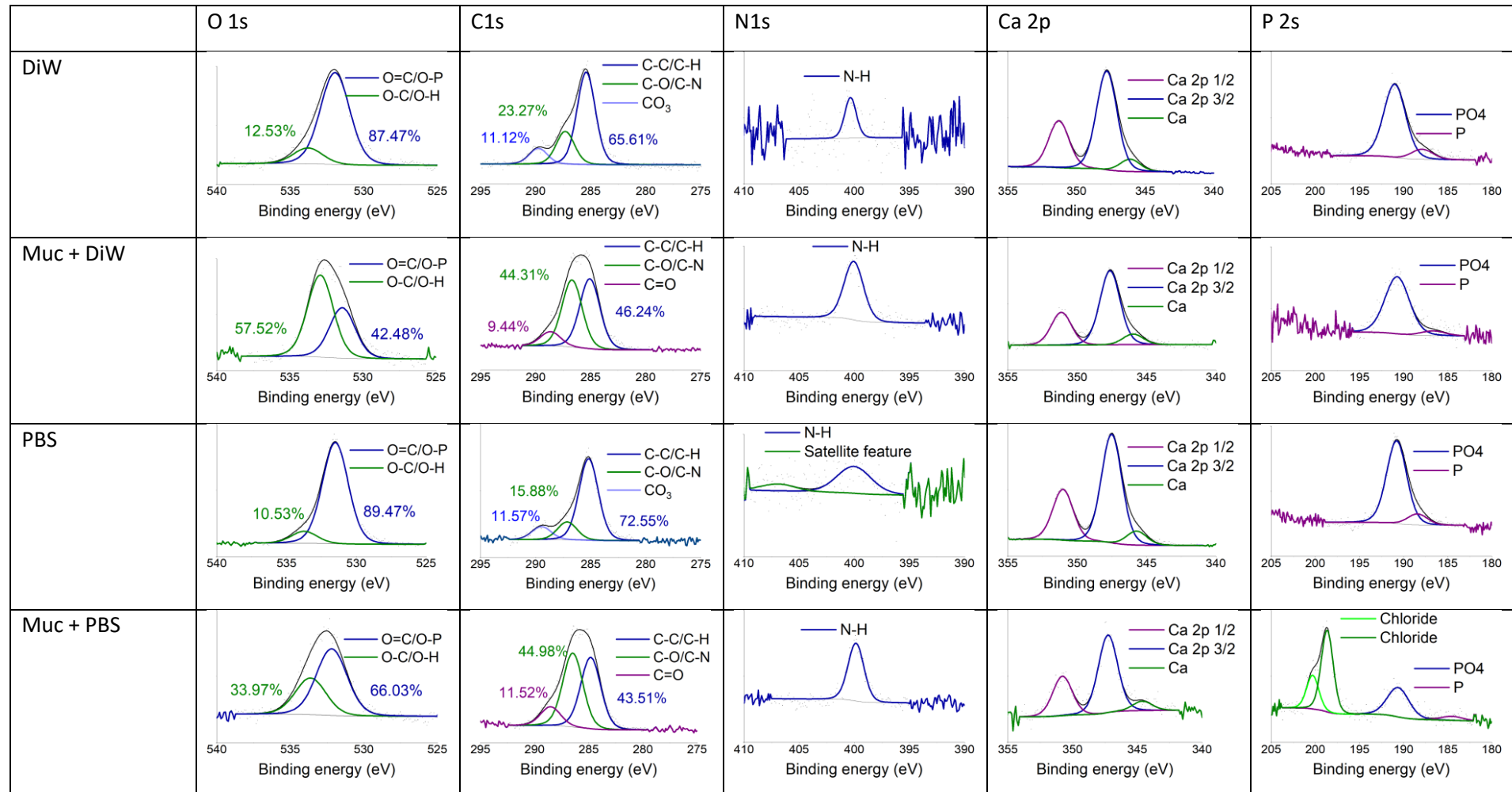
*Table 5-7 Descriptive statistics of the atomic composition, At%, of reference bovine enamel samples.*

Element	Min At %	Max At %	Mean At %	SD	% Coefficient of variance
O (n=6)	11.86	31.00	22.44	7.03	31.33
C (n=6)	44.45	72.83	60.69	12.84	21.15
N (n=5)	4.13	6.94	5.92	0.99	16.70
Ar (n=6)	2.32	9.23	6.02	2.31	38.32
Ca (n=4)	0	7.74	2.93	3.61	123.40
P (n=3)	0	6.23	1.99	2.71	136.10
Ca/P ratio (n=3)			1.59	0.54	

### Post tribo-test samples

After benchmarking of the bovine enamel samples, tribological tests were performed on them. These tests followed the same methods used earlier in this chapter and used the same test solutions. After testing, these were then rinsed and brushed in deionised water with a toothbrush before re-examination with XPS. Surveys and scans were taken both within the wear scar areas and away from the wear scar area to determine any potential differences due to test solution, tribological interaction, or a combination of the two. Table 5-8 and Table 5-9 present the modelled peak components and associated binding energies from inside the wear scars, while Table 5-10 and Table 5-11 present the same for outside the wear area.

Table 5-8 XPS surveys of O 1s, C 1s, N 1s, Ca 2p and P 2s for bovine enamel samples post tribo-test focussing within the wear area (inside wear scar).



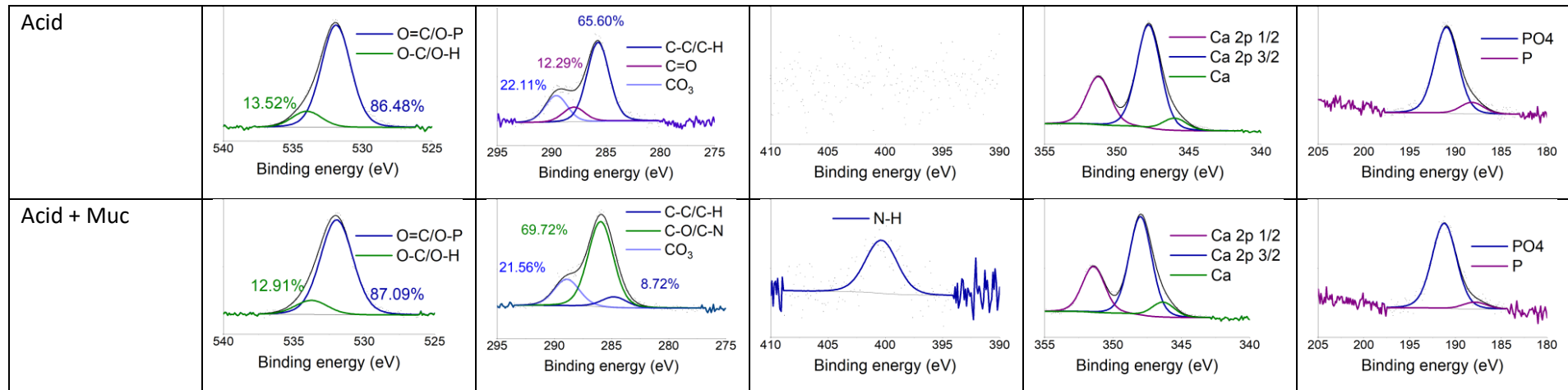
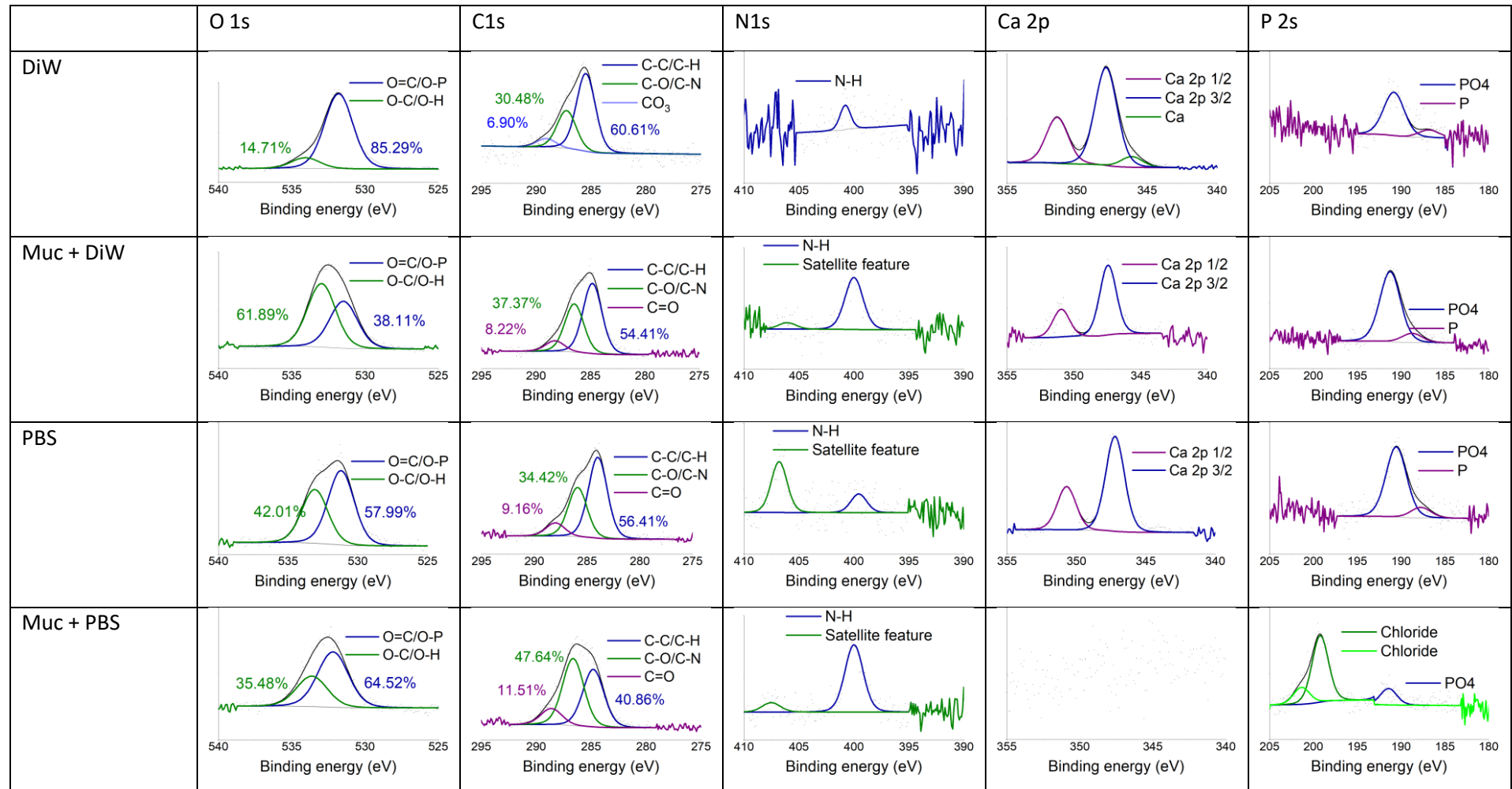


Table 5-9 Peak positions of bovine enamel samples after tribo-tests within the scar area (inside).

Species	O 1s		C 1s				N 1s		Ca 2p			P 2s		Metal chloride	
	O-C/H	O=C/O-P	C-C/H	C-O/N	C=O	CO <sub>3</sub>	N-H	Satellite	1/2p	3/2p	Ca	PO <sub>4</sub>	P	Cl	Cl
DiW	534.06	531.80	285.41	287.30	-	289.75	400.34	-	351.29	347.80	346.10	191.00	187.88	-	-
Muc + DiW	532.96	531.46	285.07	286.65	288.65	-	400.04	-	351.15	347.64	345.97	190.72	186.64	-	-
PBS	533.74	531.51	285.18	287.13	-	289.46	400.03	406.91	351.03	347.51	345.72	190.78	188.41	-	-
Muc + PBS	532.77	531.36	284.82	286.47	288.47	-	399.84	-	350.79	347.27	344.61	190.60	184.52	198.66	200.30
Acid	535.00	532.90	285.74		287.97	289.59	-	-	352.27	348.79	346.99	191.97	189.19	-	-
Acid + Muc	534.96	532.96	284.78	285.96	-	288.92	401.33	-	352.42	348.98	347.34	192.22	188.88	-	-

Table 5-10 XPS surveys of O 1s, C 1s, N 1s, Ca 2p and P 2s for bovine enamel samples post tribo-test focussing outside of the wear area (outside wear scar).



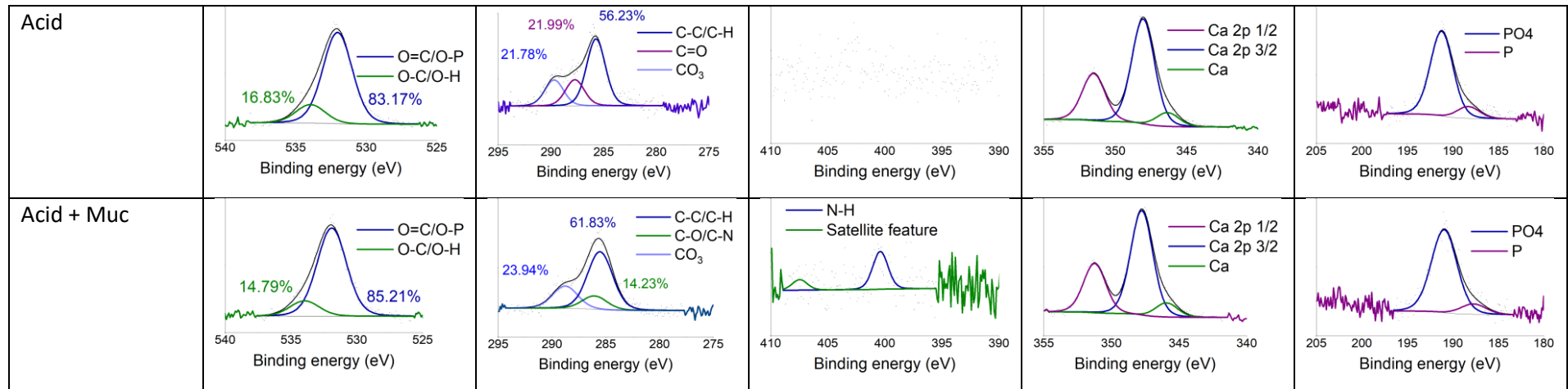
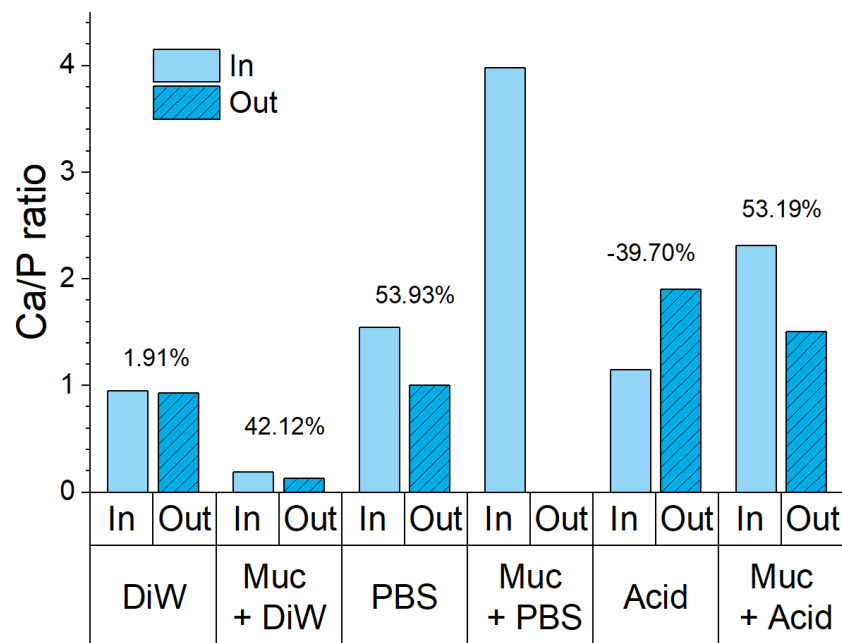


Table 5-11 Peak positions of bovine enamel samples after tribo-tests outside the scar area (outside).

Position (eV)	O 1s		C 1s				N 1s		Ca 2p			P 2s		Metal chloride	
	O-C/H	O=C/O-P	C-C/H	C-O/N	C=O	CO <sub>3</sub>	N-H	Satellite	1/2p	3/2p	Ca	PO <sub>4</sub>	P	Cl	Cl
<b>DiW</b>	533.80	531.96	285.48	287.24		289.10	400.79	-	351.43	347.93	346.10	191.24	188.74	-	-
<b>Muc + DiW</b>	532.92	531.41	284.82	286.49	288.27		400.00	406.07	350.94	347.44	-	190.91	-	-	-
<b>PBS</b>	533.08	531.20	283.98	285.90	288.00		399.56	406.81	350.71	347.22	-	190.54	187.74	-	-
<b>Muc + PBS</b>	533.62	532.18	284.80	286.64	288.62		399.99	407.52	--	-	-	191.42	-	199.22	201.35
<b>Acid</b>	534.95	533.03	285.74		287.73	289.70	-	-	352.52	349.05	347.33	192.22	189.30	-	-
<b>Acid + Muc</b>	533.97	531.90	285.62	286.13		288.86	400.39	407.46	351.24	347.76	345.92	190.94	187.73	-	-

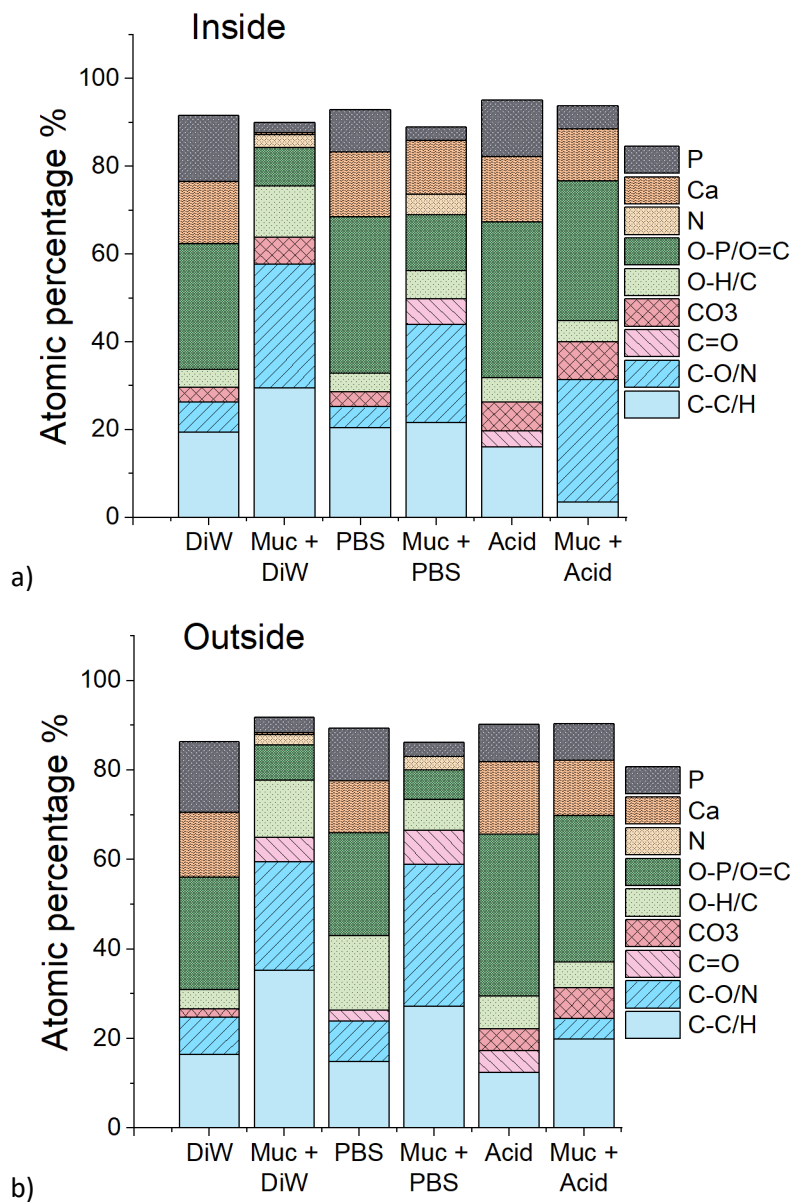
Figure 5-14 shows how the Ca/P ratio varied across the enamel samples in the different solutions, with percentage difference labels comparing the Ca/P ratio within the wear area compared to outside the wear area. For reference, the stoichiometric ratio of calcium to phosphate in hydroxyapatite is 1.67, derived from the chemical formula  $\text{Ca}_{10}(\text{PO}_4)_6(\text{OH})_2$  (i.e., 10 Ca:6 P). No differences for the Ca/P ratio were observed inside and out the wear areas in DiW. The addition of mucins to the test environment reduced the Ca/P from 0.94 to 0.18 inside the wear area and 0.92 to 0.13 on the outside. In PBS, the wear area differed from the surrounding enamel, with a ratio of 1.54 compared to 1.00 respectively, where the former was closer to the mean ratio of the reference samples (1.59). Muc + PBS increased the ratio inside the wear area to 3.97, the largest of all samples, whereas no calcium was detected in the surrounding location and a Ca/P ratio wasn't calculated. In Acid the Ca/P ratio inside the wear area was 1.15, less than outside, with 1.90. With mucin, the reverse was observed with an increased Ca/P of 2.31 inside and lower ratio of 1.51 outside.



*Figure 5-14 Ca/P ratios of enamel samples after tribo-tests, inside and outside the wear areas. Percentage labels relate to the % difference between the Ca/P ratio within the wear area compared to the Ca/P outside the wear area.*

Figure 5-15a) and b) shows the deconvoluted chemical composition, as an atomic percentage, inside and outside the wear area respectively. These were determined using the same methodology as the reference samples. General observations show a larger atomic percentage of calcium and phosphorus was observed in non-mucin samples compared to their reference composition in Figure 5-13, within the range of 11.72 – 16.01% for calcium and 8.46 – 15.73 % for phosphorus. Furthermore, N 1s peaks were observed on to Muc + DiW and Muc + PBS, but not Muc + Acid, which differed from reference samples.

Additionally, the proportion of N 1s within the wear scar regions, 3.04 % and 4.67% for Muc + DiW, and Muc + PBS respectively, were greater compared to outside this area with 2.26% and 2.94%. This was greater with Muc + PBS compared to Muc + DiW. No N 1s peaks were observed in Muc + Acid, which suggested negligible mucin was present. O=C/O-P bonds were more pronounced within DiW and PBS samples, between 25-35% of the surveyed composition. This was greater in PBS compare to DIW. O=C/O-P bonds were less pronounced in Muc + DiW, and Muc + PBS, In Acid and Muc + Acid, enamel samples presented similar O=C/O-P composition to DiW and PBS samples, making up approximately 30% of the total scan composition.

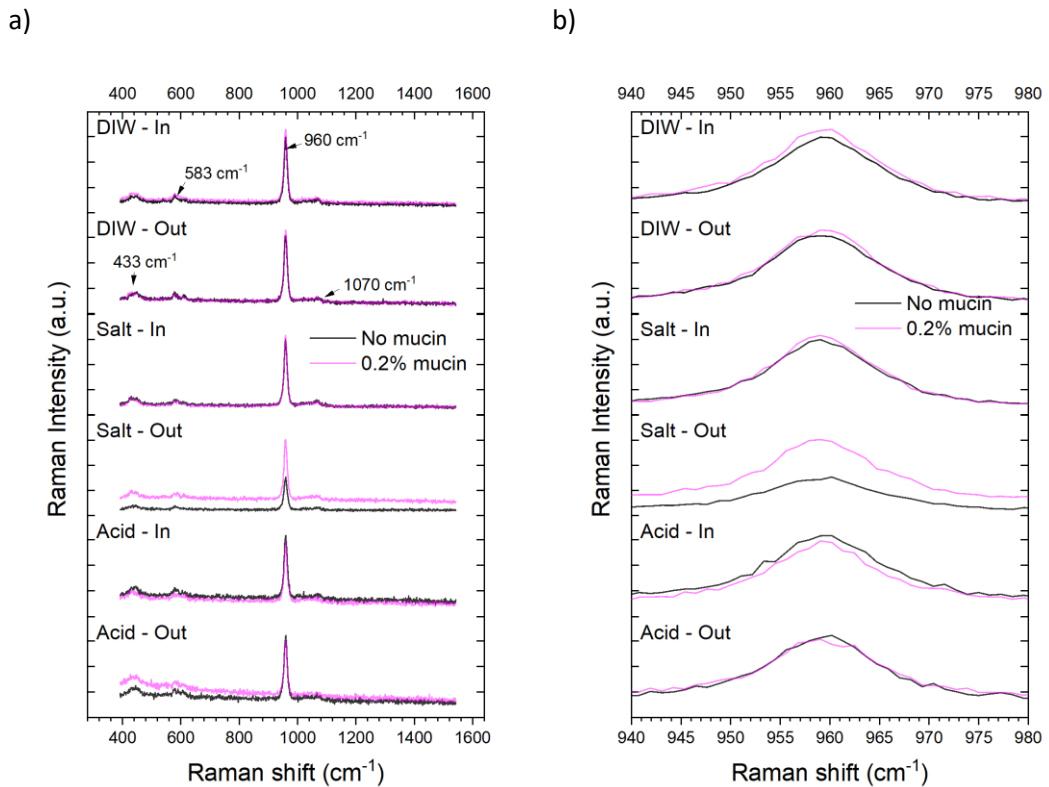


**Figure 5-15** Chemical composition of post tribo-test bovine enamel samples shown by atomic percentage %, showing a) inside the wear area and b) the surrounding surface outside the wear area. Composition is shown for tests in DiW, Muc + DiW, PBS, Muc + PBS, Acid, and Muc + Acid solutions.



### 5.2.5.2 Raman spectroscopy

Raman spectroscopy was used to further examine structural and compositional changes of bovine enamel samples after tribocorrosion tests. Figure 5-16 shows the Raman spectra for all post-test enamel samples inside and outside wear locations for environments with and without mucin. Raman peaks were observed in all samples as  $433\text{ cm}^{-1}$ ,  $583\text{ cm}^{-1}$ ,  $960\text{ cm}^{-1}$  and  $1070\text{ cm}^{-1}$  which were attributed to the different vibrational modes for  $\text{PO}_4^{3-}$  groups,  $\nu_2$  – symmetrical bending,  $\nu_4$  - asymmetrical bending,  $\nu_1$  – symmetrical stretching and  $\nu_2$  – asymmetrical stretching, respectively [212, 257].



**Figure 5-16** Raman spectra of post-test enamel samples inside and outside wear locations, with and without mucins. The full spectra are shown in a) while b) shows the  $\nu_1$  phosphate peak scaled in.

Peak analyses were performed on the  $\nu_1$   $\text{PO}_4^{3-}$  peak to give an insight into the crystallinity of the phosphate-based mineral in bovine enamel. Position shifts and changes to the full width half maximum (FWHM) were assessed and are summarised in in Table 5-12. Inside the wear track broader peaks were observed for Acid and PBS samples when compared to DiW sample. This indicated minor changes to the crystallinity of the bovine enamel. Muc + DiW reduced the FWHM of the  $\nu_1$   $\text{PO}_4^{3-}$  peak inside the wear track compared to PBS and Acid. Small changes occur for DiW samples. An increased FWHM was observed for DiW samples outside the wear track, independent of the presence of mucin. A reduction in the FWHM was observed with PBS outside the wear track compared to inside. Additionally, an increase in the FWHM was observed with Muc + PBS outside the wear track compared to inside. A

similar behaviour was observed with the FWHM of Acid outside of the track compared to inside, and a small decrease in FWHM was outside the wear area was observed with Muc + Acid.

Assessment of the degree of demineralisation (DD) demonstrates that a larger percentage of demineralisation occurs in the Acid and Muc + Acid environments, shown in Table 5-12. A greater proportion of demineralisation occurred in both Muc + Acid locations, 37.58% and 38.91% compared to 31.12% and 31.15% in Acid. Less demineralisation was observed within the wear area in this environment (when considering the raw DD). In PBS, a lower v1 peak intensity was observed outside of the wear track which indicated a higher DD compared to all samples, at 46.5%. Despite this, when the inside of the wear track was considered, the DD was negative indicating minimal demineralisation. It was assumed a  $DD \leq 0$  indicated no demineralisation of the surface.

*Table 5-12 Peak analysis of v1 PO<sub>4</sub><sup>3-</sup> peak comparing the full width half maxima (FWHM), band position and degree of demineralisation, DD, for all bovine enamel samples.*

<b>Solution</b>	<b>Wear location</b>	<b>FWHM</b>	<b>Band position (cm<sup>-1</sup>)</b>	<b>DD (raw)</b>	<b>DD (normalised)</b>
<b>DiW</b>	Inside	13.60	959.39	-5.91%	4.80%
<b>DiW</b>	Outside	14.31	959.22	-	-
<b>Muc + DiW</b>	Inside	13.58	959.28	-16.60%	3.68%
<b>Muc + DiW</b>	Outside	14.26	959.23	-7.40%	1.45%
<b>PBS</b>	Inside	14.30	959.16	-1.40%	3.35%
<b>PBS</b>	Outside	13.99	959.07	46.50%	7.14%
<b>Muc + PBS</b>	Inside	14.05	959.17	-10.66%	0.33%
<b>Muc + PBS</b>	Outside	14.36	959.12	-3.69%	3.91%
<b>Acid</b>	Inside	14.34	959.46	31.12%	6.58%
<b>Acid</b>	Outside	14.25	959.22	31.15%	7.37%
<b>Muc + Acid</b>	Inside	13.44	959.31	37.58%	10.83%
<b>Muc + Acid</b>	Outside	13.43	959.28	38.91%	9.60%

### 5.2.5.3 XRD analysis of bovine enamel surfaces before and after dynamic tribology experiments

The surface substructure of bovine enamel was investigated with XRD methods on reference samples and post tribo-test samples. Given the size of the wear area, post-test XRD analyses was assess as a composite value. Figure 5-17 shows the XRD survey of the reference (in black) and post tribo-test (in magenta) bovine enamel samples over a  $2\theta$  range of 10-70°. Most reference samples were consistent with high intensity spikes at approximately 25.6°, 31.9°, 49.17° and 52.9° corresponding to the miller indices (002), (211), (230) and (004) respectively, corresponding to  $2\theta$  positions and peak intensities when compared to a powder hydroxyapatite reference diffraction spectrum (reference 00-001-1008) [258]. This demonstrated that most reference samples exhibited similarities to the Hap reference, presenting a hexagonal closed packed lattice arrangement. The PBS reference sample was an exception, presenting a less intense peak at 25.6° compared to the intensity of this peak seen on the Hap reference and the other bovine enamel samples.

Interesting patterns emerged after dynamic testing of bovine enamel samples. Post tribo-test samples without mucin presented similar diffraction patterns to their pre-test counterparts with minor changes. No changes were noted for post tribo-test DiW diffraction patterns. Post tribo-test PBS patterns presented a split peak between at 31.7° and 32.2°, corresponding to (211) and (112). Post tribo-test Acid patterns presented a loss in diffraction peaks at 27.8°, 43.6° and 61.4°, corresponding to (102), (113), and (124). Tests with the addition of Muc presented considerably changes to the reference diffraction patterns. Post tribo-test Muc + DiW and Muc + PBS diffraction patterns present a singular peak at 28.8°, corresponding to (210). No clear peaks were observed over the rest of the post tribo-test diffraction patterns of Muc + DiW and Muc + PBS, and no clear peaks were observed for Muc + Acid. This indicated that the structure's crystallinity reduced to a more amorphous structure when mucin was present in the tribo-test environment. Interestingly, this behaviour was not observed in Muc + PBS with Raman spectroscopy, where an increased crystallinity was observed. On the other hand, an increased DD was observed Muc + Acid which supports the reduced crystallinity observed with XRD.

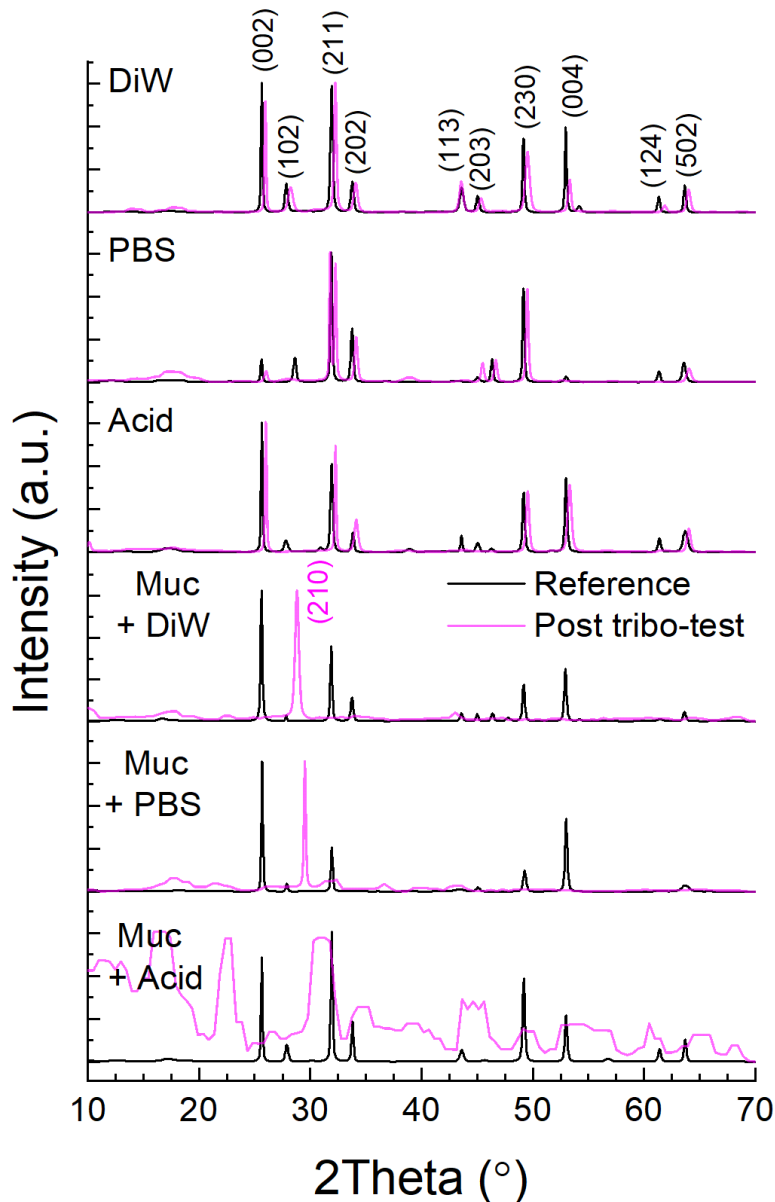


Figure 5-17 XRD sweep of bovine enamel showing pre-test reference and post tribo-test sample spectra.

Data was further processed to assess the crystallinity of samples by determining the full width half maximum (FWHM) of peaks, the mean crystallite size and unit cell parameters. The FWHM of all peaks was determined for each raw observed diffraction pattern and used to calculate the mean crystallite size.

Table 5-13 shows the FWHM data for peaks at (002), (211) and (230) before and after tribocorrosion tests respectively. These peaks presented the most intense diffraction peaks for comparison of all samples and permitted an assessment of variation to the sample surface crystallinity, as well as being examined in other studies [40, 211]. The largest FWHM changes ( $> \pm 0.01$ ) were observed for peaks at (230), broadening in DiW and Acid after tribo-

tests from 0.28743 to 0.29934 and 0.25565 to 0.27528 respectively. The opposite was observed after the PBS tribo-test, narrowing from 0.26183 to 0.23464.

The data shows the peak position,  $2\theta$ , generally increased after tribo-tests for all measurable peaks in all test environments. Two things may have caused this shift: surface structural transformation from induced residual stresses or due to or error [259]. Load cycling during tribo-tests, samples moisture content or a combination of the two may have induced compressive strain within the subsurface structure, indicating a change to the lattice configuration. Alternatively, this may be the result of a zero error in the  $2\theta$  value. As a mean shift in  $2\theta$  by  $0.35^\circ \pm 0.02^\circ$  was observed for all peaks, the zero-error explanation was favoured. However, further insight into the crystallite size was required to conclude this.

*Table 5-13 Comparison of full width half maximum (FWHM) of reference and post tribo-test bovine enamel samples for indices (002), (211) and (230).*

Reference	(002)		(211)		(230)	
	$2\theta$ ( $^\circ$ )	FWHM	$2\theta$ ( $^\circ$ )	FWHM	$2\theta$ ( $^\circ$ )	FWHM
<b>DIW</b>	25.64	0.16	31.91	0.23	49.19	0.29
<b>PBS</b>	25.63	0.11	31.89	0.21	49.16	0.26
<b>Acid</b>	25.64	0.16	31.92	0.23	49.18	0.26
<b>Muc + DIW</b>	25.62	0.17	31.89	0.21	49.16	0.26
<b>Muc + PBS</b>	25.68	0.15	31.96	0.20	49.24	0.19
<b>Muc + Acid</b>	25.65	0.16	31.93	0.21	49.20	0.26
<b>Ref Average</b>	<b>25.64</b>	<b>0.15</b>	<b>33.78</b>	<b>0.20</b>	<b>31.92</b>	<b>0.22</b>
<b>SD</b>	<b>0.02</b>	<b>0.02</b>	<b>0.03</b>	<b>0.04</b>	<b>0.02</b>	<b>0.01</b>

Post-test	(002)		(211)		(230)	
	$2\theta$ ( $^\circ$ )	FWHM	$2\theta$ ( $^\circ$ )	FWHM	$2\theta$ ( $^\circ$ )	FWHM
<b>DIW</b>	25.98	0.15	32.25	0.24	49.52	0.30
<b>PBS</b>	-	-	32.24	0.22	49.46	0.23
<b>Acid</b>	26.02	0.16	32.28	0.22	49.54	0.28

The mean crystallite size,  $D$ , was determined using the Scherrer equation, as defined by in Chapter 3. Section 3.2.7.5. This assessed crystallite size any changes that occurred in the

samples from the dynamic load cycling of tribo-tests in different artificial saliva solutions. This is summarised in Table 5-14. Decreased crystallite sizes were observed after tribo-tests in DiW and PBS, however t-tests did not show significance ( $P > 0.05$ ). The opposite was observed in the acidic environment; an increased crystallite size was observed after tribocorrosion testing, but not significantly ( $P > 0.05$ ).

*Table 5-14 Mean crystallite sizes for all reference samples and samples after tribo-tests with standard deviation between crystallite sizes of individual peaks.*

Reference	D (nm)	SD	Post tribo-test	D (nm)	SD
DiW ref	36.53	5.56	DiW	32.86	8.62
PBS ref	43.26	14.16	PBS	41.07	7.12
Acid ref	39.76	5.87	Acid	44.77	14.88
Muc + DiW ref	37.29	5.57	Muc + DiW	30.27	-
Muc + PBS ref	49.69	8.90	Muc + PBS	-	-
Muc + Acid ref	43.01	6.54	Muc + Acid	-	-

### 5.3 Discussion

To further develop preventative therapies that maximise the protection of tooth enamel, the contributions of overall tooth degradation need to be understood. This is especially the case in corrosive and tribocorrosive environments from interactions with citric acid which have been previously investigated [30, 260, 31, 261, 262, 27, 263, 209, 264, 265]. This present study aimed to demonstrate how different compositions of artificial saliva (mucin only, PBS only, mucin and PBS, acid only and, mucin and acid) can impact tooth degradation of bovine enamel in static and dynamic conditions. In general, increased degradation was observed in a tribocorrosive environment compared to a corrosion only one and that the solution composition influences the degree of surface wear observed. The addition of porcine gastric mucins to artificial saliva was also observed to influence certain aspects of degradation and that this glycoprotein behaved differently depending on the experimental conditions and environment.

#### 5.3.1 Lubrication performance of steatite

As discussed in Chapter 4, limited similarities exist between steatite and bovine enamel due to core differences in surface properties, static interactions with mucin and mechanical properties. To confirm that steatite was not feasible from a friction and lubrication point of view, dynamic tribo-tests were performed alongside bovine enamel test. It was clearly observed that steatite displayed different behaviour in all test solutions. Furthermore, Muc

+ PBS did not improve lubrication, with an observed increase in friction, opposing the friction behaviour observed on bovine enamel. Another point of interest was the reduction in steatites coefficient of friction compared to other test solutions. This behaviour is not commented on in the literature. Without further investigation of the surface chemistry and structure, this reason behind this was unknown. Given the differences between steatite and bovine enamel in terms of their coefficient of friction over time, and overall lubrication within the same test solutions, it was decided that these two materials were not similar. It was therefore confirmed that steatite was not a feasible alternative tooth material to conduct further tribological, adsorption and surface assessments on.

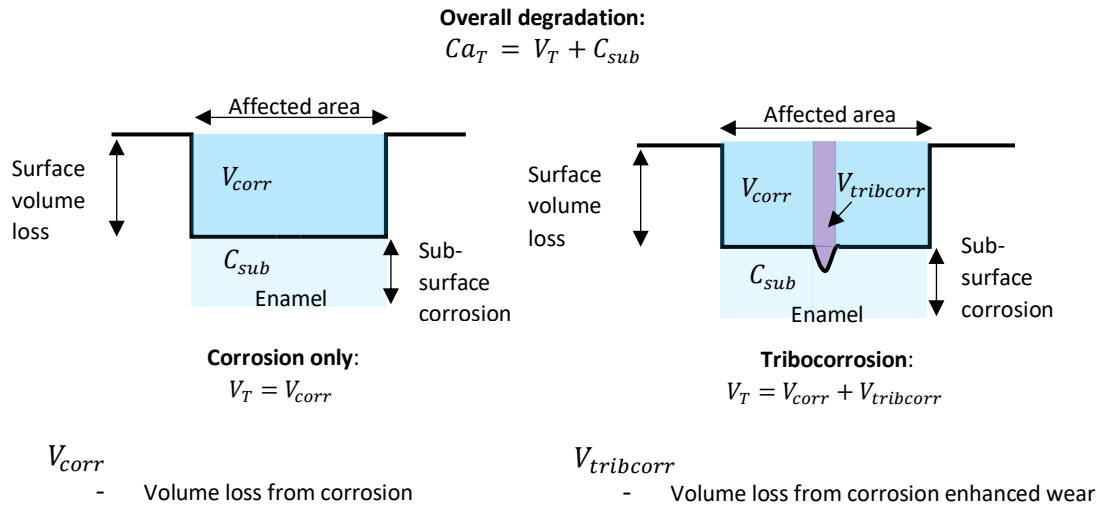
### 5.3.2 Influence of static vs dynamic conditions on overall tooth degradation

Previous work on tooth tribocorrosion has primarily focused on depth profiling of the corroded surface and the wear scar profile as an estimate to the overall wear [27, 263, 182]. Other studies have also performed pre and post-test micro indentations to examine the changes to surface hardness and modulus properties [30, 31, 27, 209]. These methods investigated the impacts of a corrosive environment in different conditions, but not the contributions to the overall degradation. In the present study the measurement of calcium release from static and dynamic experiments provided further insight into the contributions to the total degradation of tooth enamel in an acidic environment. This technique has been observed in corrosion only studies [183, 260, 264, 265] and has shown a linear relationship with changing surface micro hardness [264]. In the present study, significantly more calcium is released in a tribocorrosive environment compared to corrosion alone. This result supports the hypothesis that combining mechanical interactions with a corrosive environment can be more detrimental to the tooth enamel. As mentioned previously, enamel within a corrosive environment begins to soften due to demineralisation of the hydroxyapatite prisms [38, 181]. The enamel surface also begins to roughen and form a 'honeycomb' like structure as the core of enamel rods corrode at a greater rate compared to the outer regions of the rod [30, 31]. This mechanism ensures the enamel surface is more susceptible to material loss from mechanical interactions after it has been attacked by an acid by breaking off protruding outer rod enamel [266]. In the present study, the additional calcium release may therefore be attributed to the mechanical sliding of the YTZP cusp against the softened enamel where the corrosion is enhancing the surface wear and, subsequently, tooth degradation.

### **Breaking down the contributions of tribocorrosion in bovine enamel**

These results add an additional perspective to the field of tooth tribocorrosion where controversy exists regarding the role of corrosion within an enamel tribosystem. This may arise from primarily examining the wear scar characteristics without considering additional effects corrosion may have. Wu et al [27] observed higher wear volume loss under distilled water lubrication while low volume loss was seen with a pH 3.2 citric acid. Under similar lubrication conditions this was also seen by Eisenburger et al [263] and it was generally concluded that enamel on enamel wear was higher in neutral pH conditions compared to the low pH conditions. On the other hand, Weigand et al [182] performed similar sliding tests with different material pairs, including enamel on enamel and ceramic on enamel, and found that tribocorrosion in citric acid yielded the most surface wear, approximately 70 times more than the mineral control solution for the ceramic on enamel pairing. From only examining the wear scar characteristics in the present study, scar width under deionised water and citric acid conditions are the same, while the depth slightly increased under acid conditions. This behaviour was not attributed to changes on the Y-TZP balls, given that post-test VSI inspections demonstrated no signs of surface wear. Upon examination of the scar volume, the acid scar volume is larger than deionised water and PBS solution scars. These results agree with what has been observed with Weigand et al [182]. Other studies which consider acetic acid as the lubricating solution also show contrasting results in terms of wear rate examination, where on the one hand a lower wear rate was observed in pH 3 acetic acid compared to deionised water [261], whereas on the other hand the reverse was seen [267]. This highlights the variation in tribocorrosion studies and the requirement for additional measures to break down the contributions to overall degradation which have been alluded to and employed in the present study. This contribution would be the sub-surface corrosion resulting from acid penetration into the surface which has previously been seen up to a depth of 12  $\mu\text{m}$  [181, 268]. Therefore, it may be assumed that the calcium release is a measure of overall tooth degradation ( $Ca_T$ ) which is a combination of surface volume lost ( $V_T$ ) plus sub-surface corrosion. This has been described by Figure 5-18 as a schematic of the degradation contributions for a corrosion only environment and a tribocorrosive environment.





**Figure 5-18 Schematic of hypothesised wear contributions of bovine enamel under corrosive and tribocorrosive conditions (below the critical pH 5.5).**

### 5.3.3 Influence of mucins on overall tooth degradation

The application of a mucin component in an artificial saliva has been used in several in-vitro studies on enamel [89, 106, 183, 269, 270, 271], focusing of aspects of demineralisation before, or, remineralisation after corrosive challenge and influences on tribological behaviour. Much like with tooth tribocorrosion, there are conflicting studies which argue what type of saliva is most beneficial in terms of protection [89, 183, 106, 269, 260, 271].

Batista et al [183] investigated the protective ability of artificial saliva by pre-treating enamel surfaces and measuring the surface hardness change after corrosion in pH 2.5 hydrochloric acid. This included a mucin containing artificial saliva, other artificial saliva without mucin and human saliva for in-vitro pre-treatment procedures. No significant differences were observed between the pre-treatment solutions, all of which being comparable to the protective capability of human saliva in-vitro. On the other hand, a mucin containing artificial saliva provided similar protection to human saliva under demineralisation conditions compared to the same artificial saliva without mucin and the deionised water control [106]. Bauman et al [260, 265] also examined the interplay between mineral ions and proteins in pre-treatment solutions. A dialysed human saliva, a protein only solution, was compared to a salt only artificial saliva, artificial saliva/dialysed saliva combination and human saliva [260]. The protein only solution provided superior protection after corrosion cycles in terms of surface hardness and calcium release compared to human and other artificial saliva. It was hypothesised that less competition exists between protein and mineral ions in solution which facilitates a better level of surface coverage and therefore protection from demineralisation. A later study also showed that artificial saliva solutions which were under

saturated with respect to calcium were likely to hinder protection from demineralisation [265]. Mucin within an artificial saliva has also been seen to reduce remineralisation, despite being comparable to human saliva [269]. This may be partly be a result of the mucin-surface interactions forming a viscous layer reducing diffusion of calcium ion to the enamel surface [269]. It may also relate to the mucin-ion interactions where calcium ions are complexed by the mucins which is more prevalent in a neutral to alkaline pH environment [272, 273].

In the present study, only the interactions between the test solution and enamel were examined and all solutions used were under-saturated with respect to calcium ion concentration, i.e. no remineralisation took place. It was observed that neutral pH solutions containing mucin, salt or both yielded an increased level of calcium release compared to deionised water alone. Assuming there is no competition between salts and mucins in the single component solutions [260], direct surface interaction occurs with the calcium ions on the enamel surface [70]. Sodium and potassium ions within the PBS may substitute with calcium, releasing free calcium ions into the test solutions [274, 38]. In the presence of PBS salts and mucins, any subsequent free calcium ions may be complexed by free mucins in the solution [272, 273]. Despite an observed increase in calcium release from solution interactions, this does not translate across to the friction and wear behaviour. These results suggest the addition of mucin within a dynamic neutral pH environment enhances enamel protection with significantly improved lubrication and less surface damage. These results agree to similar studies which examined different mucin types in PBS solutions compared to human saliva [270, 271]. In the present study the addition of PBS salts fortified the enamel surface under dynamic test conditions. Despite being under saturated with respect to calcium ions, the combination of phosphate, sodium and potassium ions in PBS and their interactions with the surface had a role to play in reducing the surface wear. In the acidic pH environment, the mucin does not appear to have a significant impact on enamel protection. These results suggest that the mucin is influenced in some way by the mechanical interactions between the YTZP ball and the enamel surface as seen by a significant reduction in calcium release. However, these results cannot explain why this may be occurring, especially as there is no effect of mucin on the coefficient of friction. Most of the previous work has examined the influence of proteins and mineral ion interplay in a corrosion only setting, either after corrosive attack and surface remineralisation. However, to further understand the influence of these solution components in a dynamic environment, future work is needed that focuses on surface interactions in static and dynamic conditions and how they influence overall degradation.

#### 5.3.4 Influence of the sliding environment of bovine enamel

An assessment into the superficial surface structure and chemistry aimed to further expand on the behaviour observed for these tribocorrosion experiments. This was to determine whether the solution influenced changes to the structure and/or chemistry which might impact tooth degradation from both chemical and mechanical influences. Furthermore, chemical analysis aimed to determine whether the presence of mucin could be detected on the enamel surfaces and whether a mucin rich layer was present within the wear locations owing to mechanical interactions.

##### 5.3.4.1 Surface chemistry

###### **Reference sample chemistry and sample preparation**

The use of an ambient pressure XPS enabled the assessment of enamel surfaces up to a depth of 10 nm without having to dehydrate samples prior. This therefore meant that samples could be assessed with minimal surface treatment rather than the prolonged process of dehydrating samples in incremental concentrations of ethanol. Instead, all samples were thoroughly rinsed in isopropanol and deionised water after sample preparation. XPS investigations prior to tribocorrosion tests highlighted a large degree of elemental variation between bovine enamel samples, specifically related to the presence, and proportions of calcium and phosphorus in each sample. Samples tested in DiW, PBS, and Muc + Acid were absent of calcium and/or phosphorus all together. This was interesting as samples were prepped with the same methods and were made up of hydroxyapatite (a calcium phosphate mineral). In addition to the expected adventitious carbon on air exposed surfaces, the data in the reference samples suggests a greater level of contamination than expected. This is shown by the larger composition of carbon in most reference samples, an average of 60.69% which is larger than the 29-54 % observed for similar studies of tooth enamel [275, 217, 256, 218, 276, 222].

Individual samples that did not present calcium or phosphorus peaks presented an overall carbon content over 65%, with those under this percentage displaying both. Given the porous nature of enamel and the sensitivity of XPS to surface chemistries within the top 10 nm of a surface, it was hypothesised that the excess carbon in reference samples was attributed to the preparation and experimental methodologies. Enamel samples were ground with silicon carbide paper, polished in a sub-micron, oil-based diamond suspension, rinsed in isopropanol and deionised water, dried in compressed air and stored in a petri dish. Assuming enamel samples varied in porosity, rinsing may not have fully removed oil residues from the polishing process adequately, with samples therefore showing different

compositions of carbon in the reference XPS surveys [277]. On the other hand, post tribo-test samples did not show as much carbon in comparison to reference samples, which may have related to additional pre tribo-test cleaning in addition to submersion within test solutions for a given period. It could therefore be inferred that sample preparation refinements would improve future analysis, by allowing additional time to soak samples before analysis to remove excess contamination, preferable with ultrasonic agitation [278]. Furthermore, argon ion sputtering was not adopted given the time constraints of analysis, and the associated damage to the surface's chemistry [277]. However, this may also reduce the effects of contamination so long as caution is used to not damage the surface chemistries [277].

#### **Post tribo-test surface chemistries inside and outside of wear locations and the presence of mucin - Calcium and phosphate within post tribo-test samples**

Ca/P ratios were examined to assess the proportion of calcium to phosphate on the surface of tooth enamel, providing an insight into the stability of hydroxyapatite within the XPS scan area. The ratio decreases with an excess adsorption of phosphate groups, substitution or removal of calcium with other elements, or incorporation of trace elements [256]. Biological appetites, like tooth enamel, generally have lower ratios and are termed as "calcium-deficient" [218]. It should be noted that Ca/P provides a proportion of the calcium and phosphate groups within a given sample, but does not suggest absolute values. Mean Ca/P ratios in reference samples were within what was observed in the literature by XPS, with  $1.59 \pm 0.54$  compared to 0.84-1.51 [275, 217, 256, 218, 276, 222].

In all samples tested within mucin solutions, the absolute proportion of calcium and phosphorus was generally lower compared to samples tested without mucin, which was attributed to a combination of mucin interactions with enamel surfaces and carbon contamination, as evidence by the larger proportion of phosphate bonds attributed to O-P/O=C species in non-mucin samples. Despite PBS containing phosphate ions, a reduction in surface phosphate was observed compared to DiW, however both PBS, and Muc + PBS presented a higher Ca/P ratio than both DiW, and Muc + DiW. This suggested that without salts, enamel may partially demineralise and lose calcium ions to the bulk solution, as observed when enamel was immersed in DiW under static conditions. This also suggested that PBS, and Muc + PBS essentially simulated phosphate-rich saliva solutions that could effectively remineralise enamel by substituting in for carbonates, stabilising surface calcium ions [279]. This behaviour is observed both within and outside PBS and Muc + PBS sample wear areas, supporting the occurrence phosphate induced remineralisation. However, this

does not explain the lack of calcium outside the Muc + PBS sample wear area, presenting a Ca/P ratio of 0.0. Within acidic environments the higher Ca/P ratios were related to the preferred demineralisation pathway, where  $H^+$  ions target phosphate groups in hydroxyapatite, resulting in an overall loss of phosphate groups from the surface [38].

Wear areas were also compared with the surrounding enamel to understand whether any preferential dissolution occurred from tribo-tests in different test solutions. This aimed to uncover whether mucin provided additional benefit under mechanical interactions. Ca species, not associated with Ca<sub>1/2p</sub> and Ca<sub>3/2p</sub>, were observed within all enamel wear area, which has been suggested to be described as a transitory species between  $CaH_2O^+$  and dissolved  $Ca^{2+}$  [280]. This was also observed outside the Acid, and Muc + Acid wear areas. This indicated that some degree of dissolution occurring within wear areas for neutral pH solutions, while this occurred all over enamel in acidic pH solution. Furthermore, all samples, excluding the Acid sample, presented a lower composition of phosphate within the wear area compared to outside. Calcium composition was observed to be unchanged for DiW and Muc + DiW samples between both areas, while calcium composition was lower within Acid and Muc + Acid scar areas. Only the PBS sample presented a higher calcium composition within the wear scar compared to outside. When considering the impact of mucin on the Ca/P ratios of enamel samples, a greater proportion was observed inside the wear location for Muc + PBS and Muc + Acid samples.

Given the bulk solution composition, it can be proposed that mucin provides additional benefit to enamel within a neutral pH saline solution. This is evidenced by a higher degree of minerality shown by the Ca/P ratio in addition to the low degree of demineralisation observed with Raman spectroscopy. This explains the reduced wear volume observed under this condition after tribo-tests. Contrary to this, mucin within the citric acid environment presented a greater Ca/P ratio within the wear area, but was observed to cause more surface wear when surveyed with VSI and optical microscopy, with a much larger degree of demineralisation. Further examination the surface species was required to further elucidate the mucin/wear scar interaction.

### **Neutral pH solution interactions**

N 1s, C 1s and O 1s surveys characterised the organic species present on enamel surfaces, relating to mucin, carbon species, and organic species within citric acid. N1s peaks indicated the presence N-H bond associated with organic matrices relating to amino groups and peptide carbons along with C 1s species at binding energies around 287 eV attributed to C-O/N groups [281, 282]. In Muc + DiW, and Muc + PBS environments, N 1s peaks were

observed along with a larger percentage of C-O/N, both within and outside wear areas compared to DiW and PBS samples. This suggested that mucin may be present on the surface, however this is only partly supported by the O 1s peaks. Veeregowda et al [109] employed XPS to calculate the glycosylation of dehydrated salivary films, from C-O-H species within the O1s peak, at a binding energy of 532.7 eV. This corresponded to the lubrication of these films at the nanoscale. Inside the wear areas of enamel samples of the current work, the degree of glycosylation was 11% and 6.5% in for Muc + DiW, and Muc + PBS respectively, compared to 4% and 4% in DiW and PBS samples with no mucin. This demonstrated the presence of mucin within the wear area. This also supported the improvement in lubrication with mucin, however glycosylation cannot fully describe lubrication performance given that Muc + PBS outperformed Muc + DiW with less % glycosylation. Outside the wear location, a higher degree of glycosylation was observed with 12.8% in Muc + DiW, and 6.8% in Muc + PBS. This suggests that mucin can absorb both inside and outside the wear location, however differences in layers may occur. It was thought that layers formed outside the wear area assembled without physical interruption, whereas mucin layers subjected to mechanical interaction are either continuously broken up and reformed, or form a different viscoelastic structure under mechanical conditions. The follow chapters aim to investigate this behaviour further.

### **Acidic pH solution interactions**

Samples tested in Acid and Muc + Acid solutions presented different compositions and species compared to neutral pH solutions. No N 1s were observed in Acid or Muc + Acid samples, which supports what has been previously observed in Chapter 4. Section 4.3.4 with mucin adsorption in a citric acid environment studied by AFM. Furthermore, the degree of glycosylation of Muc + Acid samples was comparable to what was observed in Acid samples, 4.7% and 5.7% compared to 5% and 7%, for glycosylation inside and outside wear areas respectively. This provides further evidence of the lack of mucin-enamel interactions within an acidic environment, which may well have no effect on lubrication compared to citric acid alone. Any reduction in friction might be thought to be the result of enamel softening combined with the dissolution of abrasive asperities and particles [263]. However, Like Muc + DiW and Muc + PBS samples, a larger composition of C-O/N was observed within the Muc + Acid sample wear area compared the Acid sample. Furthermore, this was only observed within the wear scar, and not in the surrounding area unlike Muc + DiW and Muc + PBS samples. As no N 1s peak was observed, this thought to be attributed to citrate anions, however there was no evidence of C=O groups for the Muc + Acid sample. It was postulated

that carbohydrate fragments within the Muc + Acid solution could be present on the surface from using commercial mucin [283].

XPS studies investigating acid interactions with enamel suggested potential chemisorption of interacting acids by ionic interactions [284, 285]. Acids used for etching enamel prior to applications of dental adhesives were shown to form ionic bonds between the acid's carboxyl groups and surface calcium. This was evidenced by component peaks observed at binding energies of 288.6 - 288.8 eV and a larger C1s peak intensity [284, 285]. In the present study, no peaks occurred at this point with only peak occurrences at 288.8 – 289.7 eV indicating carbonate species. Acid, and Muc + Acid surfaces presented a greater proportion of carbonate compared to other C1s components after testing, which may be attributed to the depth changes from acid dissolution, which make the enamel more susceptible to demineralisation [38, 264, 31, 286].

#### *5.3.4.2 Surface structures of bovine enamel*

##### **XRD characterisation before and after tribo-tests**

Structural aspects of the bovine enamel surfaces were examined with XRD and Raman spectroscopic techniques to assess changes to the surface crystallinity and levels of demineralisation. Much like with the XPS analysis, the XRD was limited to examining a larger surface area compared to the areas within the wear track, however surface examination within the wear tracks were accomplished with Raman spectroscopy.

A hexagonal closed packed hydroxyapatite crystal structure was determined with XRD for all reference and post-test samples, with diffraction peaks matching the similar studies investigating tooth enamel [287, 41, 40, 211, 288, 289]. There was no indication of a monoclinic structure, with no observable peaks at  $2\theta = 37.21^\circ$  in the reference enamel diffraction patterns [290]. Not all peaks were present on some samples e.g., the lack of the (002) peak of the PBS reference sample, which was attributed to a variation that sample only. Studies which investigated bulk human enamel samples identified differences in XRD patterns when compared to powdered enamel, with bulk samples showing fewer diffraction peaks compared to powdered samples [291].

Bulk XRD patterns also provide an insight in the crystal orientation and texture, as crystals remained fixed within the bulk structure. Greater peak intensities in all reference samples at (002), (211), (230) and (004) suggested a preferential alignment of hydroxyapatite crystallites, stemming from the sample preparation methodologies used with bovine enamel sectioning and processing. No peaks were observed at between  $2\theta$  of  $28.8-30.0^\circ$  which indicated a lack of carbonate within the surface hydroxyapatite of the reference samples

[40]. However, this was the sole diffraction peak present for both Muc + DiW and Muc + PBS post tribo-tests. The lack of other any other peak in these samples is interesting, as it suggests non-crystalline behaviour. Post-Mucin tests shown in Figure 5-17 were comparable to XRD patterns observed for amorphous calcium phosphate powder formed from combining calcium chloride and sodium dihydrogenphosphate solutions in ice with a pH > 10 [292]. No peaks between 0° - 40° 2θ were observed for the amorphous calcium phosphate powder, presenting only a background spectrum [292]. However, this could not reasonably explain what was observed with the post tribo-test Muc + Acid diffraction pattern, and to the knowledge of the author neither could the literature. Further investigation with mucin layers on surfaces examined by XRD would be required.

### **Bovine enamel crystallinity assessment**

The crystallinity of tooth enamel is a measure of the apatite crystal structure and is indicative of any irregularities that might be present within a sample. Examination of the FWHM of (211) has been keyed by Featherstone et al [40] as an important measure of crystallinity in relation to the rate of material dissolution. Wider FWHMs at (211) were attributed to a greater dissolution rate in an acid solution compared to samples with a smaller FWHM [40]. An alternative method to determine the crystallinity of enamel relates to the mean crystallite a.k.a. grain size of the sample, as calculated by the Scherrer equation. The grain size has an important factor on the mechanical and hardness properties of a materials; reducing crystallite sizes up to a given critical size increases materials yield strength elastic modulus and hardness following the Hall-Petch relationship [293]. An inverse Hall-Petch relationship is observed when grain sizes are reduced further than the critical size [294]. This behaviour is observed in bovine enamel samples, where smaller crystallite sizes correlated with a greater surface microhardness (R=0.969) [295]. The reverse was seen with porcine enamel, with larger crystallite sizes and less defects increasing mechanical wear resistance [43]. These differences are attributed to structural difference between enamel samples from the respective animal [41]. The crystallite size range of 30 – 50 nm (mean = 41.58 ± 4.43 nm) presented in Table 5-14 of this study are within the size of other enamel samples measured by XRD, between 17-70 nm [288, 41, 43, 42]. No significant changes occurred to the crystal size from tribocorrosion tests, with minor decreases in size in DiW and PBS. Interestingly, there is an increase in the crystal size after tribocorrosion tests with in Acid. This can be attributed to depth changes that occur from the removal of surface material during enamel corrosion. It is also documented that the carbonate content tends to increase from the



superficial surface of enamel towards the dentine-enamel junction, reducing the crystallinity of enamel and subsequently its young's modulus and hardness [296].

#### **Raman characterisation after tribo-tests**

Raman spectroscopy provided further insight into the solution's influence of the structure of enamel after interactions with the tribocorrosion test environment, differentiating between the wear scar and surrounding areas. Changes to the  $\nu_1$   $\text{PO}_4^{3-}$  band position and FWHM provided an indication to whether the structure of enamel resemble sound health enamel compared to carious enamel [257]. Buchwald et Buchwald [257] demonstrated a link between a broader FWHM and negative shift in the  $\nu_1$   $\text{PO}_4^{3-}$  band position with enamel which was healthier, compared to a sharper FWHM and a positive band position shift. In the present study, samples treated with citric acid demonstrated a positive band position shift compared to the deionised water treated surface, supporting the formation of a more carious, low apatite enamel. However, the FWHM was only sharper for the combined citric acid and mucin samples with no change occurring the citric acid only sample. Similarly, the band position shifts in the pbs environments negatively while the FWHM varied. Lower FWHM were observed within the wear track with mucin present and in the surround area without mucin. Conversely, no change occurred without mucin in the wear track and with mucin in the surround area.

The assessment of the FWHM alone was not enough to determine how the solution and mucin affected the surface structures, given the contradictory results. The FWHM itself was dependent on the intensity of the  $\nu_1$   $\text{PO}_4^{3-}$  band position, with lower intensities reducing the perceived FWHM. Silveira et al [212] used the intensities of this band position to determine how enamel samples changed, calculating the degree of demineralisation, DD. In the current study Raman spectroscopy was only used after tribocorrosion testing and XPS/XRD examination which meant there was no pre-test reference to determine a sample specific DD. As samples prior to fabrication were stored in deionised water, it was decided that the surrounding area of the deionised water sample was used as a general reference for this application. The citric acid environment was shown to increase the DD of samples within the wear track and the surrounding area, which was enhanced in the presence of mucin. This supports what has been observed inside and outside the wear locations of the Muc + Acid sample which prevented volumetric analysis of the wear scar earlier in the chapter. In the pbs and deionised water environments the DD for most samples was much less, excluding the results for the surround area of the PBS only sample. Mucin was also able to reduce the DD to a higher degree within the wear tracks compared to outside, further supporting mucin

enhanced enamel protection under mechanical loading and shear conditions within neutral pH environments. Contrary to this, mucin was ineffective at protecting enamel in the acidic environments and contributed further to surface demineralisation from a nano structural point of view.

## 5.4 Summary

The tribocorrosion of bovine enamel was affected by a combination of mechanical, chemical and biological influences. The environment not only influences the tribological properties of enamel, but also the way mucins interact with one another and the surfaces. The key conclusions from this chapter are summarised below:

- In a neutral pH environment, the addition of mucins can be used to improve lubrication and reduce the interacting surface wear, especially with the addition of PBS. Mucin was observed to limit surface demineralisation on enamel samples to a higher degree, especially within wear locations where a greater degree of glycosylation was observed indicating presence of a mucin tribofilm.
- In an acidic pH environment, the mucins did not influence static dissolution or lubrication. This was attributed to a reduction in mucin glycosylation.
- In both environments, the additional mechanical interactions reduced the overall calcium release in the presence of mucins. However, in the acidic pH environment the acid interaction with mucin increased the level of surface demineralisation with a greater impact on the enamel structure.
- A novel method of quantifying the contributions of enamel tribocorrosion was determined through understanding individual and combined aspects of chemical and mechanical degradation.
- The wear could not be fully determined from the experiments in this chapter. Further research should investigate: surface mechanical properties over exposure time, direct changes in surface chemistry and crystal structure (with a larger sample range and more refined methods by depth profiling through progressive surface etching), corrosion depth investigations and tribo-film analyses.

## Chapter 6. Factors influencing mucin layer growth on dental surfaces

### 6.1 Introduction

This chapter probes the use of commercial porcine gastric mucin within artificial salivary solutions to understand the kinetics of protein layer formation in relation to layer viscoelastic properties and subsequent lubrication. Growth of protein layers on gold and hydroxyapatite coated quartz sensors were examined initially, using a QCM-D. Mucin in DiW, PBS and Acid solutions were examined on both surfaces to assess the influence of the material surface on layer growth kinetics and the resultant layer's viscoelastic and structural properties. Additionally, the influence of salt type and concentration were also assessed using gold coated sensors as a control surface. Finally, nanotribometer tests were performed on mucin layers grown on QCM-D sensors to identify potential links between the layer's properties and overall lubrication mechanisms. A flow chart outlining the work and analyses completed in this chapter is presented in Figure 6-1, following methodologies described in Chapter 3.

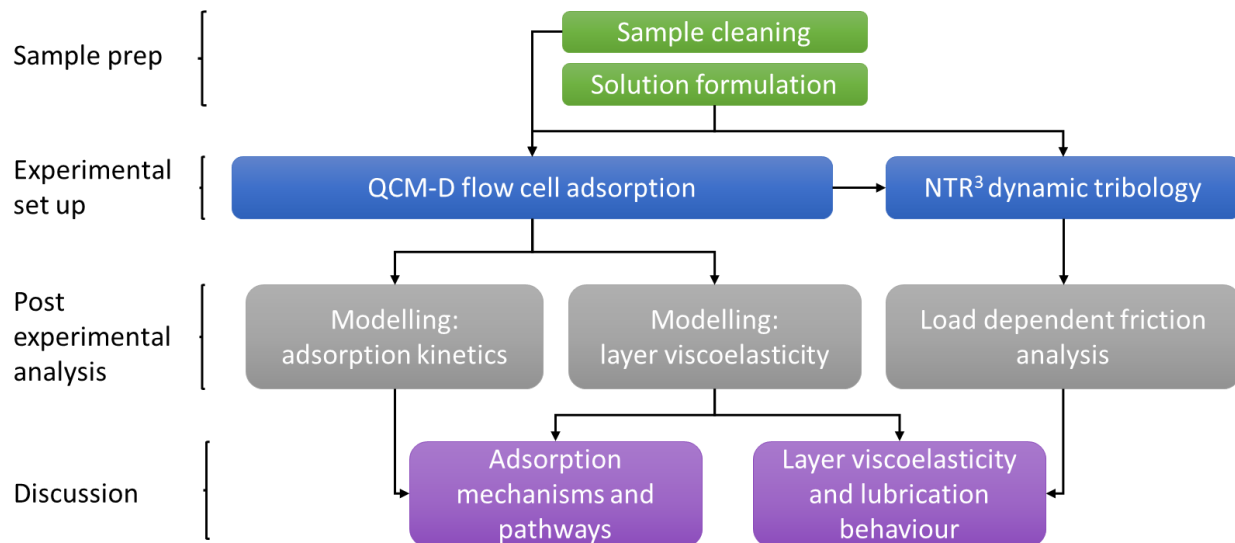


Figure 6-1 Flow chart of experimental methods and analyses Chapter 6.

## 6.2 Results

### 6.2.1 Kinetic adsorption modelling on QCM-D sensors

#### 6.2.1.1 Influence of gold and hydroxyapatite surfaces on mucin layer adsorption kinetics

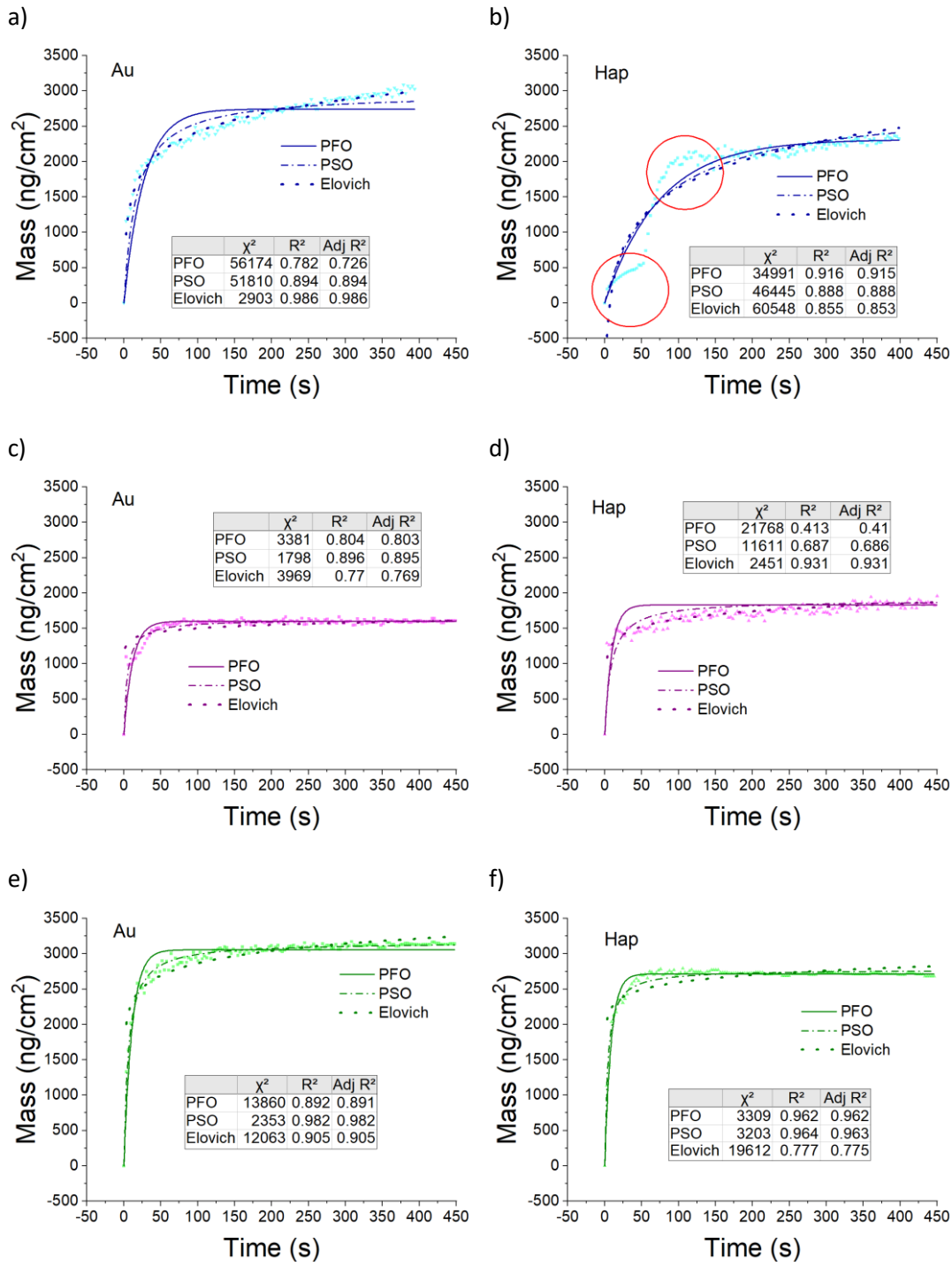
Mucin layer growth with commercial PGM was initially examined with the standard “artificial saliva” solutions used in the previous chapters: Muc + DiW, Muc + PBS and Muc + Acid. Layers were growth with each solution onto gold and hydroxyapatite coated QCM-D sensors, and the mass properties were calculated, and plotted over time as shown in Figure 6-2. To assess the adsorption pathways, rate of adsorption and approximated mass at equilibrium, Pseudo First Order (PFO), Pseudo Second Order (PSO) and Elovich adsorption models were applied for each system. Each model is presented with curve for each system along with error parameters (R squared ( $R^2$ ), adjusted R squared (Adj  $R^2$ ) and Chi squared ( $\chi^2$ )), shown in Figure 6-2. Comparison of the  $R^2$ , Adj  $R^2$ , and  $\chi^2$  fitting parameters determined the best fit out of the 3 adsorption models. The criteria for the best fit assessed how close  $R^2$  and Adj  $R^2$  were to 1 and which model possessed the lowest  $\chi^2$  result. Table 6-1 shows the model fitting parameters for each solution, adsorption model and surface material.

The Elovich model fitted both Muc + DiW adsorption to gold surfaces, as shown by  $R^2 = 0.99$  in addition to other the error parameters in Figure 6-2a). The PSO model for Muc + DiW adsorption onto gold also had a good fit,  $R^2 = 0.89$ , which was better than the PFO model,  $R^2 = 0.71$ . The PSO model fitted Muc + PBS adsorption ( $R^2 = 0.90$ ), and Muc + Acid adsorption ( $R^2 = 0.98$ ), shown in Figure 6-2c) and e). Both Elovich and PSO model fits indicated layer growth was driven by chemisorption processes onto gold surfaces, potentially strong electrostatic interactions/ electron sharing. The addition of perturbing molecules such as PBS and Acid to the mucin solution was shown to influence both the rate of adsorption and the mass adsorbed at equilibrium. If the best fitting models are considered, Muc + PBS presents the highest adsorption rate constant of  $k_1 = 1.356 \times 10^{-4}$ , followed by Muc + Acid ( $k_1 = 5.444 \times 10^{-5}$ ) and finally Muc + DiW ( $k_1 = 1.991 \times 10^{-5}$ ). Furthermore, a larger mass adsorbed at equilibrium was observed for Muc + Acid adsorption ( $q_e = 3165 \text{ ng/cm}^2$ ), followed by Muc + DiW ( $q_e = 2974 \text{ ng/cm}^2$ ), and finally Muc + PBS ( $q_e = 1626 \text{ ng/cm}^2$ ). This suggested that the presence of additional salts (PBS) increased the protein layer formation rate whilst limiting the adsorption quantity onto gold. Similarly, the presence of an acidic component (citric acid) increases the rate of protein layer formation in addition to the mass of the adsorbed layer.

On hydroxyapatite surfaces, a different behaviour was observed with Muc + DiW, and Muc + PBS solutions. Muc + DiW adsorption was observed to grow in more than one stage such that the kinetic models did not adequately fit the experimental data as evidenced by  $\chi^2$  values over 34991, shown in Figure 6-2b), compared to other  $\chi^2$  error for best fits ( $\chi^2 < 4000$ ). Muc + DiW growth was broken down into two splits, Hap1 and Hap2, which are presented in Figure 6-3 with the best fitting adsorption models displayed. The Elovich fit best described the initial stage of adsorption in Hap1 ( $R^2 = 0.97$  and  $\chi^2 = 531$ ), followed by the PFO model in Hap2 with Muc + DiW adsorption ( $R^2 = 0.77$  and  $\chi^2 = 19561$ ), reducing the overall fit error. This indicated that most of the layer's growth phase on hydroxyapatite favour physisorption processes, such as weak electrostatic interactions, hydrophobic/hydrophilic interactions, hydrogen bonding and VDW forces. Whereas the initial stages of adsorption favour more chemisorption interaction from strong electrostatic interactions.

Muc + PBS adsorption to hydroxyapatite was different to gold, with the Elovich model providing the best fit ( $R^2 = 0.93$ ) on the former surface compared to the PSO model on gold. While this suggested the chemisorption process was still dominant, the adsorption of the layer was observed to be a balance of adsorption/desorption growth compared to the other models which reach a finite mass adsorbed at equilibrium. The model fit for Muc + Acid did not change from gold with the PSO model fit ( $R^2 = 0.93$ ), suggesting similar chemisorption pathways.

Aside from adsorption pathway differences between materials, it was observed that with Muc + DiW, and Muc + PBS adsorption demonstrated a slower PSO adsorption rate constant,  $k_2$ , on hydroxyapatite compared to gold surfaces, from  $1.99 \times 10^{-5}$  to  $4.90 \times 10^{-6}$  and from  $1.35 \times 10^{-4}$  to  $6.07 \times 10^{-5}$  respectively. For Muc + Acid adsorption, the adsorption rate constant increased on hydroxyapatite to  $9.38 \times 10^{-5}$  compared to  $5.44 \times 10^{-5}$  on gold. This suggested that the material surface influenced the rate at layer formation depending the composition of the growth solution. The absorbed mass at equilibrium was observed to also differ with both Muc + DiW, and Muc + Acid adsorption onto hydroxyapatite demonstrating lower mass compared to gold, of  $q_e = 2848 \text{ ng/cm}^2$  and  $q_e = 2780 \text{ ng/cm}^2$  respectively. The adsorbed mass from Muc + PBS was observed to increase on hydroxyapatite,  $q_e = 1900 \text{ ng/cm}^2$ , suggesting that the addition of PBS salts enhance protein surface interactions more than on gold.



**Figure 6-2** Layer mass growth over time onto gold and hydroxyapatite coated QCM-D sensors with fitted kinetic adsorption models and fitting error parameters. Growth solutions used include a) and b) Muc + DiW, c) and d) Muc + PBS, and e) and f) Muc + Acid. In a), c), and e), gold (Au) surfaces adsorption is presented, while b), d), and f) show hydroxyapatite (Hap) surface adsorption. The red circles in b) present areas of poor model fit which required additional splits for analysis.

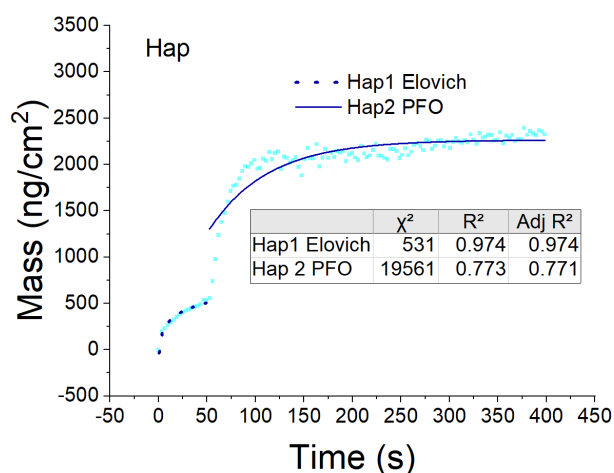


Figure 6-3 Best kinetic model splits for mucin layer growth in Muc + DiW on Hap surfaces with fitting error parameters.

Table 6-1 Kinetic adsorption model fitting parameters for mucin adsorption to gold and hydroxyapatite coated QCM-D sensors. Parameters in bold represent the best fitting model for each solution/material combination.

Material	Solution	PFO		PSO		Elovich	
		$k_1$	$q_e$	$k_2$	$q_e$	$\alpha$	$\beta$
Au	Muc + DiW	0.037	2744	$1.99 \times 10^{-5}$	2974	<b><math>1.41 \times 10^3</math></b>	<b>0.002</b>
	Muc + PBS	0.085	1602	<b><math>1.36 \times 10^{-4}</math></b>	<b>1626</b>	$1.57 \times 10^9$	0.014
	Muc + Acid	0.091	3057	<b><math>5.44 \times 10^{-5}</math></b>	<b>3165</b>	$2.25 \times 10^5$	0.004
Hap	Muc + DiW	<b>0.013</b>	<b>2314</b>	$4.90 \times 10^{-6}$	2846	$8.70 \times 10^1$	0.002
	Hap1	0.072	510	$1.22 \times 10^{-4}$	636	<b><math>1.24 \times 10^2</math></b>	<b>0.007</b>
	Hap2	<b>0.016</b>	<b>2265</b>	$8.65 \times 10^{-6}$	2601	$2.55 \times 10^2$	0.002
	Muc + PBS	0.103	1833	$6.07 \times 10^{-5}$	1900	<b><math>5.21 \times 10^4</math></b>	<b>0.006</b>
	Muc + Acid	0.117	2715	<b><math>9.38 \times 10^{-5}</math></b>	<b>2780</b>	$4.84 \times 10^7$	0.007

### 6.2.1.2 Influence of salt type and salt concentration on mucin layer adsorption kinetics

Similar to the previous section, kinetic adsorption models were applied to protein layer adsorption from salt containing mucin solutions. Figure 6-4 presents the best fitting models for a) NaCl, b) KCl, c) CaCl<sub>2</sub>, d) NaH<sub>2</sub>PO<sub>4</sub> and e) CaCl<sub>2</sub> + PBS salts at 1, 10 and 100 mmol concentrations. The fitting parameters associated with the model fits are presented in Table 6-2. At 1 mmol concentrations (excluding CaCl<sub>2</sub> + PBS), the PSO model provided the best fit with an  $R^2 > 0.96$ . 1 mmol CaCl<sub>2</sub> presented the largest adsorption rate constant,  $k_2 = 1.24 \times 10^{-5}$ , and lowest adsorbed mass at equilibrium,  $q_e = 2504$  ng/cm<sup>2</sup>. This behaviour was also closest to Muc + DiW when fitted with the PSO model ( $k_2 = 1.990 \times 10^{-5}$  and  $q_e = 2974$

ng/cm<sup>2</sup>). Conversely, 1 mmol NaCl presented the largest adsorbed mass,  $q_e = 5375$  ng/cm<sup>2</sup> with the lowest rate constant,  $k_2 = 3.44 \times 10^{-6}$ . KCl and NaH<sub>2</sub>PO<sub>4</sub> presented similar mass values at equilibrium of 3526 ng/cm<sup>2</sup> and 5371 ng/cm<sup>2</sup> respectively with adsorption constants in between NaCl and CaCl<sub>2</sub>. This behaviour, along with the adsorption model, suggests that the salt type influences the way in which commercial mucin chemisorption occurs on gold surfaces. For 1 mmol CaCl<sub>2</sub> + PBS, the PFO model provided the best fit, suggesting physisorption processes were dominant. While the adsorption rate constants are not comparable due to model differences with the other salt-mucin solutions, the mass at equilibrium was much lower than all other solutions,  $q_e = 555$  ng/cm<sup>2</sup>. This was approximately a third of the adsorbed mass observed with Muc + PBS,  $q_e = 1602$  ng/cm<sup>2</sup> with the PFO model. This suggested the Ca<sup>2+</sup> ions interactions within PBS had a negative effect on the adsorption process, both in terms of adsorption rate and adsorbed mass.

At 10 mmol concentrations, NaCl and CaCl<sub>2</sub> solutions switched from PSO to PFO models, suggesting a change to physisorption. Furthermore, the NaCl mucin solution presented higher adsorption rate constant,  $k_1 = 0.037$  compared to  $k_1 = 0.028$  with CaCl<sub>2</sub>. This demonstrated a different adsorption rate behaviour compared to both solutions at 1 mmol. The NaCl adsorption rate constant was also comparable to Muc + DiW. KCl and NaH<sub>2</sub>PO<sub>4</sub> solutions presented the same PSO fit, indicating the concentration change did not influence the chemisorption pathways. Increasing from salt concentration from 1 to 10 mmol also reduced the adsorbed mass at equilibrium parameter in all cases. For 10 mmol CaCl<sub>2</sub> + PBS, a similar PFO fit was observed, showing no change to physisorption from the salt concentration. The increased to 10 mmol CaCl<sub>2</sub> + PBS further reduced the adsorption rate constant from  $k_1 = 0.025$  to  $k_1 = 0.005$ , and reduced the adsorbed mass at equilibrium to 443 ng/cm<sup>2</sup>.

Increasing the concentration from 10 to 100 mmol indicated that physisorption was prominent with these NaCl solutions. KCl and CaCl<sub>2</sub> solutions fitted well with the PSO model, while the NaH<sub>2</sub>PO<sub>4</sub> solution fitted well with the Elovich model, indicating chemisorption behaviour. A reduction in the mass adsorbed at equilibrium was observed with increased concentration, excluding the KCl solution which increased mass adsorption. At 100 mmol CaCl<sub>2</sub> salt in PBS, an unstable mass adsorption was observed, shown in Figure 6-4e), with a poor PFO model fit ( $R^2 = 0.44$ ). Unlike other salt solutions, the increased CaCl<sub>2</sub> concentration in PBS presented an increased adsorbed mass at equilibrium,  $q_e = 1572$  ng/cm<sup>2</sup>, which was comparable to Muc + PBS.



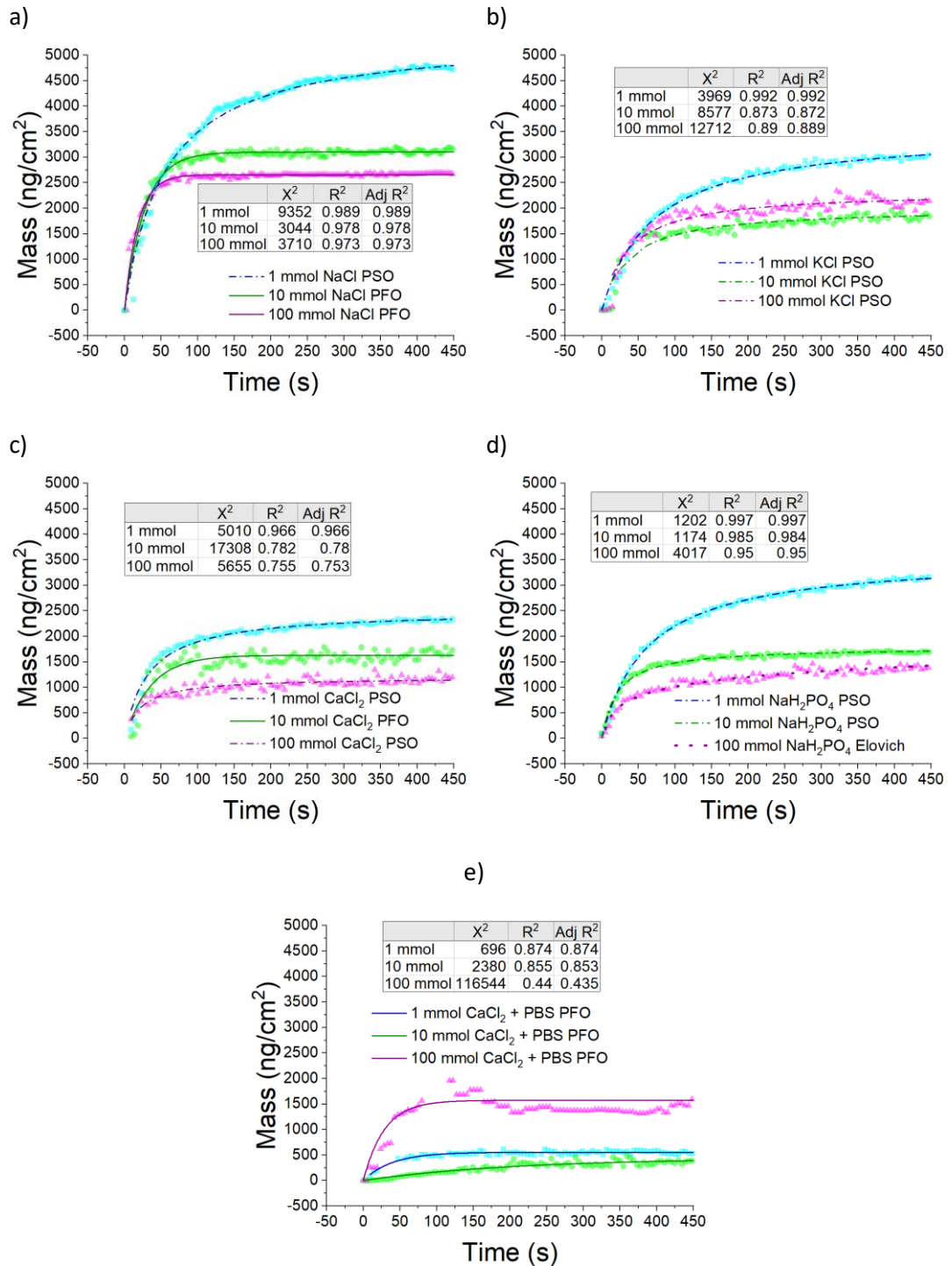


Figure 6-4 Layer mass growth over time onto gold coated QCM-D sensors with best fitting kinetic adsorption models and fitting error parameters. Growth solutions used include a) NaCl b) KCl, c)  $\text{CaCl}_2$  d)  $\text{NaH}_2\text{PO}_4$ , and e)  $\text{CaCl}_2 + \text{PBS}$ . Salt concentrations of 1, 10 and 100 mmol are presented. Solid lines represent the PFO mode, dash-dot lines represent the PSO model and dotted lines represent the Elovich model.

**Table 6-2 Kinetic adsorption model fitting parameters for salt influenced mucin adsorption to gold coated QCM-D sensors.**

Salt	Concentration	Model	$k_1/k_2/\alpha$	$\beta$	$q_e$ (ng/cm <sup>2</sup> )
<b>NaCl</b>	1	PSO	$3.44 \times 10^{-6}$	-	5375
	10	PFO	0.037	-	3101
	100	PFO	0.055	-	2656
<b>KCl</b>	1	PSO	$4.05 \times 10^{-6}$	-	3526
	10	PSO	$1.40 \times 10^{-5}$	-	2001
	100	PSO	$1.23 \times 10^{-5}$	-	2338
<b>CaCl<sub>2</sub></b>	1	PSO	$1.24 \times 10^{-5}$	-	2504
	10	PFO	0.028	-	1628
	100	PSO	$3.85 \times 10^{-5}$	-	1195
<b>NaH<sub>2</sub>PO<sub>4</sub></b>	1	PSO	$4.50 \times 10^{-6}$	-	3571
	10	PSO	$2.65 \times 10^{-5}$	-	1790
	100	Elovich	$1.09 \times 10^2$	0.004	-
<b>CaCl<sub>2</sub> + PBS</b>	1	PFO	0.025	-	555
	10	PFO	0.005	-	443
	100	PFO	0.035	-	1572

## 6.2.2 Viscoelastic modelling of mucin layers on QCM-D sensors

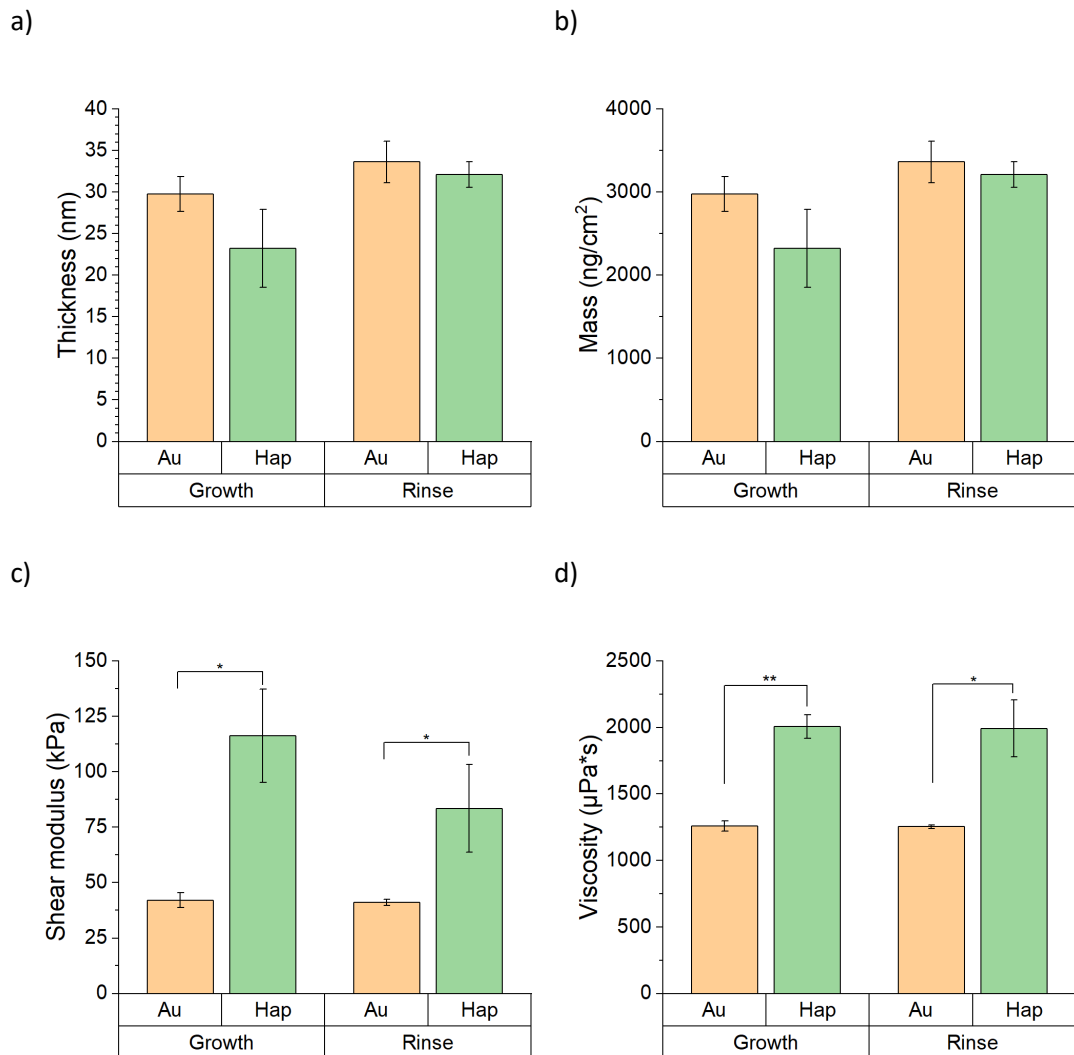
### 6.2.2.1 Influence of gold and hydroxyapatite surfaces on mucin layer viscoelastic modelling

Viscoelastic models, discussed in Chapter 3. Section 3.2.5.1, were applied to the raw frequency and dissipation to estimate the structural and viscoelastic properties of protein layers grown on gold and hydroxyapatite surfaces. Average thickness, mass, shear modulus and viscosity properties were calculated at two stages, towards the end of the mucin layer's growth phase and rinse phase. The rinse solution was the bulk solution without commercial mucin, i.e. DiW for Muc + DiW layer growth.

#### Mucin layer growth in DiW with DiW rinse

Figure 6-5 shows the average layer properties from the Muc + DiW solution onto gold and hydroxyapatite surfaces, with error bars relating to the standard deviation between samples (n=3). The average layer thickness on gold and Hap was  $29.73 \pm 2.10$  nm and  $23.2 \pm 4.69$  nm, respectively, increasing to  $33.62 \pm 2.51$  nm and  $32.10 \pm 1.52$  nm in the rinse solution, shown

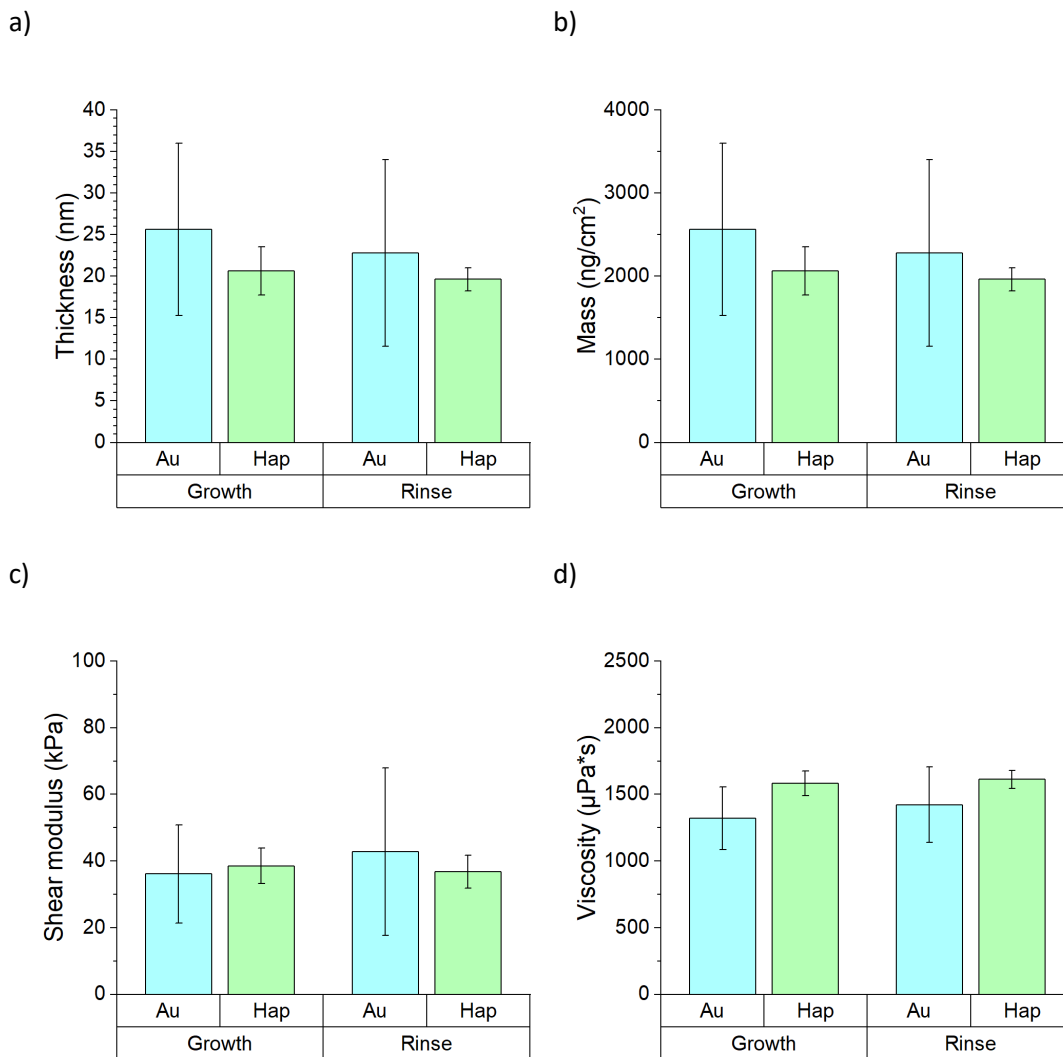
in Figure 6-5a). Similar behaviour was observed with the mass property, shown in Figure 6-5b). The average shear moduli at the end of growth phase for gold and Hap sensors was  $41.98 \pm 3.35$  kPa and  $116.16 \pm 21.12$  kPa respectively, changing to  $41.08 \pm 1.42$  kPa and  $83.50 \pm 19.71$  kPa with the rinse solution shown in Figure 6-5c). The average viscosity at the end of the growth phase for gold and Hap sensors was  $1256.95 \pm 38.75$   $\mu\text{Pa}\cdot\text{s}$  and  $2005.58 \pm 89.80$   $\mu\text{Pa}\cdot\text{s}$  respectively, changing to  $1253.80 \pm 14.20$   $\mu\text{Pa}\cdot\text{s}$  and  $1992.02 \pm 14.21$   $\mu\text{Pa}\cdot\text{s}$  during the rinse phase, shown in Figure 6-5d). The average shear modulus and viscosity properties of the mucin layers were significantly different for both gold and Hap during the growth phase ( $p = 0.035$  and  $p = 0.002$ ). During the rinse phase, only the difference in average layer viscosity remained significant between gold and Hap sensors ( $p = 0.038$ ).



**Figure 6-5 Average layer properties calculated from 'Broadfit' model comparing gold and Hap sensors after Muc + DiW adsorption and rinsing in DiW; showing a) thickness, b) mass, c) shear modulus and d) viscosity. Error bars represent standard deviation between samples ( $n = 3$ ). Asterisks refer to level of statistical significance where (\* -  $p < 0.05$ , \*\* -  $p < 0.01$  and \*\*\* -  $p < 0.001$ ).**

### Mucin layer growth in PBS with PBS rinse

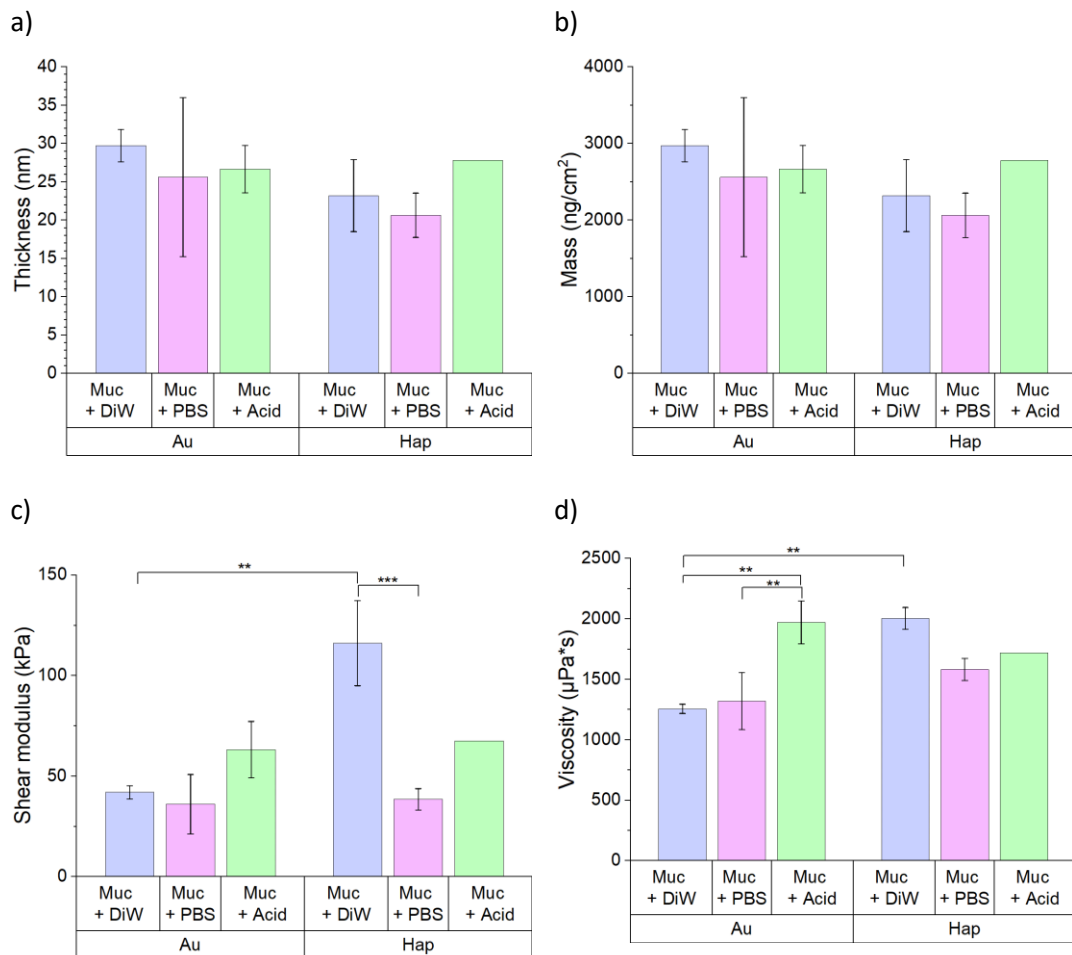
Figure 6-6 shows the average layer properties from the Muc + PBS solution onto gold and hydroxyapatite surfaces, with error bars relating to the standard deviation between samples ( $n=3$ ). The average layer thickness on gold and Hap was  $25.61 \pm 10.36$  nm and  $20.65 \pm 2.98$  nm, respectively, decreasing to  $22.80 \pm 11.22$  nm and  $19.62 \pm 1.37$  nm in the rinse solution (PBS), shown in Figure 6-6a). The average shear moduli at the end of growth phase for gold and Hap sensors was  $36.09 \pm 14.80$  kPa and  $38.52 \pm 5.34$  kPa respectively, changing to  $42.83 \pm 25.14$  kPa and  $36.74 \pm 4.97$  kPa with the rinse solution shown in Figure 6-6c). The average viscosity at the end of the growth phase for gold and Hap sensors was  $1320.40 \pm 235.83$   $\mu$ Pa.s and  $1582.57 \pm 92.67$   $\mu$ Pa.s respectively, changing to  $1421.98 \pm 284.32$   $\mu$ Pa.s and  $1611.67 \pm 67.48$   $\mu$ Pa.s during the rinse phase, shown in Figure 6-6d).



**Figure 6-6** Average layer properties calculated from 'Broadfit' model comparing gold and Hap sensors after Muc + PBS adsorption and rinsing in PBS; showing a) thickness, b) mass, c) shear modulus and d) viscosity. Error bars represent standard deviation between samples ( $n = 3$ ).

### Mucin layer growth in Acid, compared with Muc + DiW, and Muc + PBS layer growth

Figure 6-7 presents the Muc + Acid layer properties with the other solutions (Muc + DiW, Muc + PBS) for comparison during the growth phase. One Muc + Acid repeat was performed on hydroxyapatite (an active decision made due to hydroxyapatite coating degradation during measurements in citric acid). Muc + Acid layers thickness properties on gold and hydroxyapatite were comparable to the other solutions, 26.66 ± 3.10 nm and 27.82 nm respectively. However, on gold the shear modulus and viscosity of Muc + Acid layers were greater with 63.24 ± 13.99 kPa and 1971.63 ± 176.47 μPa.s respectively. For comparison to hydroxyapatite surfaces, Muc + Acid layer shear modulus and viscosity were 67.60 kPa and 1719.24 μPa.s respectively.



**Figure 6-7** Average layer properties calculated from 'Broadfit' model comparing Muc + DiW (blue), Muc + PBS (magenta), Muc + Acid (green) growth solutions on gold and Hap sensors during the growth stage; showing a) thickness, b) mass, c) shear elasticity modulus, and d) viscosity. Error bars represent standard deviation between samples ( $n = 3$ ). Asterisks refer to level of statistical significance where (\* -  $p < 0.05$ , \*\* -  $p < 0.01$  and \*\*\* -  $p < 0.001$ ).

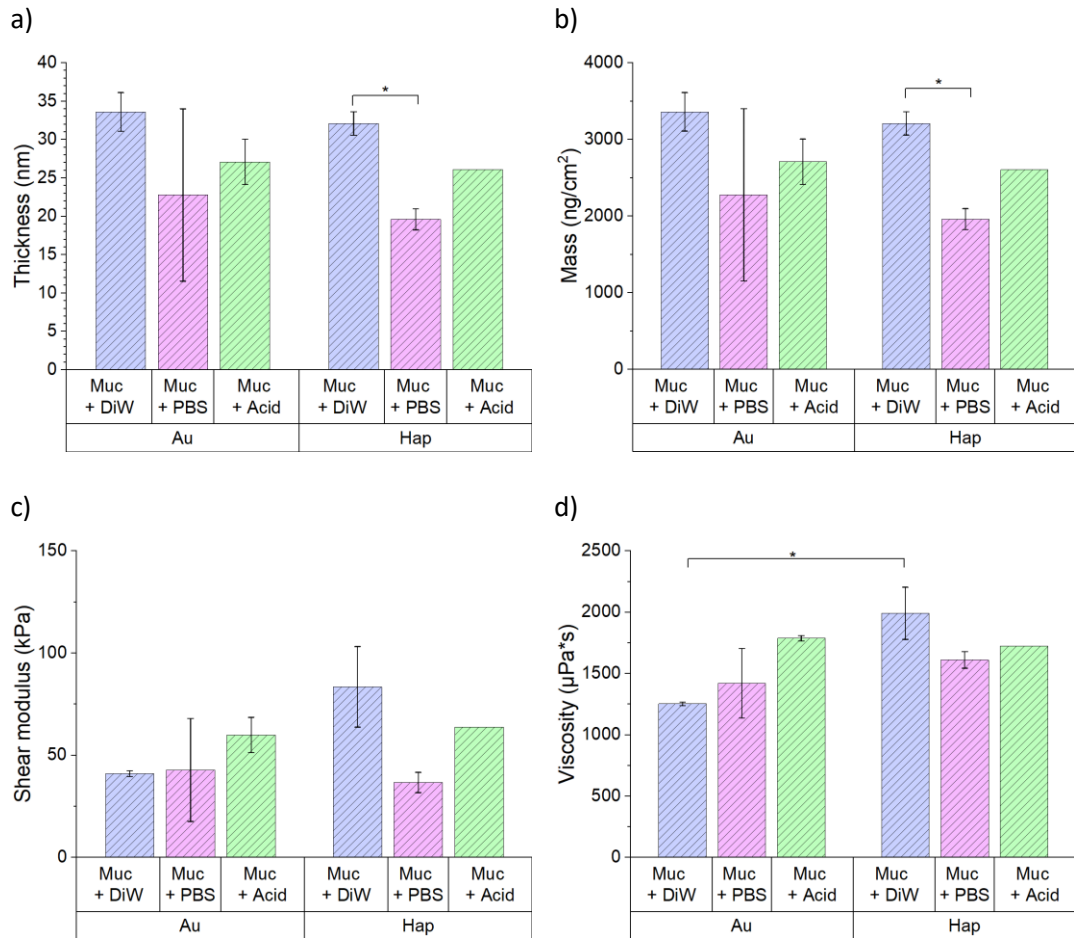
Significant differences were observed between the Muc + DiW, and Muc + PBS layer's shear properties on hydroxyapatite with  $p = 0.0008$ . On gold, significant differences between Muc + Acid and Muc + DiW, and Muc + Acid and Muc + PBS were also observed with  $p = 0.006$

and  $p = 0.005$  respectively. Between materials, significant differences were observed for Muc + DiW layers for both shear modulus and viscosity with  $p = 0.002$  and  $0.004$  respectively.

In relation the kinetic adsorption models, the average mass adsorption of Muc + DiW onto gold supported PSO fitting parameter of adsorbed mass at equilibrium,  $q_e$ , with  $2973 \pm 210$   $2974 \text{ ng/cm}^2$  compared  $2974 \text{ ng/cm}^2$ . The PSO model underestimated the equilibrium mass onto gold for Muc + PBS, but this was attributed to the large variation in the average mass,  $2561 \pm 1036 \text{ ng/cm}^2$  compared with  $1626 \text{ ng/cm}^2$ . The Muc + Acid PSO  $q_e$  parameter overestimated the adsorbed mass on gold, with an average adsorbed mass of  $2666 \pm 310 \text{ ng/cm}^2$  compared to  $3165 \text{ ng/cm}^2$ . On hydroxyapatite, the PFO  $q_e$  parameter for Muc + DiW was supported by the average adsorbed mass,  $2314 \text{ ng/cm}^2$  compared to  $2320 \pm 468 \text{ ng/cm}^2$ . Furthermore, the PSO  $q_e$  parameter for Muc + PBS was close to the average adsorbed mass,  $1900 \text{ ng/cm}^2$  compared to  $2064 \pm 289 \text{ ng/cm}^2$ .

#### **Mucin layer rinse in Acid, compared with rinse phase of Muc + DiW, and Muc + PBS layers**

Figure 6-8 presents the Muc + Acid layer properties with the other solutions (Muc + DiW, Muc + PBS) for comparison during the rinse phase. Minimal changes were observed for Muc + Acid layer thickness, shear modulus and viscosity values on gold, with values of  $27.12 \pm 2.95 \text{ nm}$ ,  $59.99 \pm 8.58 \text{ kPa}$  and  $1788.55 \pm 21.95 \text{ } \mu\text{Pa.s}$  respectively. For comparison on hydroxyapatite Muc + Acid layer thickness, shear modulus, and viscosity values were  $26.06 \text{ nm}$ ,  $63.89 \text{ kPa}$  and  $1724.76 \text{ } \mu\text{Pa.s}$  respectively. No significant differences were observed between Muc + Acid growth phase and the Acid rinse phase. Significant differences were observed between the Muc + DiW, and Muc + PBS layer's thickness and mass properties on hydroxyapatite with  $p = 0.01$  and  $p = 0.01$  respectively. Between materials, significant differences were observed for Muc + DiW layer's viscosity with  $p = 0.03$ .



**Figure 6-8** Average layer properties calculated from 'Broadfit' model comparing Muc + DiW (blue), Muc + PBS (magenta), Muc + Acid (green) growth solutions on gold and Hap sensors during the rinse stage; showing a) thickness, b) mass, c) shear elasticity modulus, and d) viscosity. Error bars represent standard deviation between samples ( $n = 3$ ). Asterisks refer to level of statistical significance where (\* -  $p < 0.05$ , \*\* -  $p < 0.01$  and \*\*\* -  $p < 0.001$ ).

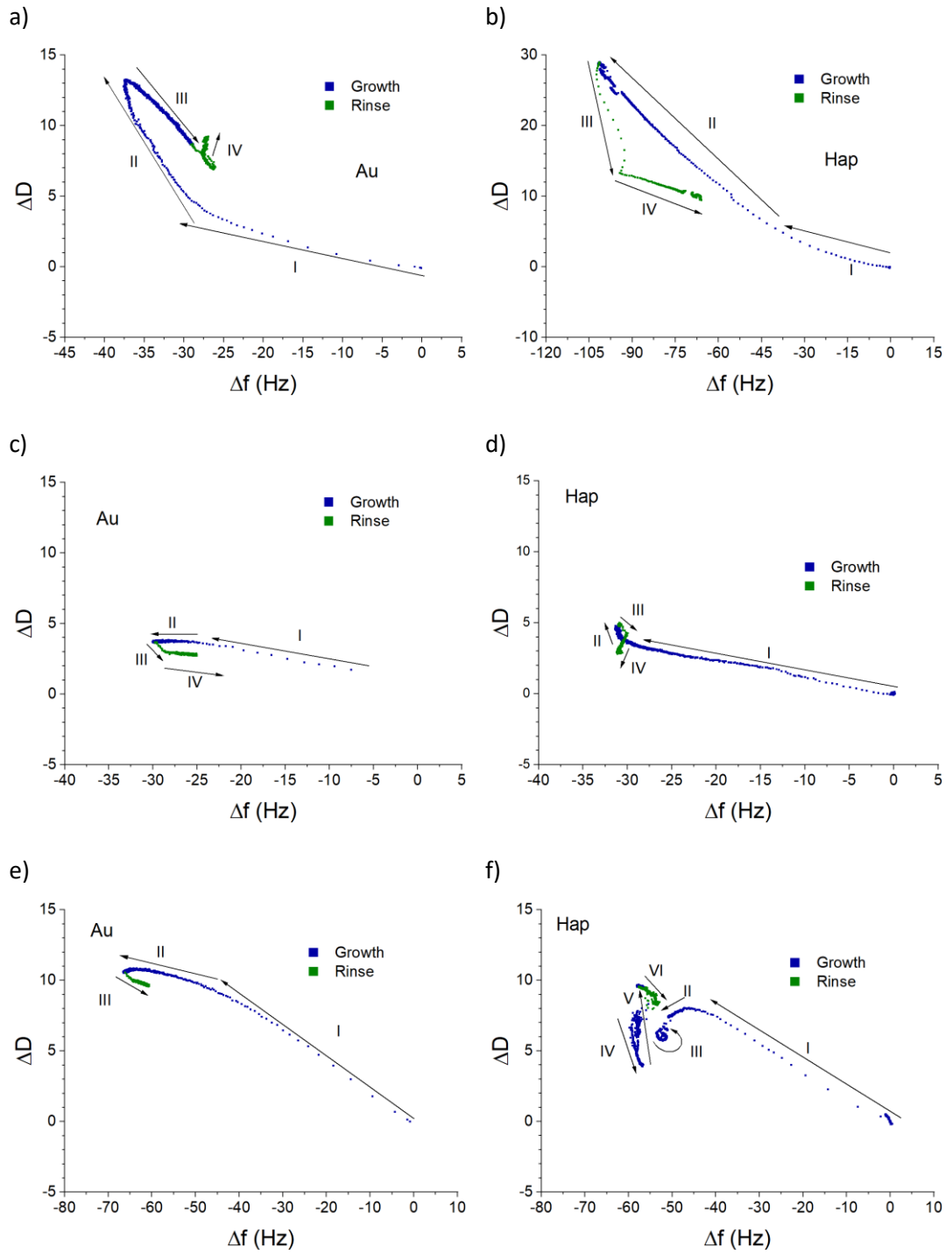
A qualitative assessment of the layer's structural properties during the growth and rinse phase was also performed, shown Figure 6-9. This provided an insight into structural changes from a mass adsorption perspective, demonstrated by the frequency change, and the stiffness/softness of the layer, demonstrated by the dissipation change. A steeper gradient relates to softer and more dissipative layer in relation to adsorbed mass, while a flatter gradient indicates a more rigid and elastic layer [110, 297]. Roman numerals in Figure 6-9 relate to stages in layer development while arrows indicate the direction of change.

On gold, multiple adsorption processes were observed with Muc + DiW, Muc + PBS, and Muc + Acid, shown in Figure 6-9a), c) and e) respectively. Muc + DiW's initial stage on gold, arrow I Figure 6-9a), indicated a more elastic and rigid layer formed initially, followed by steeper gradient change, with arrow II, that suggested a layer softening towards the layer stages. Arrow III indicated that conformation changes occurred in the layer's structure and layer desorption occurred. The reverse was observed in Muc + PBS, and Muc + Acid, with a steeper gradient initially, arrow I in Figure 6-9c) and e) respectively, followed by a flatter line with arrow II. This suggested that these layers started out soft, but changed overtime to exhibit a more elastic layer regarding the adsorbed mass.

On hydroxyapatite, Muc + DiW and Muc + PBS layers presented a similar behaviour to Muc + DiW adsorption to gold, where arrow I and II indicated an initial rigid layer followed by the formation of a softer layer, shown in Figure 6-9b) and d). A different behaviour was observed with Muc + Acid adsorption onto hydroxyapatite, where arrow I presents adsorption like other solutions but several different stages followed as illustrated by arrows II, III, IV and V in Figure 6-9f). This behaviour was attributed to citric acid interactions with the hydroxyapatite coating on the QCM-D sensor which had an impact on the perception of Muc + Acid layer properties on hydroxyapatite.

During the rinse phase, both Muc + PBS, and Muc + Acid layers on gold showed a reduction in mass with layer stiffening, shown by arrows III and IV in Figure 6-9c) and e) respectively. This behaviour suggested that loosely bound molecules on adsorbed layers were removed during the rinse phase. The Muc + DiW layer continues to follow the behaviour of arrow III, before increasing its dissipation, suggesting layer softening and dispersion with arrow IV in Figure 6-9a). On hydroxyapatite, the dissipation was observed to decrease in all solutions, which indicated layer stiffening. This change was particularly significant with Muc + DiW, as illustrated by arrows III and IV in Figure 6-9b), while this was less pronounced with Muc + PBS in Figure 6-9d).



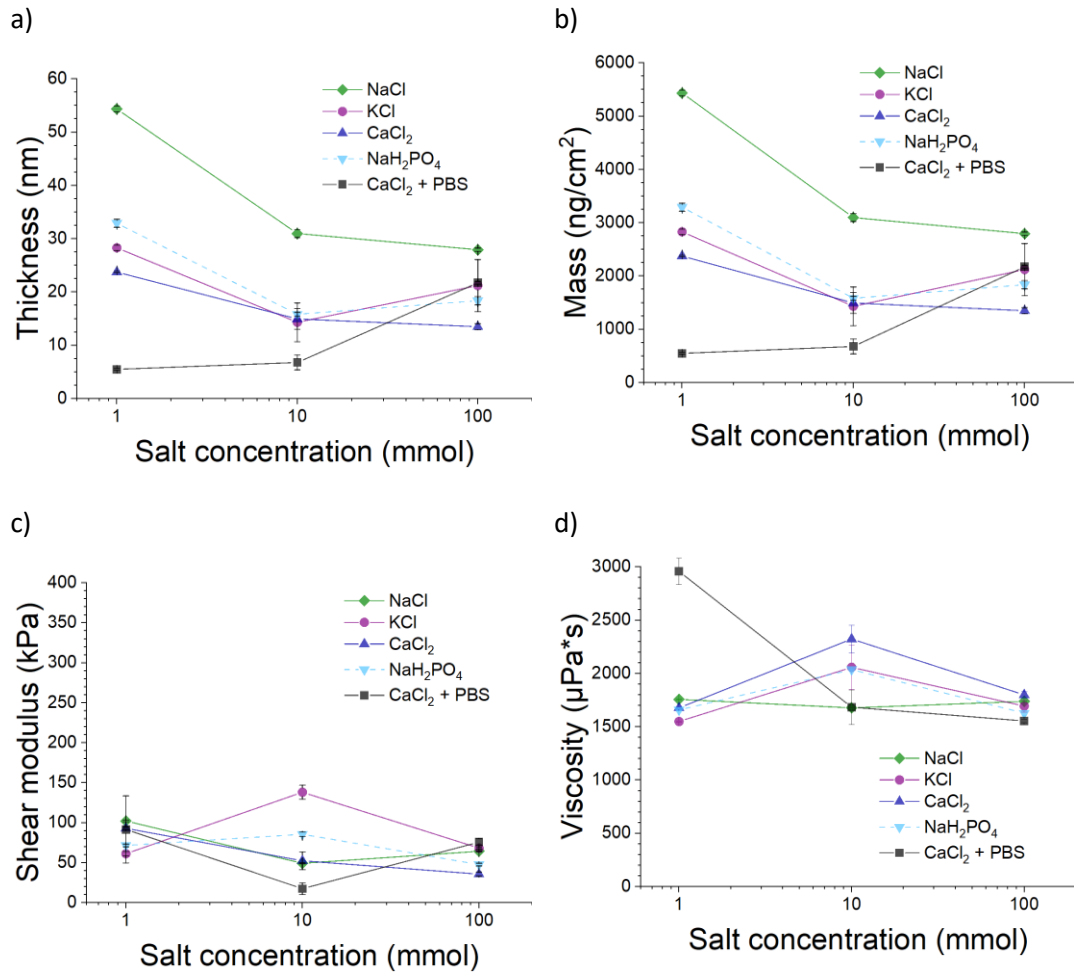


**Figure 6-9** Qualitative assessment of mucin layer viscoelasticity by comparing  $\Delta D$  vs  $\Delta f$  during the growth phase (blue), the rinse phase (green). Muc + DiW, Muc + PBS and Muc + Acid solutions onto gold are presented in a), c), and e) respectively, while the respective solutions adsorption to hydroxyapatite are presented in b), d), and f).

### 6.2.2.2 *Influence of salt type and salt concentration on mucin layer viscoelastic modelling*

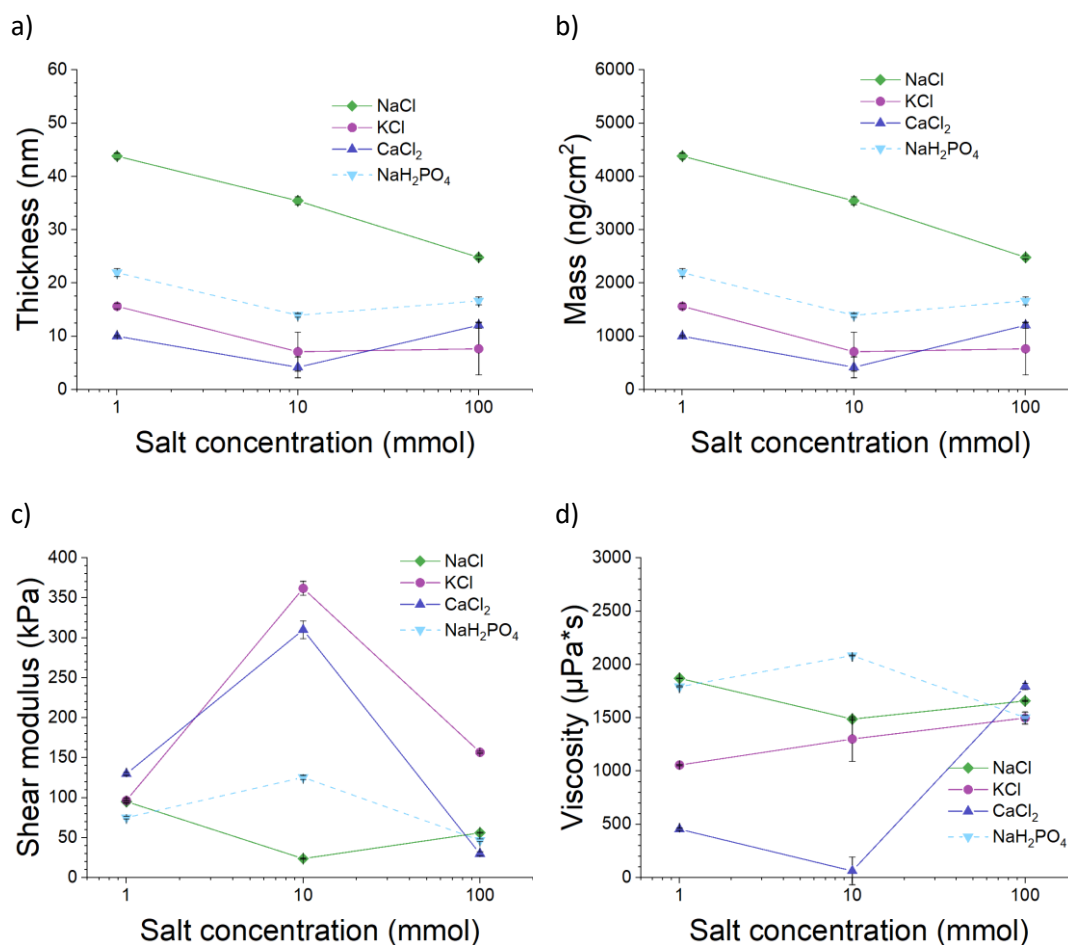
Similar to the previous section, the adsorbed layer viscoelastic properties were modelled and compared during growth and rinse phases for mucin solutions with the addition of different salt types at different concentrations. Given the number of comparisons, growth and rinse phases were separated into two figures, Figure 6-10 and Figure 6-11 respectively. For NaCl, KCl, CaCl<sub>2</sub>, and NaH<sub>2</sub>PO<sub>4</sub> layers, thickness decreased with increased salt concentrations from 1 to 10 mmol, shown in Figure 6-10a) and b). Decreased layer thickness continued with NaCl and CaCl<sub>2</sub> layers at 100 mmol salt concentrations, while KCl, and NaH<sub>2</sub>PO<sub>4</sub> layers increased in mass and thickness. NaCl layers presented the largest mass and thickness properties compared to all other layers over the experimental concentration range during the growth phase. CaCl<sub>2</sub> demonstrated the lowest adsorption in comparison to all single salt type solutions. The CaCl<sub>2</sub> + PBS layer presented a progressive increase in layer mass and thickness properties as the salt concentration increased.

Variation with salt layer's shear moduli and viscosities were observed, with maxima and minima values occurring at salt concentrations of 10 mmol, excluding the CaCl<sub>2</sub> layer. Maximum shear modulus values of 138.27 kPa and 85.65 kPa were observed with KCl and NaH<sub>2</sub>PO<sub>4</sub> layers respectively, while minimum values of 49.35 kPa and 17.48 kPa with NaCl and CaCl<sub>2</sub> + PBS respectively, shown in Figure 6-10c). Maximum viscosity values were also observed at 10 mmol concentration for KCl, CaCl<sub>2</sub> and NaH<sub>2</sub>PO<sub>4</sub> layers with 2058.45 μPa.s, 2323.60 μPa.s, and 2036.76 μPa.s respectively, shown in Figure 6-10d). The CaCl<sub>2</sub> + PBS layer presented a progressive reduction in layer viscosity with increasing salt concentration.



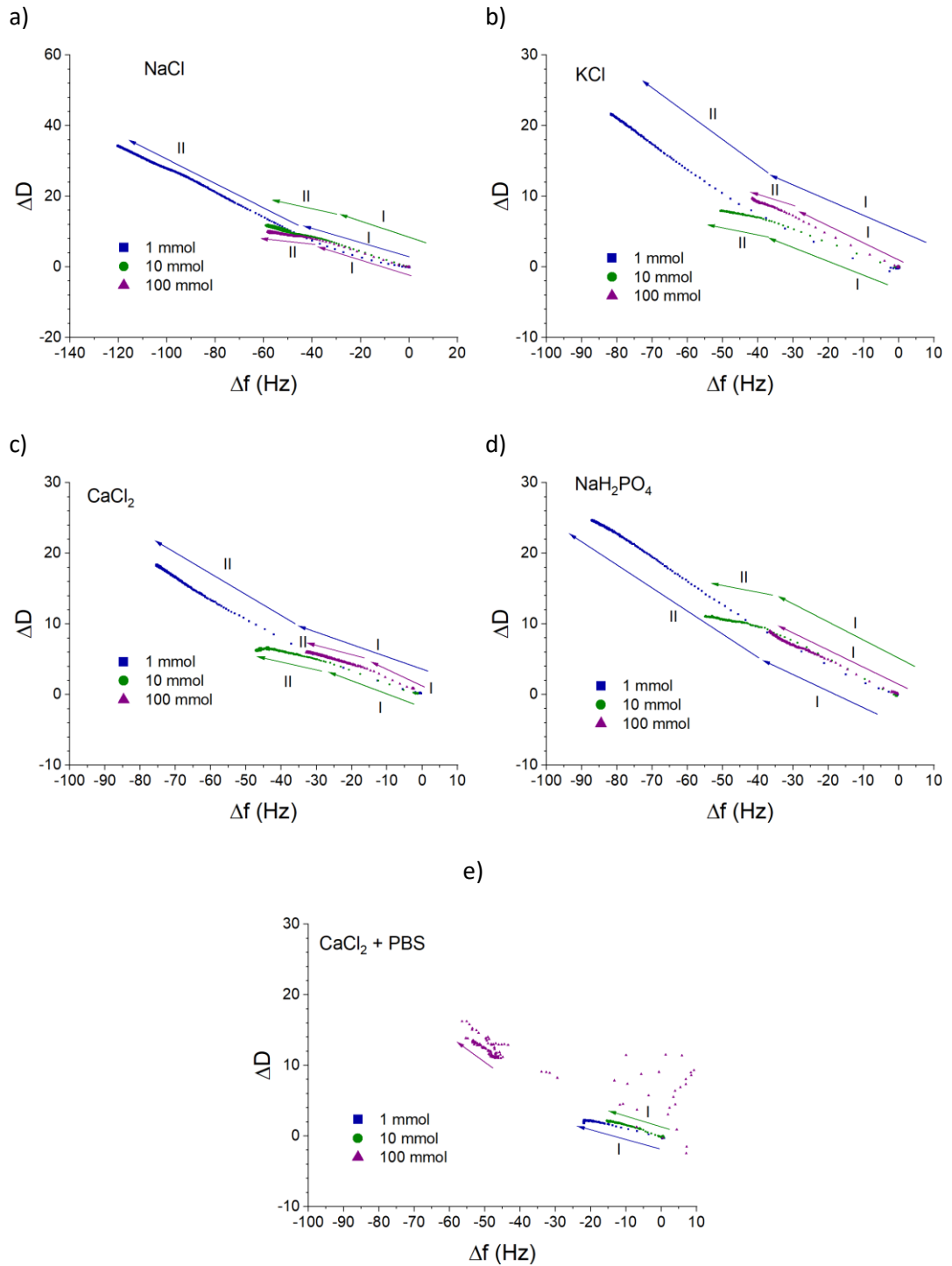
**Figure 6-10** Average layer properties calculated from 'Broadfit' model against salt concentrations comparing NaCl (green), KCl (purple), CaCl<sub>2</sub> (blue), NaH<sub>2</sub>PO<sub>4</sub> (cyan), and CaCl<sub>2</sub> in PBS (black) salt/mucin solutions on gold sensors during the growth stage; showing a) thickness, b) mass, c) shear elasticity modulus, and d) viscosity.

Changes to the salt-mucin layer properties were observed when salt only rinse solutions were introduced, presented in Figure 6-11. Instabilities with the CaCl<sub>2</sub> + PBS layer prevented viscoelastic modelling within the rinse phase. Generally, the rinse phase reduced salt-mucin layer's thickness properties in most cases by 5-15 nm. Conversely the 10 mmol NaCl layer presented an increased in thickness from 30.93 nm to 35.43 nm. Apart from the 10 mmol NaCl layer, 10 mmol KCl, CaCl<sub>2</sub> and NaH<sub>2</sub>PO<sub>4</sub> layers presented a large increase in shear modulus properties to 362.01 kPa, 351.64 kPa and 125.52 kPa, respectively, which corresponded with a reduction in layer viscosity.



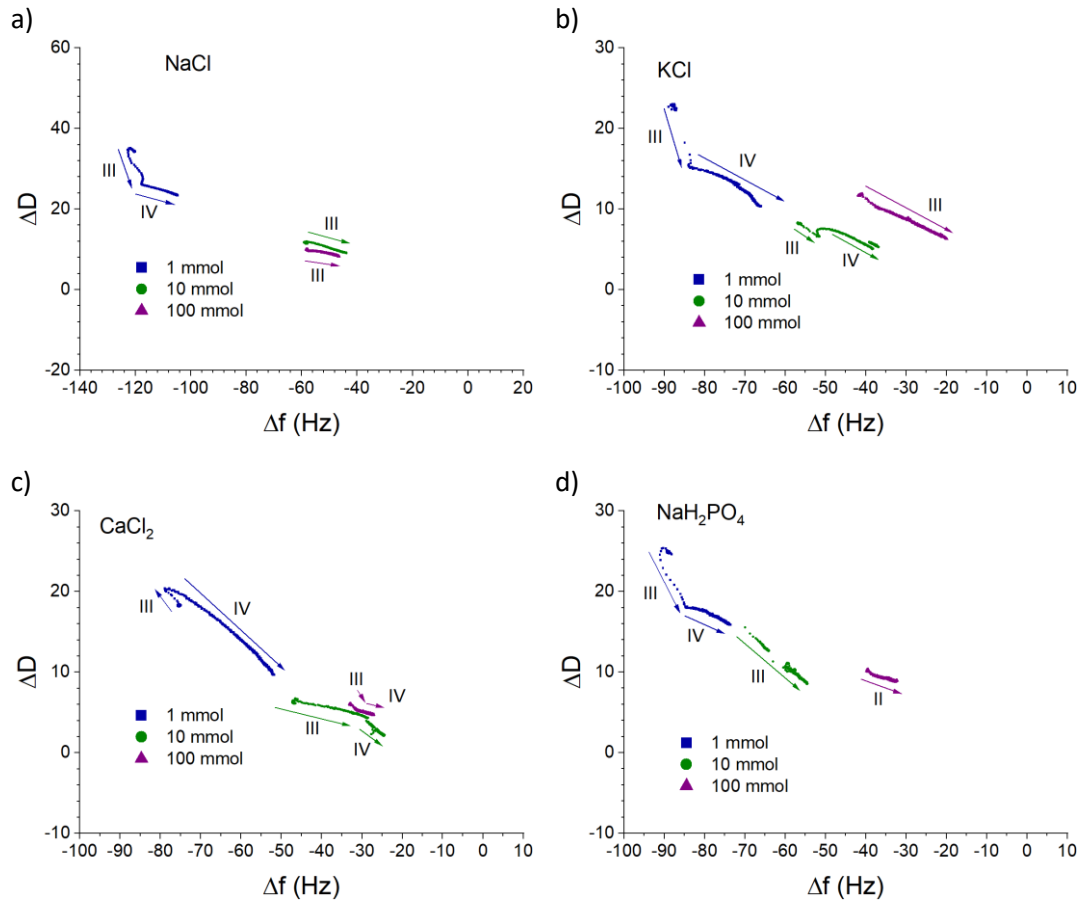
**Figure 6-11** Average layer properties calculated from 'Broadfit' model against salt concentrations comparing NaCl (green), KCl (purple), CaCl<sub>2</sub> (blue), NaH<sub>2</sub>PO<sub>4</sub> (cyan), and CaCl<sub>2</sub> in PBS (black) salt/mucin solutions on gold sensors during the rinse stage; showing a) thickness, b) mass, c) shear elasticity modulus, and d) viscosity.

A qualitative assessment of the layer's structural properties during the growth and rinse phase was also performed, shown in Figure 6-12 and Figure 6-13 respectively. Different layer properties were observed depending on the salt concentration. At 1 mmol salt concentrations a flatter gradient was observed initially, illustrated by arrow I in Figure 6-12a), b), c), and d) for NaCl, KCl, CaCl<sub>2</sub> and NaH<sub>2</sub>PO<sub>4</sub> layers respectively. Afterwards, arrow II presents a steeper gradient, indicating the formation of a softer, more dissipative layer. This behaviour was like Muc + DiW adsorption onto gold, shown in Figure 6-9a). With 10 and 100 mmol salt concentrations, a similar behaviour to Muc + PBS adsorption was observed, with steep initial gradient (arrow I) followed by a flatter gradient (arrow II), shown in Figure 6-12a), b), c), and d) for NaCl, KCl, CaCl<sub>2</sub> and NaH<sub>2</sub>PO<sub>4</sub> layers respectively. Single stage adsorption was observed with CaCl<sub>2</sub> + PBS layers, with observed instabilities at 100 mmol.



**Figure 6-12** Qualitative assessment of mucin layer viscoelasticity by comparing  $\Delta D$  vs  $\Delta f$  during the growth phase for 1, 10 and 100 mmol salt concentrations on gold with a) NaCl, b) KCl, c)  $\text{CaCl}_2$ , d)  $\text{NaH}_2\text{PO}_4$ , and e)  $\text{CaCl}_2 + \text{PBS}$ . Arrows and roman numerals indicate different phases of change and the direction of change.

During the rinse stages, a general reduction in layer mass and dissipation was observed in all salt concentrations, illustrated by arrows II, III and IV in Figure 6-13. In most cases, this suggests the removal of loosely bound molecules and an increase in layer elasticity.



**Figure 6-13** Qualitative assessment of mucin layer viscoelasticity by comparing  $\Delta D$  vs  $\Delta f$  during the rinse phase for 1, 10 and 100 mmol salt concentrations with a) NaCl, b) KCl, c)  $\text{CaCl}_2$ , d)  $\text{NaH}_2\text{PO}_4$ , and e)  $\text{CaCl}_2$  + PBS. Arrows and roman numerals indicate different phases of layer change continuing from Figure 6-12 and the direction of change.

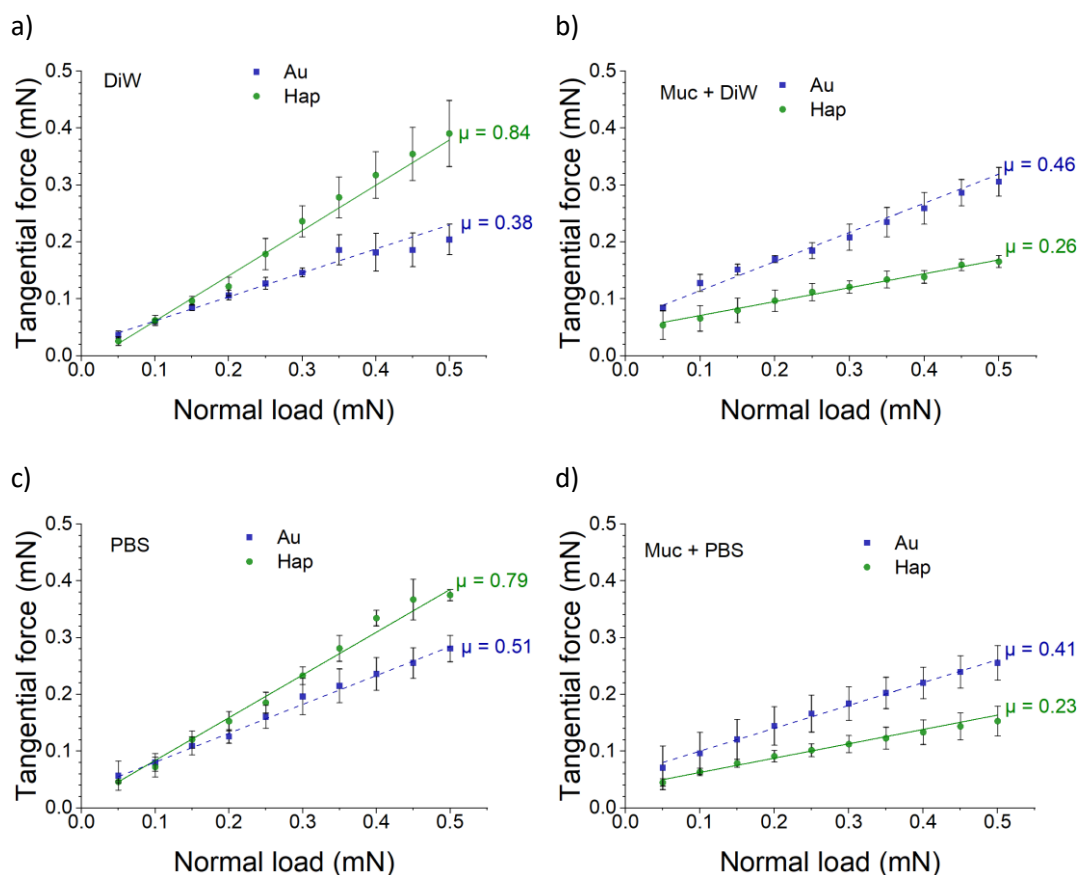
### 6.2.3 Mucin layer lubrication on QCM-D sensors

#### 6.2.3.1 *Influence of gold and hydroxyapatite surfaces on mucin lubrication and the addition of perturbing salts*

Tribo-tests were performed on QCM-D sensors to assess mucin solution lubrication on gold and hydroxyapatite surfaces to provide an indirect link to the modelled QCM-D properties. Figure 6-14 shows the resultant frictional force response to incremental normal loading for a) DiW, b) Muc + DiW, c) PBS and d) Muc + PBS. A linear  $F_t$  response was observed with increasing  $F_n$ . Error bars represent the standard deviation about the mean tangential force for all samples ( $n=3$ ) at each normal load, while the mean dynamic coefficient of friction ( $\mu$ ) and standard deviation about  $\mu$  was calculated from the linear  $F_t$  vs  $F_n$  curve fits of each sample in OriginLab (OriginLab Corp, USA). T tests assessed significance for each interaction.

Mucin lubrication was improved on the Hap surface with Muc + DiW by reducing coefficient of friction ( $\mu$ ) from  $\mu = 0.84 \pm 0.16$  in DiW to  $0.26 \pm 0.06$  ( $p < 0.001$ ). Interestingly, the gold surface's  $\mu$  increased with the adsorbed mucin layer from  $\mu = 0.38 \pm 0.09$  in DiW to  $0.46 \pm 0.07$  in Muc, but this was not observed to be significant ( $p = 0.910$ ). In Muc + PBS,  $\mu$  reduced on both surfaces, from  $0.51 \pm 0.04$  to  $0.41 \pm 0.03$  on gold ( $p = 0.890$ ), and from  $0.79 \pm 0.07$  to  $0.23 \pm 0.07$  on Hap ( $p < 0.001$ ). Mucin improved lubrication on both surfaces with PBS, which was significant on Hap but not on gold.

All Hap surfaces presented differences to gold surfaces under each condition, where  $\mu$  was greater on Hap surfaces without mucin, and where  $\mu$  was lower on Hap surfaces with mucin. The differences of  $\mu$  between Hap and gold were observed to be significant under DiW ( $p < 0.001$ ), and PBS conditions ( $p = 0.016$ ), whereas they were not observed to be significant for Muc + DiW ( $p = 0.118$ ), or Muc + PBS ( $p = 0.377$ ) conditions. The presence of perturbing salts (PBS) was also shown to have no influence on  $\mu$ , for both a PBS only solution compared to DiW on gold and Hap ( $p = 0.608$  and  $p = 0.993$  respectively), and as a Muc + PBS solution compared to Muc + DiW on gold and Hap ( $p = 0.994$  and  $p = 0.999$  respectively). Overall, these results suggest that the surface material interactions with mucin have a greater influence on resultant lubrication, independent of PBS salts, and the individual contribution of surface material and mucin. The combination of the mucin solutions with Hap surfaces demonstrates the importance of protein solution-surface interactions in promoting enhanced lubrication.



**Figure 6-14** Mean tangential force from tribo-tests on gold and hydroxyapatite QCM-D sensors over incremental normal load lubricated in a) DiW, b) Muc + DiW, c) PBS and d) Muc + PBS. Error bars represent variation between mean tangential force over the sensor material samples ( $n=3$ ) for each load increment.

### 6.2.3.2 Influence of salt type and salt concentration on mucin lubrication on gold surfaces

Tribo-tests were also performed on gold surfaces to assess the influence of salt type and concentration in relation to mucin lubrication. All tests were performed with 0.2% mucin in salt solutions. Figure 6-15 shows the resultant frictional force response to incremental normal loading for mucin and salt solutions with concentrations of 1, 10 and 100 mmol for a) NaCl, b) KCl, c) CaCl<sub>2</sub>, d) NaH<sub>2</sub>PO<sub>4</sub>, and e) CaCl<sub>2</sub> + PBS. These were fitted in the same way as results from Figure 6-14.

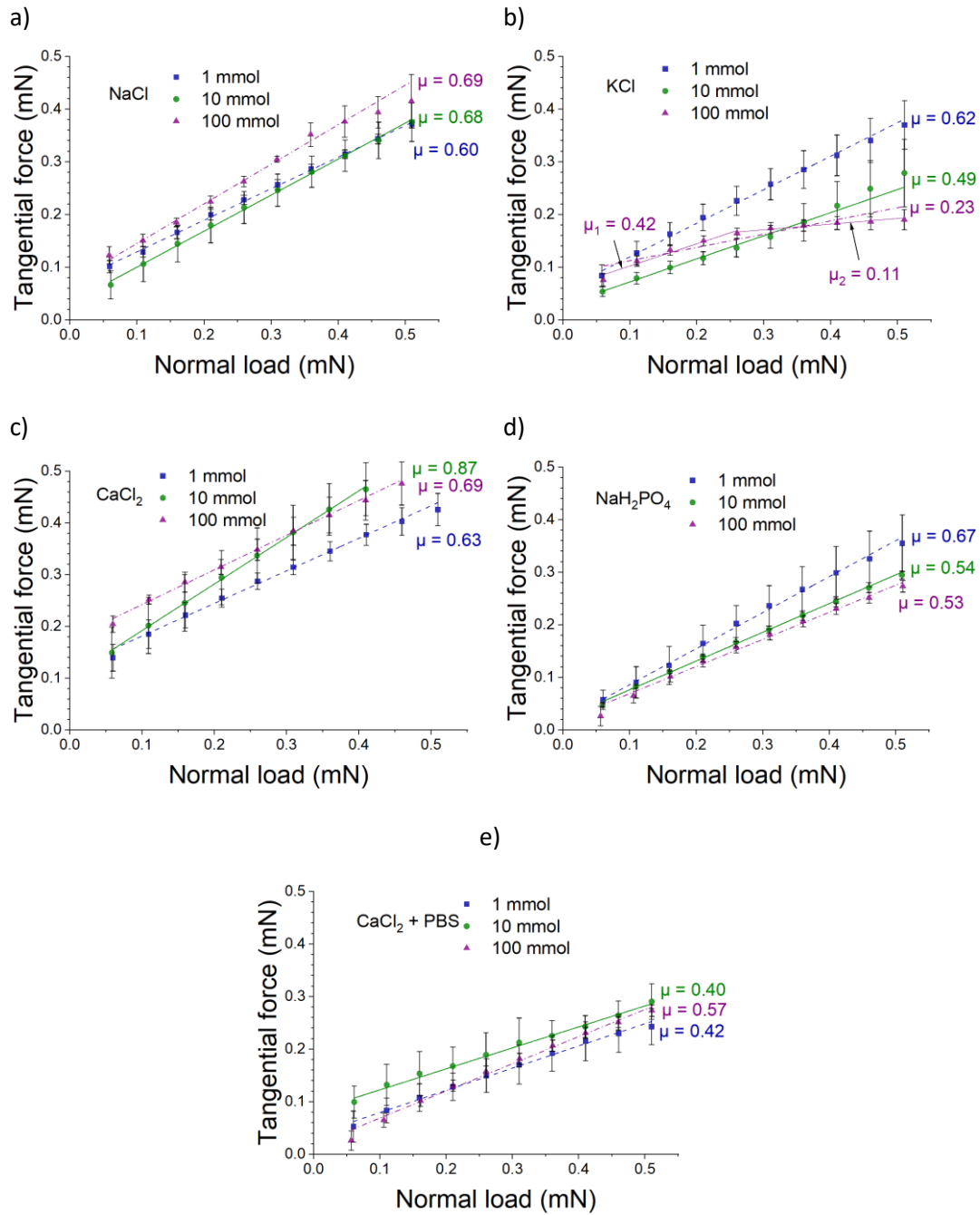
At concentrations of 1 mmol, NaCl, KCl, and CaCl<sub>2</sub> solutions presented similar values for  $\mu$ , with  $0.60 \pm 0.03$ ,  $0.61 \pm 0.09$ , and  $0.62 \pm 0.11$  respectively. The  $\mu$  was slightly larger in 1 mmol NaH<sub>2</sub>PO<sub>4</sub> with  $0.67 \pm 0.09$ , while  $\mu = 0.42 \pm 0.04$  in 1 mmol CaCl<sub>2</sub> + PBS solution which was like Muc + PBS on gold ( $0.41 \pm 0.03$ ). All salt solutions, excluding CaCl<sub>2</sub> + PBS, presented a higher  $\mu$  compared to both Muc + DiW and Muc + PBS, suggesting changes to the structural conformation of mucin in these solutions because of salt interaction. No significant differences of  $\mu$  were determined between salt types at 1 mmol concentrations.



Increasing the salt concentration to 10 mmol presented variations in  $\mu$  depending on the salt type. 10 mmol NaCl and CaCl<sub>2</sub> solutions increased  $\mu$  to  $0.68 \pm 0.06$  ( $p = 0.999$ ) and  $\mu = 0.87 \pm 0.13$  ( $p = 0.232$ ) respectively. 10 mmol KCl, NaH<sub>2</sub>PO<sub>4</sub> and CaCl<sub>2</sub> + PBS solutions were reduced  $\mu$  to  $\mu = 0.49 \pm 0.16$  ( $p = 0.947$ ),  $\mu = 0.54 \pm 0.03$  ( $p = 0.946$ ), and  $\mu = 0.42 \pm 0.05$  ( $p = 0.356$ ) respectively. Significant differences were observed between 10 mmol CaCl<sub>2</sub> and 10 mmol KCl, NaH<sub>2</sub>PO<sub>4</sub> and CaCl<sub>2</sub> + PBS solutions with significant levels of  $p = 0.004$ ,  $p = 0.024$  and  $p < 0.001$ , respectively.

Increasing the salt concentration to 100 mmol presented further variations to  $\mu$ , once again depending on the salt type. No changes were observed with 100 mmol NaCl, and NaH<sub>2</sub>PO<sub>4</sub> solutions with  $\mu = 0.69 \pm 0.15$  ( $p = 0.233$ ) and  $\mu = 0.53 \pm 0.03$  ( $p = 0.999$ ). The 100 mmol CaCl<sub>2</sub> + PBS solution increased  $\mu$  to  $\mu = 0.56 \pm 0.08$  ( $p = 0.741$ ), while  $\mu$  decreased in 100 mmol CaCl<sub>2</sub> and KCl to  $\mu = 0.69 \pm 0.16$  ( $p = 0.637$ ), and  $\mu = 0.23 \pm 0.04$  ( $p = 0.164$ ) respectively. Significant differences were observed between 100 mmol KCl mucin solutions and 100 mmol NaCl, CaCl<sub>2</sub> and CaCl<sub>2</sub> + PBS solutions with significance levels of  $p < 0.001$ ,  $p < 0.001$  and  $p = 0.018$  respectively.

An interesting behaviour was observed with the 100 mmol KCl friction curve (Figure 6-15b) where at normal loads between 0.05 – 0.25 mN a higher tangential force was observed. The resulting curve fit produced a better fit for  $\mu$ ,  $\mu_1 = 0.42 \pm 0.05$ , with  $R^2 = 0.96$  compared to  $R^2 = 0.87$  for the full data set. Above 0.25 mN to 0.50 mN the refitted curve presented a lower  $\mu$ ,  $\mu_2 = 0.11 \pm 0.01$  ( $R^2 = 0.94$ ). This suggested that under these specific conditions, higher loading improved lubrication in 100 mmol KCl mucin solutions. Furthermore, this was comparable to Muc + DiW and Muc + PBS solution lubrication on Hap surfaces, indicating a potential benefit from the addition of KCl salts at higher concentrations. Overall while salt concentration does not show significant differences in lubrication on gold for most of the salt types, it was clear that some salt types stood out as potential factors that influence lubrication. 10 mmol CaCl<sub>2</sub> and 100 mmol KCl solutions presented the largest difference to most other salts in the same concentration level which increased and decreased  $\mu$  respectively.



**Figure 6-15** Mean tangential force from tribo-tests on gold QCM-D sensors over incremental normal load lubricated in mucin + salt solutions with concentrations of 1, 10 and 100 mmol for a) NaCl, b) KCl, c) CaCl<sub>2</sub>, d) NaH<sub>2</sub>PO<sub>4</sub>, and e) CaCl<sub>2</sub> + PBS. Error bars represent variation between mean tangential force over the 3 samples for each load increment.

## 6.3 Discussion

Commercial porcine gastric mucin (PGM) has been used over the decades to simulate saliva solutions, in simulated dental and oral environments [106, 89, 298]. Use of this mucin (MUC5A), compared to lab-purified gastric mucin and other mucin types such as commercial bovine submaxillary mucin (BSM – MUC5B), has been controversial. This is attributed to the differences in sialic acid composition, structural damage and fragmentation from industrial processing, protein and inorganic salt impurities, and the inability of viscoelastic gel formation [228, 283, 225, 124]. This appears to be more important in the context of oral lubrication and associated lubrication mechanisms compared to studies relating to dental wear, corrosion, and lubrication mechanisms at the micro/macro scale. However, lab-purified gastric mucin present variations in their viscoelastic properties which vary because of non-standardised purification procedures, whereas commercial mucin can be expected to be less varied due to the controlled industrial purification procedures [124]. Commercial BSM therefore might serve as the preferred mucin alternative, given that it originates from the submaxillary gland and is more representative of salivary mucin. As commercial PGM had been used in other studies with the scope of assessing dental wear and corrosion phenomenon, this instructed initial experimental methodologies for Chapter 4. and Chapter 5. [106, 89, 298]. PGM was further investigated to complement this research. Furthermore, despite being inherently flawed, the “as-received” mucin used in this work served as a useful benchmark to assess the kinetics of protein layer formation, how different environments influenced the layer’s growth and intrinsic properties, and whether this influenced lubrication under conditions relating to mastication (direct tooth on tooth sliding).

### 6.3.1 Adsorption of commercial porcine gastric mucin onto gold and hydroxyapatite surfaces, and the influence of perturbing molecules

#### 6.3.1.1 Adsorption kinetics onto gold surfaces

#### **Recap of mucin adsorption pathways on gold**

Mucin adsorption was initially examined on gold surfaces. Gold has been previously suggested to demonstrate mirror charge properties, presenting potential sites with opposing charges to charged molecules presented to the surface when following the electrostatic model of image charges [110, 61]. This enables strong electrostatic adsorption during the initial growth phase of mucin onto gold, given presence of positive and negative sites on mucin from amine groups and sialic acid groups within carbohydrate chains respectively [97, 91, 96]. Furthermore, mucin tends to possess cysteine regions and

associated thiol groups which are known to facilitate strong covalent bonding onto gold surfaces via S-Au bonds [110, 61, 111, 125, 126]. This adsorption process has been shown to have an impact on increasing the mass adsorbed onto the surfaces of gold and increase a protein layer's resistance to elution [110, 61, 111]. However, in commercial PGM (type II) the presence of cysteine groups has been observed to be absent, due to damage in the terminal regions from industrial purification processing [228]. While cysteines are lacking within type II PGM, remnants may still exist within the peptide terminals and glycol regions to facilitate thiol-gold bonding, but to a lesser degree compared to other pathways.

Data from kinetic adsorption models suggest that chemisorption dominant pathways were mostly attributed to layer adsorptions onto gold with PSO and Elovich model fits. These exclude growth solutions with 10 and 100 mmol NaCl, 10 mmol CaCl<sub>2</sub>, and all CaCl<sub>2</sub> concentrations in PBS. In the literature there are numerous adsorption pathways for salivary protein to gold as studied by QCM-D and ellipsometry alike, both via physisorption and chemisorption [110, 61, 111, 112, 113, 117]. Salivary proteins have been shown to adsorb via electrostatic and hydrophobic interactions [110, 61, 115, 116, 91]. However, the term 'electrostatic interactions' is used broadly and does not specifically state the bonding strength associated with this type of adsorption. It may be assumed that the references to electrostatic interactions relates to the strong ionic interactions associated with chemisorption. It can therefore be inferred that the PSO and Elovich fits for mucin adsorption to gold supports the current understanding of adsorption.

#### **Impact of salt type and concentration on adsorption to gold**

Both salt type and concentration were observed to influence the rate of adsorption and total adsorbed mass. The combined salt solutions, Muc + PBS, presented the best rate of adsorption compared to all other solutions. Most notably, CaCl<sub>2</sub> salts added to Muc + DiW were observed to have the most impact on increasing the rate of adsorption whilst simultaneously reducing the adsorbed mass onto gold. Ca<sup>2+</sup> has a high affinity with mucin, and can modify its binding behaviour by enabling crosslinks between mucins [299, 110, 233]. Based on previous work in Chapter 4. Section 4.2.1, this might suggest mucin aggregation forms larger structures in solution prior to adsorption. However, the faster adsorption rate and reduced mass indicates that is not feasible when considering the Vroman effect, where smaller molecules adsorb rapidly followed by slower adsorption of larger molecules [231, 300]. As all surfaces were baselined in a non-mucin rinse solution, it could therefore be inferred that in this case a Ca<sup>2+</sup> layer was present on the surface prior to introducing the mucin solution counterpart. This preabsorbed layer could then promote rapid initial

adsorption due to the high affinity between the  $\text{Ca}^{2+}$ , which also acts to reduce overall mass growth by surface shielding and competition with surface sites.

Different behaviours observed with  $\text{CaCl}_2$  concentrations in PBS may relate to additional competition between multiple salt types and concentrations within solutions, and competition between mucin and calcium phosphate precipitates. Furthermore, the PFO model fit for  $\text{CaCl}_2 + \text{PBS}$  conditions suggests that adsorption to gold occurred from weaker electrostatic interactions. It could be hypothesised that mucin interactions with calcium phosphate precipitates may be the preferred route of interaction compared to gold. If this was the case, mucin-precipitate complexes may only form weak bond to the surface, supporting the observed physisorption pathway. This cannot be confirmed in the current work given as the mucin mass adsorbed onto hydroxyapatite is within the standard deviation of mucin adsorbed to gold in PBS conditions. Further work on both hydroxyapatite and gold surfaces with will be required to confirm this with QCM-D studies.

#### *6.3.1.2 Adsorption kinetics onto hydroxyapatite surfaces*

##### **Recap of mucin adsorption pathways on hydroxyapatite**

Hydroxyapatite surfaces possess a net negative charge, like mucin, and localised surface charges determined by the exposure of the hydroxyapatite crystal structure [68]. Calcium regions are present on 'ac' and 'bc' crystal faces which impart a positive charge in solution, while phosphate regions on 'ab' faces impart a negative charge [68]. Depending on the oral environmental conditions, mucin therefore has multiple pathways to adsorb onto the uniform, crystalline hydroxyapatite surface of the Hap QCM-D sensors. Furthermore, should mucin adsorb onto calcium regions via sialic acid or carboxylic acid groups (negatively charged groups to positively charged sites), there is also the chance of cooperative binding taking place with additional hydrogen bonding between the amine groups and the phosphate regions [129, 130].

Initial adsorption is thought to be a result of negatively charged sialic acid groups on proteins initially binding to positively charged surface calcium regions, after which H bonding may then permit coordinate bonding with other locations [130]. This is supported in the current study by the rapid adsorption in Hap P1 which shows a stronger fit with Elovich and PSO models compared to the PFO model. The adsorption at this stage is more likely to be chemisorption driven whereby calcium sites are taken up by strong electrostatic interactions. This is followed by a stronger PFO fit during the Hap P2 stage which may be attributed to a combination of coordinate bonds forming with additional H bonding and hydrophobic interactions occurring concurrently. However, given the level of model fit for

Hap 2, this may not be an adequate fit. The addition of PBS salts is shown to disrupt any physisorption, with cation interactions potentially shielding phosphate regions thus reducing H bonding, as well as altering the mucin conformation, demonstrated by the PSO adsorption fit. In the acidic environment, both citrate anions and mucin will preferably interact with  $\text{Ca}^{2+}$  at the surface while protons interact phosphate groups, disruption any physisorption processes [178].

The applications of kinetic adsorption models alone cannot be used to determine the exact pathways for adsorption. While they are useful to describe how adsorption may be occurring, additional data that measures the energy changes during adsorption would be helpful in highlighting the type of adsorption occurring. This may help in future investigations to further differentiate the mechanistic pathways for mucin adsorption.

### 6.3.2 Viscoelastic changes and rheological properties of protein layers in relation to lubrication

#### 6.3.2.1 *Changes to protein layer viscoelastic properties during adsorption*

Monitoring the changes to dissipation with respect to frequency change during layer growth and rinse cycles provides further insight into layer's formation over time. As a benchmark, the Muc + DiW layer rapidly grew a stiffer, more elastic layer followed by the growth of a softer dissipative layer. Saliva adsorption has been shown to follow a 2-phase adsorption process: an initial phase of rapid adsorption of low molecular weight proteins, followed by a slower second adsorption phase where higher molecular weight proteins (i.e. mucin) replace or anchor onto the initial layer [49, 110, 113, 301]. This creates a 2 layered structure: a rigid and compacted layer at the surface and a more diffuse layer further out. This behaviour was supported on both surfaces with the "as received" mucin solution, suggesting similarities between adsorption pathways. This could suggest mucin fragments or other protein impurities get to surface first due to their higher mobility before larger mucin subunits/structures adsorb to the surface [228]. However, additional desorption was observed on gold prior to rinsing, suggesting a restructuring of the adsorbed layer.

#### **Hypothesised PGM adsorption mechanism to gold**

Mucins adsorbed by strong electrostatic interactions possess more freedom, switching between positive and negative mirror charges on the gold surface, desorbing and reabsorbing, permitting rotational and lateral movements [117]. The movement and subsequent desorption of free mucin from the surface may free up surface sites to which three things may occur. Firstly, this could be replaced by another mucin via strong

electrostatic interactions. Secondly, this active site may drive chemisorption of mucin as a stronger S-Au bond can appropriate this location. Thirdly and finally, this site could remain unused because of the negative electrostatic repulsion of surrounding adsorbed mucin. In this system, over time the mass observed would reduce as cumulatively less mucin would be strongly bound to the gold surface. In the present study the desorption from gold during the growth phase may be attributed to conformational changes of mucin at the surface in such a way that prevents subsequent adsorption to the surface, which has been observed with salivary pellicle growth [301]. On the other hand, Barrantes et al [110] carried out similar experiments for saliva adsorption onto different surfaces using a QCM-D for a similar growth duration and no desorption was observed. The differences observed may be attributed to the more complex solutions, whole human saliva, used for these experiments. Therefore, this may suggest that, for the adsorption of a mucin layer onto gold, the presence of an ionic component in the bulk solution or additional protein/polymer may be required to prevent mucin desorption from the surface and maintain ongoing adsorption [302].

#### **Impact of salt environment on rheological properties on gold and hydroxyapatite**

The presence of individual salt concentrations and PBS salts were shown show slight changes to the layer properties during growth, generally forming a stiffer and more elastic layer compared to Muc + DiW growth. On gold, the addition of salts was observed to show no layer desorption during the growth phase, demonstrating the need for salts within a PGM solution to bolster layer adsorption to gold. The flatter gradient of dissipation/frequency curves also suggest that rigidity within the layer is enhanced by salt interactions that displace water out of the adsorbed layer [229, 230]. Similarly, the PBS salt interaction on hydroxyapatite layer formation presented an overall stiffer layer, however this still followed a two-stage adsorption process comparable to Muc + DiW on Hap, and whole human saliva [110].

#### **Impact of acid environment on rheological properties on gold and hydroxyapatite**

Interactions between Muc + Acid and hydroxyapatite are interesting, suggesting that an unstable layer formed on the surface, potentially due to dissolution of the hydroxyapatite coating. Interestingly, little mass removal occurs which might be indicative of mucin behaviour to promote remineralisation. Mucin's high affinity to  $\text{Ca}^{2+}$  is important to surface remineralisation, ensuring that a higher concentration of remains close to the surface to promote remineralisation once the pH increases above pH 5.5. Further QCM-D studies on hydroxyapatite that investigate the protective functionality of protein layers may therefore be useful in further development of saliva substitutes with an anti-corrosion benefit.

### *6.3.2.2 Viscoelastic modelled properties and suggested layer composition*

Viscoelastic modelling of layer properties aimed to further examine prediction on mucin layer composition and the role of salts on layer hydration. Mucin is the third most abundant protein within whole human saliva, accounting to between 4.5 – 17.5% of the total protein content [303]. In contrast to this, commercial mucin (PGM type II) has been observed a proportion of mucin (MUC5AC) within this range, calculated to be 7 % by one study [228]. When modelled properties are compared between the layer properties of whole human saliva in the literature, and PGM in this study, similarities are observed. In one study whole human saliva layers on gold displayed a shear modulus of 14.2 kPa, and viscosity of 1500  $\mu\text{Pa}\cdot\text{s}$ , and thickness of 23.7 nm whereas whole saliva layers on hydroxyapatite displayed a shear modulus of 170 kPa, viscosity of 2700  $\mu\text{Pa}\cdot\text{s}$  and thickness of 9.8 nm [110]. The adsorption of Muc + PBS onto gold in this work was like whole human saliva adsorption, regarding thickness and viscosity behaviour. However, on hydroxyapatite the properties for Muc + DiW were closer the properties observed for whole human saliva in the literature. This supports the choice of PGM as an artificial saliva component, given the similarities in the viscoelasticity of protein layers formed by saliva and PGM [304].

Differences can be attributed to the fact that in this study mucin was examined in the absence of other precursor salivary proteins, with the presence of inorganic salt and protein impurities [228]. By not controlling the size of mucin in the growth solutions, the adsorption behaviour was hypothesised to mimic the adsorption pathways of saliva where smaller sized mucin fragments, or other protein impurities initiate adsorption onto both Hap and gold surfaces followed by larger mucin polymers/aggregates that replace or co-mingle with bound surface proteins [231].

Gold and hydroxyapatite surfaces both show key differences between shear modulus and viscosity properties within Muc + DiW layers, supporting differences in adsorption kinetics, and suggesting differences in layer structure. The addition of individual salts components to the “as-received” PGM solution (NaCl, KCl,  $\text{NaH}_2\text{PO}_4$ ,  $\text{CaCl}_2$ ) were shown to increase layer shear modulus and viscosity compared to Muc + DiW, indicating a more compact layer with stronger surface attachment that varied with salt concentration [110]. With combined salts (Muc + PBS), both shear modulus and viscosity were comparable to Muc + DiW on gold, but very different hydroxyapatite. Overall, it appeared that a fine balance between salt type and concentration was required, in addition to surface material, to influence the viscoelastic properties of PGM layers. The physical meaning behind these properties will be discussed in the next section, with a focus on what these properties mean in terms of lubrication.



### 6.3.3 Linking tribology with protein layer structure

#### 6.3.3.1 *Lubrication by hydration*

The existence of water within a mucin layer is important for overall bio-lubrication of the system. When considering salivary films, the bio-lubrication has been hypothesised to link to two characteristics, the structure of the adsorbed layer and the degree of glycosylation of the proteins within the structure [109]. As the same mucin solutions were used to grow layers on both gold and Hap QCM sensors, the degree of glycosylation of mucin can be assumed to be the same in this study. In the absence of structural proteins, water alone is unable to bear the load of high-pressure contacts sliding over each other at low sliding speeds. This can result in boundary contact between interacting surfaces with opposing asperities coming into direct contact which generate larger coefficients of friction, as observed for the Hap surface. A structural component is required, in this case mucin, to effectively trap water molecules within its structure at the liquid surface interface and effectively provide viscous lubrication during sliding conditions [302].

Mucin has been previously shown to reduce the coefficient of friction compared to that of deionised water on bovine enamel surfaces [105]. As Hap is the main component of tooth enamel, it is no surprise that this reduction in tangential force and coefficient of friction occurs in the current study. As tribo-tests were performed in 0.2% mucin solutions, the structural properties at the end of the growth period were considered to describe the potential lubrication mechanism of “as-received” commercial PGM with various solution iterations. Aside from the viscoelastic property differences, the layer thickness may also be considered to determine the orientation of mucin at the surface interface, in addition to salt-induced compaction. Thicker layers were generally formed on gold compared to hydroxyapatite, with reduced shear viscosity and shear modulus properties, suggesting that ‘softer layers’ formed. One approach is to compare the layer’s structural properties in terms its viscoelasticity, by determining the ratio of the layer’s dissipation,  $\Delta D$ , and change in frequency,  $\Delta f$ , for a given overtone, which has been termed as the structural softness [109]. Physically this ratio is a measure of the energy lost due to the dampening effect of the layer per unit mass change, combining both shear elasticity and viscosity terms [204, 305].

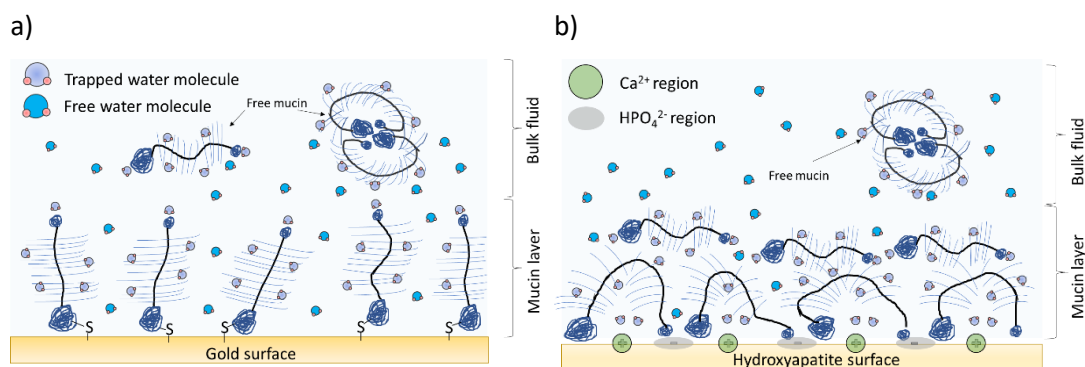
#### **Hypothesised mucin layer structure on gold**

The chemisorption pathway and subsequent desorption of the mucin layer suggested layer conformation changes occurred during the formation of the layer. This is shown by the reduced shear moduli in Figure 6-7c), indicating less interaction within the mucin layers. A “carpet fibre” mucin layer structure can therefore be considered for the gold surface, a

schematic of which is presented in Figure 6-16a). While the carbohydrate chains within mucin may trap some water to the structure, solvent flow may still be permitted throughout the layer, as well as unbound mucin/impurities. When compressed under sliding, water is not fully trapped in the contact and may be squeezed out and the resultant shear plane being closer to boundary-boundary interactions [253].

#### **Hypothesised mucin layer structure on hydroxyapatite**

Conversely, the mucin layers on the Hap surface were thinner, but exhibited a larger shear viscosity and shear modulus properties in the Muc + DiW layer. The adsorption is initially dominated by physisorption pathways with some degree of chemisorption. The more diverse bonding between mucin and hydroxyapatite may permit a stronger mucin network within the layer, forming a comparatively more rigid layer compared to what is formed on gold [302]. This is supported by a mean structural softness value of  $0.26 \pm 0.02$  which was calculated at equilibrium towards the end of the growth stage. Furthermore, the significantly larger shear viscosity of the Hap mucin layer suggests that more water molecules are trapped in the layer's structure and are less free to flow. A "bridge" like mucin layer structure can be considered, trapping water between the mucin monomer and the surface, which is presented in Figure 6-16b). This structure may also expose hydrophilic regions of mucin to the bulk fluid, permitting an extension to the hydration layer. Under sliding conditions, water is less able to flow out of the layer which may move the shear plane further away from the surface [253]. Furthermore, hydration shells of unbound mucin within the sliding contact may provide additional hydration repulsion between the mucin/Hap interface and the contacting body which in turn reduces the friction [253]. This effect may be less pronounced on the mucin/gold layer, which may explain the lack of lubrication observed for gold in the current study. These mucin structures assume mucin subunits are complete and are the only components interacting with surfaces to form hydrated layers. Further work on purified PGM would work to either support or refute this work, and the effect of protein impurities and inorganic salts can be reduced.



*Figure 6-16 Hypothesised mucin layer structure on a) gold and b) hydroxyapatite surfaces prior to sliding.*

### **Impact of salts on hypothesised mucin layer structures**

The addition of salts builds into the proposed structure when considering cations as hydration shells, integrating into the adsorbed mucin layer [253]. On gold surfaces, PBS salts had little effect the open layer structure. Muc + PBS layer shear modulus and viscosity properties were close to Muc + DiW layer properties, whilst decreasing layer thickness. This behaviour suggested that the combined salt solution did not have much of an impact on improving lubrication on gold. On the other hand, individual salt contributions appeared to have a greater effect on reducing lubrication on gold, with varying layer shear modulus and viscosity properties. NaCl, CaCl<sub>2</sub> and NaH<sub>2</sub>PO<sub>4</sub> all presented poor lubrication compared to Muc + PBS, whereas improved lubrication was observed with 10 and 100 mmol KCl mucin solutions. This indicated KCl salts were important to PGM layer lubrication compared to other salts, and may be one of the key components of PBS salts that facilitate this. Repeat work on hydroxyapatite surfaces would further determine whether this is the case. For the tests performed on hydroxyapatite, the presence of salts slightly improved lubrication, along with notable differences between shear modulus and viscosity properties. The encapsulated bridge like structure might be strengthened with hydrated salts integrated within the structure, enabling enhance load bearing properties on hydroxyapatite, supporting what was observed in Chapter 4. where hydrated mucin layers with PBS salts improved load bearing. While this may not have much of an effect on lubrication, this may enhance the protective properties of these layers, supporting the reduced wear volume and overall wear resistance observed in Chapter 5. using a Muc + PBS lubricant on bovine enamel.

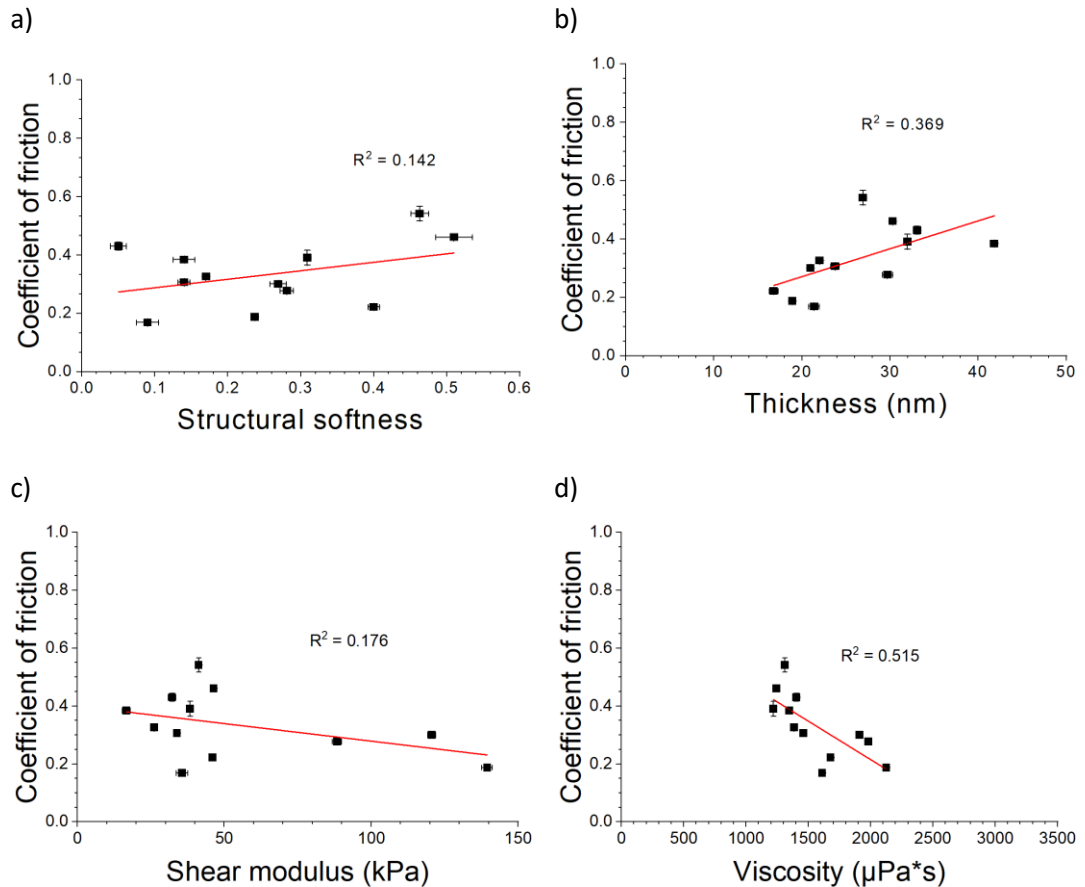
#### *6.3.3.2 Layer property relationship with friction behaviour*

Finally, to understand any possible relationship between lubrication and layer viscoelasticity the data was further scrutinised. The structural softness for hydroxyapatite results in the current study are comparable to those observed for whole saliva on the same surface in Veeregowda et al [109], which were between 0.16 – 0.23. As previously mentioned, this

viscoelasticity of salivary layers depends upon the mucin component to trap water molecules within the structure of the pellicle, as has been shown when comparing parotid and whole human saliva [301, 303, 109]. Parotid saliva does not possess a mucin component and was observed to form a more rigid layer compared to whole human saliva when examined with a QCM-D [301]. The structural softness on hydroxyapatite in the current study is outside of the range previously observed for saliva [109] and will be attributed to the additional mucin interactions with other salivary proteins that may modify the layer's structure to be more rigid [60]. Similar values were observed for bovine submaxillary mucin to PDMS in different salt concentrations, between 0.20 -0.25 [302]. The reduced competition between proteins and ions enables a more spread-out mucin structure which will impact load bearing capacity, viscous lubrication, charge density and osmotic pressure between a sliding contact [306, 253, 307]. Veeregowda et al [109] suggested that a higher structural softness and increased hydrophilicity of a protein layer might improve bio-lubrication, when examined with atomic force microscopy. Furthermore, changes to structural softness were observed in studies which modified preformed salivary films to assess the relief of dry mouth for Xerostomia patients [308, 309]. Increased structural softness was shown to improve lubrication under colloidal probe atomic force microscopy, however under a tongue-enamel friction system no changes to the coefficient of friction were observed [309]. This highlights the complexity of linking friction behaviour between the nanoscale and macroscale. Under the tongue-enamel system, increased structural softness was linked to a longer dry mouth relief period rather than an overall reduction in the coefficient of friction [308].

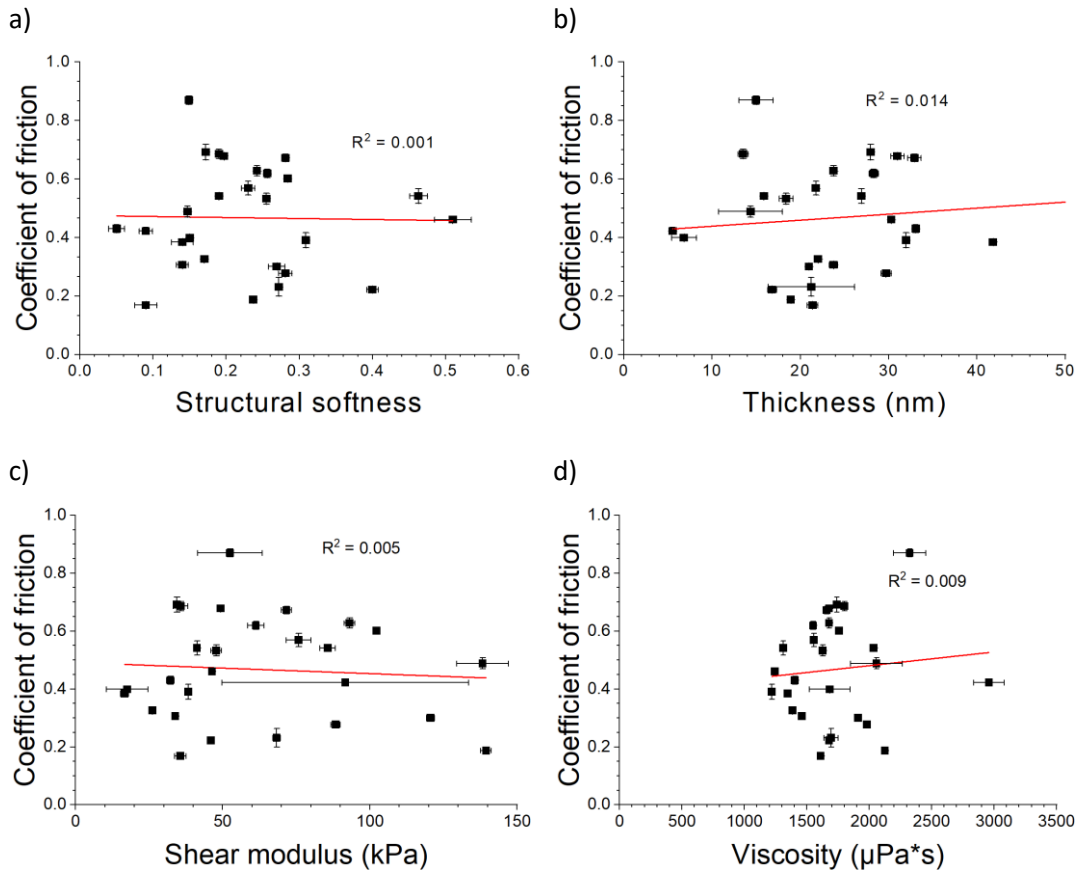
While the structural softness provides a qualitative assessment of a layer's viscoelastic properties, the calculated layer thickness, viscosity and shear modulus values may also provide additional insight. Figure 6-17b), c) and d) both show linear regression analyses comparing the measured coefficient of friction with the modelled thickness, viscosity shear modulus properties for tests performed in Muc + DiW and Muc + PBS. A weak correlation was observed between the thickness and coefficient of friction, shown in Figure 6-17b). Furthermore, a link was observed between the viscosity shown in Figure 6-17d), suggesting a lower friction result may link to viscosity. This would affect the lubricating film properties in a boundary lubrication regime, as the friction would be dependent on the viscoelasticity of the interfacial lubricating layer in addition to plastic deformation on the surface [253]. The entrapment of water within a mucin network at the surface may therefore shift the shear plane away from the surface, adopting a hydration lubrication regime similar to hydrogels. Friction behaviour of polymer hydrogels has also been observed to be influenced by elastic deformation and viscous damping components [310]. Lubrication in water was

shown to increase the viscous component of friction compared with air, and reduced the elastic deformation component of friction which reduced the overall friction force [310]. The elastic deformation of the layer was important in terms of overall friction.



**Figure 6-17** Regression analyses comparing the relationship between the coefficient of friction on gold and hydroxyapatite sensors under Muc + DiW and Muc + PBS conditions compared with a) structural softness, b) layer thickness, c) layer shear modulus, and d) layer viscosity.

However, once salts type and concentration tests were added to the regression analysis no trends were really observed, shown in Figure 6-18. Given that most tribo-tests were performed on gold surfaces, this data may be more reflective of the properties on gold surfaces. Alternatively, the salt interaction with mucin layer on hydroxyapatite were shown to have a greater observable difference in layer properties compare to Muc + DiW layer properties. This indicated that hydroxyapatite based PGM layers may be more sensitive to salt interactions, and therefore additional tribological work on hydroxyapatite surfaces with PGM, and other mucin layers may be beneficial to substantiate a link between layer viscoelasticity and lubrication. Furthermore, the structural softness should be considered with additional parameters, such as layer hydrophilicity, to further understand the link with friction in future studies. Finally, follow up studies should investigate low molecular weight mucin monomer adsorption and lubrication to gain further insight into the mechanism and impact of the initial stages of adsorption.



**Figure 6-18** Regression analyses comparing the relationship between the coefficient of friction on gold and hydroxyapatite sensors all solution conditions compared with a) structural softness, b) layer thickness, c) layer shear modulus, and d) layer viscosity.

## 6.4 Summary

The current study has shown differences in viscoelastic properties exist between mucin layers formed on gold and hydroxyapatite surfaces. Furthermore, these layers then go on to show differences in the observed friction behaviour, suggesting a potential link between layer formation and subsequent tribology. While it is suggested that a higher structural softness ratio,  $\Delta D/\Delta f$ , would provide enhanced bio-lubrication, data should also look closer at the viscosity and shear modulus properties of a layer in relation to tribological experiments. To alleviate the symptoms of xerostomia (dry mouth syndrome) and provide optimal oral protection and lubrication, further insights into potential therapies are needed. Following on from previous research to identify mucin's role on the tribocorrosion of dental tissues, this work assessed the adsorption behaviour of mucin on different dental surfaces. This included the growth and related properties of mucin layers, to gain insights into mucin's layer forming properties, and how it may link to oral lubrication. This work concludes that:

- In the absence of additional proteins and salts, mucin adsorption onto gold and hydroxyapatite was driven by surface interactions which are specific to the surface composition and may ultimately affect the resultant viscoelasticity of a fully formed mucin layer.
- The application of kinetic adsorption models in addition to  $\Delta D/\Delta f$  plots provided novel insight into the potential adsorption pathways of mucins layers onto gold and hydroxyapatite surfaces that could influence mucin layer lubrication. Stronger surface bonding is associated with mucin onto gold surfaces, while adsorption onto hydroxyapatite may be dominated by weaker physisorption mechanisms.
- Mucin layers formed on hydroxyapatite were shown to improve lubrication which may be linked to the layer's viscosity and shear modulus properties.
- This work highlighted surface materials to be a key factor in mucin layer adsorption, mucin layer properties and subsequent lubrication – namely hydroxyapatite over gold. The enamel like surface should be used for future testing of saliva and artificial saliva solutions to provide a more physiologically similar layers for in-vitro studies.

## Chapter 7. The development of an in-situ QCM-D Tribometer

### 7.1 Introduction

So far, this thesis has examined the size characteristics of PGM and the mechanical properties of mucin layers grown on tooth enamel at the nanoscale to predict how mucin may influence dental tribology. Enamel tribology was then assessed and surfaces were examined under different PGM conditions, exploring the friction, contributions to wear and the impact of testing from a surface structure and chemistry perspective. However, tribology measurements and assessment of surfaces had reached an end point, and there was a need to interrogate surface/tribological properties during mucin layer growth. To further understand the lubricating properties of the mucin layers and formation pathways, the adsorption kinetics and structural properties of mucin layers were examined under flow conditions. An indirect link was observed between the dynamic friction and the layer's structural softness, modelled viscosity and modelled shear modulus properties. To further explore this link, a more direct approach was formulated to mitigate the disturbance of mucin layers between separate testing methodologies.

The aim of this chapter was to cover the assembly and development of an in-situ QCM tribometer which could measure a mucin layer's friction behaviour and viscoelastic properties simultaneously. The bespoke tribometer (Triborig) combined a mechanical indenter test rig with an actuated sliding stage, to develop a functional reciprocating test configuration. The work in this chapter examined the load dependency of the capacitance force sensors and validity of friction results under standardised test conditions. A flow chart outlining the work and analyses completed in this chapter is presented in Figure 7-1.

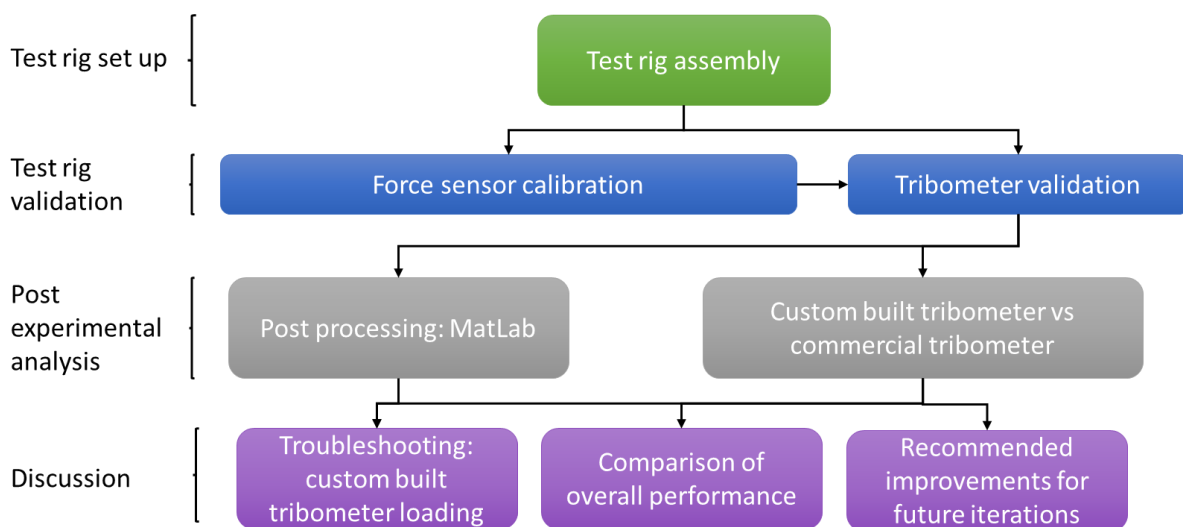


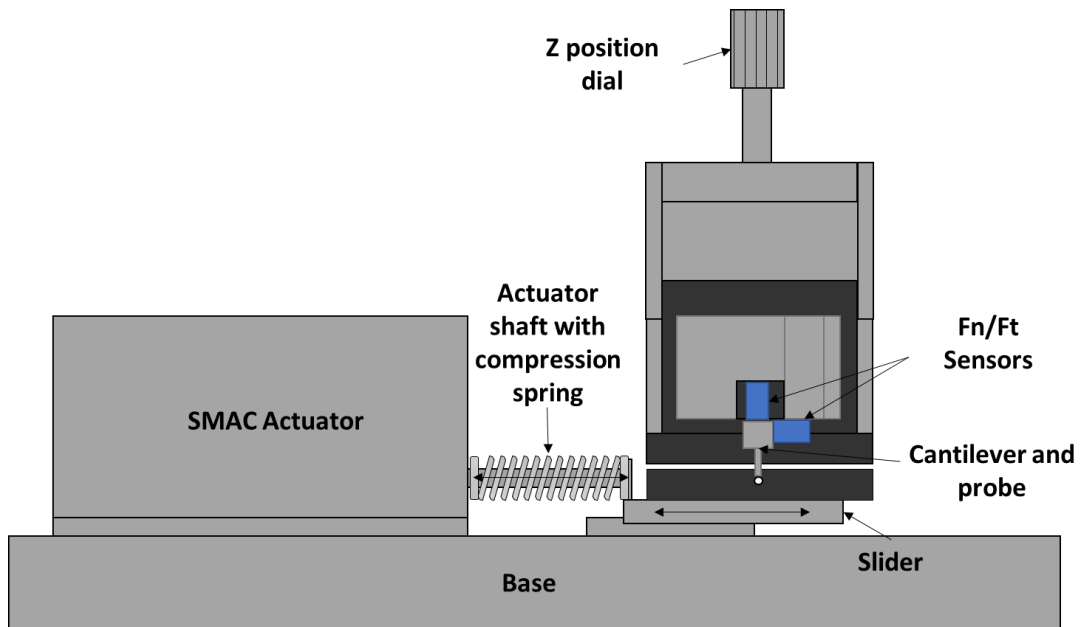
Figure 7-1 Flow chart of experimental methods and analyses Chapter 7.



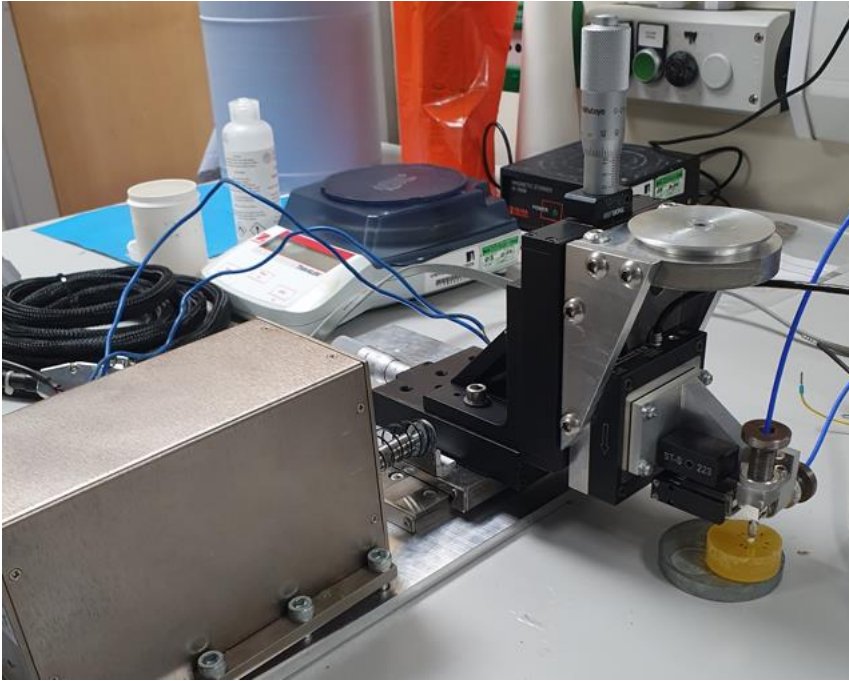
## 7.2 Triborig Instrumentation

The Triborig aimed to measure the lubrication properties of adsorbed mucin layers while the QCM-D measured the rheological properties. The setup was designed to enable benchtop friction measurements alongside a QCM-D with an open module configuration. The Triborig aimed to emulate the loading and motion achieved with the NTR<sup>3</sup> tribometer. This was for validation of the test rig and to easily compare results between the two tribometers. The design of the Triborig was advantageous, allowing a probe to move relative to a static sample. This design feature was important to accommodate the restrictions of the cumbersome QCM-D instrument and to perform tribological analyses on QCM-D sensors. Additionally, the size, weight and modular nature of the Triborig permitted relocation and fabrication of the instrument with ease within the lab-space.

Figure 7-2 shows the Triborig's schematic, Figure 7-3 shows the Triborig system and Table 7-1 details the Triborig's component specifications. The rig consisted of a bespoke mechanical indenter bolted onto a ball bearing slider stage controlled by a SMAC linear controlled actuator (LCA, SMAC Corporation, USA). The SMAC actuator-controlled stage reciprocation in the x-axis. The indenter was composed of a piezo actuated z stage (PI, Physik Instrumente, Germany) and a cantilever to mount probes.



*Figure 7-2 Schematic of the Triborig.*



*Figure 7-3 Triborig system.*

Calibrated quad beam cantilevers (Anton Paar, Austria) with a decoupled tangential and normal axis were used for this. Their stiffnesses are detailed in Table 7-1. Capacitance displacement sensors (CD, Micro-Epsilon, Germany) were placed on the top and side of the cantilever to measure the normal ( $F_n$ ) and tangential ( $F_t$ ) forces respectively. These were linear capacitive non-contact displacement sensors with a measurement range of 200  $\mu\text{m}$  and a resolution of 0.15 nm. These were chosen to provide improved sensor linearity, ( $\leq \pm 0.2\%$  full scale output) and the ability to react to very low loads. The force was based on the measured displacement of the cantilever in relation to the CD sensor,  $x$ , which was multiplied by the cantilever's stiffness,  $k$ , to provide an output force,  $F$ , in mN following Hooke's Law.

Table 7-1 System components of the Triborig.

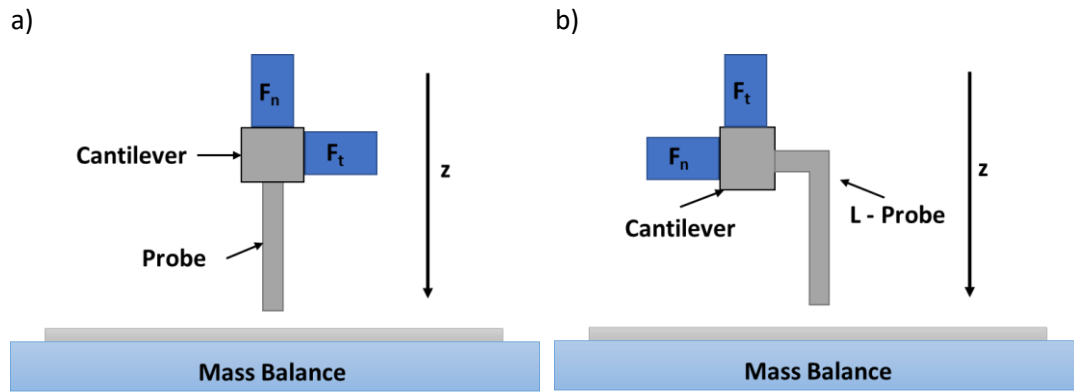
Component	Additional info
<b>Linear controlled actuator</b>	Voltage: 48V
<b>SMAC LAL95-015-85F</b>	Stroke length: 15 mm
<b>SMAC Corporation, USA</b>	Encoder resolution: 0.5 $\mu\text{m}$
<b>Capacitance displacement sensors</b>	Range: 200 $\mu\text{m}$
<b>CS02 capaNCDT 6200 system,</b>	Resolution: 0.15 nm
<b>Micro-Epsilon, Germany</b>	Linearity error: 0.2%
<b>Piezo z-stage</b>	Range: 250 $\mu\text{m}$
<b>PIHera P-622.1</b>	Resolution: 0.4 nm
<b>Physik Instrumente, Germany</b>	Linearity error: 0.02%
<b>Calibrated quad-beam cantilevers</b>	ST-S 231 calibration
<b>ST-S 231 and HR-S 220 for NTR<sup>3</sup></b>	<ul style="list-style-type: none"> <li><math>F_n</math> stiffness: 0.4808 mN/<math>\mu\text{m}</math></li> <li><math>F_t</math> stiffness: 1.1399 mN/<math>\mu\text{m}</math></li> </ul>
<b>Anton Paar, Austria</b>	HR-S 220 calibration <ul style="list-style-type: none"> <li><math>F_n</math> stiffness: 0.0591 mN/<math>\mu\text{m}</math></li> <li><math>F_t</math> stiffness: 0.1712 mN/<math>\mu\text{m}</math></li> </ul>
<b>Translation stage</b>	Actuator: micrometre dial
<b>XYZ PT3 translation stage</b>	Resolution: 0.5 mm translation per revolution
<b>Thorlabs, USA</b>	Range: 25 mm translation Engraving: 10 $\mu\text{m}$ per division
<b>Power supply unit</b>	Dual DC variable power supply
<b>Weir 4000T 30V-2A</b>	Approx. 24 V & 0.4 A output
<b>Weir Laboratory Power supplies, Unknown</b>	

The XYZ stage (Thorlabs, USA) movements were controlled manually with Z and Y micrometre dials within a 25 mm range with a resolution of 0.01 mm. The PI stage enabled finer adjustments within a 200  $\mu\text{m}$  range. The CD sensors, PI stage and LCA each had separate controllers connected to a computer, all controlled by a bespoke Triborig programme (Key Engineering Solutions LTD, UK). The output force was tared to 0 mN when the cantilever was not in contact so that any more changes to the sensor's displacement could be represented as a force.

### 7.2.1 Force sensor calibration check

A mass balance (Orion series, Bangalore) with a resolution of 0.01 g was used as a load cell to assess the loading behaviour of both normal and tangential force sensors. Two positions

were adopted to investigate the normal force ( $F_n$ ) sensor and the tangential force ( $F_t$ ) sensor. Figure 7-4 shows these configurations. To assess the normal force, the probe was loaded against the mass balance under its normal operating configuration, as shown in Figure 7-4a). The indenter stage was rotated 90° to the normal position to assess the tangential force, as shown in Figure 7-4b), and a L-shaped probe was mounted.



*Figure 7-4 Force sensor check with mass balance for a) normal force sensor loading and b) tangential force sensor loading with an L-shaped probe.*

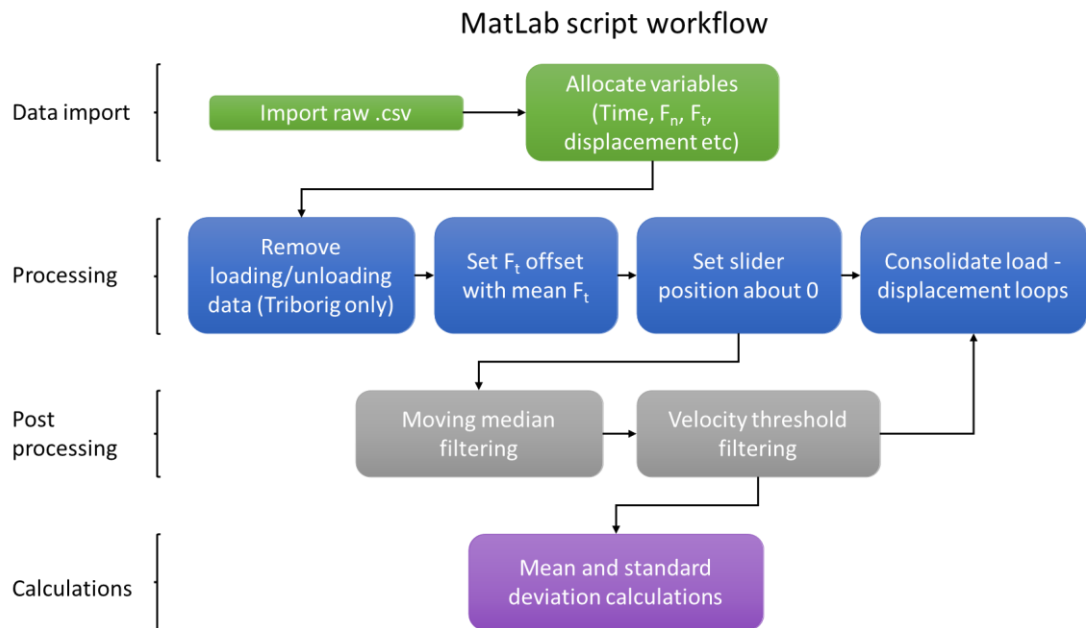
The STS-223 cantilever was used for calibration due to resolution constraints of the available mass balance. Three load sweeps were performed for each force sensor by moving the Z stage towards the mass balance in 10  $\mu\text{m}$  increments manually with the Z stage micrometre dials. Baseline mass balance readings were recorded under probe contact for each repetition. Mass readings in g (mass balance) and force output readings in mN (Triborig) were recorded at each increment and compared with the theoretical force output calculated.

### 7.2.2 Triborig validation

The micro tribometer (NTR<sup>3</sup>, Anton Paar, Austria) was used to validate the force output of the Triborig. Reciprocating sliding tests were performed on glass slides under 500  $\mu\text{L}$  deionised water (DiW) and 0.2% mucin (Muc + DiW) condition against a Y-TZP ball. A normal load sweep between 0.05 – 0.50 mN was used with 0.05 mN increments every 50 cycles. The HR-S 220 cantilever was used for both NTR<sup>3</sup> and Triborig test as the lower cantilever stiffness was preferred for QCM-D sensor tests in the next stage. The glass counter surfaces were used as a standard uniform surface that emulated the surface roughness of QCM-D sensor with an RMS roughness of less than 1 nm. The resultant coefficient of friction,  $F_n$  and  $F_t$  force outputs were compared and a regression analysis was performed.

### 7.2.3 Triborig data processing

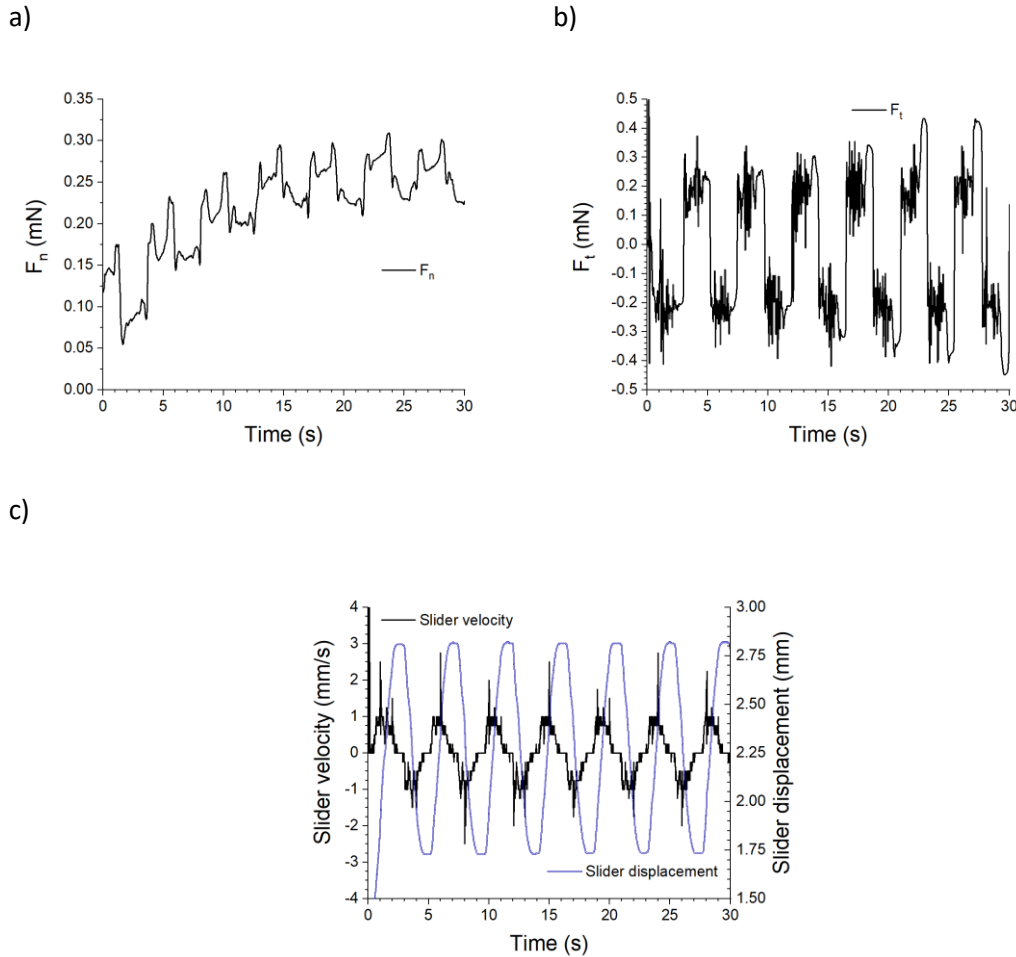
A workflow was designed to process the raw data from the NTR<sup>3</sup> and the Triborig, which was performed using MatLab (Mathworks, USA). Figure 7-5 show the workflow for the raw data processing. Raw data was in the form of a .csv file and contained the output force data from the  $F_n$  and  $F_t$  sensors in addition to slider displacement and piezo stage displacement with respect to time. For the Triborig's data, an additional step was included to remove the loading and unloading stages of the raw data when the slider was not moving, to be comparable with the NTR<sup>3</sup> data. The data was then processed further to produce load-displacement loops to understand variation throughout reciprocating cycles. To calculate mean loads during steady state sliding, a median filter was applied to remove extreme outliers, and a velocity threshold was chosen to focus only on force measurements during motion.



*Figure 7-5 Workflow diagram of MatLab script for processing NTR<sup>3</sup> and Triborig raw data.*

Figure 7-6 shows the initial 30 seconds of the test when the slider begins to move. Figure 7-6a) shows that the normal loading was delayed, as additional time is required to reach the set load of 0.25 mN. Furthermore, the loading profile exhibited an irregular shape for both trace and retrace movements. Figure 7-6b) shows the raw tangential force data and Figure 7-6c) shows the slider displacement data with the slider's velocity. Slider velocity was calculated by the change in slider displacement over the change in time. Comparing Figure 7-6b) and c) show the tangential force behaving differently when the slider is static compared dynamic sliding. To examine the dynamic friction behaviour of this system, a filter was designed to remove aspects of static friction, focusing solely on the mid cycle position.

The removal filter used the slider velocity data to remove all data where the velocity was equal to 0 mm/s.

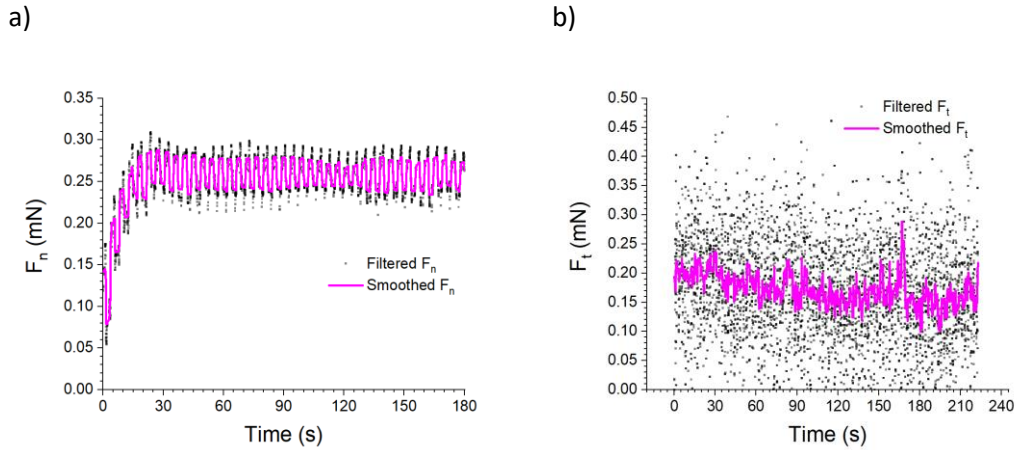


**Figure 7-6** a) Raw  $F_n$  data over time during the initial 30 seconds of Triborig testing, b) Raw  $F_t$  data over time during the initial 30 seconds of Triborig testing, and c) Raw slider displacement and calculated slider velocity, controlled by SMAC actuator over a 1.00 mm amplitude over the initial 30 seconds of Triborig testing.

To filter out some of the extreme outliers whilst also maintaining the shape of the data, a moving median filter was applied. This calculated the median based on neighbouring data points within a given data window. The data window was specified to 50 points for both Triborig and NTR<sup>3</sup> raw data. This is shown in Figure 7-7. The smoothed  $F_n$  data was then used for comparisons with NTR<sup>3</sup>  $F_n$  data and for further QCM-D Triborig work.

The  $F_t$  data required further processing as the filtered data presented both positive and negative force values about a given point. The data was offset about the mean  $F_t$  and then converted into an absolute value (changing all negative force values to positive). It was assumed that the glass slides used for validation were isotropic, presenting similar friction behaviour in all sliding directions. Therefore, the forward and reverse motion would present

a similar friction behaviour, which is why the absolute  $F_t$  was used. This was then smoothed in the same way to the  $F_n$  data. Both filtered and smoothed  $F_t$  data are displayed in Figure 7-7. The filtered data presented a lot of variation which required large window size for the median filter to get more refined output data for comparison.



**Figure 7-7 a) Filtered  $F_n$  data with static periods removed compared to smoothed  $F_n$  data and b) offset, absolute and filtered  $F_t$  data with static periods removed compared to smoothed  $F_t$  data.**

## 7.3 Results

### 7.3.1 Force sensor calibration check

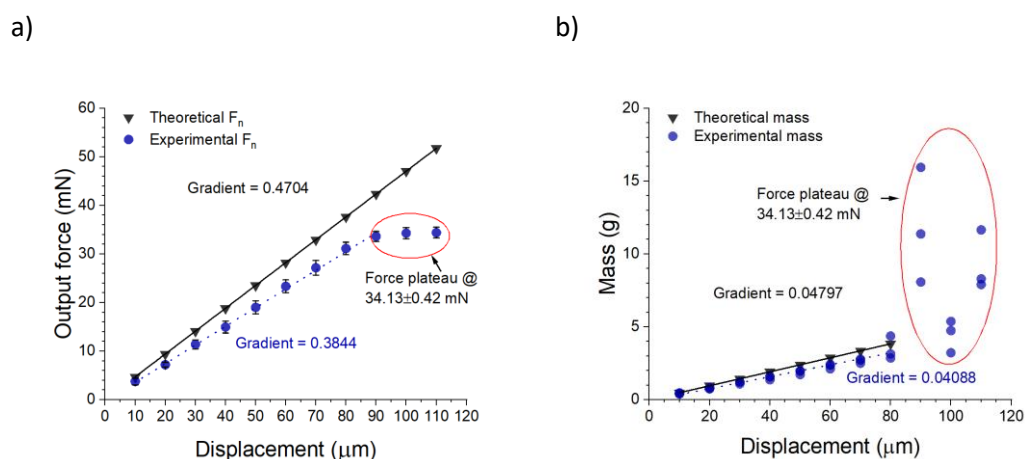
Figure 7-8a) shows the output force response with incremental probe displacement towards the mass balance compared to the theoretical force output calculated from the cantilever's calibrated  $F_n$  stiffness. A lower stiffness of  $0.3844 \text{ mN}/\mu\text{m}$  was observed experimentally compared to the previously calibrated stiffness ( $0.4704 \text{ mN}/\mu\text{m}$ ) of the cantilever, giving a percentage error of 22.4%. Furthermore, the force plateaued at  $34.13 \pm 0.42 \text{ mN}$  after  $90 \mu\text{m} \pm 10 \mu\text{m}$  displacement, which indicated the upper limit of the sensor's range where contact occurred between the cantilever and sensor.

Figure 7-8b) shows the mass balance response to the incremental probe displacement towards the mass balance. The gradient of these lines represents the ratio between the cantilever's stiffness,  $k$ , and the acceleration due to gravity,  $a$ , which was assumed to be a constant  $9.807 \text{ mN/g}$  shown in Eq. 22.

$$F = ma = kx \therefore m = \frac{k}{a}x \quad \text{Eq. 22}$$

The experimental result presented a linear relationship between the output mass response and the displacement with a gradient of  $0.04088 \text{ mN}^2/\text{g}\cdot\mu\text{m}$ , which was lower than the

theoretical gradient of  $0.04797 \text{ mN}^2/\text{g}\cdot\mu\text{m}$ . These were converted to stiffnesses of  $0.4009 \text{ mN}/\mu\text{m}$  and  $0.4704 \text{ mN}/\mu\text{m}$  for the experimental and theoretical stiffnesses respectively, giving a percentage error of 14.7%. Like Figure 7-8a, Figure 7-8b) shows the output force remained constant at  $34.13 \pm 0.42 \text{ mN}$  after  $90 \mu\text{m}$  displacement, with the mass response increasing with each  $10 \mu\text{m}$  increment hereafter.



**Figure 7-8 a) Theoretical and experimental output force vs displacement for the normal force sensor. The gradient relate relates to the cantilever stiffness in the normal direction. b) Theoretical and experimental observed mass vs normal loading.**

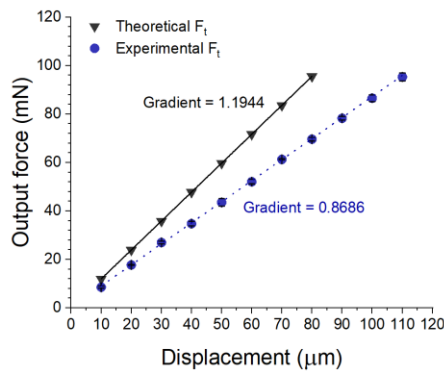
Figure 7-9a) shows the output force response to incremental probe displacement towards the mass balance compared to the theoretical force output calculated from the cantilever's calibrated  $F_t$  stiffness. Like Figure 7-8a), Figure 7-9a) shows a linear relationship between the probe's displacement and the output force. A lower stiffness of  $0.8686 \text{ mN}/\mu\text{m}$  was observed experimentally compared to the theoretical force response ( $1.1944 \text{ mN}/\mu\text{m}$ ), giving a percentage error of 27.4% for the  $F_t$  force measurement. The difference was thought to be attributed to machine compliance (impact of the entire system design and components on output force measurement), highlighting the importance of cantilever calibration on each machine. The NTR<sup>3</sup> was an overall static system, with a small reciprocating samples stage that moved in relation to a static cantilever probe system that moved only in the Z direction. The Triborig differed in configuration, where the whole system moved on a slider stage relative to a static sample outside the system, providing an additional degree of freedom to the cantilever system and additional stage connections. Any cantilever calibrated on the NTR<sup>3</sup> would therefore not fully represent the forces within Triborig system, where the additional connections and degree of freedom would induce extra elastic body deformation and overall increased flexibility within the system which is demonstrated by the lower cantilever stiffnesses. Figure 7-9b) shows the mass balance response to the incremental probe displacement towards the mass. Linear relationships were observed between the



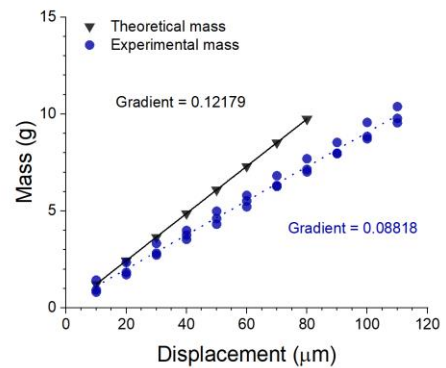
output mass response and displacement with a gradient of  $0.08818 \text{ mN}^2/\text{g}\cdot\mu\text{m}$ , converting to a stiffness of  $0.8647 \text{ mN}/\mu\text{m}$ . The percentage error of the linear relationship was 27.6 %.

The mean of the experimentally obtained percentage errors were used to approximate the  $F_n$  and  $F_t$  stiffness for the HR-S 220 cantilever, 18.55% and 27.5% respectively. The experimental  $F_n$  stiffness for the HR-S 220 cantilever was calculated to be  $0.0499 \text{ mN}/\mu\text{m}$ , and the experimental  $F_t$  stiffness was calculated to be  $0.1342 \text{ mN}/\mu\text{m}$ . These constants were applied for all remaining Triborig tests with the HR-S 220 cantilever.

a)



b)

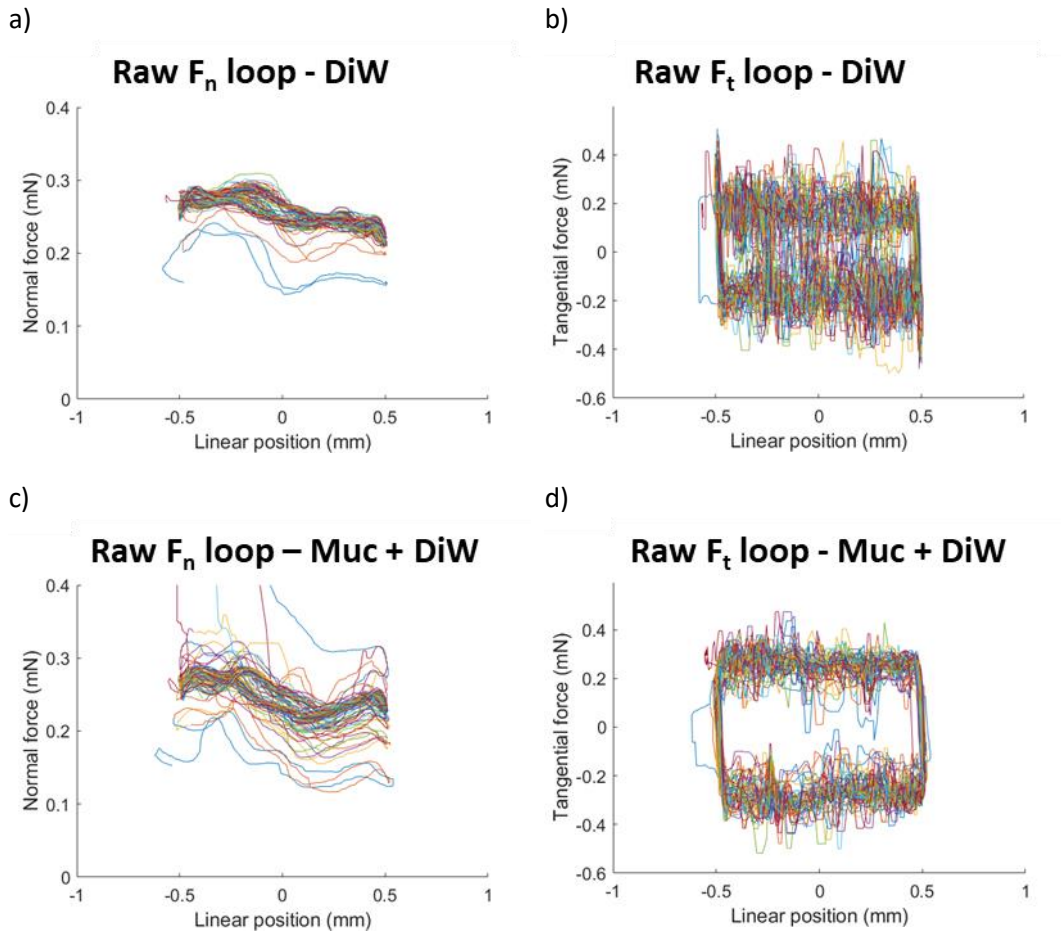


**Figure 7-9 a) Theoretical and experimental Output force vs displacement for the tangential force sensor. The gradient relate relates to the cantilever stiffness in the tangential direction. b) Theoretical and experimental observed mass vs tangential loading.**

### 7.3.2 Validation of the Triborig with the NTR<sup>3</sup>

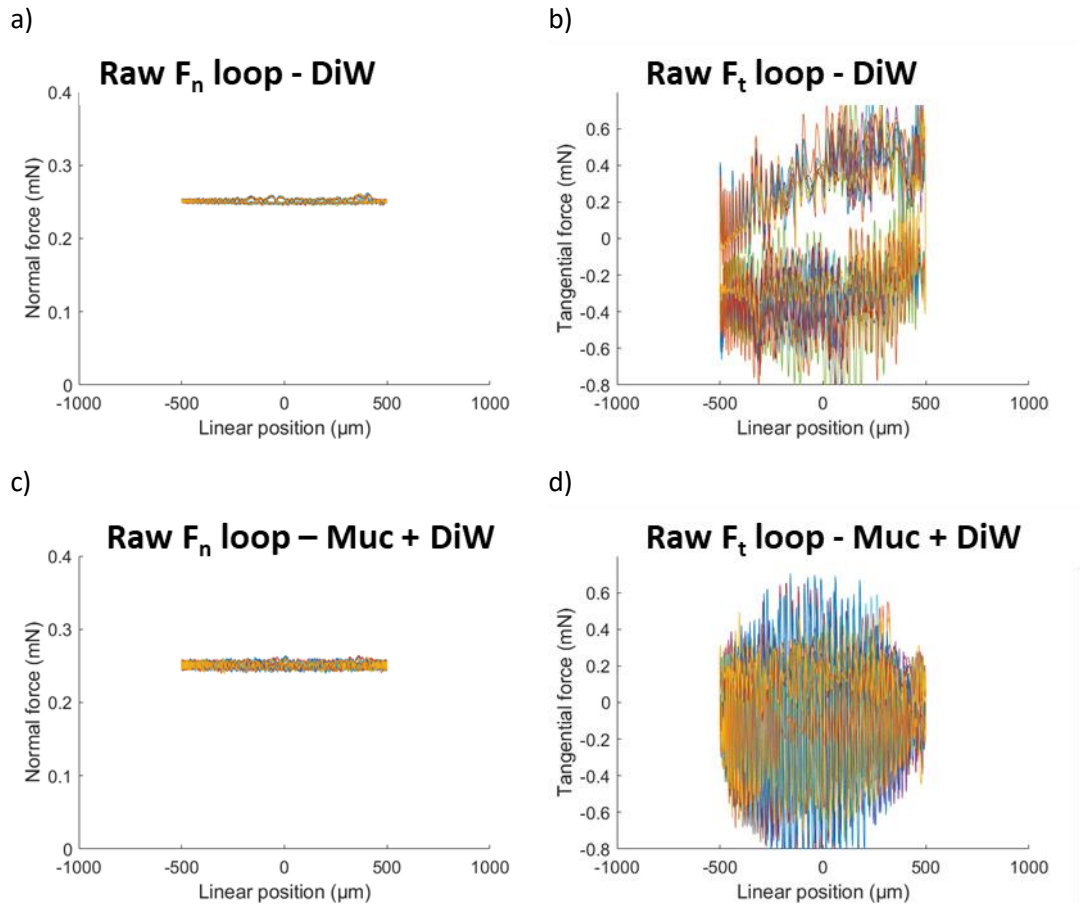
#### 7.3.2.1 Workflow validation

Initially the raw data from the Triborig and NTR<sup>3</sup> was examined using a MatLab script. Figure 7-10 and Figure 7-11 show the raw force displacement loops at  $0.25 \text{ mN}$  normal loading for the Triborig and NTR<sup>3</sup> respectively; a) and b) show the  $F_n$  and  $F_t$  response in DiW, while c) and d) show the same output in Muc + DiW. The first few cycles of the Triborig demonstrated that the system had not reached the desired normal load setpoint at the start of testing, highlighting the importance of taking the mean force measurement after this threshold. This also indicated a potential issue with the loading control settings during each cycle, which was attributed to feedback settings on the PID controller.



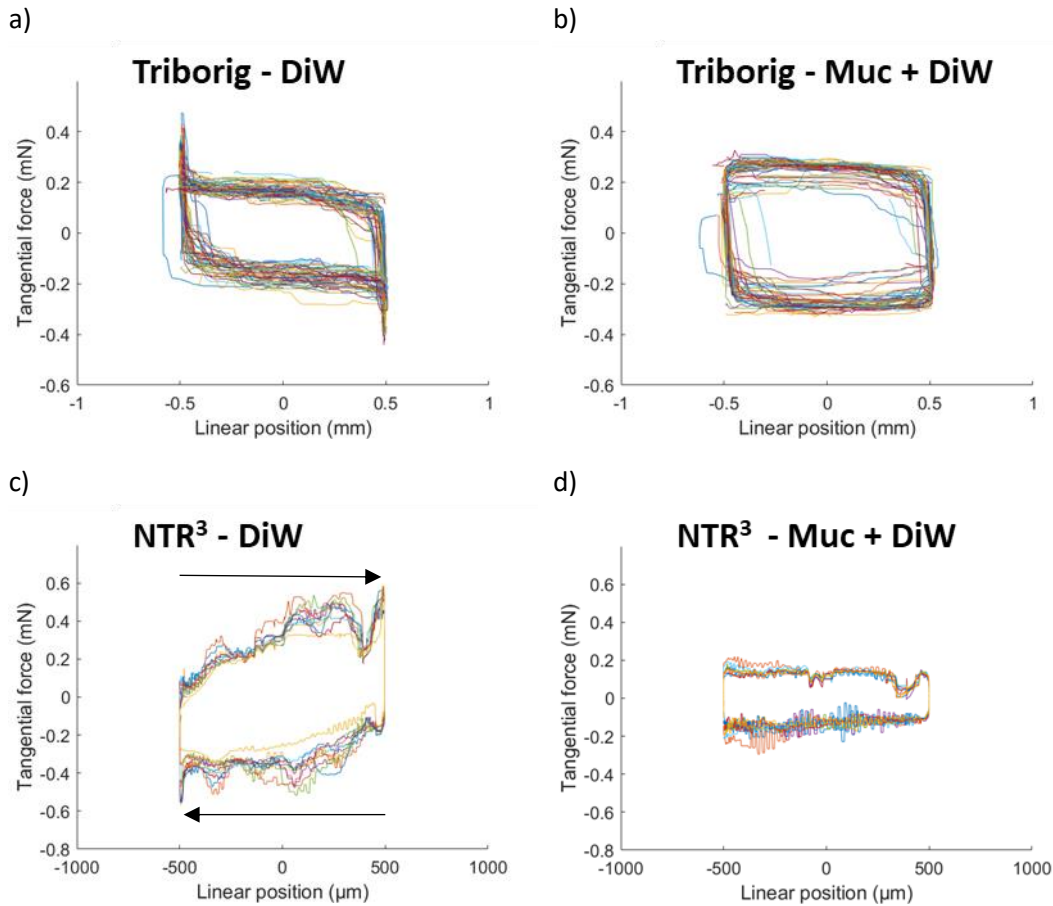
**Figure 7-10** Raw Triborig friction loops under 0.25 mN loading, showing force output over linear position for several cycles. Presenting raw a)  $F_n$  loop in DiW, b)  $F_t$  loop in DiW, c)  $F_n$  in Muc + DiW and d)  $F_t$  in Muc + DiW. The coloured lines differentiate each cycle.

The Triborig's  $F_n$  response in Figure 7-10 was not shown to be consistent within the displacement loops, exhibiting hysteresis and a visible slant where the force was greater towards -0.5 mm compared to 0.5 mm. In contrast, the NTR<sup>3</sup>'s  $F_n$  response in Figure 7-11 shows a consistent applied force with no visible hysteresis and slanting. The NTR<sup>3</sup> was able to achieve the desired load setpoint prior to data acquisition. Both NTR<sup>3</sup> and Triborig show noise within the  $F_t$  displacement loops, which was observed to be greater with the NTR<sup>3</sup> due to the 400 Hz acquisition frequency capturing more of the noise within the data, demonstrated in Figure 7-11b) and d).



*Figure 7-11 Raw NTR<sup>3</sup> friction loops under 0.25 mN loading, showing force output over linear position for several cycles. Presenting raw a)  $F_n$  loop in DiW, b)  $F_t$  loop in DiW, c)  $F_n$  in Muc + DiW and d)  $F_t$  in Muc + DiW.*

Figure 7-12 shows the output  $F_t$  displacement loops for the Triborig and NTR<sup>3</sup> after median filtering, for both DiW and Muc + DiW tests. The Triborig's  $F_t$  load displacement behaviour presented load spikes at either end of loop (Figure 7-12a), which suggest stick slip under DiW conditions for this set up. This behaviour was not observed with the NTR<sup>3</sup> under the same conditions (Figure 7-12c). Under the same conditions the NTR<sup>3</sup> presented a slanted load displacement behaviour, with the  $F_t$  load increasing over the linear displacement of the loop, shown by the arrows in Figure 7-12c).



**Figure 7-12**  $F_t$  loops under 0.25 mN loading, smoothed with a median filter using a window size of 50 to remove excess noise. Smoothed Triborig  $F_t$  loops are shown for conditions in a) DiW and b) Muc + DiW. Smoothed NTR<sup>3</sup>  $F_t$  loops are shown for conditions in c) DiW and d) Muc + DiW.

Furthermore, the NTR<sup>3</sup> presented a characteristic drop in  $F_t$  between 400-500 μm, observed in Figure 7-12c) and d). The drop in the  $F_t$  in the forward trace was thought to be attributed to the deceleration of the probe before changing direction, as highlighted by the red circle in Figure 7-13. This was observed to be a feature of the NTR<sup>3</sup> system independent of the Y-TZP probe, glass substrate and test environment. The underlying cause of this issue was not determined through this work, and for the purpose of comparison with the Triborig this area was excluded to focus on the central region of steady state sliding.

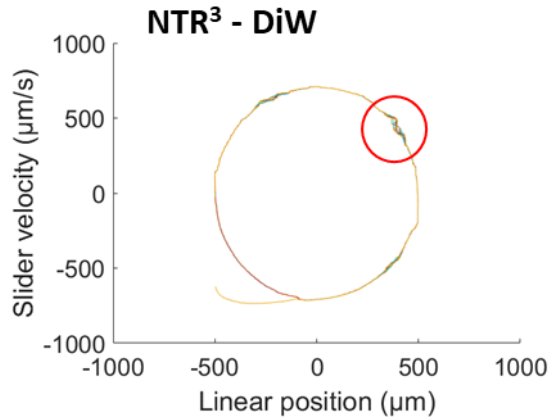


Figure 7-13 Velocity loop under 0.25 mN loading for the NTR<sup>3</sup> under DiW conditions. The red circle indicates where the velocity profile fluctuated towards the end of the NTR<sup>3</sup>'s forward trace, corresponding to the  $F_t$  drop in Figure 7-12c) and d).

To ensure the MatLab script was valid, the mean  $F_n$  and  $F_t$  results from the NTR<sup>3</sup> were exported and compared with the MatLab processed data, which is shown in Figure 7-14. The mean  $F_n$  and  $F_t$ , calculated by MatLab, were 5-6% different to the mean forces calculated by the built in Anton Paar algorithm. Furthermore, the coefficient of friction, determined by the gradient, were also similar. This indicated that the MatLab script was valid for processing the NTR<sup>3</sup>'s data, and was therefore suitable for the Triborig which followed the same workflow. This indicated that that the MatLab process was valid for processing the data in a similar way to the Anton Paar algorithm.

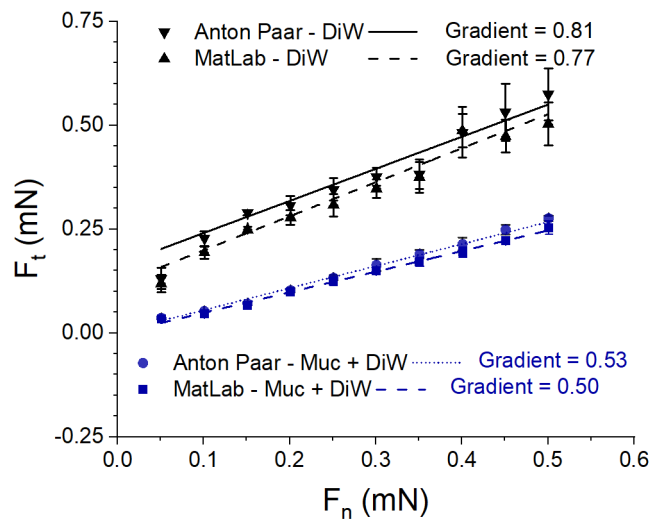
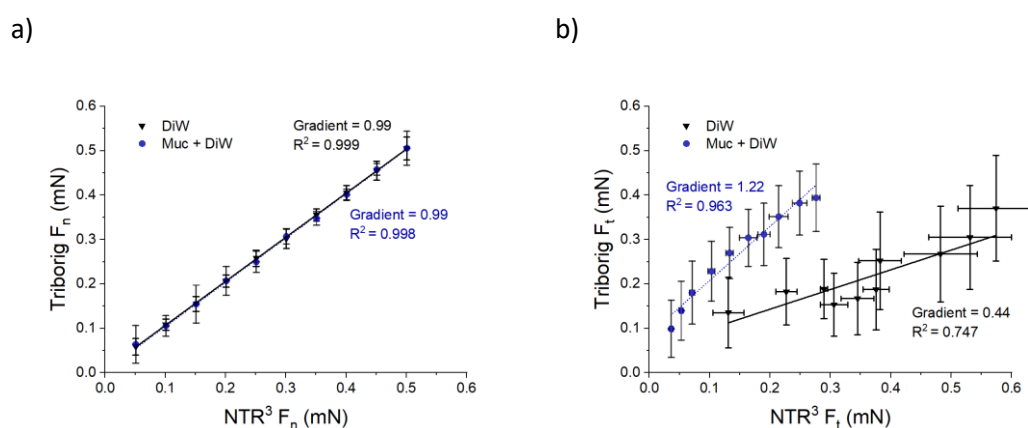


Figure 7-14 Comparison of Anton Paar's built-in algorithm to calculate the mean  $F_t$  compared to the MatLab scripted algorithm which processed the NTR<sup>3</sup>'s raw data. Figure shows results for DiW and Muc + DiW over the 0.05-0.50 mN loading range.

### 7.3.2.2 Tribometer validation

Figure 7-15a) compares the output  $F_n$  force for load dependent tribology tests with a Y-TZP ball on a glass substrate, performed on the NTR<sup>3</sup> and the Triborig. Despite the variable  $F_n$  force observed for the force displacement loops, the mean  $F_n$  from the force displacement data was comparable to the same data acquired from the NTR<sup>3</sup>. The regression lines for tests performed in DiW and Muc + DiW solutions both show a good linear fit between with  $R^2$  values of 0.99. This validated the normal force output of the Triborig for future experimentation with the QCM-D open module.



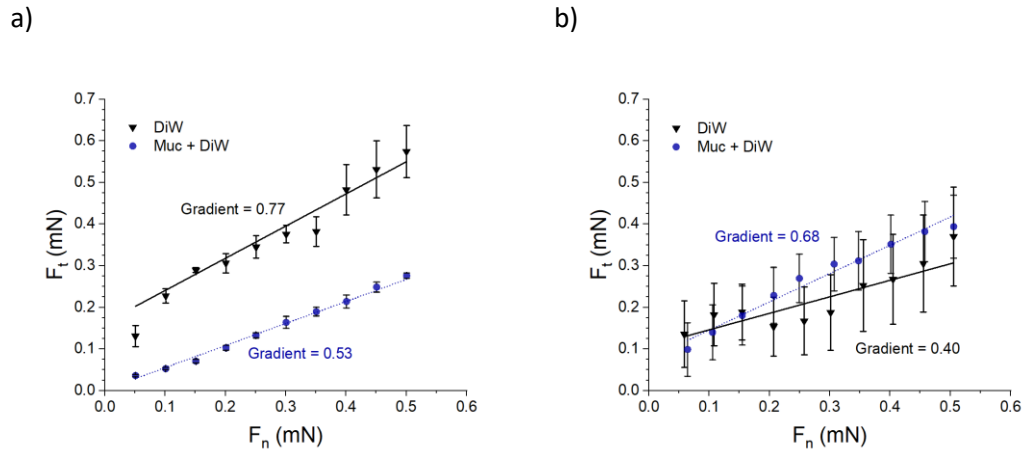
**Figure 7-15** Regression analysis comparing a) output  $F_n$  for NTR<sup>3</sup> and Triborig with SD bars for both rigs and b) output  $F_t$  for NTR<sup>3</sup> and Triborig with SD bars for both rigs. Tests were performed with a Y-TZP ball against on a glass substrate in DiW and Muc + DiW solutions. Mean and SD were taken from the last 20 cycles of each loading increment.

Figure 7-15b) compares the output  $F_t$  force for load dependent tribology tests with a Y-TZP ball on a glass substrate, performed on the NTR<sup>3</sup> and the Triborig. The output  $F_t$  force presented larger variations in the data from both rigs as shown by the error bars in Figure 7-15b). Regression lines for tests performed in DiW and Muc + DiW presented  $R^2$  values of 0.96 and 0.75 respectively. Furthermore, different behaviours were observed to be dependent on the lubricating solution used. In DiW tests, the Triborig's  $F_t$  was approximately 0.44 times the NTR<sup>3</sup>'s  $F_t$ . While in Muc + DiW tests, the Triborig's  $F_t$  was approximately 1.22 times more than the NTR<sup>3</sup>'s  $F_t$ .

This  $F_t$  behaviour has been observed with the NTR<sup>3</sup> in previous chapters, where the  $F_t$  was reduced with the application of Muc + DiW, decreasing the overall coefficient of friction on both bovine enamel and QCM-D sensors. However, this behaviour was not observed by the Triborig. This was further evidenced by the relationships between  $F_n$  and  $F_t$  for the NTR<sup>3</sup> and the Triborig, presented in Figure 7-16a) and Figure 7-16b) respectively.

Figure 7-16a) shows Muc + DiW reduced the coefficient of friction, from 0.77 to 0.53. This indicated that lubrication improved with mucin in the aqueous environment when tested

with the NTR<sup>3</sup>. On the other hand, Figure 7-16b) shows that both DiW, and Muc + DiW show no real difference as the error within both data sets overlap. Based on the tests conducted, no measurable difference could be inferred.



**Figure 7-16 Mean tangential force with SD bars over incremental load with a) the NTR<sup>3</sup> under DiW and Muc + DiW conditions on a glass substrate, and b) the Triborig under the same conditions. Mean and SD were taken from the last 20 cycles of each loading increment.**

A closer examination of Figure 7-16 showed data had deviation from the linear fit, shown by DiW in Figure 7-16a) and both solutions in Figure 7-16b). To rectify this with the data fit, different linear fits were chosen to ignore loading below 0.20 mN for both solutions with both the Triborig and NTR<sup>3</sup>. This is shown in Figure 7-17. The effective coefficient of friction (the ratio of the tangential and normal force at each load increment) was larger for both NTR<sup>3</sup> tests in DiW and Triborig tests in Muc + DiW compared to the other respective test rig. However, the load dependent coefficient of friction (the gradients in Figure 7-17) was observed to be the same under Muc + DiW, 0.57, and lower than DiW tests on the same test rig. DiW tests with the NTR<sup>3</sup> were further split due to the  $F_t$  behaviour over the loading range between 0.20-0.35 mN and 0.35 mN to 0.50 mN. The higher coefficient of friction, 1.33, at the higher loading range was not observed on the Triborig.

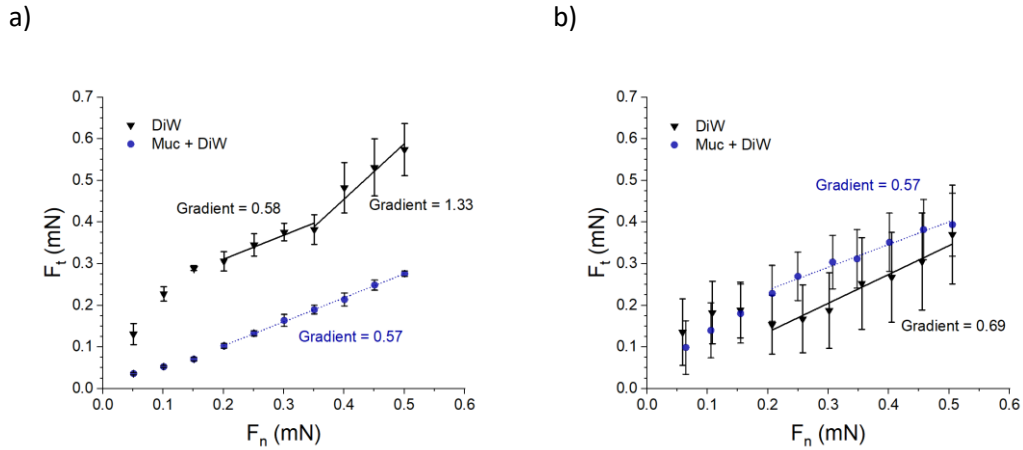


Figure 7-17 Mean tangential force with SD bars over incremental load (ignoring loads < 0.20 mN) with a) the NTR<sup>3</sup> under DiW and Muc + DiW conditions on a glass substrate, and b) the Triborig under the same conditions. Mean and SD were taken from the last 20 cycles of each loading increment.

Having shown an improved fitting for both systems when excluding the lower loading range, the tangential force regression analysis was revisited for validation. Figure 7-18 shows the tangential force output comparison between the NTR<sup>3</sup> and Triborig once more, but with linear fits excluding the lower range of acquired data. An improved linear fit was observed for both DiW and Muc + DiW  $F_t$  outputs, with  $R^2 = 0.93$  and  $R^2 = 0.98$  respectively. While it could be inferred that the DiW result could also be fitted by a horizontal line with the residual error, both gradients of the mean data were closer to 1.00 than they were previously, 0.75 for DiW and 0.95 for Muc + DiW. This was an acceptable margin for Triborig validation with the HR-S cantilever for normal loads above 0.20 mN.

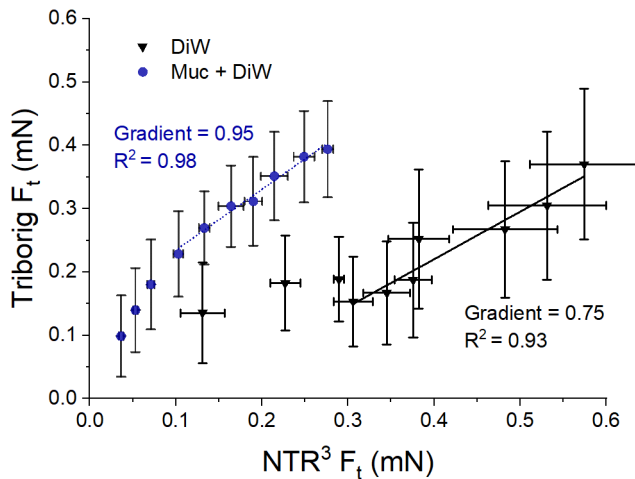


Figure 7-18 Regression analysis comparing output  $F_t$  for NTR<sup>3</sup> and Triborig with SD bars for both rigs, ignoring the output  $F_t$  corresponding to the  $F_n$  range 0.05 – 0.15 mN. Tests were performed with a Y-TZP ball against on a glass substrate in DiW and Muc + DiW solutions. Mean and SD were taken from the last 20 cycles of each loading increment.



## 7.4 Discussion

The development of the in-situ QCM-D tribometer was essential to directly observe the interaction between mucin film formation and its tribology. This required two separate experimental rigs to be arranged together, the QCM-D and the portable Triborig. Both components had their own merits and limitations when it came to functionality; this subsection aims to explore what worked and suggest improvements for future design iterations.

### 7.4.1.1 *Pre-loading limitations and troubleshooting*

The Triborig was converted from a bespoke indentation test rig with the addition of a slider stage, mounting system, and tangential force sensor. Limitations emerged relating to the pre-test loading and loading control during the first few cycles of Triborig experiments. Before testing, the cantilever's position needed to be adjusted to ensure any displacements would not exceed the sensor's working range. The caveat was that this could only be performed on the sensor manufacturer's software which couldn't be accessed when the Triborig's software was operational. Furthermore, there was no clear indicator of the probe contacting the surface on the Triborig's software. This required the user to switch between both programmes to ensure the sensors were within range for a given test, which increased the lab time required for testing.

Prior to the stage movement the normal load was expected to reach its loading setpoint within a set time based on the chosen loading rate of 0.01 mN/s. Instead, loading continued after the expected time threshold and the sliding stage started to move at this point. This behaviour suggested the loading rate was lower than 0.01 mN/s, therefore the software wrongly assumed the load setpoint had been earlier. To improve on this, the normal force should be monitored as a loading threshold before triggering slider movement.

The NTR<sup>3</sup> overcame both limitations, as controlling the sensor's range was a built-in feature to the experimental set up prior to testing. Furthermore, lowering the probe was not an issue with the NTR<sup>3</sup> as a contact load was pre assigned to notify the user when the probe had surpassed this threshold. Finally, the NTR<sup>3</sup> started data acquisition when the sample loading had reached the load setpoint. These features should be considered to further improve the Triborig's usability.

#### 7.4.1.2 Performance of the Triborig vs the NTR

##### Sensor calibration

One of the key differences between the NTR<sup>3</sup> and Triborig is the sliding stage configuration. For the NTR<sup>3</sup> the glass slide was mounted onto a reciprocating stage which moved relative to a static probe mounted to NTR<sup>3</sup> system. The Triborig moved relative to a static glass sample, as the whole system was mounted to a sliding stage controlled by an actuator. Differences between the two system configurations will have influenced the output force measurement independent of the precalibrated cantilevers and software design. System calibration was completed with the ST-S cantilever for the purposes of assessing the system and software's performance. The HR-S 220 cantilever was used for tribometer validation work, and was not directly calibrated as a system. A more robust and accurate calibration system was required relative to this cantilever's stiffness; a higher resolution mass balance or load cell was not sourced. Therefore, the manufacturer's pre calibrated stiffnesses for the HR-S cantilever were weighted to mirror the effects from machine compliance with the ST-S cantilever/Triborig system. This served as an indirect form of calibration given the constraints doing the same calibration with the HR-S cantilever/Triborig system. An alternative solution would be to emulate the processes used in AFM imaging, where a series of indentations are made on a sapphire reference sample and the stiffness of the cantilever is calculated from the force-displacement response. System calibration should also be considered before NTR<sup>3</sup> tests to provide confidence in the pre-determined stiffness values.

##### Force output comparison

The performance of the Triborig was assessed against the NTR<sup>3</sup> by comparing the mean  $F_n$  and  $F_t$  output of both test rigs during standard load sweep experiments on glass substrates. Using the MatLab workflow, mean  $F_n$  and  $F_t$  forces were calculated from each force-displacement loop over the final steady state cycles of Triborig and NTR<sup>3</sup> tests. The Triborig's  $F_n$  response was validated by the NTR<sup>3</sup>, showing a very good relationship in the regression analysis (gradient = 0.99 &  $R^2 = 0.99$ ) under both test conditions. The Triborig's  $F_t$  response was also validated by the NTR<sup>3</sup> with limitations, shown in Figure 7-18. Under mucin conditions, a good relationship was observed in the regression analysis (gradient = 0.95 &  $R^2 = 0.98$ ) for normal loads greater than 0.20 mN. Under the same loading limitations in DiW, a good relationship was observed but a less strong one (gradient = 0.75 &  $R^2 = 0.93$ ). Similarities were observed between the Triborig and NTR<sup>3</sup> when the dynamic coefficient of friction for both DiW, and Muc + DiW. However, no differences could be measured between the effective coefficient of friction between DiW and Muc + DiW on the Triborig as the SD

error bars overlapped in all  $F_n$  instances. This posed a potential issue in terms of validating the Triborig as a system, as the mirrored experiments using the NTR, other work within this thesis and the literature have shown that mucin reduces friction compared to DiW alone [105, 156, 270]. It's important to address these differences in behaviour in terms of the experimental system and errors associated with it. Systematic errors were associated with the Triborig's design, cantilever calibration and the overall sensitivity of the system. Random errors were associated with uncontrollable background noise, from the operation of other equipment within the lab (air compressors, vacuum pumps etc.), which linked up with the system's sensitivity.

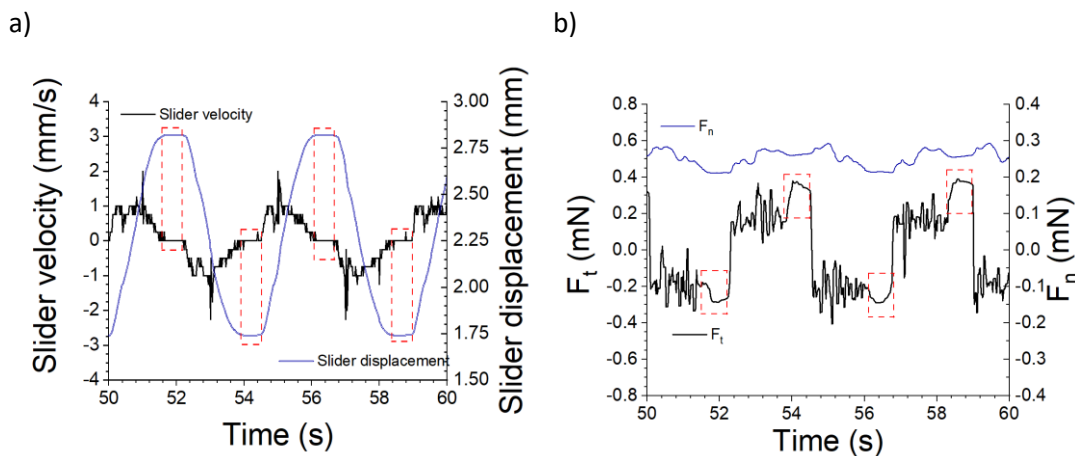
### **Acquisition frequency and data noise**

Aside from the design, the sensitivity of the HR-S 220 cantilever and acquisition frequency influenced the  $F_t$  measurements during Triborig and NTR<sup>3</sup> testing. This is demonstrated by the raw friction loops in Figure 7-10 and Figure 7-11. As very low loading was used for experiments, the use of capacitance displacement sensors was essential to detect nanometre displacements of a cantilever beam. The HR-S 220 cantilever used for validation was also 'high resolution' (defined by the manufacture) for loading from 0.005 mN up to 10 mN [311]. Together, these formed the a highly sensitive system for monitoring the force response under reciprocating sliding conditions. For validation of the Triborig, the loading was between 0.05 – 0.5 mN given the delicate nature of the QCM-D sensors that the system would eventually be tested on. The loading range was towards the cantilevers lower range, making it susceptible to random error from external noise. The NTR<sup>3</sup>'s acquisition frequency was also 8 times that of the Triborig's, 400 Hz compared to the limited 50 Hz of the Triborig system (limited by the data acquisition coding). This enabled the NTR<sup>3</sup> to be more sensitive to background noise and noise disturbances which was measured in the raw data. The test environment was also affected by uncontrolled foot traffic in addition to other users running experiments on larger, noisier test equipment. For a sensitive system such as this, additional measures should be considered to reduce the impact of external noise. One solution would be to incorporate an anti-vibration table/cabinet to house the system. While this would limit the Triborig's portability, a more robust set up and devoted test location would improve the quality of results. An alternative solution would to use a bungee system similar the one used for AFM imaging, described in Chapter 3. 3.2.5.2.

### **Triborig system design**

The Triborig was essentially a prototype tribometer meaning the overall stability of the machine was not as robust as the commercially produced NTR<sup>3</sup>. Connections were not

sufficiently shielded and were open to the lab environment; thus, communications between the PC and stage, sensors and actuator were subject to potential interference. This might have introduced internal noise within the data acquisition process, affecting the variation of collected data. Furthermore, the actuator was not fully operational; the shaft could not extend and only retract. A compression spring was used to enable shaft extension, which was crudely between the actuator body and the slider stage. This would have influenced the overall machine compliance of the system's tangential force output when the slider changed direction, characterised by a slight loss of motion slider motion. This is illustrated by red dashed boxes in Figure 7-19, showing a) the raw slider displacement, with slider velocity. These regions were ignored by the MatLab script, which only focused on the  $F_n$  and  $F_t$  data above a threshold of 25% of the set slider velocity (0.25 mm/s). Load artefacts were also observed in the  $F_t$  signal, which appear to be linked to the final deceleration of the slider/actuator before reaching a static point, illustrated by the red boxes in Figure 7-19b).



**Figure 7-19 Raw  $F_t$  and  $F_n$  output, a), from the Triborig during 0.25 mN tests on glass in Muc + DiW and b) slider displacement and slider velocity between 50 - 60 seconds of testing. Red circles indicate where spikes in the slider's velocity occurred and red dashed boxes indicate dead zones where the slider's velocity remained a 0 mm/s and the slider was static.**

The slider's velocity profile was seen to be consistent throughout testing, but unsmooth with spikes occurring at the slider's mid-point. This behaviour was thought to be attributed to the combined system resolution for speed control, which would be influenced by: Triborig loading on the slider, internal friction of the slider, connections between the slider and spring-modified actuator shaft, the actuator speed specification and operating condition, and the software's speed control design in relation to the whole system. Future considerations should be made regarding the actuator and slider mechanism to ensure smooth slider transition during tests. One approach would be to critically assess the actuator requirements for the system in terms of required force output and speed output to move the Triborig with the current slider stage, and upgrade this system component. This may also

be considered with a more robust and well lubricated slider stage, as the both actuator and slider stage movements are influence by Triborig loading. Altering the system design to consider a slider stage with a build in actuator may also be a suitable design change. Finally, whatever design is chosen should be accompanied by whole system testing to optimised the software design for the specific system.

## 7.5 Conclusion

As a prototype system, the Triborig's use was assessed in terms of its minimum viable capabilities. Despite the issues identified and discussed in this section, the Triborig was capable of functioning as a tribometer, providing data which was mostly comparable to an industrially, precision manufactured system such as the NTR<sup>3</sup> regarding  $F_n$  signal. A key limitation to the system was the  $F_t$  response at  $F_n$  loads below 0.15 mN, which provided a minimum operating load for the Triborig system be viable to work. It was decided that a load of 0.25 mN would be suitable for Tribo-QCM-D tests on QCM-D sensors. Further optimisation of the Triborig system may serve to reduce the impact of system errors with subsequent errors measure in the output force data. to optimise any future systems.

Table 7-2 summarises the Triborig features, issues and suggested improvements on the next page. Recommendations are also made on additional investigations to optimise any future systems.

*Table 7-2 Summary of Triborig design issues, improvements and investigations.*

System feature	Issue	Improvement/ Investigation
<b>Slider stage and loading</b>	Triborig's weight supported by slider, potentially more resistance to motion within the slider bearings.	Ensure slider bearings enable free movement. Investigate friction behaviour under uniform test conditions whilst loading/unloading mass to the Triborig system on the slider. Consider actuated slider.
<b>Vibration control</b>	No anti-vibration features to compensate for system sensitivity within a shared lab environment.	Implement antivibration measures like an anti-vibration table (the NTR <sup>3</sup> system has an integrated anti vibration column). An alternative to this would be to suspend the whole system from a hook with a thick bungee cable – a system which was adopted for less noisy AFM multimode imaging in Chapter 4. Consider a quieter lab environment or out of hours use to minimise traffic.
<b>Actuator</b>	Patched up with compression spring to facilitate extension.	Replace or repair actuator to perform a smooth sinusoidal velocity profile without pausing when reversing direction. Optimise speed controls by

		testing as a whole system, depending on system design
<b>Cantilever</b>	Pre-determined cantilever stiffness used with calibration weighting for Triborig, already optimised for the NTR <sup>3</sup> .	Complete a series of calibration tests in the desired test environment prior to commencing tribometer testing. Apply system calibrated stiffnesses to subsequent tests.
<b>Ease of use</b>	Timely procedure to properly set up experiments.	Improve the workflow within the Triborig's software to emulate NTR <sup>3</sup> system setting the cantilever's position within the working range. Add a contact threshold notification for user.
<b>Data acquisition</b>	Data acquisition limited to 50 Hz per displacement sensor. Sample still loading at start of tribometer test.	Adjust software/PC specification to increase data acquisition frequency cap. Use a force-based threshold to attain force setpoint, rather than time and loading rate-based force set point.
<b>PID control</b>	Triborig PID control setting not particularly responsive maintaining a constant $F_n$ during testing.	Optimised and determine best approach for PID controller settings, either by increasing the feedback sensitivity throughout the test cycle, or modifying settings to be uncontrolled throughout the cycle with adjustment to normal force every full of half cycle (while static).
<b>Output data</b>	Effective coefficient of friction differences compared under DiW and Muc + DiW solutions compared to NTR <sup>3</sup> .	Perform multiple repeats of standard glass tests in DiW and Muc + DiW, on different days with different users to assess repeatability and reproducibility of system.

## Chapter 8. The application of an in-situ QCM-D Tribometer

### 8.1 Introduction

Following on from the work of chapter 6, this chapter aimed to directly examine the trends of mucin layer viscoelasticity measured in-situ whilst simultaneously assessing the lubrication regime. Tribo-tests were performed with an aim of observing:

- the trends between friction on an established mucin layers and whether tribological interference had an observable impact on layer properties;
- the impact of layer rinsing and removal of mucin solutions on the layer properties and subsequent friction behaviour; and,
- the change in mucin layer properties over time and associated friction behaviour.

This would provide an insight into the integrity of mucin layers and build on what properties were essential in promoting optimal boundary film lubrication. This work was assess using the Triborig, developed in the previous chapter, which was paired with the QCM-D open

module and QCM-D system. A flow chart outlining the work and analyses completed in this chapter is presented in Figure 8-1.

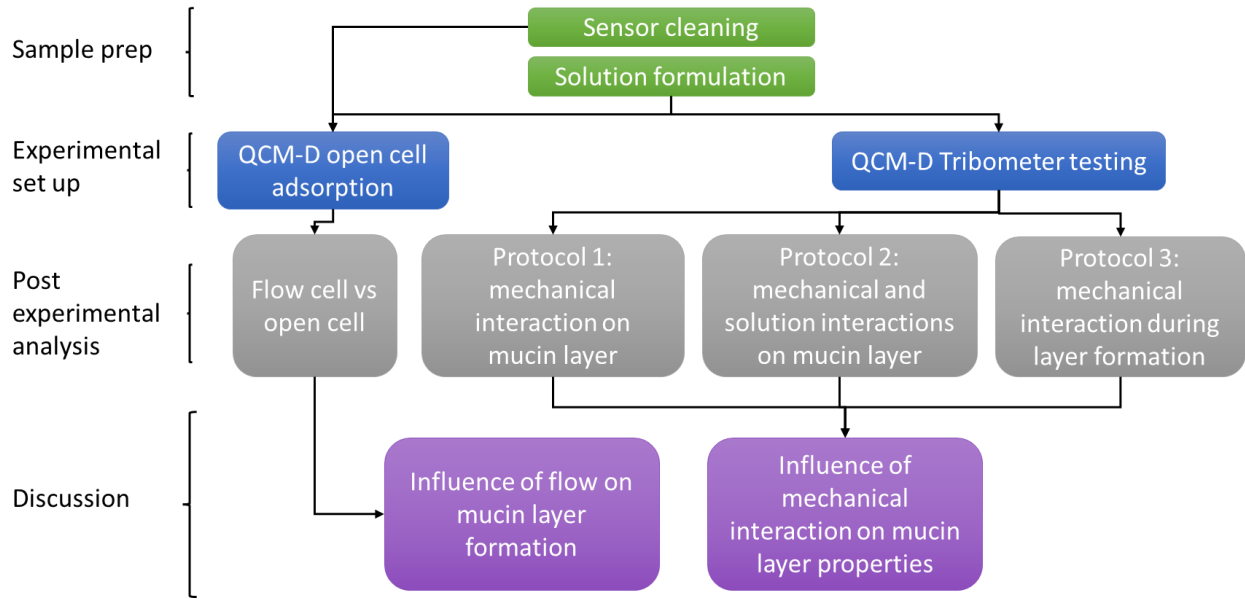
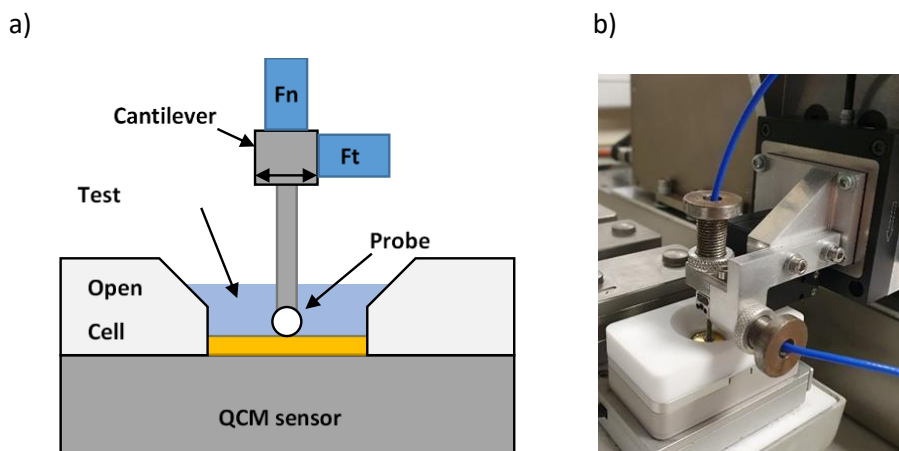


Figure 8-1 Flow chart of experimental methods and analyses Chapter 8.

## 8.2 QCM-D arrangement with Triborig

The open module allowed direct access to interact with the gold coated quartz sensor. The Triborig was positioned to allow the probe to interact with the QCM-D sensor's surface when mounted to the open module. A diagram and picture of this interaction is shown in Figure 8-2a) and b) respectively. Macroscale movements of the probe towards the sensor was controlled by the z-direction micrometre dial, while finer adjustments were controlled by the PI stage. This set up enabled tribological tests on mucin layers grown on this surface, monitored by the QCM-D. Similar to previous tribometer tests, un-used Y-TZP balls were used for each test setup, which represented the cusp of a tooth.



*Figure 8-2 Triborig interaction with QCM-D open module, a) schematic of interaction and b) image of interaction.*

### 8.2.1 Experimental protocol with QCM-D Triborig

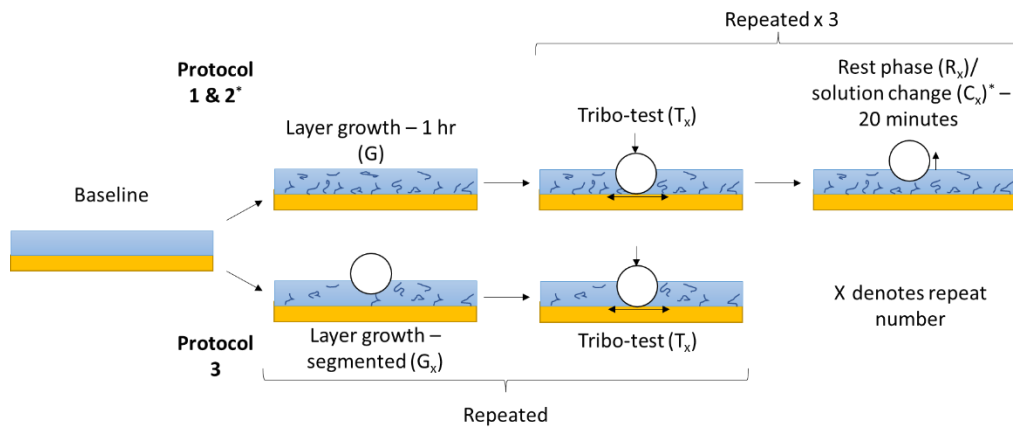
The set up aimed to examine various aspects of tribology in relation to the layer's viscoelastic and thickness properties. The following experimental protocols were chosen to investigate these mucin layers after baseline measurements were attained, shown in Table 8-1.



*Table 8-1 Experimental protocols and rationale for QCM-D Triborig after baseline attained.*

<b>Protocol</b>	<b>Rationale</b>	<b>Process</b>
<b>1)</b>	To observe the interactions between mucin film formation and tribological processes	<ol style="list-style-type: none"> <li>1. Grow mucin layers on gold for 60 minutes with a mucin growth solution;</li> <li>2. Assess tribology with Triborig in the same solution (0.25 mN for 50 cycles);</li> <li>3. Allow layer to rest after tribo-test for 20 minutes;</li> <li>4. Repeat steps 2. and 3.</li> </ol>
<b>2)</b>	To assess whether environmental changes on a mature mucin film influences mucin layer tribology	<ol style="list-style-type: none"> <li>1. Grow mucin layers on gold for 60 minutes with a mucin growth solution;</li> <li>2. Assess tribology with Triborig in the same solution (0.25 mN for 50 cycles);</li> <li>3. Rinse layer with MilliQ water after tribo-test and allow to rest for 20 minutes;</li> <li>4. Assess tribology with Triborig in the rinse solution;</li> <li>5. Rinse layer with growth solution after tribo-test and allow to rest for 20 minutes;</li> <li>6. Perform final tribo-test.</li> </ol>
<b>3)</b>	To examine the impact of tribology on mucin layer growth	<ol style="list-style-type: none"> <li>1. Grow mucin layers on gold for 5 minutes;</li> <li>2. Assess tribology with Triborig in the same solution (0.25 mN for 50 cycles);</li> <li>3. Continue layer growth;</li> <li>4. Repeat steps 2. and 3., performing tribo-tests at 15, 30, 45, and 60 minutes from test start.</li> </ol>

These three protocols aimed to provide further understanding on mucin layer removal and repair over short time periods, and whether mechanical interactions promote beneficial changes to a mucin layer. Figure 8-3 outlines the process of these experiments. Tribo-tests used the HR-S 220 cantilever ( $F_n$  stiffness -  $0.0591 \text{ mN}/\mu\text{m}$ ,  $F_t$  stiffness -  $0.1712 \text{ mN}/\mu\text{m}$ ), which was lowered to the surface at test commencement. After tests, the probe was lifted from the surface.

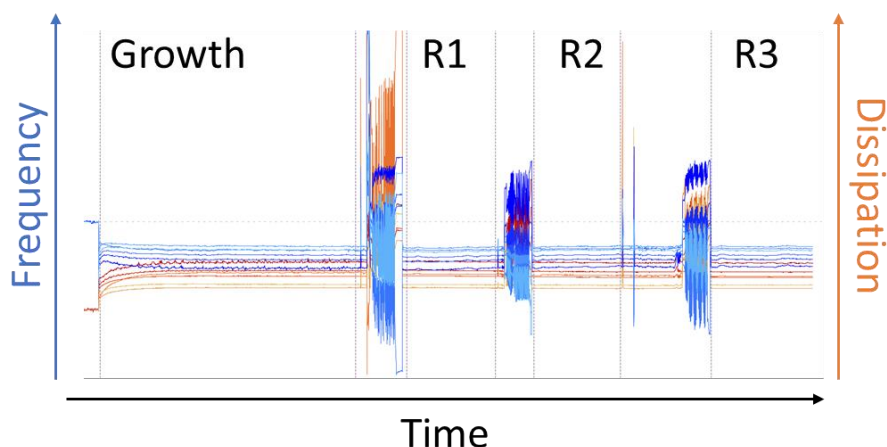


**Figure 8-3** Experimental protocols and timeline for QCM-D tribo-tests on mucin layers.

Two solutions were examined by the three protocols: Muc + DiW, and PBS solution with 0.2% mucin (Muc + PBS). A modification was made after the second rest phase of protocol 2) for the Muc + PBS tests. An additional rinse step with PBS was included before reintroducing mucin in this environment. This aimed to remove all MilliQ water and replace it with PBS to return the solution back to its baseline environment.

### 8.2.2 QCM-D data processing

The raw frequency and dissipation data required additional processing before Broadfit modelling, described in to Chapter 3. section 3.2.5.1. Figure 8-4 presents an example of the raw QCM-D data on Dfind (Qsense, Sweden) showing the frequency and dissipation data were highly sensitive to sensor interaction and tribo-tests. These regions were ignored for the viscoelastic modelling.



*Figure 8-4 Example of raw QCM-D data on Dfind software showing frequency and dissipation sensitivity during tribo-tests. R numbers represent rest phases during throughout protocol 1).*

Further analysis of the Broadfit model weighting was also performed to optimise the modelling parameters. The model's fit quality was determined by the weighted  $\chi^2$  error of the data over the test's timeline, providing a quality measure between 0-1 determined by the software. A model with a fit quality close to 1 suggested that the experimental frequency and dissipation data was very similar to the simulated results of the model. This can be affected by removing and including specific overtones used in the model, in addition to applying different model fitting weights. Adjusting the fitting weight influences the signal quality of different overtones, measure by the signal to noise ratio.

The flow module used for experiments in Chapter 6. provided a smooth signal and the default fitting weight observed to be optimal. This weighting impacted the modelled viscoelastic properties of the mucin layers. Conversely, the open module was found to be sensitive to the surrounding noise, and a suboptimal fitting quality under the default weighting. A sensitivity analysis was performed to investigate the effect of model fit weighting, with the top 3 fit qualities (default, flat FD and Mov av (3-13)) over all samples displayed in Table 8-2. To ensure consistent viscoelastic modelling of the mucin layers, the same modelling method was required for all measurement. Using the sensitivity analysis, the flat FD model, which weights all harmonics equally with a lower weighting on the 13<sup>th</sup> harmonic according to the modelling software (QSense Dfind, Biolin Scientific, Sweden), was chosen for this purpose.

*Table 8-2 Model quality for all experimental protocols using default, moving average and flat FD fitting weights.*

Solution	Protocol	Default	Mov av (3-13)	Flat FD
<b>Muc + DiW</b>	1	0.34	0.3	0.54
	2	0.72	0.92	0.56
	3	0.9	0.81	0.91
<b>Muc + PBS</b>	1	0.64	0.64	0.78
	2	0.93	0.89	0.93
	3	-0.31	0.66	0.81
<b>Mean</b>		0.54	0.70	<b>0.76</b>
<b>SD</b>		0.47	0.23	<b>0.17</b>

### 8.2.3 QCM-D module comparison

The frequency and dissipation response from the open module was compared with the flow module's response from the previous chapter to compare static and dynamic flow conditions on layer growth. System sensitivities and the modelled viscoelastic properties were also compared. Muc + DiW solution conditions were used for layer growth. The flow module followed the standard protocol documented in Chapter 3. section 3.2.5.1, while the open module followed protocol 1). The Flat FD fitting weight was applied to both data sets during viscoelastic model processing.

## 8.3 Results

### 8.3.1 QCM-D module comparison

Figure 8-5 shows the raw frequency and dissipation response for a) the flow module and b) the open module. Changing the solution from DiW to Muc + DiW presented different responses. As observed previously in the Chapter 6. , the mucin layer growth was initially rapid, followed by an adsorption limit before subsequent desorption shown by the change in frequency in Figure 8-5a). Growth within the open module presented a large initial frequency drop, followed by a brief recovery (frequency increase) and layer stabilisation for the remainder of the phase. The spread of the frequency and dissipation overtones was larger within the open module, suggesting structural differences between the mucin layers grown in the two modules. Finally, the open module was more susceptible to noise than the flow module, shown by the frequency and dissipation spikes in Figure 8-5b).

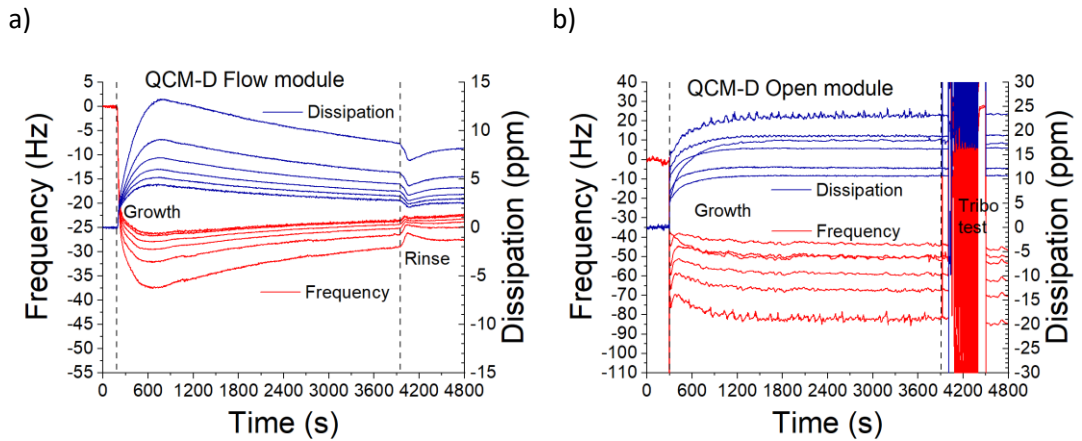


Figure 8-5 Raw QCM-D data from a) flow and b) open modules. Both show growth the growth phase in Muc + DiW solution.

Figure 8-6 presents the structural softness of the mucin layers from both QCM-D modules, calculated from the 3<sup>rd</sup> harmonic overtone by  $\Delta D/\Delta f$  and taking a mean/standard deviation of the final 500 seconds of the growth phase. The structural softness of the flow module's mucin layer was  $0.32 \pm 0.01$  compared to  $0.27 \pm 0.007$  in the open module. These results provided evidence of a more rigid mucin layer within the open module compared to the relatively softer flow module mucin layer.

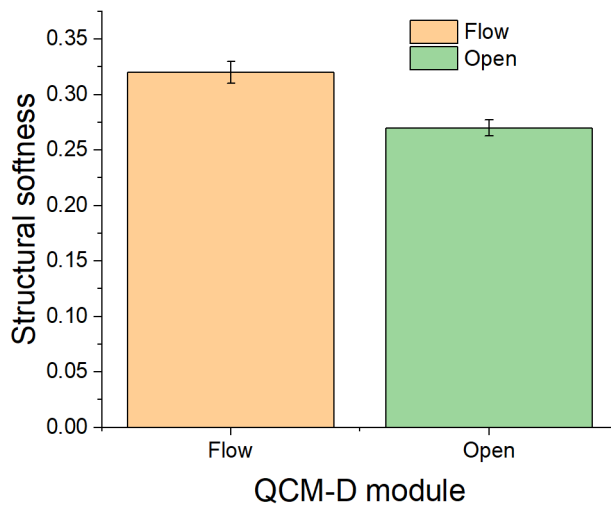
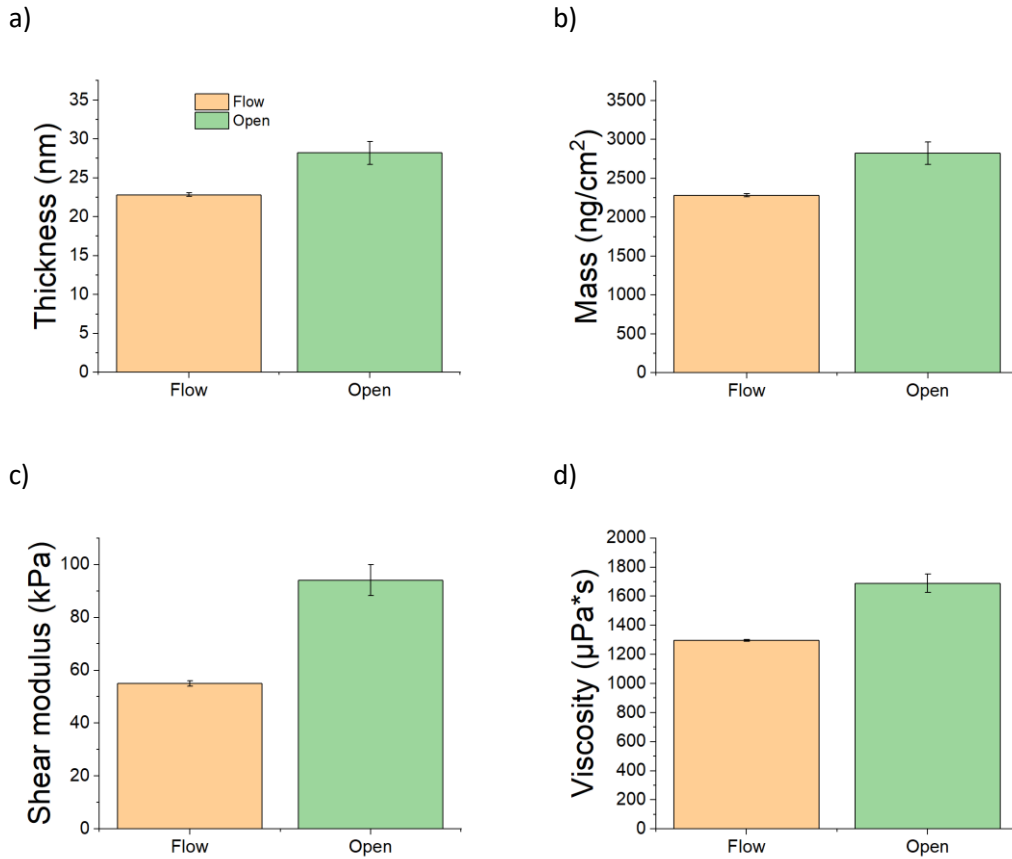


Figure 8-6 Mean Structural softness of growth phase calculated from the 3<sup>rd</sup> overtone by  $\Delta D/\Delta f$ .

The modelled layer thickness and mass properties from the two QCM-D modules are shown in Figure 8-7a) and b), while layer viscosity and shear modulus properties are shown in Figure 8-7b) and c). Additional mass absorbed onto sensors within the open module,  $2822.51 \pm 143.20$  ng/cm<sup>2</sup> compared to  $2282.12 \pm 22.88$  ng/cm<sup>2</sup> within the flow module. This imparted a larger layer thickness of  $28.20 \pm 1.46$  nm compared to  $22.82 \pm 0.23$  within the flow module. The open module mucin layer also presents greater viscosity and elastic shear modulus

properties of  $1688.50 \pm 62.32 \mu\text{Pa}\cdot\text{s}$  and  $94.03 \pm 5.84 \text{ kPa}$  respectively compared to the layer grown in the flow module. The latter showed a viscosity of  $1295.98 \pm 5.18 \mu\text{Pa}\cdot\text{s}$  and a shear modulus of  $55.05 \pm 1.03 \text{ kPa}$ . These findings clearly indicated a dependence on the system conditions (fluid flow or stagnant growth) in relation to the adsorption and physical properties of mucin layers.

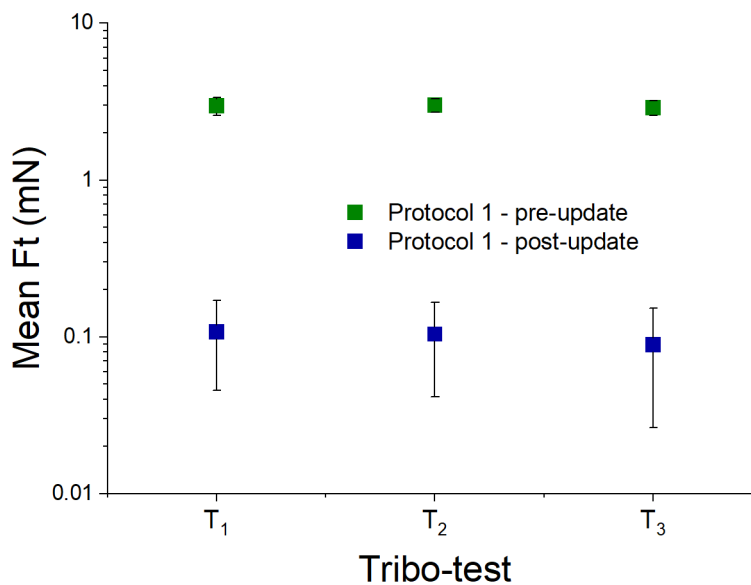


**Figure 8-7** Average layer properties calculated from 'Broadfit' model comparing flow and open modules under Muc + DiW conditions; a) thickness b) mass, c) shear modulus and d) viscosity.

### 8.3.2 Combined QCM-D properties and tangential force response trends

#### 8.3.2.1 Tangential force measurements and software updates

In between Triborig validation and combined QCM-D tribometer testing, the Triborig's software experienced a bug which began to incorrectly interpret the tangential force calculated from the HR-S cantilever's stiffness and the stage displacement. This occurred after moving the Triborig to a different lab to enable combined testing with the QCM-D. The issues manifested as an incorrect output tangential force an order of magnitude greater than what was observed during Tribometer validation. During the processes of troubleshooting this software issue, combined QCM-D tribometer tests were carried out in the interim with a focus on the trends of tangential force changes. To overcome this issue, both the software and system were assessed by a contractor, who subsequently applied a software patch to the Triborig. Protocol 1 was repeated to reassess the system updated system. The results of this are shown in Figure 8-8, comparing the tangential force response before the update with after the update. The updated output  $F_t$  response was an order of magnitude lower than before the update, of  $0.11 \pm 0.06$  mN in  $T_1$  reducing to  $0.08 \pm 0.06$  mN by  $T_3$  compared to  $2.97 \pm 0.39$  mN reducing to  $2.88 \pm 0.31$  mN.



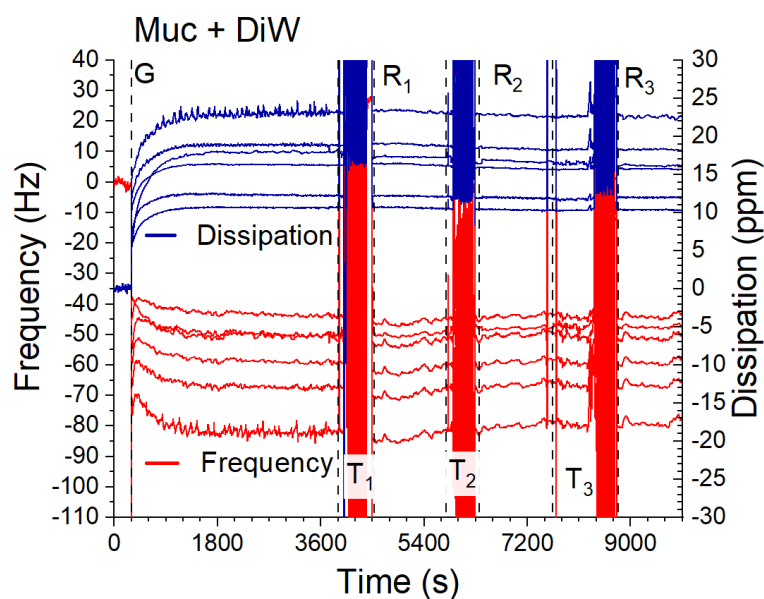
**Figure 8-8** Retest of tribo- tests from protocol 1 under Muc + DiW conditions compared to pre-update  $F_t$  results.

The friction response over protocol 1 remained consistent during the retest after the software update, with little to no change over the duration of the protocol. The mean coefficient of friction was also determined to be  $0.41 \pm 0.03$  for the repeat tests in Muc + DiW conditions. This was closer to the coefficient of friction of Muc + DiW on gold QCM-D sensors, similar to  $0.52 \pm 0.03$  as observed in the NTR<sup>3</sup> experiments in the previous chapter.

This suggested that the repeat friction measurements were more representative of the absolute friction response (in terms of scale). The other friction measurements, used in the primary tests of protocol 1 and protocols 2 to 3, were therefore more representative of the friction behaviour response due to changes to the software. However, data presented over the next subsections relate to data acquired prior to this update.

### 8.3.2.2 Mechanical interactions on established mucin layers

Investigation between mucin layer physical properties and friction started off with protocol 1. The frequency and dissipation response for protocol 1 under Muc + DiW conditions is displayed in Figure 8-9. An initial growth phase was observed (G) followed by consecutive tribo-tests (T) and rest phases (R), corresponding to Figure 8-3. The interactions between the Triborig and the QCM-D are clearly observed by larger noise in both frequency and dissipation response. Overtones were shown to remain separated after mechanical interactions with the Triborig.

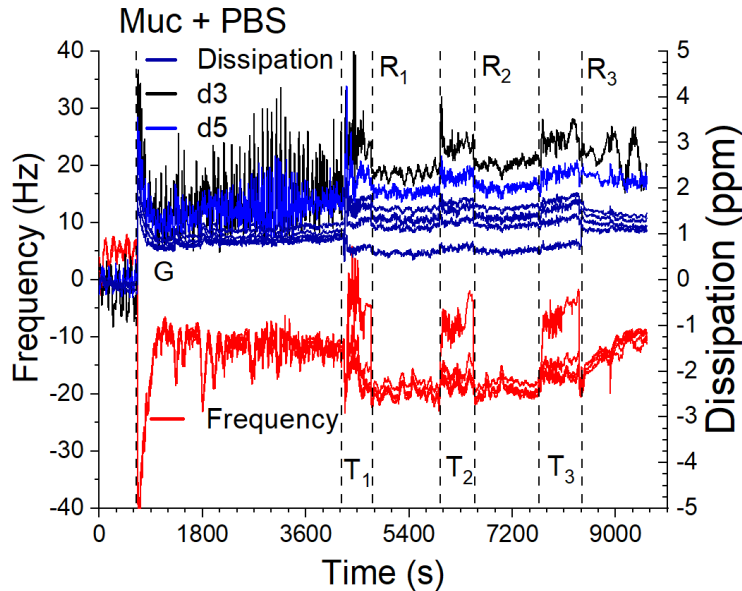


*Figure 8-9 Protocol 1 - frequency and dissipation response over time under Muc + DiW conditions. Starting initially with a growth phase (G), followed by consecutive tribo-tests (T) and rest phases (R).*

Figure 8-10 shows the frequency and dissipation response for protocol 1 under Muc + PBS conditions. Under these conditions, greater noise was observed in the dissipation data for the 3<sup>rd</sup> and 5<sup>th</sup> overtones, shown by the different coloured lines, d3 and d5, in Figure 8-10. The frequency response differed from Muc + DiW conditions by a reduced frequency drop, approx. -12 Hz in Muc + PBS compared to approx. -80 Hz when comparing the 3<sup>rd</sup> overtone. The frequency overtone spread was further reduced, suggesting the Muc + PBS layers behaved like a rigid layer rather than a softer layer. The dissipation response of Muc + PBS



mirrored the frequency with a small change of 2.50 ppm compared to 22.50 ppm, which further supported rigid layer characteristics. However, as the dissipation response was greater than 0, and the dissipation overtones were not all overlapping, the 'Broadfit' viscoelastic model was still applicable under these conditions to determine the layer properties.



*Figure 8-10 Protocol 1 - frequency and dissipation response over time under Muc + PBS conditions. Starting initially with a growth phase (G), followed by consecutive tribo-tests (T) and rest phases (R).*

Figure 8-11 compares the mean layer properties under Muc + DiW and Muc + PBS conditions over each phase of the experiment, excluding the tribo-tests. Tribo-tests were excluded due to the additional noise and interaction with the sensor during measurement that would produce an inaccurate representation of the layer. Figure 8-11a) presents the changes in the layer's structural softness overtime, calculated from  $\Delta D/\Delta f$  of the 3<sup>rd</sup> overtone. Under Muc + DiW this remained unchanged after repeated mechanical interactions with the layer of  $0.282 \pm 0.005$ , while under Muc + PBS conditions this decreased after tribo-test 1 ( $T_1$ ) from  $0.155 \pm 0.04$  to  $0.119 \pm 0.005$  but increased hereafter. The PBS induced a more rigid layer, as evidenced by the lower structural softness of  $0.15 \pm 0.04$  compared to Muc + DiW ( $0.28 \pm 0.05$ ). Muc + PBS structural softness variation in G was attributed to the additional noise of  $\Delta D_3$  (3<sup>rd</sup> dissipation overtone).

Figure 8-11b) shows the thickness changes of the mucin layers over protocol 1. Under Muc + DiW conditions, the thickness was shown to gradually decrease after each tribo-test from  $28.45 \pm 2.01$  nm in G to  $26.95 \pm 0.60$  nm by  $R_3$ . An initial drop in thickness was observed from G to  $R_1$  in Muc + PBS, from  $4.49 \pm 2.54$  nm to  $3.85 \pm 1.18$  nm, which then increased to  $5.56 \pm 1.88$  nm in  $R_2$  and  $6.13 \pm 3.02$  nm in  $R_3$ . Figure 8-11c) and d) shows the shear modulus and

viscosity properties of the mucin layers tested under protocol 1. The Muc + DiW layer presented small differences in the shear modulus after each tribo-test phase, of no more than  $\pm 10$  kPa for each phase. The viscosity of the Muc + DiW layer decreased from  $1690.28 \pm 65.31 \mu\text{Pa}\cdot\text{s}$  in G to  $1604.20 \pm 31.23 \mu\text{Pa}\cdot\text{s}$  by  $R_3$ . Larger differences were observed under Muc + PBS conditions. Layer shear modulus and viscosity properties changed from  $110.41 \pm 89.80$  kPa and  $1546.51 \pm 399.70 \mu\text{Pa}\cdot\text{s}$  in G, to  $64.42 \pm 7.35$  kPa and  $1923.38 \pm 146.72 \mu\text{Pa}\cdot\text{s}$  in  $R_1$  respectively. Shear modulus and viscosity properties both decreased in  $R_2$  before resting at  $62.77 \pm 39.18$  kPa and  $1399.83 \pm 220.08 \mu\text{Pa}\cdot\text{s}$  in  $R_3$  after the final tribo-test ( $T_3$ ). The Muc + DiW, and Muc + PBS layer properties for protocol 1 are summarised in Table 8-3.

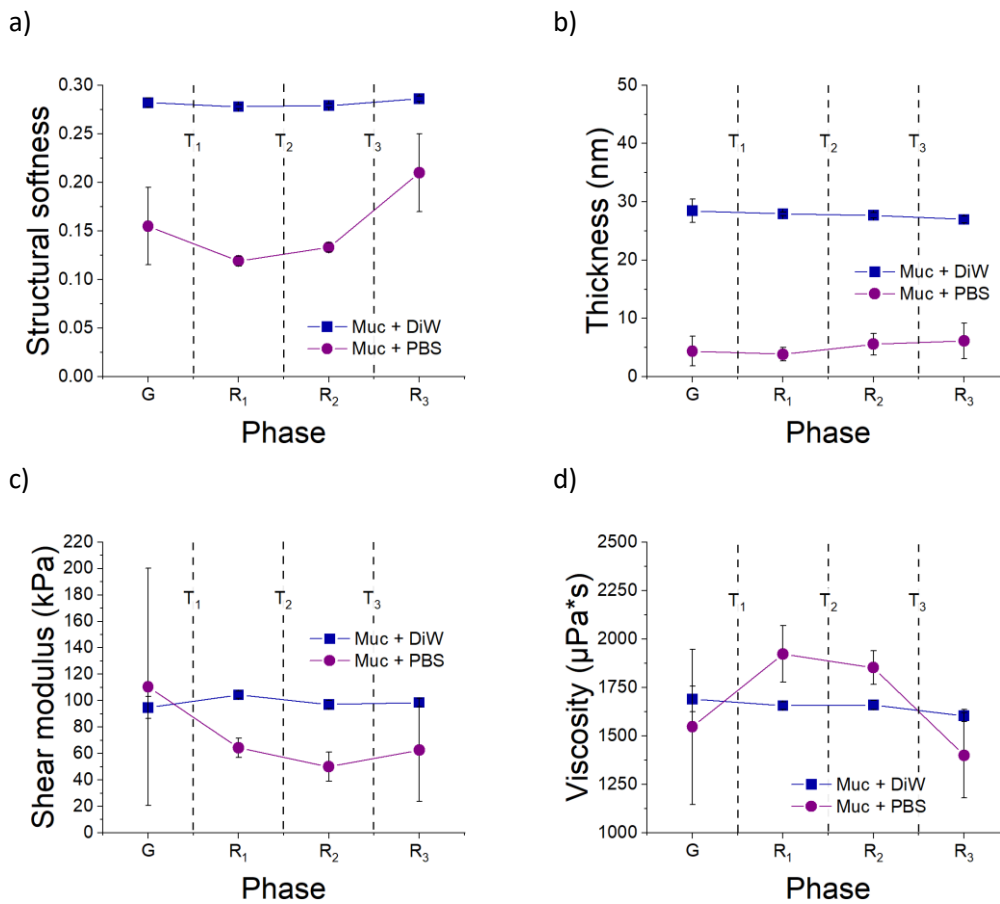
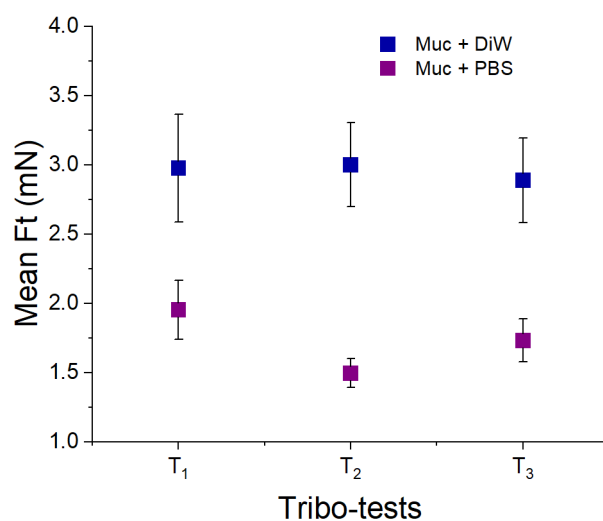


Figure 8-11 Comparison of Muc + DiW and Muc + PBS layer properties for each phase of protocol 1 showing a) structural softness, b) thickness, c) shear modulus and d) viscosity.

**Table 8-3 Mean QCM-D layer properties at the end of each phase of protocol 1 for Muc + DiW and Muc + PBS conditions.**

Phase	Structural softness		Thickness (nm)		Shear modulus (kPa)		Viscosity ( $\mu\text{Pa}\cdot\text{s}$ )	
	Muc + DiW	Muc + PBS	Muc + DiW	Muc + PBS	Muc + DiW	Muc + PBS	Muc + DiW	Muc + PBS
<b>G</b>	0.282	0.155	28.45	4.39	94.75	80.27	1690.29	1546.51
	$\pm 0.005$	$\pm 0.04$	$\pm 2.01$	$\pm 2.54$	$\pm 8.32$	$\pm 37.50$	$\pm 65.31$	$\pm 399.70$
Tribo-test 1								
<b>R<sub>1</sub></b>	0.278	0.119	27.97	3.85	104.42	64.42	1656.00	1923.38
	$\pm 0.002$	$\pm 0.005$	$\pm 0.33$	$\pm 1.18$	$\pm 2.79$	$\pm 7.35$	$\pm 19.44$	$\pm 146.72$
Tribo-test 2								
<b>R<sub>2</sub></b>	0.279	0.133	27.70	5.56	97.16	50.01	1660.02	1852.19
	$\pm 0.002$	$\pm 0.005$	$\pm 0.45$	$\pm 1.88$	$\pm 3.01$	$\pm 10.96$	$\pm 23.45$	$\pm 87.20$
Tribo-test 3								
<b>R<sub>3</sub></b>	0.286	0.210	26.96	6.13	98.67	62.77	1604.20	1399.83
	$\pm 0.003$	$\pm 0.04$	$\pm 0.61$	$\pm 3.02$	$\pm 3.28$	$\pm 39.18$	$\pm 31.23$	$\pm 220.08$

As the layer properties could not be assessed during tribo-tests, it was assumed that the layer properties of the previous phase applied throughout the tribo-test phase. Subsequently, Figure 8-12 serves to present differences in  $F_t$  after each phase. Under Muc + DiW condition the mean  $F_t$  reduced from  $2.97 \pm 0.39$  mN to  $2.88 \pm 0.31$  mN from  $T_1$  to  $T_3$ .  $F_t$  was lower under Muc + PBS conditions with  $2.15 \pm 0.32$  mN in  $T_1$  decreasing to  $1.56 \pm 0.19$  mN in  $T_2$ , followed by  $1.63 \pm 0.20$  mN by  $T_3$ .



**Figure 8-12 Mean  $F_t$  for each tribo-test stage during protocol 1.**

### 8.3.2.3 *Mechanical and solution interactions on established mucin layers*

Protocol 2 aimed to examine the impact of a rinse solution on the mucin layer properties and its implications on the subsequent friction response. Figure 8-13 and Figure 8-14 both show the frequency and dissipation response following protocol 2. Like protocol 1, this commenced with a growth phase (G) using Muc + DiW, or Muc + PBS, followed by the first tribo-test ( $T_1$ ) and a rest phase ( $R_1$ ) in the same solution to allow surface to re-equilibrate before solution change. Shifting away from protocol 1, the solution was replaced with MilliQ water during the change phase ( $C_1$ ) for 20 minutes, removing any free proteins from the solution. After a subsequent tribo-test ( $T_2$ ) and rest phase ( $R_2$ ), the solution was changed once more ( $C_2$ ), whereby a fresh mucin growth solution was reintroduced. To reintroduce the same concentration as before, 250  $\mu\text{L}$  of MilliQ water was removed, and replaced with a 0.4% Muc solution, thus achieving 0.2% mucin in the final solution. This was a two-step process for Muc + PBS, whereby a PBS rinse fully replaced the MilliQ water in  $C_2$ , followed by the above step described above but with 0.4% mucin in PBS in  $C_3$ .

The dissipation dropped at the start of  $C_1$  under both test conditions when the growth solution was removed and replaced with MilliQ water. This was from 25.06 ppm to 13.54 ppm in Muc + DiW, and 2.66 ppm to 0.69 ppm in Muc + PBS for the 3<sup>rd</sup> overtone. For the same overtone, no frequency shift was observed under Muc + DiW conditions, however in Muc + PBS the frequency shifted from approx. 18.81 Hz to 24.49 Hz. This increase was attributed to the movement of water into the Muc + PBS layer. At the same time a reduction in the spread of overtones was observed in both Figure 8-13 and Figure 8-14, indicating changes to the structure of the layer by the removal of loosely bound/unbound mucin. When the growth solution was reintroduced, the overtone spread and dissipation shift returned to pre  $C_1$  levels in  $C_2$  for Muc + DiW and  $C_3$  for Muc + PBS.

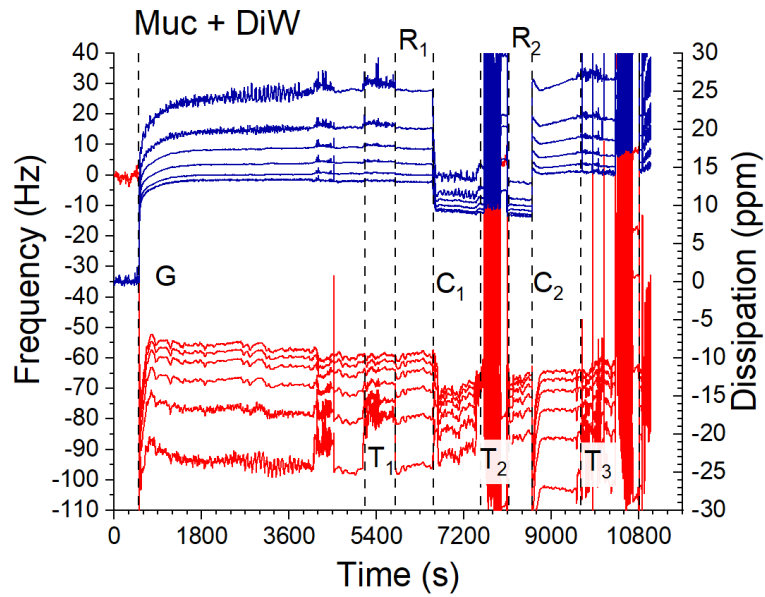


Figure 8-13 Protocol 2 - frequency and dissipation response over time under Muc + DiW conditions. Starting initially with a growth phase (G), followed by consecutive tribo-tests (T), rest phases (R) and solution changes (C).

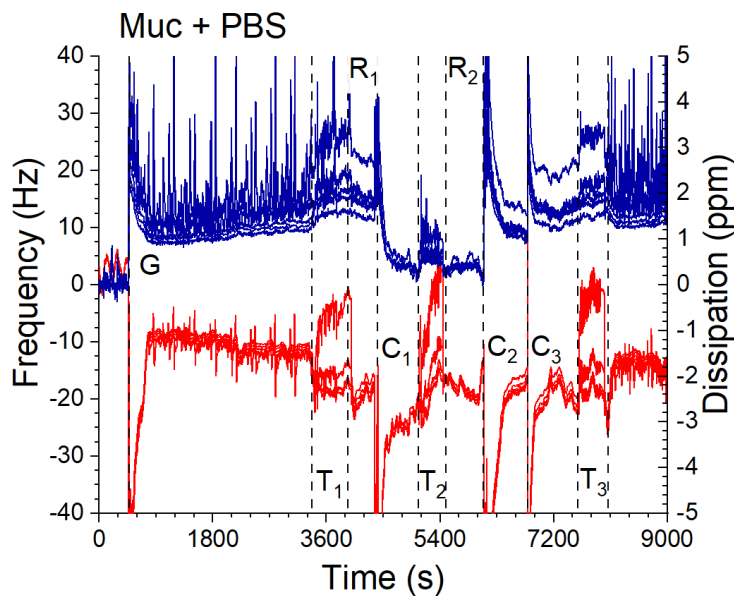
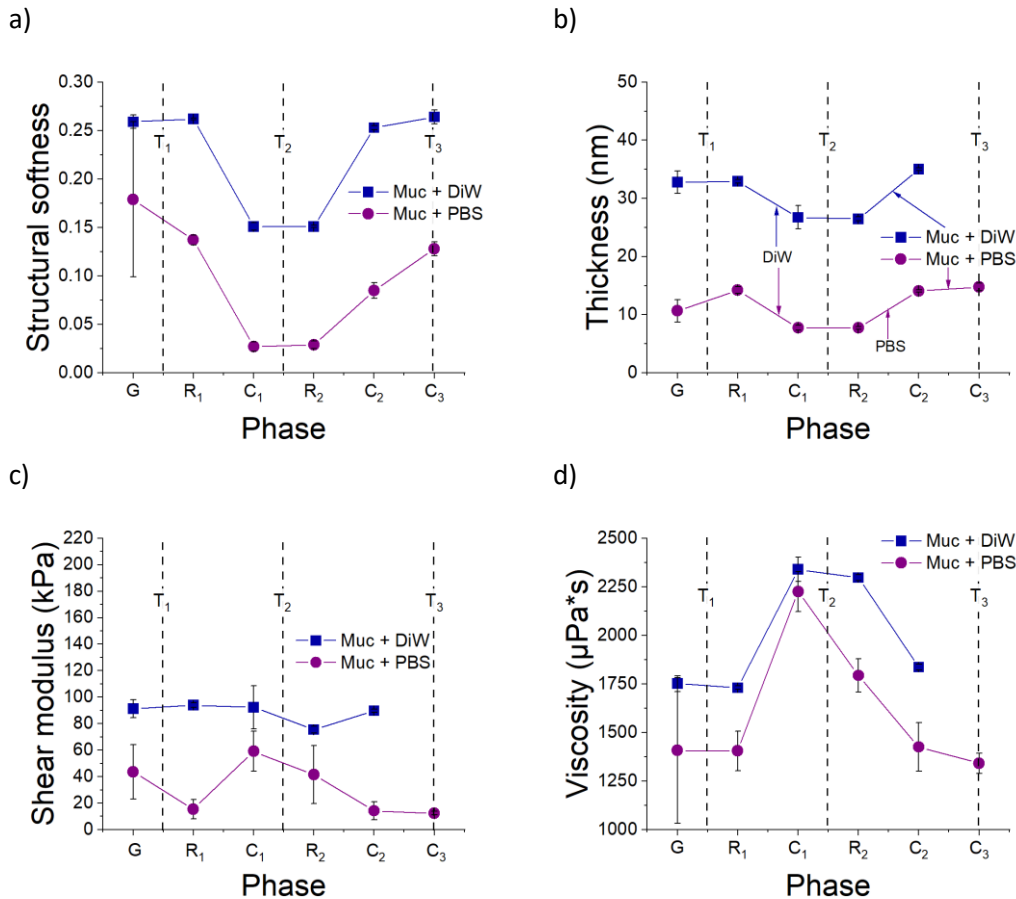


Figure 8-14 Protocol 2 - frequency and dissipation response over time under Muc + PBS conditions. Starting initially with a growth phase (G), followed by consecutive tribo-tests (T), rest phases (R) and solution changes (C).

The layer properties for each phase of protocol 2 are displayed in Figure 8-15. The MilliQ water rinse at C<sub>1</sub> impacted the layer's structural softness, thickness and viscosity under both conditions, shown in Figure 8-15a), b) and d) respectively. No change was observed for the Muc layer's shear modulus; however, an increase was observed for the Muc + PBS layer, shown in Figure 8-15c).



**Figure 8-15 Comparison of Muc + DiW and Muc + PBS layer properties for each phase of protocol 2 showing a) structural softness, b) thickness, c) shear modulus and d) viscosity.**

The transition between G and R<sub>1</sub> presents similar trends to protocol 1. No changes occurred after T<sub>1</sub> under Muc + DiW conditions, and a similar decrease was observed for structural softness and shear modulus properties with Muc + PBS. Different behaviours were observed between protocols 1 and 2 under Muc + PBS. The layer's thickness increased and its viscosity did not change in protocol 2, while viscosity increased in protocol 1, shown in Figure 8-11d). These inconsistencies suggested instabilities within the Muc + PBS layers.

Between C<sub>1</sub> and R<sub>2</sub>, a reduction in the shear modulus and viscosity properties was observed under both conditions, with a large drop in viscosity under Muc + PBS conditions. Layer thickness and structural softness remained the same during this phase transition after T<sub>2</sub>. Reintroduction of the growth solution enabled layer recovery, back to R<sub>1</sub> levels. The mean QCM-D properties for all phases of protocol 2 under Muc + DiW, and Muc + PBS conditions are summarised in Table 8-4.

*Table 8-4 Mean QCM-D properties at the end of each phase of protocol 2 for Muc + DiW and Muc + PBS conditions.*

Phase	Structural softness		Thickness (nm)		Shear modulus (kPa)		Viscosity ( $\mu\text{Pa}\cdot\text{s}$ )	
	Muc + DiW	Muc + PBS	Muc + DiW	Muc + PBS	Muc + DiW	Muc + PBS	Muc + DiW	Muc + PBS
<b>G</b>	0.259 $\pm 0.007$	0.179 $\pm 0.08$	32.78 $\pm 1.94$	10.66 $\pm 1.93$	91.36 $\pm 6.88$	43.64 $\pm 20.69$	1751.61 $\pm 40.69$	1407.51 $\pm 374.90$
Tribo-test 1								
<b>R<sub>1</sub></b>	0.262 $\pm 0.001$	0.137 $\pm 0.005$	32.94 $\pm 0.28$	14.20 $\pm 0.57$	93.95 $\pm 1.62$	15.41 $\pm 7.41$	1730.53 $\pm 9.11$	1405.18 $\pm 101.25$
Solution Change 1								
<b>C<sub>1</sub></b>	0.151 $\pm 0.004$	0.027 $\pm 0.005$	26.73 $\pm 2.00$	7.75 $\pm 0.45$	75.52 $\pm 2.41$	59.07 $\pm 15.13$	2339.70 $\pm 62.00$	2225.79 $\pm 102.58$
Tribo-test 2								
<b>R<sub>2</sub></b>	0.151 $\pm 0.001$	0.029 $\pm 0.004$	26.48 $\pm 0.34$	7.74 $\pm 0.23$	89.79 $\pm 1.27$	41.51 $\pm 21.94$	2297.19 $\pm 15.66$	1793.58 $\pm 85.14$
Solution Change 2								
<b>C<sub>2</sub></b>	0.253 $\pm 0.002$	0.085 $\pm 0.008$	35.02 $\pm 0.27$	14.08 $\pm 0.23$	89.79 $\pm 1.27$	14.26 $\pm 6.68$	1836.85 $\pm 14.95$	1425.67 $\pm 124.28$
Solution Change 3 (Muc + PBS)								
<b>C<sub>3</sub></b>	-	0.128 $\pm 0.007$	-	14.76 $\pm 0.65$	-	12.45 $\pm 1.31$	-	1342.16 $\pm 51.85$
Tribo-test 3								
<b>R<sub>3</sub></b>	0.264 $\pm 0.007$	0.169 $\pm 0.005$	-	11.05 $\pm 2.08$	-	45.72 $\pm 12.04$	-	1452.24 $\pm 324.53$

Figure 8-16 presents the mean tangential friction response,  $F_t$ , for each tribo-test phase in protocol 2. A comparison between Figure 8-15 and Figure 8-16 highlighted potential trends between mucin layer property changes and the tangential force response. A drop in the structural softness was observed from  $0.26 \pm 0.001$  to  $0.15 \pm 0.004$  which corresponded to a similar reduction in the output  $F_t$  under Muc + DiW conditions, from  $2.88 \pm 0.30$  mN to  $1.69 \pm 0.17$  mN. It should be noted that prior to  $T_2$ , the Muc + DiW layer's viscosity reduced. The  $F_t$  output increased under Muc + PBS conditions, from  $1.71 \pm 0.16$  mN to  $1.84 \pm 0.21$  mN with the rinse, while a similar drop in structural softness from  $0.14 \pm 0.005$  to  $0.03 \pm 0.005$  and increased layer viscosity. However, when Muc + PBS was reintroduced the  $F_t$  output increased again to  $1.89 \pm 0.17$  mN while the structural softness and viscosity recovered.

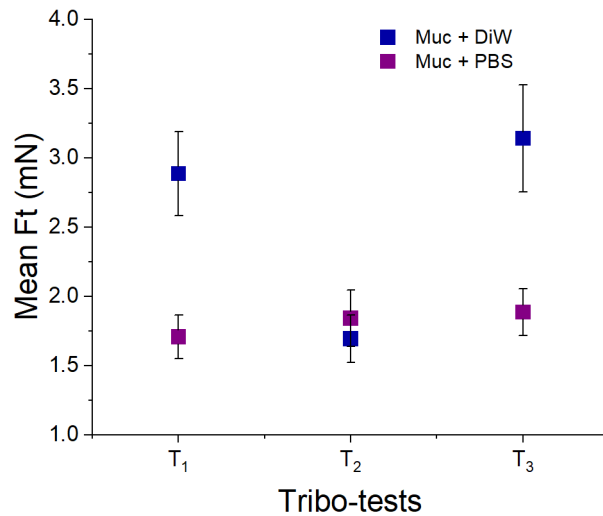


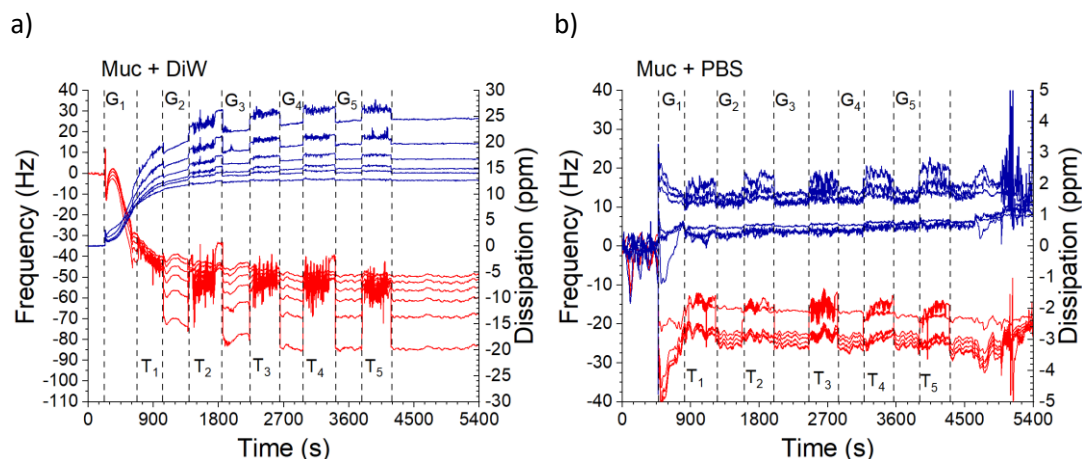
Figure 8-16 Mean Ft for each tribo-test stage during protocol 2.

#### 8.3.2.4 Mechanical interactions on unestablished mucin layers

Protocol 3 aimed to examine the effect on mucin layer growth and its properties on friction. Figure 8-17 a) and b) show the frequency and dissipation response following protocol 3 under Muc + DiW, and Muc + PBS conditions respectively. Layer growth was separated by 5 tribo-tests ( $T_1$  to  $T_5$ ) into short growth phases ( $G_1$ - $G_5$ ). Similarities between the previous protocols and protocol 3 were observed in relation to overtone spread, frequency and dissipation shift. Under Muc + DiW conditions, shown in Figure 8-17, the final frequency and dissipation shift was 84.58 Hz and 24.41 ppm respectively for the 3<sup>rd</sup> overtone. This was comparable to the frequency and dissipation response after the G phase in protocol 1 and 2 (Figure 8-9 and Figure 8-13, respectively).

This behaviour was partially observed for Muc + PBS conditions in Figure 8-17b), with a similar dissipation shifts to the previous protocols, of 2.12 ppm. However, the frequency shift was greater in protocol 3 compared to previous protocols, with a shift of 27.70 Hz. This suggested that addition mass may have adsorbed onto the gold surface after mechanical interactions under Muc + PBS conditions. Furthermore, examination of the dissipation overtones highlighted a different spread behaviour compared to the previous protocols. The 9<sup>th</sup>, 11<sup>th</sup> and 13<sup>th</sup> dissipation overtone remained close together, approx. less than 1 ppm, leaving a gap between the remaining overtones.





**Figure 8-17 Protocol 3 - frequency and dissipation response over time under a) Muc + DiW and b) Muc + PBS conditions. Starting initially with a growth phase (G), followed by consecutive tribo-tests (T) and rest phases (R).**

Figure 8-18 shows the layer properties over each test phase in protocol 3. The structural softness was shown to be stable over the duration of protocol 3, with no large changes between each tribo-test phase as shown in Figure 8-18a). This remained mostly at  $0.28 \pm 0.002$  and  $0.07 \pm 0.002$  for Muc + DiW and Muc + PBS respectively. The thickness of the Muc + DiW layer presented a large variation during  $G_1$  of  $37.79 \pm 28.17$  nm, which stabilised afterwards and settled at  $33.45 \pm 0.41$ . The increased frequency shift in Muc + PBS conditions correlated to the thickness change throughout protocol 3. After  $G_1$  the layer thickness was  $5.23 \pm 0.59$  nm, which increased to  $5.65 \pm 0.13$  nm by the end of protocol 3. This thickness was greater than the mucin layer at the end of protocol 1's growth phase, but much lower than the layer thickness at the end of the same phase of protocol 2. Figure 8-18c) and Figure 8-18d) present the most interesting results of protocol 3, exhibiting changes to the shear modulus and viscosity over the first few growth phases. The Muc + DiW layer's shear modulus increased after each phase from  $10.74 \pm 3.81$  kPa, to a plateau after  $G_4$  of  $66.67 \pm 2.90$  kPa. The same layer's viscosity started relatively low at  $1158.15 \pm 66.19$   $\mu\text{Pa}\cdot\text{s}$ , which then peaked at  $1737.86 \pm 23.20$   $\mu\text{Pa}\cdot\text{s}$  and decreased to  $1675.11 \pm 9.43$   $\mu\text{Pa}\cdot\text{s}$

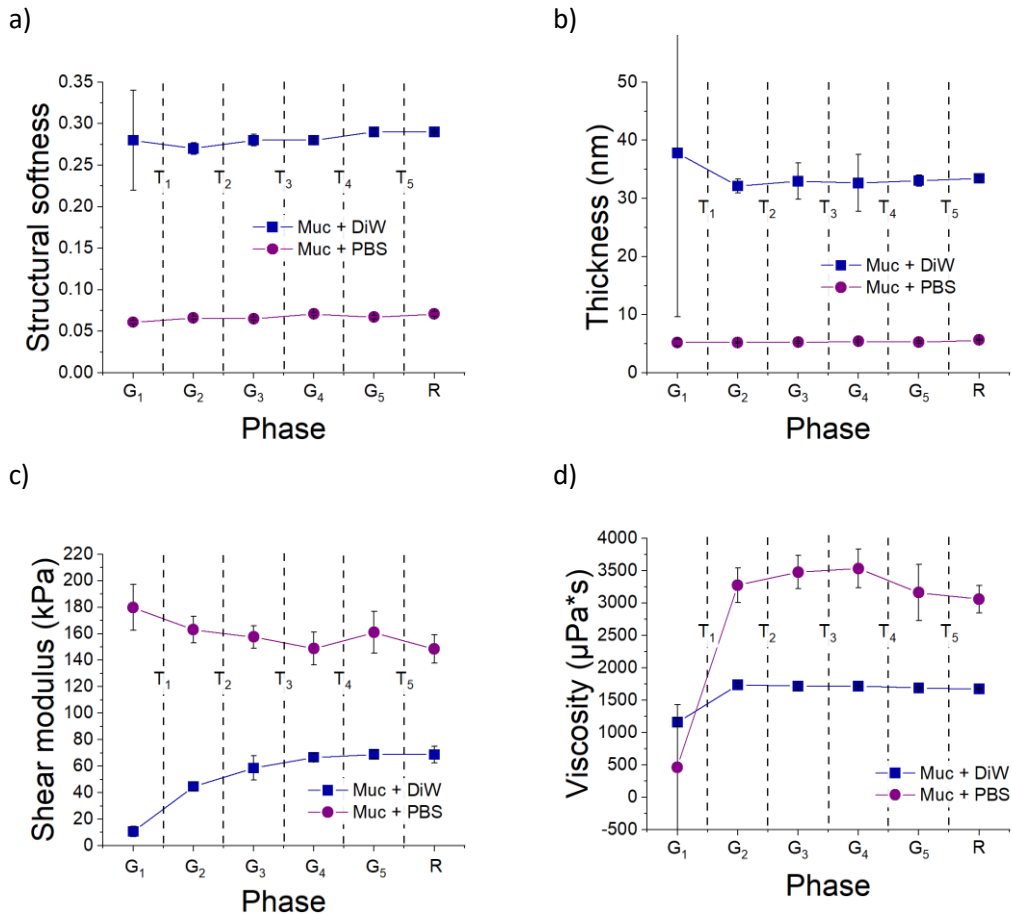


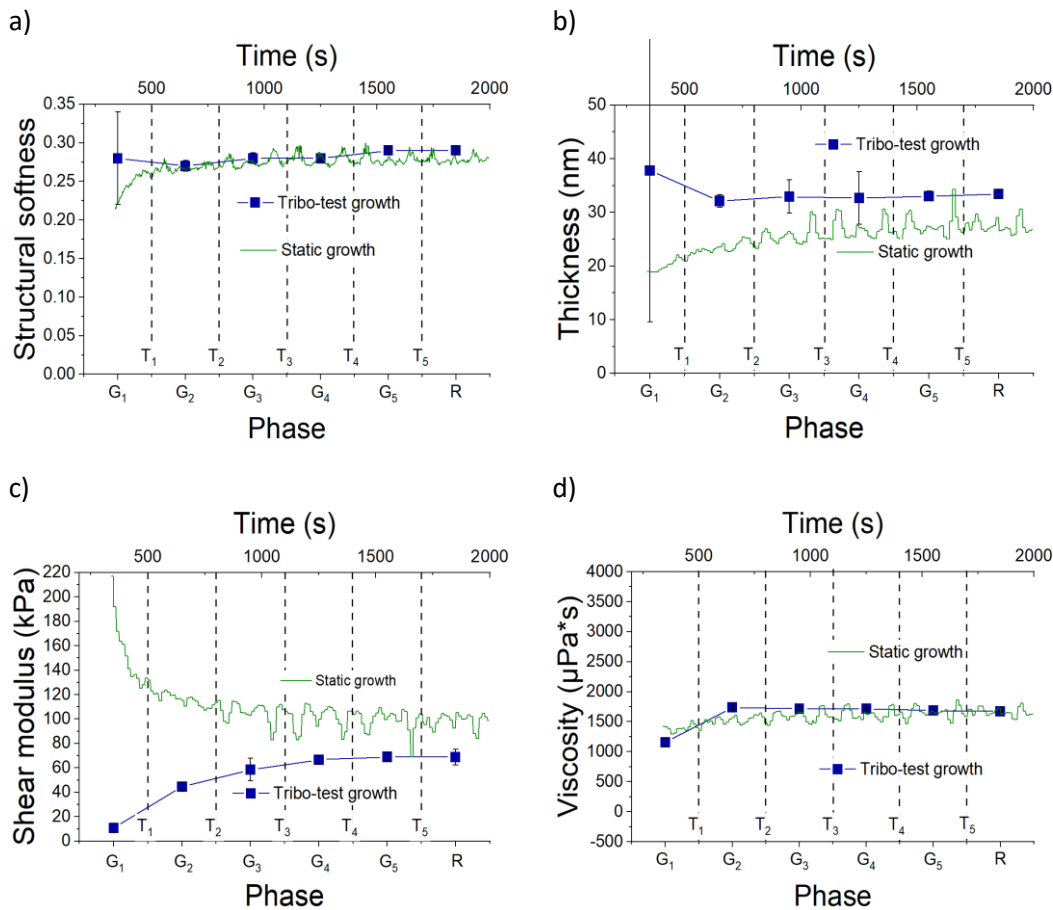
Figure 8-18 Comparison of Muc + DiW and Muc + PBS layer properties for each phase of protocol 3 showing a) structural softness, b) thickness, c) shear modulus and d) viscosity.

Table 8-5 summarises the mean layer properties of protocol 3 for Muc + DiW, and Muc + PBS. Protocol 3's Muc + PBS layer's shear and viscosity properties differed from layer properties observed protocol 1 and 2. The layer's viscosity started low with a large variation,  $463.41 \pm 966.41 \mu\text{Pa}\cdot\text{s}$ , which increased to  $3273.80 \pm 267.44 \mu\text{Pa}\cdot\text{s}$  by the next phase. This continued to increase until G<sub>4</sub>, after which it reduced. On the other hand, the shear modulus started high at  $179.85 \pm 17.20 \text{ kPa}$  and gradually reduced to  $148.43 \pm 10.7 \text{ kPa}$ . The magnitude of both the shear modulus and viscosity seem irregular, given the different values observed in Table 8-3, Table 8-4 and the previous chapter. This behaviour was attributed to the overtone spread behaviour observed in Figure 8-17b).

**Table 8-5 Mean QCM-D properties at the end of each phase of protocol 3 for Muc + DiW and Muc + PBS conditions.**

Phase	Structural softness		Thickness (nm)		Shear modulus (kPa)		Viscosity ( $\mu\text{Pa}\cdot\text{s}$ )	
	Muc + DiW	Muc + PBS	Muc + DiW	Muc + PBS	Muc + DiW	Muc + PBS	Muc + DiW	Muc + PBS
<b>G<sub>1</sub></b>	0.28	0.061	37.79	5.23	10.74	179.85	1158.15	463.41
	$\pm 0.06$	$\pm 0.002$	$\pm 28.17$	$\pm 0.59$	$\pm 3.81$	$\pm 17.20$	$\pm 66.19$	$\pm 966.41$
Tribo-test 1								
<b>G<sub>2</sub></b>	0.27	0.066	32.14	5.20	44.65	162.92	1737.86	3273.80
	$\pm 0.007$	$\pm 0.002$	$\pm 1.18$	$\pm 0.13$	$\pm 3.50$	$\pm 10.01$	$\pm 23.20$	$\pm 267.44$
Tribo-test 2								
<b>G<sub>3</sub></b>	0.28	0.065	32.96	5.23	58.57	157.47	1716.20	3476.61
	$\pm 0.007$	$\pm 0.002$	$\pm 3.11$	$\pm 0.13$	$\pm 9.17$	$\pm 8.50$	$\pm 31.33$	$\pm 256.73$
Tribo-test 3								
<b>G<sub>4</sub></b>	0.28	0.071	32.66	5.45	66.67	148.67	1716.36	3532.24
	$\pm 0.002$	$\pm 0.002$	$\pm 4.92$	$\pm 0.15$	$\pm 2.90$	$\pm 12.43$	$\pm 9.53$	$\pm 298.47$
Tribo-test 4								
<b>G<sub>5</sub></b>	0.29	0.067	33.05	5.26	68.96	160.96	1685.99	3161.29
	$\pm 0.003$	$\pm 0.002$	$\pm 0.93$	$\pm 0.19$	$\pm 2.98$	$\pm 15.81$	$\pm 14.09$	$\pm 435.71$
Tribo-test 5								
<b>R</b>	0.29	0.071	33.45	5.65 $\pm$ 0.13	68.80	148.43	1675.11	3057.16
	$\pm 0.001$	$\pm 0.003$	$\pm 0.41$		$\pm 6.29$	$\pm 10.7$	$\pm 9.43$	$\pm 209.79$

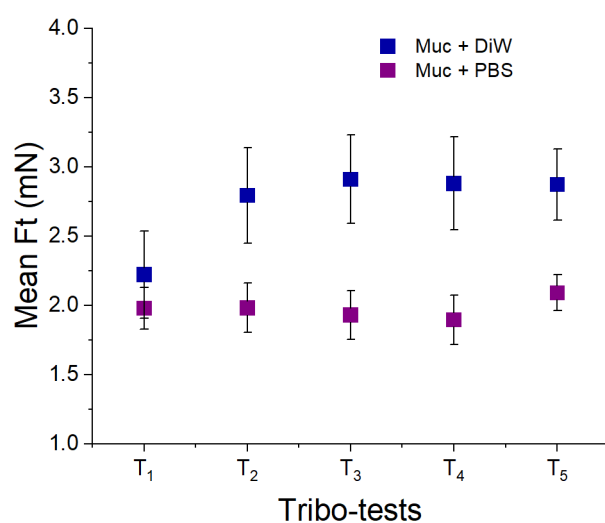
The influence of tribology on mucin layer growth in Muc + DiW was compared to the growth phase of protocol 1 to assess any differences in the layer properties over time without tribological interactions, shown in Figure 8-19. Protocol 3's structural softness and layer viscosity were shown to be in line with the same properties over time in protocol 1, evidenced in Figure 8-19a) and d) respectively. Differences were observed between Muc + DiW layer thickness and shear modulus properties, evidenced in Figure 8-19b) and c) respectively. Furthermore, protocol 1 showed a high shear modulus initially whereas in protocol 3 this property started low and increased with each phase.



**Figure 8-19 Comparison of Muc + DiW properties for each phase of protocol 3 compared with the growth phase of protocol 1 showing a) structural softness, b) thickness, c) shear modulus and d) viscosity.**

Figure 8-20 presents the mean tangential friction response,  $F_t$ , for each tribo-test phase in protocol 3. The Muc + PBS layer presented a lower  $F_t$  compared to the Muc + DiW layer. Over the duration of protocol 3, the  $F_t$  response on the Muc + DiW layer increased with each stage until after  $G_3$ , from  $2.22 \pm 0.32$  mN to  $2.91 \pm 0.32$  mN. After this peak, the  $F_t$  response decreased towards  $2.87 \pm 0.26$  mN at  $T_5$ . The  $F_t$  response of the Muc + PBS layer remained stable at approx.  $1.98 \pm 0.15$  mN until this increased at  $T_5$  to  $2.09 \pm 0.13$  mN.

Comparison of the layer properties over protocol 3 with the tangential force highlighted a trend between the shear modulus and friction response for the Muc + DiW layer. The shear modulus initially increased after each growth increment, which was linked to the increase in the tangential force response. Once the shear modulus of the Muc + DiW layer stabilised, so too did the friction response. No trends were noted between the Muc + PBS layer properties and the friction response with time, and displacement, for protocol 3.



*Figure 8-20 Mean Ft for each tribo-test stage during protocol 3.*

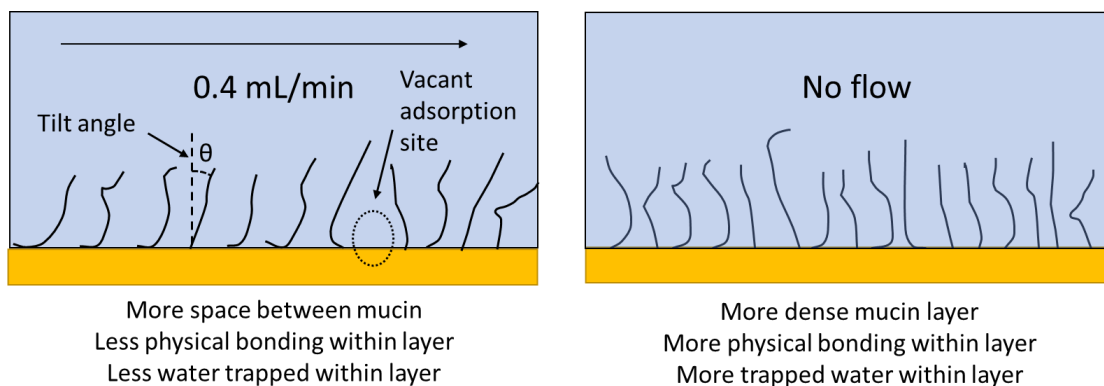
## 8.4 Discussion

Currently, to the knowledge of the author, little work exists which provides a direct correlation to the physical properties of an aqueous protein layer and lubrication. The main body of research provides an indirect assessment of a protein layer by determining the ratio between the dissipation and frequency,  $\Delta D/\Delta f$ , (termed as structural softness) [109, 309, 308]. In some cases, this parameter was then indirectly compared to a given friction response using an AFM, or a micro tribometer like the previous chapter [109, 309, 308]. These arrangements introduced additional processes between the layer growth within a QCM-D flow module and tribological testing, potentially introducing unwanted layer dehydration, removal or contamination. It was therefore important to mitigate this by developing an in-situ approach for directly assessing the lubrication of an aqueous protein layer. The discussion is split into subsections that explore the QCM-D set up with the open cell, the relationships between friction and layer properties for each protocol, and finally a critical assessment of the QCM-D Triborig assembly.

### 8.4.1 Influence of flow on mucin deposition

The adsorption of mucin under static and flow conditions was investigated to understand the differences between the layer growth methodologies. It was observed that under flow conditions, less mucin mass adsorbed onto the QCM-D sensor compared to static conditions. This behaviour has been partly observed in previous studies, implicating the effects of flow rate on the surface adsorption of non-ionic surfactants and fibrinogen.

The study examined the static and dynamic adsorption of non-ionic surfactants (Triton-X 100) onto sandstone, where the surface's maximum adsorption capacity reduced with increasing bulk flow rate [312]. It was suggested that this occurred from two potential mechanisms; monomer tilting or fluid shear interactions. The adsorbed monomers were thought to tilt under flow conditions, with a greater tilt angle as the flow rate increased, which reduced the effective surface area for additional adsorption [312]. Alternatively, the shear stresses at the surface from the fluid flow was greater than the physical bond interactions between the surface and adsorbate, again preventing additional adsorption from weaker surface bonding [312]. Another study, examining the adsorption of fibrinogen from blood plasma onto glass and polyethylene tubes, presented similar observations [300]. While the study did not comment on the mechanisms of flow rate on adsorption directly, under static conditions a greater quantity of adsorbed fibrinogen was observed on both material surfaces. Adsorption also appeared to decrease with increased flow rate [300]. The flow rate also influenced adsorption rates and subsequent displacement of adsorbed fibrinogen, which was also a surface dependent behaviour [300]. This was partially observed for the adsorption of mucin under flow conditions within this chapter, where the desorption, or displacement, of the mucin layer occurred as shown in Figure 8-5a) after reaching peak adsorption. Unlike fibrinogen and Triton-X 100, mucin is a larger hydrated molecule by weight with multiple contact sites to facilitate adsorption to a surface and network with adjacent mucin [313, 314, 315]. It could be speculated that the tilting - shielding mechanism reduced the number of mucins and therefore the number mucin-mucin interactions within the layer. This supports the reduced adsorption of mucin under flow conditions observed, with lower layer viscosity and shear modulus properties compared to static conditions. This has been illustrated for mucin monolayers in Figure 8-21.



**Figure 8-21 Hypothesised influence of flow on mucin monolayer layer structure and viscoelastic layer properties. Under 0.4 ml/min flow rate, adsorbed mucin tilt to shield additional mucin from adsorbing to the surface leaving vacant sites, reducing potential H bonding within the mucin layer. Without any flow, mucin adsorbs on all available contact sites. Due to increased layer density, more H bonding within layer can take place, stiffening the layer and promoting the entrapment of water.**

The effect of flow rates on multi-component solutions such as saliva have previously been investigated, showing similarities to the work in this chapter. Zeng et al [113] observed a decrease in salivary film thickness with an increased flow rates from 10, 50 and 500  $\mu\text{L}/\text{min}$  when assessing adsorption onto hydroxyapatite QCM-D surfaces. However, the structural softness of salivary films ( $k$  value in the paper) was shown to decrease with flow rate whereas the opposite was observed in this chapter between static and flow conditions, inferring that saliva layer properties were more elastic and stiffer compared to the more viscous PGM layers [113]. This may also be influenced by the quality of proteins within both solutions, whereby fresh whole human saliva would contain submaxillary mucin of a higher sialic acid content, and therefore improved water trapping abilities within the protein layer, compared to the highly processed and partially purified gastric mucin [97]. Growth solution composition and surface material dependent adsorption will have influenced these protein layer structures, with more complex adsorption pathways with human saliva onto hydroxyapatite surfaces compared to the mucin solution onto gold.

#### **Structural softness and test contact pressure relationship**

Interestingly, Zeng et al [113] demonstrated, with nano-scratch experiments on human tooth enamel, that a reduced salivary film's structural softness was paired with a lower coefficient of friction. Tests were performed with a conical diamond tip with a 10  $\mu\text{m}$  radius with 5 mN of normal load, applying a Hertzian mean contact pressure of approximately 2.36 GPa. Under these extreme conditions, a lower structural softness was preferred from a lubrication point of view, whilst reducing overall wear resistance at the same time. This supports what has been observed in Chapter 6, where a low structural softness is preferential for enamel lubrication on hydroxyapatite, contradicting other research that has suggested a higher structural softness enhances lubrication [109, 308, 309]. It may also infer that structural softness is not a helpful parameter to approximate lubrication under differing scales and material conditions. The key implication here is that contact pressures applied to these protein layers vary and may be a further parameter to investigate when it comes to linking the layer's structural softness with lubrication. Higher contact pressures used in this thesis, 40 – 140 MPa, and Zeng et al [113] 2.36 GPa rely on a lower structural softness to provide enhanced lubrication, whereas in other research it appears low contact pressures, observed in tongue-enamel systems, require a higher structural softness for improved lubrication [308, 309]. Conversely, mean contact pressures of 0.9 GPa achieved improved lubrication with a higher structural softness at the nanoscale with Veeregowda's work [109], prompting a reassessment of the rationale behind the measure of structural softness

regarding the scales of testing. Further investigations of contact pressure, structural softness, and tribological systems reflecting the simulated environment will therefore be important to further understand artificial saliva lubrication in enamel systems.

### **Simulating xerostomia conditions**

While it is not clear from these results how different flow rates influence the amount of mucin adsorption onto the gold QCM-D surfaces, this does provide an in-vitro comparison to what may be expected under healthy salivary flow compared to xerostomia. The flow module effectively simulated a consistent flow of salivary solutions to the sensor, while the open module is more suited to stagnant liquid measurements. The latter may be important for simulating the application of an artificial saliva under xerostomia (zero flow) conditions. This could effectively measure the adsorption behaviour in the absence of agitation within the oral cavity, using hydroxyapatite and PDMS coated QCM-D sensors to simulate layer adsorption onto hard and soft oral tissues.

### **Open cell test protocol consistency and limitations**

The open module itself is seldom used to measure adsorption of saliva or saliva substitutes onto surfaces in the literature. This may be attributed to the variations in methodologies used and limitations associated with this arrangement in other studies. The open module exposes the sensor-liquid interface to the lab environment which is a fundamental component of the combined QCM-D Tribometer. This comes with the additional cost of temperature variations from both the environment and the introduction/removal of liquids to the sensor. Conversely the flow module is enclosed around the sensor and liquids passed through a maze of channels that heat liquids to the desired temperature before meeting the sensor. This difference also introduces limitations in terms the applied volume of liquid to the sensor. QSense suggest minimised volumes between 10-50  $\mu\text{L}$  of liquid with the open module, however other studies investigating lipid membrane interactions and ligand – cell adhesion have used 300  $\mu\text{L}$  and 1 mL respectively [316, 317]. This differs from the flow module's sample volume, which at any point in time is approximately 200  $\mu\text{L}$  for comparison. It is unclear how the liquid volume influenced the frequency and dissipation response and may need further investigation and standardisation for similar tests.

Other limitations with the open module were attributed to its susceptibility to noise, either from being exposed to the lab environment or microbubble formation on the surface attenuating the signal response [318]. Removal of the open module's lid accessory after establishing a baseline response has also been documented to cause reversible frequency



and dissipation shifts when used [316]. As such, the lid was not used, which promoted interference from air fluctuations, temperature and any air-borne contamination.

Unlike the flow module which permitted a complete solution exchange at a given setpoint, a partial solution exchange needed to be adopted for the open module. This was done to avoid exposing the sensor's surface to air when switching solution, using pipettes to remove and replace equivalent quantities of solution each time [316]. The changeover process was uncontrolled from a timing point of view depending on the type of solution change required. This therefore limited the analyses of the immediate shift response after a solution change from a rate of change point of view. Furthermore, mechanical perturbation of the adsorbed layer was resultant limitation of the open module's solution change process, which has been observed in a cell adhesion study using the same module [319].

Despite these limitations, the open cell permitted direct interaction between the Triborig and the layer's grown on the QCM-D sensors. It was observed that these mucin layers were different in terms of thickness, structural softness, viscosity and shear modulus, compared to the same established layers in flow conditions, as shown in Figure 8-7. This was hypothesised to be linked to larger adsorbed mass on the sensor's surface, increasing the probability the entrapment and movement of water within the layer. Therefore, the following sections discuss the link between mucin layers adsorbed under static conditions with the mechanical interactions of the Triborig. Further design iterations ought to consider the addition of a pump system to circulate solution and simulate salivary flow conditions in the open module, that could be validated with the flow module arrangement. This would permit a direct tribological evaluation of layers grown under flow conditions.

#### 8.4.2 Influence of mechanical interactions and solutions changes on the properties of established and unestablished layers

##### **Area of mechanical interactions**

The complexity of mucin structures in relation to mechanical interactions were investigated, in relation to the average properties of the whole mucin layer on the sensor's surface. The Hertzian contact diameter (i.e.  $2a$ ) of the Tribo-pair was calculated to be  $3\ \mu\text{m}$ . This meant the area under direct mechanical interaction accounted for 0.0027 % of the total active surface area of the QCM-D sensor (surface area  $\approx 113.09\ \text{mm}^2$  based on  $\varnothing 12\ \text{mm}$  active area [320]). The interaction area was negligible in comparison and therefore the measured mucin layer properties did not wholly account for potential changes under direct mechanical interaction. Instead, mucin layer changes were attributed to indirect mechanical interactions, by the agitation of the solution provided by the Triborig.

### **Influence of mechanical interactions on established mucin layers**

The established Muc + DiW layer properties didn't change under repeated mechanical agitation. Minimal changes came from a slight reduction in the layer's viscosity and thickness which followed a slight reduction in the friction force. The mechanical agitation enabled localised solution flow within the open cell, providing opportunities for lateral interactions with adjacent adsorbed mucin molecules to occur [321]. These lateral interactions may occur after the first tribo-test of P1, evidenced by the increase in the layer's shear modulus, and could suggest entanglement of adsorbed mucin molecules. This effectively closes the layer's structure slightly, reducing the water held within it as active sites for water molecule interactions are replaced by mucin-mucin interactions.

The addition of salt ions presented greater variations to the established mucin layer. While salts potentially reduce the hydration of mucin layers, weak ion crosslinking within the layer is beneficial for surface protection, shown by improved wear resistance at high loads (5 N) on pre adsorbed salivary films [322]. The effect of solution agitation may provide enough shear to break crosslinks as shown by a reduced mucin layer shear modulus after the initial tribo-tests of P1 and P2. Active sites therefore are freed up, permitting water molecule interactions within the layer, increasing the layer's viscosity as solution flows within the layer. The increase in layer thickness can be attributed to more solution with the mucin layer, or the additional adsorption of free mucin competing with surface bound ions at the surface. The friction force on the Muc + PBS layer was shown to permanently change after the initial tribo-test of P1, despite the structural properties changing without reaching a stable value.

The solution was shown to have a more pronounced effect on changing the structural properties of both mucin layers, reducing the friction force under Muc + DiW conditions (comparable to the Muc + PBS layer). Removal of free mucin and ions effectively diluted the environment, forming a high concentration gradient of mucin/salt ions at the surface. The osmotic pressure would have enabled water molecules to flow into these layers, shown by an increased layer viscosity. Furthermore, a reduced structural softness of the Muc + DiW layer and increased layered viscosity correlated with a reduction in frictional force. However, this was not observed in the salt environment, presenting no change to the friction force response despite similar structural changes. Different behaviours have been observed in previous studies. Reducing the salt ion concentration within a salivary layer was shown to reduce its resistance to wear under tribological conditions despite presenting a thick, more hydrated layer [322]. A later study also demonstrated higher friction from a thin salivary film after a pure water rinse, while a thicker diluted salivary film exhibited lower friction after

rinsing [323]. In this current study, low friction was observed in the Muc + DiW layer during the rinse phase, which can be thought of as a dilute mucin layer given the lack of salt ions in the growth solution. However, changes to the friction force do not occur in the ion rich mucin layer where an increase might be expected.

#### **Influence of PBS salts on open cell measurements**

One of the drawbacks of these results is the inconsistent measurement of the PBS and mucin structural properties between all protocols. Flow modules experiments in the previous chapter already present larger variations in the measured structural properties of PBS mucin layers compared to mucin only layers on gold and hydroxyapatite surfaces. This might suggest that in the presence of a PBS solution, the mucin layer's which form a relatively unstable as there is more competition between free mucin and salt ions for layer interactions. This occurs less in the mucin only environment as less competition exists. Furthermore, the larger PBS layer viscosity and shear modulus, almost 2 and 3 time more than the mucin layer's properties respectively, suggested an unstable QCM-D measurement. However, given the variable nature of commercial porcine gastric mucin this may be a combined result of "as-received" mucin with PBS solution [97, 324]. Nevertheless, a stabilisation element may be required to form layers with consistent structural properties under both static and flow conditions on gold surfaces.

#### **Influence of mechanical interactions on the formation of a mucin layer**

The frictional force also increased in the Muc + DiW shear modulus property over the course of P3. The lack of mucin-surface and mucin-mucin interactions within the layer was attributed to this. Hydrated mucin may slide over the surface initially, reducing the frictional force between the probe and surface as an entrained lubricating molecule. As mucin layer interactions develops, less mucin entrainment occurs with layer maturation leading to more cohesion between the layer and probe which requires an additional force to permit movement. Repeat tests will be required to build on and confirmed how the structure softness, shear modulus and viscosity influence the friction force, after additional improvements to the combined QCM-D Tribometer.

## 8.5 Conclusion

The work completed in this chapter aimed to assess whether a link existed between the physical structural properties of mucin layers and lubrication. This was trialled using a bespoke combined tribometer and QCM-D arrangement. The combined QCM-D Tribometer was more suited to examining the influence of protein layer structures on lubrication rather than assessment of mechanically induced tribo-films and structural changes to protein layers. This work highlighted:

- Muc layers grown statically in an open modules QCM-D presented a thicker layer, with increased rigidity (lower structural softness), increased shear modulus and viscosity properties when compared to flow conditions in the flow module. While lubrication was not compared between the two modules, statically grown Muc layers were thought to possess an increased water composition, attributed to additionally mucin-surface interactions and mucin-mucin interactions.
- The use of a novel QCM-D tribometer to examine the role of mechanical interactions with protein layers.
- Triborig tests provided additional evidence that a lower structural softness was favourable for improved mucin lubrication under higher contact pressures, with an increased layer viscosity property, supporting previous research within this thesis.
- Layers properties may change after initial mechanical interactions from tribo-tests. This was hypothesised to relate mechanical shear forces of the probe squeezing water from Muc layers, and enabling mucin-mucin interactions to occur.
- A QCM-D Tribometer could serve as a test bed for further development of artificial saliva substitutes to optimise oral/dental lubrication under different loading environments with further experimental design amendments.

## Chapter 9. Overall discussion, conclusions and future work

### 9.1 Overall discussion

This thesis presents an investigation into the behaviour of porcine gastric mucin as an artificial saliva component solution. This emerged from the need to understand whether a widely available mucin component derived from a pig's stomach, Type II PGM, could provide added benefit to enamel protection from a tribological and tribocorrosive stand point. This work was undertaken with the purpose of enhancing lubrication and wear resistance under mechanical and tribocorrosive conditions, to justify further development of beneficial therapies for xerostomia patients. The influence of surface material, salt type and concentration, and interactions with citric acid on mucin structures, both in solution and adsorbed onto surfaces, have been investigated and discussed in detail. Furthermore, the work presented in this thesis progressively uncovered methodologies to further investigate key parameters by the development of a benchtop in-situ QCM-D tribometer, with respect to mucin layer lubrication mechanisms. This chapter concludes the experimental findings, highlighting limitations of study whilst also proposing the direction of future work.

Both the solution environment and surface material were demonstrated to be critical factors that influenced the adsorption rate, initial adsorption pathways, and surface coverage of mucin layers. Solution composition was shown to play an important role within "as-received" mucin solutions, with salt and acid additions inferring changes to mucin size and stability. Complex salt solutions (PBS) were shown to reduce the mean aggregate size of mucin and improved the stability of free mucin in solution when investigated by DLS and zeta potential studies in Chapter 4 Section 4.2.1. Size alteration within the bulk fluid has further implications on adsorption behaviour where smaller protein structures are more mobile to interact with surfaces [231]. PBS therefore provided the optimal salt composition to facilitate an enhance rate of adsorption onto gold and hydroxyapatite surfaces when adsorption kinetics behaviour was investigated by QCM-D experiments. Simple salt solutions were not as effective, highlighting the importance of salt interplay with mucin and other protein impurities when it comes to surface-solution interactions. AFM investigations into mucin adsorption on both steatite and bovine enamel also highlighted differences in mucin coverage, particularly on steatite where areas of preferential adsorption occurred onto specific locations. Furthermore, comparing mucin adsorption onto gold and hydroxyapatite surfaces further highlighted the dependence on surface chemistry and surface charge regarding adsorption pathways. This is important to understand in the context of developing

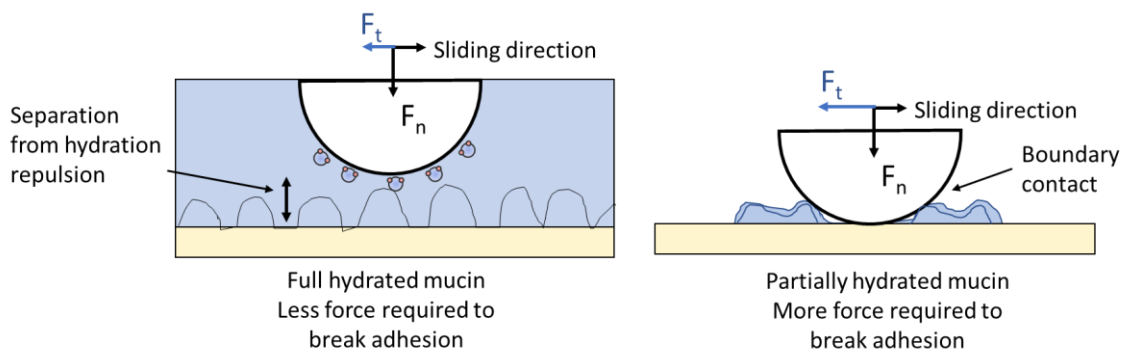
film forming therapies to target dry mouth syndromes, to effectively optimise surface coverage and layer formation on healthy and degraded tooth enamel surfaces.

Following surface adsorption, surfaces were further investigated to understand the restructuring of layers in the absence of tribology, and with mechanical interactions, to understand what this meant in terms of load bearing, hydration and lubrication. Mucin layers were observed to influence lubrication on bulk steatite and bovine enamel surfaces, as well as gold and hydroxyapatite coated quartz sensors, with an observable reduction in the coefficient of friction compared to tests performed in deionised water and PBS solutions only. AFM and QCM-D investigations provided evidence into the layers' properties that might influence this, using QNM to measure layer adhesion and tip deformation alongside viscoelastic modelling of mucin layer shear modulus and viscosity properties. The properties related to the water content and the networking within a layer to be able to bare normal and tangential loads, which related to the presence of water within these layers. The results in this thesis supported other studies which investigated saliva or mucin layer lubrication, where protein layer hydration and glycosylation impact mucin's lubricating ability [60, 302, 247, 249, 109].

Hydration has been observed to impact lubrication behaviour of whole human saliva, presenting friction coefficient of 0.02 compared to 2-3 for air dried saliva [325]. The adhesive nature of the air-dried saliva was alluded to as the reason behind the significantly larger friction results [325]. Furthermore, a suggested mechanism of dry mouth related the functional impairment of salivary mucin on oral surfaces, due to reduced mucin glycosylation (water trapping locations) which are unable to permit rehydration [326]. This highlighted both the importance of hydration in oral lubrication when considering xerostomia patients and the condition of the protein used to promote lubrication.

It could be hypothesised that a combination of the mucin layers adhesion property and load bearing capacity of the mucin layer, dependent on the surface coverage and hydration state, contributed to the potential bio-lubrication of the system as illustrated in Figure 9-1. The pellicle has been considered as a boundary lubricating layer however it is unclear within the literature as to how this boundary layer provides low friction with high wear resistance simultaneously. It has been proposed that mucin within salivary pellicles lowers energy dissipation when exposed to shear (when fully hydrated), similar to polymer brushes, arising from a lack of interpenetration and hydration lubrication [253, 327]. This is closely supported by the observed reduction in layer dissipation on hydrated mucin-bovine enamel surface layers compared to partially hydrated mucin layers, shown by AFM QNM in this thesis. This

was considered with the measured adhesion response between the AFM cantilever and mucin structures, in addition to the supporting lubrication observed on hydroxyapatite QCM-D sensors. Furthermore, the measured deformation property of these mucin layers builds into how adhesion and dissipation, and therefore friction, is reduced by bearing the load between the probe and the surface. The induced separation between contacts reduced direct boundary interactions, independent on layer thickness, which can be attributed to the water molecules within the structure of mucin and the hydration repulsion these provide. Given that the porcine gastric mucin used contains approximately 0.5-1.5% sialic acids within its structure, a directly purified mucin alternative, commercial BSM or an alternative glycoprotein like polymer with a higher proportion of sialic acid groups or similar, will have a greater influence on improving lubrication through this mechanism.



*Figure 9-1 Hypothesised influence of mucin coverage and hydration in a tribological interface. Entrapment of water molecules within mucin's structure permit load bearing, separating surface from direct boundary contact, aided by repulsion of hydration layers. When partially hydrated with limited coverage, surfaces are more likely to come into boundary contact requiring a greater force to break adhesion forces.*

In the literature, mucin and saliva studies tend to focus towards pellicle formation on soft tissues/physiologically representative materials and lubrication as opposed to enamel layer lubrication [302, 309, 308, 53, 122, 102]. Investigations into salivary layers on human tooth enamel only go as far as prescribing the improved lubrication to the presence of mucin or statherin compared to a bare enamel surface, and that salivary layer composition influences lubrication [328, 54]. However, it was also observed that alcohol stimulated salivary pellicles on enamel presented reduced lubrication with increased adhesion properties, indicating that the measure of surface adhesion was a good indicator to layer lubrication [328].

Other studies investigated layer properties from the perspective of soft-to-hard contact, simulating the oral tissue lubrication with dental surfaces, suggesting increased structural softness was an important property to consider regarding lubrication [109, 309]. A higher structural softness is generally associated with a higher level of energy dissipation per unit mass absorbed onto a surface, however the QNM work indicated mucin on bovine enamel lowered the dissipation and lowered the coefficient of friction. This suggested a reverse relationship between the structural softness property and coefficient friction in the mucin enamel system.

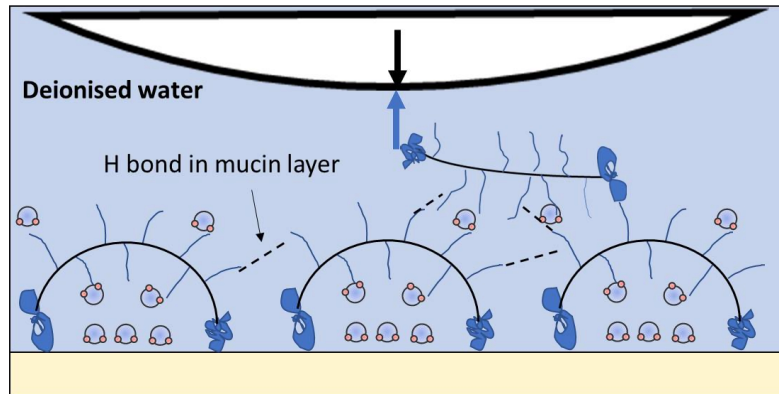
The work presented in this thesis suggests that for hard surfaces interacting with hard counter faces, a mucin layer's shear moduli and viscosity properties might provide a greater insight into the layer's structure and how it may influence lubrication, as proposed in Figure 6-16, which also supports the above interaction proposed Figure 9-1. It was hypothesised that structures with a higher shear modulus and viscosity were indicative of the load bearing properties, as demonstrated by tribo-tests between gold and hydroxyapatite. The higher shear modulus suggested an increased amount of water entrapment in the layers, while the viscosity related to the flow response within the layer. This behaviour can be disrupted by PBS salts, reducing mucin networking by competing with areas where H bonding may facilitate entrapment, however stronger electrostatic interaction between cations and ionic regions may maintain a layer's viscosity property. Furthermore, surface bound mucin interactions with PBS salts provide these localised structures with further rigidity as shown by AFM QNM. The following mechanism in Figure 9-2 outlines this hypothesised process in a) deionised water and b) in PBS.



a)

More water within layer from additional mucin networking

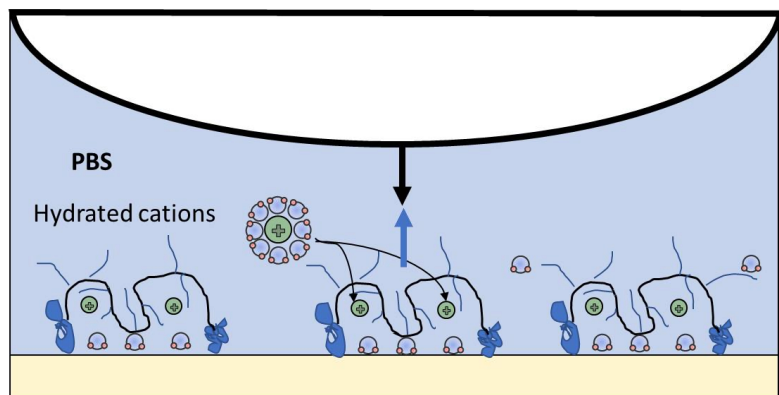
Structure and networking resist flow within layer, providing load bearing benefit



b)

PBS salt incorporated into mucin structure reducing water and networking within layer

Incorporated salts resistant to movement due to strong electrostatic bonding with mucin, promoting load bearing



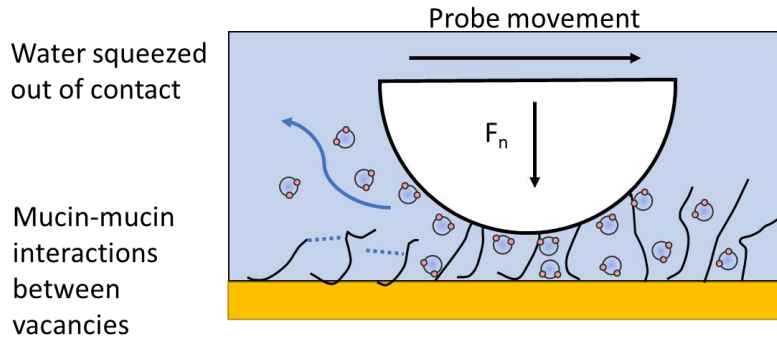
*Figure 9-2 Hypothesis load bearing of mucin structures in a) deionised water and b) PBS solution.*

The observed properties of mucin layers may therefore be used to describe the wear resistance of bovine enamel surfaces under mucin conditions, which was further enhanced with PBS salts. AFM investigations demonstrated that PBS enhanced mucin layer load bearing properties on bovine enamel, as illustrated previously in Figure 4-37. PBS demonstrated an overall improvement in wear resistance on bovine enamel during tribometer tests on bovine enamel compared to mucin alone, which was partly attributed to the mucin layer interaction with salts and some evidence of reduced enamel degradation, indicated by an improved surface crystallinity observed by Raman spectroscopy. However, enhanced mucin lubrication with PBS was not observed on hydroxyapatite surfaces, with comparable coefficient of friction to mucin layers without PBS. Furthermore, examination of mucin layer's shear modulus and viscosity properties suggested PBS reduced water within the mucin layers compared layers without PBS, although this was shown to have limited effect on lubrication under the two conditions. Nevertheless, from a surface protection point of view, the ability to bear greater loads may explain the improved wear resistance of bovine enamel, as separation between the Y-TZP probe and surface is maintained, preventing direct boundary contact.

Finally, this work expanded on the wear mechanism of bovine enamel under tribological and tribocorrosion conditions, highlighting the importance of a corrosion measurement (calcium release) when assessing overall tooth degradation within the wear area and the surrounding area in contact with the bulk solution. To the author's knowledge, this work presented novel insights into tooth tribocorrosion, combining methods taken from static corrosion cycling methodologies and applying it to a tribological setting to provide a quantitative evaluation of degradation compared to qualitative relationships with degradation and surface mechanical properties, illustrated in Figure 5-18. Raman spectroscopy and XPS investigations provided further insight into mucin's role on tribocorrosion, specifically differences identified within wear scar locations. Tribo-tests under mucin conditions demonstrated a reduced degree of demineralisation compared to tests within non- mucin environments, suggesting improved surface protection in the tribo-contact. A higher proportion of mucin was also identified to be present within the wear areas of samples tested in neutral pH mucin solution.

Overall, this suggested that a potential tribofilm was formed providing protection of the enamel surface. It was hypothesised that this could form from mechanical squeezing of water from the established layer, promoting mucin-mucin interactions at the tribological interface, as indicated by Triborig experiments and changes to mucin layer shear modulus properties after mechanical interaction. An illustration of how this could form is presented in Figure 9-3, with the proposed layer formation mechanism under mechanical conditions from studies on gold in Figure 9-3a), what this could suggest to the distribution of mucin on bovine enamel in Figure 9-3b), and how this reduces calcium ion release under DiW and PBS conditions in Figure 9-3c). Repeat work on hydroxyapatite will be required to confirm this behaviour with the QCM-D Tribometer.

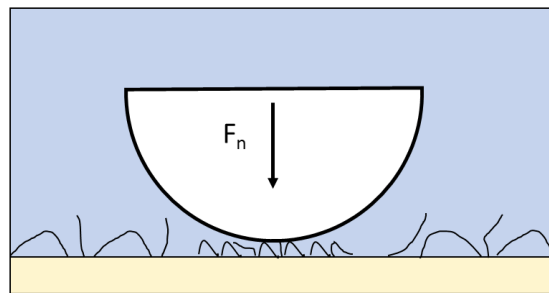
a)



b)

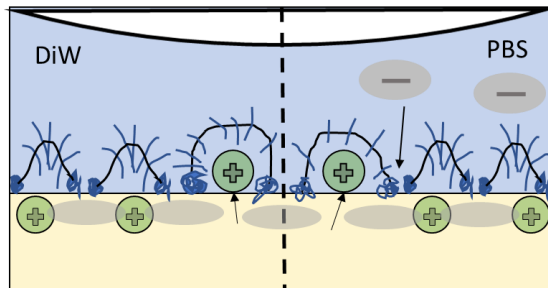
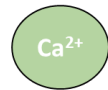
Mucin concentrated within wear location

Mucin dispersed outside wear location



c)

Mucin tribofilm prevents release of  $\text{Ca}^{2+}$  ions by forming a layer to reduce internal flow



Phosphate ions within PBS provide additional support to enamel crystal structure



*Figure 9-3 Hypothesised mucin tribofilm illustration showing a) proposed mechanism of water movement out of mucin layers on gold leading to more elastic layers by mucin-mucin interactions, b) propose difference in mucin structures on bovine enamel after mechanical interactions leading to a more condense layer within the wear contact, and c) the effect of the condensed mucin layer on trapping calcium ions close to enamel's surface, with additional fortification provided by phosphate ions in PBS.*

In the acidic environments, mucin's presence appeared to provide limited protection, having only been shown to reduce tooth degradation compared to the acid only environment. AFM, NTR<sup>3</sup>, optical microscopy and VSI methods<sup>3</sup> all indicated that demineralisation was the dominant surface interaction, with the addition of mucin causing additional surface damage to bovine enamel. This is in line with recent work investigating the "anti-erosive" impact of mucin, where mucin only and combinations of mucin/chitosan combinations were shown to provide no protective effects on human tooth enamel demineralisation [298]. However, other research suggests mucin within an artificial saliva was comparable to human saliva in

corrosion prevention [106]. Differences in erosion behaviour relate to the solution composition used and the application of mucin within studies. On the one hand enamel samples were treated for 2 hours in a mucin solution which contained additional salts, glucose, ascorbic acid and urea, and presented similar protection after citric acid demineralisation cycles to human saliva compared to solutions without mucin [106]. On the other hand, citric acid demineralised enamel samples were treated with mucin solutions without addition salt and additives [298]. In this work, citric acid/mucin solutions were introduced to surfaces which had been immersed in mucin only solutions, where little protection was observed. This highlights the importance of additive components within artificial saliva solutions, concluding that mucin alone cannot provide adequate protection to tooth enamel.

## 9.2 Conclusions

The research questions initially proposed in the aims and objectives have been addressed by the work presented in this thesis. This served to further explore the methodologies used to investigate and understand the implication of mucin layers and their role on the tribology and tribocorrosion of dental materials. The key messages of this work are summarised as follows:

- Commercial porcine gastric mucin type II demonstrated enhanced lubrication on bovine enamel, and hydroxyapatite surfaces within deionised water, and PBS environments. The lubrication was associated with the reduced adhesion between tribological contacts that mucin provided, which was considered to linked with the hydrophilic nature of both mucin and hydroxyapatite-based surfaces.
- Surface chemical composition played a key role in mucin layer adsorption kinetics, mature layer properties and mucin lubrication. Mucin layer properties were also influenced by bulk solution composition, where hydroxyapatite surfaces demonstrated a higher sensitivity to the addition of complex salts to the bulk solution, while this was limited on gold.
- Steatite was demonstrated to not be a feasible alternative to bovine enamel for research which aimed to investigate mucin layer adsorption and tribology. Surfaces prepared by the same methods as bovine enamel presented rougher surface features, and the voids in the trifocal structure were not comparable to the ordered and anisotropic structure of bovine enamel.
- The tribocorrosion of bovine enamel was determined to be a combination observable surface wear and unknown wear below the surface, culminating as an

overall calculation of tooth degradation. Surface investigation methods in this thesis proved to be insufficient in quantifying subsurface wear, however the proposed mechanism will guide future investigation into overall tooth enamel degradation.

- There was no added benefit of mucin to lubrication, surface wear, surface integrity and corrosion protection within a pH 3.1 citric acid environment.

### 9.3 Limitations of study and future work

#### 9.3.1 Use of physiologically relevant mucin type and purity

The work presented in the thesis provided a benchmark understanding to how type II PGM influenced aspects of viscoelastic layer formation on a range of surfaces and how this improved lubrication and wear protection on bovine enamel. Given that the use of this type of mucin is considered controversial outside of dental tribology, it would be beneficial to compare how other mucin types influence layer formation, density, thickness, rheological and structural properties, and how this impacts protection against tribocorrosion. A molecule with a larger proportion of water trapping groups, such as sulphates, sialic acids or others, and the ability to form a highly crosslinked network may provide benefits to general enamel wear protection and lubrication under most environments. Bovine submaxillary mucin is another commercially available mucin type, derived from salivary glands, which has an increased proportion of sialic acid groups and is more intact compared to type II PGM [97, 228]. Furthermore, purification of commercial mucin to remove the impact of salt and other protein impurities may serve to build onto the adsorption behaviour and layer properties discussed in this work. At the time of writing, further work is currently being carried out to understand the implications of purification.

#### 9.3.2 Use of XRD on bovine enamel samples

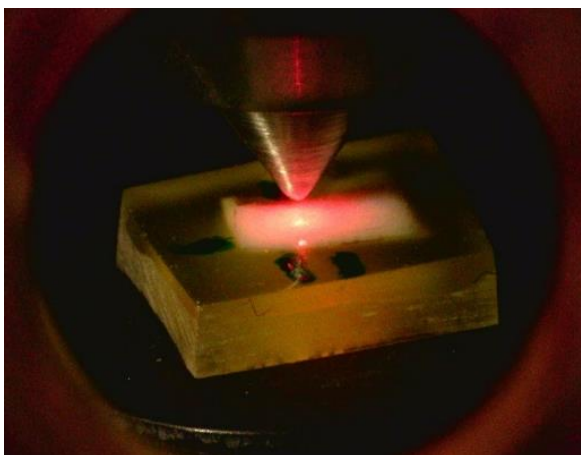
One question which was not addressed in this thesis was whether a surface's crystalline structure and bulk composition influenced mucin layer properties and subsequent mucin lubrication. A homogeneous hydroxyapatite coating onto quartz only provided an insight into the surface chemistry impact of layer formation and lubrication, while the structurally orientated hydroxyapatite prisms and rods in bovine enamel, examined by XRD in this thesis, may expose a more specific interface for mucin-surface and mucin-solution interactions [329]. It would be beneficial to examine hydroxyapatite crystallinity in relation to mucin or salivary layer formations in relation bovine and human tooth enamel materials to provide a feasible relation in layer's measures with one surface compared to layer's tested on another.

### 9.3.3 Use of a static or incremental load profile for all tribometer tests

The tribology results presented in this thesis relate to a dynamically controlled constant loading force applied during a sliding cycle, providing an insight into peak force sliding conditions observed in mastication. However, a dynamic loading regime over a single cycle may provide further insight into dental wear and tribocorrosion under more physiological related loading profiles. Furthermore, the behaviour of mucin layers under dynamic load profiles could be further investigated from a lubrication point of view. This could be done with a modified QCM-D tribometer arrangement, examining structural behaviour from impact, loading and sliding behaviours. The nanoindentation module of the Triborig would also compliment investigations.

### 9.3.4 Use of XPS and location targeting specific areas

The XPS system was limited due to the lack of ability to properly target specific locations on enamel surfaces. As wear scars were approximately 1 mm in length, a precise survey could not be attained directly within the wear track. Three cameras and a laser were used to target the centre of the scar using markers on the sample, where Figure 9-4 provides an example of the scan area highlighted by the laser. Despite this limitation, this investigation does highlight some interesting differences between the wear scar area and areas further away from the scar. An in-depth characterisation of a potential tribo-films therefore could not be completed under the current experimental set up, however this should be re-examined with more samples, a larger wear scar area and refinements in location targeting to directly uncover site specific chemistries, within different locations of the wear scar.

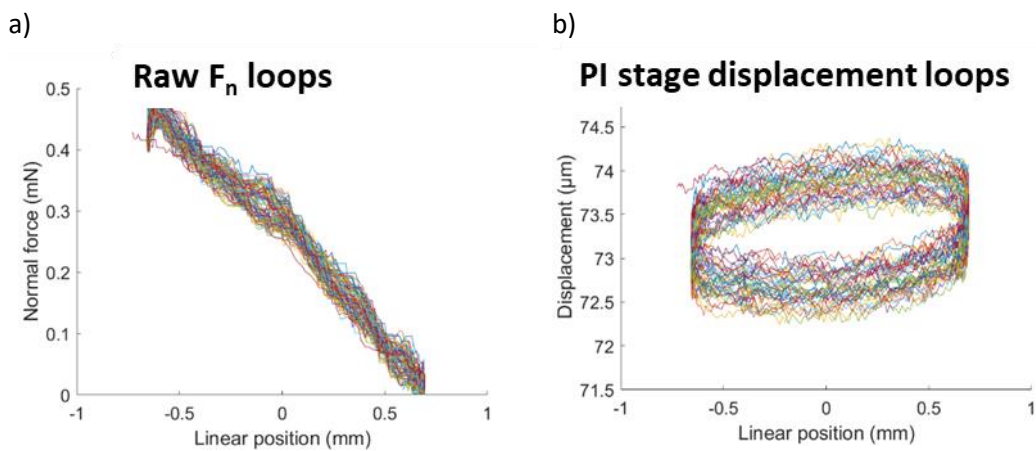


*Figure 9-4 Example of targeting the wear scar location with XPS system.*

### 9.3.5 Use of the Triborig system combined with the QCM-D

The Triborig system, when paired with the QCM-D, presented a limitation regarding sample slanting (sample's top and bottom surfaces not parallel) and software corrections. Figure 9-5

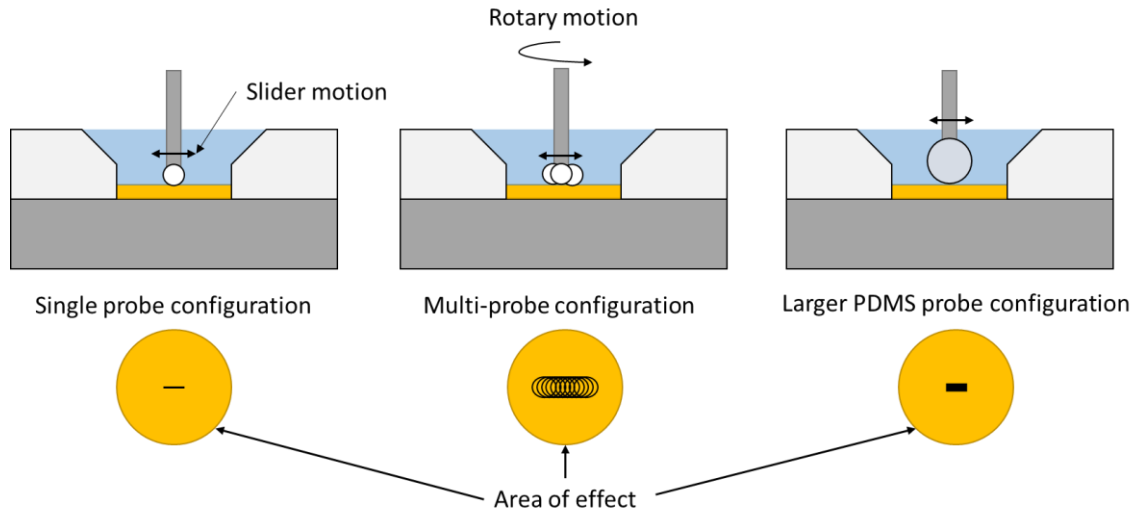
shows the raw displacement loops for  $F_n$  and the piezo stage displacement, highlighting an area for improvement. The normal force is slanted due to the position of the Triborig in relation to QCM-D, shown in Figure 9-5a). In contrast the piezo stage displacement is not slanted, shown in Figure 9-5, presenting a systematic error where the normal force was not corrected over the course of the displacement loop. This was attributed to the PID (proportional integral derivative) control of the feedback loop which control the  $F_n$ . More responsive settings should be tested to ensure the piezo stage is dynamically controlled to output a more consistent/ constant normal force. This would benefit future tests to ensure a constant load is applied over a slightly slanted surface.



*Figure 9-5 Raw displacement loops for a)  $F_n$  and b) the piezo (PZ) stage displacement.*

### 9.3.6 Use of linear sliding motion on QCM-D sensors with the QCM-D tribometer

Future iterations of the test arrangement to examine structural changes to layers from direct mechanical interactions should consider an alternative probe material and design. Changing the probe to softer material like polydimethylsiloxane (PDMS), and increasing the probe diameter, will enable a greater area for direct mechanical interaction to investigate changes to the directly affected area. Additionally, a rotating multi-probe set up should also be considered to maximise the interaction area on the QCM-D sensor. This configuration has been used to maximise interaction area of a cobalt chromium molybdenum (CoCrMo) alloy pins on CoCrMo coated QCM-D sensors [330]. The radius of the multi-probe arrangement can be adjusted depending on the size and softness of each probe component. The effect has been illustrated in Figure 9-6. By interacting with a larger surface area on the QCM-D sensor, the measured frequency and dissipation properties would provide a more accurate representation of a mechanically altered layer to further explain tribofilm behaviour.



**Figure 9-6** Illustration of how the Triborig's probe configuration can increase the area of effect on the QCM-D sensor.

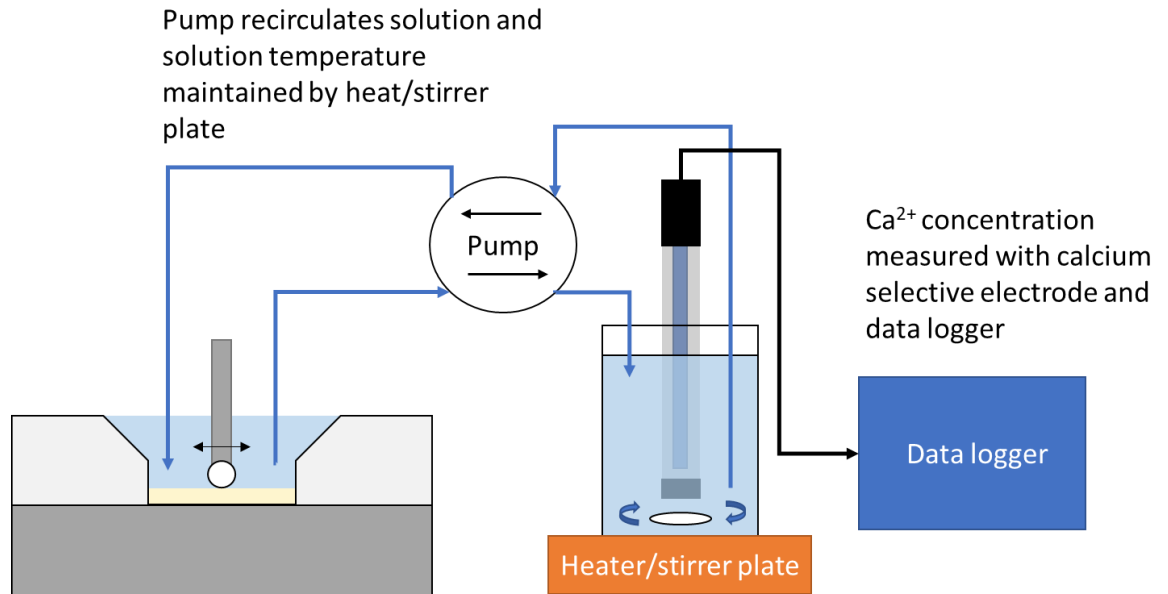
### 9.3.7 Use of high contact pressure during tribo-tests, generally, and with the QCM-D tribometer

A lot of mucin layer studies linked to lubrication tend to focus around softer, low contact pressure applications rather than the higher contact pressures associated with tooth-on-tooth interactions. Additional research addressing the latter would provide further knowledge of the importance of protein layers on protection under these conditions. Upon confirmation, artificial saliva solutions can be developed with this method of in-situ testing.

### 9.3.8 Use of static flow conditions with the QCM-D tribometer and NTR<sup>3</sup> tribo-tests

Addition features such as a circulating solution pump will enable the simulation of flow condition with QCM-D tribometer arrangement, which could be used to provide further insight into layer degradation in-situ. The flow inlet and outlet would be positioned perpendicular to the direction of sliding to minimise any directional forces in the  $F_t$  direction from the flow. Flow rates should also be representative of salivary flow, similar to the flow conditions used in QCM-D tests in Chapter 6. Should hydroxyapatite coated QCM-D sensors be used, the addition of a calcium selective electrode would provide an insight into the protection of mucin layer under corrosion and tribocorrosion conditions. Under this proposed arrangement, the structural properties of the mucin layers could be linked with the calcium concentration in the circulating solution as the schematic in Figure 9-7 illustrates.





*Figure 9-7 Proposed modification to Tribo-QCM-D for tribocorrosion measurements of hydroxyapatite coated sensors.*

#### 9.4 Closing statement

From the work documented in this thesis it can be concluded that while mucin may be a viable additive for artificial salivas within a neutral pH environment, it is not sufficient to protect dental surfaces within an acidic environment alone. For artificial salivas to provide additional benefit to xerostomia patients, further work should focus on either an alternative “anti-corrosive” component within formulations, or to identify which components are crucial to enable mucin to provide protection during demineralisation and tribocorrosion in general.

## Chapter 10. References

- [1] A. Lussi, "Erosive tooth wear - A Multifactorial Condition of Growing Concern and Increasing Knowledge," in *Dental Erosion*, Basel, Karger, 2006, pp. 1-8.
- [2] Global Burden of Disease Collaborative Network, "Global Burden of Disease Study 2019 (GBD 2019)," Institute of Health Metrics and Evaluation (IHME), Seattle, 2020.
- [3] M. Vujjic and S. Listl, "An Economic perspective of the global burden of dental caries," in *ACFF Make Cavities History Taskforce*, 2021.
- [4] J. M. Cate, "Toothpaste abrasivity: an introduction to the symposium.," *International Dental Journal*, vol. 52, pp. 397-398, 2002.
- [5] GBD 2017 Disease and Injury Incidence and Prevalence Collaborators, "Global, regional, and national incidence, prevalence, and years lived with disability for 354 diseases and injuries for 195 countries and territories, 1990–2017: a systematic analysis for the Global Burden of Disease Study," *Lancet*, vol. 392, no. 10159, pp. 1789-1858, 2018.
- [6] A. Lussi and T. Jaeggi, "Erosion - diagnosis and risk factors," *Clinical Oral Investigations*, vol. 12, no. suppl, pp. S5-S13, 2008.
- [7] D. L. Gambon, H. S. Brand and E. C. I. Veerman, "Dental erosion in the 21st Century: what is happening to nutritional habits and lifestyle in our society.," *British Dental Journal*, vol. 213, pp. 55-57, 2012.
- [8] D. White, N. Pitts, J. Steele, K. Sadler and B. Chadwick, "2: Disease and related disorders - a report from the Adult Dental Health Survey 2009," The NHS Information Centre for Health and Social Care, 2011.
- [9] "Cost of dental treatment," Queensway Dental Clinic, 2019. [Online]. Available: <https://www.queensway.co.uk/costs/treatment-fees/>. [Accessed 06 05 2021].
- [10] Private Healthcare UK, "Tooth extraction," LaingBuisson International Limited, 2020. [Online]. Available: [https://www.privatehealth.co.uk/conditions-and-treatments/tooth-extraction/costs/?product\\_id=375](https://www.privatehealth.co.uk/conditions-and-treatments/tooth-extraction/costs/?product_id=375). [Accessed 06 05 2021].

- [11 NHS Services, "How much will I pay for NHS dental treatment?," 21 01 2021. [Online].  
] Available: <https://www.nhs.uk/nhs-services/dentists/dental-costs/how-much-will-i-pay-for-nhs-dental-treatment/>. [Accessed 06 05 2021].
- [12 M. Armstrong, "The poor state of the nation's teeth: can anyone be bothered?,"  
] NuffieldTrust QualityWatch, 02 11 2017. [Online]. Available:  
<https://www.nuffieldtrust.org.uk/news-item/the-poor-state-of-the-nation-s-teeth-can-anyone-be-bothered>. [Accessed 06 05 2021].
- [13 Public Health England, "Hospital tooth extractions of 0 to 19 year olds," in *Public Health  
] England*, London, 2019.
- [14 Public Health England, "Health Matters: Child dental health," in *Public Health England*,  
] London, 2017.
- [15 P. Blackburn, "LaingBuisson's comprehensive study into the UK's dental care market,"  
] 2019.
- [16 NHS Dental Statistics, "NHS Dental statistics for England - 2020-21 Annual Report:  
] Annex 1 (Tables and Charts)," in *NHS Dental Statistics*, 2021.
- [17 C. H. Wilder-Smith, A. Materna, L. Martig and A. Lussi, "Gastro-oesophageal reflux is  
] common in oligosymptomatic patients with dental erosion: A pH-impedance and  
endoscopic study," *United European Gastroenterol J*, vol. 3, no. 2, pp. 174-181, 2015.
- [18 B. A. Agostini, G. O. Cericato, E. R. Silveira, G. G. Nascimento, F. dos Santos Costa, W.  
] M. Thomson and F. Demarco, "How common is Dry Mouth? Systematic Review and  
Meta-Regression Analysis of Prevalence Estimates," *Brazilian Dental Journal*, vol. 29,  
no. 6, pp. 606-618, 2018.
- [19 A. Villa, C. L. Connel and S. Abati, "Diagnosis and management of xerostomia and  
] hyposalivation," *Therapeutics and Clinical Risk Management*, vol. 11, pp. 45-51, 2015.
- [20 J. M. Plemons, I. Al-Hashimi and C. L. Marek, "Managing Xerostomia and salivary gland  
] hypofunction: Executive summary of a report from the American Dental Association  
Council on Scientific Affairs," *The Journal of the American Dental Association*, vol. 145,  
no. 8, pp. 867-873, 2014.
- [21 U. Lendenmann, J. Grogen and F. G. Oppenheim, "Saliva and dental pellicle: a review,"  
] *Advances in Dental Research*, vol. 14, pp. 22-28, 2000.

- [22 I. C. Berg, M. W. Rutland and T. Arenbrant, "Lubricating properties of the initial salivary pellicle – an afm study," *Biofouling*, vol. 19, no. 6, pp. 365-369, 2003.
- [23 S. P. Humphrey and R. T. Williamson, "A review of saliva: Normal composition, flow, and function," *Journal of Prosthetic Dentistry*, vol. 85, no. 2, pp. 162-169, 2001.
- [24 C. E. Christersson, L. Lindh and T. Arnebrant, "Film-forming properties and viscosities of saliva substitutes and human whole saliva," *European Journal of Oral Sciences*, vol. 108, no. 5, pp. 418-425, 2000.
- [25 A. Vissink, H. A. Waterman, E. J. 's Gravenmade, A. K. Panders and A. Vermey, "Rheological properties of saliva substitutes containing mucin, carboxymethylcellulose or polyethylenoxide," *Journal of Oral Pathology*, vol. 13, pp. 22-28, 1984.
- [26 G. W. Stachowiak and A. W. Batchelor, "13. Corrosive and Oxidative Wear," in *Engineering Tribology (4th Edition)*, Elsevier, 2014, pp. 597-620.
- [27 Y. Q. Wu, J. A. Arsecularatne and M. Hoffman, "Effect of acidity on attrition-corrosion of human dental enamel," *Journal of the Mechanical Behaviour of Biomedical Materials*, vol. 44, pp. 23-34, 2015.
- [28 Y. Zhang, J. A. Arsecularatne and M. Hoffman, "The effects of three different food acids on the attrition-corrosion wear of human dental enamel," *Journal of Physics D Applied Physics*, vol. 48, no. 285401, pp. 1-10, 2015.
- [29 E. Sajewicz, "Tribological behaviour of human enamel in red wine and apple juice environments," *Wear*, vol. 262, pp. 308-315, 2007.
- [30 J. Zheng, F. Xiao, L. M. Qian and Z. Zhou, "Erosion behaviour of human tooth enamel in citric acid solution.," *Tribology International*, vol. 42, no. 11-12, pp. 1558-1564, 2009.
- [31 J. Zheng, F. Xiao, L. Zheng, L. M. Qian and Z. R. Zhou, "Erosion behaviour of human teeth at different depths.," *Tribology International*, vol. 43, pp. 1262-1267, 2010.
- [32 L. Zheng, J. Zheng, L. Q. Weng, L. M. Qian and Z. R. Zhou, "Effect of remineralization on the nanomechanical properties and microtribological behaviour of acid-eroded human tooth enamel," *Wear*, vol. 271, no. 9-10, pp. 2297-2304, 2011.

- [33 A. Bardow, F. Lagerlof, B. Nauntofte and J. Tenovuo, "Chapter 11: The role of saliva," ]  
] in *Dental Caries: The disease and its clinical management 2nd ed*, London, Blackwell, 2008, pp. 190-207.
- [34 B. G. Cooper, C. Bordeianu, A. Nazarian, B. D. Snyder and M. W. Grinstaff, "Active ]  
] agents, biomaterials, and technologies to improve biolubrication and strengthen soft tissues," *Biomaterials*, vol. 181, pp. 210-226, 2018.
- [35 B. Staff, "Tooth Anatomy - Medical Gallery of Blausen Medical 2014," *WikiJournal of ]  
] Medicine*, vol. 1, no. 2, p. 66, 2014.
- [36 Y. H. Zhang, W. Du, X. D. Zhou and H. Y. Yu, "Review of research on the mechanical ]  
] properties of the human tooth," *International Journal of Oral Science*, vol. 6, no. 2, pp. 61-69, 2014.
- [37 M. Braden, "Biophysics of the Tooth," *Frontiers of oral physiology*, vol. 2, pp. 1-7, 1975. ]  
]
- [38 J. D. B. Featherstone and A. Lussi, "Understanding the chemistry of Dental Erosion. ]  
] Lussi, A (ed): Dental Erosion," *Monographs in Oral Science. Basel, Karger*, vol. 20, pp. 66-76, 2006.
- [39 E. Lee, P. Wadhwa, M. Kim, H. B. Jiang, I. Um and Y. Kim, "Organic Matrix of Enamel ]  
] and Dentin and Developmental Defects," in *Human Teeth – Structure and Composition of Dental Hard Tissues and Developmental Dental Defects* , London, United Kingdom, IntechOpen, 2021.
- [40 J. D. B. Featherstone, C. P. Shields, B. Khademazad and M. D. Oldershaw, "Acid ]  
] reactivity of carbonated apatites with strontium and fluoride substitutions," *Journal of Dental Research*, vol. 62, no. 10, pp. 1049-1053, 1983.
- [41 A. J. Ortiz-Ruiz, J. D. Teruel-Fernandez, L. A. Alcolea-Rubio, A. Hernandez-Fernandez, Y. ]  
] Martinez-Beneyto and F. Gispert-Guirado, "Structural differences in enamel and dentin in human, bovine, porcine and ovine teeth," *Annals of Anatomy*, vol. 218, pp. 7-17, 2018.
- [42 J. Xia, L. Hua, L. Chen, Z. Zhou, L. Qian and P. S. Ungar, "Enamel crystallite strength and ]  
] wear: nanoscale responses of teeth to chewing loads," *Journal of The Royal Society Interface*, vol. 14, no. 20170456, pp. 1-8, 2017.

- [43 A. Kallistova, R. Skala, M. Slouf, P. Cejchan, I. Matulkova and I. Horacek, "Enamel apatite crystallinity significantly contributes to mammalian dental adaptations," *Scientific Reports*, vol. 8, no. 5544, pp. 1-9, 2018.
- [44 R. Halgas, J. Dusza, J. Kaiferova, L. Kovaksova and N. Markovska, "NANOINDENTATION TESTING OF HUMAN ENAMEL AND DENTIN," *Ceramics*, vol. 57, no. 2, pp. 92-99, 2013.
- [45 J. de Dios Teruel, A. Alcolea, A. Hernandez and A. J. Ortiz Ruiz, "Comparison of chemical composition of enamel and dentine in human, bovine, porcine and ovine teeth," *Archives of Oral Biology*, vol. 60, pp. 768-775, 2015.
- [46 L. J. Oesterle, W. C. Shellhart and G. K. Belanger, "The use of bovine enamel in bonding studies," *American Journal of Orthodontics and Dentofacial Orthopedics*, vol. 114, no. 5, pp. 514-519, 1998.
- [47 C. Wang, Y. Li, X. Wang, L. Zhang, Tiantang and B. Fu, "The Enamel Microstructure of Bovine Mandibular Incisors," *The Anatomical Record*, vol. 295, pp. 1698-1706, 2015.
- [48 G. Yassen, J. Platt and A. Hara, "Bovine teeth as substitute for human teeth in dental research: a review of literature," *Journal of Oral Science*, vol. 53, no. 3, pp. 273-282, 2011.
- [49 W. L. Siqueira, H. C. Margolis, E. J. Helmerhorst, F. M. Mendes and F. G. Oppenheim, "Evidence of intact histatins in the in vitro acquired enamel pellicle," *Journal of Dental Research*, vol. 89, pp. 626-630, 2010.
- [50 P. D. V. de Almeida, A. M. T. Gregio, M. A. N. Machado, A. A. S. de Lima and L. R. Azevedo, "Saliva Composition and Functions: A Comprehensive Review," *The Journal of Contemporary Dental Practice*, vol. 9, no. 3, pp. 72-80, 2008.
- [51 M. Moritsuka, Y. Kitasaki, M. F. Burrow, M. Ikeda, J. Tagami and S. Nomura, "Quantitative assessment for stimulated saliva flow rate and buffering capacity in relation to different ages," *J Dent*, vol. 34, no. 9, pp. 716-720, 2006.
- [52 J. B. D. Featherstone, "Dental Caries: a dynamic disease process," *Australian Dental Journal*, vol. 53, pp. 286-291, 2008.
- [53 A. Sarkar, E. Andablo-Reyes, M. Bryant, D. Dowson and A. Neville, "Lubrication of soft oral surfaces," *Current Opinion in Colloid & Interface Science*, vol. 39, pp. 61-75, 2019.

- [54 Y. F. Zhang, J. Zheng, L. Zheng, X. Y. Shi, L. M. Qian and Z. R. Zhou, "Effect of adsorption time on the lubrication properties of the salivary pellicle on human tooth enamel," *Wear*, vol. 301, no. 1-2, pp. 300-307, 2013.
- [55 W. L. Siqueira, M. T. B. R. Santos, E. Oliveira and J. Nicolau, "Comparison of electrolyte concentrations in whole saliva of individuals with and without cerebral palsy," *Quintessence International*, vol. 38, no. 4, pp. 301-306, 2007.
- [56 G. E. Youngburg, "Salivary Ammonia and its Relation to Dental Caries," *Journal of Dental Research*, vol. 15, no. 5, pp. 247-264, 1935.
- [57 P. S. Hench and M. Aldrich, "The concentration of urea in saliva," *Journal of the American Medical Association*, vol. 79, no. 17, pp. 1409-1412, 1922.
- [58 D. Esser, G. Alvarez-Llamas, M. P. de Vries, D. Weening, R. J. Vonk and H. Roelofsen, "Sample Stability and Protein Composition of Saliva: Implications for Its Use as a Diagnostic Fluid," *Biomark Insights*, vol. 3, pp. 25-27, 2008.
- [59 A. Ash, P. J. Wilde, D. J. Bradshaw, S. P. King and J. R. Pratten, "Structural modifications of the salivary conditioning film upon exposure to sodium bicarbonate: implications for oral lubrication and mouthfeel," *Soft Matter*, vol. 12, pp. 2794-2801, 2016.
- [60 A. A. Feiler, A. Sahlholm, T. Sandberg and K. D. Caldwell, "Adsorption and viscoelastic properties of fractionated mucin (BSM) and bovine serum albumin (BSA) studied with quartz crystal microbalance (QCM-D)," *Journal of Colloid and Interface Science*, vol. 315, no. 2, pp. 475-481, 2007.
- [61 T. Halthur, T. Arnebrant, L. Macakova and A. Feiler, "Sequential adsorption of bovine mucin and lactoperoxidase to various substrates studied with quartz crystal microbalance with dissipation," *Langmuir*, vol. 26, no. 7, pp. 4901-4908, 2010.
- [62 M. S. Park, J. W. Chung, Y. K. Kim, S. C. Chung and H. S. Kho, "Viscosity and wettability of animal mucin solutions and human saliva," *Oral Diseases*, vol. 13, no. 2, pp. 181-186, 2007.
- [63 J. F. Prinz, E. A. de Wijk and L. Huntjens, "Load dependency of the coefficient of friction of oral mucosa," *Food Hydrocolloids*, vol. 21, no. 3, pp. 402-408, 2007.
- [64 B. Staff, "Salivary glands - Medical Gallery of Blausen Medical 2014," *WikiJournal of Medicine*, vol. 1, no. 2, p. 23, 2014.

- [65 K. C. Dee, D. A. Puleo and R. Bizios, "Chapter 2: Proteins," in *An Introduction to Tissue-Biomaterial Interactions*, Hoboken, New Jersey, Wiley & Sons, inc., 2002, pp. 15-35.
- [66 K. C. Dee, D. A. Puleo and R. Bizios, "Chapter 3: Protein-Surface Interactions," in *An Introduction to Tissue-Biomaterial Interactions*, Hoboken, New Jersey, Wiley & Sons, inc., 2002, pp. 37-52.
- [67 I. C. H. Berg, Y. M. Elofsson, A. Joiner, M. Malmsten and T. Arnebrant, "Salivary adsorption onto hydroxyapatite and sds-mediated elution studied by in situ ellipsometry," *Biofouling*, vol. 17, no. 3, pp. 173-187, 2001.
- [68 K. Kandori, T. Shimizu, A. Yasukawa and T. Ishikawa, "Adsorption of bovine serum albumin onto synthetic calcium hydroxyapatite: influence of particle texture," *Colloids and Surfaces B: Biointerfaces*, vol. 5, pp. 81-87, 1995.
- [69 W. L. Siqueira, W. Custodio and E. E. McDonald, "New insights into the composition and functions of the acquired enamel pellicle," *Journal of Dental Research*, vol. 91, no. 12, pp. 1110-1118, 2012.
- [70 M. Hannig and A. Joiner, "The structure, function and properties of the acquired pellicle," *Monographs in Oral Science*, vol. 19, pp. 29-64, 2006.
- [71 A. Joiner, A. Schwarz, C. J. Philpotts, T. F. Cox, K. Huber and M. Hannig, "The protective nature of pellicle towards toothpaste abrasion on enamel and dentine," *Journal of Dentistry*, vol. 36, no. 5, pp. 360-368, 2008.
- [72 W. L. Siqueira, W. Zhang, E. J. Helmerhorst, S. P. Gygi and F. G. Oppenheim, "Identification of protein components in in vivo human acquired enamel pellicle using LC-ESI-MS/MS," *Journal of Proteome Research*, vol. 6, no. 6, pp. 2152-2160, 2007.
- [73 Z. Cheaib and A. Lussi, "Impact of acquired enamel pellicle modification on initial dental erosion," *Caries Research*, vol. 45, no. 2, pp. 107-112, 2011.
- [74 N. M. A. Chaudhury, P. Shirlaw, R. Pramanik, G. H. Carpenter and G. B. Protor, "Changes in Saliva Rheological Properties and Mucin Glycosylation in Dry Mouth," *Journal of Dental Research*, vol. 94, no. 12, pp. 1660-1667, 2015.
- [75 B. Liu, M. R. Dion, M. M. Jurasic, G. Gibson and J. A. Jones, "Xerostomia and salivary hypofunction in vulnerable elders: prevalence and etiology," *Oral Medicine*, vol. 114, no. 1, pp. 52-60, 2012.



- [76 S. B. Jensen, A. M. L. Pedersen, A. Vissink, E. Andersen, C. G. Brown, C. G. Brown, A. N. Davies, J. Dutilh, J. S. Fulton, L. Jankovic, N. N. F. Lopes, A. L. S. Mello, L. V. Muniz, C. A. Murdoch-Kinch, R. G. Nair, J. J. Napenas, A. Nogueira-Rodrigues, D. Saunders, B. Stirling, I. von Bultzingslowen, D. S. Weikel, L. S. Elting, F. K. L. Spijkervet and M. T. Brennan, "A systematic review of salivary gland hypofunction and xerostomia induced by cancer therapies: prevalence, severity and impact on quality of life," *Support Care Cancer*, vol. 18, no. 8, pp. 1039-1060, 2010.
- [77 B. Malicka, U. Kaczmarek and K. Skoskiewicz-Malinowska, "Prevalence of xerostomia and the salivary flow rate in diabetic patients," *Advances in Clinical and Experimental Medicine*, vol. 23, no. 2, pp. 225-233, 2014.
- [78 V. K. Jarvinen, I. I. Rytomaa and O. P. Heinonen, "Risk factors in dental erosion," *Journal of Dental Research*, vol. 70, no. 6, pp. 942-947, 1991.
- [79 M. G. Cersosimo, G. B. Raina, C. R. Calandra, A. Pellene, C. Gutierrez, F. E. Micheli and E. E. Benarroch, "Dry mouth: an overlooked autonomic symptom of Parkinson's disease," *Journal of Parkinson's Disease*, vol. 1, no. 2, pp. 169-173, 2011.
- [80 R. M. Lopez-Pintor, E. Casanas, J. Gonzalez-Serrano, J. Serrano, L. Ramirez, L. de Arriba and G. Hernandez, "Xerostomia, Hyposalivation, and Salivary Flow in Diabetes Patients," *Journal of Diabetes Research*, vol. 2016, pp. 1-15, 2016.
- [81 W. M. Thomson, "Issues in the epidemiological investigation of dry mouth," *Gerodontology*, vol. 22, no. 2, pp. 65-76, 2005.
- [82 R. S. Percival, S. J. Challacombe and P. D. Marsh, "Flow Rates of Resting Whole and Stimulated Parotid Saliva in Relation to Age and Gender," *Journal of Dental Research*, vol. 73, no. 8, pp. 1416-1420, 1994.
- [83 M. Fusconi, F. Candelori, L. Weiss, A. Riccio, R. Priori, R. Businaro, L. Mastromanno, I. Musy, M. de Vincentiis and A. Greco, "Qualitative mucin disorders in patients with primary Sjögren's syndrome: a literature review," *Medicina Oral, Patologia Oral y Cirugia Bucal*, vol. 26, no. 1, pp. e71-e77, 2021.
- [84 S. Hahnel, M. Behr, G. Handel and R. Burgers, "Saliva substitutes for the treatment of radiation-induced xerostomia -- a review," *Support Care Cancer*, vol. 17, no. 11, pp. 1331-1343, 2009.

- [85 J. Mellema, H. J. Holterman, H. A. Waterman, C. Blom and E. J. Gravenmade,  
] “Rheological aspects of mucin-containing solutions and saliva substitutes,”  
*Biorheology*, vol. 29, no. 2-3, pp. 231-249, 1992.
- [86 W. A. Van der Reijden, E. C. Veerman and A. V. Nieuw Amerongen, “Rheological  
] properties of commercially available polysaccharides with potential use in saliva  
substitutes,” *Biorheology*, vol. 31, no. 6, pp. 631-642, 1994.
- [87 A. Aguirre, B. Mendoza, M. S. Reddy, F. A. Scannapieco, M. J. Levine and M. N. Hatton,  
] “Lubrication of selected salivary molecules and artificial salivas,” *Dysphagia*, vol. 4, no.  
2, pp. 95-100, 1989.
- [88 W. A. Van der Reijden, M. J. Buijs, J. J. Damen, E. C. Veerman, J. M. ten Cate and A. V.  
] Nieuw Amerongen, “Influence of polymers for use in saliva substitutes on de- and  
remineralization of enamel in vitro,” *Carries Research*, vol. 13, no. 3, pp. 216-223, 1997.
- [89 F. C. Ionta, F. L. Mendonca, G. C. Oliveira, A. R. B. Alencar, H. M. Honorio, A. C.  
] Magalhaes and D. Rios, “In vitro assessment of artificial saliva formulations on initial  
erosion remineralization,” *Journal of Dentistry*, vol. 42, pp. 175-179, 2014.
- [90 H. Meyer-Lueckel, W. Hopfenmuller, D. Klinggraff and A. M. Kielbassa,  
] “Microradiographic study on the effects of mucin-based solutions used as saliva  
substitutes on demineralised bovine enamel in vitro,” *Archives of Oral Biology*, vol. 51,  
no. 7, pp. 541-547, 2006.
- [91 R. Bansil and B. S. Turner, “Mucin structure, aggregation, physiological functions and  
] biomedical applications,” *Current Opinion in Colloid & Interface Science*, vol. 11, pp.  
164-170, 2006.
- [92 G. D. Offner and R. F. Troxler, “Heterogeneity of High-molecular-weight Human Salivary  
] Mucins,” *Advances in Dental Research*, vol. 14, no. 1, pp. 69-75, 2000.
- [93 S. A. Rayment, B. Liu, G. D. Offner, F. G. Oppenheim and R. F. Troxler,  
] “Immunoquantification of human salivary mucins MG1 and MG2 in stimulated whole  
saliva: factors influencing mucin levels,” *Journal of Dental Research*, vol. 79, no. 10, pp.  
1765-1772, 2000.

- [94 M. J. Levine, M. S. Reddy, L. A. Tabak, R. E. Loomis, E. J. Bergey, P. C. Jones, R. E. Cohen,  
] M. W. Stinson and I. Al-Hashimi, "Structural aspects of salivary glycoproteins," *Journal of Dental Research*, vol. 66, no. 2, pp. 436-441, 1987.
- [95 S. P. Authimoolam and T. D. Dziubla, "Biopolymeric Mucin and Synthetic Polymer  
] Analogs: Their Structure, Function and Role in Biomedical Applications," *Polymers*, vol. 8, no. 71, pp. 1-28, 2016.
- [96 J. M. Coles, D. P. Chang and S. Zauscher, "Molecular mechanisms of aqueous boundary  
] lubrication by mucinous glycoproteins," *Current Opinion in Colloid & Interface Science*, vol. 15, pp. 406-416, 2010.
- [97 A. Sarkar, F. Xu and S. Lee, "Human saliva and model saliva at bulk to adsorbed phases  
] – similarities and differences," *Advances in Colloid and Interface Science*, vol. 273, pp. 1-11, 2019.
- [98 D. J. Thornton, K. Rousseau and M. A. McGuckin, "Structure and formation of the  
] polymeric mucins in airway mucus," *Annual Review of Physiology*, vol. 70, pp. 459-486, 2008.
- [99 J. Dekker, J. W. A. Rossen, H. A. Buller and A. W. C. Einerhand, "The MUC family: an  
] obituary," *Trends in Biochemical Sciences*, vol. 27, no. 3, pp. 126-131, 2002.
- [10 B. T. Kasdorf, F. Weber, G. Petrou, V. Srivastava, T. Crouzier and O. Lieleg, "Mucin-  
0] Inspired Lubrication on Hydrophobic Surfaces," *Biomacromolecules*, vol. 18, pp. 2454-2462, 2017.
- [10 Y. Znamenskaya, J. Sotres, J. Engblom, T. Arnebrant and V. Kockerbitov, "Hydration on  
1] structural and thermodynamic properties of Pig gastric and bovine submaxillary gland mucins," *The Journal of Physical Chemistry B*, vol. 116, pp. 5047-5055, 2012.
- [10 T. Crouzier, K. Boettcher, A. R. Geonnotti, N. L. Kavanaugh, J. B. Hirsch, K. Ribbeck and  
2] O. Lieleg, "Modulating Mucin Hydration and Lubrication by Deglycosylation and Polyethylene Glycol Binding," *Advanced Materials Science*, vol. 2, no. 18, pp. 1-7, 2015.
- [10 G. J. Strous and J. Dekker, "Mucin-type glycoproteins," *Critical Reviews in Biochemistry  
3] and Molecular Biology*, vol. 27, no. 1-2, pp. 57-92, 1992.
- [10 N. Jentoft, "Why are proteins O-glycosylated," *Trends in Biochemical Sciences*, vol. 15,  
4] pp. 291-294, 1990.

- [10 P. Smart, A. Neville and M. Bryant, "Tribocorrosion of dental tissues: The role of  
5] mucin," *Tribology International*, vol. 148, pp. 1-8, 2020.
- [10 M. C. Jordao, F. Q. Ionta, B. T. Bergantin, G. C. Oliveira, M. J. Moretto, H. M. Honorio,  
6] T. C. Silva and D. Rios, "The effect of mucin in artificial saliva on erosive rehardening  
and demineralization," *Caries Research*, vol. 51, pp. 136-140, 2017.
- [10 M. Levine, "Development of artificial salivas," *Critical reviews in oral biology and  
7] medicine*, vol. 4, no. 3/4, pp. 279-286, 1993.
- [10 H. Teixeira, A. C. Branco, I. Rodrigues, D. Silva, S. Cardoso, R. Colaco, A. P. Serro and C.  
8] G. Figueiredo-Pina, "Effect of albumin, urea, lysozyme and mucin on the triboactivity  
of Ti6Al4V/zirconia pair used in dental implants," *Journal of the Mechanical Behaviour  
of Biomedical Materials*, vol. 118, 2021.
- [10 D. H. Veeregowda, H. J. Busscher, A. Vissink, D.-J. Jager, P. Sharma and H. C. Van der  
9] Mei, "Role of Structure and Glycosylation of Adsorbed Protein Films in Biolubrication,"  
*PloS one*, vol. 7, no. 8, pp. 1-10, 2012.
- [11 A. Barrantes, T. Arnebrant and L. Lindh, "Characteristics of saliva films adsorbed onto  
0] different dental materials studied by QCM-D," *Colloids and Surfaces A: Physicochemical  
and Engineering Aspects*, vol. 442, pp. 56-62, 2014.
- [11 E. Yoshida and T. Hayakawa, "Adsorption study of pellicle proteins to gold, silica and  
1] titanium by quartz crystal microbalance method," *Dental Materials Journal*, vol. 31, no.  
6, pp. 883-887, 2013.
- [11 M. Glumac, C. Ritzoulis and J. Chen, "Surface properties of adsorbed salivary  
2] components at a solid hydrophobic surface using a quartz crystal microbalance with  
dissipation (QCM-D)," *Food Hydrocolloids*, vol. 97, no. 105195, pp. 1-8, 2019.
- [11 Q. Zeng, G. Ma, H. Xaio, D. Yang, L. Zheng and Z. Zhou, "Effect of saliva flow rate on the  
3] adsorption kinetics and lubrication of salivary pellicle on human tooth enamel surface,"  
*Wear*, Vols. 426-427, pp. 180-185, 2019.
- [11 K. C. Dee, D. A. Puleo and R. Bizios, "Chapter 3: Protein-Surface Interactions," in *An  
4] Introduction to Tissue-Biomaterial Interactions*, Hoboken, New Jersey, Wiley & Sons,  
inc, 2002, pp. 37-52.

- [11 M. A. Al-Ghuoti and D. A. Da'ana, "Guidelines and interpretation of adsorption  
5] isotherms models: A review," *Journal of Hazardous Materials*, vol. 493, pp. 1-22, 2020.
- [11 M. Lundin, T. Sandberg, K. D. Caldwell and E. Blomberg, "Comparison of the adsorption  
6] kinetics and surface arrangement of "as received" and purified bovine submaxillary  
gland mucin (BSM) on hydrophilic surfaces," *Journal of Colloid and Interface Science*,  
vol. 336, pp. 30-39, 2009.
- [11 I. Svendsen, L. Lindh, U. Elofsson and T. Arnebrant, "Studies on the exchange of early  
7] pellicle proteins by mucin and whole saliva," *Journal of Colloid and Interface Science*,  
vol. 321, no. 1, pp. 52-59, 2008.
- [11 B. Lassen, K. Holmberg, C. Brink, C. Carlen and J. Olsson, "Binding of salivary proteins  
8] and oral bacteria to hydrophobic and hydrophilic surfaces in vivo and vitro," *Colloid  
and Polymer Science*, vol. 272, no. 9, pp. 1143-1150, 1994.
- [11 L. Lindh, I. E. Svendsen, M. Cardenas and T. Arnebrant, "The salivary mucin MUC5B and  
9] lactoperoxidase can be used for layer-by-layer film formation," *Journal of Colloid and  
Interface Science*, vol. 310, no. 1, pp. 74-82, 2007.
- [12 K. Haberska, O. Svenson, S. Shleev, L. Lindh, T. Arnebrant and T. Ruzgas, "Activity of  
0] lactoperoxidase when adsorbed on protein layers," *Talanta*, vol. 76, p. 1159-1164,  
2008.
- [12 Z. Feldoto, T. Pettersson and A. Dedinaite, "Mucin-electrolyte Interactions at the Solid-  
1] Liquid Interface Probed by QCM-D," *Langmuir*, vol. 26, no. 7, pp. 4901-4908, 2008.
- [12 M. Cardenas, U. Elofsson and L. Lindh, "Salivary Mucin MUC5B could be an important  
2] component of in vitro pellicles of human saliva: an in situ ellipsometry and atomic force  
microscopy study," *Biomacromolecules*, vol. 8, no. 4, pp. 1149-1156, 2007.
- [12 G. Ma, Y. Tang, Q. Zeng and J. Zheng, "On adhesion mechanism of salivary pellicle-  
3] PDMS interface," *Biosurface and Biotribology*, vol. 5, no. 3, pp. 93-96, 2019.
- [12 S. Lee, M. Muller, K. Rezwan and N. D. Spencer, "Porcine Gastric Mucin (PGM) at the  
4] water/Poly(Dimethylsiloxane)(PDMS) Interface: Influence of pH and Ionic strength on  
its conformation, adsorption, and aqueous lubrication properties," *Langmuir*, vol. 21,  
no. 18, pp. 8344-8353, 2005.

- [12 L. Wang, J. Li, X. Jiang, Y. Ji, Y. Qu, Y. Zhao, X. Wu and C. Chen, "Revealing the binding  
5] structure of the protein corona on gold nanorods using synchrotron radiation-based  
techniques: understanding the reduced damage in cell membranes," *Journal of the  
American Chemical Society*, vol. 135, no. 46, pp. 17359-17368, 2013.
- [12 S. Nakata, N. Kido, M. Hayashi, M. Hara, H. Sasabe, T. Sugawara and T. Matsuda,  
6] "Chemisorption of proteins and their thiol derivatives onto gold surfaces:  
characterization based on electrochemical nonlinearity," *Biophysical Chemistry*, vol.  
62, pp. 63-72, 1996.
- [12 H. W. Choi, H. J. Lee, K. J. Kim, H. M. Kim and S. C. Lee, "Surface modification of  
7] hydroxyapatite nanocrystals by grafting polymers containing phosphonic acid groups,"  
*Journal of Colloid and Interface Science*, vol. 304, no. 1, pp. 227-281, 2006.
- [12 J. L. Meyer and G. H. Nancollas, "The influence of Multidentate Organic Phosphonates  
8] on the Crystal Growth of Hydroxyapatite," *Calcified Tissue International*, vol. 13, pp.  
295-303, 1973.
- [12 J. A. Lori, S. Z. Kazaure and S. M. Dangoggo, "Mechanism for the adsorption of mucin  
9] on hydroxyapatite," *Nigerian journal of chemical research*, vol. 10, pp. 21-29, 2005.
- [13 M. Johnsson, M. J. Levine and G. H. Nancollas, "Hydroxyapatite binding domains in  
0] salivary proteins," *Critical Reviews in Oral Biology and Medicine*, vol. 4, no. 3/4, pp.  
371-378, 1993.
- [13 T. Nagasaki, F. Nagata, M. Sakuri and K. Kato, "Effects of pore distribution of  
1] hydroxyapatite particles on their protein adsorption behaviour," *Journal of Asian  
Ceramic Societies*, vol. 5, no. 2, pp. 88-93, 2017.
- [13 Y. Yang, M. Yu, F. Boke, Q. Qin, R. Hubner, S. Knust, S. Schiderek, G. Grundmeier, H.  
2] Fischer and A. Keller, "Effect of nanoscale surface topography on the adsorption of  
globular proteins," *Applied Surface Science*, vol. 535, no. 147671, pp. 1-9, 2021.
- [13 K. Rechendorff, M. B. Hovgaard, M. Foss, V. P. Zhdanov and F. Besenbacher,  
3] "Enhancement of Protein Adsorption Induced by Surface Roughness," *Langmuir*, vol.  
22, no. 26, pp. 10885-10888, 2006.

- [13 A. Dolatshahi-Pirouz, K. Rechendorff, M. B. Hovgaard and M. Foss, "Bovine serum  
4] albumin adsorption on nano-rough platinum surfaces studied by QCM-D," *Colloids and Surfaces B: Biointerfaces*, vol. 66, no. 1, pp. 53-59, 2008.
- [13 G. W. Kajjumba, S. Emik, A. Ongen, H. K. Ozcan and S. Aydin, "Modelling of Adsorption  
5] Kinetic Processes—Errors, Theory and Application," in *Advanced Sorption Process Applications*, IntechOpen, 2018.
- [13 J. Wang and X. Guo, "Adsorption kinetic models: physical meanings, applications and  
6] solving methods," *Journal of Hazardous Materials*, vol. 390, no. 122156, pp. 1-18, 2020.
- [13 S. Xie, Z. Wen, H. Zhan and M. Jin, "An experimental study on the adsorption and  
7] desorption of Cu (II) in silt clay," *Geofluids*, vol. 2018, no. 3610921, pp. 1-12, 2018.
- [13 K. Riahi, S. Chaabane and B. B. Thayer, "A kinetic modelling study of phosphate  
8] adsorption onto Phoenix dactylifera L. date palm fibers in batch mode," *Journal of Saudi Chemical Society*, vol. 21, pp. S143-S152, 2017.
- [13 Y. S. Ho and G. McKay, "Sorption of dyes and copper ions onto biosorbents," *Process  
9] Biochemistry*, vol. 38, no. 7, pp. 1047-1061, 2003.
- [14 Y. S. Ho, "Review of second-order models for adsorption systems," *Journal of  
0] Hazardous Materials B*, vol. 136, pp. 681-689, 2006.
- [14 J. Kou and S. Xu, "In situ kinetics and conformation studies of dodecylamine adsorption  
1] onto zinc sulfide using quartz crystal microbalance with dissipation (QCM-D)," *Colloids and Surfaces A: Physicochemical and Engineering aspects*, vol. 490, pp. 110-120, 2016.
- [14 X. Guo and J. Wang, "A general kinetic model for adsorption: Theoretical analysis and  
2] modelling," *Journal of Molecular Liquids*, vol. 288, pp. 1-8, 2019.
- [14 T. Sandberg, H. Blom and K. D. Caldwell, "Potential use of mucins as biomaterial  
3] coatings. I. Fractionation, characterization, and model adsorption of bovine, porcine and human mucins," *Journal of Biomedical Materials Research Part A*, vol. 91A, no. 3, pp. 762-772, 2008.
- [14 B. M. Manzi, M. Werner, E. P. Ivanova, R. J. Crawford and V. A. Baulin, "Simulations of  
4] Protein Adsorption on Nanostructured Surfaces," *Scientific Reports*, vol. 9, no. 4694, pp. 1-13, 2019.

- [14 Y. Zheng, K. Bashandeh, A. Shakil, S. Jha and A. A. Polycarpou, "Review of dental tribology: Current status and challenges," *Tribology International*, vol. 166, no. 107354, pp. 1-21, 2022.
- [14 International Standards Organisation, "Dental materials - guidance on testing of wear - Part 2: wear by two and/or three body contact," *ISO TS 14569 - 2:2001*, 2001.
- [14 F. Soleimani, H. Jalali, A. Z. Mostafavi, S. Zeighami and M. Memarian, "Retention and Clinical Performance of Zirconia Crowns: A Comprehensive Review," *International Journal of Dentistry*, vol. 2020, no. 8846534, pp. 1-6, 2020.
- [14 Y. Zhang and B. R. Lawn, "Novel Zirconia Materials in Dentistry," *Journal of Dental Research*, vol. 97, no. 2, pp. 140-147, 2017.
- [14 J. Grech and E. Antunes, "Zirconia in dental prosthetics: A literature review," *Journal of Materials Research and Technology*, vol. 8, no. 5, pp. 4956-4964, 2019.
- [15 R. W. Wassell, J. F. McCabe and A. W. G. Walls, "A Two-body Frictional Wear Test," *Journal of Dental Research*, vol. 73, no. 9, pp. 1546-1553, 1994.
- [15 J. Chevalier, L. Gremillard and S. Deville, "Low-temperature degradation of zirconia and implications for biomedical implants," *Annual Review of Materials Research*, vol. 37, pp. 1-32, 2007.
- [15 K. Furuya, S. Takemoto, S. Yamashita, H. Sekine, Y. Yajima and M. Yoshinari, "Low-temperature degradation of high-strength Y-TZP (yttria-stabilized tetragonal zirconia polycrystal)," *Dental Materials Journal*, vol. 39, no. 4, pp. 577-586, 2020.
- [15 Matweb, "Steatite (Magnesium Silicon Oxide)," Matweb, [Online]. Available: [https://www.matweb.com/search/datasheet\\_print.aspx?matguid=9e9ad98b717b44e695621cd67e5ff262](https://www.matweb.com/search/datasheet_print.aspx?matguid=9e9ad98b717b44e695621cd67e5ff262).
- [15 STC Material Solutions, "Steatite," STC Material Solutions, 2022. [Online]. Available: <https://www.ceramics.net/ceramic-materials-solutions/silicates/steatite#:~:text=Steatite%20is%20a%20low%20cost,loss%2C%20and%20high%20voltage%20insulation..>
- [15 A. C. Shortall, X. Q. Hu and P. M. Marquis, "Potential countersample materials for in vitro simulation wear testing," *Dental Materials*, vol. 18, no. 3, pp. 546-254, 2002.



- [15 E. Andrysewicz, J. Mystkowska, J. R. Dabrowski and R. Olchowik, "Influence of self-  
6] made saliva substitutes on tribological characteristics of human enamel," *Acta of  
Bioengineering and Biomechanics*, vol. 16, no. 2, pp. 67-74, 2014.
- [15 C. P. Turssi, D. F. Messias, S. M. Corona and M. C. Serra, "Viability of using enamel and  
7] dentin from bovine origin as a substitute for human counterparts in an intraoral  
erosion model," *Brazilian Dental Journal*, vol. 21, no. 4, pp. 332-336, 2010.
- [15 E. Sajewicz and Z. Kulesza, "A new tribometer for friction and wear studies of dental  
8] materials and hard tooth tissues," *Tribology International*, vol. 40, no. 5, pp. 885-895,  
2007.
- [15 K. Nishigawa, E. Bando and M. Nakano, "Quantitative study of bite force during sleep  
9] associated bruxism," *Journal of Oral Rehabilitation*, vol. 28, no. 5, pp. 485-491, 2001.
- [16 "What Is Bruxism?," The Bruxism Association - Somnowell, [Online]. Available:  
0] <http://www.bruxism.org.uk/what-is-bruxism.php>. [Accessed 21 June 2018].
- [16 B. Rilo, J. Fernandez, L. D. Silva, A. Martinez and U. Santana, "Frontal-plane lateral  
1] border movements and chewing cycle characteristics," *Journal of Oral Rehabilitaion*,  
vol. 28, no. 10, pp. 930-936, 2001.
- [16 Z. R. Zhou, H. Y. Yu, J. Zheng, L. M. Qian and Y. Yan, "Biomechanics of human teeth," in  
2] *Dental Biotribology*, New York, Springer Science+Business Media, 2013.
- [16 C. C. Peck, "Biomechanics of occlusion - implications of oral rehabilitation," *Journal of  
3] Oral Rehabilitation*, vol. 43, pp. 205-214, 2016.
- [16 D. J. Anderson, "Measurement of stress in Mastication," *Journal of Dental Research*,  
4] vol. 35, no. 5, pp. 644-670, 1956.
- [16 B. Dejak, A. Mlotkowski and M. Romanowicz, "Finite Element Analysis of Stess in  
5] Molars during Clenching and Mastication," *The Journal of Prosthetic Dentistry*, vol. 90,  
no. 6, pp. 591-597, 2003.
- [16 L. H. Mair, "Wear in dentistry - current terminology," *Journal of Dentistry*, vol. 20, pp.  
6] 140-144, 1992.

- [16 K. W. Hemmings, A. Truman, S. Shah and R. Chauhan, "Tooth wear guidelines for the  
7] BSRD part 1: Aetiology, diagnosis and prevention," *Dental Update*, vol. 45, no. 6, pp.  
483-495, 2018.
- [16 P. Lambrechts, M. Braem, M. Vuylsteke-Wauters and G. Vanherle, "Quantitative in vivo  
8] Wear of Human Enamel," *Journal of Dental Research*, vol. 68, no. 12, pp. 1752-1754,  
1989.
- [16 F. Lutz, R. W. Phillips, J. F. Roulet and J. C. Setcos, "In vivo and in vitro wear of potential  
9] posterior composites," *Journal of Dental Research*, vol. 63, no. 6, pp. 914-920, 1984.
- [17 D. DeLong, "Intra-oral restorative materials wear: Rethinking the current approaches:  
0] How to measure wear," *Dental Materials*, vol. 22, pp. 702-711, 2006.
- [17 O. Borrero-Lopez, A. Pajares, P. J. Constantino and B. R. Lawn, "A model for predicting  
1] wear rates in tooth enamel," *Journal of the Mechanical Behaviour of Biomedical  
Materials*, vol. 37, pp. 226-234, 2014.
- [17 E. d'Incau and P. Saulie, "Understanding dental wear," *Journal of Dentofacial  
2] Anomalies and Orthodontics*, vol. 15, no. 1 (104), pp. 1-19, 2012.
- [17 G. W. Stachowiaz and A. W. Batchelor, "11. Abrasive, erosive and cavitation wear," in  
3] *Engineering Tribology 4th ed*, Elsevier, 2014.
- [17 J. M. ten Cate and T. Imfeld, "Dental erosion, summary," *European Journal of Oral  
4] Sciences*, vol. 104, no. 2 (Pt 2), pp. 241-244, 1996.
- [17 A. Lussi, N. Schleuter, E. Rakhmatullina and C. Ganss, "Dental erosion - an overview  
5] with emphasis on chemical and histopathic aspects," *Caries Research*, vol. 45, no. Suppl  
1, pp. 2-12, 2011.
- [17 E. A. A. Neel, A. Aljabo, A. Strange, S. Ibrahim, M. Coathup, A. M. Young, L. Bozec and  
6] V. Mudera, "Demineralization-remineralization dynamics in teeth and bone,"  
*International Journal of Nanomedicine*, vol. 19, no. 11, pp. 4743-4763, 2016.
- [17 M. A. R. Bazulaf, A. R. Hannas and M. T. Kato, "Saliva and dental erosion," *Journal of  
7] Applied Oral Science*, vol. 20, no. 5, pp. 493-502, 2012.
- [17 J. A. Hughes, N. X. West, D. M. Parker, R. G. Newcome and M. Addy, "Development and  
8] evaluation of a low erosive blackcurrant juice drink 3. Final drink and concentrate,

- formulae comparisons in situ and overview of the concept.," *Journal of Dentistry*, vol. 27, no. 5, pp. 345-350, 1999.
- [17 R. S. Austin, J. M. Rodriguez, S. Dunne, R. Moazzez and D. W. Bartlett, "The effect of  
9] increasing sodium fluoride concentrations on erosion and attrition of enamel and dentine in vitro," *Journal of Dentistry*, vol. 38, no. 10, pp. 782-787, 2010.
- [18 P. Scheutzel, "Etiology of dental erosion - Intrinsic factors," *European Journal of Oral  
0] Sciences*, vol. 144, pp. 178-190, 1996.
- [18 Y. Q. Wu, J. A. Arsecularatne and M. Hoffman, "Attrition corrosion of human dental  
1] enamel: a review," *Biosurface and Biotribology*, vol. 3, pp. 196-210, 2017.
- [18 A. Weigand , A. Crede, C. Tschammler, T. Attin and T. T. Taubock, "Enamel wear by  
2] antagonistic restorative materials under erosive conditions," *Clinical Oral Investigations*, vol. 21, pp. 2689-2693, 2017.
- [18 G. R. Batista, C. R. G. Torres, B. Sener, T. Attin and A. Weigand, "Artificial saliva  
3] formulations versus human saliva pretreatment in dental erosion experiments.," *Caries Research*, vol. 50, pp. 78-86, 2016.
- [18 H. Li and Z. R. Zhou, "Wear behaviour of human teeth in dry and artificial saliva  
4] conditions," *Wear*, vol. 249, no. 10-11, pp. 980-984, 2002.
- [18 G. Guidoni, M. Swain and I. Jager, "Nano-scale sliding contact deformation behaviour  
5] of enamel under wet and dry conditions," *Journal of Materials Science: Materials in Medicine*, vol. 21, no. 4, pp. 1195-1203, 2010.
- [18 J. Zheng and Z. R. Zhou, "Friction and wear behaviour of human teeth under various  
6] wear conditions," *Tribology International*, vol. 40, pp. 278-284, 2007.
- [18 S. Ranjitkar, J. A. Kaidonis, G. C. Townsend, A. M. Vu and L. C. Richards, "An in vitro  
7] assessment of the effect of load and pH on wear between opposing enamel and dentine surfaces," *Archives of Oral Biology*, vol. 53, no. 11, pp. 1011-1016, 2008.
- [18 J. Zheng, H. Huang, M. Y. Shi, L. Zheng, L. M. Qian and Z. R. Zhou, "In vitro study on the  
8] wear behaviour of human tooth enamel in citric acid solution.," *Wear*, vol. 271, pp. 2313-2321, 2011.

- [18 S. S. Gao, L. M. Qian, S. B. Huang and H. Y. Yu, "Effect of gallic acid on the wear  
9] behaviour of early carious enamel," *Biomedical Materials*, vol. 4, no. 3, pp. 1-5, 2009.
- [19 A. V. N. Amerongen, C. H. Oderkerk and A. A. Driessen, "Role of Mucins from Human  
0] Whole Saliva in the Protection of Tooth Enamel against Demineralization in vitro,"  
*Caries Research*, vol. 21, pp. 297-309, 1987.
- [19 M. Mutahar, G. Carpenter, D. Bartlett, M. German and R. Moazzez, "The presence of  
1] acquired enamel pellicle changes acid-induced erosion from dissolution to a softening  
process," *Scientific Reports*, vol. 7, no. 10920, pp. 1-8, 2017.
- [19 M. Mutahar, S. O'Toole, G. Carpenter, D. Bartlett, M. Andiappan and R. Moazzez,  
2] "Reduced statherin in acquired enamel pellicle on eroded teeth compared to healthy  
teeth in the same subjects: An in-vivo study," *PLoS One*, vol. 12, no. 8, pp. 1-11, 2017.
- [19 A. Ash, M. J. Ridout, A. R. Mackie, G. R. Burnett and P. J. Wilde, "Effect of calcium ions  
3] on in vitro pellicle formation from parotid and whole saliva," *Colloids and Surfaces B:  
Biointerfaces*, vol. 102, pp. 546-553, 2013.
- [19 L. H. Hove, A. Young and A. B. Tveit, "An in vitro study on the effect of TiF(4) treatment  
4] against erosion by hydrochloric acid on pellicle-covered enamel," *Caries Research*, vol.  
41, no. 1, pp. 80-84, 2007.
- [19 D. H. Veeregowda, H. C. van der Mei, H. J. Busscher and P. K. Sharma, "Influence of  
5] fluoride-detergent combination on the visco-elasticity of adsorbed salivary protein  
films," *European Journal of Oral Sciences*, vol. 119, no. 1, pp. 21-16, 2011.
- [19 A. A. Algarni, M. C. M. Mussi, E. B. Moffa, F. Lippert, D. T. Zero, W. L. Siqueira and A. T.  
6] Hara, "The impact of stannous, fluoride ions and its combination on enamel pellicle  
proteome and dental erosion," *PLoS One*, vol. 10, no. 6, pp. 1-11, 2015.
- [19 A. Kensche, J. Kirsch, S. Mintert, F. Enders, S. Potschke, S. Basche, B. Konig, C. Hannig  
7] and M. Hannig, "Impact of customary fluoride rinsing solutions on the pellicle's  
protective properties and bioadhesion in situ," *Scientific Reports*, vol. 7, no. 16584, pp.  
1-11, 2017.
- [19 B. Machines, "Steatite grinding balls," Baan Machines, 2018. [Online]. Available:  
8] [https://www.baanmachines.com/products/grinding-media/steatite-grinding-balls-bs-  
64/](https://www.baanmachines.com/products/grinding-media/steatite-grinding-balls-bs-64/).

- [19 A. White, C. Yorath, V. ten Hengel, S. D. Leary, M.-C. D. N. J. M. Huysmans and M. E. 9] Barbour, "Human and bovine enamel erosion under 'single drink' conditions," *European Journal of Oral Sciences*, vol. 118, no. 6, pp. 604-609, 2010.
- [20 T. S. Carvalho, A. Lussi, N. Schlueter and T. Baumann, "Differences in susceptibility of 0] deciduous and permanent teeth to erosion exist, albeit depending on protocol design and method of assessment," *Scientific Reports*, vol. 12, no. 4153, pp. 1-9, 2022.
- [20 ThermoFisher Scientific, Ambio applied Biosystems, "AM9626 PBS pH 7.4 data sheet," 1] 2008. [Online]. Available: [https://www.thermofisher.com/document-connect/document-connect.html?url=https%3A%2F%2Fassets.thermofisher.com%2FTFS-Assets%2FLSG%2Fmanuals%2Fsp\\_9625.pdf](https://www.thermofisher.com/document-connect/document-connect.html?url=https%3A%2F%2Fassets.thermofisher.com%2FTFS-Assets%2FLSG%2Fmanuals%2Fsp_9625.pdf).
- [20 J. T. Dominici, P. D. Eleazer, S. J. Clark, R. H. Staat and J. P. Scheetz, 2] "Disinfection/sterilization of extracted teeth for dental student use.," *Journal of Dental Education*, vol. 65, no. 11, pp. 1278-1280, 2001.
- [20 G. Sauerbrey, ""The Use of Quartz Oscillators for Weighing Thin Layers and for 3] Microweighing,"," *Zeitschrift für Physik*, vol. 155, no. 2, pp. 206-222, 1959.
- [20 M. V. Voinova, M. Rodahl, M. Jonson and B. Kasemo, "Viscoelastic acoustic response 4] of layered polymer films at fluid-solid interfaces: continuum mechanics approach," *Physica Scripta*, vol. 59, no. 5, pp. 391-396, 1999.
- [20 W. P. Mason, R. N. Thurston and W. Philipoff, "Relaxation in Polymer Solutions, Liquids 5] and Gels," in *Physical Acoustics: Principles and Methods*, New York, Academic Press, 1965.
- [20 S. B. Kaemmar, "Application Note #133 Introduction to Bruker's ScanAsyst and 6] PeakForce Tapping AFM Technology," *Bruker Corporation*, pp. 1-12, 2011.
- [20 B. V. Derjaguin, V. M. Muller and Y. P. Toporov, "Effect of contact deformations on the 7] adhesion of particles," *Journal of Colloid and Interface Science*, vol. 53, no. 2, pp. 314-326, 1975.
- [20 B. Pittenger, N. Erina and C. Su, "Quantitative Mechanical Property Mapping at the 8] nanoscale with PeakForce QNM," *Bruker Corporation*, pp. 1-12, 2010.

- [20 Y. Zhang, J. A. Arsecularatne and M. Hoffman, "The effects of three different food acids  
9] on the attrition-corrosion wear of human dental enamel.," *Journal of Physics D: Applied Physics*, vol. 48, pp. 1-10, 2015.
- [21 E. Feki, J. M. Savariault, B. Salah and M. Jernal, "Sodium and Carbonate Distribution in  
0] Substituted Calcium Hydroxyapatite," *Solid State Sciences*, vol. 2, pp. 577-586, 2000.
- [21 H. Hong, L. Tie and T. Jian, "The crystal characteristics of Enamel and Dentin by XRD  
1] method," *Journal of Wuhan University of Technology - Mater. Sci. Ed.*, vol. 21, no. 1, pp. 9-12, 2006.
- [21 J. Silveira, S. Countinho, D. Marques, J. Castro, A. Mata, M. L. Carvalho and S. Pessanha,  
2] "Raman spectroscopy analysis of dental enamel treated with whitening agent product - Influence of saliva in the remineralization," *Spectrochimica Acta Part A: Molecular and Biomolecular Spectroscopy*, vol. 198, pp. 145-149, 2018.
- [21 A. Santini and V. Miletic, "Quantitative micro-Raman assessment of dentine  
3] demineralization, adhesive penetration, and degree of conversion of three dentine bonding systems," *European Journal of Oral Sciences*, vol. 116, pp. 177-183, 2008.
- [21 A. V. Naumkin, A. Kraut-Vass, S. W. Gaarenstroom and C. J. Powell, "NIST X-ray  
4] Photoelectron Spectroscopy Database, Version 4.1," National Institute of Standards and Technology, 2012. [Online]. Available: <https://srdata.nist.gov/xps/>.
- [21 T. F. S. Inc., "XPS Reference Table of Elements," Thermo Fisher Scientific Inc., 2021.  
5] [Online]. Available: <https://xpssimplified.com/periodictable.php>.
- [21 J. F. Moulder, W. F. Stickle, P. E. Sobol and K. D. Bomben, Handbook of X-ray  
6] Photoelectron Spectroscopy, Eden Prairie: Perkin-Elmer Corporation, 1992.
- [21 S. S. N. a. GmbH, "XPS surface analysis of human tooth samples with EnviroESCA,"  
7] *Application Note #000396*.
- [21 F. Taube, R. Ylmen, A. Shchukarev, S. Nietzsche and J. G. Noren, "Morphological and  
8] chemical characterization of tooth enamel exposed to alkaline agents," *Journal of Dentistry*, vol. 38, pp. 72-81, 2010.
- [21 Y. C. G. Kwan, G. M. Ng and C. H. A. H, "Identification of functional groups and  
9] determination of carboxyl formation temperature in graphene oxide using XPS O 1s spectrum," *Thin Solid Films*, vol. 590, pp. 40-48, 2015.

- [22 A. E. Nelson, N. K. S. Hildebrand and P. W. Major, "Mature Dental Enamel [Calcium  
0] Hydroxyapatite,  $\text{Ca}_{10}(\text{PO}_4)_6(\text{OH})_2$ ] by XPS," *Surface Science Spectra*, vol. 9, pp. 250-  
259, 2002.
- [22 M. Schmidt and S. G. Steinemann, "XPS studies of amino acids adsorbed on titanium  
1] dioxide surfaces," *Fresenius' Journal of Analytical Chemistry*, vol. 341, pp. 412-415,  
1991.
- [22 A. Lehmann, A. Rueppell, A. Schindler, I. Zylla, H. J. Seifert, F. Nothdurft, M. Hannig and  
2] S. Rupf, "Modification of Enamel and Dentin Surfaces by Non-Thermal Atmospheric  
Plasma," *Plasma Processes and Polymers*, vol. 10, pp. 262-270, 2013.
- [22 R. Franke, T. Chasse, P. Streubel and A. Meisel, "Auger parameters and relaxation  
3] energies of phosphorus in solid compounds," *Journal of Electron Spectroscopy and  
Related Phenomena*, vol. 56, pp. 381-388, 1991.
- [22 E. Perez and J. E. Proust, "Forces between Mica Surfaces Covered with Adsorbed Mucin  
4] across Aqueous Solution," *Journal of Colloid and Interface Science*, vol. 118, no. 1, pp.  
182-191, 1987.
- [22 J. B. Madsen, J. Sotres, K. I. Pakkanen, P. Elfer, B. Svensson, M. A. Hachem, T. Arnebrant  
5] and S. Lee, "Structural and Mechanical Properties of Thin Films of Bovine Submaxillary  
Mucin versus Porcine Gastric Mucin on a Hydrophobic Surface in Aqueous Solutions,"  
*Langmuir*, vol. 32, no. 38, pp. 9687-9696, 2016.
- [22 T. M. Riddick, *Control of Colloid Stability through Zeta Potential: With a closing chapter  
6] on its relationship to cardiovascular disease*, Livingston Publishing Company, 1968.
- [22 G. V. Lowry, R. J. Hill, S. Harper, A. F. Rawle, C. O. Hendren, F. Kluessig, U. Nobbmann,  
7] P. Sayre and J. Rumble, "Guidance to improve the scientific value of zeta-potential  
measurements in nanoEHS," *Environmental Science Nano*, vol. 3, pp. 953-965, 2016.
- [22 M. Marczynski, K. Jiang, M. Blakeley, V. Srivastava, F. Vilaplana, T. Crouzier and O.  
8] Lieleg, "Structural Alterations of Mucins Are Associated with Losses in Functionality,"  
*Biomacromolecules*, vol. 22, pp. 1600-1613, 2021.
- [22 T. Pettersson, Z. Feldoto, P. M. Claesson and A. Dedinaite, "The effect of salt  
9] concentration and cation valency on interactions between mucin-coated hydrophobic  
surfaces," *Progress in Colloid and Polymer Science*, vol. 134, pp. 1-10, 2008.

- [23 H. N. Xu, Y. Liu and L. Zhang, "Salting-out and salting-in: competitive effects of salt on  
0] the aggregation behavior of soy protein particles and their emulsifying properties," *Soft matter*, vol. 11, pp. 5926-5932, 2015.
- [23 S. L. Hirsh, D. R. McKenzie, N. J. Nosworthy, J. A. Denman, O. U. Sezerman and M. M.  
1] M. Bilek, "The Vroman effect: Competitive protein exchange with dynamic multilayer protein aggregates," *Colloids and Surface B: Biointerfaces*, vol. 103, pp. 395-404, 2013.
- [23 R. Gelli, F. Martini, M. Geppi, S. Borsacchi, F. Ridi and P. Baglioni, "Exploring the  
2] interplay of mucin with biologically-relevant amorphous magnesium-calcium phosphate nanoparticles," *Journal of Colloid and Interface Science* 594, vol. 594, pp. 802-811, 2021.
- [23 B. D. E. Raynal, T. E. Hardingham, J. K. Sheehan and D. J. Thornton, "Calcium-dependent  
3] Protein Interactions in MUC5B Provide Reversible Cross-links in Salivary Mucus," *The Journal of Biological Chemistry*, vol. 278, no. 31, pp. 28703-28710, 2003.
- [23 R. Kuver and S. Lee, "Calcium binding to biliary mucins is dependent on sodium ion  
4] concentration: relevance to cystic fibrosis," *Biochemical and Biophysical Research Communications*, vol. 314, pp. 330-334, 2004.
- [23 M. L. Singh and A. S. Papas, "Long-term clinical observation of dental caries in salivary  
5] hypofunction patients using a supersaturated calcium-phosphate remineralizing rinse," *Journal of clinical dentistry*, vol. 20, no. 3, pp. 87-92, 2009.
- [23 I. Kleinberg, "A new saliva-based anticaries composition," *Dent today*, vol. 18, no. 2,  
6] pp. 98-103, 1999.
- [23 E. C. Reynolds, "Remineralization of Enamel Subsurface Lesions by Calcium  
7] Phosphopeptide-stabilized Calcium Phosphate Solutions," *Journal of Dental Research*, vol. 76, no. 9, pp. 1587-1595, 1997.
- [23 J. Zhao, Y. Liu, W. Sun and H. Zhang, "Amorphous calcium phosphate and its application  
8] in dentistry," *Chemistry Central Journal*, vol. 5, no. 40, pp. 1-7, 2011.
- [23 H. Meyer-Lueckel, N. Umland, W. Hopfenmuller and A. M. Kielbassa, "Effect of Mucin  
9] Alone and in Combination with Various Dentifrices on in vitro Remineralization," *Caries Research*, vol. 38, pp. 478-483, 2004.



- [24 A. Terzic, N. Obradovic, V. Pouchy, J. Stojanovic, K. Maca and V. B. Pavlovic,  
0] "Microstructure and phase composition of steatite ceramics sintered by traditional and  
spark plasma sintering," *Science of Sintering*, vol. 50, pp. 299-312, 2018.
- [24 k. Makovsek, I. Ramsak, V. Bobnar and D. Kuscer, "Processing of steatite ceramic with  
1] a low dielectric constant and low dielectric losses," *Journal of microelectronics,  
electronic components and materials*, vol. 46, no. 2, pp. 100-105, 2016.
- [24 M. Han, A. Sethuraman, R. S. Kane and G. Belfort, "Nanometer-Scale Roughness having  
2] little effect on the amount or structure of adsorbed protein," *Langmuir*, vol. 19, no. 23,  
pp. 9868-9872, 2003.
- [24 X. D. Zhu, H. S. Fan, D. X. Li, H. J. Zhang, T. Luxbacher and X. D. Zhang, "Effect of surface  
3] structure on protein adsorption to biphasic calcium-phosphate ceramics in vitro and in  
vivo," *Acta Biomaterialia*, vol. 5, no. 4, pp. 1311-1318, 2009.
- [24 M. M. H. Antink, S. Beutal, K. Rezwan and M. Maas, "Tailoring electrostatic surface  
4] potential and adsorption capacity of porous ceramics by silica assisted sintering,"  
*Materiala*, vol. 12, no. 100735, pp. 1-11, 2020.
- [24 H. Park, G. Junren, B. K. Yoon, N. J. Cho and J. A. Jackman, "Comparing Protein  
5] Adsorption onto Alumina and Silica Nanomaterial Surfaces: Clues for vaccine adjuvant  
development," *Langmuir*, vol. 21, pp. 1306-1314, 2021.
- [24 F. Hosseinali and J. A. Thomasson, "Probing of Nanoscale Friction and Mechanical  
6] Characteristics of Cotton Fiber's Surface," *Fibers*, vol. 7, no. 64, pp. 1-16, 2019.
- [24 J. S. Yoneda, A. J. Miles, A. P. U. Araujo and B. A. Wallace, "Differential dehydration  
7] effects on globular proteins and intrinsically disordered proteins during film  
formation," *Protein Science*, vol. 26, no. 4, pp. 718-726, 2017.
- [24 J. Carmichael, P. Atri, S. Sharma, S. Kumar, R. C. Venkata, P. Kulkarni, R. Salgia, D. Ghersi,  
8] S. Kaur and S. K. Batra, "Presence and structure-activity relationship of intrinsically  
disordered regions across mucins," *Federation of American Societies for Experimental  
Biology*, vol. 34, no. 2, pp. 1939-1957, 2020.
- [24 Y. Z. Falk, J. Engblom, J. S. Pedersen, T. Arnebrant and V. Kocherbitov, "Effect of  
9] hydration on structure and phase behaviour of pig gastric mucin elucidated by SAXS,"  
*The Journal of Physical Chemistry B*, vol. 122, pp. 7539-7546, 2018.

- [25 N. I. Uzhegova, A. L. Svistkov, B. Lauke and G. Heinrich, "The influence of capillary effect  
0] on atomic force microscopy measurements," *International journal of engineering science*, vol. 75, pp. 67-78, 2014.
- [25 S. Zhang, Y. Weng and C. Ma, "Quantitative Nanomechanical Mapping of Polyolefin  
1] Elastomer at Nanoscale with Atomic Force Microscopy," *Nanoscale Research Letters*, vol. 16, no. 113, pp. 1-11, 2021.
- [25 Y. Znamenyaka, J. Sotres, S. Gavryushov, J. Engblom, T. Arnebrant and V. Kocherbitov,  
2] "Water Sorption and Glass Transition of Pig Gastric Mucin Studied by QCM-D," *The Journal of Physical Chemistry B*, vol. 117, pp. 2554-2563, 2013.
- [25 J. Klein, "Hydration lubrication," *Friction*, vol. 1, no. 1, pp. 1-23, 2013.  
3]
- [25 Y. Nekrashevych, M. Hannig and L. Stosser, "Assessment of enamel erosion and  
4] protective effect of salivary pellicle by surface roughness analysis and scanning electron microscopy," *Oral Health and Preventative Dentistry*, vol. 2, no. 1, pp. 5-11, 2004.
- [25 R. Barac, J. Gasic, N. Trutic, S. Sunaric, J. Popovic, P. Djekic, G. Radenkovic and A. Mitic,  
5] "Erosive effect of different soft drinks on enamel surface in vitro: Application of stylus profilometry," *Medical Principles and Practice*, vol. 24, pp. 451-457, 2015.
- [25 L. Lou, A. E. Nelson, H. Giseon and P. W. Major, "Surface chemical composition of  
6] human maxillary first premolar as assessed by X-ray photoelectron spectroscopy (XPS)," *Applied Surface Science*, vol. 254, no. 21, pp. 6706-6709, 2008.
- [25 T. Buchwald and Z. Buchwald, "Assessment of the Raman spectroscopy effectiveness  
7] in determining the early changes in human enamel caused by artificial caries," *Analyst*, vol. 144, pp. 1409-1419, 2019.
- [25 J. D. Hanawalt, H. W. Rinn and L. K. Frevel, "Chemical Analysis by X-ray Diffraction.,"  
8] *Analytical Chemistry*, vol. 10, pp. 475-512, 1938.
- [25 M. Ermich and D. Opper, "XRD for the analyst - getting acquainted with the principles,"  
9] in *X-RAY powder diffraction*, Almelo, The Netherlands, PANalytical GmbH, 2011.

- [26 T. Baumann, J. Kozik, A. Lussi and T. S. Carvalho, "Erosion protection conferred by whole human saliva, dialysed saliva, and artificial saliva," *Scientific Research*, vol. 6, no. 34670, pp. 1-8, 2016.
- [26 K. A. Kaidonis, L. C. Richards, G. C. Townsend and G. D. Tansley, "Wear of human enamel: quantitative in vitro assessment," *J Dent Res*, vol. 77, no. 12, pp. 1983-1990, 1998.
- [26 N. X. West, J. A. Hughes and M. Addy, "Erosion of dentine and enamel in vitro by dietary acids: The effect of temperature, acid character, concentration and exposure time," *Journal of Oral Rehabilitation*, vol. 27, pp. 875-880, 2000.
- [26 M. Eisenburger and M. Addy, "Erosion and attrition of human enamel in vitro part 1: Interaction effects," *Journey of Dentistry*, vol. 30, pp. 341-347, 2002.
- [26 T. S. Carvalho and A. Lussi, "Susceptibility of enamel to initial erosion in relation to tooth type, tooth surface and enamel depth.," *Caries Research*, vol. 49, pp. 109-115, 2015.
- [26 T. Bauman, R. Bereiter, A. Lussi and T. S. Carvalho, "The effect of different salivary calcium concentrations on the erosion protection conferred by the salivary pellicle.," *Scientific Reports*, vol. 7, no. 12999, pp. 1-9, 2017.
- [26 A. Weigand, L. Kowing and T. Attin, "Impact of brushing force on abrasion of acid-softened and sound enamel," *Archives of Oral Biology*, vol. 52, no. 11, pp. 1-9, 2007.
- [26 M. Shabanian and L. Richards, "In Vitro wear rates of materials under different loads and varying pH," *The Journal of Prosthetic Dentistry*, vol. 87, no. 6, pp. 650-656, 2002.
- [26 N. Cougot, T. Doulard, F. Dalmas, N. Pradelle, R. Gauthier, C. Sanon, B. Grogogeat, P. Colon and J. Chevalier, "Towards quantitative analysis of enamel erosion by focused ion beam tomography," *Dental Materials*, vol. 34, pp. e289-e300, 2018.
- [26 A. T. Hara, C. Gonzalez-Cabezas, B. M. Sener, T. Attin and A. Weigand, "The effect of human saliva substitutes in an erosion-abrasion cycling model," *European Journal of Oral Sciences*, vol. 116, pp. 552-556, 2008.
- [27 J. Mystlkowska, W. Karalus, J. Sidorenko, J. R. Dabrowski and B. Kalska-Szostko, "Biotribological properties of dentures lubricated with artificial saliva," *Journal of Friction and Wear*, vol. 37, no. 6, pp. 746-754, 2016.

- [27 J. Klimek, E. Hellwig and G. Ahrens, "Fluoride taken up by plaque, by the underlying  
1] enamel and by clean enamel from three fluoride compounds in vitro.," *Caries Research*,  
vol. 16, pp. 156-161, 1982.
- [27 H. Meyer-Lueckel, W. Hopfenmuller, D. Klinggraff and A. M. Kielbassa, "Micro  
2] radiographic study on the effects of mucin-based solutions used as saliva substitutes  
on demineralised bovine enamel in vitro," *Archives of Oral Biology*, vol. 51, pp. 541-  
547, 2006.
- [27 R. Kuver and S. P. Lee, "Calcium binding to biliary mucins is dependent on sodium ion  
3] concentration: relevance to cystic fibrosis," *Biochemical and Biophysical Research  
Communications*, vol. 314, pp. 330-334, 2003.
- [27 A. Secilmis, E. Dilber, F. Gokmen, N. Ozturk and T. Telatar, "Effect of storage solutions  
4] on mineral contents of dentin," *Journal of Dental Sciences*, vol. 6, pp. 189-194, 2011.
- [27 C. Zamudio, R. Contreras-Bulnes, R. Scougall-Vilchis, R. A. Morales Luckie, L. E.  
5] Rodriguez Vilchis and O. F. Olea-Mejia, "Morphological, chemical and structural  
characterisation of deciduous enamel: SEM, EDS, XRD, FTIR and XPS analysis,"  
*European Journal of Paediatric Dentistry*, vol. 15, no. 3, pp. 275-280, 2014.
- [27 P. S. Viana, M. O. Orlandi, A. C. Pavarina, A. L. Machado and C. E. Vergani, "Chemical  
6] composition and morphology study of bovine enamel submitted to different  
sterilization methods," *Clinical Oral Investigations*, vol. 22, pp. 733-744, 2018.
- [27 F. A. Stevie, R. Garcia, J. Shallenberger, J. G. Newman and C. Donley, "Sample handling,  
7] preparation and mounting for PS and other surface analytical techniques," *Journal of  
Vacuum Science & Technology A*, vol. 38, no. 063202, pp. 1-11, 2020.
- [27 V. Santak, A. Vesel, R. Zaplotnik, M. Biscan and S. Milosevic, "Surface Treatment of  
8] Human Hard Dental Tissues with Atmospheric Pressure Plasma Jet," *Plasma Chem  
Plasma Process*, vol. 37, pp. 401-413, 2017.
- [27 R. L. Karlinsey, A. C. Mackey, D. D. Blanken and C. S. Schwandt, "Remineralization of  
9] eroded enamel lesions by simulated saliva in vitro," *The Open Dentistry Journal*, vol. 6,  
pp. 170-176, 2012.

- [28 T. Thirioux, P. Baillif, J. C. Touray and J. P. Ildefonse, "Surface reactions during  
0] fluorapatite dissolution-recrystallization in acid media (hydrochloric and citric acids)," *Geochimica et Cosmochimica Acta*, vol. 54, pp. 1969-1977, 1990.
- [28 C. Gruian, E. Vanea, S. Simon and V. Simon, "FTIR and XPS studies of protein adsorption  
1] onto functionalized bioactive glass," *Biochimica et Biophysica Acta (BBA) - Proteins and Proteomics*, vol. 1824, no. 7, pp. 873-881, 2012.
- [28 A. Lebugle, M. Subirade and J. Gueguen, "Structural characteristics of globular protein  
2] investigated by X-ray photoelectron spectroscopy: comparison between a legumin film and a powdered legumin," *Biochimica et Biophysica Acta*, vol. 1248, pp. 107-114, 1995.
- [28 O. Svensson and T. Arnebrant, "Mucin layers and multilayers - Physicochemical  
3] properties and applications," *Current Opinion in Colloid & Interface Science*, vol. 15, no. 6, pp. 395-405, 2010.
- [28 B. Fu, J. Yuan, W. Qian, Q. Shen, X. Sun and M. Hannig, "Evidence of chemisorption of  
4] maleic acid to enamel and hydroxyapatite," *European Journal of Oral Sciences*, vol. 112, pp. 362-367, 2004.
- [28 Y. Yoshida and S. Inoue, "Chemical analyses in dental adhesive technology," *Japanese  
5] Dental Science Review*, vol. 48, pp. 141-152, 2012.
- [28 R. Z. Legeros, T. Sakae, C. Bautista, M. Retino and J. P. Legeros, "Magnesium and  
6] Carbonate in Enamel and Synthetic Appatites," *Advances in Dental Research*, vol. 10, no. 2, pp. 225-231, 1996.
- [28 C. Wang, Y. Zhang, J. Wei and S. Wei, "Effects of different pH Conditions on enamel  
7] erosion repair by nano fluorapatite paste," *Journal of Nanoscience and Nanotechnology*, vol. 12, pp. 1-8, 2012.
- [28 R. K. Brundavanum, G. E. J. Poinern and D. Fawcett, "Modelling the crystal structure of  
8] a 30 nm sized particle based hydroxyapatite powder synthesised under the influence of ultrasonic irritation from X-ray powder diffraction data," *American Journal of Materials Science*, vol. 3, no. 4, pp. 84-90, 2013.
- [28 N. Sabel, A. Karlsson and L. Sjolín, "XRMA analysis and X-ray diffraction analysis of  
9] dental enamel from human permanent teeth exposed to hydrogen peroxide of varying pH," *Journal of Clinical and Experimental Dentistry*, vol. 11, no. 6, pp. e512-e520, 2019.

- [29 J. Reyes-Gasga, E. L. Martinez-Pineiro and E. F. Bres, "Crystallographic structure of  
0] human tooth enamel by electron microscopy and x-ray diffraction: hexagonal or  
monoclinic?," *Journal of Microscopy*, vol. 248, p. 102.109, 2012.
- [29 M. Behroozibakhsh, H. Hajizamani, K. Shekofteh, M. Otadi, M. Ghavami-Lahiji and N. S.  
1] F. Nazari, "Comparative assessment of the crystalline structures of powder and bulk  
human dental enamel by X-ray diffraction analysis," *Journal of Oral Biosciences*, vol. 61,  
no. 3, pp. 173-178, 2019.
- [29 T. Ito, M. Saito, T. Uchino and M. Senna, "Preparation of injectable auto-forming  
2] alginate gel containing simvastatin with amorphous calcium phosphate as a controlled  
release medium and their therapeutic effect in osteoporosis model rat," *Journal of  
Materials Science: Materials in Medicine*, vol. 23, pp. 1291-1297, 2012.
- [29 G. E. Fougere, J. R. Weertman, R. W. Siegel and S. Kim, "Grain-size dependent  
3] hardening and softening of nanocrystalline Cu and Pd," *Scripta Metallurgica et  
Materialia*, vol. 26, pp. 1879-1883, 1992.
- [29 A. H. Chokshi, A. Rosen, J. Karch and H. Gleiter, "On the validity of the Hall-Petch  
4] relationship in nanocrystalline materials," *Scripta Metallurgica*, vol. 23, pp. 1679-1684,  
1989.
- [29 H. Eimar, E. Ghadimi, B. Marelli, H. Vali, S. N. Nazhat, W. M. Amin, J. Torres, O. Ciobanu,  
5] R. F. Albuquerque Jnr and F. Tamimi, "Regulation of enamel hardness by its  
crystallographic dimensions," *Acta Biomaterialia*, vol. 8, pp. 3400-3410, 2012.
- [29 C. Xu, R. Reed, J. P. Gorski, Y. Wang and M. P. Walker, "The Distribution of Carbonate  
6] in Enamel and its Correlation with Structure and Mechanical Properties," *Journal of  
Materials Science*, vol. 47, no. 23, pp. 8035-8043, 2012.
- [29 G. A. Mccubbin, S. Praporski, S. Piantavigna, D. Knappe, R. Hoffman, J. H. Bowie, F.  
7] Separovic and L. L. Martin, "QCM-D fingerprinting of membrane-active peptides,"  
*European Biophysics Journal*, vol. 40, pp. 437-446, 2011.
- [29 B. Luka, V. Arbter, K. Sander, A. Duerrschnabel and N. Schlueter, "Impact of mucin on  
8] the anti-erosive/anti-abrasive efficacy of chitosan and/or F/Sn in enamel in vitro,"  
*Scientific Reports*, vol. 11, no. 5285, pp. 1-12, 2021.

- [29 R. Sturmer, S. Harder, H. Schluter and W. Hoffman, "Commercial Porcine Gastric Mucin  
9] Preparations, also used as Artificial Saliva, are a Rich Source for the Lectin TFF2: In Vitro  
Binding Studies," *ChemBioChem*, vol. 19, pp. 2598-2608, 2018.
- [30 P. Wojciechowski and J. L. Brash, "The Vroman effect in tube geometry: the influence  
0] of flow on protein adsorption measurements," *Journal of Biomaterials Science, Polymer  
Edition*, vol. 2, no. 3, pp. 203-216, 1991.
- [30 A. Ash, G. R. Burnett, R. Parker, M. J. Ridour, N. M. Rigby and P. J. Wilde, "Structural  
1] characterisation of parotid and whole mouth salivary pellicles adsorbed onto DPI and  
QCMD hydroxyapatite sensors," *Colloids and Surfaces B: Biointerfaces*, vol. 116, pp.  
603-611, 2014.
- [30 F. Xu, E. Lamas, M. Bryant, A. F. Adedeji, E. Andablo-Reyes, M. Castronovo, R. Ettelaie,  
2] T. V. J. Charpentier and A. Sarkar, "A Self-assembled Binary Protein Model Explains High  
Performance Salivary Lubrication from Macro to Nanoscale," *Advanced Materials  
Interfaces*, vol. 7, no. 1901549, pp. 1-17, 2020.
- [30 F. G. Oppenheim, E. Salih, W. L. Siqueira, W. Zhang and E. J. Helmerhorst, "Salivary  
3] Proteome and its Genetic Polymorphisms," *Annals of the New York Academy of  
Sciences*, vol. 1098, pp. 22-50, 2007.
- [30 E. C. Veerman, M. Valentijn-Benz and A. V. N. Amerongen, "Viscosity of human salivary  
4] mucins: effect of pH and ionic strength and role of sialic acid," *Journal de biologie  
buccale*, vol. 17, no. 4, pp. 297-306, 1989.
- [30 F. Höök, M. Rodahl, B. Kasemo and P. Brzezinski, "Structural changes in hemoglobin  
5] during adsorption to solid surfaces: Effects of pH, ionic strength, and ligand binding,"  
*Proceedings of the National Academy of Sciences of the United States of America*, vol.  
95, pp. 12271-12276, 1998.
- [30 J. An, A. Dedinaite, A. Nilsson, J. Holgersson and P. M. Claesson, "Comparison of a  
6] Brush-with-Anchor and a Train-of-Brushes Mucin on Poly(methyl methacrylate)  
Surfaces: Adsorption, Surface Forces, and Friction," *Biomacromolecules*, vol. 15, pp.  
1515-1525, 2014.
- [30 J. L. Lanigan, S. Fatima, T. V. Charperntier, A. Neville, D. Dowson and M. Bryant,  
7] "Lubricious ionic polymer brush functionalised silicone elastomer surfaces,"  
*Biotribology*, vol. 16, pp. 1-9, 2018.

- [30 K. Vinke, H. J. Kaper, A. Vissink and P. K. Sharma, "Dry mouth: saliva substitutes which adsorb and modify existing salivary condition films improve oral lubrication," *Clinical Oral Investigations*, vol. 24, pp. 4019-4030, 2020.
- [30 H. Wan, A. Vissink and P. K. Sharma, "Enhancement in Xerostomia Patient Salivary Lubrication Using a Mucoadhesive," *Journal of Dental Research*, vol. 99, no. 8, pp. 914-921, 2020.
- [31 H.-Y. Ren, M. Mizukami, T. Tanabe, H. Furukawa and K. Kurihara, "Friction of polymer hydrogels studies by resonance shear measurements," *Soft Matter*, vol. 11, pp. 6192-6200, 2015.
- [31 Anton Paar, "User Manual - Nano Tribometer NTR3 - Tribometer Software Version 7".
- [31 W. Kwok, H. A. Nasr-El-Din, R. E. Hayes and D. Sethi, "Static and dynamic adsorption of non-ionic surfactant on Berea sandstone," *Colloids and Surfaces A: Physicochemical and Engineering Aspects*, vol. 78, pp. 193-209, 1993.
- [31 Sigma-Aldrich, "Triton X-100 (T8532) - Product Information Sheet," [Online]. Available: <https://www.sigmaaldrich.com/deepweb/assets/sigmaaldrich/product/documents/160/855/t8532pis.pdf>.
- [31 Sigma-Aldrich, "Mucin from porcine stomach (M2378) - Product Information Sheet," 2019. [Online]. Available: <https://www.sigmaaldrich.com/deepweb/assets/sigmaaldrich/product/documents/722/220/m2378pis.pdf>.
- [31 M. Ciesla, Z. Adamczyk, J. Barbasz and M. Wasilewska, "Mechanisms of Fibrinogen Adsorption at Solid Substrates at Lower pH," *Langmuir*, vol. 29, pp. 7005-7016, 2013.
- [31 R. Frost and S. Svedhem, "Characterization of nanoparticle-lipid membrane interactions using QCM-D," *Methods in Molecular Biology*, vol. 991, pp. 127-137, 2013.
- [31 L. Sandrin, D. Thakar, C. Goyer, P. Labbe, D. Boturyn and L. Coche-Guerente, "Controlled surface density of RGD ligands for cell adhesion: evidence for ligand specificity by using QCM-D," *Journal of Materials Chemistry B*, vol. 3, no. 27, pp. 5577-5587, 2015.



- [31 A. D. Easley, T. Ma, C. I. Eneh, J. Yun, R. M. Thakur and J. L. Lutkenhaus, "A practical  
8] guide to quartz crystal microbalance with dissipation monitoring of thin polymer films,"  
*Journal of Polymer Science*, pp. 1-18, 2021.
- [31 J. Chen, M. Garcia, L. Penn and J. Xi, "Use of the Quartz Crystal Microbalance with  
9] Dissipation Monitoring for Pharmacological Evaluation of Cell Signalling Pathways  
Mediated by Epidermal Growth Factor Receptors," *Methods in Pharmacology and  
Toxicology*, vol. 53, pp. 253-268, 2015.
- [32 Quartz PRO, "QCM 5 MHz 14 mm Ti/Au (compatible with Q-SENSE™ jig)," Quartz  
0] PRO, 2021. [Online]. Available: <https://www.quartzpro.com/product.html/qcm-varor-16>.
- [32 A. Sethuraman and G. Belfort, "Protein Structural Perturbation and Aggregation on  
1] Homogenous Surfaces," *Journal of Biophysics*, vol. 88, no. 2, pp. 1322-1333, 2005.
- [32 L. Macakova, G. E. Yakubov, M. A. Plunkett and J. R. Stokes, "Influence of ionic strength  
2] on the tribological properties of pre-adsorbed salivary films," *Tribology International*,  
vol. 44, pp. 856-962, 2011.
- [32 N. M. Harvey, G. E. Yakubov, J. R. Stokes and J. Klein, "Lubrication and load-bearing  
3] properties of human salivary pellicles adsorbed ex vivo on molecularly smooth  
substrata," *Biofouling*, vol. 28, no. 8, pp. 843-856, 2012.
- [32 V. J. Schomig, B. T. Kasdorf, C. Scholz, K. Bidmon, O. Lieleg and S. Berensmeier, "An  
4] optimized purification process for porcine gastric mucin with preservation of its native  
functional properties," *RSC Advances*, vol. 6, no. 50, pp. 44932-44943, 2016.
- [32 J. H. H. Bongaerts, D. Rossetti and J. R. Stokes, "The lubricating properties of Human  
5] Whole Saliva," *Tribology Letters*, vol. 27, pp. 277-287, 2007.
- [32 R. Pramanik, S. M. Osailan, S. J. Challacombe, D. Urquhart and G. B. Proctor, "Protein  
6] and Mucin retention on oral mucosal surfaces in dry mouth patients," *European  
Journal of Oral Sciences*, vol. 118, no. 3, pp. 245-253, 2010.
- [32 N. M. Harvey, G. E. Yakubov, J. R. Stokes and J. Klein, "Normal and Shear forces between  
7] Surfaces Bearing Porcine Gastric Mucin, a High-Molecular-Weight Glycoprotein,"  
*Biomacromolecules*, vol. 12, pp. 1041-1050, 2011.

- [32 Q. Zeng, L. Zheng, J. Zhou, H. Xiao, J. Zheng and Z. Zhou, "Effect of alcohol stimulation  
8] on salivary pellicle formation on human tooth enamel surface and its lubricating  
performance," *Journal of the Mechanical Behaviour of Biomedical Materials*, vol. 75,  
pp. 567-573, 2017.
- [32 A. C. Juriaanse, M. Booij, J. Arends and J. J. Ten Bosch, "The adsorption in vitro of  
9] purified salivary proteins on bovine dental enamel," *Archives of Oral Biology*, vol. 26,  
pp. 91-96, 1981.
- [33 R. Pourzal, E. J. Martin, S. Vajpayee, Y. Liao, M. A. Wimmer and K. R. Shull,  
0] "Investigation of the role of tribofilms in self-mating CoCrMo systems utilizing a quartz  
crystal microtribometer," *Tribology International*, vol. 72, pp. 161-171, 2014.
- [33 S. Habelitz, S. J. Marshall, G. W. Marshall and M. Balooch, "Mechanical properties of  
1] human dental enamel on the nanometre scale," *Archives of Oral Biology*, vol. 46, no. 2,  
pp. 173-183, 2001.